Design, Testing and Simulation of Grip ‘n’ Grab Ratcheting, Tension-only Devices for Seismic Energy Dissipation Systems

Jarrod Cook

A thesis submitted for the degree of

Doctor of Philosophy

in Mechanical Engineering

at the University of Canterbury, Christchurch, New Zealand

2018

Abstract

This thesis details the development of a ratcheting, tension-only mechanism for use with seismic energy dissipation systems, known as the Grip 'n' Grab (GNG). The development is taken from initial design concepts through to construction and testing of two prototype devices, as well as development of a material model algorithm to simulate the hysteretic response of the devices, and a finite element flexible rocking system model to assess the behaviour of a controlled rocking system instrumented with the GNG device. The GNG devices developed use single direction engagement to provide resistance to system displacements while allowing for re-centring and closure of rocking joints. Concerns around buckling and residual compressive forces in the dissipater, which can exist in traditional tension-compression solutions are ameliorated. The ratcheting mechanism reduces the take-up prior to engagement on cycles after previous engagement of the dissipater element has occurred, increasing resistance to displacement and improving energy dissipation capability.

The completed schedule of monotonic compressive and cyclic experiments, with 14 yielding steel dissipaters, has provided insight into operational issues and design considerations. Careful detailed design was used in both prototypes to ensure a low-cost and easy to machine device, to increase likelihood of uptake. The results of the testing of the two prototype devices, and the subsequent numerical analyses, show the potential of the GnG concept to be a favourable option in supplementary damping and bracing systems. Robust, repeatable operation of both prototype mechanisms, with redundancy in engagement, was observed, with negligible compressive forces recorded. The GNG ratcheting, tension-only devices developed provide a unique solution which can be implemented with a range of energy dissipation mechanisms as desired. The ratcheting mechanism itself is generalisable and could be attached to the dissipater element through a range of interfaces, depending on what is required for a given application.

The GNG material model algorithm developed allowed for the device behaviour to be simulated in numerical analysis, providing a basis for the inclusion of a GNG device within a structural design. The finite element controlled rocking system model also developed in this thesis was used to simulate the behaviour of a rocking frame and provide insight into GNG behaviour in a rocking structure and the impact on the overall behaviour of the controlled rocking system. Multiple parameter studies were conducted involving over 18000 individual time-history analyses looking at the response of a range of structures to a ULS seismic event based in the Wellington region. The study of rocking system response and demand in the GNG devices completed in this thesis provides a tentative guide for implementation and required capacity in deployment.

Table of Contents

Abstract i
List of Figures viii
List of Tables xvi
1. Introduction 1
1.1. Summary 1
1.2. Earthquake damage 1
1.3. Design approaches and expectations 2
1.3.1. Expectations 2
1.3.2. Conventional design 3
1.3.3. Low damage design 4
1.4. Base isolation 4
1.5. Energy dissipation mechanisms 6
1.5.1. Metallic dampers 6
1.5.2. Friction dampers 8
1.5.3. Viscoelastic solid dampers 9
1.5.4. Viscous fluid dampers 10
1.5.5. Other developments 11
1.6. Issues with current dissipaters 12
1.7. Tension-only devices 13
1.8. The Grip ‘n’ Grab Device 17
1.8.1. Introduction 17
1.8.2. Possible applications 17
1.8.3. Research scope 18
1.9. Chapter Overview 19
2. First Prototype Design, GNG1 21
2.1. Summary 21
2.2. Hysteresis behaviour 21
2.3. Concept Overview 23
2.4. Design Overview 28
2.4.1. Dissipater Subassembly 28
2.4.2. Pawl subassembly 33
2.4.3. Tension springs 35
2.5. Experimental Test Design 36
2.6. Design analysis 40
2.6.1. Load Paths 40

2.6.2. Pawl Interface 42
2.6.3. Bearing Loads 43
2.7. Conclusions 45
3. Testing of GNG1 Device 47
3.1. Summary 47
3.1. Data Acquisition 47
3.2. Monotonic Testing 48
3.3. Cyclic Testing 51
3.4. Hysteresis 54
3.4.1. GNG-dissipater System 54
3.4.2. Dissipater element 57
3.5. Ratchet Mechanism Behaviour 60
3.6. System Overview 65
3.7. Material model algorithm 66
3.7.1. Menegotto-Pinto material model 66
3.7.2. Comparison to experimental results 68
3.8. Conclusions 71
4. Second Prototype Design, GNG2 75
4.1. Summary 75
4.2. Concept Overview 75
4.3. Design Overview 81
4.3.1. Dissipater Subassembly 81
4.3.2. Collet Subassembly 83
4.3.3. Compression spring 87
4.4. Design analysis 88
4.4.1. Load Paths 88
4.4.2. Collet to collet guide taper surface 90
4.4.3. Rack-collet Interface 91
4.4.4. Thread stripping 93
4.5. Prototype Comparison 94
4.6. Conclusions 95
5. Testing of GNG2 Device 97
5.1. Summary 97
5.2. Monotonic Testing 97
5.3. Cyclic Testing 101
5.4. Hysteresis 104

5.4.1. GNG-dissipater System 104
5.4.2. Dissipater element 109
5.5. Ratchet Mechanism Behaviour 112
5.5.1. Effective pitch 113
5.6. System Overview 116
5.7. Comparison to numerical model 117
5.8. Conclusions 119
6. Controlled Rocking Systems 123
6.1. Summary 123
6.2. First rocking systems 123
6.3. Testing overview 125
6.4. Selected modern applications 127
6.5. Idealised system behaviour 130
6.5.1. Overview 131
6.5.2. Controlled rocking system with post-tensioning and yielding energy devices 132
6.5.3. Effect of ratcheting behaviour 140
6.6. Conclusions 143
7. Rocking Model Development 145
7.1. Summary 145
7.2. Model introduction 145
7.3. Model parameters 147
7.4. Material models 148
7.4.1. Horizontal supports 148
7.4.2. GNG and rocking edge 149
7.4.3. Post-tensioning 150
7.5. Analysis settings 151
7.6. Design spectra 152
7.7. Sample structure 154
7.8. Conclusions 162
8. System Response and Analysis 165
8.1. Summary 165
8.2. Main parameter study 165
8.2.1. Study details 165
8.2.2. Roof deflection, roof drift, base rotation, and uplift 169
8.2.3. Ratcheting 176
8.2.4. Inelastic dissipater demand 181

8.2.5. Demand ratio 183
8.3. Code-based method results and capacity recommendation 190
8.3.1. Peak uplift approximation from code methods 190
8.3.2. Comparison of peak uplift values from simulations and code methods 193
8.3.3. Recommended capacity in the dissipater and rack 197
8.4. Effect of response reduction factor 198
8.4.1. Roof deflection, roof drift, base rotation, and uplift 198
8.4.2. Inelastic dissipater demand and demand ratio 203
8.5. Effect of dissipater strength 206
8.5.1. Study details 206
8.5.2. Roof deflection, roof drift, base rotation, and uplift 207
8.5.3. Ratcheting 210
8.5.4. Inelastic dissipater demand and demand ratio 212
8.5.5. Energy dissipation 214
8.6. System configuration 216
8.6.1. Device placement 216
8.6.2. Connection options 218
8.7. Conclusions 221
9. Conclusions 223
9.1. Summary 223
9.2. Tension-only device design 223
9.3. Device engagement and behaviour 224
9.4. GNG and rocking wall modelling 226
9.5. Dissipater demand 226
9.6. Implementation 228
9.7. Conclusions 229
10. Directions of Future Research 231
10.1. Summary 231
10.2. Design revision 231
10.3. Use of other dissipaters 231
10.4. Large-scale system testing 232
10.5. System sensitivities 232
10.6. Higher mode effects and frame design 232
10.7. Code method approximations 233
10.8. Field deployment 233
References 234

Appendix A Prototype device engineering drawings 1
A1 GNG1 prototype engineering drawings 1
A2 GNG2 prototype engineering drawings 14
Appendix B System stiffness rearrangement 1
Appendix C OpenSEES material model files 1
C1 Header file: GNGMaterial.h 1
C2 Main file: GNGMaterial.cpp 4
Appendix D Sample OpenSEES analysis files 1
D1 Model file: finalData.tcl 1
D2 Parameter study file: run_finalData.tcl 6
Appendix E Additional parameter study results 1
E1 Roof deflection 1
E1.1 Results by pitch 1
E1.2 Results by aspect ratio 2
E2 Roof drift 3
E2.1 Results by pitch 3
E2.2 Results by aspect ratio 4
E3 Base rotation 5
E3.1 Results by pitch 5
E3.2 Results by aspect ratio 6
E4 Uplift 7
E4.1 Results by pitch 7
E4.2 Results by aspect ratio 8
E5 Ratchet count 9
E5.1 Results by pitch 9
E5.2 Results by aspect ratio 10
E6 Rack demand 11
E6.1 Results by pitch 11
E6.2 Results by aspect ratio 12
E7 Dissipater demand 13
E7.1 Results by pitch 13
E7.2 Results by aspect ratio 14
E8 Relative dissipater demand 15
E8.1 Results by aspect ratio 15
E9 Demand ratio 16
E9.1 Results by pitch 16

List of Figures

Figure 1.1 The Pyne Gould Corporation building [CERC 2012]: a) before the February 2011 earthquake, and b) after the event. 2
Figure 1.2 Structure performance criteria as desired for future guidelines [CERC 2012]. 3
Figure 1.3 Response of idealised base isolation systems: a) rollers, and b) bearings. 5
Figure 1.4 Friction pendulum bearings in situ [Calvi 2010]. 6
Figure 1.5 Metallic damper: a) example shear fuse construction [Eatherton and Hajjar 2014], and b) idealised hysteretic behaviour [Symans et al. 2008]. 7
Figure 1.6 Friction damper: a) basic construction [Grigorian et al. 1993], and b) idealised hysteretic behaviour. 8
Figure 1.7 Actions and hysteretic behaviour of the SHJ during cyclic deformations [MacRae et al. 2010]. 9
Figure 1.8 Viscoelastic solid damper: a) basic construction [Xu et al. 2016], and b) hysteretic behaviour [Chang et al. 1993]. 9
Figure 1.9 Viscous fluid damper: a) basic construction [Symans et al. 2008], and b) idealised hysteretic behaviour. 10
Figure 1.10 HF2V damper [Rodgers et al. 2008]: a) photograph of the device, and b) schematic showing typical dimensions (mm). 11
Figure 1.11 Buckled EMD [Gultom and Ma 2015]: a) during the experiment, and b) after removal. . 13
Figure 1.12 Damper-cable bracing mechanism [Phocas and Pocanschi 2003]. 14
Figure 1.13 Seesaw vibration control system [Kang and Tagawa 2013]. 15
Figure 1.14 Wedge spring device [Lei et al. 2014]: a) before deformation, b) under seismic load, and c) after deformation. 15
Figure 1.15 Non-buckling segmented brace [Hao 2015]: a) schematic sketch, and b) prototype with controlled compression resistance. 16
Figure 1.16 Compression-free brace [Thammarak et al. 2017]: a) mechanism, and b) test apparatus. 16
Figure 1.17 Possible GNG locations (shown in red) for two structural applications: a) energy dissipation in a controlled rocking system, and b) for stability and re-alignment in an out-of-plumb moment resisting frame structure. 18
Figure 2.1 GNG-dissipater system hysteresis model under cyclic displacement input A-C-E-H, shown in insert. 22
Figure 2.2 Types of ratchet gearing [Oberg et al. 2000] 24
Figure 2.3 Friction device concept 25
Figure 2.4 Step device concept 25
Figure 2.5 Linear ratchet concept with two pawls, showing motion of parts with black arrows and centreline of tension spring in red 26
Figure 2.6 GNG1 prototype assembly with front view on left and section view on right 27
Figure 2.7 The first GNG prototype: a) exploded view, and b) approximate load paths during tensile engagement of the dissipater element (tension ←→ and compression→←). 28
Figure 2.8 Yielding dissipater subassembly 29
Figure 2.9 Early GNG concept using a sharper pawl design with a leaf spring variation 30
Figure 2.10 Rack part showing tooth profile 31
Figure 2.11 Racks with two different pitch sizes shown interacting with the same set of pawls: a) larger pitch, and b) smaller pitch, with reduced contact area. 32
Figure 2.12 Main support body of the GNG1 device, showing key features. 33
Figure 2.13 Plan section view of GNG1 prototype assembly showing lower rack supports 34

Figure 2.14 Pawl profile with relief section shown by dotted line 35
Figure 2.15 GNG1 prototype pawl forces: a) tension spring between pawls, and b) uneven restoring forces during horizontal orientation 36
Figure 2.16 Experimental setup showing distribution of space 37
Figure 2.17 Sample cyclic loading profile using 20 mm pitch, with initial reloading position labelled A 38
Figure 2.18 Free travel present when pawls are between tooth edges, as can initially occur on reloading (position A in **Figure 2.17**) 39
Figure 2.19 Approximate load path for tensile forces through the first GnG prototype. 41
Figure 2.20 GNG1 rack-pawl interface with loading areas labelled. 42
Figure 2.21 Isometric cross-section view of bearing areas of first GnG prototype. 44
Figure 2.22 Projected bearing areas of first GnG prototype. 44
Figure 3.1 GNG prototype test apparatus with accelerometer placement shown in insert 48
Figure 3.2 Maximum forces recorded during monotonic compressive testing 50
Figure 3.3 Force displacement results of the monotonic tests with the GNG1 prototype. 51
Figure 3.4 Maximum compressive forces recorded during cyclic testing 53
Figure 3.5 Yield and ultimate tensile forces recorded for the cyclic experiments 54
Figure 3.6 Force-displacement hysteresis loops for cyclic testing of 20 mm pitch rack. 55
Figure 3.7 GNG device at bottom of travel during C2 test with free-travel shown. 56
Figure 3.8 Force displacement hysteresis loops for cyclic testing with 40 mm pitch rack 56
Figure 3.9 Rack resting on closed pawls, representing the starting position for cyclic testing, with the spring removed for visibility 57
Figure 3.10 Dissipater behaviour for cyclic testing with 20 mm pitch rack 58
Figure 3.11 Hysteretic dissipater behaviour for cyclic testing with 40 mm pitch rack 59
Figure 3.12 Hysteretic behaviour comparison of dissipater element and overall GNG-dissipater system 60
Figure 3.13 View of ratcheting mechanism, showing enlarged region used in **Figure 3.14** 61
Figure 3.14 Closure of pawl captured by high speed camera during the M40-100 monotonic test (where each frame is 1 ms apart).The outline of the pawl and rack are highlighted in the first image for clarity, as they are partially obscured by the spring. The section of the device shown here is indicated in **Figure 3.13**. 61
Figure 3.15 Ram speed and misalignment time for the tests captured with high speed camera footage. 63
Figure 3.16 Accelerometer signals taken from C20-15-0.25$_1$ test: a) during unloading cycle, and b) close-up of signals during ratcheting 64
Figure 3.17 Rack and pawls with suggested placement of additional rack constraints 65
Figure 3.18 Overview of all recorded signals during C20-15-0.25$_1$ test, indicating free-travel time. The acceleration unit scale is omitted. 66
Figure 3.19 Menegotto-Pinto material model. 68
Figure 3.20 Comparison of experimental and numerical hysteresis loops for the GNG-dissipater system. 69
Figure 3.21 Comparison of experimental and numerical hysteresis loops for the dissipater element. 70
Figure 3.22 Comparison of experimental and numerically created dissipater elongation behaviour. 70
Figure 3.23 Numerical hysteresis loops for the GNG-dissipater system with 20 mm, 10 mm, 5 mm, and 3 mm pitch sizes. 71
Figure 4.1 Early axisymmetric GNG prototype design with revolved pawls supported by either a pin or ring 76

Figure 4.2 Partial assembly with collet guide, collets and rack 77
Figure 4.3 Second prototype concept with rack and two collets, showing motion of parts..... 77
Figure 4.4 Engaged collet position shown on left and collet position immediately prior to ratcheting on right. 78
Figure 4.5 The second GNG prototype: a) Exploded view, and b) approximate load paths during tensile engagement of the dissipater element (tension ←→ and compression→←). 79
Figure 4.6 Second prototype GNG assembly with front view on left and section view on right. The location of the compression spring is shown in red on the right. 80
Figure 4.7 Dissipater subassembly..... 81
Figure 4.8 Rack-collet tooth interface 82
Figure 4.9 Collet-rack thread like interface: a) example design, and b) selected available screw thread types 83
Figure 4.10 Main support body with central and side slots 84
Figure 4.11 Isometric section view of second generation assembly with spring-bearing washer removed 85
Figure 4.12 Ratchet assembly showing spring-bearing washer and collet reset access 86
Figure 4.13 Collet position with reset collar tightened to provide clearance between rack and collets and allow for simple rack adjustment: a) system cross-section, and b) close up of clearance. 87
Figure 4.14 Approximate load path for tensile forces through second prototype GnG device. 89
Figure 4.15 Collet to collet guide interface. 90
Figure 4.16 Rack and collet interface. 91
Figure 4.17 GNG tooth profile detail. 92
Figure 4.18 External thread form [Fastenal 2005]..... 94
Figure 4.19 The two prototype GNG devices: a) The GNG1 linear prototype, and b) the GNG2 axisymmetric prototype..... 95
Figure 5.1 Second GNG prototype test apparatus..... 98
Figure 5.2 Maximum forces from monotonic compressive testing with second prototype 100
Figure 5.3 Force displacement results of the monotonic tests with the GNG2 prototype. 100
Figure 5.4 Yield and ultimate tensile forces for dissipaters used with second prototype 103
Figure 5.5 Force-displacement hysteresis loops for cyclic testing of second prototype with 10 mm tooth pitch, showing tests C10-10-0.50$_1$, C10-10-1.00$_1$, and C10-10-1.50$_1$ with no fracture of dissipater element. Input displacements are shown inset. 105
Figure 5.6 Force-displacement hysteresis loops for cyclic testing of second prototype with 10 mm tooth pitch, showing tests C10-10-0.50$_2$, C10-10-1.00$_2$, and C10-10-1.50$_2$ with fracture of dissipater element. Input displacements are shown inset. 106
Figure 5.7 Comparison of free-travel reduction and increased energy dissipation with the use of the finer pitch rack in the GNG2 prototype. Displacement inputs are shown inset. 107
Figure 5.8 Force-displacement hysteresis loop for cyclic testing of GNG2 prototype with 3 mm pitch rack for test C03-05-0.50 with 5 mm input displacement amplitude..... 109
Figure 5.9 Force-displacement hysteresis behaviour for dissipater elements in cyclic testing of second prototype with 10 mm pitch, showing tests C10-10-0.50$_1$, C10-10-1.00$_1$, and C10-10-1.50$_1$ with 5 input displacement cycles and no fracture of dissipater element. 110
Figure 5.10 Force-displacement hysteresis behaviour for dissipater elements in cyclic testing of second prototype with 10 mm pitch, showing tests C10-10-0.50$_2$, C10-10-1.00$_2$, and C10-10-1.50$_2$ with 6 input displacement cycles and fracture of dissipater elements 111
Figure 5.11 Dissipater behaviour comparison of the device with 3 mm pitch, when subjected to 5 and 10 mm amplitude input displacement cycles. 112

Figure 5.12 Accelerometer signals taken from C10-10-0.50$_2$ test: a) during unloading cycle, and b) close up of signals during ratcheting showing simultaneous collet response. 113
Figure 5.13 Ram force and displacement during monotonic compressive test M10-025$_2$ indicating initial pitch discrepancy. 114
Figure 5.14 Effective pitch concept, showing initial collet position on left and collet position after 10 mm, or one tooth pitch, of rack travel on right. Note that additional rack movement is required for ratcheting to occur. 115
Figure 5.15 Effective pitch concept, showing initial collet position on left and collet position required for ratcheting on right. Note that the required rack movement is greater than the pitch. 115
Figure 5.16 Overview of all recorded signals during C10-10-0.50$_2$ test, with acceleration shown in g 116
Figure 5.17 Overview of all recorded signals during C03-10-0.50 test, with acceleration shown in g 117
Figure 5.18 Comparison of experimental and numerical hysteresis loops for the GNG-dissipater system with the GNG2 prototype. 118
Figure 5.19 Comparison of experimental and numerical hysteresis loops for the dissipater element with the GNG2 prototype. 119
Figure 5.20 Comparison of experimental and numerically created dissipater elongation behaviour. 119
Figure 6.1 Model used by Muto et al. [1960]. 124
Figure 6.2 RC bridge pier designed to step [Beck and Skinner 1974]: a) typical A-frame pier, and b) energy absorber arrangement 124
Figure 6.3 Early large scale testing: a) 3-storey single bay frame [Clough and Huckelbridge 1977], and b) 5 storey PRESSS building [Priestley et al. 1999]. 125
Figure 6.4 Column splice connections [Wada et al. 2001]: a) conventional joint, and b) proposed new joint. 126
Figure 6.5 Controlled rocking system [Eatherton et al. 2014]: a) schematic, and b) test apparatus. 127
Figure 6.6 The controlled rocking system at the Orinda City Hall, with looped post-tensioning cables highlighted. A specimen of the bolted moment joint is shown at right [Mar 2010]. 128
Figure 6.7 Ringfeder friction spring behaviour [Tait et al. 2013]: a) prior to uplift, b) at ULS deflection, c) at MCE deflections, and d) CBF column-base connection. 129
Figure 6.8 The controlled rocking system at Forte Health [Wiebe 2013]: a) coupled steel braced frames, and (b) paired energy dissipation devices at the base. 130
Figure 6.9 Floor to frame slotted connection [Latham et al. 2013]: a) tongue plate, b) slot in frame, and c) frame-superstructure schematic by author. 130
Figure 6.10 Loading response of uplifting rocking frame systems: a) elastic rocking frame only, b) frame and post-tensioning, and c) frame, post-tensioning and energy devices. 132
Figure 6.11 Mechanics of the controlled rocking system with post-tensioning and yielding energy devices: a) definition of flexible rocking system, b) lateral deflection prior to uplift, c) lateral deflection after uplift, d) lateral deflection after uplift and device yield, and e) hysteresis behaviour. 134
Figure 6.12 Base rocking moment allocation and resulting flag shapes: a) 25% from energy devices, b) 33% from energy devices, c) 50% from energy devices, and d) 66% from energy devices. 136
Figure 6.13 Comparison of rocking system hysteresis loops for tension-only and tension-compression energy dissipation systems. 140

Figure 6.14 Force-displacement responses with ratcheting behaviour: a) frame and post-tensioning system, b) Grip 'n' Grab device system, c) combined controlled rocking system, and d) uplift profile. 142
Figure 7.1 Flexible rocking model implemented in OpenSEES. 146
Figure 7.2 Constitutive material models defining frame-ground interaction from a sample study. Clockwise from right: RHS shear restraint, RHS ground contact and GNG device, post-tensioning, LHS ground contact and GNG device, LHS shear restraint. 148
Figure 7.3 Force-displacement relationships for the horizontal supports at the rocking edges, from a sample study: a) LHS (node 5) and b) RHS (node 6)..... 149
Figure 7.4 The parallel ENT and GNG material models used to represent the vertical response at the rocking edges, from a sample study: a) The full hysteresis, and b) a close up of the positive displacement behaviour, controlled by the GNG. The ground motion input used to produce these results, record la01: Imperial Valley, is shown inset. 150
Figure 7.5 The elastic post-tensioning model with initial strain, from a sample study..... 151
Figure 7.6 The elastic site hazard spectrum for a Wellington based structure, produced from NZS1170.5. 153
Figure 7.7 A sample of the ground motion records scaled for a structure period of 0.7 seconds..... 154
Figure 7.8 The scaled ground motion acceleration record input to the fixed base nodes (period = 0.7 s, record la01: Imperial Valley). 156
Figure 7.9 Frame top (Node 10) drift (pitch = 5 mm, period = 0.7 s, aspect ratio = 4, R = 4, ζ = 3%, record la01: Imperial Valley)..... 157
Figure 7.10 Base rocking uplift on left (Node 3) and right (Node 4) sides of the frame (pitch = 5 mm, period = 0.7 s, aspect ratio = 4, R = 4, ζ = 3%, record la01: Imperial Valley). 157
Figure 7.11 Comparison of the ground motion record, roof drift and uplift for the first 50 seconds of the response (pitch = 5 mm, period = 0.7 s, aspect ratio = 4, R = 4, ζ = 3%, record la01: Imperial Valley). 158
Figure 7.12 A force-displacement plot of the flexible rocking frame (pitch = 5 mm, period = 0.7 s, aspect ratio = 4, R = 4, ζ = 3%, record la01: Imperial Valley). 159
Figure 7.13 Cumulative plastic strain in the dissipater elements (pitch = 5 mm, period = 0.7 s, aspect ratio = 4, R = 4, ζ = 3%, record la01: Imperial Valley)..... 160
Figure 7.14 Static cyclic hysteresis response (pitch = 5 mm, period = 0.7 s, aspect ratio = 4, R = 4).161
Figure 7.15 Cumulative ratchet count in the GNG devices (pitch = 5 mm, period = 0.7 s, aspect ratio = 4, R = 4, ζ = 3%, record la01: Imperial Valley). 161
Figure 7.16 A force-displacement plot of the flexible rocking frame without supplementary energy dissipation devices: (pitch = 5 mm, period = 0.7 s, aspect ratio = 4, R = 4, ζ = 3%, record la01: Imperial Valley). 162
Figure 8.1 Combinations of aspect ratio and period selected for simulation. 167
Figure 8.2 Schematics for the four aspect ratios used in the parameter study, with leaning columns omitted for clarity. 168
Figure 8.3 Geometric mean of peak roof deflections (pitch = 5 mm, R = 4, ζ = 3%). 170
Figure 8.4 Structure stiffness and elastic site hazard spectrum for the period range considered. ... 171
Figure 8.5 Relative changes in structure stiffness and elastic site hazard spectrum with period..... 171
Figure 8.6 Geometric mean peak roof deflections, showing the effect of pitch size (aspect ratio = 4, R = 4, ζ = 3%). 172
Figure 8.7 Geometric mean peak roof drifts, showing the contribution to roof drift from base rotation (R = 4, ζ = 3%): a) effect of aspect ratio (pitch = 5 mm), and b) effect of pitch size (aspect ratio = 4)..... 173

Figure 8.8 Geometric mean base rotation angles (R = 4, ζ = 3%): a) effect of aspect ratio (pitch = 5 mm), and b) effect of pitch size (aspect ratio = 4). 174
Figure 8.9 Geometric mean peak uplift, for left and right sides (pitch = 5 mm, R = 4, ζ = 3%). 175
Figure 8.10 Geometric mean peak uplift (aspect ratio = 4, R = 4, ζ = 3%). 176
Figure 8.11 Geometric mean ratchet count, for left and right side devices (pitch = 5 mm, R = 4, ζ = 3%). 176
Figure 8.12 Geometric mean ratchet count, for all devices (both sides) (aspect ratio = 4, R = 4, ζ = 3%). 177
Figure 8.13 Geometric mean GNG rack demand, for left and right side devices (pitch = 5 mm, R = 4, ζ = 3%). 178
Figure 8.14 Pitch size effect on GNG rack demand and free-travel. 179
Figure 8.15 System hysteresis comparison (aspect ratio = 4, period = 0.6 s, R = 4, ζ = 3%, record la02): a) pitch size = 1 mm, and b) pitch size = 5 mm. 179
Figure 8.16 Schematic showing roof displacement occurring during free-travel of the GNG. 180
Figure 8.17 Geometric mean GNG rack demand, for all devices (both sides) (aspect ratio = 4, R = 4, ζ = 3%). 181
Figure 8.18 Geometric mean inelastic dissipater demand, for left and right side devices (pitch = 5 mm, R = 4, ζ = 3%). 182
Figure 8.19 Geometric mean inelastic dissipater demand, for all devices (both sides) (aspect ratio = 4, R = 4, ζ = 3%). 182
Figure 8.20 Geometric mean relative dissipater demand, for all devices (both sides) (aspect ratio = 4, R = 4, ζ = 3%). 183
Figure 8.21 Inelastic dissipater demand and peak uplift, for all devices (both sides) (R = 4, ζ = 3%) 184
Figure 8.22 Geometric mean of demand ratio, for all devices (both sides) (R = 4, ζ = 3%): a) aspect ratio = 2, b) aspect ratio = 4, c) aspect ratio = 6, and d) aspect ratio = 8. 185
Figure 8.23 Demand ratio spread (aspect ratio = 4, period = 0.2 s, R = 4, ζ = 3%). 186
Figure 8.24 Cumulative distribution function of the demand ratio data, showing the CDF fit. 188
Figure 8.25 Histogram and probability distribution of the demand ratio data. The y-axis shown applies to the histogram. 188
Figure 8.26 Schematic of ULS peak lateral deflection estimated from code method. 192
Figure 8.27 SCNZ 110:2015 peak uplift values and OpenSEES simulation geometric mean peak uplift values (pitch = 1 mm, R = 4, ζ = 3%). 194
Figure 8.28 Ratio of OpenSEES simulation geometric mean peak uplift values to SCNZ peak uplift values (pitch = 1 mm, R = 4, ζ = 3%). 194
Figure 8.29 Ratio of OpenSEES simulation geometric mean peak uplift values to SCNZ peak uplift values (pitch = 20 mm, R = 4, ζ = 3%). 195
Figure 8.30 Spread of ratio of OpenSEES simulation geometric mean peak uplift values to SCNZ peak uplift values (pitch = 1 mm, R = 4, ζ = 3%). 197
Figure 8.31 Geometric mean peak roof deflections (pitch = 5 mm, ζ = 3%). 199
Figure 8.32 Geometric mean peak roof drifts (pitch = 5 mm, ζ = 3%). 200
Figure 8.33 Geometric mean contribution to peak roof drift from base rotation (pitch = 5 mm, ζ = 3%). 201
Figure 8.34 Geometric mean peak base rotation angles (pitch = 5 mm, ζ = 3%). 201
Figure 8.35 Geometric mean peak uplift, using both left and right sides (pitch = 5 mm, ζ = 3%). 202
Figure 8.36 Ratio of OpenSEES simulation geometric mean peak uplift values to SCNZ peak uplift values (pitch = 1 mm, ζ = 3%). 203
Figure 8.37 Geometric mean inelastic dissipater demand, for all devices (both sides) (pitch = 5 mm, ζ = 3%). 203

Figure 8.38 Geometric mean of demand ratio, for all devices (both sides) (pitch = 5 mm, ζ = 3%).. 204
Figure 8.39 Geometric mean of demand ratio, normalised to SCNZ uplift values (pitch = 5 mm, ζ = 3%). 205
Figure 8.40 Inelastic dissipater demand vs peak uplift for all time-history analyses (ζ = 3%): a) R = 2, b) R = 4, c) R = 6, and d) all results. 206
Figure 8.41 Geometric mean peak roof deflections (aspect ratio = 4, period = 0.7 s, pitch = 5 mm, R = 4, ζ = 3%). 208
Figure 8.42 Geometric mean peak roof drifts, showing the contribution to roof drift from base rotation and the total roof drift (aspect ratio = 4, period = 0.7 s, pitch = 5 mm, R = 4, ζ = 3%). 208
Figure 8.43 Geometric mean peak base rotation angles (aspect ratio = 4, period = 0.7 s, pitch = 5 mm, R = 4, ζ = 3%). 209
Figure 8.44 Peak base rotation angle spread (aspect ratio = 4, period = 0.7 s, pitch = 5 mm, R = 4, ζ = 3%). 210
Figure 8.45 Geometric mean peak uplifts, for left and right sides (aspect ratio = 4, period = 0.7 s, pitch = 5 mm, R = 4, ζ = 3%). 210
Figure 8.46 Geometric mean ratchet count, for all devices (both sides) (aspect ratio = 4, period = 0.7 s, pitch = 5 mm, R = 4, ζ = 3%). 211
Figure 8.47 Geometric mean GNG rack demand, for all devices (both sides) (aspect ratio = 4, period = 0.7 s, pitch = 5 mm, R = 4, ζ = 3%). 212
Figure 8.48 Geometric mean inelastic dissipater demand, for all devices (both sides) (aspect ratio = 4, period = 0.7 s, pitch = 5 mm, R = 4, ζ = 3%) 213
Figure 8.49 Geometric mean demand ratio, for all devices (both sides) (aspect ratio = 4, period = 0.7 s, pitch = 5 mm, R = 4, ζ = 3%). 213
Figure 8.50 Demand ratio spread (aspect ratio = 4, period = 0.7 s, pitch = 5 mm, R = 4, ζ = 3%). 214
Figure 8.51 Geometric mean energy dissipation, for all devices (both sides) (aspect ratio = 4, period = 0.7 s, pitch = 5 mm, R = 4, ζ = 3%). 215
Figure 8.52 Geometric mean equivalent viscous damping: (aspect ratio = 4, period = 0.7 s, pitch = 5 mm, R = 4, ζ = 3%). 216
Figure 8.53 Example controlled rocking system configurations: a) devices at outer edges and PT at centre, b) devices and PT at outer edges, c) device at centre and PT at outer edges, and d) device and PT at centre. 217
Figure 8.54 GNG-dissipater connection detail with pawl or collet subassembly connected to the frame: a) initial position, and b) following inelastic demand in the dissipater. Device location shown in insert. 219
Figure 8.55 GNG-dissipater connection detail with pawl or collet subassembly connected to the ground: a) initial position, and b) following inelastic demand in the dissipater. Device location shown in insert. 220
Figure E.1 Geometric mean peak roof deflections (R = 4, ζ = 3%): a) pitch = 1 mm, b) pitch = 2 mm, c) pitch = 5 mm, d) pitch = 10 mm, and e) pitch = 20 mm. 1
Figure E.2 Geometric mean peak roof deflections (R = 4, ζ = 3%): a) aspect ratio = 2, b) aspect ratio = 4, c) aspect ratio = 6, and d) aspect ratio = 8. 2
Figure E.3 Geometric mean peak roof drifts, showing the contribution to roof drift from base rotation (R = 4, ζ = 3%): a) pitch = 1 mm, b) pitch = 2 mm, c) pitch = 5 mm, d) pitch = 10 mm, and e) pitch = 20 mm. 3
Figure E.4 Geometric mean peak roof drifts, showing the contribution to roof drift from base rotation (R = 4, ζ = 3%): a) aspect ratio = 2, b) aspect ratio = 4, c) aspect ratio = 6, and d) aspect ratio = 8. 4

Figure E.5 Geometric mean base rotation angles (R = 4, ζ = 3%): a) pitch = 1 mm, b) pitch = 2 mm, c) pitch = 5 mm, d) pitch = 10 mm, and e) pitch = 20 mm. 5
Figure E.6 Geometric mean base rotation angles (R = 4, ζ = 3%): a) aspect ratio = 2, b) aspect ratio = 4, c) aspect ratio = 6, and d) aspect ratio = 8. 6
Figure E.7 Geometric mean peak uplift (R = 4, ζ = 3%): a) pitch = 1 mm, b) pitch = 2 mm, c) pitch = 5 mm, d) pitch = 10 mm, and e) pitch = 20 mm 7
Figure E.8 Geometric mean peak uplift (R = 4, ζ = 3%): a) aspect ratio = 2, b) aspect ratio = 4, c) aspect ratio = 6, and d) aspect ratio = 8 8
Figure E.9 Geometric mean ratchet count(R = 4, ζ = 3%): a) pitch = 1 mm, b) pitch = 2 mm, c) pitch = 5 mm, d) pitch = 10 mm, and e) pitch = 20 mm. 9
Figure E.10 Geometric mean ratchet count (R = 4, ζ = 3%): a) aspect ratio = 2, b) aspect ratio = 4, c) aspect ratio = 6, and d) aspect ratio = 8 10
Figure E.11 Geometric mean GNG rack demand (R = 4, ζ = 3%): a) pitch = 1 mm, b) pitch = 2 mm, c) pitch = 5 mm, d) pitch = 10 mm, and e) pitch = 20 mm. 11
Figure E.12 Geometric mean GNG rack demand (R = 4, ζ = 3%): a) aspect ratio = 2, b) aspect ratio = 4, c) aspect ratio = 6, and d) aspect ratio = 8. 12
Figure E.13 Geometric mean inelastic dissipater demand (R = 4, ζ = 3%): a) pitch = 1 mm, b) pitch = 2 mm, c) pitch = 5 mm, d) pitch = 10 mm, and e) pitch = 20 mm 13
Figure E.14 Geometric mean inelastic dissipater demand (R = 4, ζ = 3%): a) aspect ratio = 2, b) aspect ratio = 4, c) aspect ratio = 6, and d) aspect ratio = 8. 14
Figure E.15 Geometric mean relative dissipater demand (R = 4, ζ = 3%): a) aspect ratio = 2, b) aspect ratio = 4, c) aspect ratio = 6, and d) aspect ratio = 8. 15
Figure E.16 Geometric mean of demand ratio (R = 4, ζ = 3%): a) aspect ratio = 2, b) aspect ratio = 4, c) aspect ratio = 6, and d) aspect ratio = 8. 16

List of Tables

Table 2.1 Selected properties of the prototype design 40
Table 3.1 Summary of monotonic compressive testing of the first GNG prototype 49
Table 3.2 Input test parameters for cyclic testing of the GNG1 prototype 52
Table 3.3 Summary of results for cyclic testing of the GNG1 prototype 52
Table 3.4 Summary of ratcheting mechanism behaviour 62
Table 4.1 Compression spring properties 88
Table 4.2 Comparison of the two GNG prototypes 95
Table 5.1 Monotonic testing results for second GNG device 99
Table 5.2 Input test parameters for cycling testing of the GNG2 prototype 101
Table 5.3 Cycling testing results for the GNG2 prototype 102
Table 5.4 Energy dissipation per cycle in kN.mm 108
Table 6.1 Guide to parameters presented in **Figure 6.11**. 133
Table 6.2 Summary of system stiffness during different stages of rocking behaviour. 137
Table 6.3 Calculation of the required post-tensioning and initial device stiffness values for a desired stiffness ratio in the rocking system. 138
Table 7.1 OpenSEES analysis command settings 152
Table 7.2 Site conditions used to create the elastic site hazard spectrum. 152
Table 7.3 Values of the parameterised variables selected for the sample model 155
Table 8.1 Properties of the simulated structures. 167
Table 8.2 Percentage contributions of base rotation to total roof drift. 173
Table 8.3 Effect of pitch size on peak uplift. 175
Table 8.4 Summary statistics of the demand ratio analysis. 187
Table 8.5 Log-normal distributions and confidence intervals. 187
Table 8.6 Cases captured by 3 standard deviation distributions of the demand ratio data. 189
Table 8.7 Pitch size influence on demand ratio. 189
Table 8.8 Parameters in the approximation of the code method to find peak base uplift. 191
Table 8.9 Variation of ratio of geometric mean simulated peak uplift values to SCNZ peak uplift values. 195
Table 8.10 Spread of peak uplift ratios. 197
Table 8.11 Geometric mean peak roof deflections at min. and max. periods (pitch = 5 mm, ζ = 3%). 199
Table 8.12 Max. and min. geometric mean peak roof drifts (pitch = 5 mm, ζ = 3%). 200
Table 8.13 Range of geometric mean peak base rotations and peak uplifts (pitch = 5 mm, ζ = 3%). 202
Table 8.14 Range of geometric mean demand ratios (pitch = 5 mm, ζ = 3%). 204
Table 8.15 Range of geometric mean demand ratios, normalised to SCNZ uplift values (pitch = 5 mm, ζ = 3%). 205
Table 8.16 Properties of the simulated structure for the dissipater strength study 207
Table 8.17 Changes in GNG rack demand with increasing device contribution to uplift moment. 212

1. Introduction

1.1. Summary

This chapter outlines the background, need and scope of the research presented in this thesis. The issues of the disruption that earthquakes cause to the built environment and its inhabitants are briefly outlined, followed by conventional and new, low-damage design approaches to mitigate these issues. More detail on energy dissipation mechanisms is then provided, with a focus on tension-only developments. The issues with these energy dissipation systems are discussed, and the Grip 'n' Grab concept, that is the basis for this research, is introduced and the scope of the research is defined. An outline of the thesis chapters and layout is provided at the end of the chapter.

1.2. Earthquake damage

Large earthquakes, such as the Canterbury earthquakes of 2010 and 2011, and more recent events in Japan, Chile and Kaikoura, among many others, have caused significant disturbance to communities.The cost of the Christchurch rebuild following the earthquakes of 2010 and 2011 has been estimated to be as high as $40 billion NZD [English 2013]. Despite the massive cost involved with rebuilding the second largest city in New Zealand, the majority of structures remained stable enough to avoid collapse and allow the safe exit of occupants. This level of performance was in line with the expectations of current civil engineering design philosophy.

There were a few tragic exceptions, involving the collapse of some large structures, such as the Pyne Gould Corporation building shown in **Figure 1.1**, and the loss of 185 lives. This collapse occurred during the main 22 February 2011 event, which had spectral acceleration about twice the level explicitly considered in design, at some periods. Hence, for the size of this event ~5 months after a major event in September 2010, the vast majority of structures performed well.

Canterbury, New Zealand, is not the only region of the world experiencing issues with earthquake resilience. Despite advances in earthquake engineering, a 2008 report from the United States Geological Survey (USGS), which endeavoured to find accurate projections of the physical, social and economic effects of a magnitude 7.8 earthquake in southern California, shows the extent of damage that could occur from a major seismic event. Due to relevant mitigation measures, the financial impact of the simulated earthquake was estimated to be limited to $200 billion USD, and the event was predicted to claim 1800 lives in this highly populated region [USGS 2008]. Even in this region, where research and planning for earthquakes has continued for many years, there is evidently much work that can yet be done to reduce the vulnerability of the community to earthquake damage. Recent updates to the earthquake forecast for California's complex fault system supported previous

predictions that the chance of at least one magnitude 6.7 or larger earthquake occurring in California in the coming 30 years is greater than 99% [USGS 2015].

Figure 1.1 *The Pyne Gould Corporation building [CERC 2012]:*
a) before the February 2011 earthquake, and b) after the event.

The Kobe, Japan earthquake of 1995 killed more than 6000 people and severely damaged over 100,000 buildings, leaving more than 300,000 people homeless. The financial impact of this earthquake was thought to be over $100 billion USD. Despite the massive impact of the earthquake, the recovery of the Kobe area was surprisingly rapid, with manufacturing in the greater Kobe region returning to 98% of pre-earthquake levels within 15 months [Horwich 2000]. It has been commonly thought that the region escaped any true long term financial effect. However, this interpretation has recently been challenged by duPont and Noy [2015], who argue that the true cost of the Kobe earthquake is more than twice the generally accepted figures of US$95-147 billion and that the long-term impact includes a 12% reduction in per capita GDP for the region, from which it has not yet fully recovered. This updated information highlights that historically there is always a significant long term impact on a region following a large scale seismic event.

1.3. Design approaches and expectations

1.3.1. Expectations

The aftermath of these events has outlined and altered the different expectations of structural engineers and the general public in terms of the expected structural response. By design, the engineering community expected that a severe seismic event would leave many structures in a damaged state but avoid loss of life [SEAOC 1995, Pampanin 2012]. Based on this criteria, most structures performed well. However, the expectation of much of the general public that buildings would remain operable following the earthquakes was not met and is not a part of typical design expectations.

There is thus a strong motivation in the earthquake engineering community to develop means to meet these high expectations and to prevent prohibitively expensive damage occurring to structures during large earthquakes, while still maintaining the same high level of life safety. This desired adjustment in performance criteria was outlined in the Low Damage Building Technologies report to the Canterbury Earthquakes Royal Commission (CERC) [CERC 2012]. **Figure 1.2** illustrates criteria for future guidelines, where it is desired for all structures to remain operational and reparable following any earthquake event.

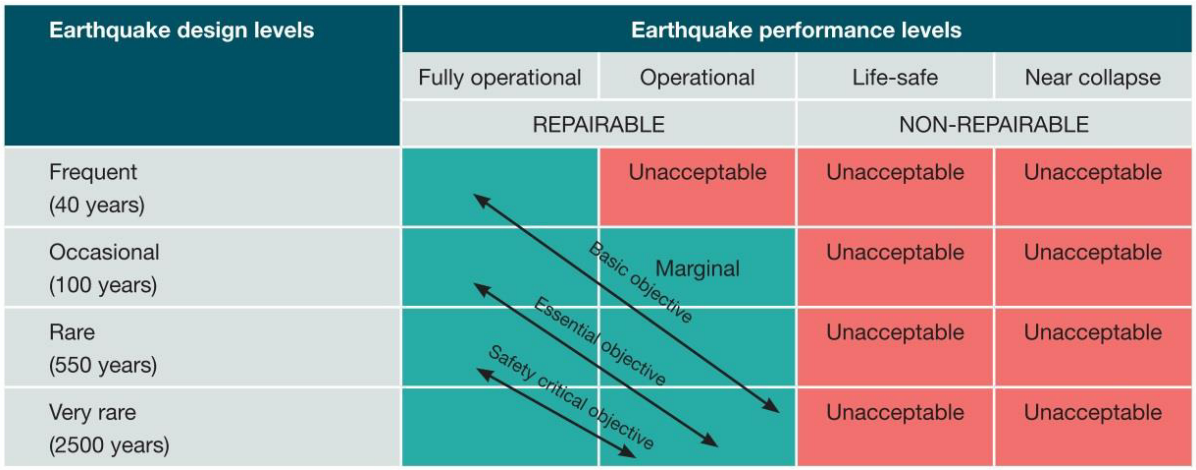

Figure 1.2 *Structure performance criteria as desired for future guidelines [CERC 2012].*

1.3.2. Conventional design

Preventing damage to structures during an earthquake requires dealing with the large amounts of energy released during a seismic event. Most structures have low inherent damping within their elastic response range, and are unable to absorb or dissipate the large forces induced by earthquakes without suffering damage through hysteretic damping or plastic deformation. Conventional design thinking has focused on capacity design. Capacity design provides a hierarchy of strength in the system, leading to the 'strong-column, weak-beam' design approach. The end of the beam, where it connects to the column, is designed to yield and form a plastic hinge before it transfers damaging forces to the column. Explicitly, the beam is designed with a lower moment capacity than the column. Beam damage may lead to floor slab damage or unlevelled floors, and a reduction in the stiffness of the overall structure. By design, these hysteretic damping mechanisms in the beams are employed prior to column damage, which risks collapse of the overall structure.

As experienced during the Canterbury earthquakes, exploiting inelasticity in conventional structures to dissipate energy can help provide life safety, but results in extensive structural damage. This damage leads to delays in reoccupation of the structures and can require significant, sometimes uneconomical, restoration to achieve acceptable levels of safety and functionality. These delays lead

to both immediate and long term economic and social impacts, as seen already in Canterbury. Hence, the energy of the earthquake can be absorbed by the main structure itself, but at an extremely high cost in damage, as well as longer term social and economic impacts.

1.3.3. Low damage design

CERC produced some interesting documents summarising the state of available structural and earthquake engineering technologies. Low damage structural technology is a large field covering much of the work that is being completed as engineers work towards improving building performance levels following seismic events. Buchanan et al. [2011] summarised and grouped low damage technology into two key strategies.

The first approach is to increase the strength and stiffness of a structure, so that it can remain in the elastic response region to the greatest extent possible. By remaining fully elastic a structure can avoid any permanent damage and residual stresses or displacements. However, adding the required materials to achieve such an increase in strength and stiffness can lead to excessive increases in building costs when compared to a basic structure, particularly for multi-storey buildings. This approach might be categorised as better materials and design, and generally requires the strength and stiffness of the structure to be considered interdependently.

The other method is to implement specific energy dissipation mechanisms to absorb the energy of the earthquake and reduce damage to the main structure. Low damage design approaches are commonly divided into two categories of how this outcome can be achieved. One way is via base isolation, which can reduce the response of the building by isolating it from the motion of the ground. The other common option is to attach specific damping devices to the structure to resist motion. This strategy allows for a non-linear and ductile response within the damping devices, resisting damage or restricting the location to allow for easy replacement of certain elements after an earthquake. This approach can be categorised as supplemental damping and isolation, and allows for decoupling of the strength and stiffness of the system. Details of some available options are outlined below.

1.4. Base isolation

An effective way to limit the forces induced in a structure during an earthquake is to decouple the motion of the structure from the earthquake ground motion. Using connections or bearings mounted between the ground and the structure, base isolation can prevent the transfer of large forces into the structure. In an ideal case, the building would remain completely still while the ground moved freely beneath it.

In **Figure 1.3** two types of base isolation are shown: frictionless rollers and rubber bearings. The frictionless rollers represent the idea of complete decoupling of structure and ground motions. The ground moves freely underneath the structure, transferring no forces. However, the location of the building following ground motion is not restricted and can have serious consequences. Alternatively rubber bearings allow some transfer of forces into the structure, but the structure remains in the same location, within the range of allowable motion of the bearings. Through careful design, only small forces are induced in the structure, and displacements and forces felt are greatly reduced compared to a fixed base structure.

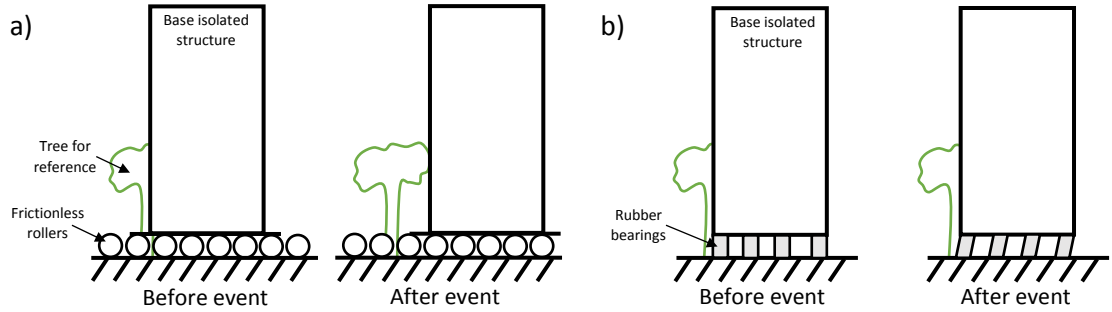

Figure 1.3 *Response of idealised base isolation systems: a) rollers, and b) bearings.*

In practice, the two common approaches to base isolation involve either friction pendulum bearings or elastomeric bearings. Friction pendulum bearings take the concept of the rollers and place them on a concave bed to limit their range of motion and use kinematical stability to provide some re-centring capability. Motion of the rollers away from the centre of the concave bed induces gravitational potential effects which move the rollers back toward the original location. Elastomeric bearings are usually implemented via laminated rubber bearings or lead rubber bearings. Both designs provide horizontal flexibility to convert strong horizontal ground shaking into gentle movement of the bearings and the structure, while continuing to support vertical gravity loads.

Calvi [2010] details the use of modern friction pendulum devices installed in buildings housing 4500 apartments constructed in Italy. Eleven buildings were dynamically tested on site with outstanding performance. 400 devices were tested in a laboratory and thousands of non-linear analyses were completed. Part of this construction in shown in **Figure 1.4**.

Figure 1.4 *Friction pendulum bearings in situ [Calvi 2010].*

Ryan and Dao [2016] observed horizontal-vertical coupling in a full-scale shake table experiment of a 5-story moment frame building isolated with triple pendulum bearings. Three-dimensional shaking caused a significant increase in horizontal floor accelerations when compared to horizontal only shaking with comparable input motions. A numerical study and modelling of the test structure showed the vertical component of ground acceleration introduced a high-frequency component into the base shear that can excite higher modes of the base-isolated structure. It was concluded that this phenomenon is possible in any multi-storey structure using friction bearings for isolation, and should be evaluated on a case-by-case basis.

1.5. Energy dissipation mechanisms

There is a wide range of mechanisms available to provide supplementary energy dissipation in structures, and research in this area continues to expand. Symans et al. [2008] describes how energy dissipation is commonly provided for structures through the use of four broadly categorised types of damping: hysteretic or metallic dampers, friction dampers, viscoelastic solid dampers and viscous fluid dampers. These devices are generally designed to provide repeatable, robust dissipation, and thus not need repair. A brief overview of these four main mechanisms is provided below, along with two of the many alternative options.

1.5.1. Metallic dampers

Metallic or hysteretic dampers commonly use the plastic deformation of material yielding to dissipate energy in the system. This approach is similar to traditional sacrificial design, but confined to replaceable elements. As such, these devices may need post event replacement. These dampers are typically constructed of metal, usually steel, and can be designed to yield in different loading scenarios such as in tension and compression, bending or torsion. Hysteretic dampers are generally considered

to be load-rate independent. The large body of knowledge available on the response of steel elements under loading makes hysteretic dampers a popular choice. An example construction and idealised hysteresis loop are presented in **Figure 1.5**.

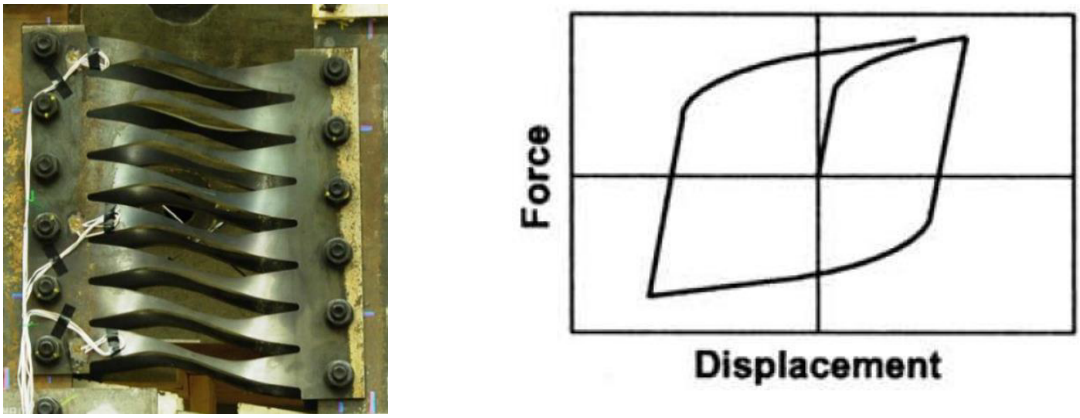

Figure 1.5 *Metallic damper:*

a) example shear fuse construction [Eatherton and Hajjar 2014], and b) idealised hysteretic behaviour [Symans et al. 2008].

Replaceable steel dissipaters have been used in seismic design work for several decades. Some of the early testing of yielding steel dissipaters in different arrangements was undertaken by Kelly and collaborators, and included U-shaped flexural plates (UFP) [Kelly et al. 1972] and yielding steel bars [Kelly and Tsztoo 1977]. Following testing of yielding steel bars at the base of a 3-storey structure with uplifting columns, the researchers remarked: “the device was shown not only to have substantial energy-absorbing capacity over an extended period of time, but also to deteriorate in a gradual, predictable manner independent of loading rate.”

More recently Eatherton et al. [2014] has used replaceable metallic shear fuses to extend the elastic response of a rocking braced frame up to drift ratios of 2.5%. Another interesting development is the use of a piston metallic damper (PMD), with a set of parallel hollow circular plates that interconnect an inner shaft to an outer pipe [Jarrah et al. 2019]. The PMD was shown to dissipate significant seismic input energy with stable hysteretic behaviour.

Metallic dampers are commonly buckling restrained to prevent failure during compressive loading. Buckling restrained braces (BRBs) use an un-bonded steel core encased in a steel tube filled with grout or concrete. The steel core carries axial loads, while the filled outer tube provides lateral support and prevents buckling. Black et al. [2004] completed a comprehensive component testing program on one commercially available BRB product. The system was found to deliver substantial and repeatable energy absorption capability.

1.5.2. Friction dampers

Friction dampers absorb energy via sliding forces between two surfaces, and are rate independent. Steel plates separated by small shims of special friction materials carry high forces when sliding against each other moving in opposite directions. The shims help to provide stable coefficients of friction and predictable behaviour. Usually the steel plates are bolted together with a design clamping force, which defines the friction force when slip will occur. An example construction and idealised hysteresis loop are presented in **Figure 1.6**.

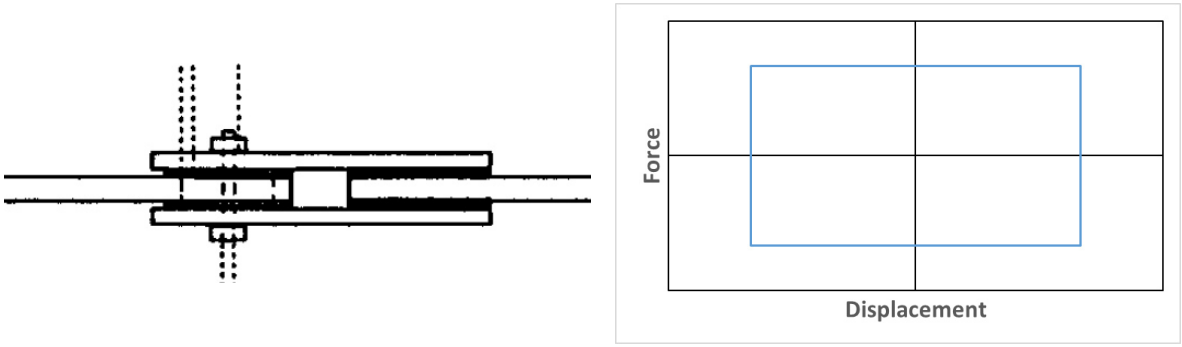

Figure 1.6 *Friction damper:*

a) basic construction [Grigorian et al. 1993], and b) idealised hysteretic behaviour.

In an idealised model, friction dampers act as a perfectly elasto-plastic system, producing a rectangular hysteresis loop shape, and providing large energy dissipation capability in each cycle. The initially near-rigid behaviour of friction dampers at forces below the slip force adds stiffness to the structure prior to slip occurring. Additional restoring forces, from the device or the structural frame, are required to avoid permanent deformation.

Slotted bolted connections (SBCs) are a common application of friction connections used for energy dissipation. Grigorian et al. [1993] was among the first to test specimens of steel plates fitted with brass inserts. More recent applications of friction connections include the sliding hinge joint (SHJ). This design was developed in New Zealand by Clifton [2005] as a low-damage alternative to the traditional beam-column welded connections of moment resisting steel frames. The top flange plate pins the top corner of the beam to the column. During seismic loading, the SHJ remains very stiff until the sliding resistance provided by the bottom flange friction connection is exceeded, the friction connection will then slide, allowing for inelastic rotation in the joint, dissipating energy through friction, while confining yielding to the bolts. The sliding of plates and hysteretic behaviour of the SHJ during cyclic deformations is shown in **Figure 1.7** [MacRae et al. 2010]. Current SHJ developments include work on a low-yielding, self-centring, rocking column base joint with friction dampers [Latour et al. 2019]. This design aims to improve the self-centring performance of SHJs through implementation of pre-loaded threaded bars and disk springs.

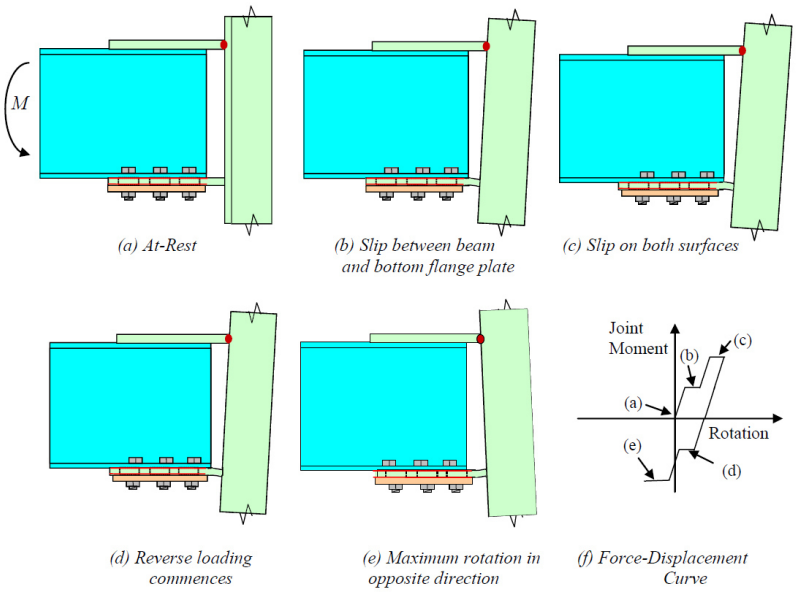

Figure 1.7 *Actions and hysteretic behaviour of the SHJ during cyclic deformations [MacRae et al. 2010].*

1.5.3. Viscoelastic solid dampers

Viscoelastic solid dampers typically use solid elastomeric pads of viscoelastic material bonded to steel plates. Relative motion between the steel plates causes shear deformations and dissipates energy in the structure. Viscoelastic solid dampers are rate-dependent and are commonly incorporated into diagonal bracing. An example construction and idealised hysteresis loop are presented in **Figure 1.8**.

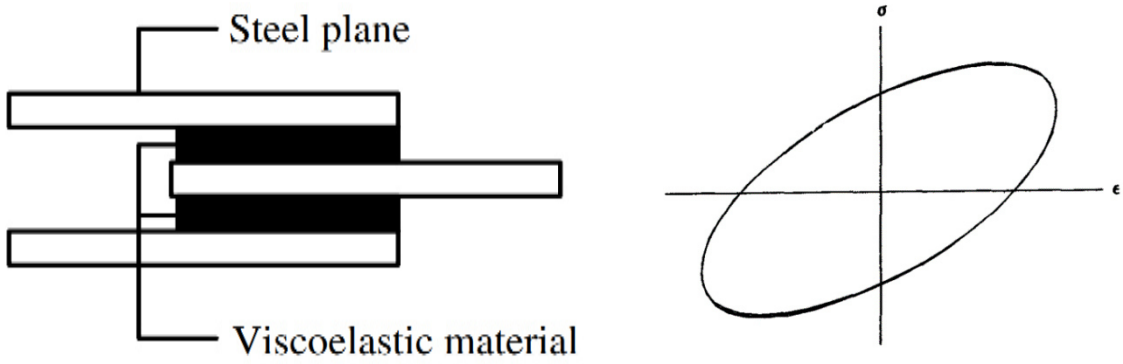

Figure 1.8 *Viscoelastic solid damper:*

a) basic construction [Xu et al. 2016], and b) hysteretic behaviour [Chang et al. 1993].

Extensive experimental work has been completed with viscoelastic dampers in seismic applications with steel frames. Early work by Chang et al. [1993] showed that structural response was significantly reduced in testing with a 2/5 scale 5-story steel frame prototype structure, with the addition of viscoelastic dampers. Shen et al. [1995] retrofitted a 1/3 scale model 3-story structure, previously damaged in shake table tests, with viscoelastic diagonal braces. Inter-story drifts and story shears in the columns were substantially reduced at all floors. Most of the energy dissipation was transferred from the columns to the viscoelastic dampers, and the hysteresis behaviour of the dampers during an

actuator test demonstrated a highly consistent response. Development of viscoelastic dampers as a structural control device continues, with recent work exploring several kinds of viscoelastic materials based on different matrix rubbers [Xu et al. 2016].

1.5.4. Viscous fluid dampers

In viscous fluid dampers, high velocity fluid flow through orifices is used to attenuate shock and dissipate energy. A piston with orifices alters the flow characteristics of the fluid and the response is proportional to the velocity of the piston within the damping fluid, and is therefore rate-dependent. Energy is dissipated by heat in the fluid, and various oils or silicone-based fluids with different performance coefficients are commonly used to fill the damper [Constantinou et al. 1998]. Correctly designed and fabricated viscous dampers suffer very little wear and deterioration over time [Lee and Taylor 2001]. An example construction and idealised hysteresis loop are presented in **Figure 1.9**.

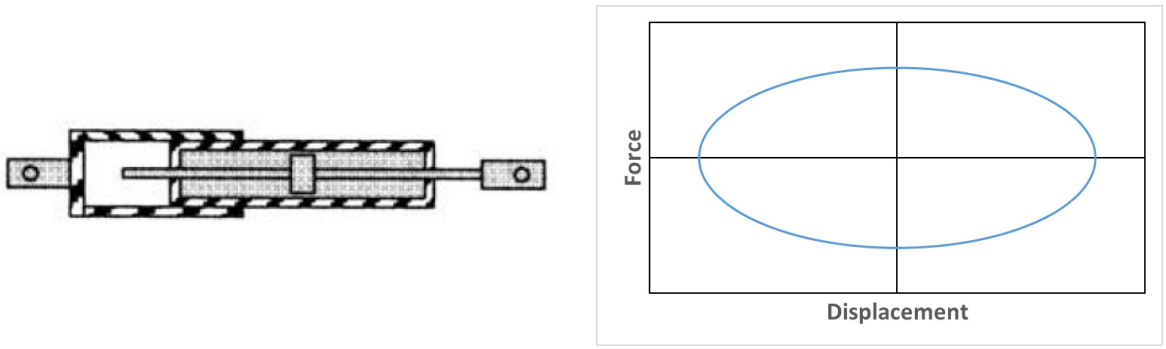

Figure 1.9 *Viscous fluid damper:*
a) basic construction [Symans et al. 2008], and b) idealised hysteretic behaviour.

Above a predetermined cut-off frequency, fluid dampers show strong stiffness in addition to energy dissipation capabilities. Early work of Constantinou and Symans [1992, 1993] demonstrated that the addition of fluid dampers to a 3 story 1:4 scale steel frame model increased damping and stiffened the structure by reducing the period of higher modes. Tremblay et al. [2008] used viscous dampers, mounted vertically between the foundation and column bases of a controlled rocking system, to dissipate energy and control lateral displacement, while also limiting the impact forces induced in the columns. Dynamic cyclic loading tests performed on individual dampers demonstrated load-displacement response approximately followed a simple non-linear relationship.

One variation of non-linear viscous damper is an extrusion damper, utilising the plastic deformation of materials such as lead. These dampers are highly non-linear and represent a combination of viscous and metallic damper response characteristics, bordering on being rate-independent. Robinson and Greenbank [1975, 1976] completed early testing of devices extruding lead back and forth through an orifice. A number of tested devices displayed nearly rectangular hysteretic behaviour and little rate

dependence. The deformed lead recrystallizes immediately, recovering its original mechanical properties between each extrusion. The amount of energy absorbed is then limited by the heat capacity of the device, and not by work hardening or fatigue of the lead. Any force reduction through heating is recovered after the motion stops and the device cools. Further development of lead extrusion damper technology was completed through the 90s, including work by the Institute of Geological and Nuclear Sciences (GNS) [Cousins and Porritt 1993, Zhao et al. 2000].

Recent research has included development of the high force-to-volume (HF2V) lead-extrusion damper, shown in **Figure 1.10**. The design uses a central shaft with a bulge encased in lead. During movement of the shaft, the bulge displaces the lead from one side to the other, and can sustain a constant force upon yielding [Rodgers et al. 2008].

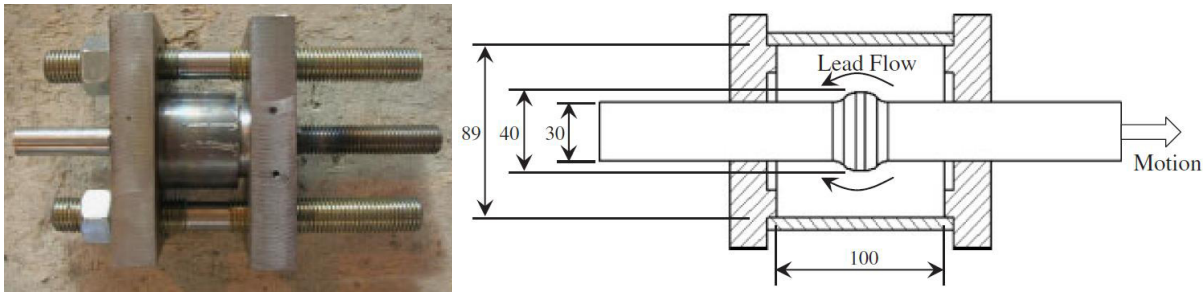

Figure 1.10 *HF2V damper [Rodgers et al. 2008]:*
a) photograph of the device, and b) schematic showing typical dimensions (mm).

1.5.5. Other developments

There are many alternative energy dissipation mechanisms available and in development, with varying degrees of adoption. A couple of interesting developments include phase transformation dampers, tuned masses and tuned liquids. These concepts are briefly mentioned here to highlight the large diversity of options available in energy dissipation, and this is not intended to be a comprehensive overview of alternatives.

Shape memory alloys (SMAs) are a type of smart material that is able to undergo reversible transformation between high-temperature and low-temperature phases. These alloys are named for their ability to 'remember' their original un-deformed shape, and return to this shape when heated following deformation. Another property of SMAs is super-elasticity, which is the ability to recover high amounts of strain triggered by mechanical stress. These reversible strains can exceed 20% in a few special alloys [Ma et al. 2010]. Recent work by Tian et al [2018] proposed a novel shape memory alloy tuned mass damper for the seismic protection of power transmission towers. Several types of SMA materials were modelled and non-linear time history analysis showed that installing the damper reduced seismic responses by up to 60%, compared to a standard structure.

Tuned mass dampers (TMDs) reduce structure motion by using an added spring-mass-damper system to absorb energy imparted to the structure. The added system is tuned to the excitation frequency, and in an ideal case the main structure remains stationary while the added system moves and dissipates energy. TMDs can only be tuned to one frequency, making them most effective when the first mode dominates the response in MDOF structures. The 509 metre tall Taipei 101 building in Taipei, Taiwan uses a 660-tonne steel pendulum TMD suspended from the 92nd to 87th floors to sway and offset wind motion in the structure [Poon et al. 2004].

Tuned liquid dampers (TLDs) use a similar concept to TMDs and absorb energy through viscous fluid actions and wave breaking [Constantinou et al. 1998]. The passage of liquid through an orifice has inherent head loss characteristics, and TLD systems have been used in several applications to reduce wind-induced and seismic vibrations in structures. TLD systems installed in the Tokyo International Airport Tower, consisting of around 1400 shallow cylinders filled with a mixture of water, floating particles and preservatives, have been shown to reduce the acceleration response under wind loading to about 60% of the response without the TLD system [Tamura et al. 1995].

1.6. Issues with current dissipaters

Yielding dissipaters, often using steel, remain a desirable option due to their low cost, simple design, and their performance. This is broadly similar to conventional sacrificial design principles. While the tensile performance of steel dissipaters is often desirable, slender steel members may be susceptible to buckling under low compressive loads. Slender bracing, that yields in tension and buckles in compression, has low energy dissipation because it only dissipates energy during the part of an earthquake displacement cycle where the force is tensile, and the displacement in tension is greater than the yield displacement experienced during previous cycles. Specifically, plastic deformation on prior cycles will increase the unstressed member length and result in a “dead-zone” with take-up on subsequent cycles. During earthquakes with multiple loading cycles this limitation can significantly reduce the energy dissipation capacity, as subsequent cycles will provide delayed engagement. As a result, structures may be in an impaired state for large aftershocks soon after a main earthquake event. Also, if the bracing does yield during compressive loading, this can severely reduce the cyclic deformation capacity.

BRBs are common and restrain buckling of the yielding member during compressive loading. However, residual compressive stresses after a seismic event limit the ability to allow the re-centring of a structure post-earthquake, and also impair their performance in subsequent loading cycles. For example, this can be a problem in rocking systems, where the restoring forces are usually provided by the frame weight and the clamping action of post-tensioning. Residual compressive forces in BRBs and

other dissipaters can act against the restoring forces in the system, reducing the resistance to uplift and altering system performance on subsequent cycles. Residual drifts of up to 0.52% were observed by Eatherton et al. [2014] for lower self-centring ratios.

The increased dissipater length during tensile yielding also induces large compressive loads during cyclic behaviour, and out-of-plane buckling can occur if connection details are not carefully designed. Low cycle fatigue of the brace itself, and the 3-D performance of the braces and their gusset plates, is a topic of current concern given the lack of testing and analysis of these systems under realistic earthquake demands [MacRae and Clifton 2015, Sitler et al. 2017]. Furthermore, small BRB-like externally mounted dissipaters (EMDs) have experienced premature failure due to buckling and concentrated rotation around the ends of the buckling restraint during pseudo-dynamic tests of a rocking column involving multi-directional loading [Gultom and Ma 2015]. The buckled EMD is shown in **Figure 1.11**. Insufficient testing of full size BRBs under multi-directional loading has been completed to fully address these concerns.

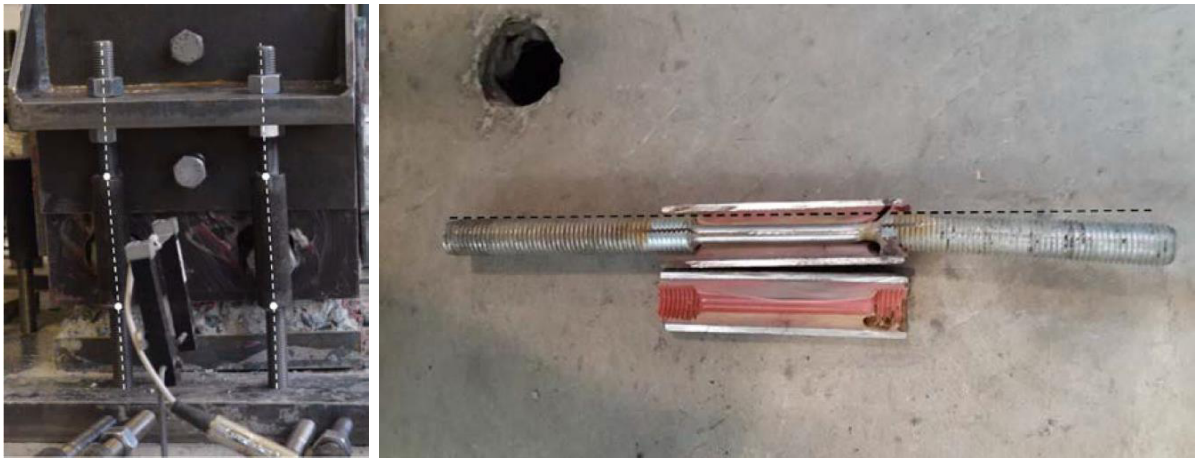

Figure 1.11 *Buckled EMD [Gultom and Ma 2015]:*
a) during the experiment, and b) after removal.

1.7. Tension-only devices

To avoid compression and buckling related issues, several tension-only solutions have been developed. Among these solutions is a cable cross-brace system with hysteretic dampers, which resists only tension [Phocas and Pocanschi 2003, Phocas and Sophocleous 2013]. As shown in **Figure 1.12**, the diagonals of the system are fixed at the bottom of the columns and are free to move at the top corners of the frame via rotation or slipping mechanisms. When the length of one diagonal cross-cable increases, the length of the other diagonal cross-cable decreases by the same amount. As a result, both cross-braces are permanently under tension during cyclic loading. A hysteretic damper

connected between the frame and the horizontal cable member prevents free relative motion, but can yield during strong ground motions to allow relative motion between the bracing and the frame.

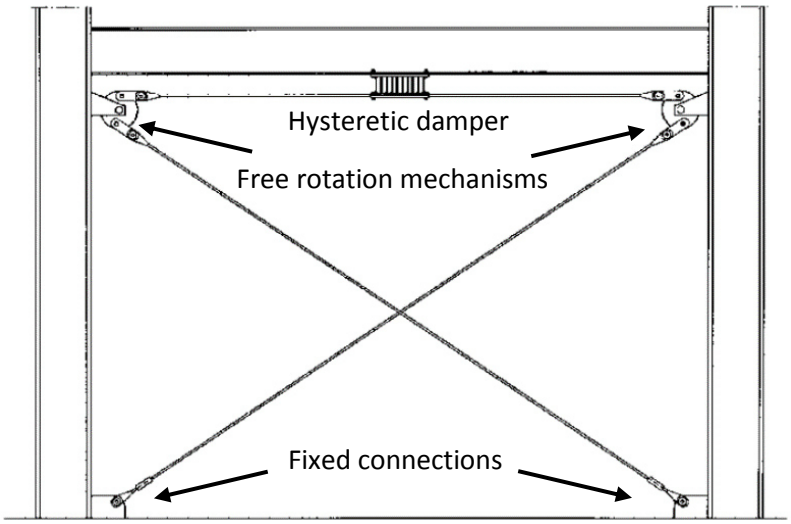

Figure 1.12 *Damper-cable bracing mechanism [Phocas and Pocanschi 2003].*

Tagawa and collaborators [Kang and Tagawa 2013, Tagawa et al. 2016] developed a seesaw vibration control mechanism with viscoelastic dampers, presented in **Figure 1.13**. The proposed system comprises three main parts: a brace, seesaw member and viscoelastic dampers, with only tensile forces appearing in the bracing members. The seesaw member sits on a pinned connection and is attached to the floor via dampers at each side. Tension rods are connected to the top corners of the columns and opposing sides of the seesaw member, crossing slightly. When the frame deforms, the dampers undergo shear deformations and dissipate seismic energy. Reversals in the load direction generate tensile axial forces in an opposite tension rod.

Eatherton et al. [2014] proposed adding self-centring capability to BRB systems. Pre-tensioned SMA rods were used in conjunction with the BRBs to allow the system to return to near zero displacement.

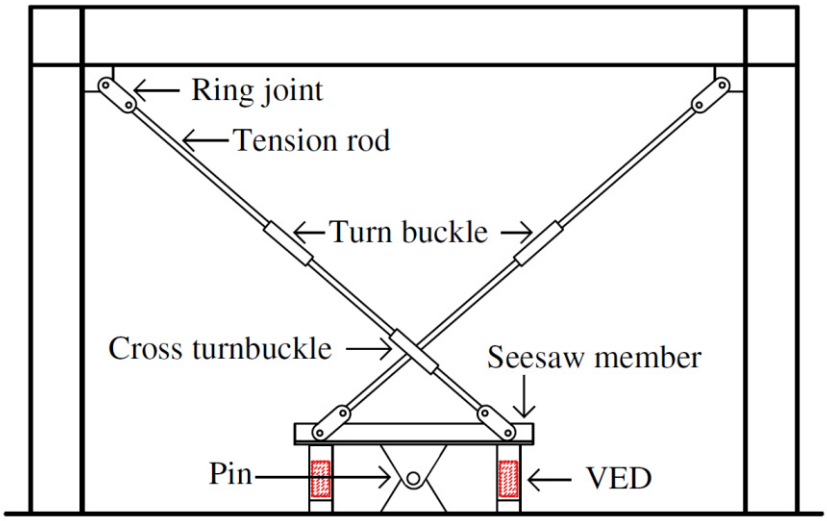

Figure 1.13 *Seesaw vibration control system [Kang and Tagawa 2013].*

Lei et al. [2014] have used wedge spring devices to offset anchor bolt elongation in column connections. **Figure 1.14** shows the operation of this system, where a spring driven wedge block moves into the gap caused by plastic deformation of the anchor bolts and provides continued resistance to uplift.

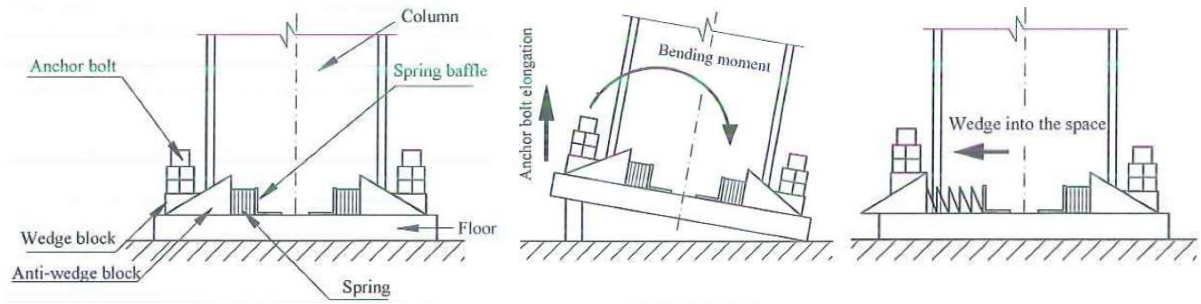

Figure 1.14 *Wedge spring device [Lei et al. 2014]:*
a) before deformation, b) under seismic load, and c) after deformation.

A non-buckling segmented brace system with sliding joints has been proposed by Hao [2015]. Segments of the device are connected by sliding joints which transmit tension forces, but allow the brace to slide under compression. In a single segment assembly, such as that shown in **Figure 1.15**, each segment is welded on one side to a stiff end plate and pinned at the other end. The end plates of adjacent segments are connected together by threaded rods, with nuts on the outer sides of the end plates to prevent tensile movement. The threaded rods carry tensile forces, while the end plates can slide together in compression. A compression spring between the end plates can be added to provide certain compressive force resistance.

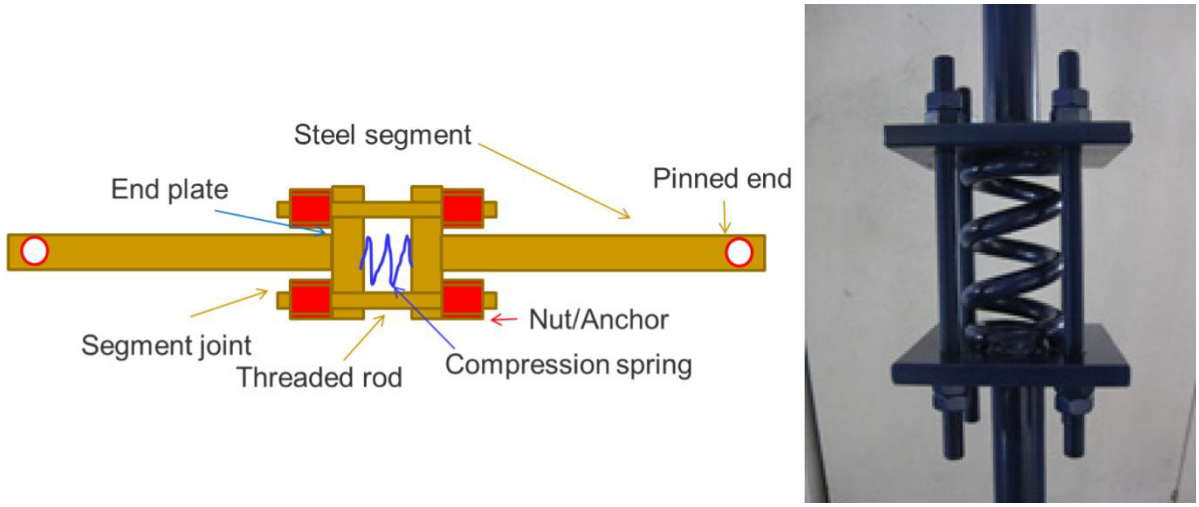

Figure 1.15 *Non-buckling segmented brace [Hao 2015]:*

a) schematic sketch, and b) prototype with controlled compression resistance.

A further project addressing these issues is a Compression-Free Device (CFD) for energy dissipative braces using an arrangement of cams and rollers with a slim steel coupon [Thammarak et al. 2017]. Two rotary cams, pinned to the body of the CFD, are used to grip a mild steel core by friction forces under tension, allowing for tensile yielding of the core, as presented in **Figure 1.16**. The cams have an eccentric pear-shaped profile and disengage readily under compressive loading. The steel core is convenient to replace.

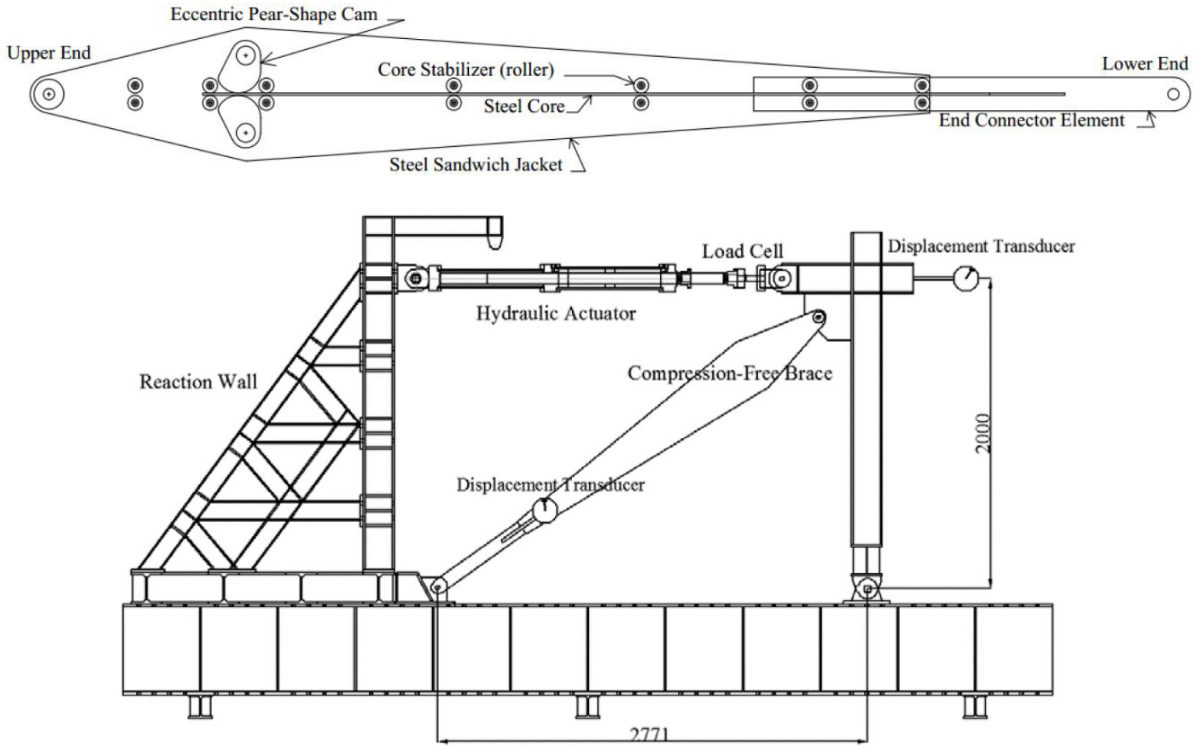

Figure 1.16 *Compression-free brace [Thammarak et al. 2017]:*

a) mechanism, and b) test apparatus.

Despite several promising designs present in the research, there has been little adoption of tension-only systems in the structural design industry. The need for a simple, low-cost, solution remains, with a focus on robustness due to the importance of this mechanism.

1.8. The Grip 'n' Grab Device

1.8.1. Introduction

A solution has been developed to address the practical issues mentioned above through the use of a tension-only device with a ratcheting function. The proposed device, referred to as Grip 'n' Grab (GNG), offers a novel alternative. The idea behind the GNG is to allow the dissipater to yield in tension, absorbing seismic energy, while offering almost no resistance to compressive loading, to allow for re-centring to occur. The single direction engagement eliminates residual compressive forces and removes the need for buckling restraint. A ratcheting mechanism will be used to offset any increase in the length of the dissipater element, reducing take-up as the energy dissipation method engages more rapidly on subsequent cycles, and reducing the effect of impact loading. The ratcheting, tension-only engagement mechanism is designed to be used in conjunction with a dissipater, where the energy dissipation in the GNG-dissipater system can be provided by various mechanisms such as yielding or friction.

When used with a yielding dissipater mechanism, both the design and cost of the replaceable yielding element itself can be greatly simplified, as the use of buckling restraints in current designs is a major contributor to the complexity of the design as well as a significant expense. These expensive, heavy restraints to prevent buckling would not be required with the new tension-only type device. Notably, while there is added complexity in the form of the ratcheting mechanism, it is a one-off cost, as opposed to the yielding dissipater, which may need to be replaced several times over the lifetime of the structure. Hence, a small addition of complexity and cost could be covered by greater savings in time and cost later.

1.8.2. Possible applications

Two possible applications of the GNG device are shown in **Figure 1.17**. The lack of resistance to compressive loading makes this device particularly suitable for use with low damage controlled rocking type structures, discussed in detail in Chapter 6. **Figure 1.17**a shows a potential GNG configuration for use with a rocking frame by using one or more devices on either side of the rocking structure to provide resistance to motion in either direction. The device located at the rocking edge will not be engaged, while the device on the opposite side will undergo tensile engagement during uplift, but will not provide any major residual compression forces upon joint closure. This application is considered in detail in this thesis in Chapters 6, 7, and 8.

Post-earthquake permanent deformations in steel structures are a serious issue and can leave the building out-of-plumb [Rad et al. 2015]. It may be possible to use the GNG device to provide a directional stiffness to assist in re-aligning structures that have a residual displacement after an earthquake. This application would require installation of the devices after the initial earthquake has occurred and induced a residual displacement. The approximate positioning is illustrated in **Figure 1.17**b. This application requires significant additional research to assess the viability of using the device to assist with realigning an out-of-plumb structure. The GNG configuration in **Figure 1.17**b should be carefully designed to disengage once the structure returns to centre, to avoid inducing a large drift in the opposite direction to the original out-of-plumb direction.

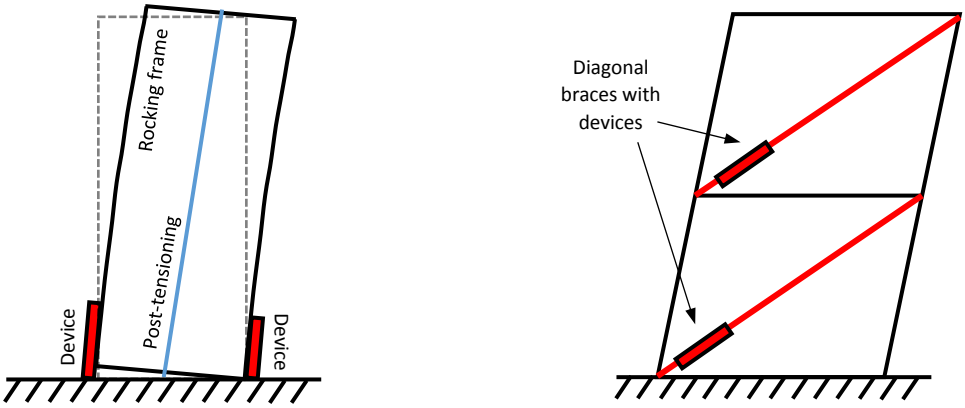

Figure 1.17 *Possible GNG locations (shown in red) for two structural applications: a) energy dissipation in a controlled rocking system, and b) for stability and re-alignment in an out-of-plumb moment resisting frame structure.*

1.8.3. Research scope

The GNG device, conceived by MacRae and inspired by the performance of plastic cable ties, was originally modelled for a rocking system by Gunning and Weston [2013]. However, this was only a computational investigation and no physical prototype or design details were investigated. Several important factors need to be investigated to enable deployment of this technology. Key steps include ensuring the robustness of the mechanism and assessing the engagement timing. Maximum compressive forces, ratcheting pitch, and cumulative inelastic displacement demand imposed on the energy dissipation mechanism, should all be investigated and quantified. This research assesses the ratcheting mechanism acting with a yielding steel energy dissipation system, but the mechanism could equally be applied to friction devices, HF2V dampers, or any other energy dissipation mechanism.

This thesis details the design, construction and testing of two prototype GNG devices, as well as modelling of device performance in a controlled rocking system. This work addresses the need outlined above by developing solutions to the following research questions:

1) Can devices be designed and built to dissipate energy under tensile earthquake loading without carrying compressive loads, and with reduced take-up on subsequent loading cycles to maximise energy dissipation?

2) Can the devices respond with appropriate speed of engagement for use during seismic loading of structures?

3) Can the experimental devices exhibit desirable hysteresis behaviour, similar to theoretical predictions?

4) Can a model be developed to describe the GNG hysteretic performance, together with that of a rocking wall?

5) What is the system response, including the cumulative plastic demand generated in the dissipative element, and how does this vary with key design parameters such as the ratchet pitch size?

6) How should GNG rocking wall systems be designed?

1.9. Chapter Overview

Chapter 1 outlined the background, need and scope of the research presented in this thesis. Conventional and next generation seismic design were discussed with an emphasis on energy dissipation mechanisms and tension-only devices. Current issues were detailed and the Grip 'n' Grab concept, that is the basis for this research, was introduced, and the scope of the research was defined.

Chapter 2 defines the desired behaviour of a ratcheting, tension-only mechanism for use with seismic energy dissipation systems, and details the design process to produce an initial experimental prototype device. Basic design equations are also presented. This chapter addresses research question 1.

Chapter 3 describes the testing of the initial experimental prototype to prove the concept and characterise the response. This initial system is tested with a number of yielding steel dissipaters in a monotonic compression and cyclic testing schedule. A computational algorithm for modelling the hysteretic behaviour of the GNG-dissipater system is created and compared to experimental results. This chapter addresses research questions 2, 3 and 4.

Chapters 4 presents the design of a second, more advanced experimental prototype to develop the capabilities and robustness of the system. Basic design equations are also presented. This chapter further addresses research question 1.

Chapter 5 outlines testing of the advanced prototype with a number of yielding steel dissipaters in a monotonic compression and cyclic testing schedule. A comparison between the responses of the two prototype systems is made. This chapter further addresses research questions 2 and 3.

Chapter 6 presents an overview of controlled rocking systems with details of the mechanics of the system and literature on existing testing and implementation. The model of system behaviour is expanded for use with the GNG devices developed. This chapter addresses research question 4.

Chapter 7 presents the development of a finite element flexible rocking model, incorporating effects of gravity forces, post-tensioning and energy dissipation devices. This chapter further addresses research question 4.

Chapter 8 presents the findings of multiple parameter studies conducted using the finite element model developed in Chapter 7. The influence of a range of device and structure parameters on the system response, and important relationships are investigated. Design guidelines for using the Grip 'n' Grab device in practice, including attachment and required capacity calculations are proposed and discussed. This chapter addresses research questions 5 and 6.

Chapter 9 presents the overall conclusions to the research, and the unique contributions from this research and thesis to the earthquake engineering field.

Chapter 10 discusses possible extensions to the research and issues to be addressed in future work.

2. First Prototype Design, GNG1

2.1. Summary

This chapter defines the desired behaviour of a ratcheting, tension-only mechanism for use with seismic energy dissipation systems to address the concerns outlined in Chapter 1, including buckling and residual compressive forces. The design process to produce an initial experimental prototype device is then detailed. The initial prototype is focussed on creating a functional device using a conservative design approach, and represents the transition of the GNG concept from a novel hysteresis loop in a computational study [Gunning and Weston 2013], into a physical system of mechanical parts producing a desired response to loading input. A basic stress analysis of the first prototype device design is also presented, focussing on the unique design interfaces and high stress areas.

This chapter addresses research question 1: Can devices be designed and built to dissipate energy under tensile earthquake loading without carrying compressive loads, and with reduced take-up on subsequent loading cycles to maximise energy dissipation?

2.2. Hysteresis behaviour

The desired GNG-dissipater system behaviour features single direction engagement, where the device will resist tensile loading, while offering negligible resistance in compression. This approach avoids compressive loading on the components and associated buckling concerns, while allowing for the unimpeded restoring motion of an underlying structure, such as a controlled rocking frame. **Figure 2.1** shows the idealized behaviour for a system where the GNG device is used with a bi-linear dissipater with strain hardening. In **Figure 2.1** the GNG-dissipater system is exposed to cyclic displacement pattern A-C-E-H, as shown in the inset graph.

For tensile loading from the origin at A, the material exhibits a high initial stiffness, followed by a greatly reduced stiffness after the yield point at B. Between B and C the force rises due to strain hardening. When the loading is reversed at C, elastic strain is recovered in a linear fashion, until there is no load present at D. During compressive loading, there is only a very low compressive force produced in the system and the force-displacement curve in **Figure 2.1** passes essentially along the horizontal axis and through the origin at A towards E.

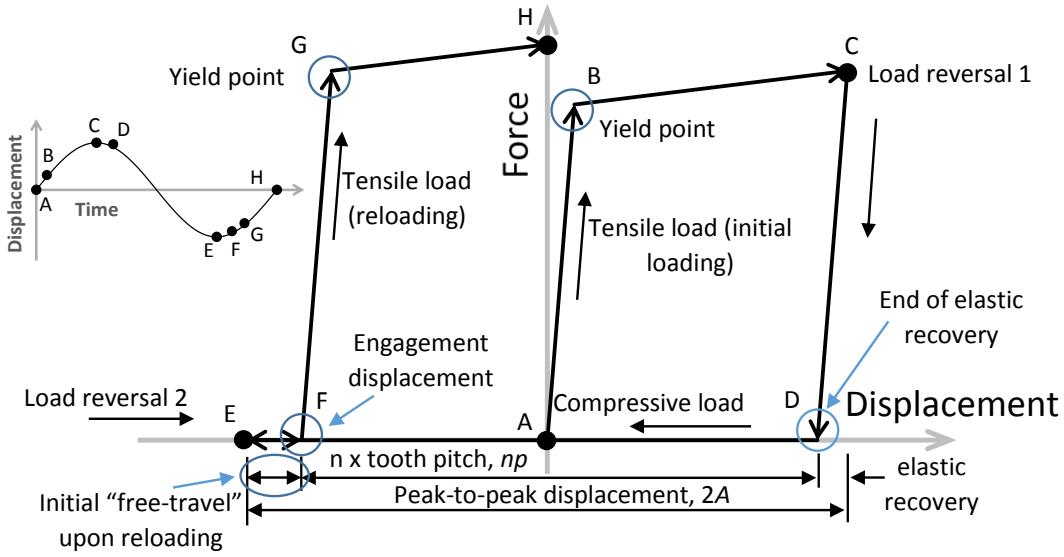

Figure 2.1 *GNG-dissipater system hysteresis model under cyclic displacement input A-C-E-H, shown in insert.*

This horizontal section of the hysteresis plot near the x-axis, between points D and E on **Figure 2.1**, represents the very low strength of the GNG-dissipater system in compression. This compressive displacement must exceed the tooth pitch of the ratcheting mechanism for ratcheting to occur. Multiple ratcheting actions can occur in each cycle, reducing the displacement datum where engagement begins by any integer multiple of the tooth pitch size. Thus, this displacement offset from ratcheting is used to redefine the displacement where tensile elastic strain will resume, represented by point F in **Figure 2.1**. Upon initial change of displacement from the negative to the positive direction, between points E and F, there may initially be no tensile force, indicating some "free-travel". This free-travel is directly related to the tooth pitch (p) and is defined by:

$$x_{\text{free-travel}} = 2A - \delta_{\text{elastic}} - np \qquad (2.1)$$

where $2A$ is the displacement in the negative direction from the previous positive displacement where there was yielding, δ_{elastic} is the elastic recovery displacement of the system during unloading, p is the tooth pitch and n is the largest integer value where $(2A - \delta_{elastic}) > np$. Multiple ratcheting actions can occur when $(2A - \delta_{elastic}) > 2p$, and the total displacement between points D and F represents an integer multiple, n, of the pitch size. These terms are shown in **Figure 2.1**.

When loading in the positive direction from E, once the displacement exceeds the new displacement datum for engagement at point F, tensile elastic strain resumes and a new yield point is reached at G. The yield force value at point G is dependent upon any strain hardening that may be exhibited during the previous loading cycle. In this model, the strength at point G is the same as that at point C, because the inelastically deforming component is behaving essentially in a piecewise monotonic manner due to the absence of compressive yielding loads. It should be noted that the hysteretic response in **Figure**

2.1 includes strain hardening and as such is specific to a yielding steel component as the dissipater element. However, any alternate dissipater element, such as a lead dissipater or friction connection, could be used and would have a broadly similar overall response.

2.3. Concept Overview

To replicate the hysteretic behaviour outlined above, the GNG1 device was designed from scratch, taking much inspiration from other applications of mechanisms that lock in only one direction, such as cable ties and bicycle free-hubs. To achieve the desired single direction engagement and hysteretic behaviour, the principle of a ratchet, generally used in rotational applications, has been applied to the linear motion of the dissipater in tension and compression. In a basic ratchet mechanism, a lever arm known as a pawl rests against a toothed ratchet wheel, where the tooth profile is designed to allow the wheel to rotate in only one direction. The teeth lock against the pawl when the ratchet wheel is rotated in one direction, while rotation in the other direction results in the pawl sliding off the back of the tooth, allowing free rotation. **Figure 2.2** demonstrates several types of ratchet mechanism [Oberg et al. 2000]. **Figure 2.2**b illustrates an ordinary ratchet and pawl mechanism, while other, more complex designs are also presented. This ordinary, very common mechanism represents the most analogous concept to the GNG1 device design.

Several variations of ratcheting mechanisms are available, with some making use of multiple pawls, offset by a fraction of the tooth pitch, to achieve a fine feed without reducing the size of the teeth. Such designs could be applied to the GNG device to reduce take-up between engagements without reducing the size of the ratchet teeth, which would increase contact stresses and complicate the manufacturing process. **Figure 2.2**d gives one example of how this approach could be adopted. There are two pawls attached to the same pivot point, and one pawl is half of the tooth pitch longer than the other. As a result, the pitch is effectively reduced by one-half, while maintaining the same contact area. The GNG design presented in this thesis is focused on an initial proof-of-concept prototype and does not incorporate these options. However, the prototype can be easily modified to incorporate these additional features, if and as necessary for a given application.

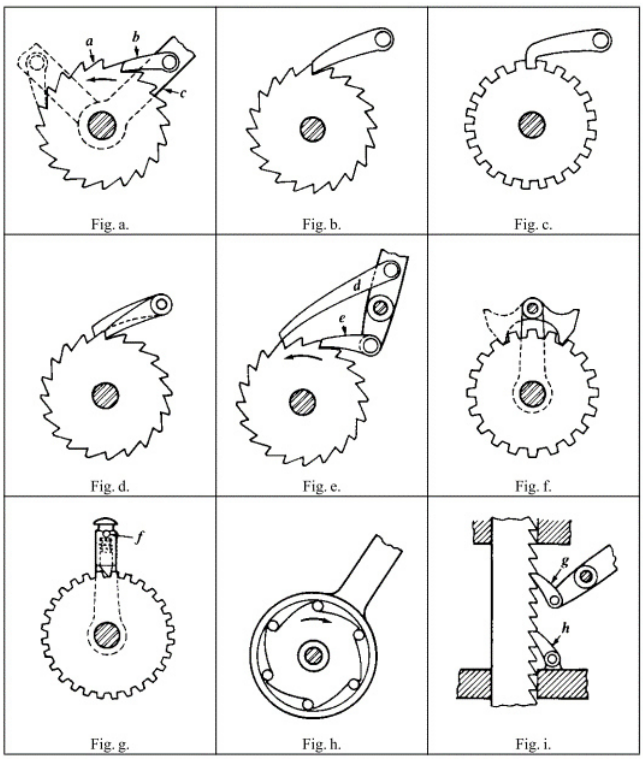

Figure 2.2 *Types of ratchet gearing [Oberg et al. 2000]*

Some initial concepts for the GNG device were systems with few parts, consisting of a yielding component with a built-in rack interface, and a structure interface at either end, one of which included the ratcheting mechanism. These systems were quite impractical due to the complexity of the parts. Of particular concern with this approach was the complexity of the yielding component with the built-in rack interface. The yielding component is the replaceable part of the system and so it is desirable to keep it as simple and easily accessible as possible to reduce post-event repair costs. In addition, complex devices require complex machining and manufacture, which increases cost. Development of the design progressed toward the use of more parts that were simpler, and in particular the isolation and simplification of the replaceable yielding component.

A number of alternative concepts were considered, including designs making use of friction or stepped interfaces to provide the required single direction engagement. Particular attention was given to reliable engagement, low manufacturing cost and robustness of the design concepts. For successful deployment in the field, the device must be low-cost and ensure a high level of confidence in performance due to the importance of its function in a structure. A friction type device, as seen in **Figure 2.3**, offers the ability for an effectively continuous range of resolution, or pitch of engagement, while the stepped concept in **Figure 2.4** represents a more discretised pitch system.

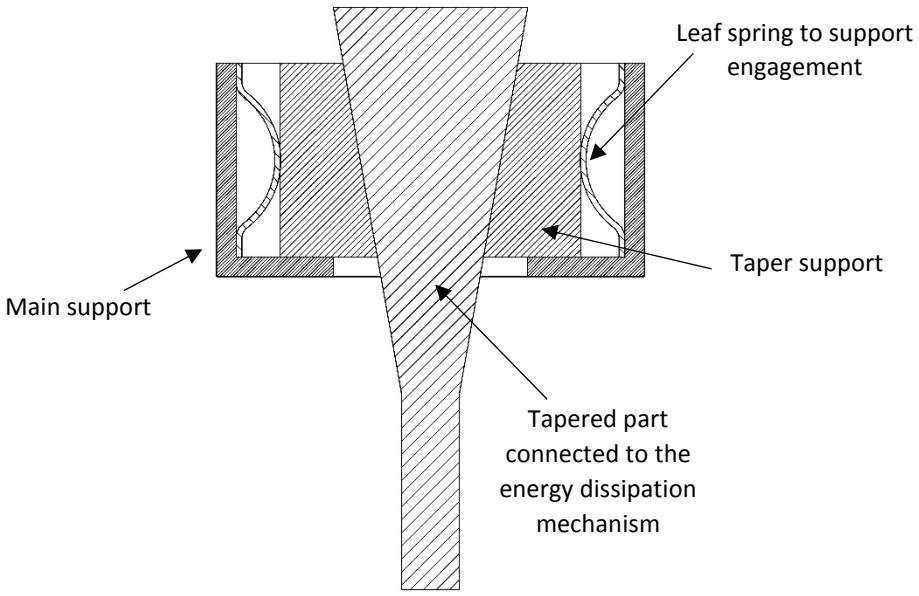

Figure 2.3 *Friction device concept*

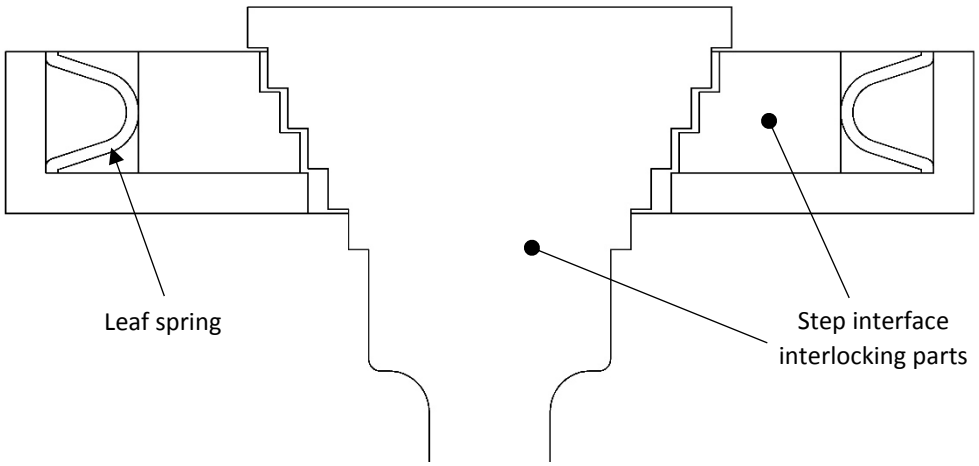

Figure 2.4 *Step device concept*

For the friction concept, engagement of the device acts against the leaf springs and becomes weaker as the position of the tapered yielding element changes. The stepped concept also experiences variance in spring force as operation progresses. The early alternative designs offered variations on the GNG concept and could be developed further. However, a conservative approach was used for the initial proof-of-concept device detailed in this work, and a more reliable engagement mechanism was developed and used for the chosen GNG prototype outlined below.

A symmetric design was selected for the GNG1 device, utilising two pawls and a rack with teeth on both sides, as shown in **Figure 2.5**. The form of the teeth on the rack component allows the rack to slide past the pawls during upward motion of the rack, whilst downward motion will result in the teeth locking on the pawls. This engagement will activate the connected energy dissipation mechanism. This approach is a linear analogy to the ratchet wheel mechanism in **Figure 2.2**. The design minimises

asymmetrical forces on the components and provides two contact areas for the transmission of force through the pawls, reducing bearing stresses.

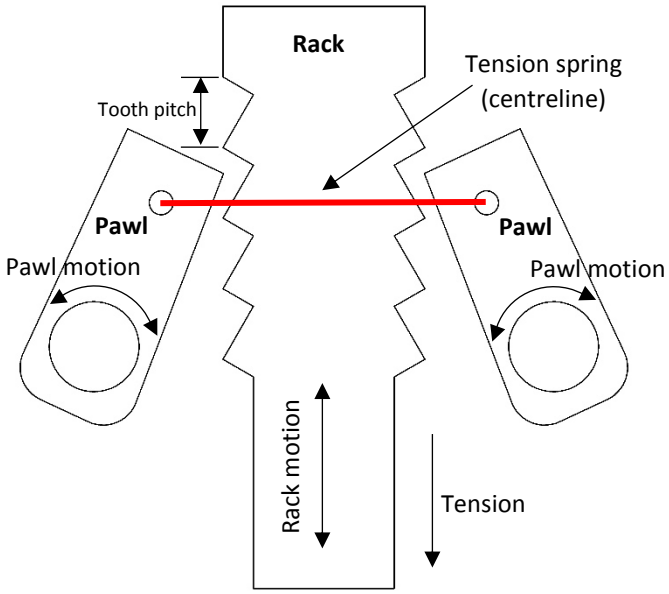

Figure 2.5 *Linear ratchet concept with two pawls, showing motion of parts with black arrows and centreline of tension spring in red*

A tension spring fitted between the pawls is used to aid initial engagement during tensile loading. After initial engagement the clamping force between the pawls and the rack increases as the tension force increases. The interface is self-stabilising and the tension spring facilitates initial engagement only. The centreline position of the spring is indicated on **Figure 2.5**. There is also a spring fitted between the pawls across the opposite face of the rack. The use of two springs maintains symmetry and provides redundancy of the initial engagement mechanism.

The two pawls rotate about pins located within a rectangular main support, as seen in Figure 2.6 and Figure 2.7. The main support makes use of a modified RHS profile for simplicity and cost reduction. The main support body also accommodates lateral supports to limit the motion of the rack to vertical displacements and ensure that the rack moves in-plane, to stay in correct alignment with the location of the pawls. These supports can be seen in the detailed drawings in Figure 2.6.

Figure 2.6 shows a section view of the full design assembly. Sacrificial damage in the GNG-dissipater system is isolated to the dissipater element through a capacity design process. To allow easy replacement of the yielding component, the rack is created as a separate component and attached to the dissipater via a threaded connection.

It should be noted that the mounting arrangements used with the prototype designs are specific to the hydraulic testing apparatus, and do not limit the possible connection types and applications for

the device in service. The initial prototype features a rectangular tongue at either end, designed to allow the device to be held in the hydraulic jaws of the MTS-810 test machine used for the experiments. These proof-of-concept tests were focussed on the ratcheting action and engagement aspects of the device. The exact details of mounting the GNG device into a structure, including the device orientation and end connections, will be dependent on the application, and will likely vary to those presented here.

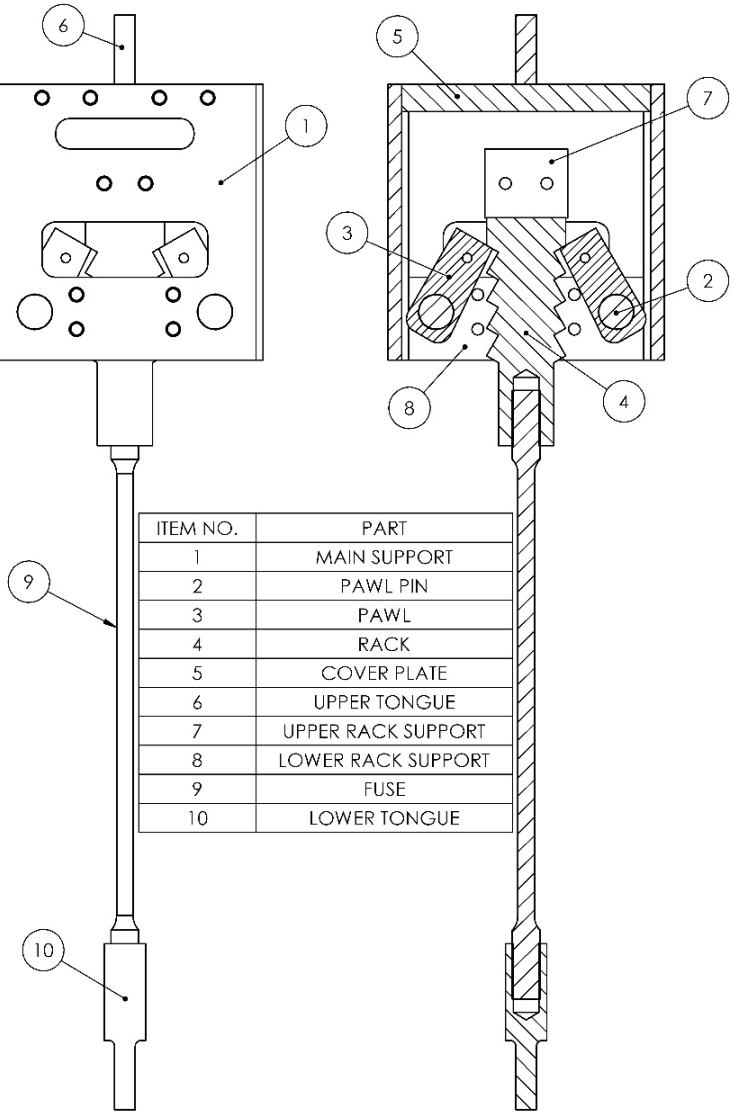

ITEM NO.	PART
1	MAIN SUPPORT
2	PAWL PIN
3	PAWL
4	RACK
5	COVER PLATE
6	UPPER TONGUE
7	UPPER RACK SUPPORT
8	LOWER RACK SUPPORT
9	FUSE
10	LOWER TONGUE

Figure 2.6 *GNG1 prototype assembly with front view on left and section view on right*

Figure 2.7 shows an exploded view of the full assembly and the load paths of tensile loads in the device. Tensile forces in the dissipater are transferred to the rack, which induces compressive forces in the pawls. These forces then transfer into the main support body via bearing contact areas on the pawl pins. Cap screws connect the cover plate with the main support body. The tooth profile on the rack has a 90° internal angle to avoid interference with pawl rotation and to allow for simple machining

processes, eliminating the need for complicated profile milling or other specialist manufacturing processes.

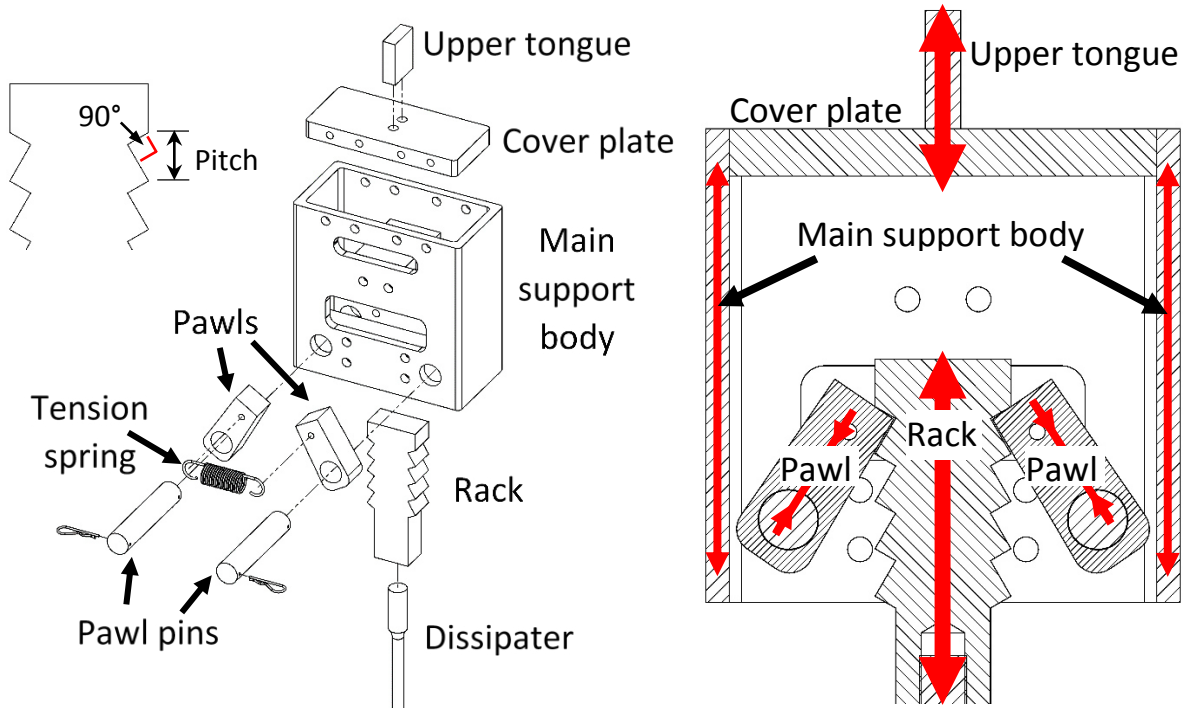

Figure 2.7 *The first GNG prototype:*
a) exploded view, and b) approximate load paths during tensile engagement of the dissipater element (tension ←→ and compression →←).

In the initial prototype AISI 1040 steel was used for several components, including the yielding dissipater element, due to availability. Superior AISI 4140 or equivalent is used for parts subjected to higher stresses and contact forces to ensure the longevity of the non-yielding components. The main support makes use of a modified RHS profile for simplicity and cost reduction. A complete assembly drawing of the prototype device, with the springs omitted for clarity, is provided in Appendix A1, along with full manufacturing drawings for the required parts.

2.4. Design Overview

2.4.1. Dissipater Subassembly

The overall function of the GNG device prototype design can be described by two subassemblies that interact to provide the desired system response. One of these subassemblies is the dissipater subassembly, which consists of three parts: the lower tongue, the dissipater and the rack. This subassembly is shown in **Figure 2.8**. The lower tongue has a flat feature to be held in a hydraulic wedge grip in the MTS-810 test machine. The part then widens to accommodate an M20 fine pitch tapped hole used to secure the dissipater.

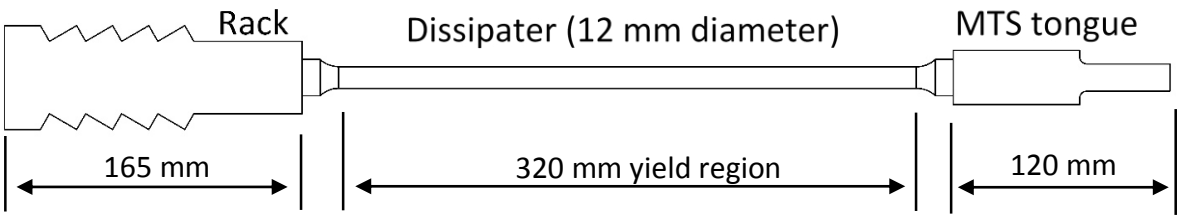

Figure 2.8 *Yielding dissipater subassembly*

The dissipater is circular with a 320 mm long section in the middle turned down to a diameter of 12mm. This section of the dissipater is the yielding region and will provide the plastic displacement capacity to dissipate energy in the system. This diameter was selected to place the yield force and ultimate tensile force of the dissipater within the safe operating capacity of the test machine, with a design UTS of 70 kN that is less than the 90-100 kN machine capacity. With an elongation to fracture of approximately 28%, this dissipater design will provide ~90 mm of plastic displacement capacity upon which to test GNG action.

The dissipaters underwent a full annealing cycle at Heat Treatments Limited (Auckland, New Zealand) to ensure maximum ductility. The dissipater diameter increases at the ends to 20 mm via a large radii fillet to avoid stress concentrations. Each end is threaded with M20 fine pitch thread to secure the dissipater into the lower tongue and rack. The fine pitch was selected to ensure a strong thread with plastic deformation only occurring in the reduced-diameter section of the dissipater to enable easy disassembly and replacement. A larger pitch thread would reduce the root diameter of the thread, possibly requiring a reduced diameter of the yielding section if thread failure was to be avoided.

One end of the rack is rectangular and accommodates an M20 fine pitch tapped hole, for securing the dissipater. The remainder of the rack contains the teeth to interact with the pawls. These teeth create the engagement between the two subassemblies to provide the GNG behaviour when the dissipater yields.

The rack-pawl interface evolved during the design period of the project. Initial designs included sharp variants of the pawls, creating a ‘puzzle piece’ effect, with the rack and pawls locking together in a secure manner. An example of an early concept with this type of design is shown in **Figure 2.9**.

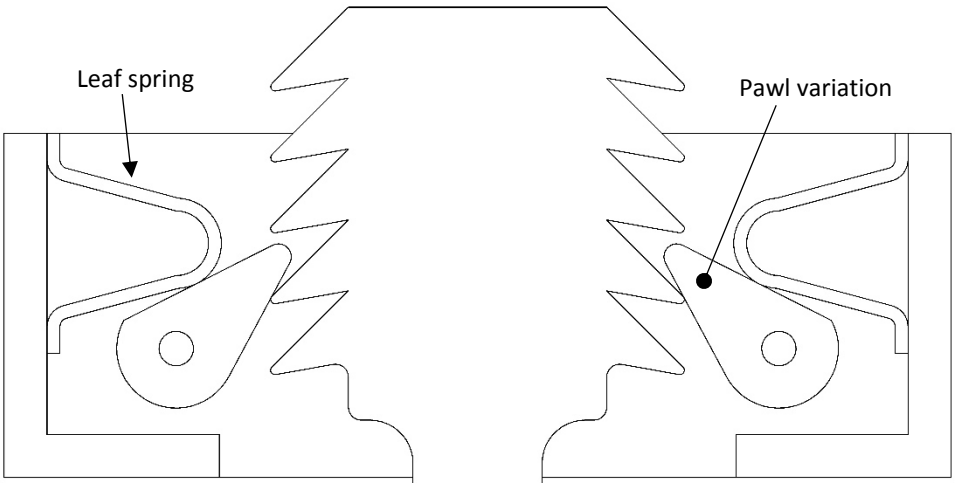

Figure 2.9 *Early GNG concept using a sharper pawl design with a leaf spring variation*

While this type of design provides a secure locking effect, the small internal angle of the teeth on the rack presents issues to the pivoting of the pawls for disengagement. The pawls need to be able to rotate freely to disengage when the rack moves in the upwards direction during compressive loading. This 'locked in' type of interface does not allow for the rotation of the pawls necessary for them to move out of the way and allow for the reverse, compressive, motion of the device.

Moreover, reduced internal angles for the tooth profile will induce higher stresses and complicate the manufacturing process. Figure 2.2b shows a rotational ratchet mechanism with an internal tooth angle of less than 90°. The linear mechanism in the GNG prototype has different geometric constraints.

In particular, the 90° internal angle of the rack tooth profile, as adopted in the first prototype, allows for the unhindered rotation of the pawl required for disengagement during compressive loading. There is no unwanted interference between the pawls and the rack when the rack moves in compression. This profile is shown in **Figure 2.10**.

This design is simple and allows a wide range of manufacturing options. Some of the methods that could be employed to create the part with this basic design geometry include:

- Wire cutting
- Electrical discharge machining (EDM)
- Casting (as used for jack stands)
- Milling or profile cutting
- Laser cutting
- Water-jet cutting

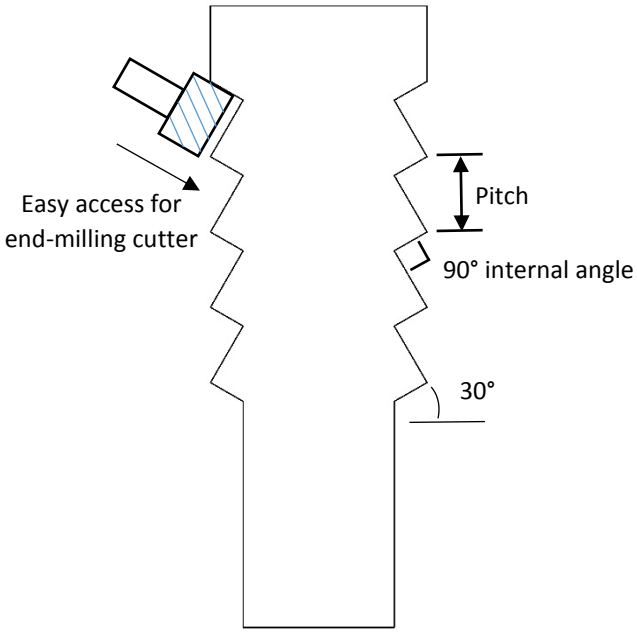

Figure 2.10 *Rack part showing tooth profile*

These options each have varying levels of complexity and associated cost. Among the lowest cost of these manufacturing options is end milling. By using an internal angle of 90° for the teeth, the chosen design allows for easy access of the milling cutter to remove the required material to make the part. This material removal process can be completed in a single pass for each level of cut depth required to step down to the total depth of the profile, as shown in **Figure 2.10**. This approach thus also allows for a basic rectangular pawl design, preventing complex interaction between the teeth and the pawls, allowing them to slide easily during the ratcheting motion.

The bottom edge of each tooth is rotated 30° above the horizontal, as also shown in **Figure 2.10**. This angle position provides a suitable contact area with the pawl and allows the pawls to sit at a reasonable offset from the rack to prevent undesired interference, allowing for easy rotation of the pawls. During engagement, the load direction through the pawls is primarily vertical, meaning there is solid engagement and the pawls will not slip.

The motion of the pawls is indicated previously on Figure 2.5. More complex pawl and tooth design could be utilised to assist with initial engagement, but would also limit the manufacturing options and increase production costs. The use of tooth detail to aid the initial engagement of the pawls is an important aspect of the design that could be considered in future development to help avoid any possible failure of engagement, which is an important consideration for this application. However, it should be noted that the current design has multiple springs to provide initial engagement with redundancy, and is a reliable yet easily machined solution.

In addition, the prototype design is a self-stabilising system. The tension spring provides only the initial engagement. Contact forces then strengthen the engagement and location of the pawls onto the rack.

The simple tooth design also allows for the assembly to accommodate racks with different tooth sizes to vary the pitch of ratcheting for a specific application. The same pawls can be used with racks with different sized teeth, as seen in Figure 2.11. For a smaller tooth size/pitch, the contact area between the pawl and rack is reduced. This reduced contact area increases the stresses developed in the parts during operation, and in the extreme case, increases the chance of the mechanism failing to engage or skipping teeth on the rack, which needs to be avoided in practice. A small clearance is shown between the rack and pawls in **Figure 2.11**. This gap is due to the relief section added to the pawl design, which is discussed later in this section.

However, the advantage of reducing the tooth pitch is that during successful operation the magnitude of impact loading is reduced. Since the motion of the system prior to engagement is reduced, the system velocity at the time of engagement will likely be lower, as will the displacement or drift of the structure. Therefore, a smaller pitch will lessen the chance of damage to the structure prior to the onset of yielding in the dissipater and energy dissipation occurring.

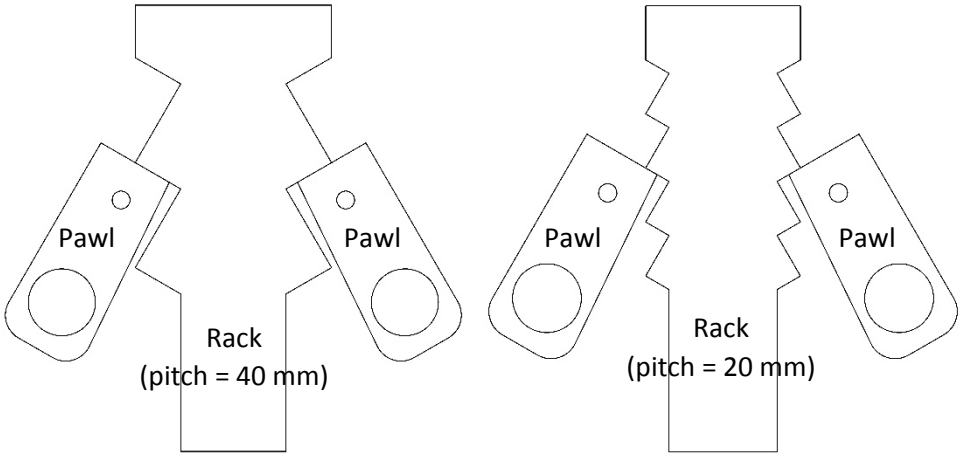

Figure 2.11 *Racks with two different pitch sizes shown interacting with the same set of pawls: a) larger pitch, and b) smaller pitch, with reduced contact area.*

Finally, a reduction in pitch leads to greater overall plastic displacement demand for the dissipater. In particular, a smaller loading cycle is then required to trigger the ratcheting effect of the system. This engagement during smaller loading cycles is expected to lead to a larger cumulative displacement demand within the dissipater.

Racks containing teeth with two different pitch sizes, 20 mm and 40 mm, were designed for this initial prototype. These two values were chosen to assess the suitability of the pawls to work with different pitch sizes. The smaller case also tests its ability to operate near the expected limits of functionality.

2.4.2. Pawl subassembly

The upper subassembly is the pawl subassembly, which contains the ratcheting mechanism. This subassembly contains the upper tongue, cover plate, main support, rack supports, two pawl pins and two pawls. The upper tongue is a flat feature, which is held in a hydraulic wedge grip in the test machine. A cover plate is used to connect the upper tongue, which mounts into the test machine, with the main support body, which holds the components of the ratcheting mechanism. Cap screws are used to fasten the tongue to the cover plate and the cover plate to the main support. The tapped holes for these connections are visible in Figure 2.7.

The main support body makes use of a modified 200x100x10 mm RHS section, shown in Figure 2.12. A rack vision slot is located near the top of the RHS section to enable viewing of the rack as it moves through the RHS and approaches the top cover plate. The position of the cover plate limits the ratcheting capacity of the device as the rack moves upwards toward the cover plate during ratcheting. In applications that require more ratcheting actions, and therefore a longer rack, it will be necessary to design additional space inside the main support body to allow for the movement of the rack during operation.

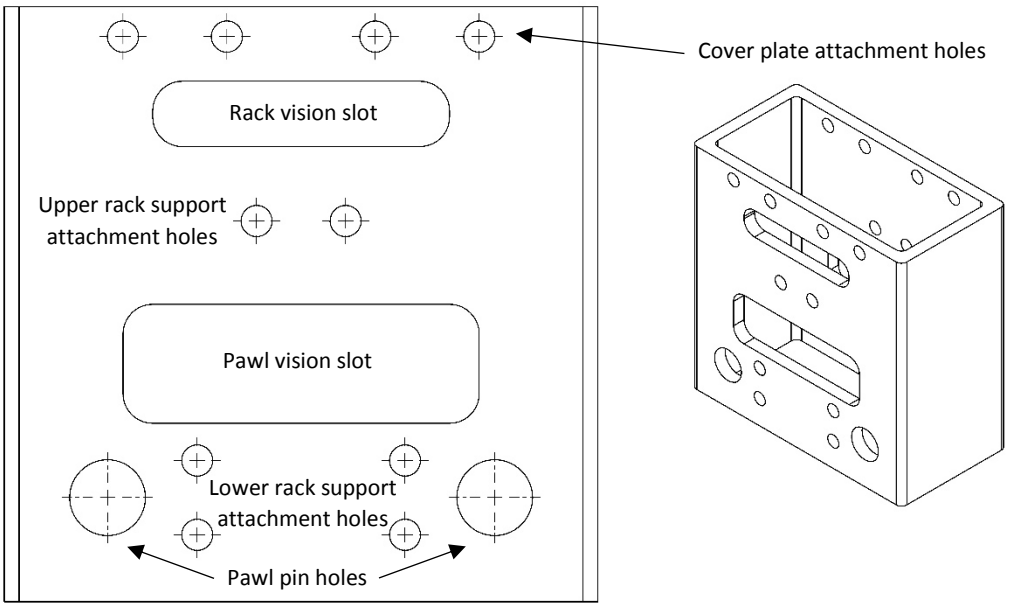

Figure 2.12 *Main support body of the GNG1 device, showing key features.*

Upper and lower rack supports are attached to the main support to prevent out-of-plane motion of the rack. A large pawl vision slot in the lower region of the RHS section allows the viewing of the ratcheting mechanism during operation, and enables easy access to fit and remove the tension springs fitted to the pawls. This slot also provides clearance for the tension springs which protrude out from the pawls. Two 25.5 mm diameter through holes towards the base of the main support locate the pawl pins, which set the location of the pawls.

The rack supports are fastened to the inside of the main support on each long side of the RHS, with the upper rack supports located between the rack vision slot and the pawl vision slot, while the two lower rack supports are positioned below the pawl vision slot. The two supports on one side of the rack can be seen in Figure 2.6, labelled as parts 7 and 8. These supports ensure that the rack moves in-plane to stay in correct alignment with the location of the pawls as the rack moves through the main support body.

Figure 2.13 is a plan cross section of the assembly, cut through the centre of the pawl pins, showing the lower rack supports. The lower rack supports increase the bearing area between the pawl pins and the main support body, reducing bearing stresses, as well as ensuring that the pins act predominantly in shear and are not subjected to significant bending stresses. These rack supports were necessary due to the aspect ratio of the standard RHS section used for the main support body. Alternatively, a custom support body could be machined, which might actually simply the overall assembly.

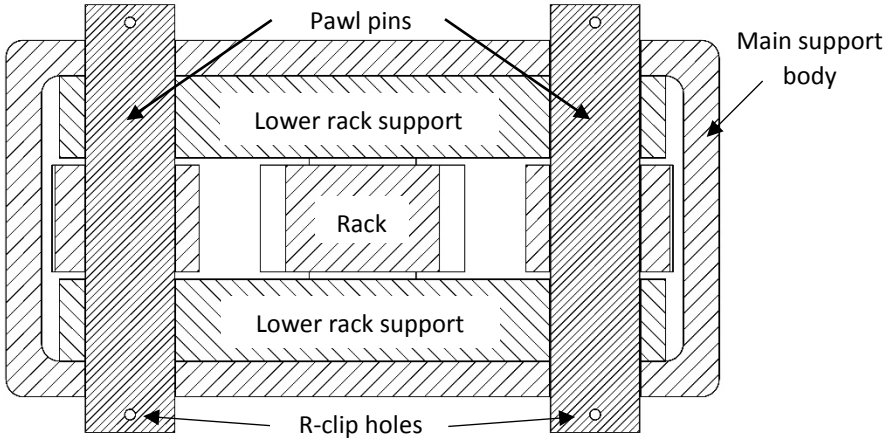

Figure 2.13 *Plan section view of GNG1 prototype assembly showing lower rack supports*

Two pawl pins, 25 mm in diameter, locate the pawls and allow them to rotate. The pawl pins fit through holes in the main support and are prevented from sliding all the way through by R clips fitted into 3 mm diameter holes near the ends of the pawl pins. These holes are visible in Figure 2.13.

The pawls are approximately rectangular 80x35 mm lever arms with a 25.5 mm diameter hole at one end to locate the respective pawl pins. They each contain a tapped M8 through hole to accommodate two cap screws, which hold the tension springs used to provide initial engagement. One cap screw is threaded in from each side. Each pawl has a relief on the inward side, in contact with the rack, to limit the range of motion of the pawl. This limit prevents it from moving too far outward when the rack teeth slide past during compressive motion. This feature should also allow a more rapid return to the neutral position for the pawls. The relief section is shown in **Figure 2.14**.

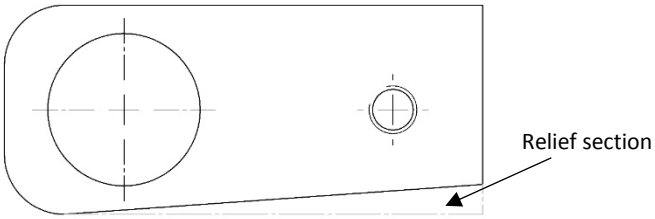

Figure 2.14 *Pawl profile with relief section shown by dotted line*

2.4.3. Tension springs

In a rotational ratchet mechanism, the pawl can be positioned above the ratchet wheel to use gravitational effects to keep the pawl in contact with the ratchet wheel. This orientation is shown previously in **Figure 2.2**b. However, the linear analogy used in the GNG1 design with two pawls cannot be positioned to provide such an inherent centring effect to both pawls, and, in practice, the system could be used in a variety of orientations. Without additional restraint, provided by the springs, the pawls may be prone to rotating further outward than required for the movement of the rack under compression loading, and would not inherently return to a neutral position where they were able to engage with the rack teeth. Hence, the fitting of springs to the assembly provides an aid to initial engagement and returns the pawls to a neutral position after the passing of rack teeth during compressive motion and ratcheting.

Several variants of spring type and position were considered during the design of this GNG prototype. Leaf springs and compression springs were considered and could have been positioned in the main housing to control the motion of the pawls. Tension springs, as used in the final design, were favoured primarily due to the ease of installation compared to compression type springs, which must be fitted in a closed area with pretension. In addition, the use of tension springs limited the number of parts, as a single tension spring can be fitted between the two pawls instead of having a separate compression or leaf spring for each pawl, such as in Figure 2.3, Figure 2.4 and Figure 2.9.

To provide redundancy during initial engagement of the ratcheting mechanism, a tension spring is fitted between the two pawls on each side of the device. These springs limit the range of motion of the pawls and pull them inward after ratcheting past a tooth on the rack. This inward pull will be of particular importance to avoid any delay of engagement following load reversal from compression, when it is desirable for the device to take only a very limited load, to tension, when the device is required to engage and support large tensile loads to facilitate the yielding of the dissipater element to absorb structural response energy.

The springs are fitted to cap screws protruding from the pawls, with washers used to give a secure fit, as shown in Figure 2.15a. The addition of the tension springs offers some minimal resistance to

compressive motion, as the outward motion of the pawls must stretch the tension springs. However, only a small force is required to overcome this resistance and slide the rack teeth past the pawls. This approach thus allows the adjoined structure to return to its original location, preventing residual compressive loads.

These springs will operate most effectively when the device is in an upright position as in Figure 2.6. In an angled orientation the mass of one of the pawls may not act inward toward the rack, creating uneven pawl restoring forces. This concept is illustrated in **Figure 2.15**b. However, the rack will centre under loading as the contact and spring forces should be specified to be much greater than the weight of the pawls.

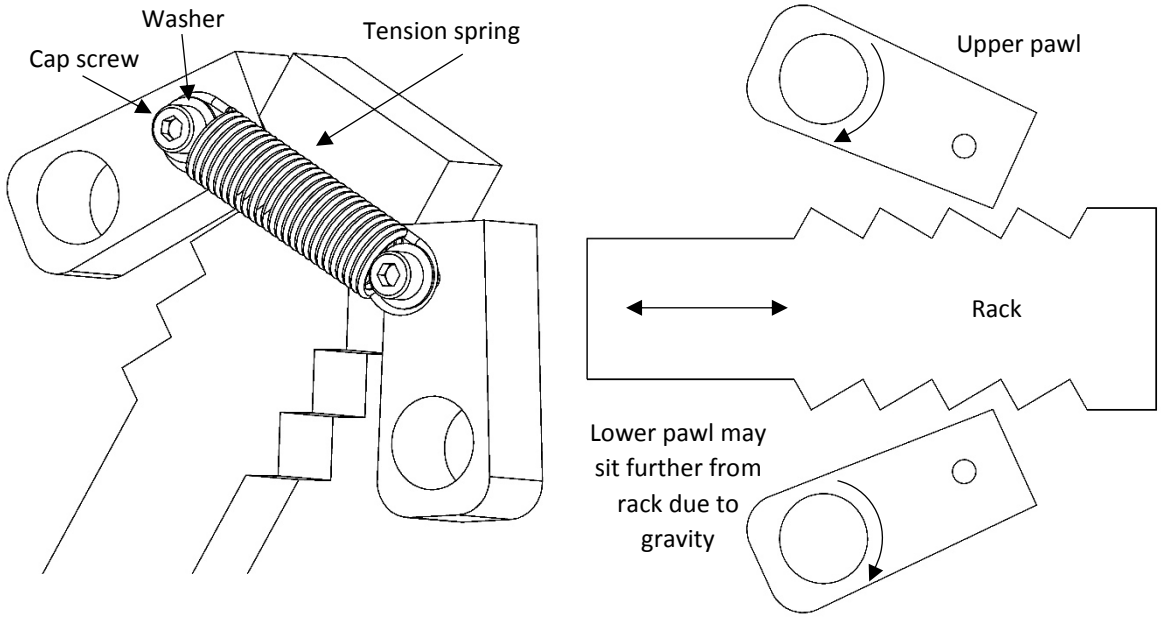

Figure 2.15 *GNG1 prototype pawl forces:*

a) tension spring between pawls, and b) uneven restoring forces during horizontal orientation

2.5. Experimental Test Design

Considering the limited test space available with the MTS machine, and the dissipater length required to attain a reasonable amount of plastic deformation in the element prior to fracture, the design of the MTS experiment required careful thought. The available space between crossheads on the test machine is occupied by the combination of the following four lengths, also shown in **Figure 2.16**:

1. The length of the upper tongue and the cover plate thickness
2. The space inside the RHS section between the top of the rack and the cover plate (which accommodates rack motion due to ratcheting)
3. The length of the dissipater subassembly

4. The remaining hydraulic ram displacement capacity for displacement inputs

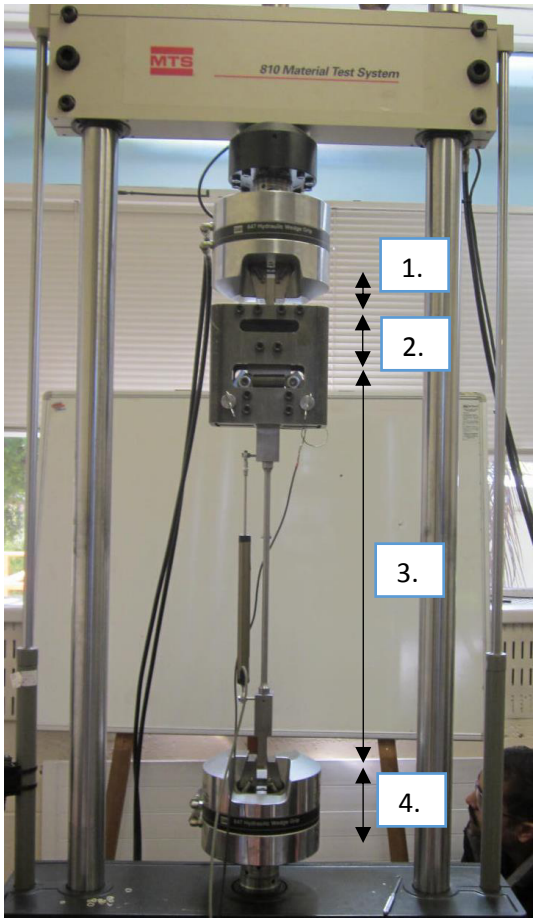

Figure 2.16 *Experimental setup showing distribution of space*

These lengths are defined by the design of the prototype and the total crosshead capacity of the test machine. To make the most of the approximately 700 mm of space available, a compromise needed to be made between extending the length of the dissipater, to allow greater plastic displacement capacity, extending the length of the RHS section, to accommodate greater ratcheting capacity, and selecting the remaining available ram displacement capacity, to allow for loading cycles with a suitable amplitude to demonstrate full system behaviour. A yielding region length of 320 mm for the dissipater provides a predicted plastic displacement capacity of approximately 90 mm prior to fracture.

To make use of the ratcheting mechanism during the unloading period of cyclic testing, it was required that the hydraulic ram displacement capacity be sufficient to allow a peak-to-peak displacement greater than the tooth pitch. If the plastic deformation of the dissipater on each cycle was not equal to or greater than the tooth pitch, ratcheting would not occur. Hence, the experiments were designed to provide ample compressive motion to ensure ratcheting would take place and the full range of system behaviour could be observed.

For the 40 mm and 20 mm pitch sizes used, initial experimental tests allowed for the ratcheting of the rack for a minimum of 1 and 2 teeth, respectively, during a monotonic compressive test with 50 mm displacement. A cyclic loading pattern was used for further testing, and ratcheting was expected to coincide with each unloading or compressive period. A total of 2 or 4 teeth, for 40 mm and 20 mm pitch sizes respectively, could be used during a full cyclic experiment, due to the 90 mm plastic displacement capacity available. **Figure 2.17** shows the loading pattern, where positive displacement is tensile. The occurrence of ratcheting motion during compressive loading, after elastic recovery, is highlighted.

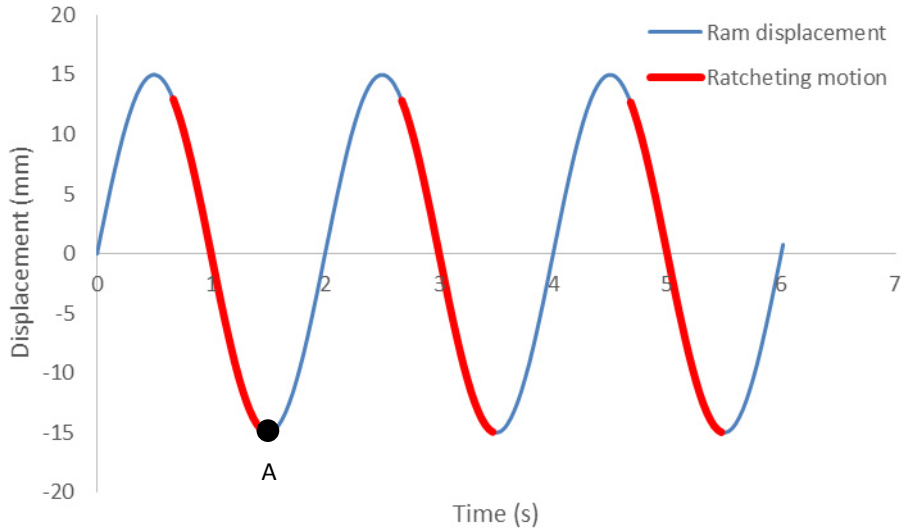

Figure 2.17 *Sample cyclic loading profile using 20 mm pitch, with initial reloading position labelled A*

The peak-to-peak loading displacement, and subsequently the magnitude of compressive loading phases, is deliberately selected to significantly exceed the pitch. This magnitude is chosen to achieve ratcheting, while also allowing for elastic displacement in the assembly elements and any period of non-engagement or free-travel when the pawls are between consecutive teeth. The free-travel effect is discussed in greater detail later in this section and in Chapter 3. This loading profile allows for the experimental examination of the influence of impact loads, elastic take-up and cumulative yield displacement.

Free-travel is possible if the pawls are not engaged up against a tooth at the start of a cycle, such as position A on Figure 2.17, due to prior plastic dissipater deformation and where the compressive displacement in a cycle is not equal to an integer number of pitches. The amount of free travel, and thus the velocity and magnitude of impact loading, is directly proportional to tooth pitch. This concept of free-travel is illustrated in **Figure 2.18**.

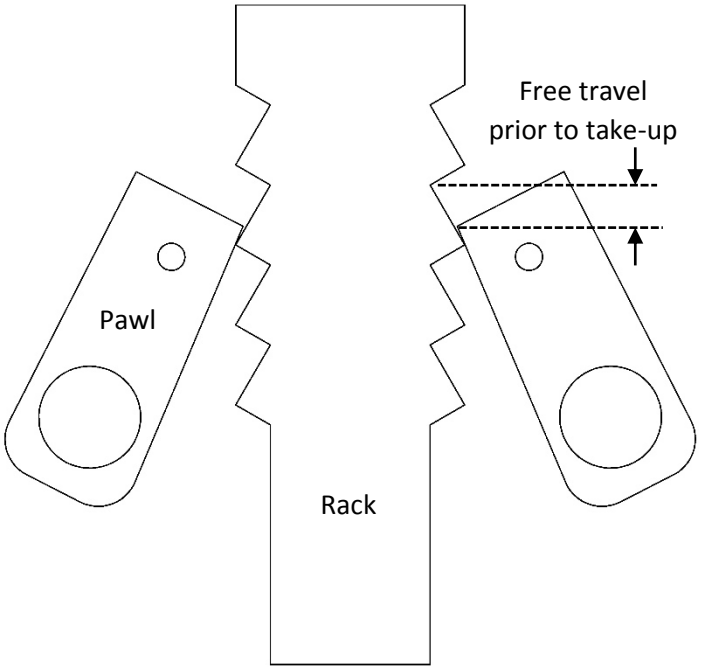

Figure 2.18 *Free travel present when pawls are between tooth edges, as can initially occur on reloading (position A in* ***Figure 2.17****)*

Due to limitations with the test equipment used, the initial prototype was built with limited force and plastic displacement capacity. As a result of these limitations, the tests completed are of a limited number of cycles. However, the engagement mechanism is validated and some of the tests still progress to the fracture of the dissipater, and thus capture the full spectrum of dissipater behaviour. The overall goal is to validate the device design and kinematics, which is achievable and will generalise to larger devices.

The effectiveness of the ratchet mechanism can be seen from the data acquired, which is presented in Chapters 3 and 5. The primary purpose of these tests was to investigate the effectiveness of the ratcheting mechanism engagement in tension, as well as the ability for the rack to slide past the pawls in compression. The effects of an increase in length of the yielding steel dissipater are easily modelled based on the well-known plastic behaviour of steel. To generalise the design, the important parameters of the GNG1 prototype design are shown in **Table 2.1**.

Table 2.1 Selected properties of the prototype design

Property	Value
Yield force (dissipater)	42.3 kN
Ultimate force (dissipater)	66.7 kN
Pitch (rack teeth)	20 mm, 40 mm (two designs)
Dissipater length (reduced region for yield)	320 mm
Plastic displacement capacity (dissipater)	90 mm (28% elongation at fracture)

2.6. Design analysis

This section presents a basic stress analysis of the GNG1 prototype device design, focussing on the unique design interfaces and high stress areas. The load paths through the ratcheting mechanism are discussed, followed by simple stress calculations at regions of interest. The discussion is focussed on the ratcheting mechanism assembly that is unique to the GNG, and not the details of the dissipater. The ratchet mechanism is viable to use with a range of energy dissipation mechanisms, including yielding steel, friction connections and extrusion devices. Due to the wide range of possible energy dissipation options, this component of the system is not considered here and is left open for special considerations based on individual applications.

2.6.1. Load Paths

During testing of the GNG1 prototype, as detailed in the following chapter, tensile forces were introduced to the GNG-dissipater system via downward displacement of the lower tongue, which was gripped in the hydraulic ram of the MTS test machine. The greatest design force considered in the system is equal to the ultimate tensile force of the dissipater (F_{UTS}). This value is used as the true strength of the dissipater, and over-strength factors could be included to ensure a capacity design where failure occurs only in the desired dissipative region when the device is added to a structure. The transmission of forces through the assembly during tensile engagement is given by the following load path and is illustrated for the upper section of the assembly in Figure 2.19:

- Input displacement to lower tongue via hydraulic gripper (tension)
- Lower tongue to dissipater element via threaded connection (tension)
- Dissipater element to rack via threaded connection (tension)
- Rack to pawls via tooth interface (compression)
- Pawls to pawl pins via bearing surface (compression)

- Pawl pins to main support body and lower rack supports via bearing surface (compression/shear)
- Main support body to cover plate via cap screws (tension/shear)
- Cover plate to upper tongue via cap screws (tension)
- Upper tongue to stationary upper machine crosshead via hydraulic gripper (tension)

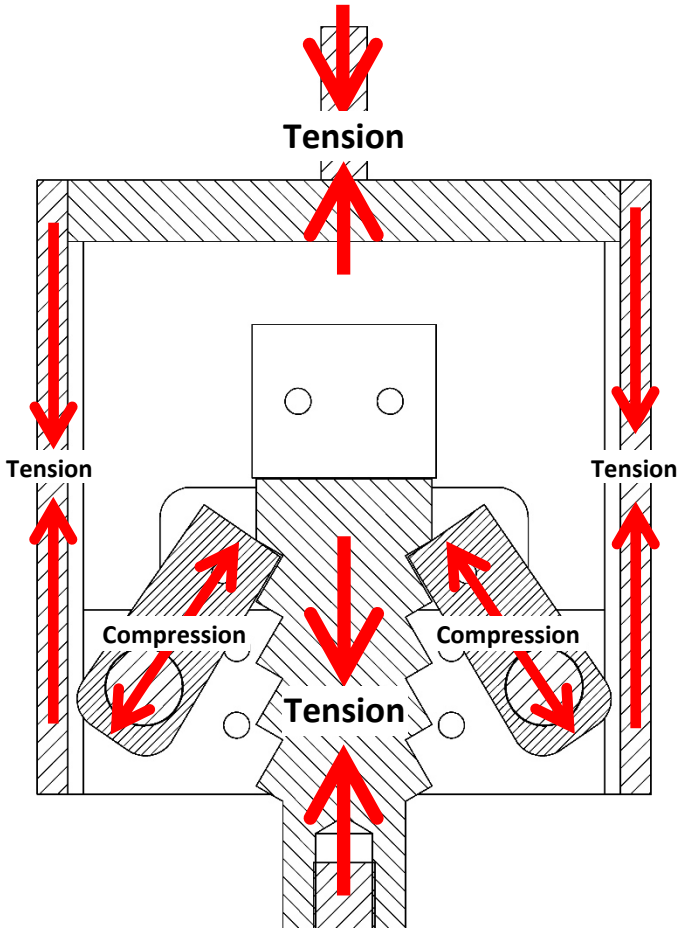

Figure 2.19 *Approximate load path for tensile forces through the first GnG prototype.*

When considering the device prototypes, it is important to realise that the upper and lower tongues are specific to the hydraulic test machine used during the testing outlined in Chapters 3 and 5. For an in-situ device, it is recognised that the upper and lower tongues would be replaced with a suitable interface for connection to the rocking frame or anchoring to the ground, or other relevant structural features. The forces in the system could be transferred from the device to the frame via a modified main support body, and the top cover plate may not be required. Given these practical alterations that would be required for a deployable device, this brief design assessment addresses the more general components of the system that comprise the ratchet mechanism itself, which will be consistent in any device of this design, regardless of the specific application. Several key points of

interest are present including the interface between the rack and the pawls, the bearing load between the pawls and the pawl pins, and the bearing load between the pawl pins and the main support body. Loading at these key interfaces is addressed below.

2.6.2. Pawl Interface

For this design analysis, a change has been made to the profile of the pawls, compared with the design that was used during the experiments with the device. The angle at the contact edge of the pawl, previously referred to as the relief, has been removed. The original desired effect of this feature was to limit the outward rotation of the pawl and improve the speed of ratcheting. However, following testing this effect is believed to be insignificant, and the design of the pawl can be simplified to a square edge. By removing the angled edge, the end of the pawl sits parallel to the tooth surface when the pawl is rotated fully inward, allowing for more secure engagement with a slightly larger contact area. This removed feature is indicated in Figure 2.20, which shows the rack-pawl interface.

The rack experiences the most significant loading at the interface with the pawls, where failure may occur via the two distinct mechanisms of crushing or shearing of the tooth. The areas where these stresses occur are indicated on Figure 2.20 and are projected into the page, which represents the thickness of the respective parts. Figure 2.20 also shows the bearing area for the load between the pawls and the pawl pins.

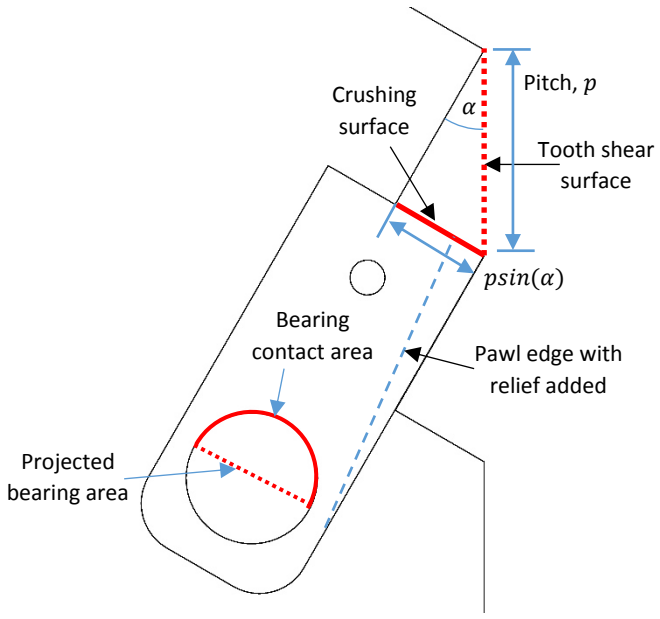

Figure 2.20 *GNG1 rack-pawl interface with loading areas labelled.*

Crushing may occur on the lower edge of the tooth due to excess bearing stress. The crushing area is equal to the length of the tooth edge $(psin(\alpha))$ multiplied by the thickness of the rack (t_{rack}), which is the distance into the page in Figure 2.20. The force perpendicular to this crushing surface at each

rack-pawl interface is equal to the force in the system divided by $\cos(\alpha)$. The force in each pawl is then:

$$F_{pawl} = \frac{F_{UTS}}{2cos(\alpha)} \tag{2.2}$$

The angle α and other features are labelled in Figure 2.20. Assuming the two pawls share the load evenly, the crushing stress at the tooth interface, $\sigma_{crushing}$, can be calculated by:

$$\sigma_{crushing} = \frac{F_{pawl}}{psin(\alpha)t_{rack}} \tag{2.3}$$

where t_{rack} is the thickness of the rack. Shearing of the tooth may occur due to excess shear forces in the rack at the tooth base. The shear area is equal to the tooth pitch multiplied by the thickness of the rack. The force parallel to this surface is equal to half the force in the system. Assuming the two pawls share the load evenly, the shear stress at the tooth interface can be calculated by:

$$\tau_{tooth} = \frac{F_{UTS}}{2pt_{rack}} \tag{2.4}$$

2.6.3. Bearing Loads

Figure 2.21 shows the location of a cross-section through the centre of the pawl pins used to show the position of the projected bearing areas, which are shown in Figure 2.22. Figure 2.22 provides a plan view showing the projected bearing areas for the loads moving from the pawls to the pawl pins, and from the pawl pins to the main support body and lower rack supports. The green and red shaded areas in Figure 2.22 indicate the location of bearing between the pawl pin and the other parts, as labelled.

The full force in the system is transferred through these bearing areas. The projected bearing area at each interface is equal to the pin diameter (d_{pin}) multiplied by the thickness of the mating part. These thickness are the pawl thickness (t_{pawl}), the thickness of the lower rack support $(t_{support})$, and the thickness of the main support body (t_{body}), respectively, and are labelled in Figure 2.22. Note that the lower rack supports were added to reduce bending stresses in the pawl pins and to improve alignment of the rack.

Each pawl pin is in contact with one of the pawls and the two associated projected bearing areas are coloured green and labelled as 1A and 1B, respectively, in Figure 2.22. A small bending moment is also induced in the pawl pins. By minimising the gap between the pawls and the lower rack supports, while still allowing for the free rotation of the pawls, this bending moment can be further reduced.

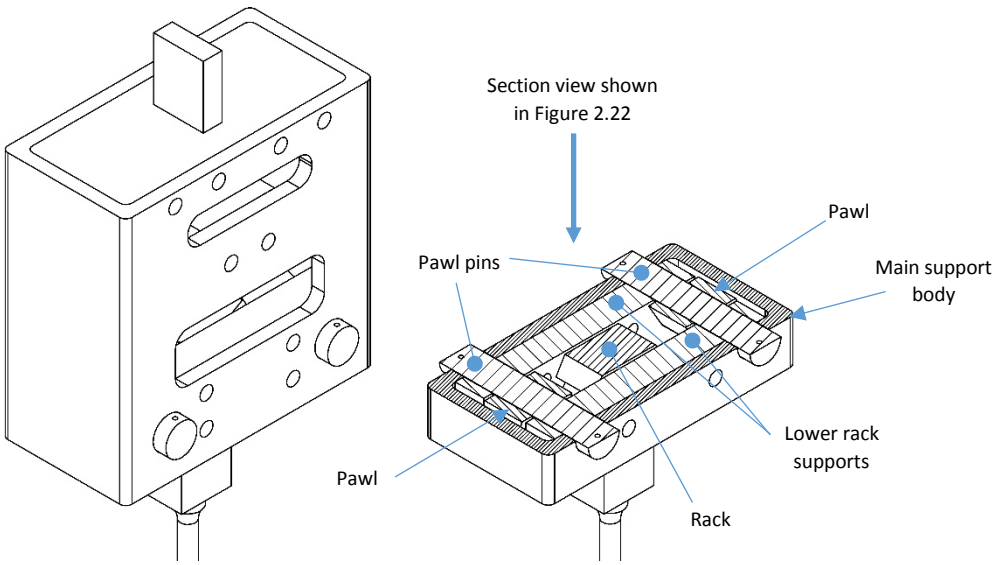

Figure 2.21 *Isometric cross-section view of bearing areas of first GnG prototype.*

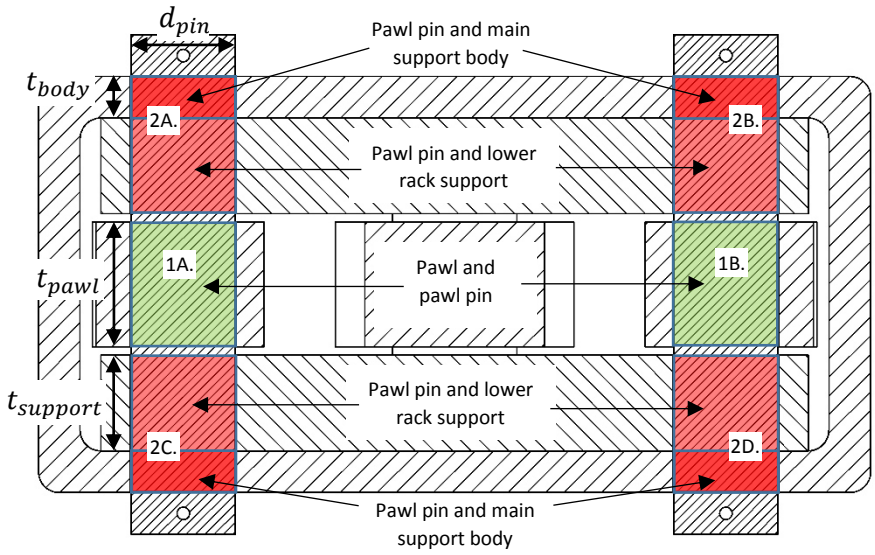

Figure 2.22 *Projected bearing areas of first GnG prototype.*

Each pawl pin is in contact with the main support body in two places and with both lower rack supports. For the transfer of forces from the pawl pins into the supports, the load is shared across the bearing area with both the main support body and the lower rack supports. This bearing load is spread across four contact points in total, and these contact points are coloured red and labelled as 2A to 2D, respectively, in Figure 2.22. In a future design, the rack supports could be incorporated into the main support body as one part. Assuming the two pawls share the load evenly, the bearing stresses at these interfaces are defined by:

$$\sigma_{pawl} = \frac{F_{UTS}}{2d_{pin}t_{pawl}} \quad (2.5)$$

$$\sigma_{body} = \frac{F_{UTS}}{4d_{pin}(t_{body} + t_{support})} \quad (2.6)$$

Other interfaces in the first GNG prototype are specific to the mounting required for the MTS test machine, or use threaded and bolted connections which are not unique to this design.

2.7. Conclusions

This chapter has defined the desired behaviour of a ratcheting, tension-only mechanism for use with seismic energy dissipation systems, and detailed the design process to produce an initial experimental prototype GNG1 device to achieve the desired hysteretic behaviour. These actions address research question 1:

Can devices be designed and built to dissipate energy under tensile earthquake loading without carrying compressive loads, and with reduced take-up on subsequent loading cycles to maximise energy dissipation?

- A ratcheting mechanism has been designed for tension-only engagement of the energy dissipation system.
- The device employs a conservative design approach using a simple and reliable rack and pawl engagement interface.
- Careful detailed design was used to ensure a low-cost and easy to machine device, to increase likelihood of uptake.
- A yielding steel dissipater element was designed to be used with the ratcheting device for proof-of-concept testing outlined in Chapter 3.
- Multiple rack designs were produced to experimentally test the influence of tooth pitch.
- A series of basic stress calculations, related to pitch size, are provided. These are specific to the particular GNG1 device design used in this thesis.

3. Testing of GNG1 Device

3.1. Summary

This chapter describes the testing of the initial experimental GNG1 prototype. Experimental proof-of-concept testing on 6 dissipater elements in a monotonic compression and cyclic testing schedule was used to demonstrate the function of the ratcheting mechanism and assess the hysteretic behaviour of the dissipater element and the overall GNG-dissipater system. The dissipaters were heat treated with a full annealing cycle to give maximum ductility in the relatively short length that was used due to testing machine limitations. This process resulted in a yield forces of ~45 kN and ultimate tensile forces of ~65 kN in the dissipater elements. High speed camera footage of the ratcheting mechanism was recorded to assess engagement timing with two different pitch sizes of 20 mm and 40 mm. Also, a computational algorithm for modelling the hysteretic behaviour of the GNG-dissipater system was created and compared to the experimental results.

This chapter addresses research questions 2, 3 and 4: Can the devices respond with appropriate speed of engagement for use during seismic loading of structures? Can the experimental devices exhibit desirable hysteresis behaviour, similar to theoretical predictions? Can a model be developed to describe the GNG hysteretic performance, together with that of a rocking wall?

3.1. Data Acquisition

A data acquisition system recorded five outputs against time during the experiments. The force and displacement of the hydraulic ram, at the lower end of the device, were recorded from the test machine. Note that the upper crosshead, indicated in **Figure 3.1**, remained stationary. A linear potentiometer displacement sensor was used to directly record changes in the length of the dissipater element, and was mounted to the device via rod ends bolted to the lower region of the rack and the upper end of the lower tongue, as shown in **Figure 3.1**. The remaining two signals were taken from a pair of single-axis accelerometers mounted on the lower ends of the two pawls, as shown in the insert in **Figure 3.1**.

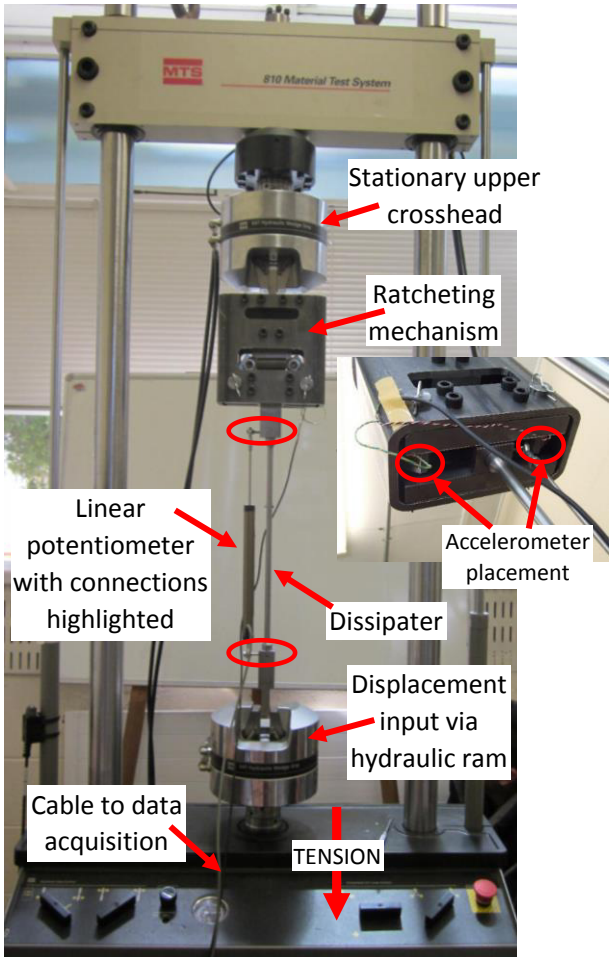

Figure 3.1 *GNG prototype test apparatus with accelerometer placement shown in insert*

The accelerometers were used to capture acceleration spikes during ratcheting and to quantify engagement timing, as engagement creates small acceleration spikes upon impact between the rack and pawls. All data was sampled at 1000 Hz to ensure all frequencies were captured. High speed camera footage was recorded for several of the tests to measure pawl engagement time using a FASTCAM SA5 model 775K-C3 camera operating at 1000 frames per second.

A test setup with the ratcheting mechanism and the rack revealed that the frequency of impacts occurring between the pawls and the rack were above the 400 Hz bandwidth of the accelerometers. Subsequently, it is not assumed that the full behaviour of the impact is captured by accelerometer data and values recorded do not necessarily represent the peak acceleration of the pawls. In any case, the peaks recorded in the data are useful to show the timing of the engagement of the ratcheting mechanism with respect to the other system behaviour.

3.2. Monotonic Testing

Several tests of monotonic compressive loading were completed to characterise the ratcheting function of the device without yielding the dissipater elements. During these tests the device was

displaced in compression by 50 mm. This displacement enabled ratcheting of 1 or 2 teeth, when used with the 40 mm and 20 mm pitch racks, respectively. These tests were completed at different ram velocities and a summary of the monotonic testing is presented in **Table 3.1**, including the maximum compressive forces recorded. The reference numbers indicate an M for monotonic, followed by the rack pitch in mm, and the ram velocity in mm/s, separated by a hyphen. Subscripts are used to differentiate any tests completed under the same conditions. For example, M20-025$_1$ is the first of three monotonic tests with a 20 mm pitch rack completed at 25 mm/s.

Table 3.1 *Summary of monotonic compressive testing of the first GNG prototype*

Rack Pitch (mm)	Velocity (mm/s)	Test Ref.	Max. Compressive Force (kN)
40	50	M40-050	0.72
	100	M40-100	1.14
20	25	M20-025$_1$	0.24
	25	M20-025$_2$	0.47
	25	M20-025$_3$	0.47
	50	M20-050$_1$	0.48
	50	M20-050$_2$	0.76
	50	M20-050$_3$	0.48
	100	M20-100	0.32

A reference structure with a 1.2 s period, peak uplift rotation of 2% (0.02 radians), and 1 m eccentricity of the GNG dissipater system from the rocking edge, would experience a peak uplift of 20 mm. Based on a harmonic sine wave motion with 10 mm displacement amplitude, or 20 mm peak to peak displacement, this will give a peak velocity of approximately 52 mm/s.

Higher speeds could be used to simulate shorter period structures, or greater peak uplift values. Given the limitations of the MTS hydraulic test machine, reported via saturation velocity as assessed by a colleague, ram speeds of up to 220 mm/s could have been used during the cyclic testing with the reported peak forces, if the saturation velocity of the machine was approached.

A series of dynamic tests were completed, and it is believed that the results would generalise to such an increase in ram speeds, without significant impact on the observed behaviour of the GNG dissipater systems tested. The functionality of the ratcheting mechanism was observed to be very robust. Also, the steel dissipaters used in the testing have low rate dependence. Friction connections, which could be used as an alternative energy dissipation mechanism with the GNG device, are rate independent.

The maximum force experienced by the device during the monotonic compressive tests was 1.14 kN. This result occurred during a test with the 40 mm pitch rack, where the ram velocity was 100 mms^{-1}. This result fits with the expectation that slightly larger compressive forces would be experienced by the device with the use of a larger pitch rack. The larger teeth force the pawls to rotate slightly further outward, increasing the tension force in the spring which must be overcome for ratcheting to occur.

An exception to this expectation occurred during a test with the 20 mm pitch rack, where the ram velocity was 50 mms^{-1}. In this test, a maximum compressive force of 0.76 kN was recorded, which exceeds the 0.72 kN force recorded for a test with the 40 mm pitch rack and a ram velocity of 50 mms^{-1}. **Figure 3.2** shows the maximum compressive forces from the monotonic compressive tests against ram velocity.

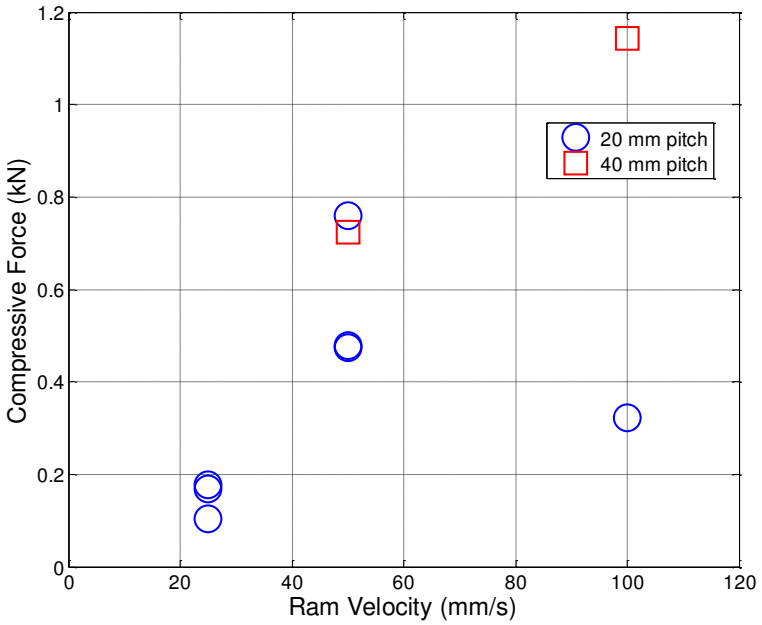

Figure 3.2 *Maximum forces recorded during monotonic compressive testing*

It is expected that imperfect symmetry of the pawls and springs during operation contributed to the variability of the recorded compressive force values. Overall, there is a rough correlation between ram velocity and the compressive force. However, all values of compressive force are less than approximately 1.2 kN, representing negligible compressive forces as expected by design.

Figure 3.3 shows the force displacements results for the monotonic testing with the GNG1 prototype. Only small forces are recorded, as desired by design. There is some variation across the results, and this is expected to be primarily due to small differences in alignment during the testing.

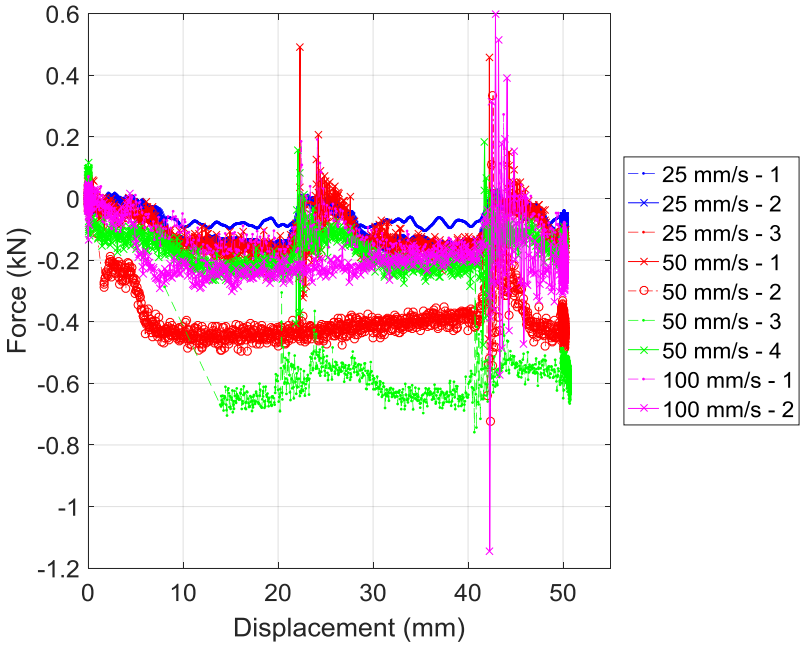

Figure 3.3 *Force displacement results of the monotonic tests with the GNG1 prototype.*

3.3. Cyclic Testing

Cyclic tests were completed to assess the hysteretic behaviour of the dissipater element and the overall GNG-dissipater system. A summary of the cyclic testing parameters is presented in Table 3.2 and results from testing follow in Table 3.3. The reference numbers indicate a C for cyclic, followed by the rack pitch in mm, then the input displacement amplitude in mm and the input frequency in Hz, with the three numbers separated by a hyphen. Subscripts are used to differentiate any tests completed under the same conditions. For example, C20-15-0.25$_1$ is the first of three cyclic tests with a 20 mm pitch rack and a displacement input amplitude of 15 mm, completed at 0.25 Hz.

Test amplitudes were selected to clearly present a single ratcheting action during each compressive loading cycle. Initial machine overload limits meant that the C20-15-0.50 test was interrupted after approximately one cycle before resuming to completion. Where no value is stated for dissipater elongation to fracture, it indicates that the sample did not fracture during testing.

Table 3.2 Input test parameters for cyclic testing of the GNG1 prototype

Rack pitch (mm)	Amplitude (mm)	Frequency (Hz)	Test Ref.	No. cycles
40	25	0.25	C40-25-0.25	2
		0.50	C40-25-0.50	2
20	15	0.25	C20-15-0.25$_1$	3
			C20-15-0.25$_2$	3
			C20-15-0.25$_3$	3
		0.50	C20-15-0.50	3

Table 3.3 Summary of results for cyclic testing of the GNG1 prototype

Test Ref.	Yield Force (kN)	Ultimate Tensile Force (kN)	Dissipater Elongation to Fracture (mm)	Max. Compressive Force (kN)
C40-25-0.25	44.1	66.7	75.2	1.27
C40-25-0.50	46.0	67.1	71.4	0.53
C20-15-0.25$_1$	42.4	65.1	65.2	0.30
C20-15-0.25$_2$	43.5	65.3	--	0.35
C20-15-0.25$_3$	46.5	65.0	--	0.28
C20-15-0.50	49.9	65.7	71.4	0.49

Due to the limited rack displacement capacity of the prototype device, the cyclic tests with the 40 mm pitch rack, C40-25-0.25 and C40-25-0.50, were both completed in two sets of a single cycle to avoid interference of the rack with the top cover plate. Between cycles the springs were removed from the pawls, to allow the dissipater subassembly to be moved back to its approximate original position before reassembly. Data recordings were zeroed prior to the second cycle and some reconstruction was required to obtain the effective force displacement figures. It is important to note that this process was required as a result of the limited space within the specific test machine used for these experiments, and is not an inherent feature of the GNG ratchet mechanism design.

The maximum compressive force experienced by the device during any of the cyclic loading experiments was 1.27 kN. This result occurred during a test with the 40 mm pitch rack operating at 0.25 Hz. During the cyclic testing the two largest maximum compressive forces occurred during the two tests with the larger pitch rack. However, there was little difference, approximately 8%, between

the largest of the maximum compressive forces recorded for the smaller pitch experiments and the lower value for the two larger pitch experiments.

The maximum compressive forces are shown in Figure 3.4. In all tests, the compressive forces are very low, as intended by design. The dissipater behaviour was reasonably consistent, with an average yield force of 45.4 kN and an average ultimate tensile force of 65.8 kN. Therefore, the largest maximum compressive force represents less than 2% of the average ultimate tensile force recorded. The yield and ultimate tensile forces are presented in Figure 3.5. Any differences are likely due to normal manufacturing or test variation.

The average elongation to fracture was 70.8 mm. This value represents ~79% of the expected 90 mm, based on 28% elongation at break, for AISI 1040 steel. Therefore, the assumed uniform plastic strain of 28% throughout the entire dissipater length may not have been obtained during the dynamic cyclic testing. The actual uniform elongation at fracture was about 22%, based on the 70.8 mm average elongation at 320 mm active fuse length.

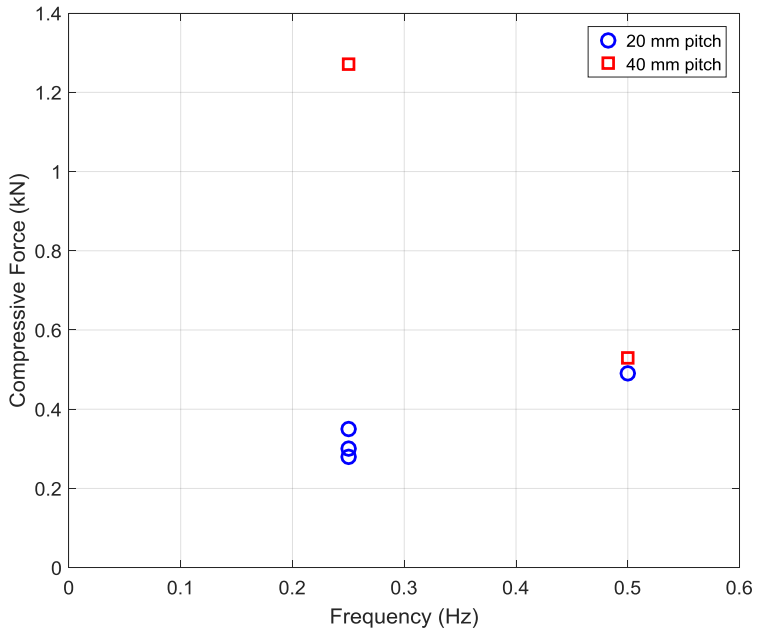

Figure 3.4 *Maximum compressive forces recorded during cyclic testing*

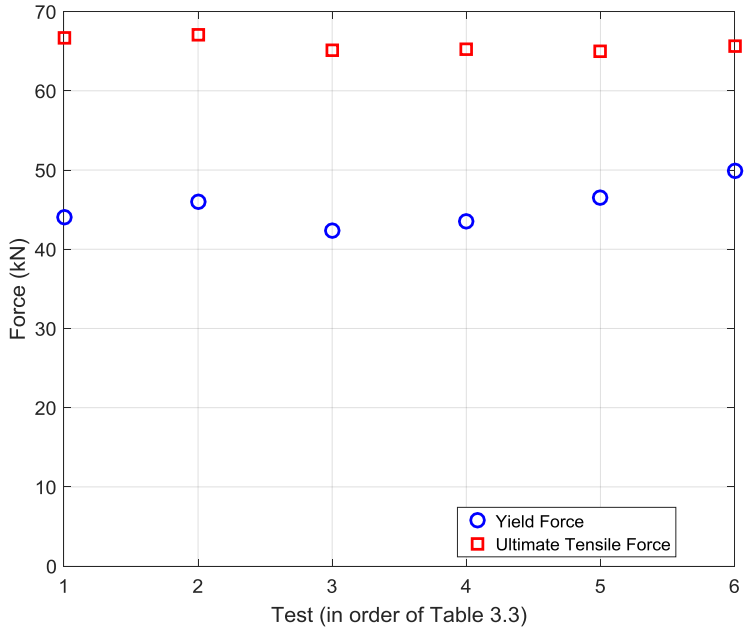

Figure 3.5 *Yield and ultimate tensile forces recorded for the cyclic experiments*

Hydraulic test machine limitations, most notably a maximum force of 100 kN, dictated the maximum dissipater diameter used for this testing. The ratcheting mechanism is capable of withstanding much larger forces if required and exhibited no visible signs of yielding or other damage following testing. Additionally, while these results use yielding steel dissipaters for energy dissipation, various dissipation methods, such as friction connections [MacRae et al. 2010] and lead dissipaters [Rodgers et al. 2008], could be implemented with the ratcheting mechanism as required for specific applications and force or yield levels. Most importantly, these specific tests were only designed to validate the functionality of the GNG device, which was demonstrated, and is not specific to the yielding steel dissipater.

3.4. Hysteresis

3.4.1. GNG-dissipater System

The effect of the ratcheting mechanism produces unique hysteresis behaviour for the GNG-dissipater system. A force-displacement plot of results from the cyclic tests with the 20 mm pitch rack is presented in Figure 3.6. Note that the input displacement amplitude is 15 mm.

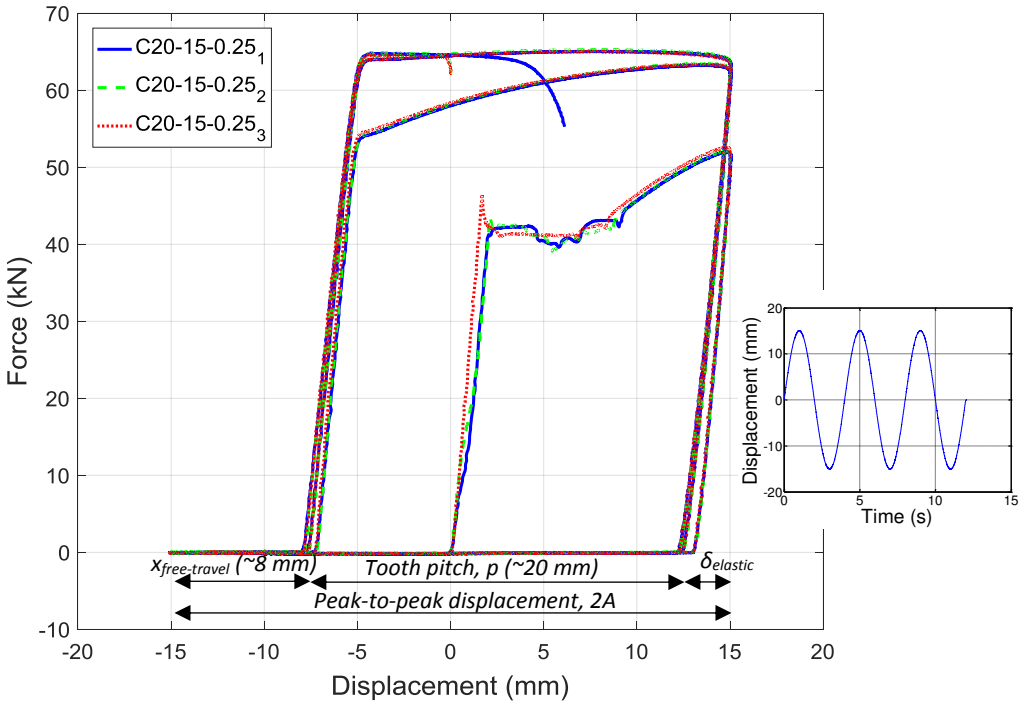

Figure 3.6 *Force-displacement hysteresis loops for cyclic testing of 20 mm pitch rack.*

The hysteresis loops begin by displaying typical elastic behaviour, yielding and strain hardening before the first load reversal. After input displacement reversal, elastic recovery is followed by a period of negligible force in compression. The bottom of the hysteresis loop lies essentially on the horizontal axis, indicating that only very small compressive forces are induced during the unloading phase of the cycle. This reflects the key elements of the idealised hysteresis behaviour outlined in Chapter 2.

The 30 mm peak-to-peak input displacement exceeds the combined value of the tooth pitch of the rack, p, and the elastic displacement of the dissipater, $\delta_{elastic}$. As a result, the displacement at which the GNG device engages during the next loading cycle is offset by an amount equal to the tooth pitch. This effect is shown in Figure 3.6, where it can be seen that during the unloading phase of the initial cycle, zero force is achieved at a displacement of approximately 13 mm, indicating approximately 2 mm of elastic recovery from the 15 mm displacement peak. However, during the following cycle the onset of elastic strain behaviour of the system occurs at a displacement of approximately - 7 mm, with respect to the initial position. The hydraulic ram reaches a minimum position of -15 mm, and Figure 3.6 indicates that up to 8 mm of free-travel ($x_{free\text{-}travel}$) exists before engagement occurs after load reversal.

Similar behaviour occurs for the subsequent loading and unloading cycles, with a slight offset in position. This slight shifting of the response is due to an increase in elastic displacement within the dissipater as a result of the increased force within the yielding steel element from strain hardening.

This free-travel is shown in Figure 3.7. Figure 3.7 shows a frame from the high speed camera recordings, where the device is at the bottom of its travel during the C20-15-0.25$_1$ test. Similar behaviour was exhibited in tests with the larger 40 mm pitch rack, with around 7 mm of free-travel upon reloading, as seen in the hysteresis loops in **Figure 3.8**.

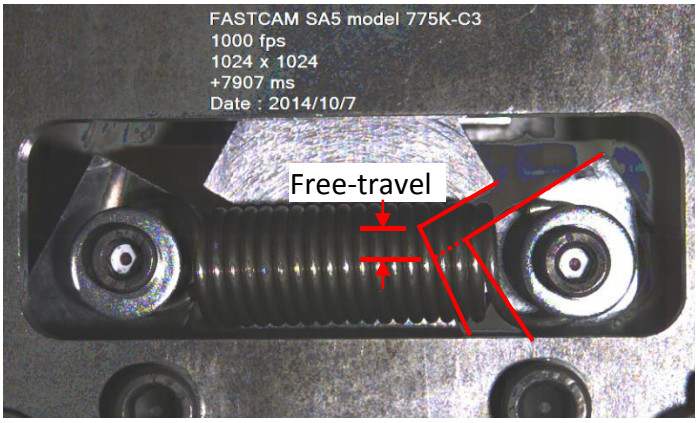

Figure 3.7 *GNG device at bottom of travel during C2 test with free-travel shown.*

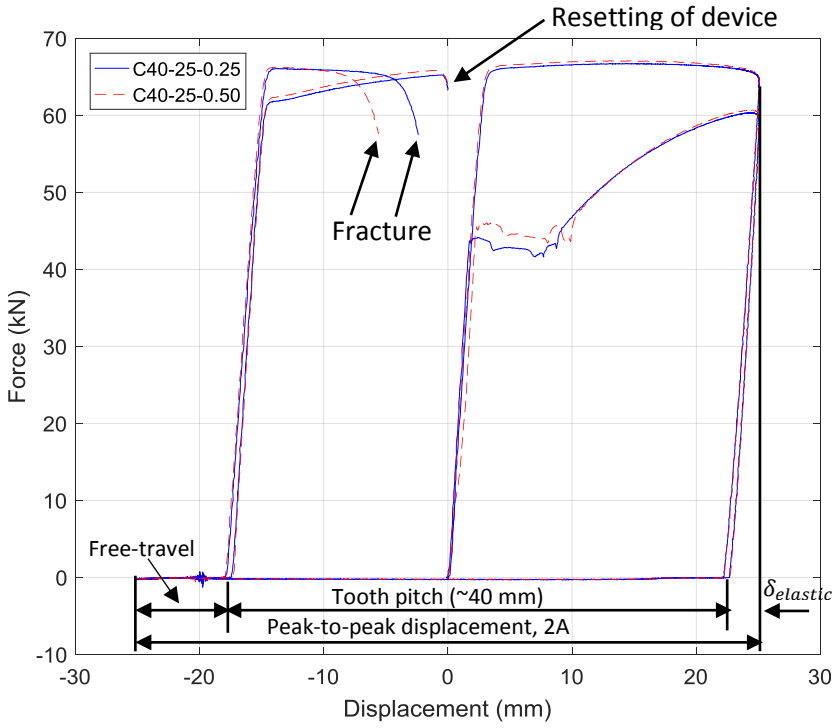

Figure 3.8 *Force displacement hysteresis loops for cyclic testing with 40 mm pitch rack*

During reloading displacements of -15 mm to -7.5 mm in Figure 3.5 and between -25 mm and -17.5 mm in **Figure 3.8**, reloading occurs with negligible resistive force. This free-travel ($x_{\text{free-travel}}$) is directly proportional to tooth pitch (p) and can be approximated by Equation (2.1), as described in the Chapter 2 and repeated here for convenience:

$$x_{\text{free-travel}} = 2A - \delta_{\text{elastic}} - np \quad (3.1)$$

where A is the amplitude of the displacement input cycle, δ_{elastic} is the elastic recovery displacement of the device during unloading, and n is the largest integer value where $(2A - \delta_{elastic}) > np$. Multiple ratcheting actions can occur when $(2A - \delta_{elastic}) > 2p$. These terms are expressed on **Figure 3.6** and **Figure 3.8**. Values for the displacement datum for engagement to begin are consistent for tests with the same rack due to approximately equal starting positions. In particular, the rack rests on the closed pawls, as shown in **Figure 3.9**, at the start of the test.

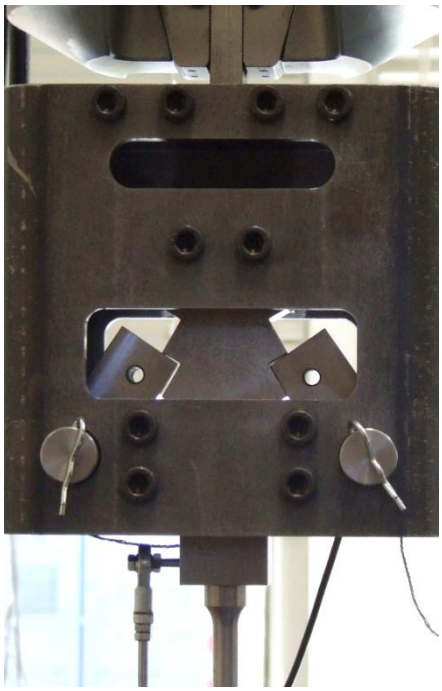

Figure 3.9 *Rack resting on closed pawls, representing the starting position for cyclic testing, with the spring removed for visibility*

It is clear that the hysteretic behaviour of the system closely matches the desired system behaviour outlined in Chapter 2, with more complex material yielding behaviour observed in the physical system. The results presented in **Figure 3.6** and **Figure 3.8** differ from a standard piecewise monotonic yield response due to the ratcheting mechanism essentially shifting the zero displacement datum. The amount of free-travel prior to re-engagement of the yielding mechanism on subsequent cycles is reduced due to the absence of compressive loads. The input displacement does not need to exceed that experienced on prior cycles before energy dissipation can occur, which is a limitation with simple tension bracing that is ameliorated here by the GNG device.

3.4.2. Dissipater element

Figure 3.10 and **Figure 3.11** show the hysteretic behaviour of the dissipater element during the cyclic testing for the 20 mm and 40 mm pitch racks, respectively. These figures use the linear potentiometer

reading, which gives true dissipater displacement, rather than the hydraulic ram displacement, which was used to generate the system hysteresis loops in **Figure 3.6** and **Figure 3.8**. As such, **Figure 3.10** and **Figure 3.11** do not include the ratcheting behaviour. Usual hysteresis curve features are visible including elastic strain, yielding, strain hardening and necking. The responses are essentially piecewise versions of a conventional monotonic tension test.

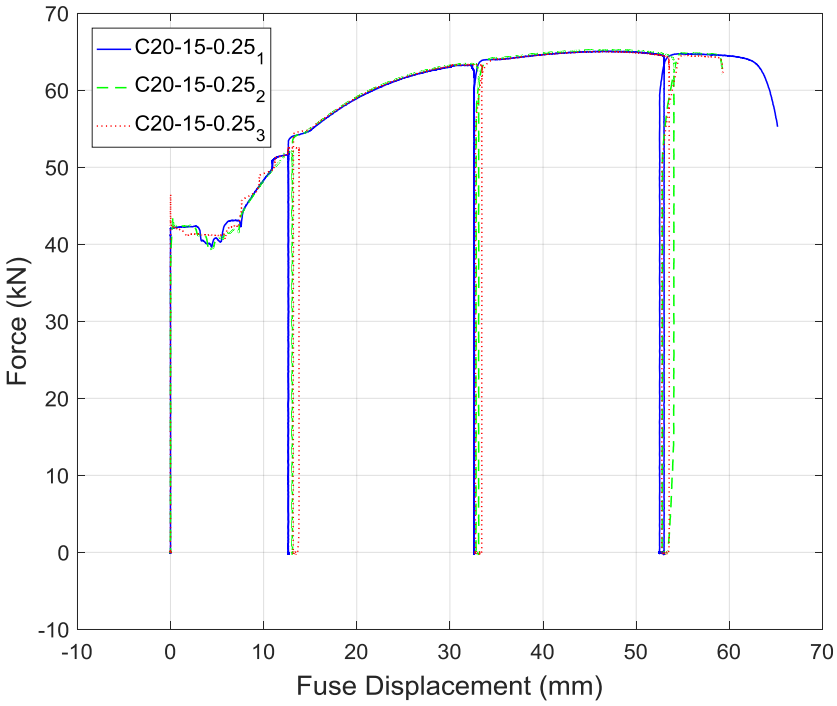

Figure 3.10 *Dissipater behaviour for cyclic testing with 20 mm pitch rack*

As expected from the three cycles in the test input, there are three occurrences of load reversal shown. The second load reversal shown for the C40-25-0.25 and C40-25-0.50 samples in **Figure 3.11** is a result of the resetting that was required between cycles for the larger 40 mm pitch rack. The potentiometer data for the two parts of each of these two respective tests are concatenated to present the overall results in **Figure 3.11**. Only minimal compressive loading was experienced, and there is thus very little elastic compressive strain observed, less than 0.01%. Note that the C20-15-0.25$_2$ and C20-15-0.25$_3$ samples, shown in **Figure 3.10**, have not been tested to fracture.

The elastic stiffness of the dissipater does not appear to be fully captured by the potentiometer data. There are several small connections which may have contributed to this discrepancy. Each end of the potentiometer instrument used to record the displacement of the dissipater has a rod end containing a spherical plain bearing. Small bolts through the bearings were used to connect the potentiometer to the rack and the lower tongue at the respective ends. Nuts were used to hold these bolts securely in the bores of the spherical bearings, which were not threaded. If these nuts were not sufficiently

secured, extra free movement would be available in the connection. This movement could lead to a lack of engagement of the potentiometer and a lack of force data prior to the yielding of the dissipater. There is another nut securing the rod end to the potentiometer, which may also have been a little loose. Additionally, there is a small amount of movement possible between the inner and outer races of the bearings.

Each of these connections can only contribute a small amount of free movement in the system. However, the expected elastic displacement prior to yielding of the dissipater is only around 0.64 mm, based on the dimensions and yield force of the dissipater, and assuming an elastic modulus of 200 GPa. This effect could be reduced in future work by carefully ensuring the nuts securing the bolts into the bores of the bearings, as well as the rod end nut, are tightened appropriately. In addition, more grease could be added to the bearings to reduce free movement between the inner and outer races of the bearings.

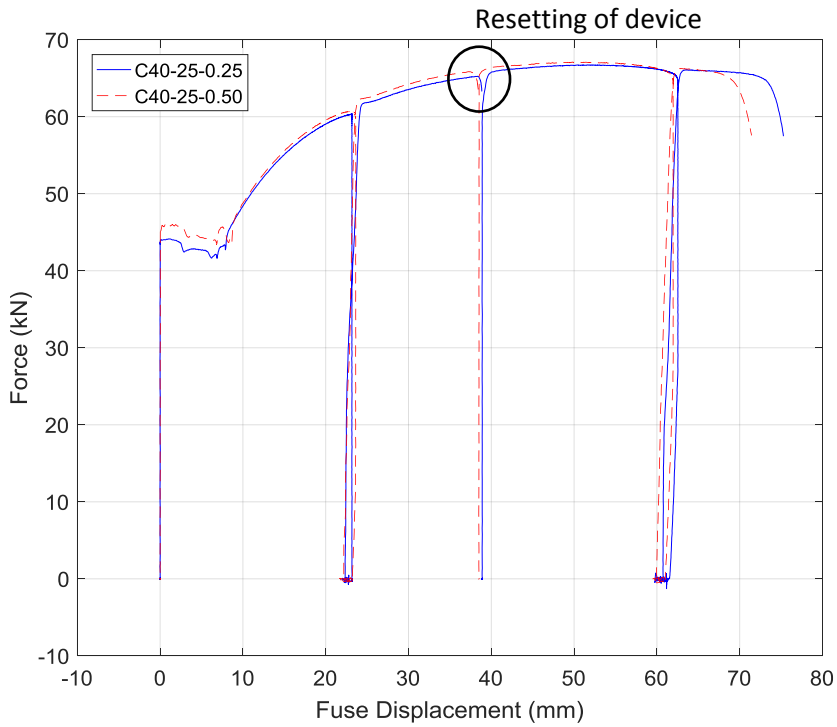

Figure 3.11 *Hysteretic dissipater behaviour for cyclic testing with 40 mm pitch rack*

Figure 3.12 provides a comparison of the hysteretic behaviours of the yielding steel dissipater alone and the response of the GNG-dissipater system as a whole for test C20-15-0.25$_1$. The displacements clearly vary between the two systems. This variation is due to the ratcheting behaviour of the GNG device, which results in a condensed hysteresis curve where sequential loading cycles are overlaid.

There is a lack of compressive force experienced in the dissipater element, as intended by design. The onset of tensile yielding of the GNG-dissipater system occurs when the force in the dissipater exceeds

the force at the start of the unloading phase in the previous cycle. While the test was cyclic, the steel yields only in tension and the behaviour approximates a piecewise version of a standard monotonic tensile test due to the GNG device essentially removing compressive loading in the dissipater. The stiffness during the initial loading cycle is different for the two systems shown in **Figure 3.12**. The extra components which make up the ratcheting mechanism introduce significant additional flexibility to the GNG-dissipater system, reducing the overall system stiffness compared to the dissipater element alone.

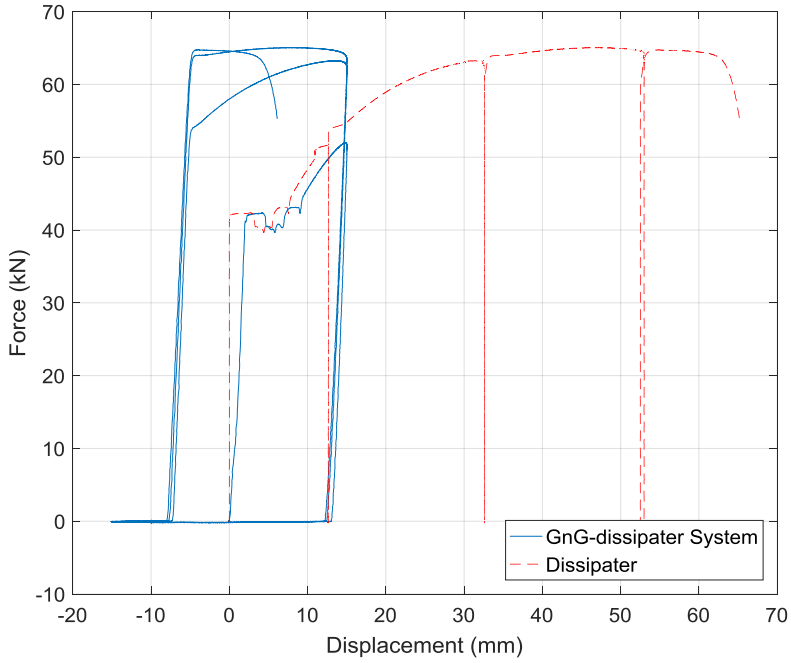

Figure 3.12 *Hysteretic behaviour comparison of dissipater element and overall GNG-dissipater system*

3.5. Ratchet Mechanism Behaviour

The high speed camera footage was used to find the closure time for the ratcheting mechanism during the tests. There is a short period immediately after the onset of each ratchet increment when the pawls are not in contact with the rack as they rotate inward after sliding past the end of a tooth. This closure time was assessed via visual inspection of the high speed camera footage. The closure times for each pawl ranged from 5 to 13 ms. A change from compressive to tensile loading in the system during this pawl closure process could limit the contact area between the pawl and the rack, increasing contact stresses. The angle of the teeth and the force of the tension springs are designed to aid the rapid return of the pawl to a position where full engagement and maximum contact area with the rack is established. **Figure 3.13** highlights the area of the system that is enlarged in **Figure 3.14**, which in turn shows a number of frames from the M40-100 monotonic test demonstrating the closure of a pawl with time stamps from the processing software. Note that each frame is 1 ms (0.001 s) apart.

Enlarged area shown in **Figure 3.14**

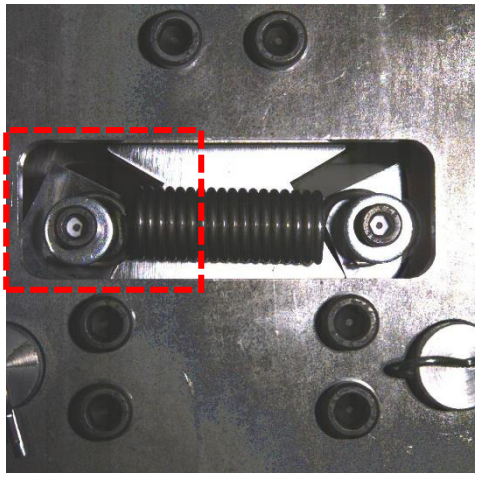

Figure 3.13 *View of ratcheting mechanism, showing enlarged region used in* ***Figure 3.14***

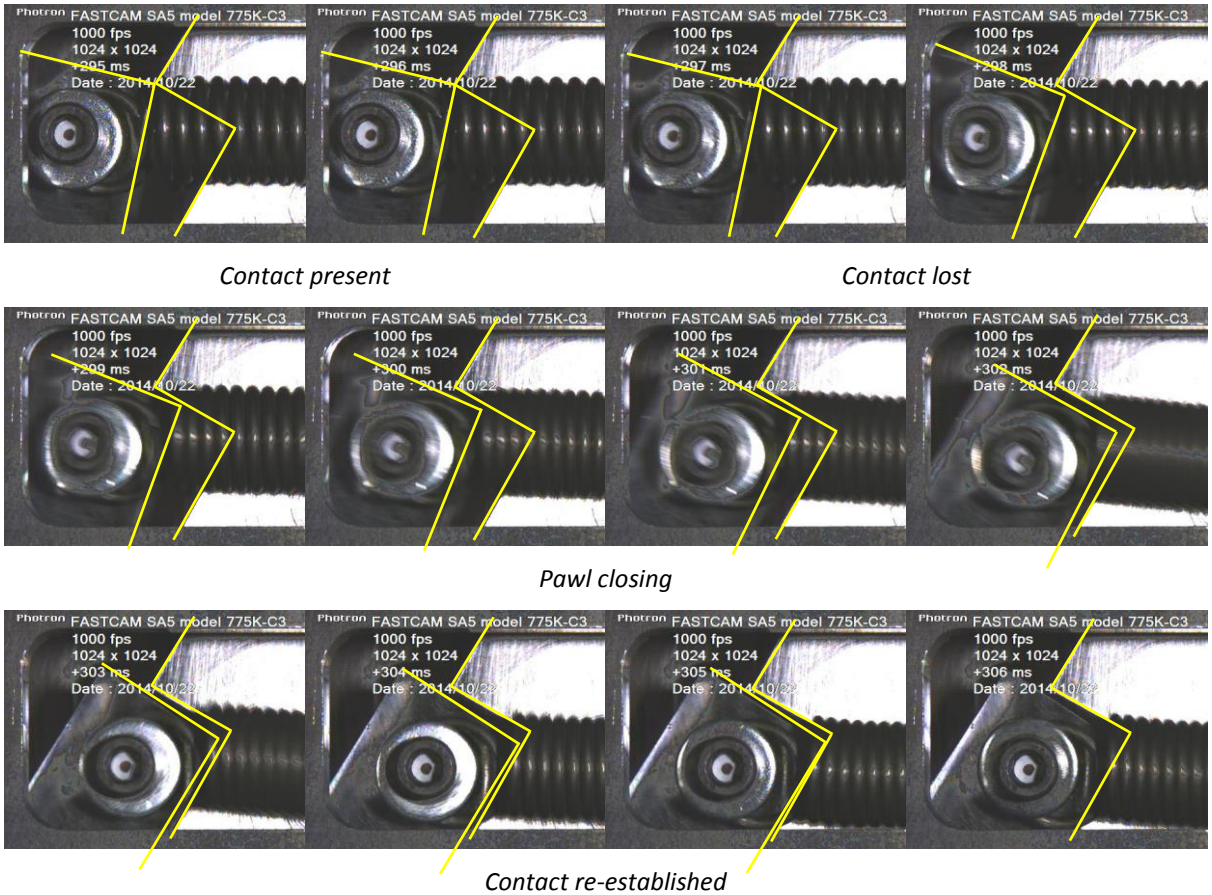

Figure 3.14 *Closure of pawl captured by high speed camera during the M40-100 monotonic test (where each frame is 1 ms apart).The outline of the pawl and rack are highlighted in the first image for clarity, as they are partially obscured by the spring. The section of the device shown here is indicated in* ***Figure 3.13****.*

A summary of the ratcheting mechanism behaviour is provided in **Table 3.4**. It was observed that in general the two pawls did not act perfectly in unison, with the ratcheting action of one of the pawls

lagging slightly behind the other. The closure times for the left and right pawls respectively are shown in square brackets using the format [left, right]. Multiple ratcheting occurrences were observed in some tests and so multiple sets of values are shown in some sections of the table. In **Table 3.4**, bold font indicates the lead pawl, where no specific trend is evident. These differences are thus likely due to natural manufacturing or test variation.

Table 3.4 *Summary of ratcheting mechanism behaviour*

Test Ref.	Individual pawl closure time (ms) [left, right]	Total closure envelope (ms)	Misalignment time (ms)
M40-100	[8, **8**]	9	1
M20-025_2	[**6**, 8] [**7**, 9]	20, 29	12, 20
M20-025_3	[**6**, 8] [**6**, 11]	14, 34	6, 23
M20-050_1	[**6**, 10] [**6**, 9]	41, 42	31, 33
M20-050_3	[**5**, 13] [**5**, 13]	21, 33	8, 20
M20-100	[**5**, 7] [**5**, 7]	22, 16	15, 9
C40-25-0.25	[**7**, 9] [11, **7**]	14, 13	5, 6
C20-15-0.25_1	[**6**, 11] [**5**, 12] [11, **6**]	18, 33, 20	7, 21, 14

The individual pawl closure time represents the time period when contact with the rack is lost as the pawl rotates inward before contact is re-established, while the total closure envelope describes the time from the beginning of closure for the lead pawl to the end of closure for the lagging pawl. The total closure time is sometimes larger than the sum of the two individual pawl closure times, indicating that occasionally one pawl had finished closing before the lagging pawl began to close. The largest total closure envelope was 42 ms. This period of time corresponds to a maximum ram displacement of approximately 4.2 mm during the test involving the fastest ram movement rate of 100 mms^{-1}. This time also represents around 2-4% of the expected 1-2 s period for many common structures, and is thus directly relevant to intended structural applications.

The smallest closure envelope recorded, 9 ms, is representative of a ram displacement of 0.90 mm at the fastest ram speed tested and is approximately 1-2% of the expected period for common structures. With careful design, reloading during the small window where only one pawl is engaged will not prevent tensile load carrying and energy dissipation capacity.

Figure 3.15 shows the misalignment time and the ram speed of each corresponding test. There is no strong correlation between ram speed and misalignment time visible. A range of misalignment times were observed for each ram speed.

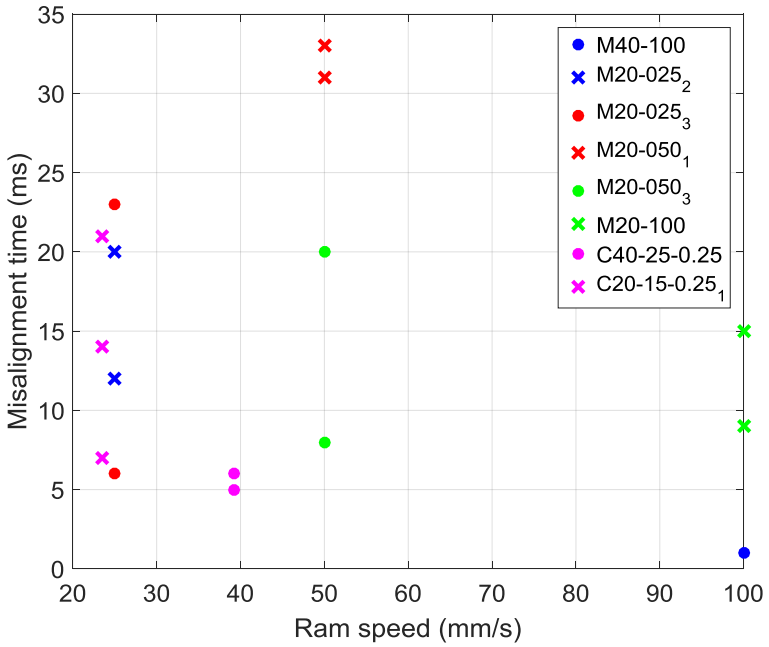

Figure 3.15 Ram speed and misalignment time for the tests captured with high speed camera footage.

This delay between pawl closures is likely due to imperfect symmetry of the pawl positions and the spring. **Figure 3.16** shows a sample of the recorded accelerometer signals from the C20-15-0.25$_1$ test highlighting the insignificance of the discrepancy, as the periods of disturbance for the two accelerometers overlap. Spikes in acceleration coincide with a ratcheting action occurring and there is little acceleration recorded at any other time during the testing. **Figure 3.16**a shows the timing of the ratcheting with respect to the sinusoidal displacement input profile, where the ratcheting action occurs near the bottom of the compressive loading phase. **Figure 3.16**b shows a close up of the accelerometer signals during ratcheting, which indicates that the two signals are closely aligned. This acceleration corresponds specifically to the pawls of the ratcheting mechanism impacting the rack, and not the acceleration of the dissipater or the structure. This acceleration would not be transferred to the structure.

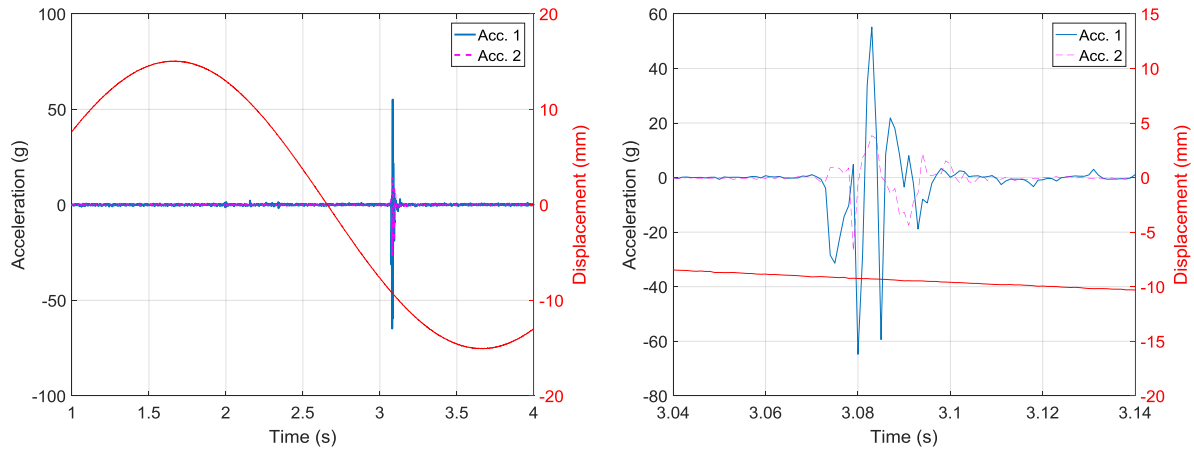

Figure 3.16 *Accelerometer signals taken from C20-15-0.25$_1$ test:*
a) during unloading cycle, and b) close-up of signals during ratcheting

As a result of the minor phase delay, there was a short period of time during which one pawl was aligned one tooth higher on the rack than the other pawl. In very rare cases, a change from compressive to tensile motion in the system during this small time window could cause the rack to be seated on one pawl only. While this misalignment could cause asymmetric forces in the system, sufficient lateral support of the rack will enable reliable force transmission in this case.

During the testing of the GNG1 device, the greatest time period of this misalignment was 33 ms. This rapid engagement is significantly faster than a typical structural period and should not significantly impact performance. With careful design of the main components, the GNG device would be able to safely support the loads of the system through one pawl, in the unlikely occurrence of this misalignment. The use of two pawls in this prototype was to increase the level of redundancy in the system, and a single-pawl design could operate reliably, but with less overall redundancy. Also, further development of the tension spring mechanism, specifically, increased spring stiffness or preload, could reduce or eliminate the period of asymmetry in the two-pawl design.

To reduce any asymmetric behaviour, additional constraints could be fitted in the main support to prevent sideways motion of the rack as it moves through the main support. These constraints would act in the same way as the existing rack supports do to prevent forward and backward motion of the rack, and are shown in **Figure 3.17**. The additional constraints would ensure that the pawls and springs were aligned correctly during operation. It is not expected that such added pieces would significantly affect the complexity or cost of the design.

The misalignment issue was addressed with the improvements made in the GNG2 design, where a compression spring was used to act equally on two collets. The GNG2 design is discussed in detail in Chapter 4. Future designs using the pawl type assembly, which was implemented in the first

prototype, could operate with just one pawl and be supported against the rocking wall or another surface on the other side, removing the misalignment issue completely.

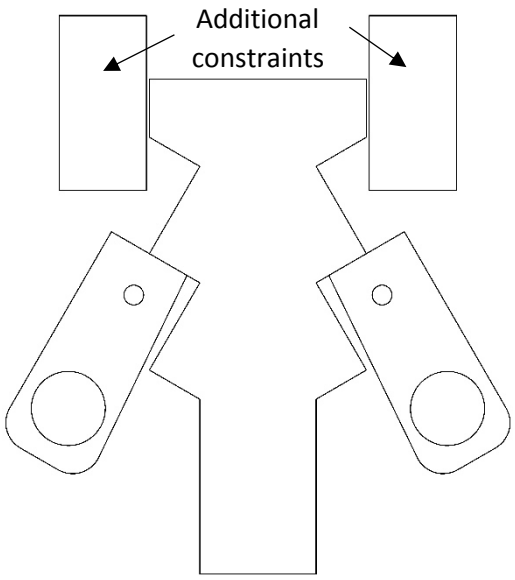

Figure 3.17 *Rack and pawls with suggested placement of additional rack constraints*

3.6. System Overview

To give a better idea of the overall system behaviour occurring during the cyclic testing, **Figure 3.18** shows all of the signals recorded against time for the C20-15-0.25$_1$ test, omitting one of the accelerometer signals as it closely matches the signal that is shown. The hydraulic ram displacement follows a sine wave profile with an amplitude of 15 mm, as programmed into the test machine. Positive displacement in **Figure 3.18** represents tensile motion, corresponding to downward motion of the hydraulic ram in Figure 3.1. The spikes in acceleration of the pawls coincide with the occurrence of ratcheting during compressive displacement of the hydraulic ram.

The ram force increases during the periods of positive displacement, following the expected stages of strain behaviour. During the periods of negative velocity, immediately after the peak displacement point, the ram force decreases, as the elastic strain in the system is recovered. Beyond this point, only negligible compressive force is recorded. There is a region of free-travel, at the beginning of each transition to tensile displacement, immediately after a displacement minima, during which there is no significant hydraulic ram force. This free-travel concept is expected with the GNG device.

This free-travel represents the movement of the rack prior to engagement with the pawls, when it is between teeth. Free-travel is also indicated in Figure 3.6 and Figure 3.7, on the hysteresis loop and the device, respectively. The time period of the region of free-travel is indicated as ‘free-travel time’ for each cycle on Figure 3.18. There is a delay in the engagement of the energy dissipation mechanism during this period of free-travel, and thus, there is no discernible ram force. The elongation of the

dissipater occurs during tensile loading and also experiences a delay in engagement due to the free-travel.

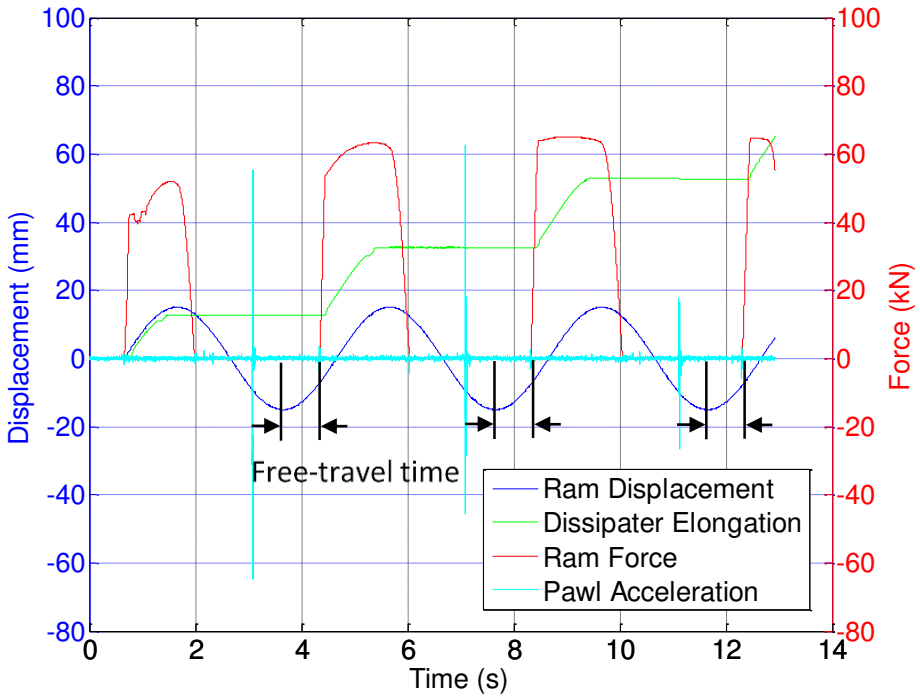

Figure 3.18 *Overview of all recorded signals during C20-15-0.25$_1$ test, indicating free-travel time. The acceleration unit scale is omitted.*

The free-travel is related to tooth pitch. A small tooth pitch, with the resulting smaller teeth, will induce higher contact and internal stresses. However, there will be less free-travel on load reversals and thus less impact loading. Additionally, there will also be a greater accumulation of inelastic displacement demand on the dissipative element due to the smaller ratcheting threshold, resulting in greater energy dissipation. This larger inelastic displacement demand must be incorporated into the dissipater design (such as having a long dissipative element with high inelastic capacity) to avoid early fracture in service.

3.7. Material model algorithm

3.7.1. Menegotto-Pinto material model

A computational algorithm for modelling the hysteretic behaviour of the GNG-dissipater system was created in MATLAB [TheMathworksInc. 2016]. Yielding behaviour of the dissipater was approximated by a bi-linear Menegotto-Pinto material model [Menegotto and Pinto 1973], which was modified to recreate the effect of the ratcheting mechanism. The bilinear response during loading can be defined by:

$$F_{loading} = \frac{K_1(x - x_{reset}) + F_{reset}}{\left(1 + \left|\frac{K_1(x - x_{reset}) + F_{reset}}{F_y sign(\dot{x})}\right|^{\beta}\right)^{\frac{1}{\beta}}} + K_2\langle x - x_y\rangle \quad (3.2)$$

where $F_{loading}$ is the force corresponding to the input displacement x, K_1 is the initial linear stiffness of the material, K_2 is the post yield stiffness of the material, F_y is the yield force, x_y is the yield displacement, x_{reset} and F_{reset} are respectively the displacement and force immediately prior to the most recent change in direction of the input displacement, $\dot{x}$ is the velocity and β is a convergence constant governing the acuteness of the force-displacement curve around the yield point. The values of x_{reset} and F_{reset} are updated for every reversal of the direction of the input displacement, and F_y is updated to take the value of F_{reset} when a load reversal occurs beyond the yield point.

In Equation (3.2), $\langle \quad \rangle$ are Macaulay brackets, indicating that when the value inside the brackets is negative it is replaced by zero. Therefore, when the material is in an un-yielded state, the second term in Equation (3.2) is taken as zero. During unloading, the model follows a linear stiffness line to represent elastic strain recovery. The corresponding force during unloading is defined by:

$$F_{unloading} = K_1(x - x_{reset}) + F_{reset} \quad (3.3)$$

Figure 3.19 gives a schematic guide to the meaning of the terms from Equation (3.2) and Equation (3.3). In **Figure 3.19**, a high value of β has been used for clarity, so yield and load reversal points appear as sharp discontinuities. Lower values of β give a more gradual, rounded-off transition.

Two main modifications to the material response model were required to incorporate the effects of the ratcheting mechanism, and were achieved using conditional statements in the MATLAB function previously developed. The first was to model the absence of compressive forces in the device. This effect was achieved by removing the response for compressive loading that occurs beyond elastic recovery. The second change was the adjustment of the displacement required for engagement of the yielding steel dissipater after ratcheting has occurred, due to the different rack location and shortening of the system. The modified model captures the idealised GNG-dissipater system hysteretic behaviour outlined in Chapter 2 well, and is compared to an experimental result below.

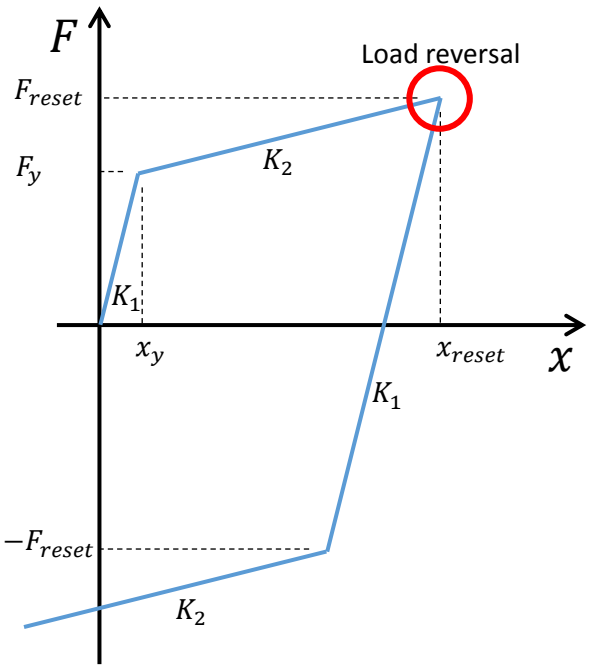

Figure 3.19 *Menegotto-Pinto material model.*

3.7.2. Comparison to experimental results

A comparison between an experimental hysteresis loop and a recreation of the result using the numerical model is provided in **Figure 3.20**. The experimental result shown is from test C20-15-0.25$_1$, which used a 20 mm pitch rack and an input displacement amplitude of 15 mm. The input displacement profile used to produce the numerical result in **Figure 3.20** was $0.015sin\left(\frac{\pi}{2}t\right)$, which mimics the input displacement used in the corresponding test.

There is some visible difference in the stiffness when comparing the experimental and numerical responses. The model was based on an analytical prediction of the stiffness of the dissipater element. The ram displacement is displayed here, and the connections between components in the ratcheting mechanism introduce additional flexibility to the assembled GNG-dissipater system. A slight variation between the true stiffness of the steel used for the dissipater and the stated material properties available is also possible.

The ratcheting behaviour from the experiment is accurately recreated by the model using the displacement input profile and other known parameters, such as the pitch and dissipater material properties. It is noted that the yielding and strain hardening behaviour of the dissipater element is not completely captured by the bi-linear material model due to the highly non-linear behaviour exhibited during yielding of the mild steel used in these tests. However, the numerical result gives a useful

reconstruction of the post-yield behaviour, and is sufficiently accurate to capture the key response mechanisms.

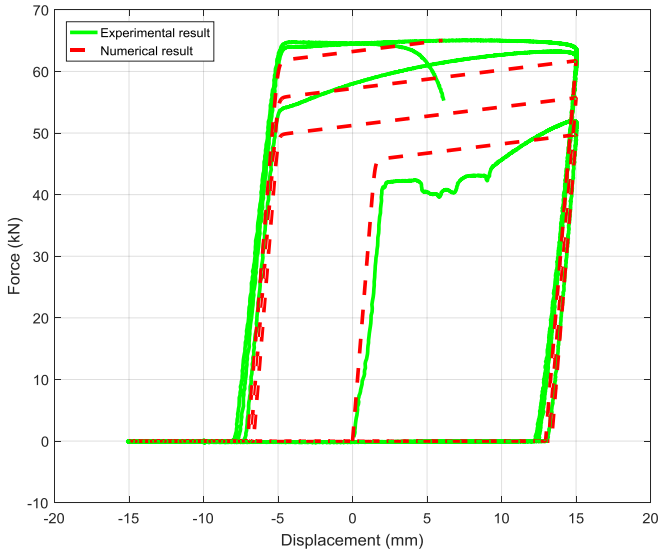

Figure 3.20 *Comparison of experimental and numerical hysteresis loops for the GNG-dissipater system.*

Figure 3.21 presents a comparison of the hysteretic behaviour of just the yielding steel dissipater in the same C20-15-0.25$_1$ experiment, compared to the numerical recreation. The ratcheting behaviour is again well represented with some discrepancies in the post-yield stiffness profile. The dissipater elongation is shown in **Figure 3.22** and a good match between the empirical and numerical results is obtained. The discrepancies in **Figure 3.21** again represent the challenge of approximating the complex, non-linear behaviour of mild steel yielding exhibited in these experiments with a simple bi-linear response model, and a displacement limit is needed to represent dissipater fracture. However, overall, the model provides useful results for design and analysis purposes. Specifically, this hysteretic model provides a means of modelling the GNG-dissipater system response which can be used to undertake dynamic structural simulations to assess performance and displacement demands within the dissipater. This material model algorithm was later recreated as a custom material in OpenSEES and the subsequent simulation work is outlined in Chapters 7 and 8.

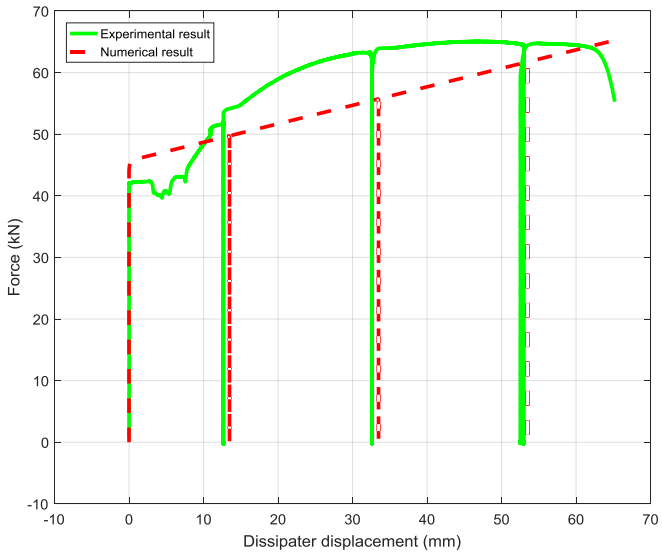

Figure 3.21 *Comparison of experimental and numerical hysteresis loops for the dissipater element.*

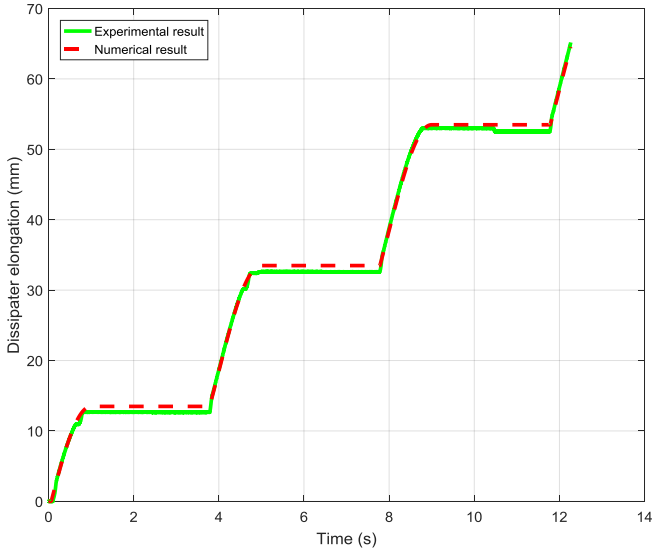

Figure 3.22 *Comparison of experimental and numerically created dissipater elongation behaviour.*

Figure 3.23 shows a comparison of the numerical result emulating experiment C20 15-0.251 with a 20 mm pitch, previously displayed in Figure 3.18, to the numerical results for pitch sizes of 10 mm, 5 mm, and 3 mm, using the same values for other inputs to the model. The response for pitch sizes of 20 mm and 10 mm is the same in this case, using the given simple sine loading cycle, as there is not an additional 10 mm of compressive motion available beyond the last ratchet point, as would be required to achieve a further ratcheting action with the 10 mm pitch device. The response for these two pitch sizes would not always be the same, and an increase in the loading amplitude by a small amount, specifically around 3 mm, would result in an additional ratcheting action on each cycle for the device

with a 10 mm pith size. With the smaller pitch sizes of 5 mm and 3 mm, fracture of the dissipater element occurs within fewer cycles due to the reduction in free travel, which causes extra engagement of the dissipater on each reloading cycle. Approximately the same amount of energy is absorbed by the dissipater in total.

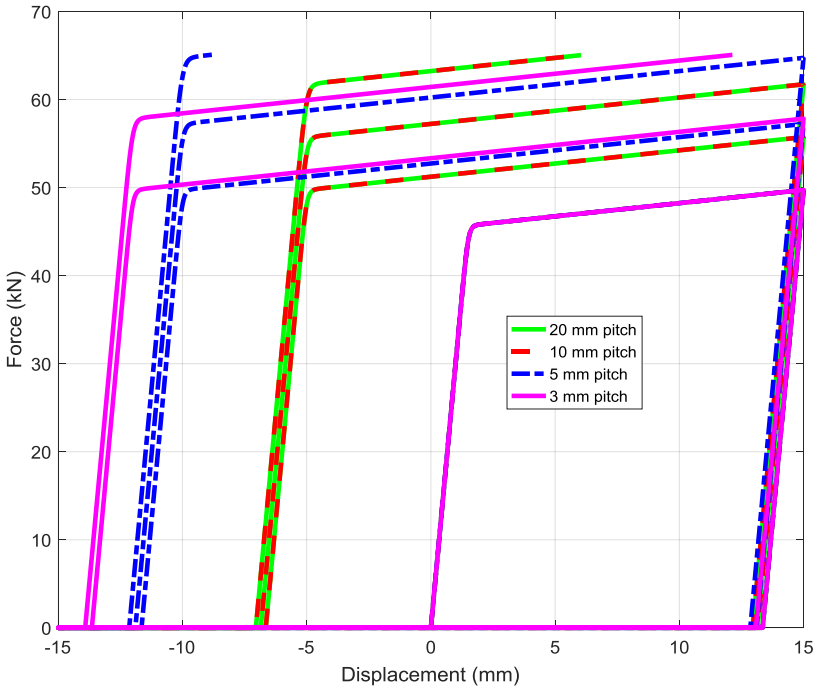

Figure 3.23 *Numerical hysteresis loops for the GNG-dissipater system with 20 mm, 10 mm, 5 mm, and 3 mm pitch sizes.*

3.8. Conclusions

This chapter has described the testing of the initial experimental GNG1 prototype to prove the concept and characterise the response. This initial system was tested with 6 yielding steel dissipaters in a monotonic compression and cyclic testing schedule. Also, a computational algorithm for modelling the hysteretic behaviour of the GNG-dissipater system was created and compared to experimental results. These actions address research questions 2, 3 and 4, and specific outcomes to note are listed for each research question below:

Can the devices respond with appropriate speed of engagement for use during seismic loading of structures?

- High speed camera footage and accelerometer recordings were used to measure engagement timing. The pawls showed rapid engagement, but experienced a short period of misalignment

of less than 33 ms. This brief misalignment is not likely to significantly impact performance during a typical earthquake, and could be addressed in future design developments. Overall, the pairs of pawls acted closely in unison producing solid engagement.

Can the experimental devices exhibit desirable hysteresis behaviour, similar to theoretical predictions?

- The ratcheting mechanism was shown to work as designed, reducing the free-travel prior to engagement on subsequent loading cycles, with the observed hysteretic behaviour closely matching the model presented previously in Chapter 2, with more complex material yielding behaviour observed in the physical system.
- The ratcheting mechanism provided rapid engagement during multi-cycle loading, providing additional energy dissipation capacity to the system.
- Robust, repeatable operation of the mechanism, with redundancy in engagement, was observed.
- 40 mm and 20 mm pitch racks were tested to investigate the experimental performance of these different tooth sizes.
- Six yielding steel dissipater elements were tested allowing peak forces of ~65 kN, with four tested to fracture. As intended by design, the steel dissipater yielded only in tension.
- Furthermore, while the test was cyclic, the dissipater behaviour approximates a piecewise version of a standard monotonic tensile test due to the GNG device removing significant compressive loading in the dissipater. In particular, the maximum compressive forces are limited to less than 2% of the ultimate tensile forces.
- No damage to the assembly beyond the dissipater was observed.
- The system can be designed for use with various other dissipation mechanisms and at higher force levels as required.

Can a model be developed to describe the GNG hysteretic performance, together with that of a rocking wall?

- A bi-linear Menegotto-Pinto material model algorithm was created and adapted to incorporate the ratcheting behaviour of the GNG device. The resulting hysteretic response showed a good match with experimental results, while not capturing the full extent of non-linear yielding behaviour.

- The model was used to recreate test results with a good match in ratcheting behaviour and some similarities in post-yield behaviour, despite the highly non-linear nature of true mild steel yielding behaviour. This hysteretic model provides a means of modelling the GNG-dissipater system response which can be used to undertake dynamic structural simulations to assess performance and displacement demands within the dissipater.

4. Second Prototype Design, GNG2

4.1. Summary

This chapter presents the design of a second, more advanced experimental prototype to develop the capabilities and robustness of the system. The GNG2 prototype device uses axial symmetry and a different engagement mechanism to provide several advantages over the initial prototype and features many changes to the original design, simplifying the assembly process and providing improved performance. In particular, the axisymmetric design is less sensitive to the effect of gravity and can be easily aligned vertically, horizontally, or in an inclined brace, without affecting the response behaviour. Contact occurs at almost 360° around the rack rather than only at two sides, as in the first prototype. This approach allows a greater contact area between the collets and the rack, which enables a smaller tooth pitch while supporting the same tensile loads. It should thus be a more robust design to achieve the same function as the initial device. Furthermore, additional threaded connections were used to reduce the use of fasteners and provide better ease of assembly. This second device was also designed to be tested in the MTS-810 test machine, and a cylindrical steel dissipater is used for the energy dissipation method, as before. A basic stress analysis of the second prototype device design is also presented, focussing on the unique design interfaces and high stress areas.

This chapter further addresses research question 1: Can devices be designed and built to dissipate energy under tensile earthquake loading without carrying compressive loads, and with reduced take-up on subsequent loading cycles to maximise energy dissipation?

4.2. Concept Overview

The second generation GNG prototype device was designed, manufactured and tested. This prototype explored the use of an axisymmetric design to make better use of space and incorporate better inherent alignment of mechanism components. **Figure 4.1** shows an early concept with revolved pawls and a circular rack. This design had issues with interference between the pivoting pawls and the rack teeth. These pivoting issues were removed by evolving the design away from the use of hinged pawls and towards collets to achieve a similar engagement without interference issues, seen in **Figure 4.2**.

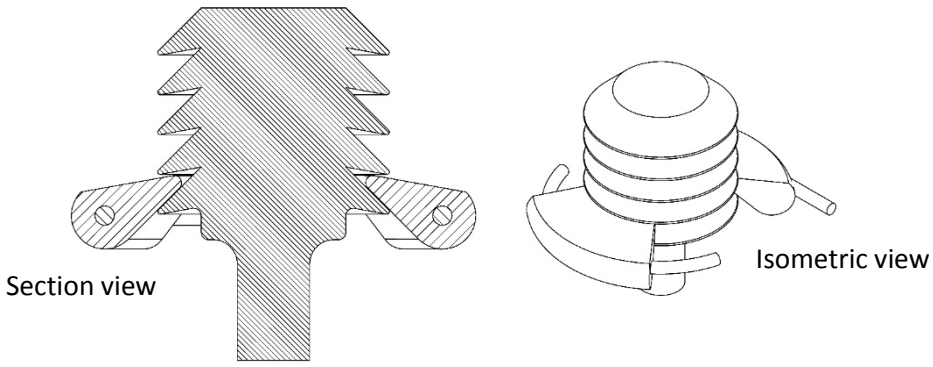

Figure 4.1 *Early axisymmetric GNG prototype design with revolved pawls supported by either a pin or ring*

The ratcheting function of the second device is achieved by two collets, which are analogous to the pawls used with the first, linear prototype design presented in Chapter 2. A compression spring acts upon the collets, which tighten around a circular rack with stepped teeth, and rest on a collet guide, as shown in **Figure 4.2** and **Figure 4.3**. Larger, easily constructed pitch sizes were used with the initial prototype to provide extremely robust engagement during proof of concept testing. After achieving a solid proof of concept response with the GNG1 prototype, smaller pitch sizes will be investigated to reduce free travel further and maximise engagement of the dissipative element. Racks with two different pitch sizes, 10 mm and 3 mm, were fabricated. Threaded connections were used for some parts in the second prototype assembly to reduce the use of fasteners and provide better ease of assembly. In this revised prototype, the collets are not hinged as the pawls were in the GNG1 device. Instead the collets are seated on a tapered base, which aligns them against the rack.

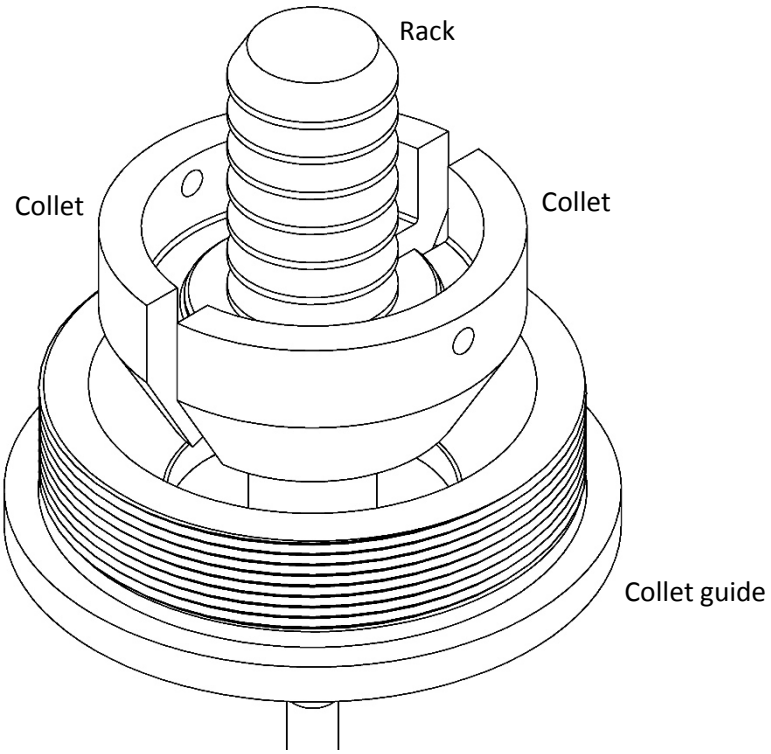

Figure 4.2 *Partial assembly with collet guide, collets and rack*

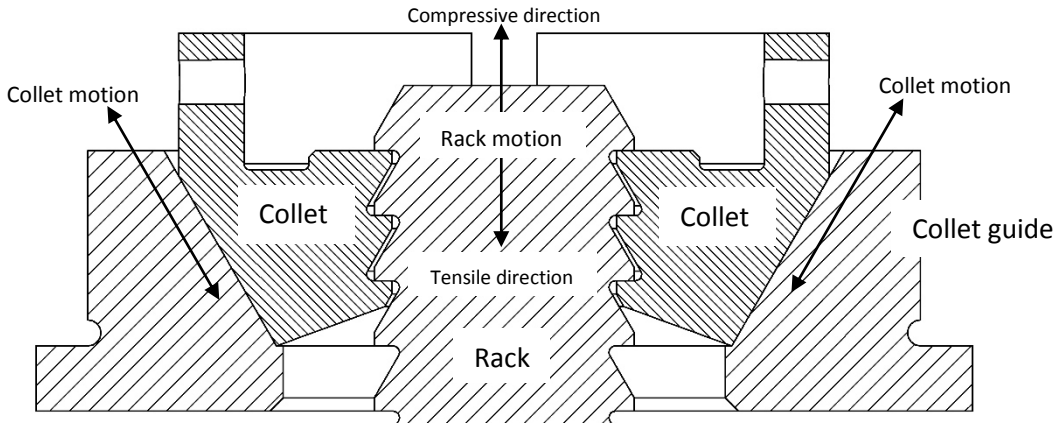

Figure 4.3 *Second prototype concept with rack and two collets, showing motion of parts*

A collet guide with a tapered bore is used to align the collets. In tension, the teeth on the rack lock with the teeth on the collets to engage the energy dissipation mechanism. The engagement is self-stabilising, where initial engagement provides a clamping force between the collets and the rack. As the tension force increases, so does the clamping force between the collets and the rack.

During compressive loading, the angled faces of the teeth on the rack and collets cause the collets to move outward as they move up the collet guide taper, while allowing the rack to slide past with minimal resistance. **Figure 4.4** shows the engaged position of the collets during tensile motion on the left, in contrast to the collet position immediately prior to a ratcheting action during compression, as seen on the right.

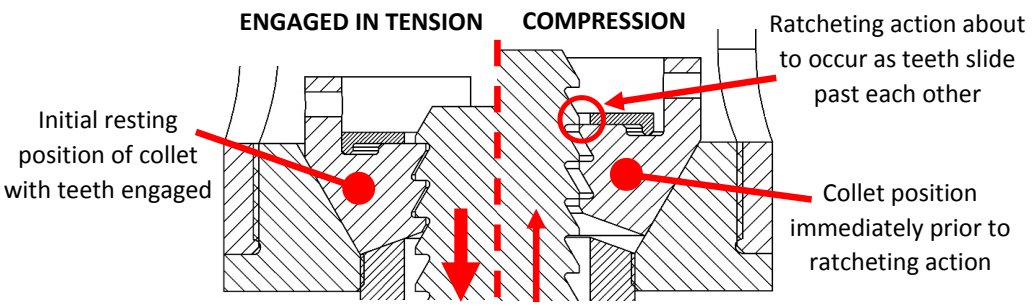

Figure 4.4 Engaged collet position shown on left and collet position immediately prior to ratcheting on right.

Figure 4.5 shows an exploded view of the GNG2 assembly and the load paths in the device during tensile loading. Tensile forces in the dissipater are transferred from the rack into compressive forces in the collets and then into the tapered collet guide. A compression spring resting atop the collets keeps them inside the collet guide, ensuring they slide on the rack during compressive motion. The spring also aids the return of the collets to a lower position to re-engage with the rack during subsequent tensile loading. At the lower end, the spring is seated on a washer that rests inside the two collets, and at the top end the spring is located by a boss on the cover plate, which sits inside the spring and is indicated on **Figure 4.5**. The collet guide and cover plate are threaded into the main support body, which uses a modified tube profile for simplicity and cost effectiveness.

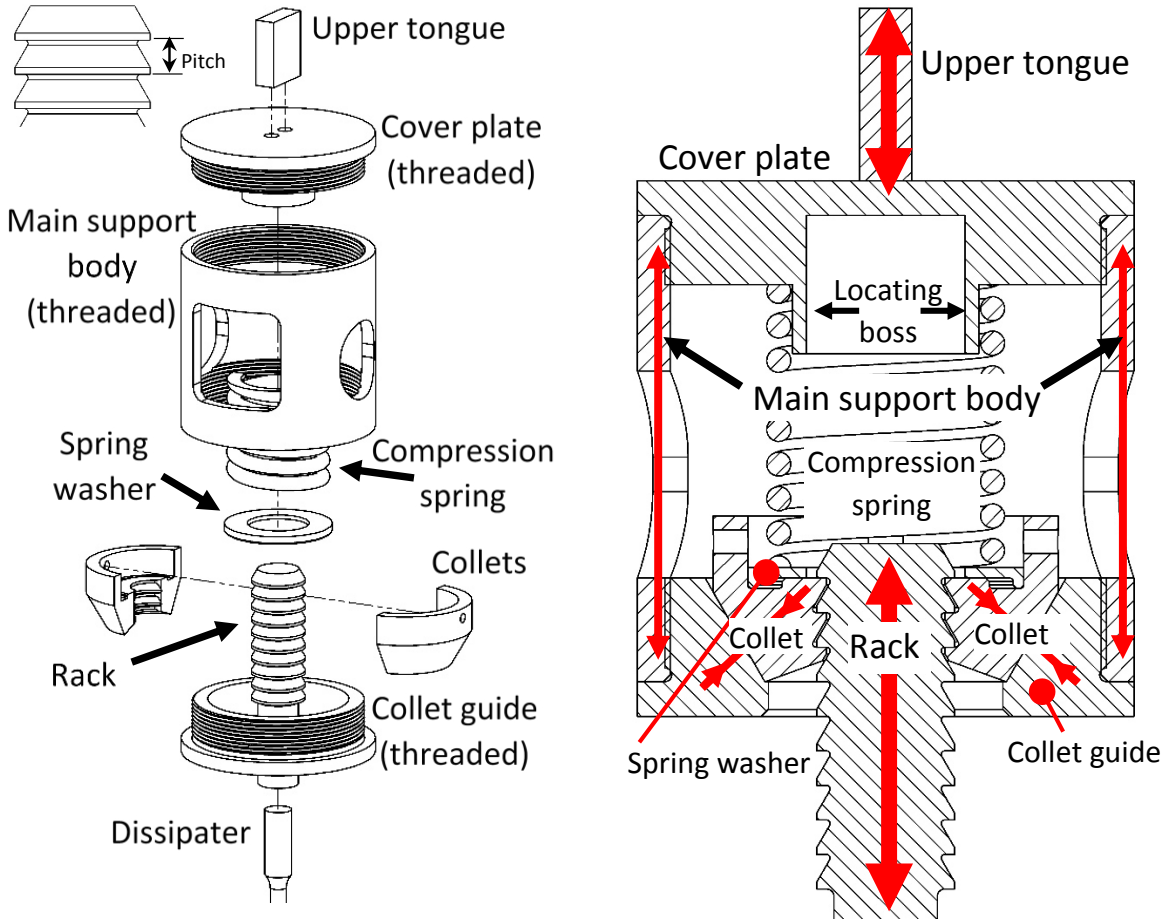

Figure 4.5 *The second GNG prototype:*

a) Exploded view, and b) approximate load paths during tensile engagement of the dissipater element (tension ←→ and compression →←).

The axial symmetry of the design makes better use of space, compared with the first design. This approach allows a greater contact area between the collets and the rack, which enables a smaller tooth pitch. The 10 mm pitch design uses three contact faces on each collet. Hence, three sets of teeth are engaged, providing more reliable and robust engagement.

The additional contact area allows for a smaller tooth pitch on the rack, in particular, without increasing contact stresses. A reduced pitch increases energy dissipation capability due to more rapid engagement and a smaller displacement threshold that must be exceeded to induce ratcheting. However, the trade-off is that the finer pitch also increases the cumulative plastic displacement demand in the dissipater, which must be considered in the design.

Both prototypes utilise a self-stabilising engagement mechanism. A spring force is used to provide initial engagement before tensile loading forces provide an increased clamping force, ensuring robust and reliable engagement in field structures. The GNG2 prototype uses a single spring acting on both of the collets. This design adds robustness and a reduction in complexity compared to the previous

design, which used two tension springs acting between the pawls. Using less parts will make the GNG2 prototype easier to assemble and may give cost savings. The designs were refined to provide ease of manufacture, eliminating complex and expensive processes, to reduce the overall construction costs. A section view of the full design assembly is shown in Figure 4.6.

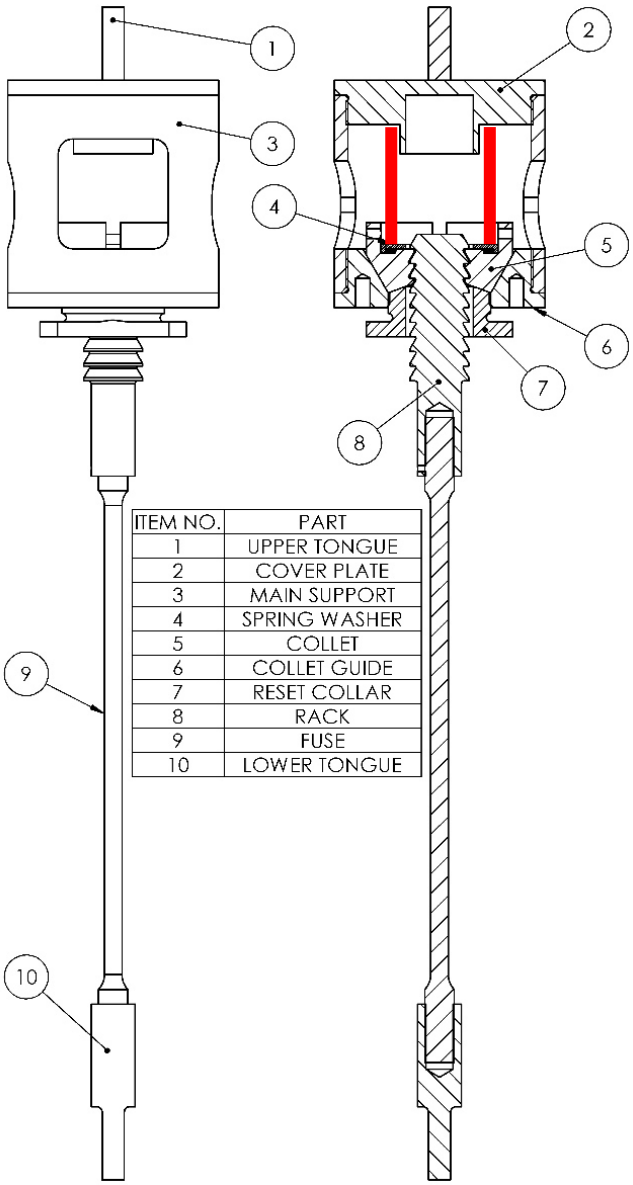

Figure 4.6 *Second prototype GNG assembly with front view on left and section view on right. The location of the compression spring is shown in red on the right.*

As with the first prototype, sacrificial damage is isolated so it only occurs in the dissipater element, which is threaded into the rack and lower tongue. The same dissipater element design from Chapter 2 was used for the testing of the second prototype to provide a direct comparison of response. The dissipaters again underwent a full annealing cycle at Heat Treatments Limited (Auckland, New

Zealand) to ensure maximum ductility. The same rectangular tongues from the first prototype were used for mounting in the test machine.

AISI 1040 steel was used for several components, including the yielding dissipater elements, with AISI 4140 or equivalent used in places to ensure durability of the non-yielding components. The main support makes use of a modified tube profile for simplicity and cost effectiveness. A complete assembly drawing of the second prototype device, with the spring omitted for clarity, is shown in Appendix A2, along with full manufacturing drawings for the required parts.

4.3. Design Overview

4.3.1. Dissipater Subassembly

The overall function of this second GNG prototype design can be described by two subassemblies that interact to provide the desired system response. One is the dissipater subassembly, which is similar to the one used with the initial prototype in Chapter 2, with the exception of the changes to the rack design. The three parts in this subassembly are the lower tongue, the dissipater and the rack, all of which are shown in **Figure 4.7**.

Figure 4.7 *Dissipater subassembly*

The rack is circular with an M20 fine pitch tapped hole at one end for securing the dissipater. The remainder of the rack contains the teeth, which interact with the collets to create engagement between the two subassemblies. A detailed view of the rack-collet tooth interface is presented in **Figure 4.8**.

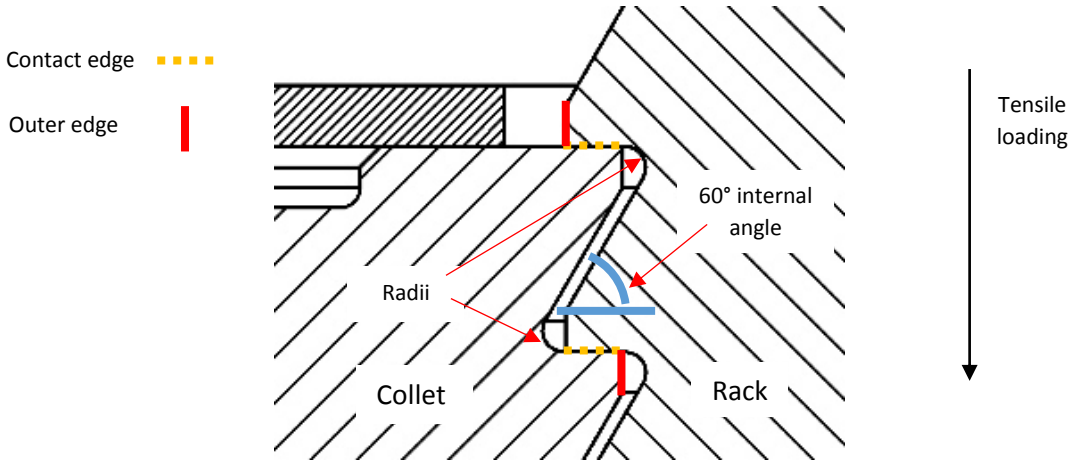

Figure 4.8 *Rack-collet tooth interface*

The design of the teeth for the axisymmetric prototype contains a horizontal contact edge to provide secure engagement. The faces of the rack and collets meet flush perpendicular to the direction of the loading on the device. A 60° internal angle is used to give a suitable taper for the rack to push the collets outward as it moves up into the main support during compressive loading, delivering the ratcheting action as required.

The radii on the inside of the profile minimises stress concentration and removes the need for specialised tooling to create the geometry, as it can be matched to common lathe tool radii. A flat outer edge is left on the outside of the tooth profile for simplicity and to avoid a tight fit, which could jam when fitted into the collets. The collet tooth design has the same profile rotated 180° to interlock with the rack teeth.

Two racks were designed, with pitches of 10 mm and 3 mm respectively, offering a reduction from the 20 mm and 40 mm pitch sizes in Chapter 2. A pitch size of 3 mm was considered as a suitable minimum pitch size to allow for easy and prompt manufacture of the prototype devices locally, while avoiding significant stresses in the parts due to small radii and features. Smaller pitch sizes could be produced if required. The 3 mm size represents the interface approaching the fine resolution of a friction type interface, but with enough initial contact to ensure reliable engagement. In contrast, the 10 mm pitch thus tests a reasonably easily achieved pitch offering good, fine resolution and thus greater potential dissipation.

Several options were considered for the collet-rack interface, including the use of a helical thread-like connection between the two parts. This thread-like profile would provide the ability to adjust or reset the zero displacement position of the rack by threading the rack into or out of the collets, without the need to remove the cover plate or adjust other components. Various thread types could be considered, including knuckle-like threads, ACME or custom threads. Part of a threaded assembly is

shown in **Figure 4.9**a and several thread types are presented in **Figure 4.9**b. A rack-collet interface with a metric thread was constructed during development of the prototype. However, the metric thread caused difficulty disengaging the collets from the rack. The stepped interface selected is an effective solution and is simple to manufacture without requiring custom tooling.

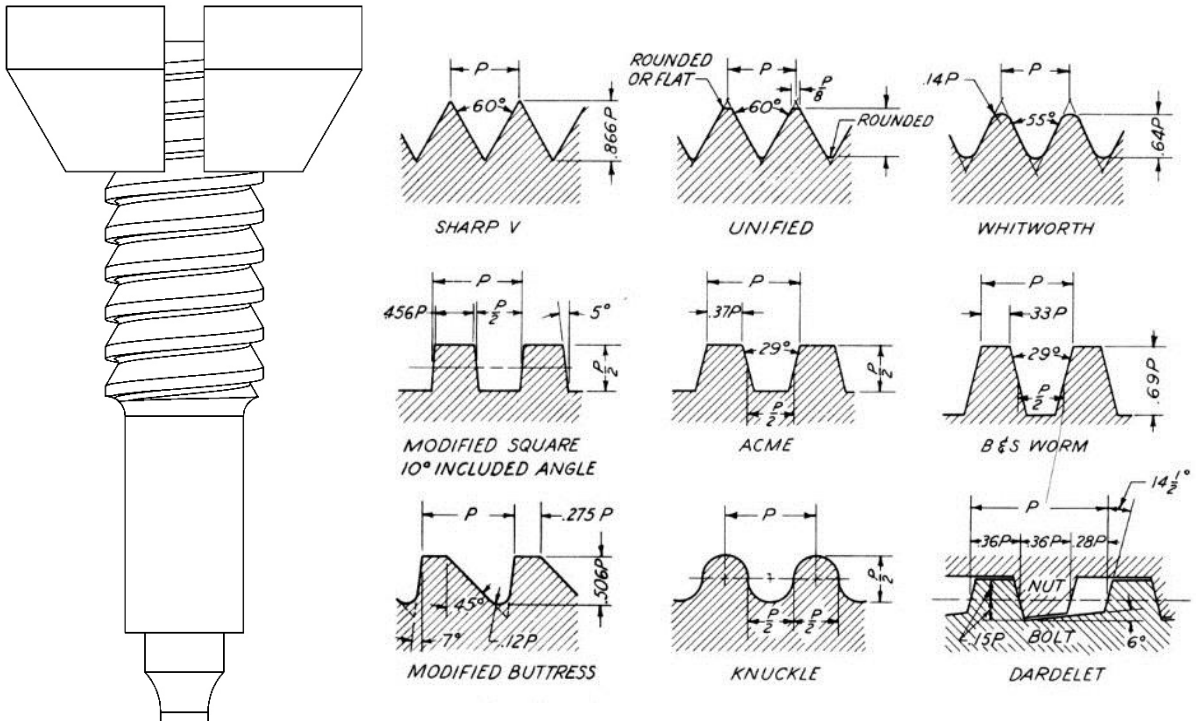

Figure 4.9 *Collet-rack thread like interface:*

a) example design, and b) selected available screw thread types

4.3.2. Collet Subassembly

The upper subassembly is the collet subassembly. Analogous to the pawl subassembly in the initial design, this subassembly contains the revised ratcheting mechanism. The parts in this subassembly are the upper tongue, cover plate, main support, collet guide, two collets, spring-bearing washer, and reset collar. These parts are shown previously in Figure 4.5 and Figure 4.6.

The upper tongue is identical to that presented in Chapter 2, and shown in Figures 2.6 and 2.7, and is attached to the cover plate via cap screws. The cover plate connects the upper tongue to the main support body, which holds the components of the ratcheting mechanism. An M125x3 mm threaded connection is used to join the cover plate and the main support body. The cover plate also includes a circular boss to locate the top of the compression spring. This boss is hollowed out in the centre to accommodate extra movement of the rack through the main support. These features are visible in Figure 4.6.

The main support is a modified 125 mm bore tube section, shown in Figure 4.10. A large central slot allows viewing of the spring and collets in operation, as well as viewing of the rack as it moves through the main support. Two side slots provide access to attach accelerometers to the collets for data acquisition. These slots will also enable access to the collets to hold them clear of the rack and allow resetting of the device, as described later in this section. These slots are primarily included for the research tests and may not be required for field usage of the system. In applications that require more ratcheting actions, and therefore a longer rack, it will be necessary to design additional space inside the main support body to allow for the movement of the rack during operation.

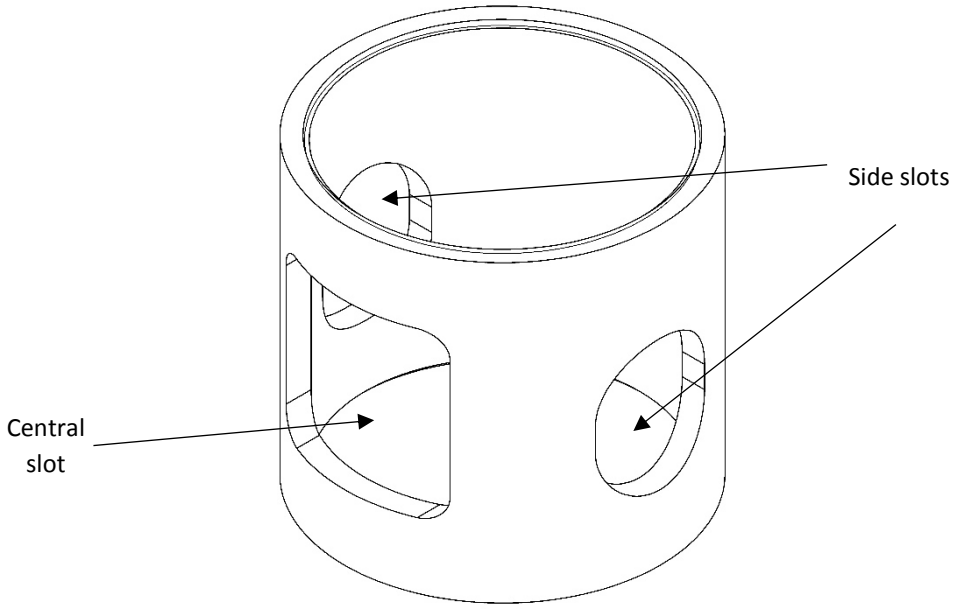

Figure 4.10 *Main support body with central and side slots*

A collet guide threads into the bottom of the main support via an M125x3 mm thread and locates the collets. A tapered bore is used to align the collets, restricting their motion and guiding them to move upward and outward when pushed in compression. The collets rest inside the collet guide and contain a complimentary tooth profile to that cut into the rack, allowing them to engage together during tensile loading.

Importantly, the larger the tensile force, the greater the clamping force between the rack and collets such that the locking interface is self-stabilising. The interface can be seen in Figure 4.3 and Figure 4.8. With the second GNG prototype, it should be noted that a different set of collets is required for each rack pitch variation.

The collets contain a channel to fit the spring-bearing washer, and also have a large shoulder at the top to locate the compression spring. These features can be seen in **Figure 4.11** and **Figure 4.12**. **Figure 4.11** presents an isometric section view as a way to see the parts held inside the main support.

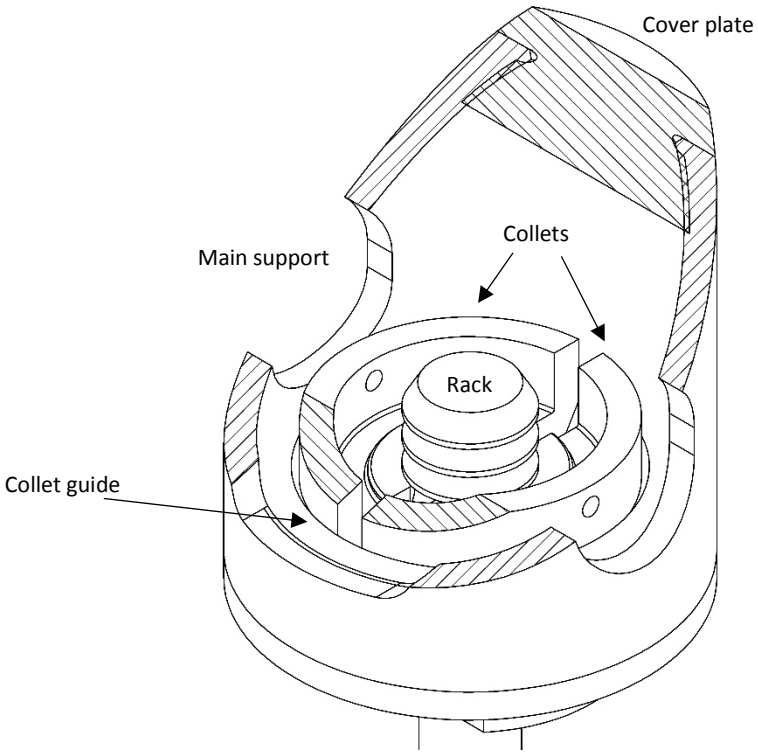

Figure 4.11 *Isometric section view of second generation assembly with spring-bearing washer removed*

A tapped hole through the shoulder on each collet is included in the prototype to assist outward lateral movement of the collets when resetting the device between experiments. To remove or reposition the rack and reset the device, the collets need to be held clear of the rack. This clearance could be achieved by using a bolt or threaded rod to pull the collet out towards the side of the main support. The collet is raised as it moves along the taper of the collet guide. The position of the bolt for this method is shown on **Figure 4.12**. This method is considered as a secondary option to the use of the reset collar shown in **Figure 4.12**, and is explained later in this section.

The spring-bearing washer is included to allow the spring to rotate while tightening the cover plate that secures the spring at the top end. The spring-bearing washer also holds the collets at an appropriate separation, to ensure they interact correctly with the rack, and helps to prevent excessive outward motion of the collets via a shoulder which catches on the channel cut into the collets. This shoulder also prevents the washer from sliding out of position and interfering with the rack or getting caught under a tooth on the rack. The spring-bearing washer and the collet channel are shown in Figure 4.12.

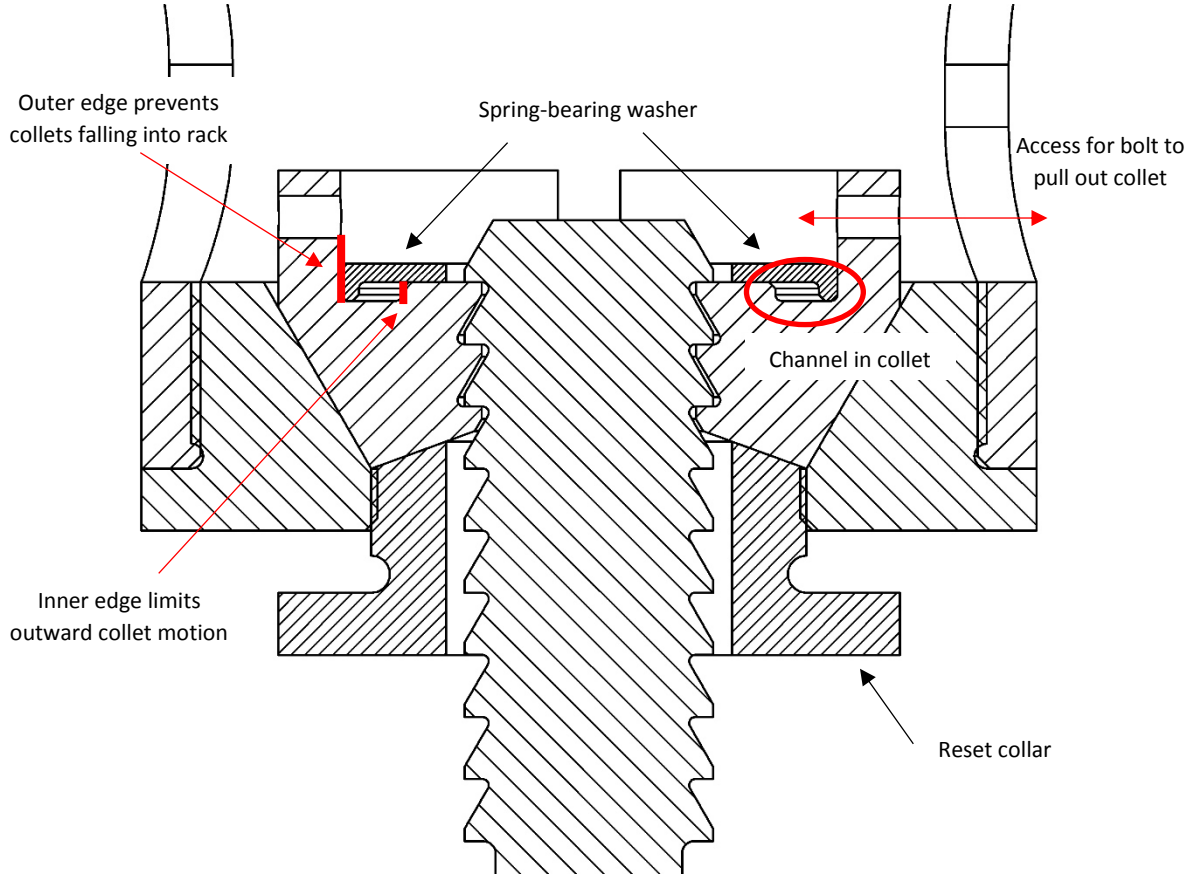

Figure 4.12 *Ratchet assembly showing spring-bearing washer and collet reset access*

The reset collar, visible in Figure 4.12, is threaded into the collet guide and can be screwed upward to push the collets outward and clear of the rack using a tapered region at the top of the reset collar. Figure 4.13 shows the reset collar in a tightened position with the collets held clear of the rack. This function is useful to allow the rack to be removed from the main support during testing to reset its position without having to disassemble the whole device and remove the compression spring. This simple removal is not otherwise possible due to the engagement of the collets during tensile loading, and may also be advantageous after an earthquake, to reset a device or when the dissipater is changed.

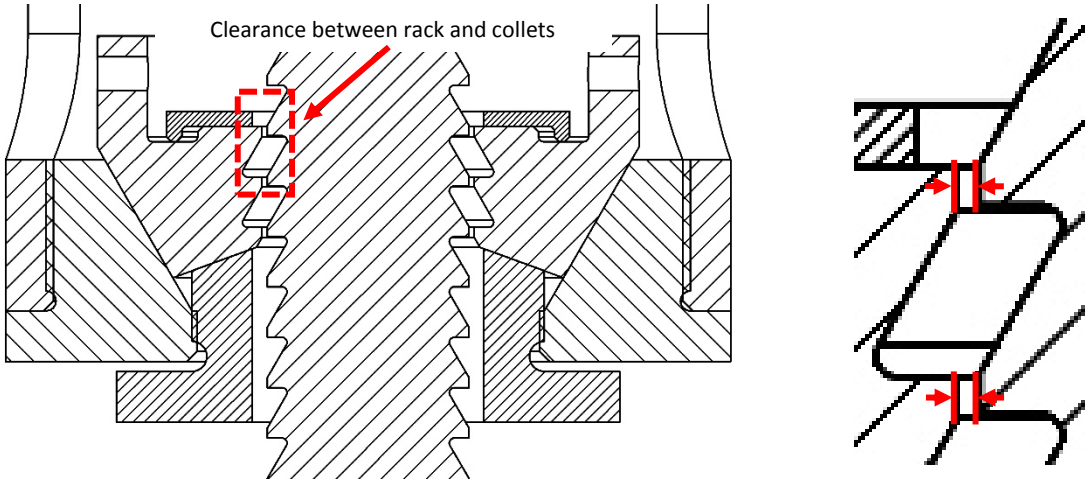

Figure 4.13 *Collet position with reset collar tightened to provide clearance between rack and collets and allow for simple rack adjustment:*
a) system cross-section, and b) close up of clearance.

As discussed earlier, a helical, thread-like collet-rack connection, in place of the stepped interface used, could remove the requirement for the reset collar. With the thread-like connection, repositioning of the rack within the collets could be done by a simple rotation. However, this choice adds significant complexity and thus cost to the device manufacture and fabrication.

4.3.3. Compression spring

To ensure initial engagement of the ratcheting mechanism, a compression spring is fitted in the device and rests against the spring-bearing washer at one end and around a boss on the cover plate at the other end. This spring limits the range of motion of the collets and holds them in a suitable position for engagement with the rack. One end of the spring rests against the spring-bearing washer, which sits on both of the collets. The use of a single compression spring, held firmly in place and acting on both collets, helps to ensure the collets act closely in unison and avoid the slight lag that was experienced by the pawls with the initial prototype in Chapter 3. This design should prevent misalignment and thus improve robustness.

The compression spring used with the second prototype was made to order by CMI springs in Christchurch and had the approximate properties shown in Table 4.1. The free length of 92 mm allows for a pretension force on the spring-bearing washer and collets of approximately 250 N, as the spring is compressed to 82 mm when fitted in the device. A further 250 N of force is estimated to be required to move the collets by an additional 10 mm to allow ratcheting to occur in the 10 mm pitch rack case.

Table 4.1 Compression spring properties

Property	Value
Internal diameter	55 mm
Wire diameter	7 mm
Free length	92 mm
Spring rate	25 Nmm^{-1}
End condition	Closed and ground

The use of a compression spring, located firmly in the device, removes any misalignment due to gravity. The prototype can thus be used in any orientation, provided the weight of the collets is offset by the spring force. However, the weight of the collets is small and an ample spring force could easily be specified to maintain correct positioning without any special spring being required.

4.4. Design analysis

This section presents a basic stress analysis of the GNG2 prototype device design, focussing on the unique design interfaces and high stress areas. The load paths through the ratcheting mechanism are discussed, followed by simple stress calculations at regions of interest. The discussion is focussed on the ratcheting mechanism assembly that is unique to the GNG, and not the details of the dissipater. The ratchet mechanism is viable to use with a range of energy dissipation mechanisms, including yielding steel, friction connections and extrusion devices. Due to the wide range of possible energy dissipation options, this component of the system is not considered here and is left open for special considerations based on individual applications.

4.4.1. Load Paths

During testing of the GNG2 prototype, as detailed in the following chapter, tensile forces are introduced to the system via downward displacement of the lower tongue, which is gripped in the hydraulic ram of the MTS test machine. The greatest design force considered in the system is equal to the ultimate tensile force of the dissipater (F_{UTS}). This value is used as the true strength of the dissipater, and over-strength factors could be included to ensure a capacity design where failure occurs only in the desired dissipative region when the device is added to a structure. The transmission of tensile forces through the second prototype assembly is given by the following load path, with the forces through the upper section of the assembly presented in Figure 4.14:

- Input displacement to lower tongue via hydraulic gripper (tension)
- Lower tongue to dissipater element via threaded connection (tension)

- Dissipater element to rack via threaded connection (tension)
- Rack to collets via tooth interface (compression)
- Collets to collet guide via taper interface (compression)
- Collet guide to main support body via threaded connection (tension)
- Main support body to cover plate via threaded connection (tension)
- Cover plate to upper tongue via cap screws (tension)
- Upper tongue to stationary upper machine crosshead via hydraulic gripper (tension)

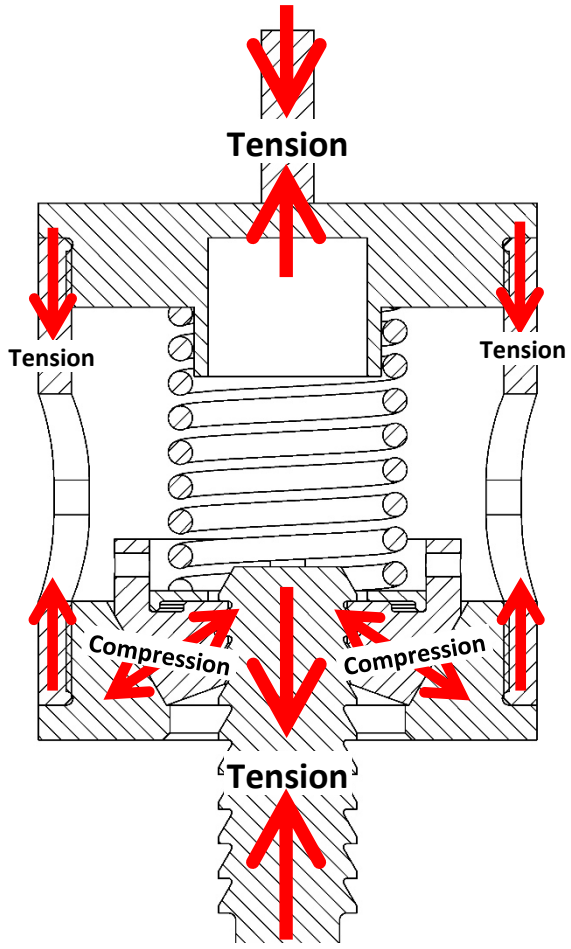

Figure 4.14 *Approximate load path for tensile forces through second prototype GnG device.*

Noting similar practical in-situ requirements to those for the first prototype, where mounting components are specific to the test machine, this design assessment is limited to the general ratchet mechanism parts of the full assembly. In practice, the cover plate may be used solely to provide a compression force on the spring, while the forces in the system could be transferred from the device

to the structural frame via a modified main support body. Therefore, tensile forces may not have to pass through the top cover plate in a field deployment of this device.

The main support body and the collet guide are connected via an ISO metric thread. Stress areas for ISO metric threads can be calculated using the thread diameter, pitch and engagement length, to ensure this connection is sufficient for the design force. However, this procedure is not unique to this design and so is not considered in detail. A brief overview of thread stripping is provided. The unique interfaces in the second ratchet mechanism system are the interface between the rack and the collets, and the interface between the collets and the collet guide. As such, these interfaces will be discussed in more detail.

4.4.2. Collet to collet guide taper surface

The collet to collet guide interface is via the contact of the tapered surfaces of the two parts. When correctly aligned, the transmission of forces between these two parts occurs over a large contact area. This large area induces only small stresses in the two parts. Figure 4.15 shows the collet to collet guide interface, where the right edge of Figure 4.15 represents the centreline of the assembly. The length of the contact region between the collet and the collet guide is rotated around a total angle (θ) of ~160° for each collet. Each collet encloses an area of less than 180° to allow for the collets to lock securely onto the rack and avoid interference between the two collets. The quotient $\frac{\theta}{180°}$ in Equation (4.1) represents the fraction of a total revolution included in the area calculation, accounting for the collet split.

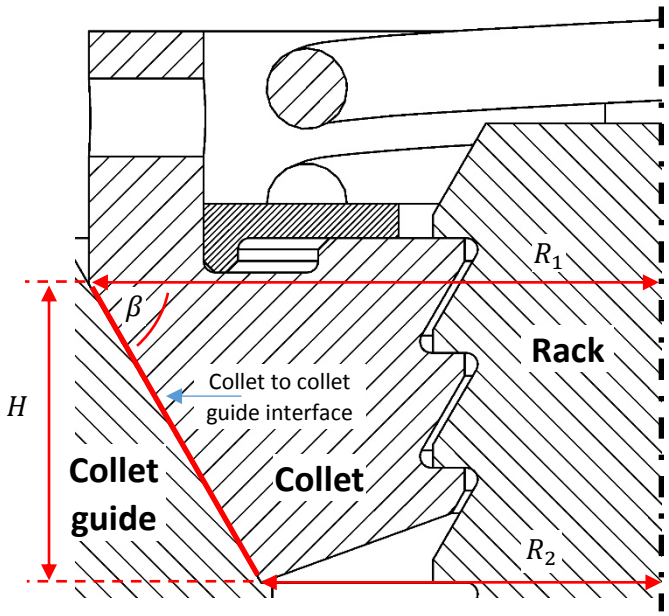

Figure 4.15 *Collet to collet guide interface.*

In Figure 4.15, H represents the height of the collet to collet guide interface and β is the angle of the taper. The radius from the centre of the rack to the outer edge of the collet to collet guide contact area is R_1 and the radius to the inner edge of the contact region is R_2. The contact area for each collet is:

$$A_{contact} = \frac{\theta}{180°} 2\pi \left(\frac{R_1 + R_2}{2}\right) \frac{H}{sin(\beta)} \tag{4.1}$$

Due to the taper angle β, the force perpendicular to this contact area is:

$$F_{collet} = \frac{F_{UTS}}{2cos(\beta)} \tag{4.2}$$

and the associated induced stress, assuming the load is shared evenly between the two collets, is approximated by:

$$\sigma_{collet\ interface} = \frac{F_{collet}}{A_{contact}} \tag{4.3}$$

4.4.3. Rack-collet Interface

From a stress perspective, the main point of interest in the second assembly is the rack to collet interface. Crushing and shearing failure mechanisms may occur at this interface, similar to the rack to pawl interface in the first prototype design. Shear of the teeth could potentially occur in the rack and also in the collets. The crushing and shearing interfaces are shown in Figure 4.16, where the right edge of Figure 4.16 represents the centreline of the assembly.

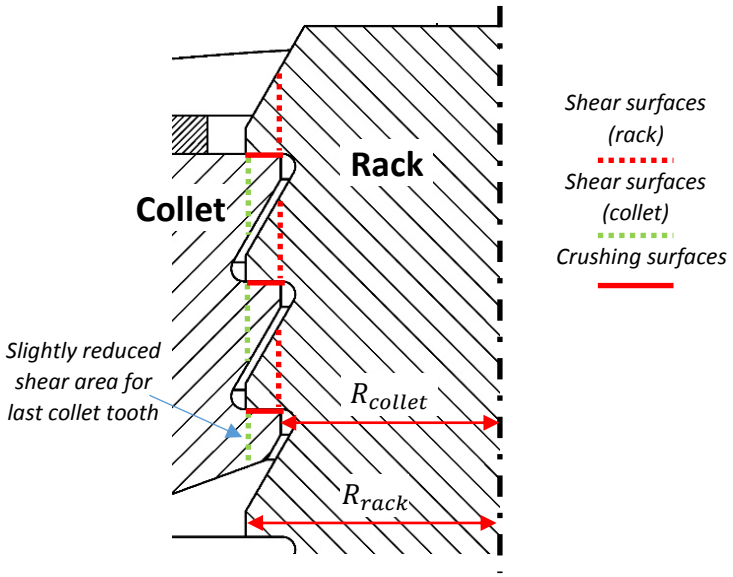

Figure 4.16 *Rack and collet interface.*

Contact between the teeth on the rack and the collets occurs on the bottom edge of the tooth, in the region between the shear surfaces of the rack and collets. The contact area for each set of teeth is enclosed by an annulus profile, where the two radii are defined by the outer radius of the rack (R_{rack}) and the bore radius of the collets (R_{collet}). There are 3 sets of teeth in contact for the 10 mm pitch GNG2 setup shown in Figure 4.16. However, the number of engaged teeth could easily be adapted in future designs, and the number of teeth engaged is represented by η in Equation (4.4). The crushing stress in the rack or collet teeth can be approximated by:

$$\sigma_{crushing} = \frac{F_{UTS}}{\eta \times \frac{2\theta}{360°}\pi\left({R_{rack}}^2 - {R_{collet}}^2\right)} \tag{4.4}$$

Figure 4.17 shows the detail of the tooth profile of the rack, with relevant quantities labelled. The vertical height of the shear area is equal to the tooth thickness at the outer edge of the rack, for shear of collet teeth, and the tooth thickness at the inner edge of the collet, for shear of rack teeth. These thicknesses are the same due to the tooth symmetry.

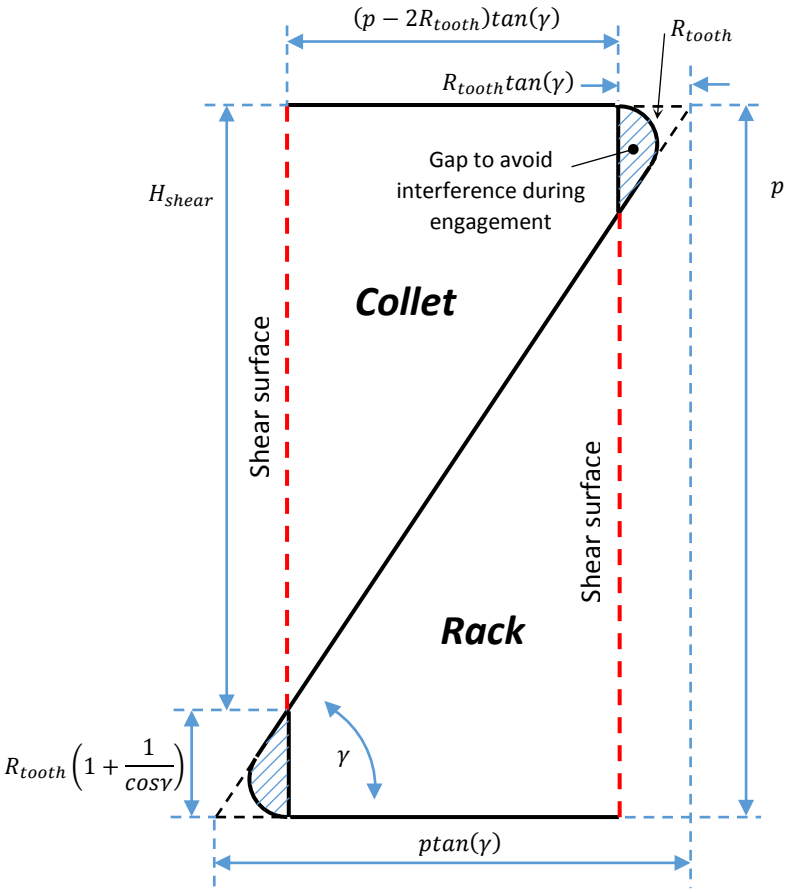

Figure 4.17 *GNG tooth profile detail.*

The vertical height of the shear surface for each engaged tooth is equal to:

$$H_{shear} = p - R_{tooth}\left(1 + \frac{1}{cos\gamma}\right) \quad (4.5)$$

where R_{tooth} is the radii on the tooth profile and γ is the tooth angle, both labelled in Figure 4.17. A tooth angle of 60° was used in the GNG2 prototype, and applying this value to Equation (4.5), the bracketed term becomes equal to 3.

The vertical height of the shear surface is then multiplied by the arc length at the radius of the shear surface from the centreline of the assembly to find the shear area. The enclosed angle of the collet (θ) can be used to find this arc length as the collet is not a complete closed revolution like the rack, due to the splitting of the collets to allow for ratcheting motion. The quotient $\frac{2\theta}{360°}$ in Equation (4.6) and Equation (4.7) represents the fraction of a total revolution included in the area calculations, accounting for the collet split.

In the GNG2 prototype constructed, the bottom tooth of the collet does not have a complete tooth profile and so has a slightly reduced shear area, as indicated in Figure 4.16. This feature was included as part of the interface with the reset collar, and a future design could easily be adapted to provide equal shear area for each tooth in contact, or more contact interfaces, if required. In Equation (4.6) and Equation (4.7) the number of teeth engaged is represented by η.

The shearing stresses in the rack and the collets, respectively, are approximated using dimensions from Figure 4.16 and Figure 4.17:

$$\tau_{rack} = \frac{F_{UTS}}{\eta \times \frac{2\theta}{360°} 2\pi R_{collet}(p - 3R_{tooth})} \quad (4.6)$$

$$\tau_{collet} = \frac{F_{UTS}}{\eta \times \frac{2\theta}{360°} 2\pi R_{rack}(p - 3R_{tooth})} \quad (4.7)$$

4.4.4. Thread stripping

Several threaded connections are included in the second prototype design. The strength of threaded connections is a standard design consideration, and so is not discussed in detail here. Instead, a brief introduction to failure of connections via thread stripping is given.

When the male and female parts of a threaded interface are made of the same material, both threads will strip simultaneously and the failure will occur at the pitch line [Fastenal 2005]. The pitch line diameter is defined by:

$$d_p = D - 0.65p \quad (4.8)$$

where D is the major diameter, equal to the bolt size in metric thread specifications, and p is the thread pitch. The shear area for calculating stresses is equal to the thickness of the teeth at the pitch line diameter $\left(\frac{p}{2}\right)$ multiplied by the number of engaged thread rotations $\left(\frac{l_e}{p}\right)$ and the circumference of the pitch line diameter (πd_p):

$$A_{shear} = \frac{l_e \pi d_p}{2} \tag{4.9}$$

where l_e is the engagement length of the threaded connection. This geometry is shown in Figure 4.18, and the resulting shear stress is then:

$$\sigma_{shear} = \frac{F_{UTS}}{A_{shear}} \tag{4.10}$$

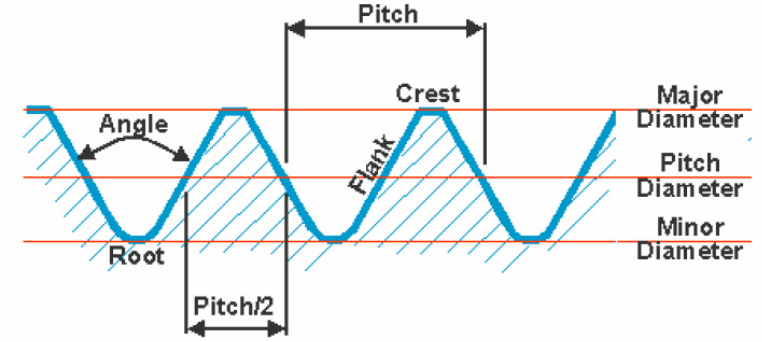

Figure 4.18 *External thread form [Fastenal 2005].*

4.5. Prototype Comparison

The second prototype provides a robust design, which is simpler to assemble and adjust than the first device, and allows much smaller pitch sizes. A comparison of some features of the two prototype designs is presented in **Table 4.2**. The number of parts stated excludes fasteners, springs, MTS tongues and dissipater elements, while the fastener count excludes springs and fasteners for the MTS tongues. The number of threaded connections does not include dissipater connections. **Figure 4.19** shows the two prototype devices in the test machine.

Table 4.2 Comparison of the two GNG prototypes

	First Prototype, GNG1	Second Prototype, GNG2
No. of parts	11, including 4 rack supports	8, including reset collar
No. of fasteners and r-clips	20 cap screws and 4 r-clips	0
No. of ISO metric thread connections	0	3, including reset collar
No. of springs	2, tension type	1, compression type
Pitch sizes	40 mm and 20 mm	10 mm and 3 mm
Adjustment or reset method	Spring removal and manipulation of pawls	Rotation of reset collar
Approximate cost for a one-off device (specific to the completed tests)	$1000	$1000

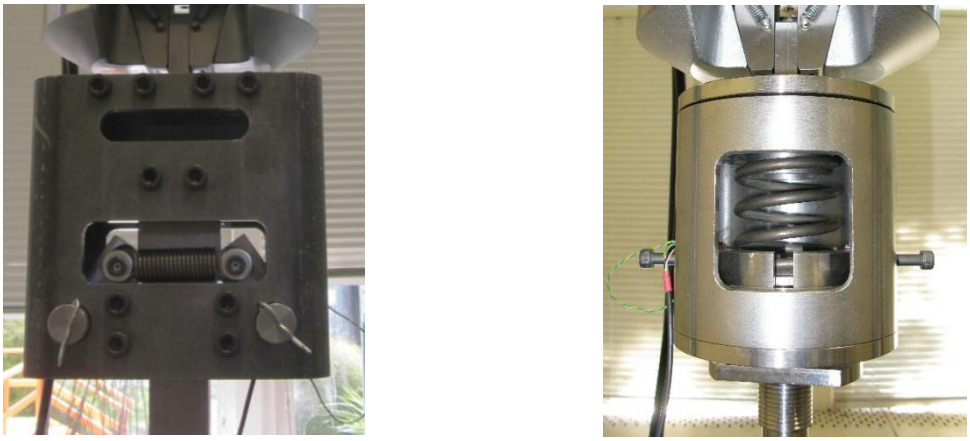

***Figure 4.19** The two prototype GNG devices:*
a) The GNG1 linear prototype, and b) the GNG2 axisymmetric prototype

4.6. Conclusions

This chapter has presented the design of a second, more advanced experimental prototype to develop the capabilities and robustness of the system. The second prototype features many changes to the original design, simplifying the assembly process and providing improved performance. These actions further address research question 1:

Can devices be designed and built to dissipate energy under tensile earthquake loading without carrying compressive loads, and with reduced take-up on subsequent loading cycles to maximise energy dissipation?

- A second ratcheting mechanism has been designed for tension-only engagement of the energy dissipation system
- The device employs a simple and reliable rack and collet engagement interface, improving robustness in operation
- The new design offers more effective operation and will be easier to reset the position of the rack between experiments, or when a dissipater is replaced after an event.
- Smaller pitch rack and collet interfaces can be used than was possible with the original rack and pawl design outlined in Chapter 2.
- Multiple rack designs were produced to experimentally test the influence of tooth pitch.
- Careful detailed design was used to ensure a low-cost and easy to machine device, to increase likelihood of uptake.
- The same yielding steel dissipater element design is incorporated into the second prototype to ensure direct comparison of performance between prototypes.
- A series of basic stress calculations, related to pitch size and the number of teeth engaged, are provided. These are specific to the particular GNG2 device design used in this thesis.

5. Testing of GNG2 Device

5.1. Summary

This chapter outlines testing of the advanced GNG2 prototype. The second, axisymmetric prototype was tested in a series of experiments similar to those for the initial prototype, described in Chapter 3. Eight dissipater elements were used in a series of monotonic and cyclic tests to demonstrate the function of the new ratcheting mechanism, and assess the hysteretic behaviour of both the dissipater element and the system as a whole, with a particular focus on assessing the impact of reduced pitch size. Two racks with 10 mm and 3 mm pitches were tested. A different set of rack-specific collets is used with each rack. Test machine and data acquisition arrangements were the same as for the first prototype, with accelerometers placed on top of the collets in this experiment. The enclosed hysteretic energy dissipation is calculated and compared for the two rack sizes, using the same input displacement profile. A comparison between the responses of the two prototype systems is also made.

This chapter further addresses research questions 2 and 3: Can the devices respond with appropriate speed of engagement for use during seismic loading of structures? Can the experimental devices exhibit desirable hysteresis behaviour, similar to theoretical predictions?

5.2. Monotonic Testing

Several tests of monotonic compressive loading were completed to demonstrate the functionality of the new ratcheting mechanism using the test apparatus shown in **Figure 5.1**. During these tests the device was displaced in compression by between 50 and 70 mm. These tests enabled the device to ratchet by a minimum of 6 teeth when using the 10 mm pitch rack and 22 teeth when using the 3 mm pitch rack, without yielding the dissipater element. These tests were completed at different ram velocities and a summary of the monotonic compressive testing is presented in **Table 5.1** for both pitches, including the maximum compressive forces recorded. The reference numbers indicate an M for monotonic, followed by the rack pitch in mm, and the ram velocity in mm/s, separated by a hyphen. Subscripts are used to differentiate any tests completed under the same conditions. For example, M10-025$_1$ is the first of two monotonic tests with a 10 mm pitch rack completed at 25 mm/s.

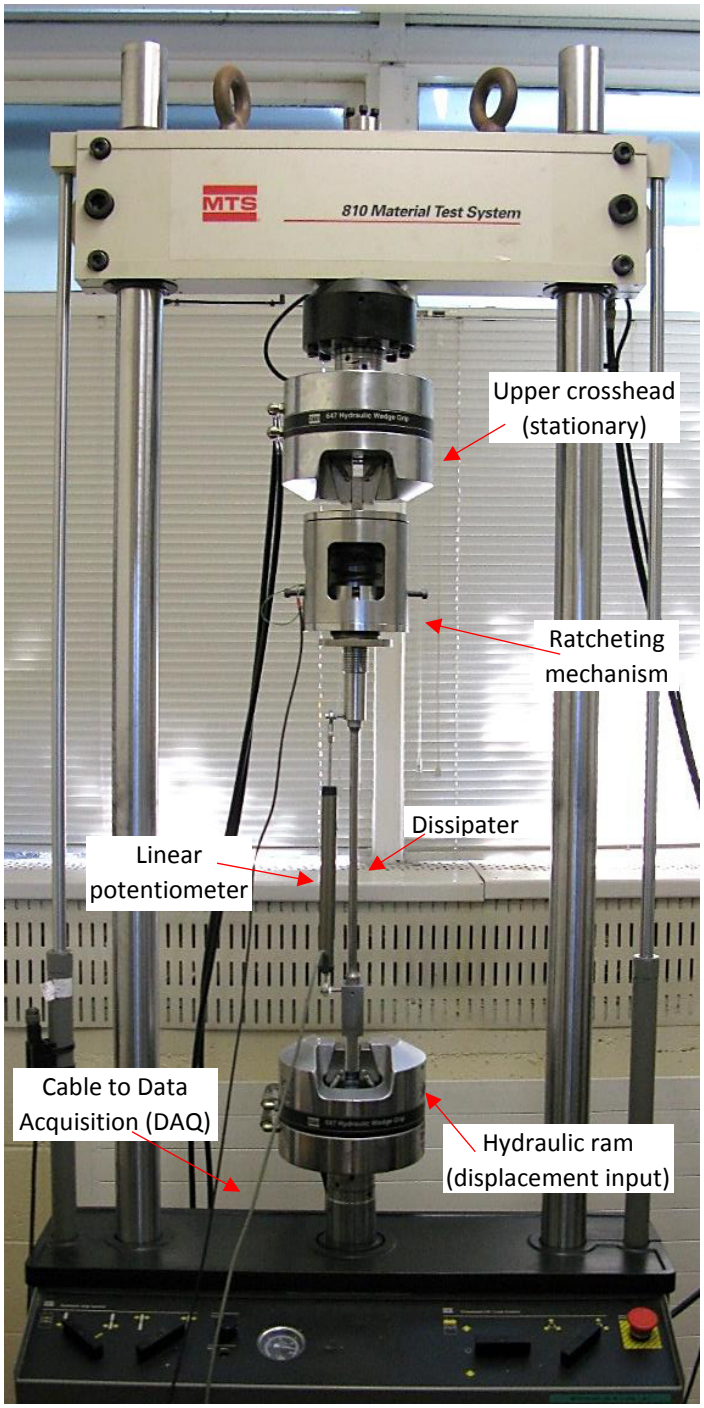

Figure 5.1 *Second GNG prototype test apparatus.*

Table 5.1 *Monotonic testing results for second GNG device*

Pitch (mm)	Velocity (mm/s)	Test Ref.	Max. Compressive Force (kN)
10	25	$M10\text{-}025_1$	0.85
		$M10\text{-}025_2$	0.89
	50	$M10\text{-}050_1$	0.85
		$M10\text{-}050_2$	0.96
	75	$M10\text{-}075_1$	0.91
		$M10\text{-}075_2$	0.76
	100	$M10\text{-}100_1$	0.70
		$M10\text{-}100_2$	0.77
3	25	$M03\text{-}025_1$	0.73
		$M03\text{-}025_2$	0.43
	50	$M03\text{-}050_1$	0.73
		$M03\text{-}050_2$	0.88
	75	$M03\text{-}075_1$	0.82
		$M03\text{-}075_2$	0.83
	100	$M03\text{-}100_1$	0.84
		$M03\text{-}100_2$	0.83

All compressive forces recorded during these tests are below 1 kN and the maximum compressive force experienced by the second prototype during any of the monotonic experiments was 0.96 kN. With the 10 mm pitch rack, the maximum compressive forces ranged from 0.70 kN to 0.96 kN. The 3 mm pitch experiments yielded a range of maximum compressive forces from 0.43 kN to 0.88 kN, showing no significant reduction on average. **Figure 5.2** shows the maximum compressive forces as a function of velocity. These results show no discernible correlation between ram velocity and compressive force, as should be expected, with the 0.43 kN value being an outlier.

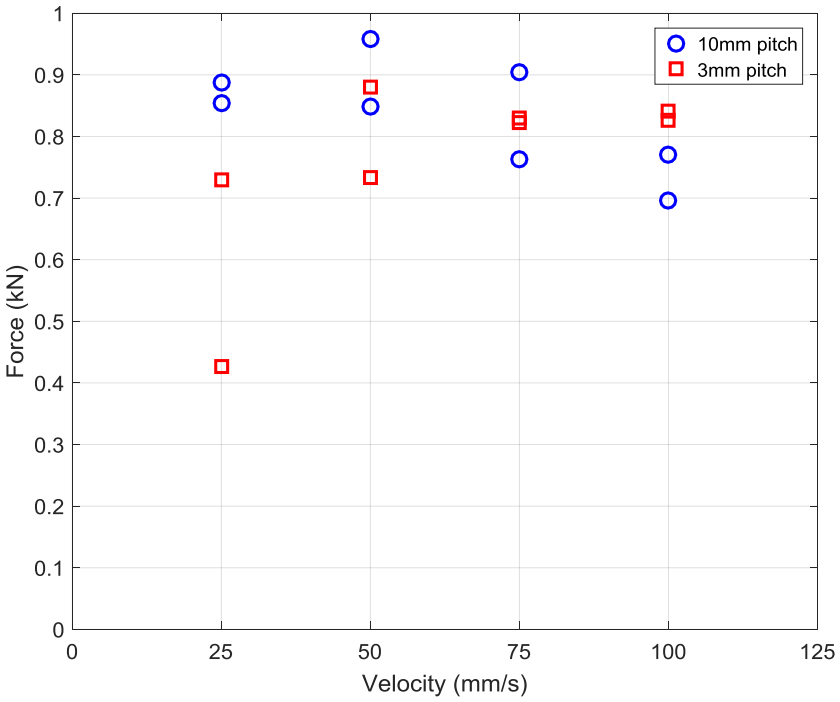

Figure 5.2 Maximum forces from monotonic compressive testing with second prototype

Figure 5.3 shows the force displacements results for the monotonic testing with the GNG2 prototype. Only small forces are recorded, as desired by design. There is little variation across the results, with better consistency observed with the GNG2 prototype, compared to the same results presented earlier in **Figure 3.3** for the GNG1 prototype.

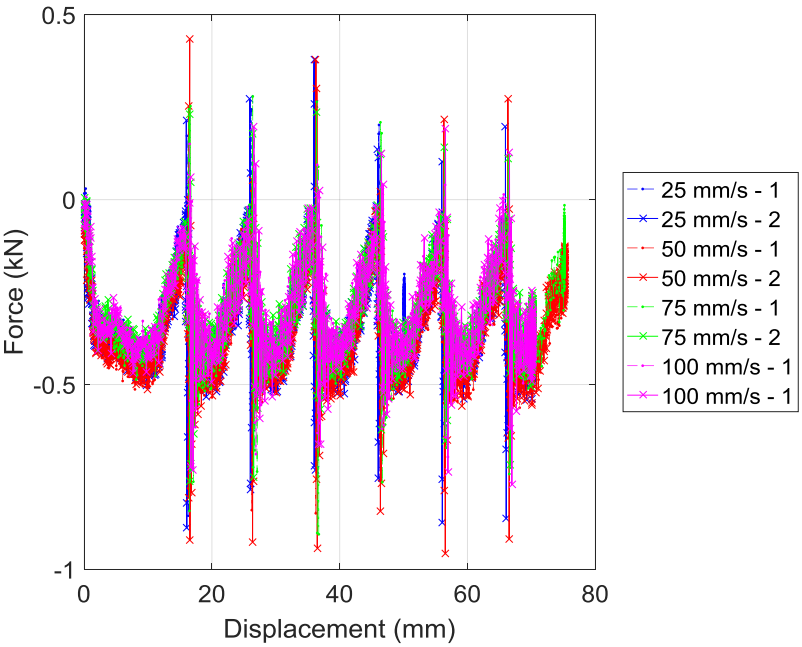

Figure 5.3 Force displacement results of the monotonic tests with the GNG2 prototype.

5.3. Cyclic Testing

Cyclic tests were completed to assess the hysteretic behaviour of the dissipater element and the overall GNG-dissipater system, as with the GNG1 prototype. A summary of the cyclic testing parameters is presented in **Table 5.2** and results from this testing follow in **Table 5.3**. The reference numbers indicate a C for cyclic, followed by the rack pitch in mm, then the input displacement amplitude in mm and the input frequency in Hz, with the three numbers separated by a hyphen. Subscripts are used to differentiate any tests completed under the same conditions. For example, C10-10-0.50_1 is the first of two cyclic tests with a 10 mm pitch rack and a displacement input amplitude of 10 mm, completed at 0.5 Hz.

Test amplitudes were selected to clearly present a single ratcheting action during each compressive loading cycle, with the exception of the 3 mm pitch test using an amplitude of 10 mm. This amplitude was chosen to provide a comparison with the behaviour from the 10 mm pitch experiments with the same input displacement amplitude. Where no value is stated for dissipater elongation to fracture, it indicates that the sample did not fracture during testing.

Table 5.2 *Input test parameters for cycling testing of the GNG2 prototype*

Rack Pitch (mm)	Amplitude (mm)	Frequency (Hz)	Test Ref.	No. Cycles
10	10	0.5	C10-10-0.50_1	5
			C10-10-0.50_2	6
		1.0	C10-10-1.00_1	5
			C10-10-1.00_2	6
		1.5	C10-10-1.50_1	5
			C10-10-1.50_2	5
3	10	0.5	C03-10-0.50	4
	5	0.5	C03-05-0.50	17

Table 5.3 Cycling testing results for the GNG2 prototype

Test Ref.	Yield Force (kN)	Ultimate Tensile Force (kN)	Dissipater Elongation to Fracture (mm)	Max. Compressive Force (kN)
C10-10-0.50$_1$	43.3	65.9	--	0.75
C10-10-0.50$_2$	43.2	66.2	63.1	0.84
C10-10-1.00$_1$	42.9	66.0	--	0.81
C10-10-1.00$_2$	43.8	66.6	62.7	0.73
C10-10-1.50$_1$	43.3	66.5	--	0.74
C10-10-1.50$_2$	45.0	66.2	56.9	0.80
C03-10-0.50	41.5	66.2	57.5	0.46
C03-05-0.50	40.7	64.3	60.9	0.32

In all tests, the compressive forces are low, as intended by design. The maximum compressive force recorded during any of the cyclic loading experiments was 0.84 kN, which is comparable to the maximum compressive force of 0.96 kN recorded during the monotonic experiments. The average maximum compressive force for the six 10 mm pitch cyclic experiments was 0.78 kN. This average was reduced to 0.39 kN for the two 3 mm pitch cyclic experiments, which is a reduction of 50%. The average yield force recorded was 43.0 kN and the average ultimate tensile force was 66.0 kN. Therefore, the largest maximum compressive force represents less than 1.5% of the average ultimate tensile force recorded. The yield and ultimate tensile forces were consistent across all of the experiments, and thus across all dissipaters, and are presented in **Figure 5.4**. Any differences are likely due to normal manufacturing or test variation.

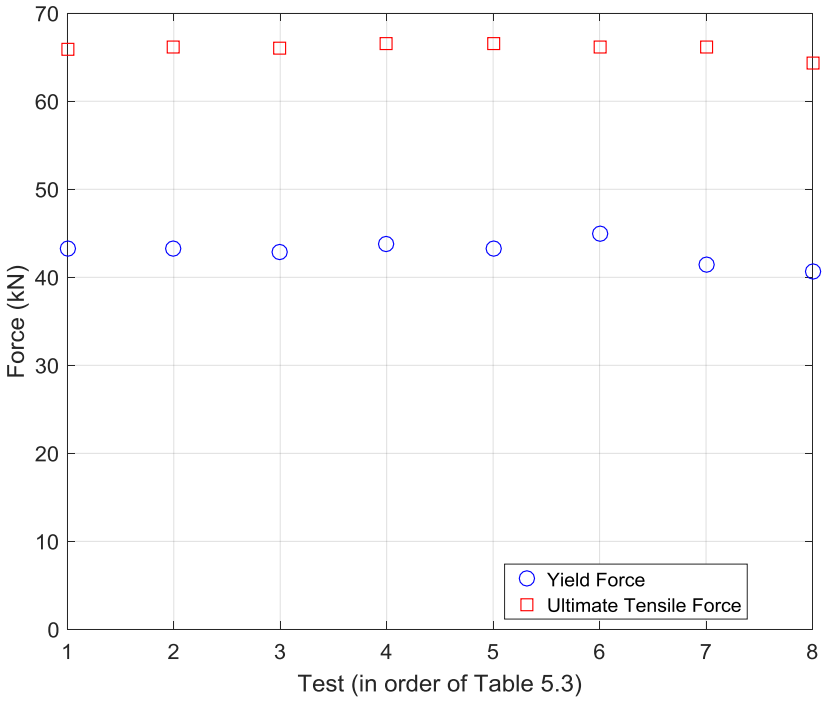

Figure 5.4 *Yield and ultimate tensile forces for dissipaters used with second prototype*

The average elongation to fracture for the dissipater elements was 60.2 mm, which represents only 67% of the expected value of 90 mm, based on 28% elongation at break for the 320 mm long dissipater yielding region. As with the testing of the first prototype, uniform plastic strain throughout the dissipater length was likely not obtained during the dynamic cyclic testing. Hence, fracture displacements were lower than theoretically calculated, a factor to consider in any dissipater design or application.

For the second prototype dissipaters, this discrepancy is at least partially attributed to manufacturing issues resulting in a non-uniform strain region. A CNC lathe was used to produce the end detail of the dissipaters and manual methods were used for turning the yield region due to the length of the part and associated clamping concerns. In error, a small irregularity was produced near the ends of the dissipater yield region, where the manufacturing method was changed. This area was subsequently polished with emery cloth, but it did not produce as smooth a transition as was present in the dissipaters used with the first prototype experiments. This discrepancy reduced the available plastic strain capacity by around 10 mm when compared to the first prototype experiments. However, there was no effect on the operation of the ratcheting mechanism.

A CNC machine was not used to produce the yield region of the dissipater, where the imperfections occurred. This decision was made at the time to address concerns about adequately clamping the part in the available machine, given its length. In future production, computer control could be used to

produce the full part. This issue was specific to the dissipative elements only, and not the GNG mechanism.

As with the first prototype testing, limitations of the test equipment restricted the size of the dissipater and the resulting forces in the system. The ratcheting mechanism itself is capable of withstanding much larger forces if required and exhibited no visible signs of yielding or other damage following testing. Furthermore, while these results use yielding steel dissipaters for energy dissipation, various dissipation methods, such as friction connections [MacRae et al. 2010] and lead dissipaters [Rodgers et al. 2008], could be implemented with the ratcheting mechanism as required for specific applications and force or yield levels. Most importantly, these specific tests were only designed to validate the functionality of the GNG device, which was demonstrated, and is not specific to the yielding steel dissipater.

5.4. Hysteresis

5.4.1. GNG-dissipater System

Similar hysteresis behaviour was recorded to that observed from the first prototype device. **Figure 5.5** shows the force-displacement recordings for the tests C10-10-0.50$_1$, C10-10-1.00$_1$, and C10-10-1.50$_1$. A displacement amplitude of 10 mm was used for these tests with the 10 mm pitch rack. Displacement input profiles for these three tests are also shown in Figure 5.4, highlighting the different frequencies used in the testing.

During these tests five cycles were completed and the dissipater elements did not fracture. However, the full hysteresis behaviour is captured. Following elastic recovery, the bottom of the hysteresis loop lies essentially on the horizontal axis, reflecting the negligible forces experienced by the system during compressive loading and ratcheting, as desired.

The displacement datum where engagement begins is reduced from ~7.5 mm to ~-2.5 mm, representing a reduction equal to the tooth pitch of 10 mm due to ratcheting. This adjustment is shown by the difference between the end of elastic recovery, where the loop meets the x-axis during unloading, and the re-engagement point, where the loop leaves the x-axis again during reloading. After reversal of the input displacement direction from compressive to tensile, some initial free-travel occurs before re-engagement of the teeth, as discussed in Chapter 3. This free-travel is again observed with approximately 7.5 mm of free-travel before re-engagement of the rack and collets during reloading with the 10 mm pitch rack.

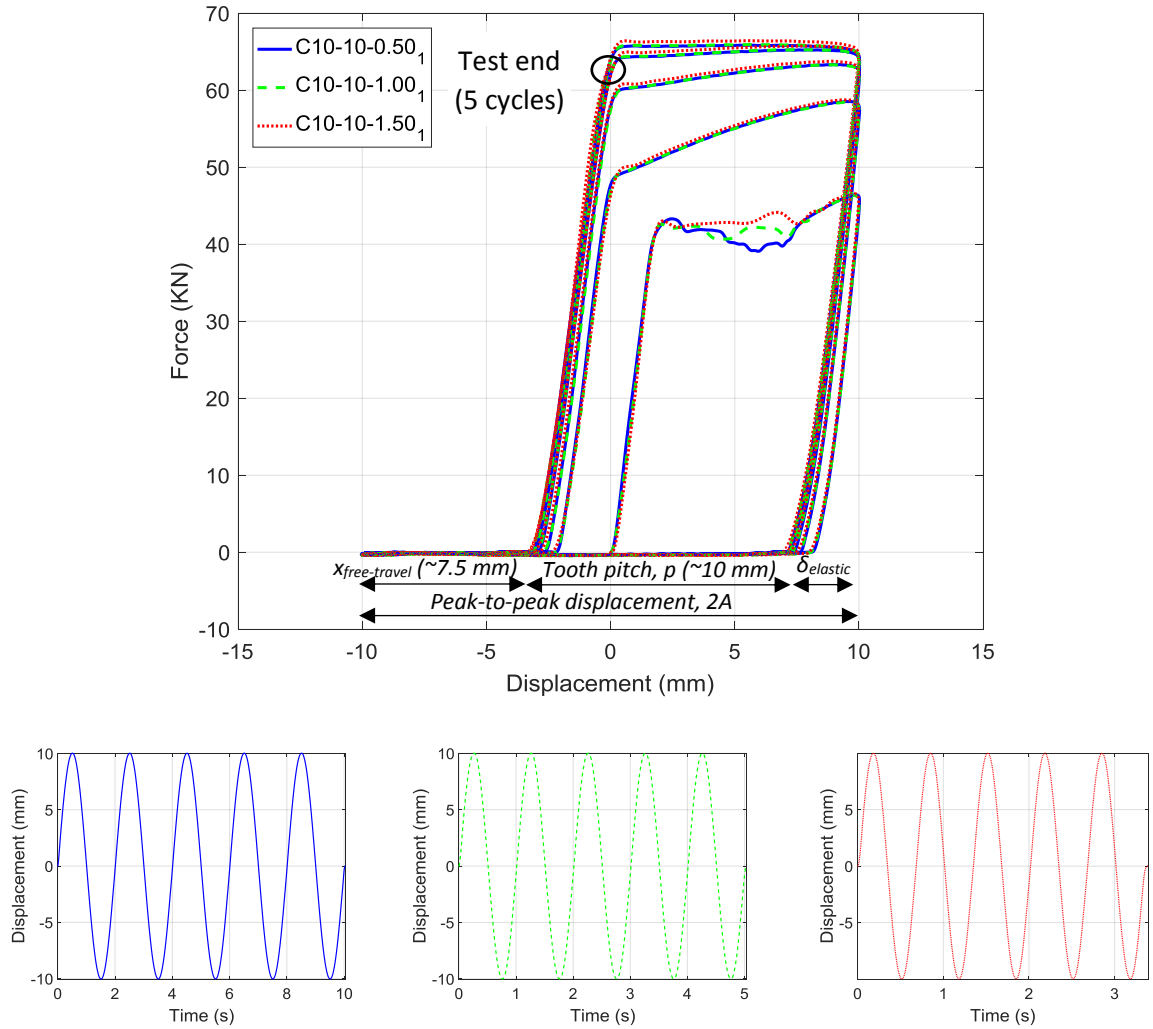

Figure 5.5 *Force-displacement hysteresis loops for cyclic testing of second prototype with 10 mm tooth pitch, showing tests C10-10-0.50$_1$, C10-10-1.00$_1$, and C10-10-1.50$_1$ with no fracture of dissipater element. Input displacements are shown inset.*

Similar results were obtained from the three tests C10-10-0.50$_2$, C10-10-1.00$_2$, and C10-10-1.50$_2$, though in these tests the dissipaters fractured after between 5 and 6 cycles. The hysteresis results from tests C10-10-0.50$_2$, C10-10-1.00$_2$, and C10-10-1.50$_2$ are shown in **Figure 5.6**. Displacement input profiles for these three tests are also shown in Figure 5.5, showing the use of the same input profile as the previous tests, and highlighting the different frequencies used in the testing and the slightly longer inputs required to fracture the dissipater elements, when compared to the previous tests in **Figure 5.5**.

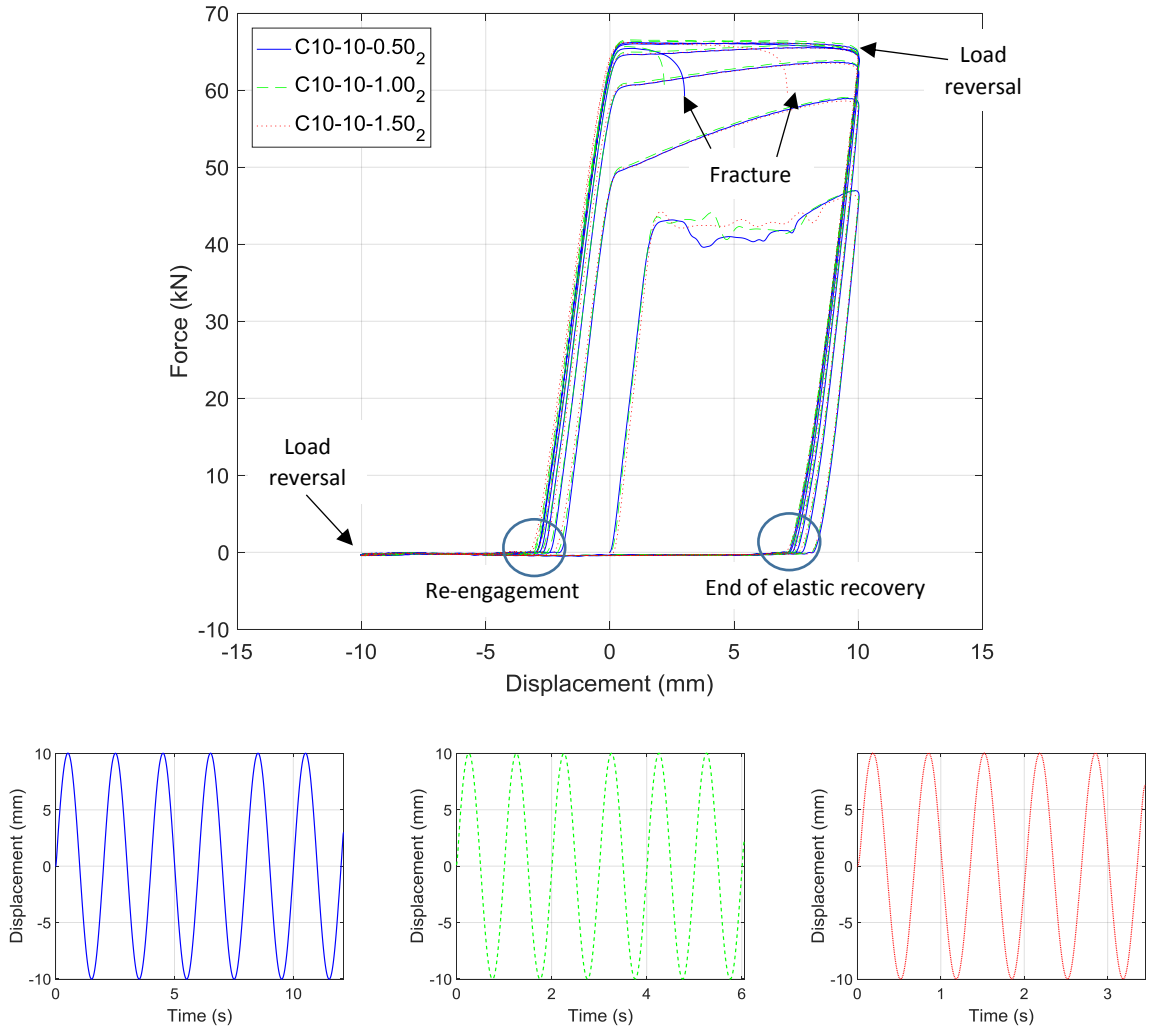

Figure 5.6 *Force-displacement hysteresis loops for cyclic testing of second prototype with 10 mm tooth pitch, showing tests C10-10-0.50$_2$, C10-10-1.00$_2$, and C10-10-1.50$_2$ with fracture of dissipater element. Input displacements are shown inset.*

Figure 5.7 compares the hysteretic behaviour of the second prototype using 10 mm and 3 mm pitch racks for cyclic loading with an input displacement amplitude of 10 mm at 0.5 Hz. This data is from tests C10-10-1.50$_1$ and C03-10-0.50, respectively. It is seen in Figure 5.6 that on subsequent loading cycles the re-engagement of the device with the 10 mm pitch occurs at a displacement of approximately -3 mm, with respect to the initial position, compared with approximately -7 mm when using the finer 3 mm pitch rack. This result represents a reduction in the free-travel that occurs prior to engagement from 7 mm to 3 mm, as expected with the finer pitch rack. A comparison to a theoretical maximum result is also included in **Figure 5.7**. The theoretical maximum result refers to a response with zero free travel, exhibiting similar post yield behaviour in the dissipater to that observed in the two experimental results presented.

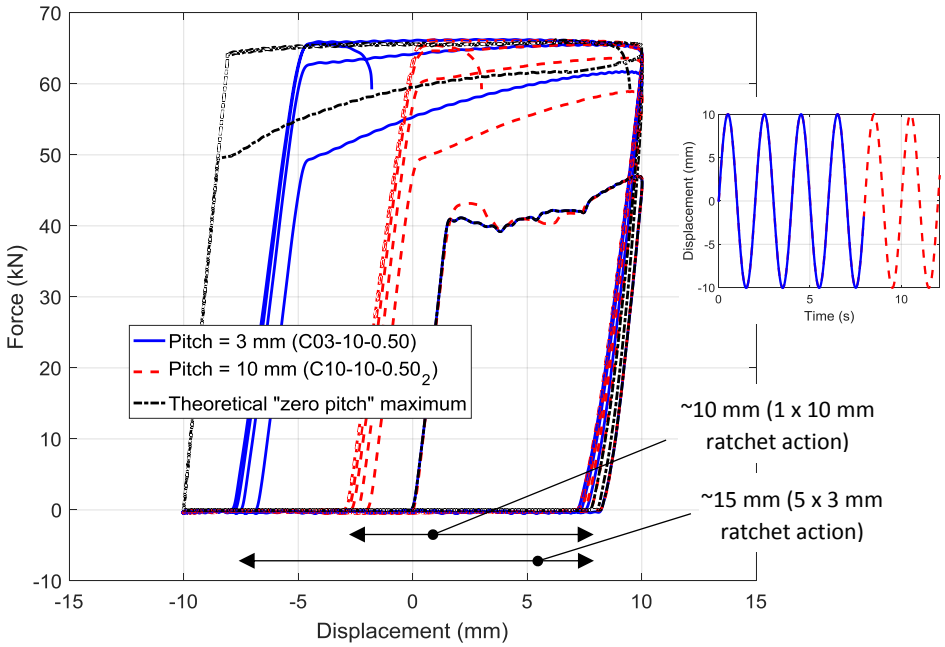

Figure 5.7 *Comparison of free-travel reduction and increased energy dissipation with the use of the finer pitch rack in the GNG2 prototype. Displacement inputs are shown inset.*

The shift in the displacement datum for engagement with the 10 mm pitch setup is ~10 mm, representing a single ratchet action for each compressive loading cycle. This shift in engagement is increased to around 15 mm when using the 3 mm pitch rack and collets, which accounts for five ratchet actions in each cycle. The enclosed area in the hysteresis loop for the finer pitched rack has thus increased by ~50%, demonstrating a significant increase in energy dissipation for the same displacement loading input.

Table 5.4 shows the enclosed hysteretic energy dissipation for each cycle, including incomplete cycles where fracture of the dissipater element occurred, using data from the two tests shown in Figure 5.7. During the four cycles completed with the 3mm pitch rack, the energy dissipation per cycle was between 143% and 164% of the energy dissipated using the 10mm pitch rack during the same loading cycle, due to the smaller pitch having less free travel. A comparison to a theoretical maximum, representing a device with no free-travel, is also included in **Table 5.4**. These results suggest that an additional 15-26% of energy dissipation could be achieved per cycle during the first three cycles, prior to dissipative element fracture on the fourth cycle for the theoretical device with an infinitely small pitch and no free-travel.

Table 5.4 Energy dissipation per cycle in kN.mm

Parameter	Cycle 1	Cycle 2	Cycle 3	Cycle 4	Cycle 5	Cycle 6	Cycle 7	Total
10mm pitch	390	564	642	672	683	680	127	3758
3mm pitch	640	923	997	963	--	--	--	3523
Theoretical max. (zero pitch)	805	1086	1147	603	--	--	--	3641
$\frac{E_{3mm}}{E_{10mm}}$ x 100	164%	164%	155%	143%	--	--	--	--
$\frac{E_{Max.}}{E_{3mm}}$ x 100	126%	118%	115%	--	--	--	--	--

These enclosed hysteretic energy values will be roughly half of what would be obtained using a tension-compression member, such as a BRB, that has the same yield force. However, the tension-only nature of the mechanism and the absence of compression force may enable a larger yield force to be used, which may lead to a closer value of enclosed hysteretic energy. For a rocking system such as a rocking wall, the relative contributions of post-tensioning and energy dissipation to the overall gap-opening moment could be modified to achieve a similar overall energy dissipation.

Additional cycles were required to produce dissipater fracture when using the larger pitch rack, as shown in the input displacements inset in Figure 5.7. The increased number of loading cycles is due to the greater free-travel and reduced inelastic action in each cycle with the larger pitch rack. Overall, the finer pitch led to less free-travel and thus greater energy dissipation, as well as larger inelastic demand per loading cycle, as expected.

A smaller displacement input amplitude of 5 mm was used for the final experiment with the 3 mm pitch rack. This result is from test C03-05-0.50 and is shown in **Figure 5.8**. The 5 mm amplitude allowed for a large number of cycles with ratcheting actions. Specifically, 19 total ratcheting actions occurred across the 17 cycles completed.

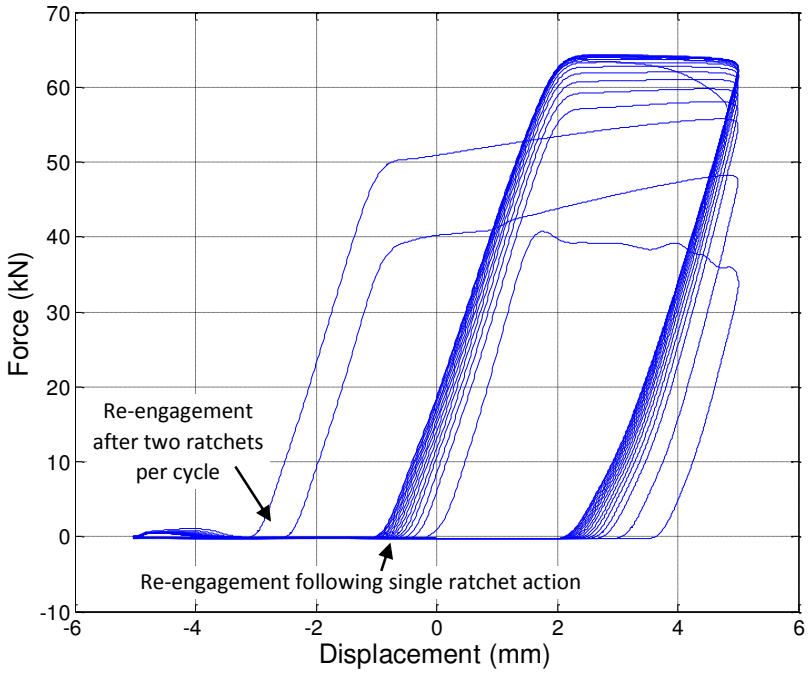

Figure 5.8 *Force-displacement hysteresis loop for cyclic testing of GNG2 prototype with 3 mm pitch rack for test C03-05-0.50 with 5 mm input displacement amplitude.*

During the first two cycles the device was ratcheting by two teeth per cycle. However, this action was reduced to one tooth per cycle on subsequent cycles due to the increase in elastic displacement during unloading as a result of higher forces in the system from strain hardening of the steel dissipater. The high number of cycles and ratcheting actions completed during this test demonstrates the repeatability of the GNG device behaviour to show that it can be a useful tool during longer duration earthquake ground motions.

5.4.2. Dissipater element

Figure 5.9 and **Figure 5.10** show the hysteretic behaviour of the dissipater element during the cyclic testing with the 10 mm pitch rack. Tests C10-10-0.50$_1$, C10-10-1.00$_1$, and C10-10-1.50$_1$ are presented in **Figure 5.9** and tests C10-10-0.50$_2$, C10-10-1.00$_2$, and C10-10-1.50$_2$ are shown in **Figure 5.10**. These figures use the linear potentiometer reading, which gives true dissipater displacement (without the offset in displacement datum due to ratcheting), rather than the hydraulic ram displacement, which represents the whole system displacement, and thus includes the ratcheting action, as well.

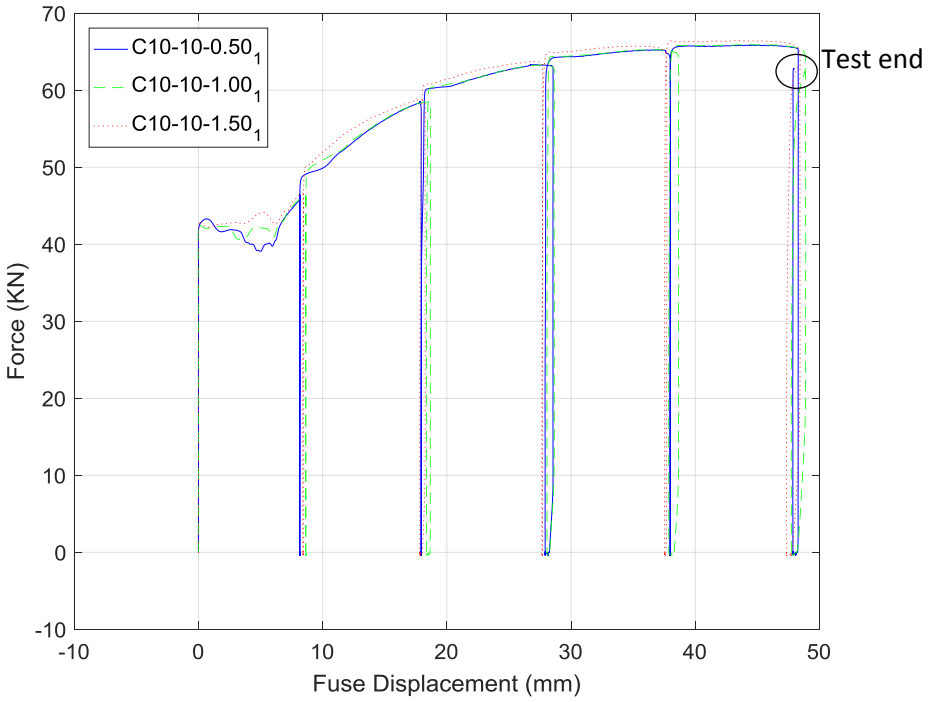

Figure 5.9 *Force-displacement hysteresis behaviour for dissipater elements in cyclic testing of second prototype with 10 mm pitch, showing tests C10-10-0.50$_1$, C10-10-1.00$_1$, and C10-10-1.50$_1$ with 5 input displacement cycles and no fracture of dissipater element.*

The hysteresis curve features are visible including elastic strain, yielding, strain hardening and necking. There are 5 or 6 load reversals shown, corresponding to the number of cycles completed in each test. As with the testing with the initial GNG prototype, the GNG system experiences negligible compressive forces and the steel dissipater yields only in tension. While cyclic tests were completed, the behaviour of the steel element approximates the response during a monotonic tensile test due to the GNG device essentially removing compressive loading in the dissipater, as it was designed to do.

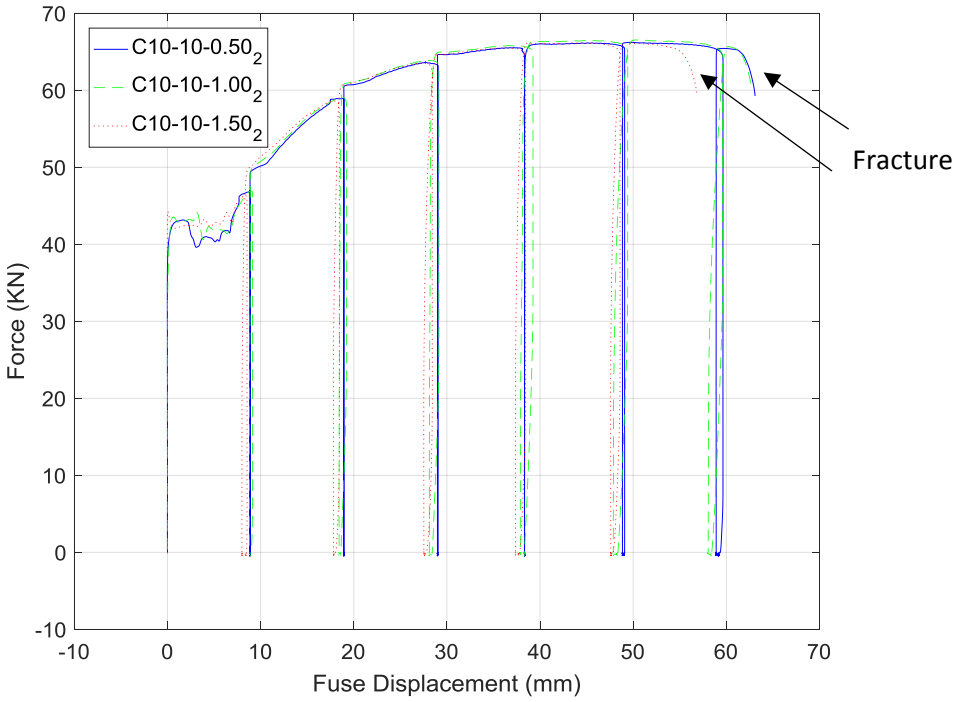

Figure 5.10 *Force-displacement hysteresis behaviour for dissipater elements in cyclic testing of second prototype with 10 mm pitch, showing tests C10-10-0.50$_2$, C10-10-1.00$_2$, and C10-10-1.50$_2$ with 6 input displacement cycles and fracture of dissipater elements*

Figure 5.11 compares the dissipater behaviours in the two cyclic tests completed with the 3 mm pitch rack. This data is from tests C03-10-0.50 and C03-05-0.50. The hysteresis curves for these tests appear in Figures 5.6 and 5.7, respectively. A similar strain hardening pattern is observed for the result from the 10 mm displacement input amplitude as for the 5 mm displacement amplitude. However, the smaller amplitude test shows 17 load reversals as there were 17 cycles completed, compared with 4 for the larger amplitude test.

It is visible in Figure 5.11 that two of the cycles during the 5 mm amplitude test produced greater strain hardening than the rest. These two cycles are labelled in Figure 5.10, and correspond to the second and third cycles of loading, which exhibited two ratcheting actions during unloading in the prior cycle due to lower elastic displacement than experienced in later cycles. This effect can also be seen in **Figure 5.8**.

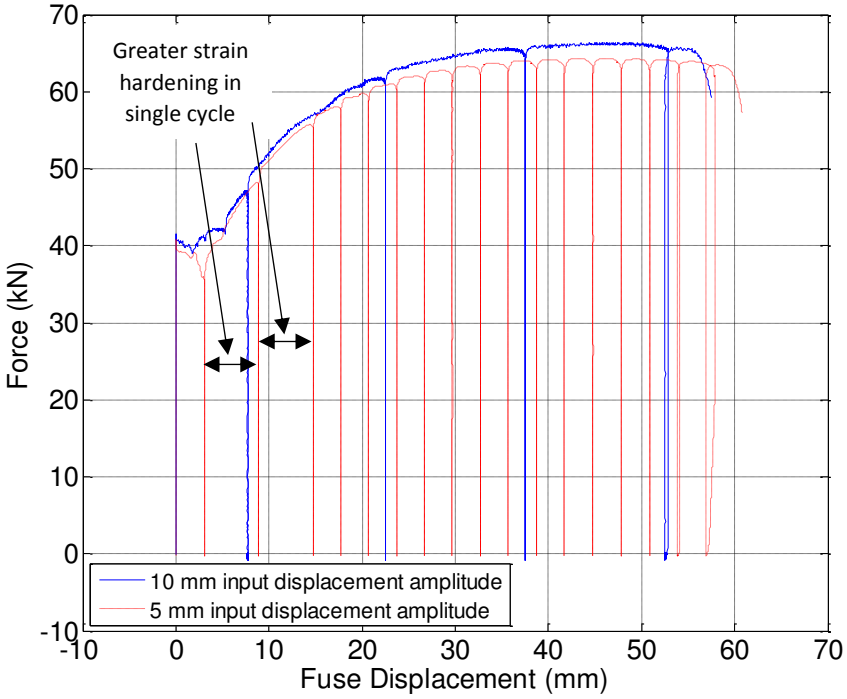

Figure 5.11 *Dissipater behaviour comparison of the device with 3 mm pitch, when subjected to 5 and 10 mm amplitude input displacement cycles.*

5.5. Ratchet Mechanism Behaviour

Due to the axial symmetry of the ratcheting mechanism in the second prototype, it is believed that the collets on this prototype act in greater unison than the pawls on the first prototype, which experienced a slight lag to varying degrees during operation. This lag was attributed to imperfect rack alignment and symmetry with the fitting of the springs between the pawls, as discussed in Chapter 3. Careful detailed design could reduce the likelihood of misalignment and ensure consistent and reliable engagement. No high speed camera footage was recorded for the testing of the second prototype. However, accelerometer readings, where one accelerometer was mounted on each collet, demonstrate the simultaneous action of the two collets during the ratcheting motion.

The ratcheting behaviour from test C10-10-0.50$_2$ is shown in Figure 5.12. Figure 5.12a shows the timing of the ratcheting with respect to the sinusoidal displacement input profile, where the ratcheting action occurs near the bottom of the compressive loading phase. Figure 5.12b shows a close up of the accelerometer signals during ratcheting. Spikes in acceleration coincide with a ratcheting action occurring and there is little acceleration recorded at any other time during the testing. As the acceleration spikes from both accelerometers are closely aligned in time, as seen in **Figure 5.12**b, the collets are deemed to move at almost exactly the same time.

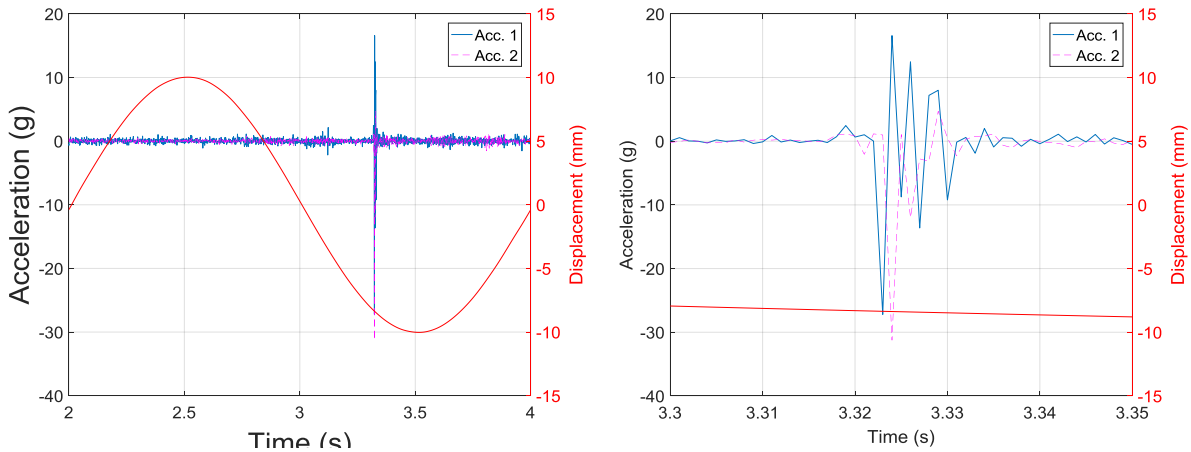

Figure 5.12 *Accelerometer signals taken from C10-10-0.50$_2$ test:*

a) during unloading cycle, and b) close up of signals during ratcheting showing simultaneous collet response.

5.5.1. Effective pitch

There was an unexpected increase in the effective pitch of the system for the first ratcheting action in the compressive loading phase of each cycle. This effect is shown in **Figure 5.13**, which shows the ram force and displacement from test M10-025$_2$, a monotonic compressive test with a 10 mm pitch. The time before the first ram force spike, representing the first occurrence of ratcheting, is greater than the time between subsequent ram force spikes, and there is a greater displacement over the longer time period due to a constant hydraulic ram speed. In particular, around 16 mm of compressive ram displacement is required to trigger the first ratcheting action in the device, while subsequent ratcheting actions in the same compressive loading phase occur once for every additional 10 mm of compressive ram displacement, matching the pitch of the teeth on the rack. This discrepancy is shown on **Figure 5.13**.

The initial increased effective pitch of ~160% of the rack teeth spacing is due to the need to displace the collets upward along the collet guide taper as well as outward away from the rack. If the collets were to only move horizontally away from the rack as it slid past, then rack movement equal to the pitch would be sufficient to trigger the ratcheting action. However, with the design implemented, the collets need to be raised upward by ~6 mm to move far enough outward to clear the teeth on the 10 mm pitch rack. Hence, the first motion takes ~16 mm in total.

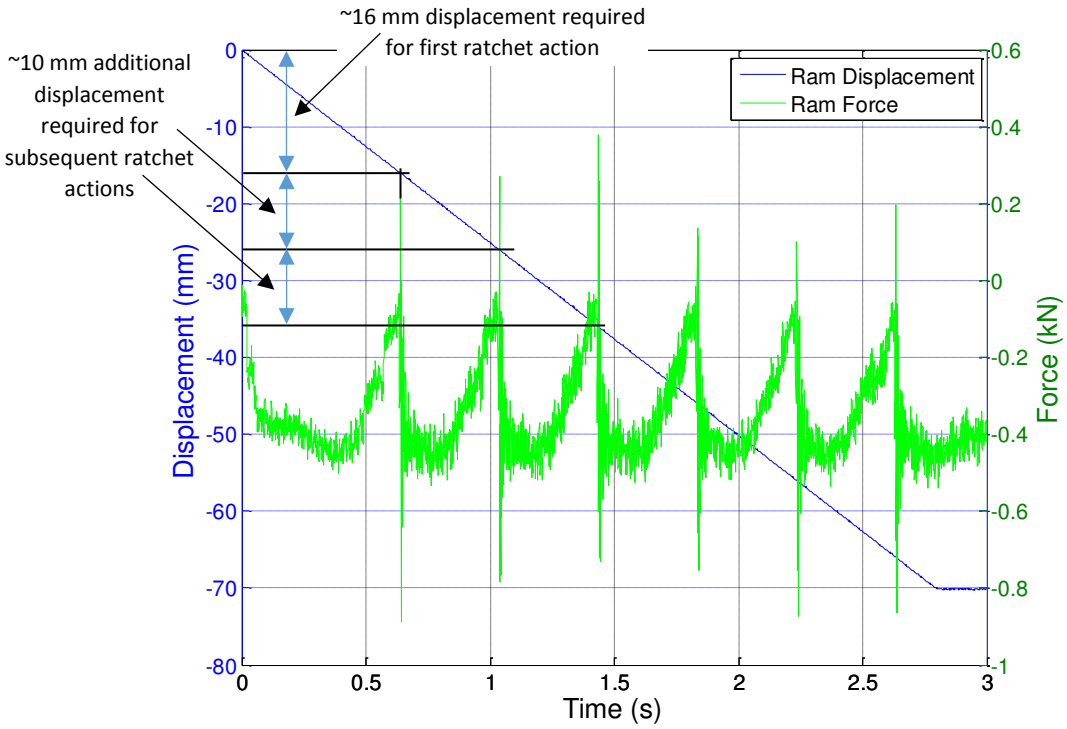

Figure 5.13 *Ram force and displacement during monotonic compressive test M10-025$_2$ indicating initial pitch discrepancy.*

The rack needs to provide this extra displacement in addition to a displacement equal to the pitch, to move past the complimentary tooth profile of the collets, for ratcheting to occur. As a result, for the first ratcheting action to occur in the compressive phase of each cycle, the rack must be raised by ~16 mm when using the 10 mm pitch rack. Additional ratcheting actions in the same compressive phase will occur at displacement intervals equal to the pitch size, as the collets have already cleared the additional 6 mm raise required for them to clear the rack.

This concept is illustrated for the 10 mm pitch rack in Figure 5.14 and Figure 5.15. Figure 5.14 shows the position of the collets after 10 mm of rack travel, equal to one tooth pitch, compared to the initial resting position of the collets. This figure demonstrates that additional rack travel is required for a ratcheting action to occur. Figure 5.15 shows the position of the rack and collets immediately prior to a ratcheting action taking place. Again, this position is compared with the initial resting position of the rack and collets. Figure 5.15 shows that around 16 mm of compressive rack motion is required to trigger the initial ratcheting action during a loading cycle.

A similar effect was observed with the 3 mm pitch testing. The effect was overlooked during the design of the second prototype. While it is undesirable for the pitch to not be solely controlled by the teeth spacing on the rack, it can be managed and factored into the design and pitch selection. This effect

could be removed in a later design iteration, and was not a factor with the first prototype design due to the different ratchet mechanism.

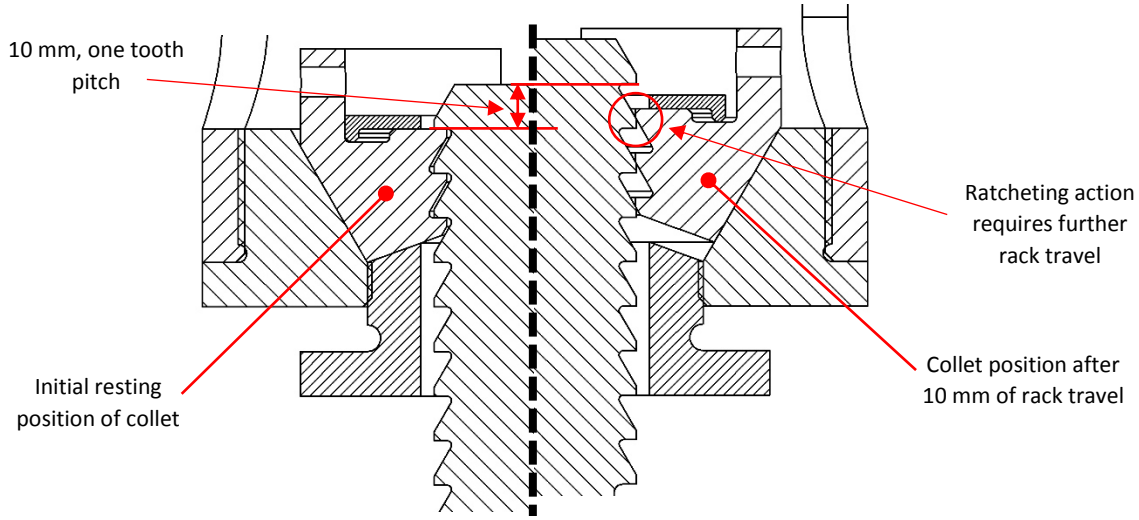

Figure 5.14 *Effective pitch concept, showing initial collet position on left and collet position after 10 mm, or one tooth pitch, of rack travel on right. Note that additional rack movement is required for ratcheting to occur.*

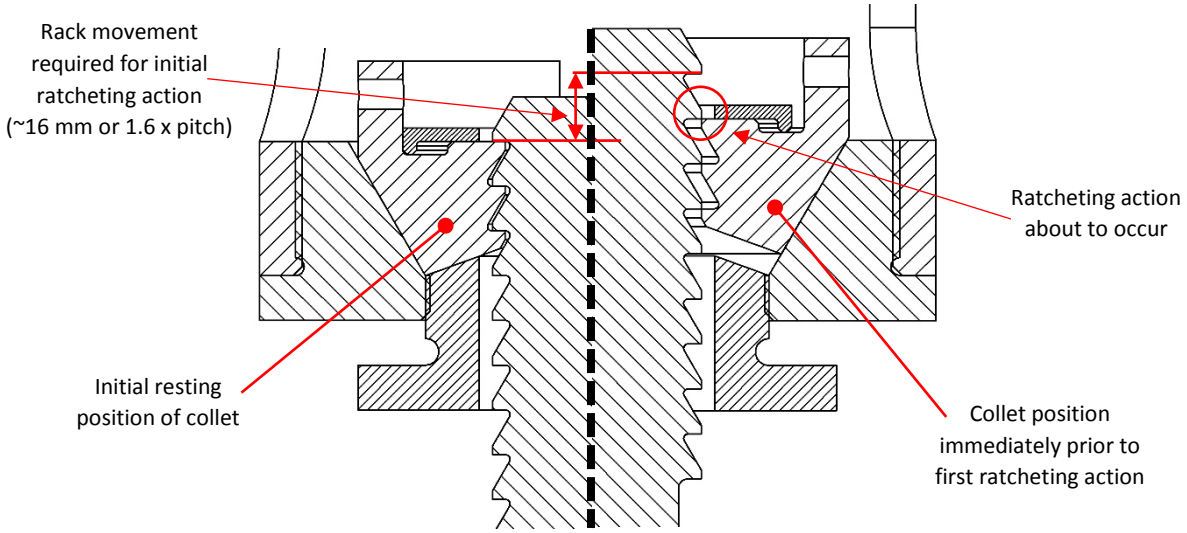

Figure 5.15 *Effective pitch concept, showing initial collet position on left and collet position required for ratcheting on right. Note that the required rack movement is greater than the pitch.*

While this effect altered the amount of compressive displacement required to trigger the ratcheting action for the first tooth in each loading cycle, it does not affect the difference in the displacement datum for engagement that occurs and is shown in the hysteresis loops. The displacement datum for engagement is still reduced in increments of the true pitch value. It also does not affect the very low forces in compression due to the ratcheting, so the overall concept is seen to work as designed. **Figure 5.5** to **Figure 5.8** demonstrate this adherence.

5.6. System Overview

Figure 5.16 and **Figure 5.17** present all the signals recorded during the C10-10-0.50$_2$ and C03-10-0.50 tests, respectively. The hydraulic ram displacement follows a sine profile with an amplitude of 10 mm as programmed into the test machine. Positive displacement in **Figure 5.16** and **Figure 5.17** represent tensile motion, so that downward motion of the hydraulic ram seen in **Figure 5.1** is positive.

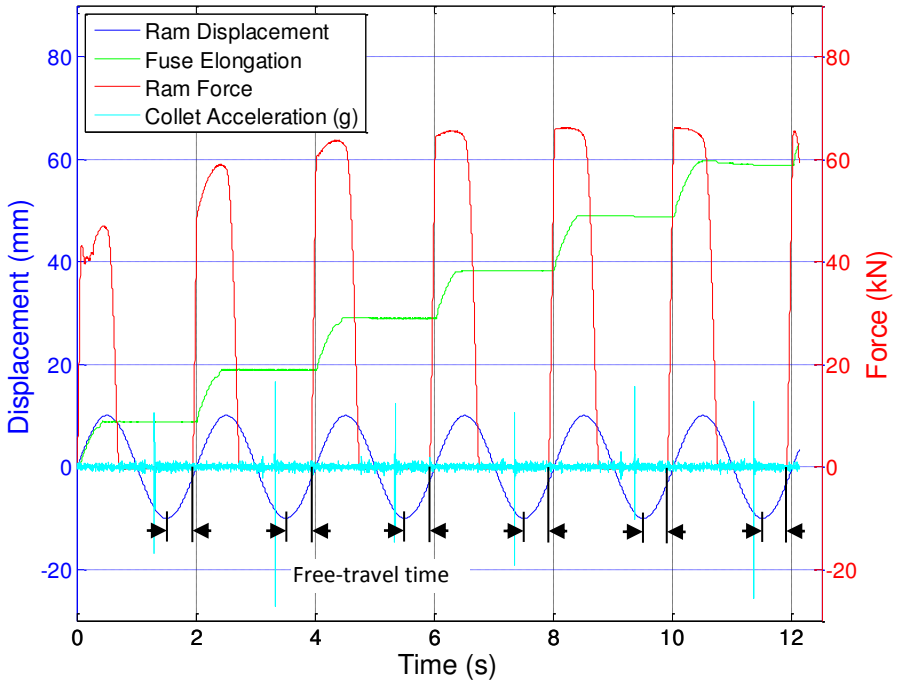

Figure 5.16 *Overview of all recorded signals during C10-10-0.50$_2$ test, with acceleration shown in g*

The spikes in acceleration of the collets coincide with the occurrence of ratcheting during compressive displacement of the hydraulic ram. As such, there is one spike for each cycle of test C10-10-0.50$_2$ shown in **Figure 5.16** and five spikes per cycle for test C03-10-0.50 shown in **Figure 5.17**. The ram force follows the stages of strain hardening behaviour experienced by the yielding steel dissipater during tensile motion and shows elastic recovery followed by minimal forces during compressive motion.

The time period of the region of free-travel is indicated as 'free-travel time' for each cycle on Figure 5.16 and Figure 5.17. There is a delay in the engagement of the energy dissipation mechanism during this period of free-travel, and thus, there is no discernible ram force. The elongation of the dissipater occurs during tensile loading and also experiences a delay in engagement due to the free-travel.

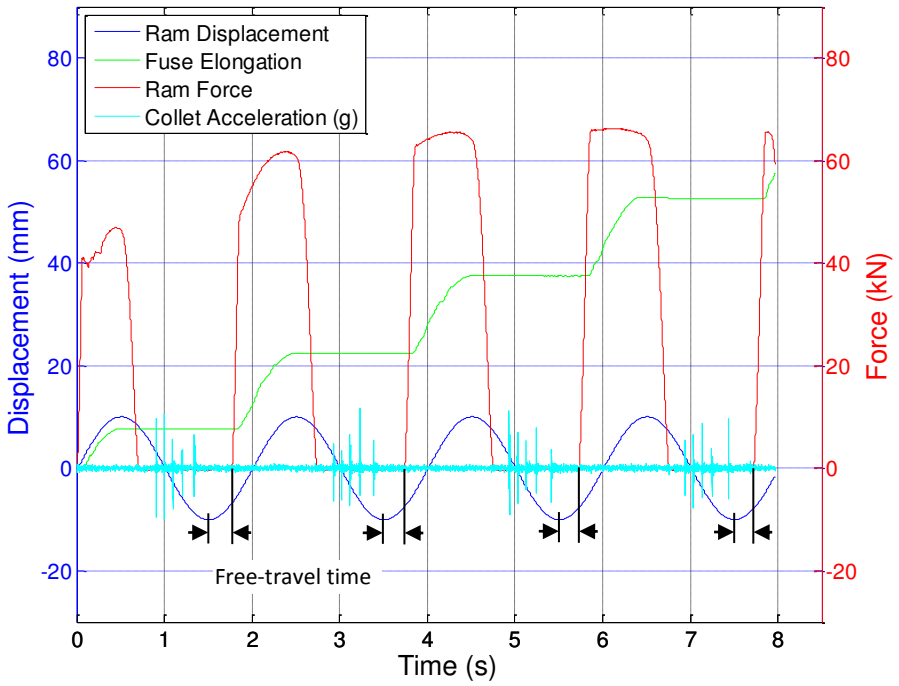

Figure 5.17 *Overview of all recorded signals during C03-10-0.50 test, with acceleration shown in g*

5.7. Comparison to numerical model

A comparison between an experimental hysteresis loop and a recreation of the result using the numerical model, previously discussed in Section 3.7, is provided in **Figure 5.18**. The experimental result shown is from test C10 10 0.502, which used a 10 mm pitch rack and an input displacement amplitude of 10 mm. The input displacement profile used to produce the numerical result in **Figure 5.18** was 0.01sin(πt), which mimics the input displacement used in the corresponding test.

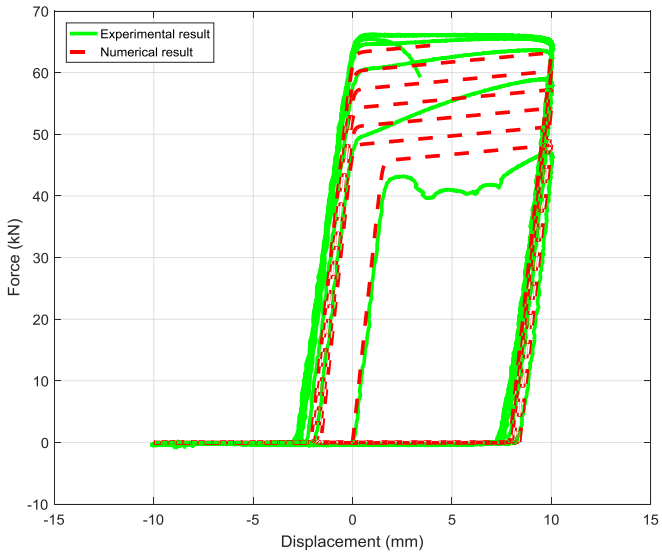

Figure 5.18 *Comparison of experimental and numerical hysteresis loops for the GNG-dissipater system with the GNG2 prototype.*

As with the previous comparison to the GNG1 C20 15 0.251 test made in Section 3.7, the ratcheting behaviour from the experiment is accurately recreated by the model using the displacement input profile and other known parameters, such as the pitch and dissipater material properties. The limitations of the bi linear model in fully capturing yielding and strain hardening behaviour are visible, as discussed in Section 3.7.

Figure 5.19 presents a comparison of the hysteretic behaviour of just the yielding steel dissipater in the same C10 10 0.502 experiment, compared to the numerical recreation. The ratcheting behaviour is again well represented with some discrepancies in the post-yield stiffness profile. The dissipater elongation is shown in **Figure 5.20** and a good match between the empirical and numerical results is obtained. This material model algorithm was later recreated as a custom material in OpenSEES and the subsequent simulation work is outlined in Chapters 7 and 8.

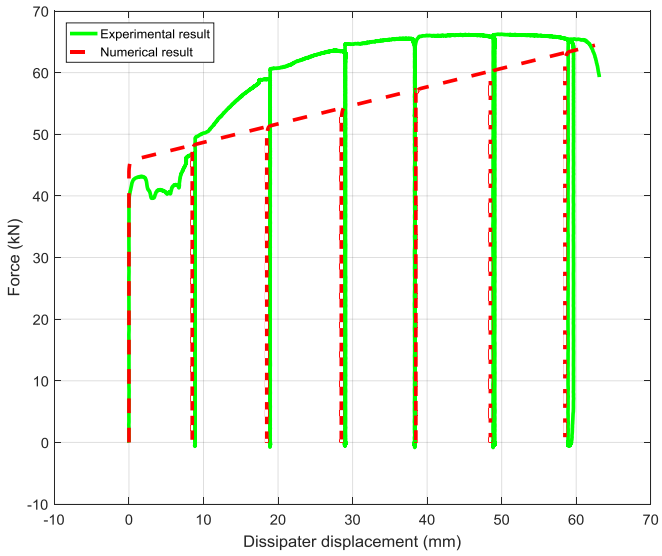

Figure 5.19 *Comparison of experimental and numerical hysteresis loops for the dissipater element with the GNG2 prototype.*

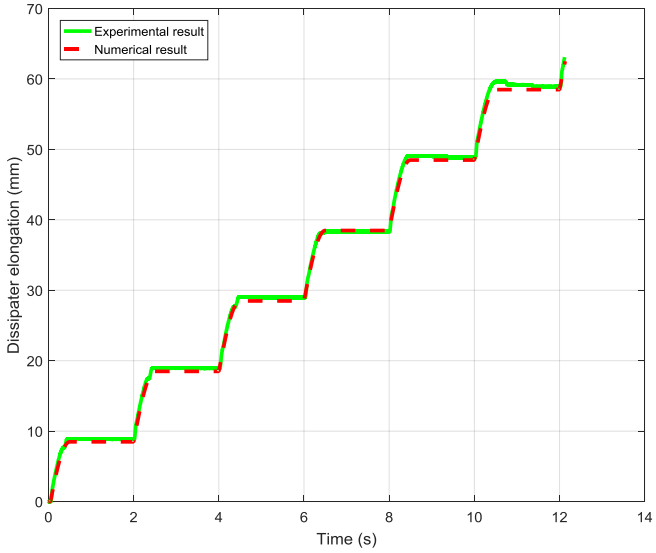

Figure 5.20 *Comparison of experimental and numerically created dissipater elongation behaviour.*

5.8. Conclusions

This chapter has outlined the testing of the advanced GNG2 prototype with eight yielding steel dissipater elements in a monotonic compression and cyclic testing schedule. The enclosed hysteretic energy dissipation was calculated and compared for 10 mm and 3 mm rack sizes, using the same input displacement profile. A comparison between the responses of the two prototype systems was made. These actions further address research questions 2 and 3, and specific outcomes to note are listed for each research question below:

Can the devices respond with appropriate speed of engagement for use during seismic loading of structures?

- Accelerometer recordings, where one accelerometer was mounted on each collet, demonstrated the approximately simultaneous action of the two collets during the ratcheting motion.
- Due to the axial symmetry of the ratcheting mechanism in the second prototype, it is believed that the collets on this prototype act in greater unison than the pawls on the first prototype, which experienced a slight lag to varying degrees during operation. Careful detailed design could reduce the likelihood of misalignment and ensure consistent and reliable engagement.

Can the experimental devices exhibit desirable hysteresis behaviour, similar to theoretical predictions?

- The ratcheting mechanism was shown to work as designed, reducing the free-travel prior to engagement on subsequent loading cycles, with the observed hysteretic behaviour closely matching the model presented previously in Chapter 2, with more complex material yielding behaviour observed in the physical system.
- The ratcheting mechanism provided rapid engagement during multi-cycle loading, providing additional energy dissipation capacity to the system.
- Robust, repeatable operation of the mechanism with redundancy in engagement was observed.
- 10 mm and 3 mm pitch racks were tested to investigate the experimental performance of these different tooth sizes, with the 3 mm case broadly representing a practical lower bound in pitch size.
- Use of the reduced pitch setup was shown to reduce free-travel and increase engagement of the energy dissipation system, resulting in increased energy dissipation.
- The enclosed hysteretic energy dissipation for the 10 mm and 3 mm rack pitch sizes was compared, with each system undergoing the same sine displacement input profile until dissipater fracture. During the four cycles completed with the 3mm pitch rack, the energy dissipation per cycle was between 143% and 164% of the energy dissipated using the 10mm pitch rack during the same loading cycle, due to the smaller pitch having less free travel. A comparison to a theoretical maximum, representing a device with no free-travel, suggests that an additional 15-26% of energy dissipation could be achieved per cycle during the first three

cycles, prior to dissipative element fracture on the fourth cycle for the theoretical device with an infinitely small pitch and no free-travel.

- Initial loading cycles, with lower forces in the system prior to strain hardening of the steel dissipater, produced less elastic displacement during unloading, allowing for more ratcheting occurrences on these initial cycles
- Due to the construction of the devices, the displacement required for the first ratcheting occurrence on each loading cycle was slightly greater than the tooth pitch
- Eight yielding steel dissipater elements were tested allowing peak forces of ~65 kN, with five tested to fracture. As intended by design, the steel dissipater yielded only in tension.
- Furthermore, while the test was cyclic, the dissipater behaviour approximates a piecewise version of a standard monotonic tensile test due to the GNG device removing significant compressive loading in the dissipater. In particular, the maximum compressive forces are limited to less than 1.5% of the ultimate tensile forces.
- No damage to the assembly beyond the dissipater was observed.
- The system can be designed for use with various other dissipation mechanisms and at higher force levels as required.
- The results of the testing of the two prototype devices show the potential of the GNG concept to be a favourable option in supplementary damping and bracing systems.

6. Controlled Rocking Systems

6.1. Summary

This chapter presents an overview of controlled rocking systems with details of the mechanics of the system and their hysteretic behaviour. Controlled rocking systems are one of the most suitable applications for the use of GNG devices. A brief overview of rocking frame development, testing and applications is provided. The idealised system behaviour used to model rocking frame response is then described. This model is adapted for application with the tension-only ratcheting GNG devices that have been developed in previous chapters of this thesis. The controlled rocking system behaviour model developed here is used to create a numerical model to simulate the response of a controlled rocking system in Chapter 7.

This chapter addresses research question 4: Can a model be developed to describe the GNG hysteretic performance, together with that of a rocking wall?

6.2. First rocking systems

An increasingly popular low damage design approach, is through controlled rocking systems. The earliest studies of the advantages of allowing uplift in structures exposed to ground motions were completed in the 1960s. Muto et al. [1960] and Housner [1963] viewed it as an anomaly that some structures which appeared classically unstable, such as elevated water tanks, tall slender petroleum cracking towers, and stone columns supporting heavy statues, survived earthquake events while seemingly more stable structures nearby were severely damaged.

In some of the first developments, Housner used rigid block dynamics to explain this unexpected stable behaviour, and Muto conducted shake table experiments on an inverted pendulum type model structure, shown in **Figure 6.1**. The seismic design technique of applying a static horizontal force to a structure was found by both Muto and Housner to greatly underestimate the stability of tall slender structures subjected to earthquake ground motions.

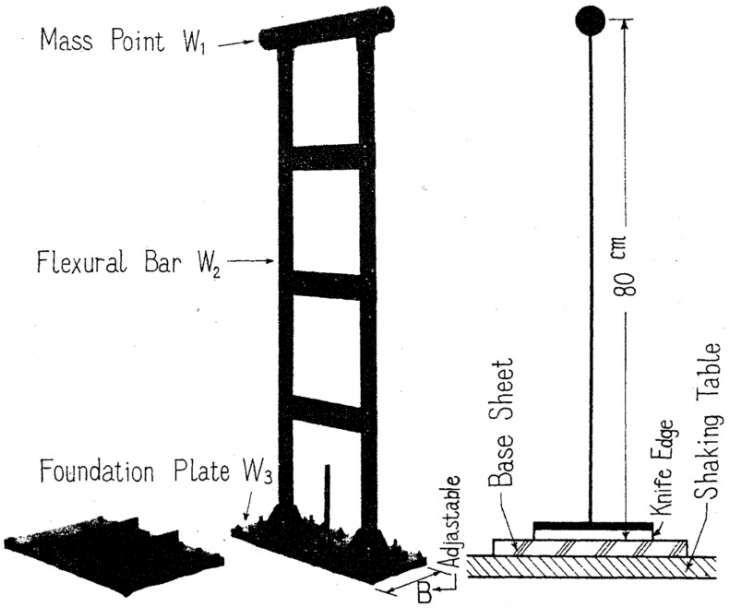

Figure 6.1 *Model used by Muto et al. [1960].*

Supplemental damping devices were first added to rocking structures by Beck and Skinner [1974]. They considered a controlled rocking system in their design of the reinforced concrete bridge pier presented in **Figure 6.2**. The stepping A-frame hollow cylinders of the bridge pier incorporated damping by energy-absorbing devices, using the plastic deformation of a steel torsion beam, to reduce side-sway motion.

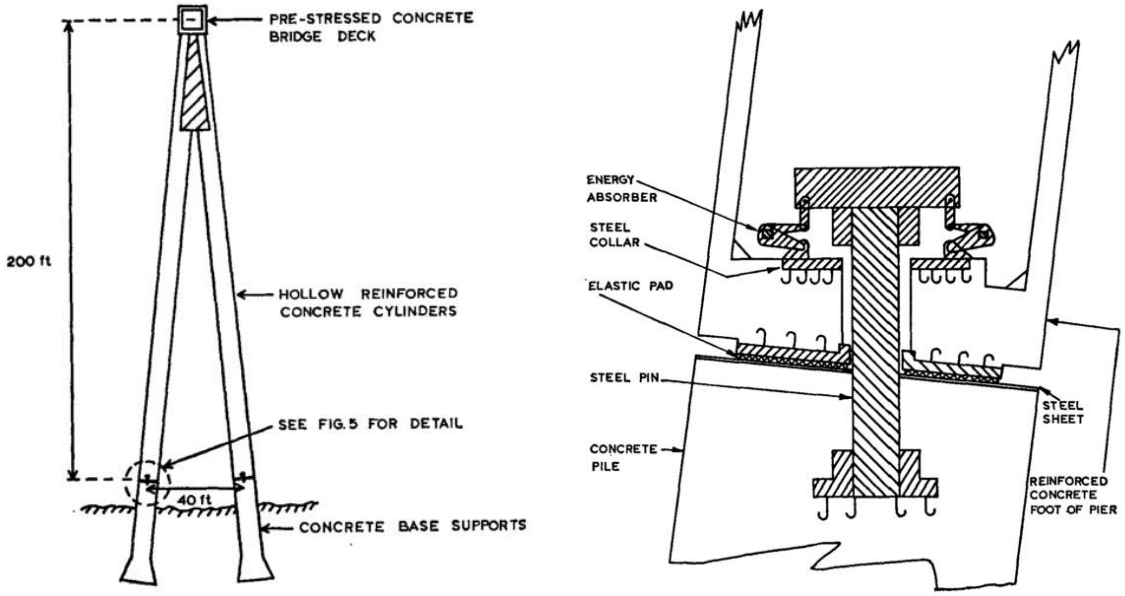

Figure 6.2 *RC bridge pier designed to step [Beck and Skinner 1974]:*
a) typical A-frame pier, and b) energy absorber arrangement

6.3. Testing overview

The first large scale tests were completed by Clough and Huckelbridge [1977]. They tested steel moment frames with uplifting columns using a 3 storey single bay frame. Energy dissipation was added to the same 3 storey structure, via yielding steel bars at the base, by Kelly and Tsztoo [1977]. Performance of the system with the energy-absorbing devices installed was greater than testing with a fixed base design or a frame freely allowed to uplift. The structure is shown in Figure 6.3. Huckelbridge [1977] also tested a 9 storey multi bay frame and observed significant reductions in lateral loading compared to the response of a fixed base structure.

The 1990s saw a significant increase in interest in controlled rocking structures from the structural engineering community following the work of Priestley and collaborators on Precast Seismic Structural Systems (PRESSS) [Priestley 1991]. PRESSS systems aimed to limit non-linear response to the connections, and these studies were the first to introduce un-bonded post-tensioning to controlled rocking systems. A 60% scale five-storey precast concrete building, shown in **Figure 6.3**, was tested at seismic levels significantly higher than required by building codes and exposed to drifts of up to 4.5% with no significant strength loss and only minimal damage [Priestley et al. 1999]. Other work in this project considered soil effects on rocking [Xiao et al. 1992].

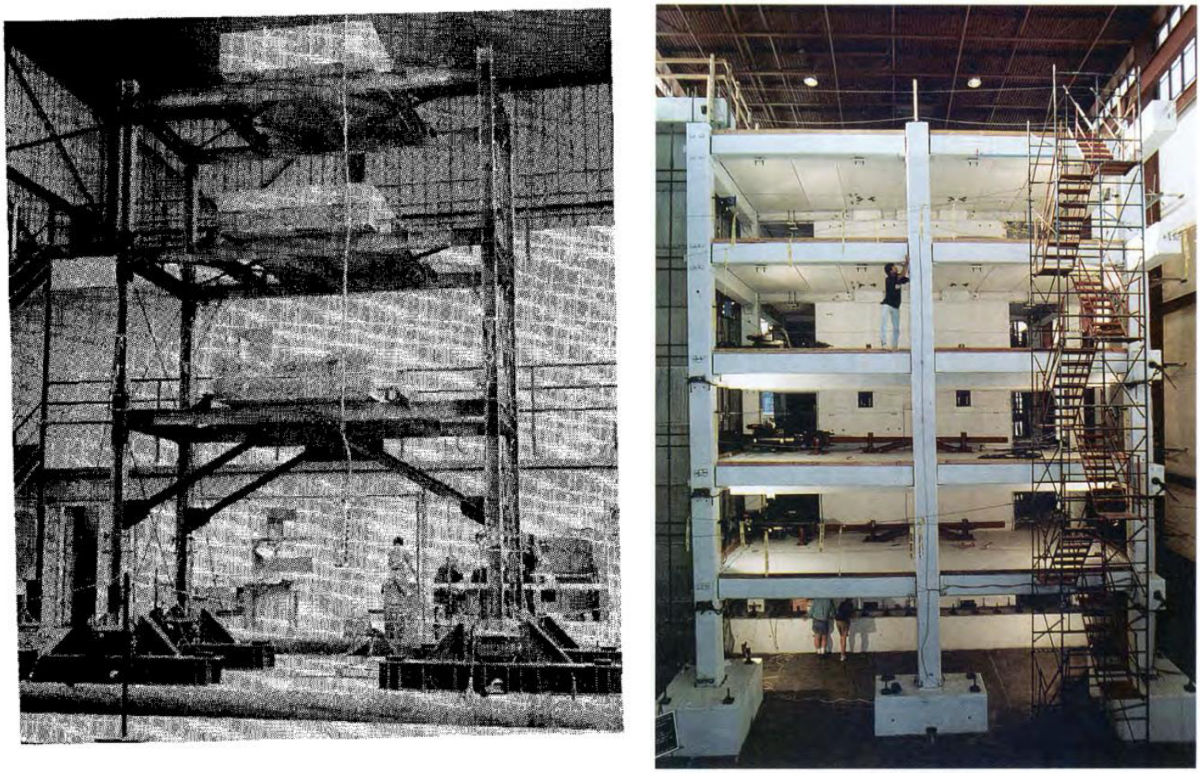

Figure 6.3 *Early large scale testing:*

a) 3-storey single bay frame [Clough and Huckelbridge 1977], and b) 5 storey PRESSS building [Priestley et al. 1999].

Some of the first work on steel framed rocking structures was undertaken by Wada et al. [2001]. An alternative column splice design using slender columns with damper joints was proposed, as shown in **Figure 6.4**. The joints are weak in tension with a large deformation capacity, and strong in compression. Results indicated that the damper joint had a promising capacity for deformation and energy absorption.

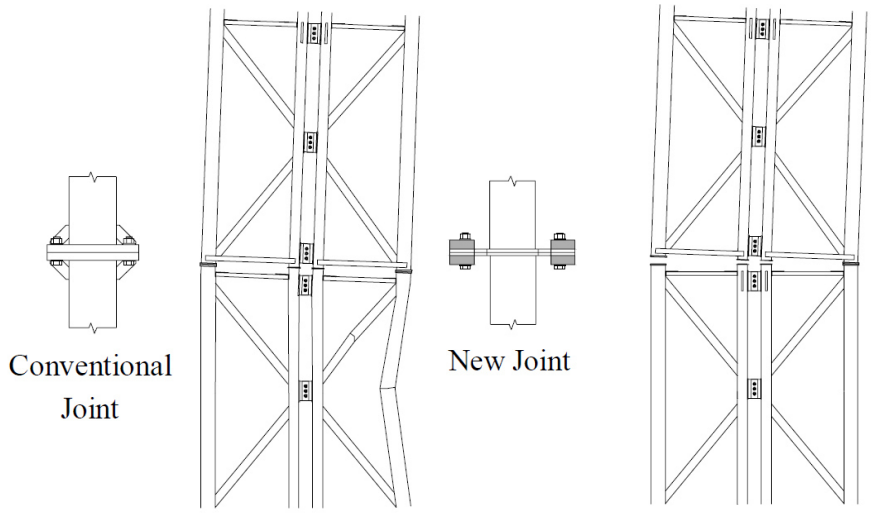

Figure 6.4 *Column splice connections [Wada et al. 2001]:*
a) conventional joint, and b) proposed new joint.

Yielding base plates were studied by Midorikawa et al. [2006, 2010] in half-scale and one-third-scale 3-storey braced steel frames. Shaking table tests using the 1940 El Centro earthquake ground motion were completed. In a comparison between yielding base plates permitting uplift and fixed base plates, column base shear was reduced by up to 52% in the structure with uplift, while maximum roof displacements were similar for both systems.

Viscous dampers, vertically mounted between the foundation and column bases of a controlled rocking steel system, were used by Tremblay et al. [2008] to dissipate energy and control lateral displacement, while also limiting the impact forces induced in the columns. A half-scale model of a two-storey rocking system was subjected to a series of ground motion shaking tests, resulting in peak inter-storey drifts of about 1.5%. No structural damage was recorded.

Controlled rocking steel frames with post-tensioning and replaceable yielding elements have been studied in detail by Eatherton et al. [2014]. A dual frame system, shown in Figure 6.5, was constructed with replaceable yielding steel plates attached between the two frames to provide supplemental energy dissipation. For drift ratios of up to 2.5%, inelastic response was confined to the replaceable shear fuses, and near-zero residual drift was recorded when lateral forces were removed. Self-centring ratios of greater than 1.0 produced the best results, where the self-centring ratio was calculated as

the ratio of restoring moment due to initial post-tensioning force and expected dead loads, divided by the resistance to self-centring caused by the fuse shear capacity.

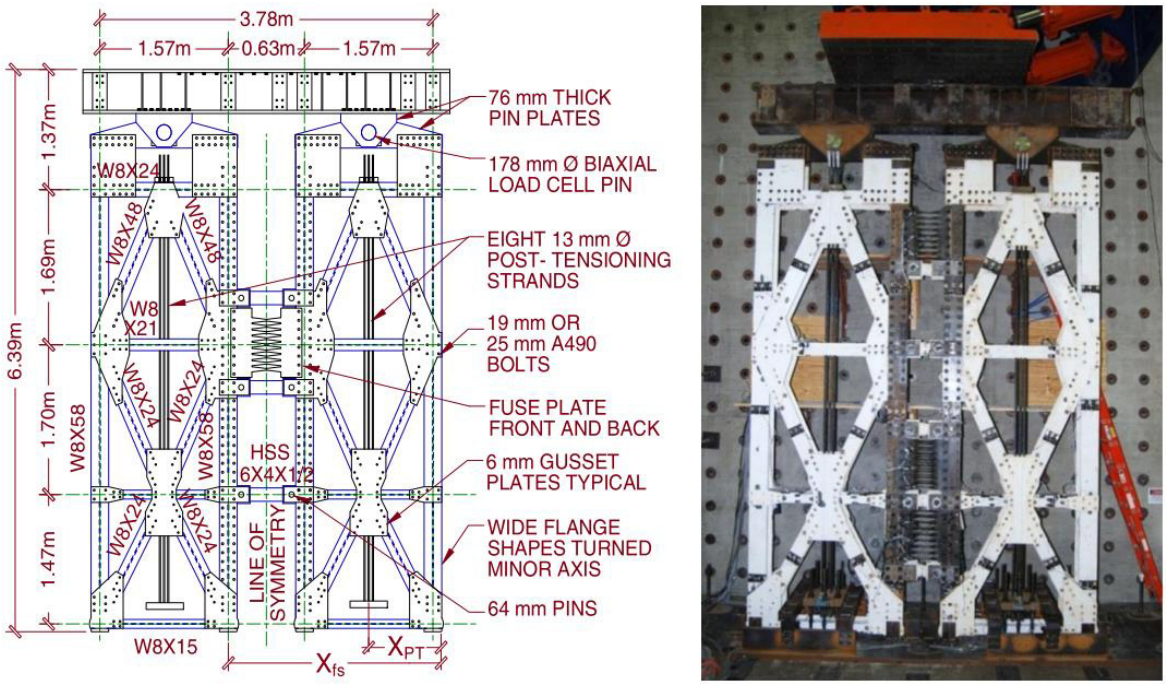

Figure 6.5 *Controlled rocking system [Eatherton et al. 2014]: a) schematic, and b) test apparatus.*

A rocking base controls the response of the first mode, but higher modes can increase structural forces even when the base moment is limited. Higher mode effects become more important for taller structures, with their associated longer periods and higher spectral displacements. Wiebe [2008] showed that providing multiple rocking sections over the height of a controlled rocking frame system substantially reduced storey shears and bending moments due to system response of the first and higher modes. Including a non-linear, self-centring shear control brace at the first level of the frame can also be used to control the peak forces in the system [Wiebe 2013, Wiebe and Christopoulos 2014]. Base rocking provides deformation capacity in the system, while the first-storey brace is only needed to limit the shears caused by the higher modes. While higher modes effects are an important consideration and an area for additional research, it is not the focus of this thesis.

6.4. Selected modern applications

Controlled rocking steel systems are being implemented in modern structures with high desired seismic performance. The Orinda City Hall in Orinda, California, houses several city services and was designed to fulfil ‘essential-use facility’ design criteria. Rocking frames with post-tensioning and replaceable bolted moment joints were used to meet these safety requirements [Mar 2010]. To

provide additional drift capacity before post-tensioning cables yield, the post-tensioning cable length was increased by looping the cables under the frame, as demonstrated in **Figure 6.6**.

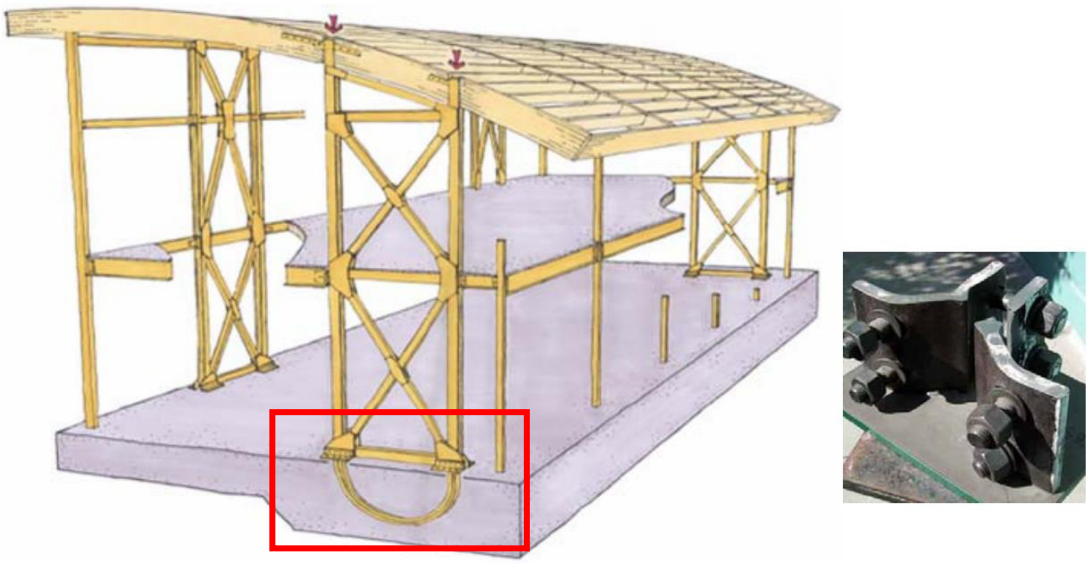

Figure 6.6 *The controlled rocking system at the Orinda City Hall, with looped post-tensioning cables highlighted. A specimen of the bolted moment joint is shown at right [Mar 2010].*

The 15-storey Elevate Apartments building, and the Fairlie Terrace student accommodation buildings (5, 10 and 11 stories respectively), all located in Wellington, New Zealand, use a controlled rocking system of concentrically braced frames with pre-stressed Ringfeder friction springs and sliding hinge joints between columns and foundation to provide low damage design performance [Gledhill et al. 2008, Tait et al. 2013]. The seismic resisting scheme developed included perimeter longitudinal moment resisting frames with transverse bracing frames reducing diaphragm spans and controlling torsion at the perimeter. A schematic of the column base system at Elevate is provided in **Figure 6.7**.

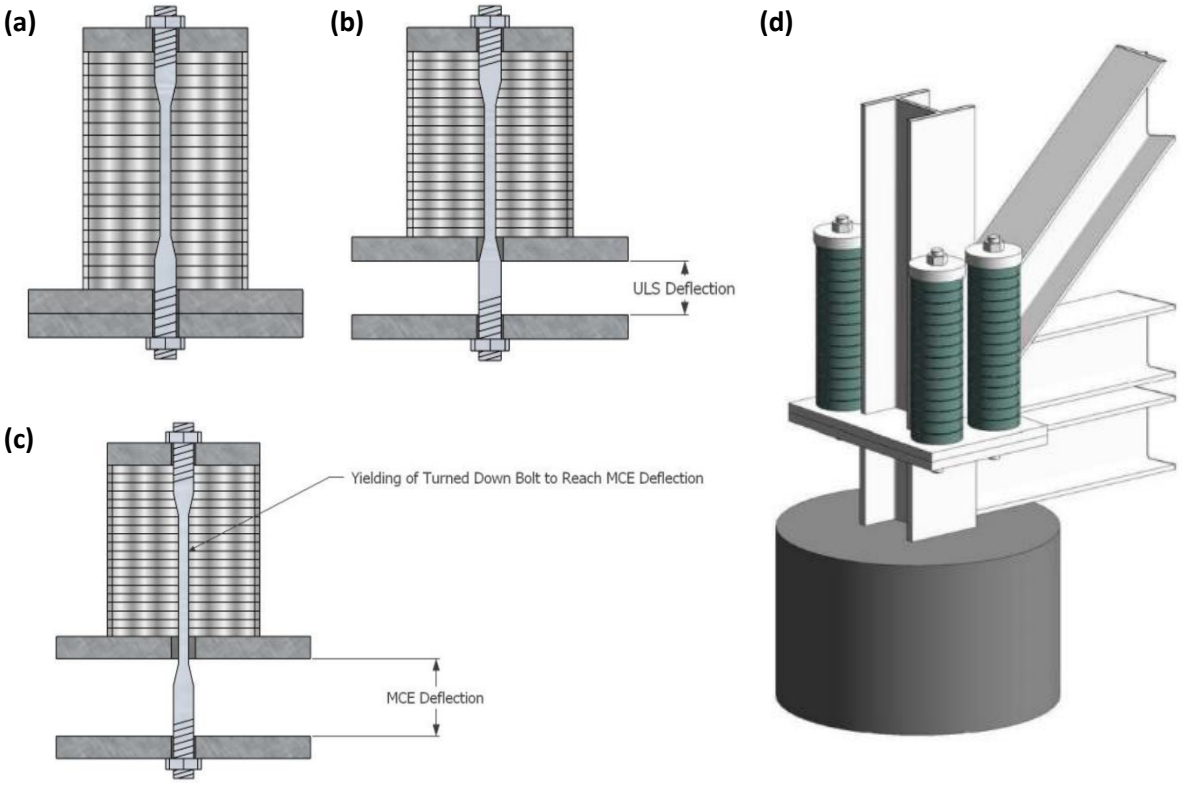

Figure 6.7 *Ringfeder friction spring behaviour [Tait et al. 2013]:*
a) prior to uplift, b) at ULS deflection, c) at MCE deflections, and d) CBF column-base connection.

The 3-storey Forte Health building, located in the CBD of Christchurch, New Zealand, uses a controlled rocking system to meet the requirements of an 'Importance Level 4' structure and protect the specialist medical facilities housed inside [Latham et al. 2013]. The system incorporates coupled steel braced frames, vertical post-tensioning, and paired energy dissipation devices. Replaceable axially-yielding mild steel dissipaters are used in conjunction with HF2V lead extrusion dampers to provide robust energy dissipation via both displacement-proportional and velocity-proportional mechanisms. The system is shown in **Figure 6.8**.

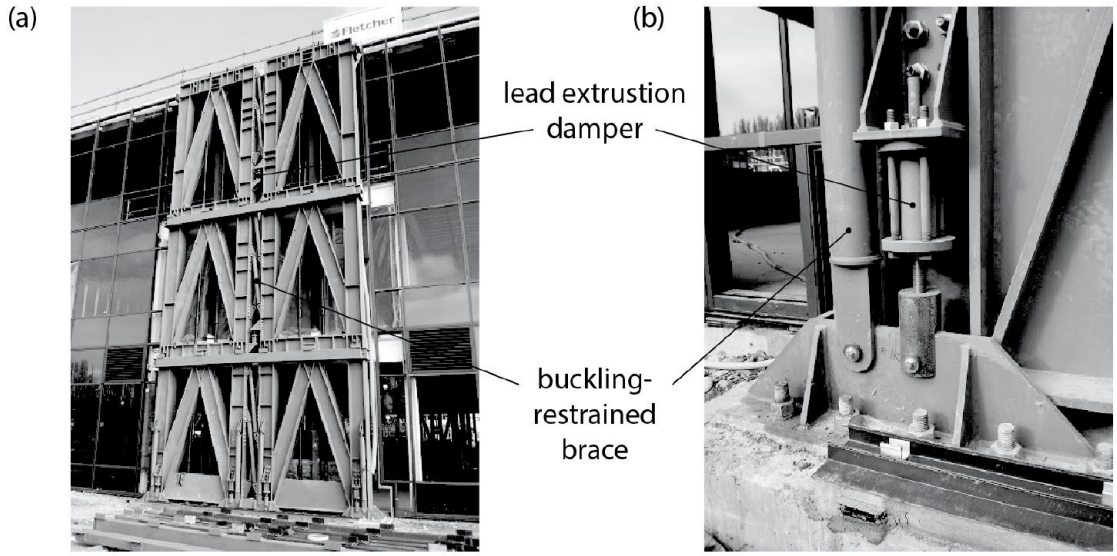

Figure 6.8 *The controlled rocking system at Forte Health [Wiebe 2013]:*
a) coupled steel braced frames, and (b) paired energy dissipation devices at the base.

This structure features special detailing at the connection between the floor diaphragms and the lateral load-resisting system to minimise displacement incompatibilities associated with uplift. A steel tongue plate, shown in **Figure 6.9**, protrudes from the floor structure and fits through a slot in the rocking frame. This slotted connection allows the tongue plate to slide up and down within the rocking frame to accommodate vertical movements experienced by the frames as they rock. Lateral loads are transferred via bearing of the steel plate onto the frames.

Figure 6.9 *Floor to frame slotted connection [Latham et al. 2013]:*
a) tongue plate, b) slot in frame, and c) frame-superstructure schematic by author.

6.5. Idealised system behaviour

The idealised system behaviour used to model rocking frame response is described below, and adapted for application with the tension-only ratcheting GNG devices that have been developed. The system behaviour model developed here is used to create a numerical model to simulate the response of a controlled rocking system in Chapter 7.

6.5.1. Overview

The hysteretic response of controlled rocking systems has been described by a range of researchers, including recent work by Wiebe [2013] and Eatherton and Hajjar [2014]. **Figure 6.10** illustrates the loading response of three types of flexible rocking frame systems. System A has a restoring force provided by gravity forces alone. The response of system A, with the elastic rocking frame only, shows a bilinear response in loading with an initially very stiff response prior to uplift due to elastic flex, followed by a negative post-uplift stiffness during rocking. The delay in the onset of uplift is due to the weight force of the frame providing an initial moment to overcome. This system can become statically unstable at large drifts.

The response of system B, where post-tensioning is added to the elastic rocking frame, also displays bilinear behaviour in loading. This system has the same very stiff response prior to uplift as system A, but the post-tensioning provides a positive stiffness after uplift. This positive post-uplift stiffness greatly increases the force carrying capability of the frame during a stable range of motion. The gravity force of the frame and the force in the post-tensioning both contribute to the initial moment to overcome to achieve uplift.

Supplementary damping mechanisms are frequently implemented along with rocking systems to achieve a more controlled response, and to increase energy dissipation, as rocking systems typically have very low inherent damping. The response of system C, where some yielding energy dissipation devices are incorporated into the post-tensioned system, can have a flag-shaped hysteresis response. The shape of the hysteresis flag is dependent on the energy dissipation mechanism installed. In this system, the weight force, post-tensioning force, and yield force of the devices all contribute to the initial uplift moment. In **Figure 6.10** the energy dissipation devices are coloured red when not engaged or during elastic behaviour, and green to indicate dissipater yielding. The mechanics of a controlled rocking system with post-tensioning and yielding energy devices is described in more detail below, and a detailed description of the system hysteresis behaviour when implementing Grip ‘n’ Grab devices is provided in Section 6.5.3.

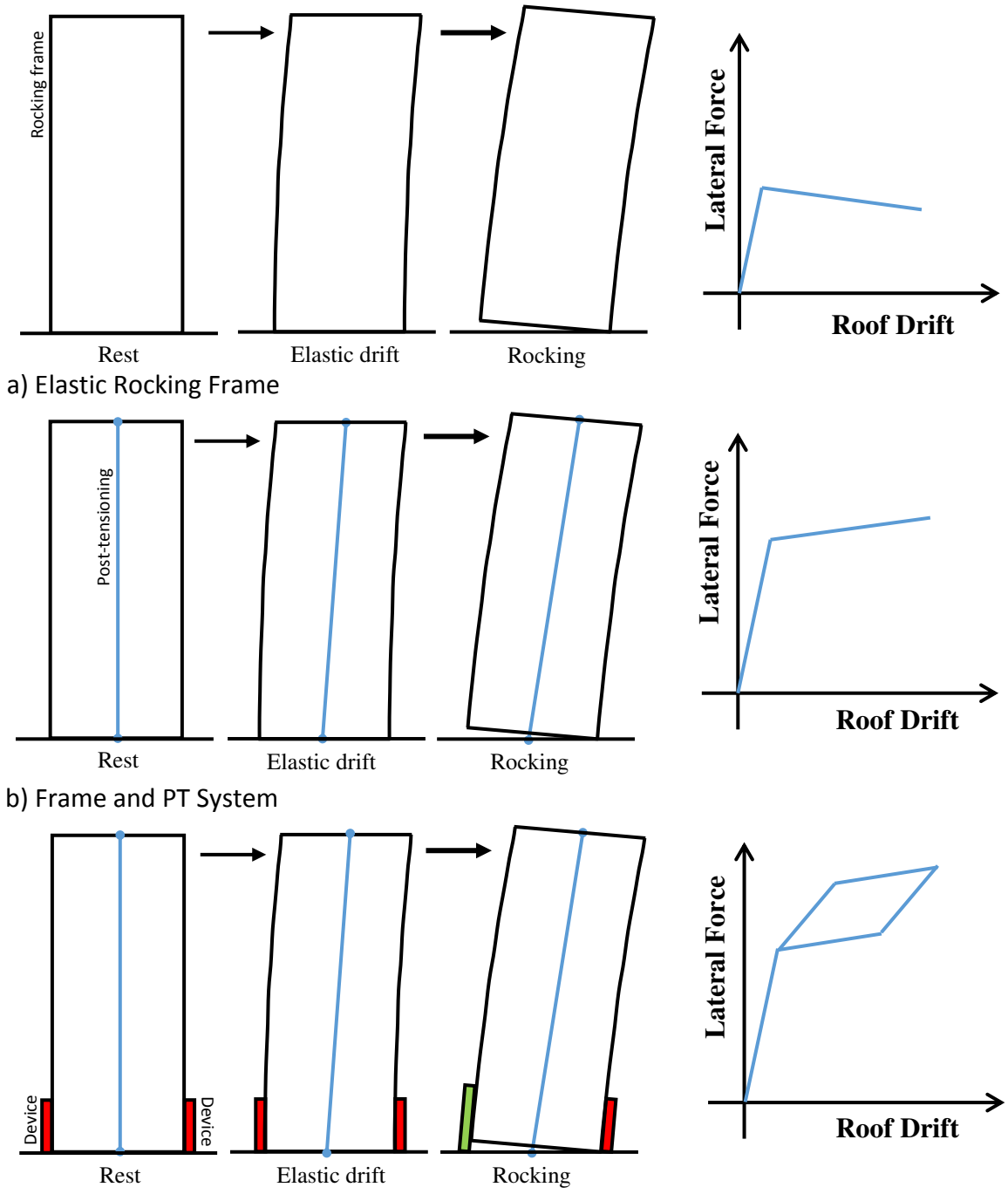

Figure 6.10 *Loading response of uplifting rocking frame systems:*

a) elastic rocking frame only, b) frame and post-tensioning, and c) frame, post-tensioning and energy devices.

6.5.2. Controlled rocking system with post-tensioning and yielding energy devices

6.5.2.1. System behaviour

Figure 6.11 shows the idealised behaviour of a detailed controlled rocking system with post-tensioning and yielding energy dissipation devices. The rocking frame, post-tensioning, leaning column (applied

to model P-Delta effects), and devices are shown in an approximate configuration. The energy dissipation devices are installed at both rocking edges and the post-tensioning is connected at the centre of the rocking frame in this example system.

The displacements due to flexure of the rocking frame and base rocking about the right hand side rocking edge, during the main stages of system motion, are labelled in Figure 6.11:

A. Definition of flexible rocking system at rest
B. Lateral deflection prior to uplift
C. Lateral deflection after uplift, prior to dissipater yielding
D. Lateral deflection after uplift, subsequent to dissipater yielding

A guide to the parameters used in **Figure 6.11** is provided in **Table 6.1**. The energy dissipation devices are coloured red when not engaged or during elastic behaviour, and green to indicate dissipater yielding. A detailed description of the system hysteresis behaviour when implemented with Grip 'n' Grab devices is provided in the subsection effect of ratcheting behaviour.

***Table 6.1** Guide to parameters presented in **Figure 6.11**.*

Symbol	Description
H	Height of the rocking frame
b	Half-width of the rocking frame
W_{frame}	Weight of the rocking frame
W_{trib}	Total tributary weight of the system
F_{PT}	Post-tensioning force
F_{ED}	Device force
d_W	Eccentricity of the frame weight from the rocking edge
d_{PT}	Eccentricity of the post-tensioning line of action from the rocking edge
d_{ED}	Eccentricity of the device line of action from the rocking edge
Δ_{flex}	Lateral displacement of the rocking frame due to flexure
Δ_{rock}	Lateral displacement of the rocking frame due to uplift
K_0	Initial lateral stiffness of the controlled rocking system
$K_{rock,ED}$	Post-uplift, pre-yield lateral stiffness of the controlled rocking system
$K_{rock,ED\ yield}$	Post-uplift, post-yield lateral stiffness of the controlled rocking system

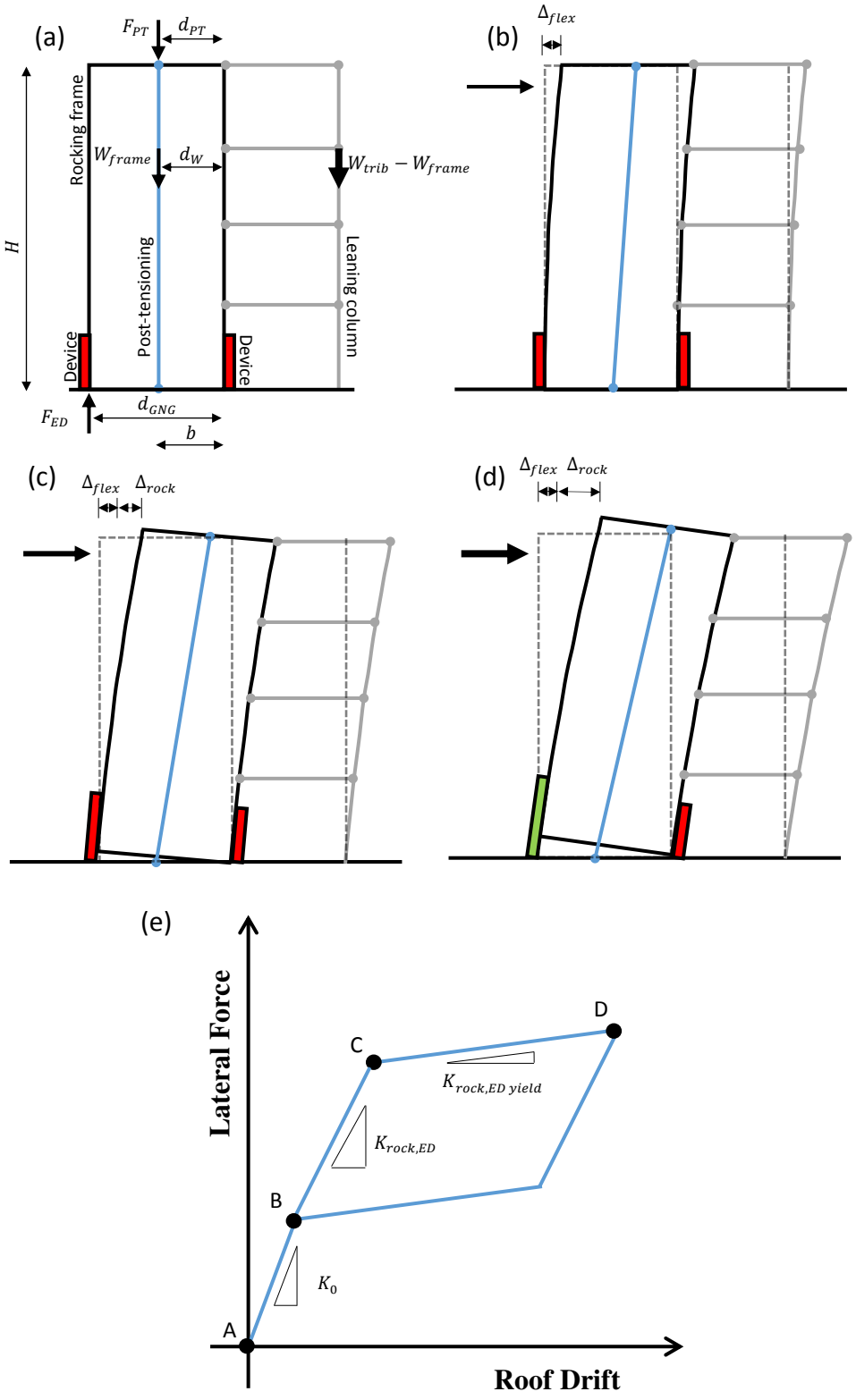

Figure 6.11 *Mechanics of the controlled rocking system with post-tensioning and yielding energy devices: a) definition of flexible rocking system, b) lateral deflection prior to uplift, c) lateral deflection after uplift, d) lateral deflection after uplift and device yield, and e) hysteresis behaviour.*

6.5.2.2. Contributions to moment at uplift

There are three components of the system contributing resistance to uplift and defining the rocking base moment required for uplift and rotation, M_{uplift}, clearly outlined by Wiebe [2015] and described below. These contributions are provided by the frame weight, M_W, the post-tensioning, M_{PT}, and the supplemental energy dissipation devices, M_{ED}, respectively. Taking moments about the rocking edge:

$$M_{uplift} = M_W + M_{PT} + M_{ED} \quad (6.1)$$

The rocking resistance caused by the weight of the rocking frame is:

$$M_W = W_{frame} \times d_W \quad (6.2)$$

where W_{frame} is the weight force of the frame and d_W is the horizontal distance from the rocking edge to the centre of mass of the frame. The resistance to uplift provided by the post-tensioning is:

$$M_{PT} = F_{PT} \times d_{PT} \quad (6.3)$$

where $F_{PT,initial}$is the initial force in the post-tensioning and d_{PT} is the horizontal distance from the rocking edge to the connection point of the post-tensioning. The remaining moment resistance is provided by the supplemental energy dissipation devices:

$$M_{ED} = F_{ED} \times d_{ED} \quad (6.4)$$

where $F_{ED}$is the force in the energy dissipation devices at uplift and d_{ED} is the horizontal distance from the rocking edge to the device. A range of these terms are illustrated in **Figure 6.11**.

Figure 6.12 shows the effect of altering the contribution of energy dissipation devices to the base rocking moment on the resulting hysteresis flag loop. Increasing the contribution of energy dissipation devices to the base rocking moment increases the height of the flag, increasing the enclosed area of the loop and the resulting energy dissipated by the device. **Figure 6.12**a shows the hysteresis flag for a moment contribution from energy dissipation devices of 25%. Displacement of the devices begins at a rocking moment of 75% of the base rocking moment at uplift, and around one quarter of the height of the hysteresis curve above the x-axis is enclosed. This enclosed area is approximately doubled in **Figure 6.12**c where energy dissipation devices contribute 50% of the base rocking moment at uplift.

The SCNZ rocking frame design guide [Wiebe et al. 2015] suggests at least 40% of the total base uplifting moment resistance be provided by energy dissipation devices. However, in the examples provided in the design guide, the requirement to ensure that the overstrength force resisting joint closure is less than the pre-stress in the post-tensioning along one column line, often results in the contribution of the energy dissipation devices to the total uplifting moment in the final calculation to be around one third. This value is based largely on the presence of residual compressive forces in the

energy dissipation devices, which do not exist when using the GNG device, so the choice could be more open in this case.

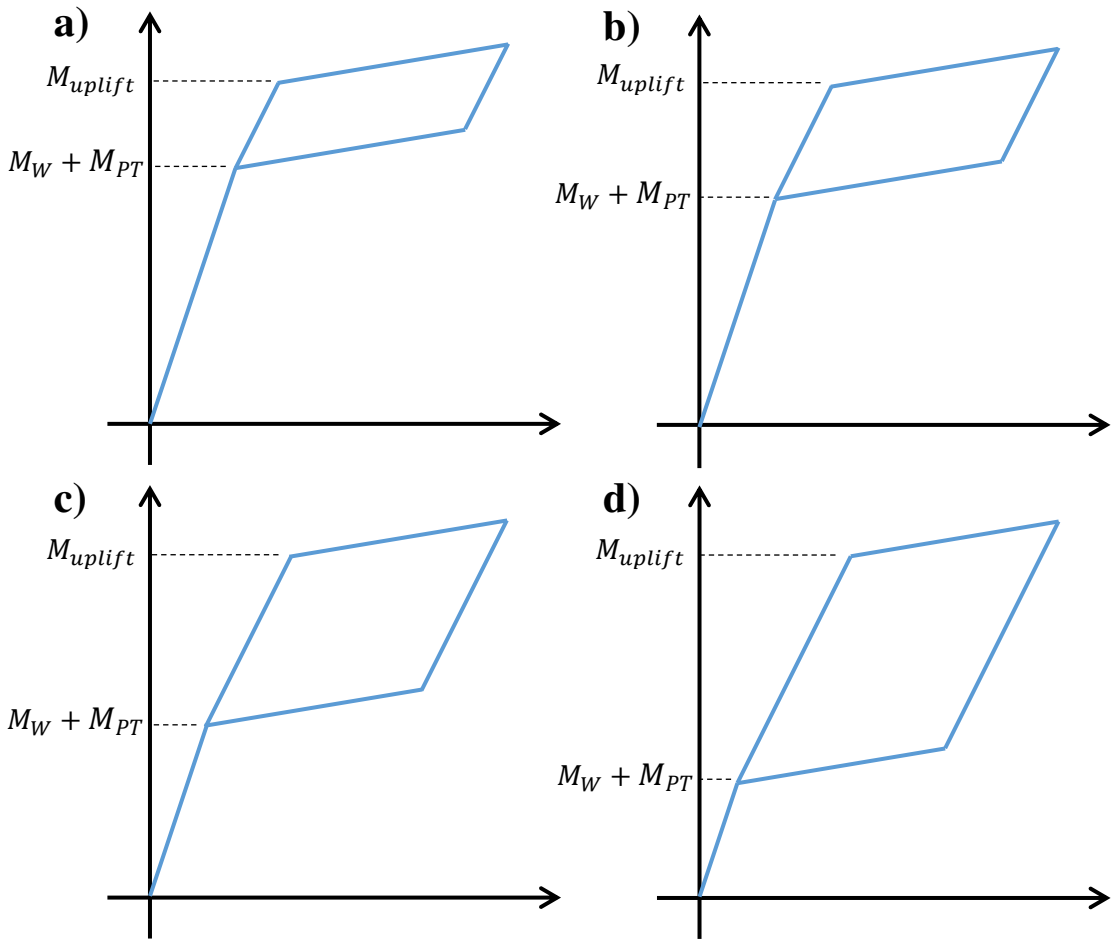

Figure 6.12 *Base rocking moment allocation and resulting flag shapes:*
a) 25% from energy devices, b) 33% from energy devices, c) 50% from energy devices, and d) 66% from energy devices.

6.5.2.3. System stiffness

The initial lateral stiffness of the controlled rocking system prior to uplift is defined by the frame properties:

$$K_0 = \frac{3E_{frame}I_{frame}}{L^3} \tag{6.5}$$

Wiebe [2013] defines the post-uplift lateral stiffness, relating F to Δ for an idealised controlled rocking system, with a load applied at height h as:

$$K_{rock} = \left(\frac{h^2}{K_{rigid\ rock}} + \frac{1}{K_0}\right)^{-1} \tag{6.6}$$

where $K_{rigid\ rock}$ is the post-uplift moment-rotation stiffness of an equivalent rigid rocking block, defined by:

$$K_{rigid\ rock} = \left(\frac{A_{PT}E_{PT}}{L_{PT}}\right) {d_{PT}}^2 - W_{trib}H_W \qquad (6.7)$$

where A_{PT}, E_{PT} and L_{PT} are the area, elastic modulus and length of the post-tensioning respectively. The weight forces in the system act at height H_W. This equation is applicable to systems with energy devices displaying perfectly plastic behaviour following uplift. For the use of devices with elastic-plastic behaviour following uplift, this definition can be extended to:

$$K_{rigid\ rock,ED} = \left(\frac{A_{PT}E_{PT}}{L_{PT}}\right) {d_{PT}}^2 + \left(\frac{A_{ED}E_{ED}}{L_{ED}}\right) {d_{ED}}^2 - W_{trib}H_W \qquad (6.8)$$

where A_{ED}, E_{ED} and L_{ED} are the area, elastic modulus and length of a yielding type device. The resulting $K_{rock,ED}$ will be applicable to the controlled rocking system following uplift, and prior to device yielding. The reduction in device stiffness following yielding alters the equivalent rigid rocking equation, which will become:

$$K_{rigid\ rock,ED\ yield} = \left(\frac{A_{PT}E_{PT}}{L_{PT}}\right) {d_{PT}}^2 + \left(\frac{A_{ED}\beta E_{ED}}{L_{ED}}\right) {d_{ED}}^2 - W_{trib}H_W \qquad (6.9)$$

where β is the post-yield stiffness to initial stiffness ratio of the device.

These equations define the stiffness of the controlled rocking system during the three main stages of hysteresis behaviour displayed in Figure 7.9. Simplifying the stiffness of the post-tensioning and the devices, and substituting the appropriate $K_{rigid\ rock}$ values, the three stiffness equations are presented in full in **Table 6.2** for completeness.

Table 6.2 *Summary of system stiffness during different stages of rocking behaviour.*

Rocking stage	**System stiffness**	
Pre-uplift	$K_0 = \frac{3 \times E_{frame}I_{frame}}{h^3}$	*(6.5)*
Post-uplift, pre-yield	$K_{rock,ED} = \left(\frac{h^2}{K_{PT}{d_{PT}}^2 + K_{ED}{d_{ED}}^2 - W_{trib}H_W} + \frac{1}{K_0}\right)^{-1}$	*(6.10)*
Post-uplift, post-yield	$K_{rock,ED\ yield} = \left(\frac{h^2}{K_{PT}{d_{PT}}^2 + \beta K_{ED}{d_{ED}}^2 - W_{trib}H_W} + \frac{1}{K_0}\right)^{-1}$	*(6.11)*

6.5.2.4. Defining a stiffness ratio for the system

Knowledge of these system stiffness equations allows for the design of a desired system stiffness ratio between the initial pre-uplift stiffness and either, or both, of the two post-uplift stiffness values:

$$\alpha = \frac{K_{rock,ED}}{K_0} \tag{6.12}$$

$$\gamma = \frac{K_{rock,ED\ yield}}{K_0} \tag{6.13}$$

When K_0, d_{PT}, d_{ED}, W_{trib}, and H_W have been defined by the geometry of the design, the required stiffness contributions from the post-tensioning and energy devices can be calculated. A further simplification can be made if the post-tensioning stiffness and the initial stiffness in the device are set equal to each other. These rearrangements are shown in **Table 6.3**.

Table 6.3 *Calculation of the required post-tensioning and initial device stiffness values for a desired stiffness ratio in the rocking system.*

Defining pre-yield stiffness ratio	**Defining post-yield stiffness ratio**	
$K_{rock,ED} = \alpha K_0$	$K_{rock,ED\ yield} = \gamma K_0$	*(6.14)*
$K_{rigid\ rock,ED} = \frac{\alpha K_0 h^2}{1-\alpha}$	$K_{rigid\ rock,ED\ yield} = \frac{\gamma K_0 h^2}{1-\gamma}$	*(6.15)*
$K_{PT}{d_{PT}}^2 + K_{ED}{d_{ED}}^2 = \frac{\alpha K_0 h^2}{1-\alpha} + W_{trib}H_W$	$K_{PT}{d_{PT}}^2 + \beta K_{ED}{d_{ED}}^2 = \frac{\gamma K_0 h^2}{1-\gamma} + W_{trib}H_W$	*(6.16)*
$K_{PT,ED} = K_{PT} = K_{ED}$		*(6.17)*
$K_{PT,ED} = \frac{\frac{\alpha K_0 h^2}{1-\alpha} + W_{trib}H_W}{{d_{PT}}^2 + {d_{ED}}^2}$	$K_{PT,ED} = \frac{\frac{\gamma K_0 h^2}{1-\gamma} + W_{trib}H_W}{{d_{PT}}^2 + \beta{d_{ED}}^2}$	*(6.18)*

Both stiffness ratios α and γ can be defined, and the required values of K_{PT} and K_{ED} calculated, using both versions of Equation (6.16). The resulting equations were used in the numerical model presented in Chapter 7. This rearrangement is omitted from the main text in the interest of clarity, and is provided in Appendix B.

6.5.2.5. Comparison of tension-only and tension-compression systems

Since the GNG acts only in tension and does not provide any compressive forces, defining an equivalent tension compression system requires some design decisions and there are multiple ways of defining the equivalence. **Figure 6.13**a shows a reference system response curve for a tension only

device, such as a GNG dissipater system, with low energy dissipation. A system response curve for a tension compression system, such as a BRB, with the same overall flag shaped hysteresis is shown in **Figure 6.13**b. The enclosed area will be essentially the same, and overall system response is expected to be closely similar. The GNG tension force will be twice that of the BRB, but will not contribute any compressive forces. The system using the tension compression device would require larger initial post tensioning forces. Alternatively, if using the same post tensioning force as the reference tension only system in **Figure 6.13**a and the same yield force in both the GNG dissipater system and the BRB, a larger enclosed area of the flag shaped hysteresis curve, and additional energy dissipation, would be achieved. This response is illustrated in **Figure 6.13**c.

Figure 6.13d shows a reference system response curve for a tension only device, such as a GNG dissipater system, with high energy dissipation. Matching this overall system response curve when using a traditional tension compression device requires a much greater post tensioning force, as demonstrated in **Figure 6.13**e. The lower initial post tensioning force required for the GNG system in **Figure 6.13**d, as compared to the system in **Figure 6.13**e, may be favourable for short rocking frames where achieving sufficient elastic deflection of the post tensioning cables can be difficult. Alternatively, if using the same post tensioning force as the reference tension only system, a larger enclosed area of the flag shaped hysteresis curve, and additional energy dissipation, would be achieved. This response is illustrated in **Figure 6.13**f. However, the compressive forces in the dissipater would lead to residual displacements after removal of all dynamic forces at the conclusion of an earthquake. These complications make a direct comparison between tension only and tension compression devices in rocking systems difficult to obtain, given the need for several design decisions and the choice of which aspect of the response is to be maintained.

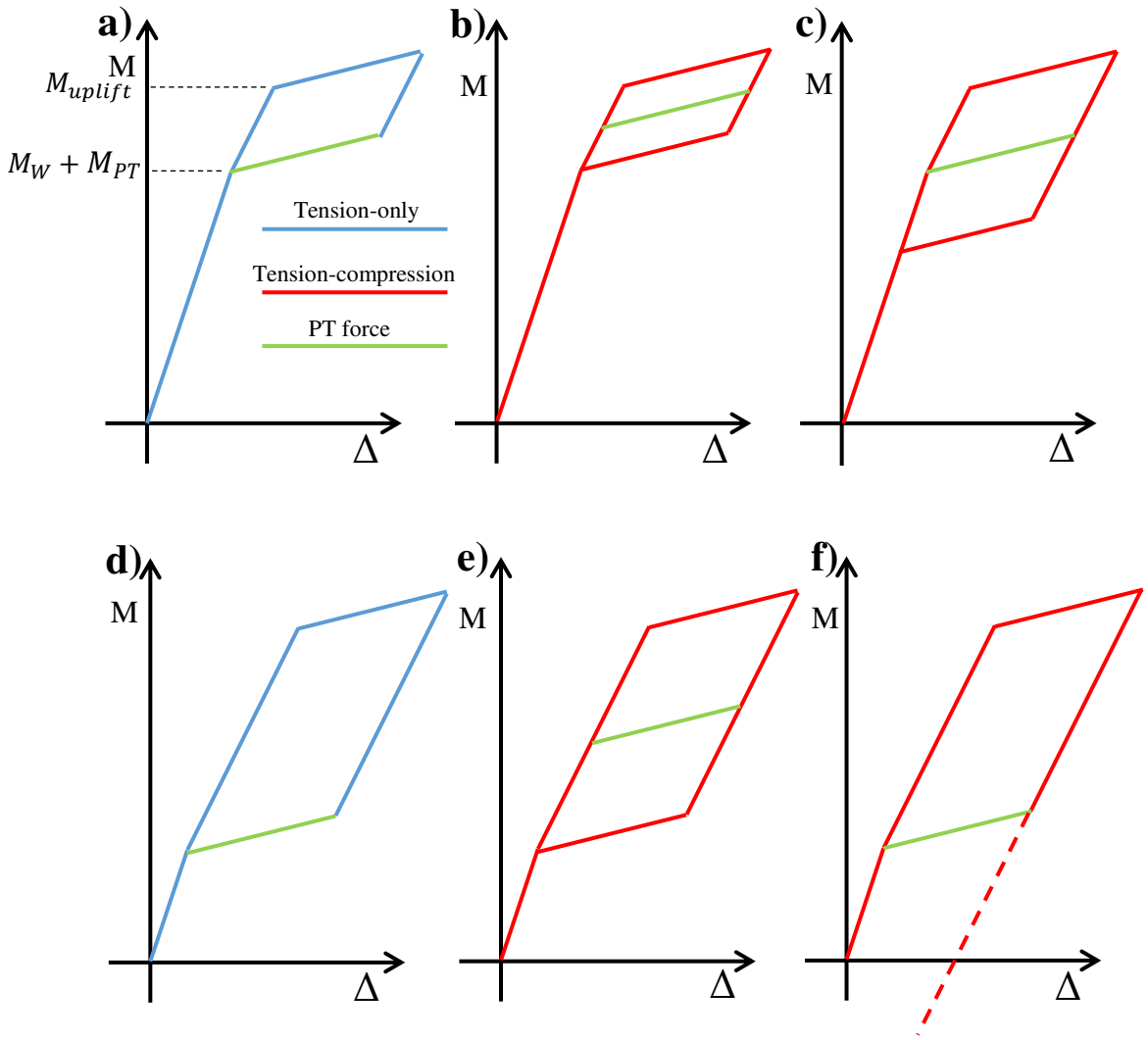

Figure 6.13 *Comparison of rocking system hysteresis loops for tension-only and tension-compression energy dissipation systems.*

6.5.3. Effect of ratcheting behaviour

Figure 6.14 demonstrates the effect of the Grip 'n' Grab ratcheting behaviour on the hysteretic response of the controlled rocking system during subsequent loading cycles. Behaviour of the two key subsystems in the controlled rocking frame system, the flexible frame and post-tensioning system (a), and the GNG device behaviour (b), are shown along with the combined response (c). The uplift profile for two consecutive uplifts of equal magnitude at the LHS rocking edge (d) is shown alongside the hysteresis. Consecutive uplifts at the same rocking edge are shown to focus on the response of a single device.

The scale of some changes in the system, such as the amount of free-travel and strain hardening, are shown in an exaggerated manner for clarity, and the key stages of the response are identified in **Figure 6.14** by sequential letters. The following stages define the response of the controlled rocking system, and are described in detail below:

Initial cycle:

A. Rest
B. Frame uplift and device engagement (no free-travel present on first cycle)
C. Dissipater yielding
D. Load reversal
E. End of elastic recovery (zero force in the device)
F. Re-contact of the frame with the ground
G. Return to initial position

Subsequent cycle:

H. Frame uplift
I. Device engagement after free-travel (depends on GNG device design – specifically rack size)
J. Dissipater yielding
K. Load reversal
L. End of elastic recovery (zero force in the device)
M. Re-contact of the frame with the ground
N. Return to initial position

The system is initially at rest at point A. Uplift of the rocking frame occurs at point B and the GNG device engages at this point as there is no free-travel present on the first loading cycle. Elastic displacement in the dissipater occurs between B and C, before yielding of the dissipater commences at point C and continues until the load reversal at point D. Elastic recovery in the dissipater occurs between D and E. Uplift reduces to zero and the rocking frame contacts the ground at point F. Elastic recovery in the frame occurs between F and G and the frame has returned to its initial location at rest at point G.

On the second uplift cycle, the GNG ratcheting behaviour alters the profile of the flag hysteresis in Figure 6.14c in a similar way to the device hysteresis shown in Figure 6.14b and described in detail in Chapter 2. The second uplift of the frame begins at point H. The presence of free-travel on subsequent loading cycles causes a delay to engagement of the device between H and I. Elastic displacement in the dissipater occurs between I and J, before dissipater yielding commences at point J.

If using a yielding steel dissipater as is presented here, strain hardening in the device shifts the yield point of the device and raises the position of the post-yield curve in the combined system hysteresis response. After the load reversal at K, the increase in forces due to strain hardening results in greater elastic recovery on subsequent cycles, and so the bottom side of the hysteresis flag is slightly shorter than on previous loading cycles with equivalent displacement in the system. Elastic recovery in the dissipater ends at L and the frame contacts the ground at M, before returning to the initial rest position at N.

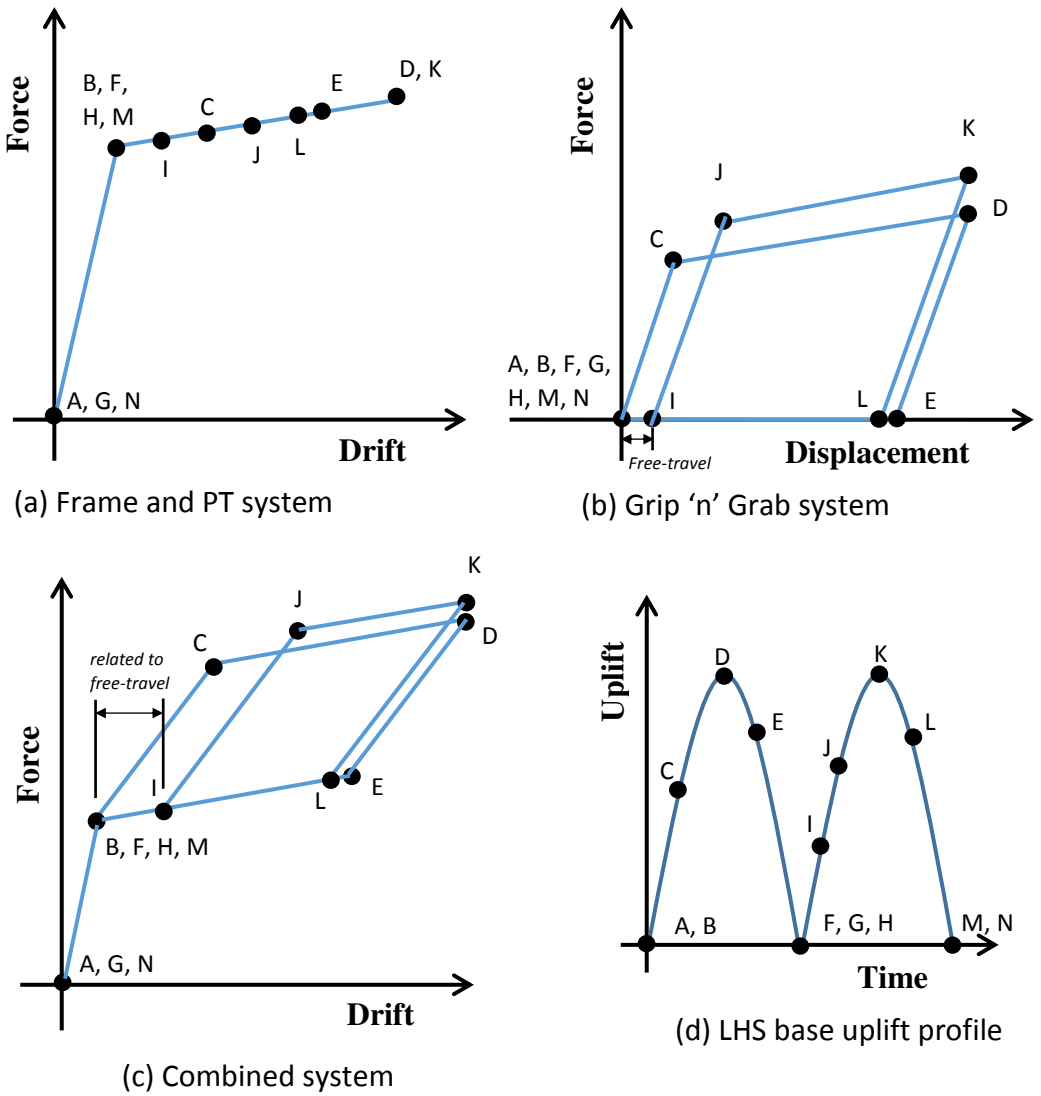

Figure 6.14 *Force-displacement responses with ratcheting behaviour:*
a) frame and post-tensioning system, b) Grip 'n' Grab device system, c) combined controlled rocking system, and d) uplift profile.

6.6. Conclusions

This chapter has presented an overview of controlled rocking systems with details of the mechanics of the system and literature on existing testing and implementation. The idealised system behaviour used to model rocking frame response has been described, and adapted for application with the tension-only ratcheting GNG devices that have been developed. These actions address research question 4:

Can a model be developed to describe the GNG hysteretic performance, together with that of a rocking wall?

- Supplementary damping mechanisms are frequently implemented along with rocking systems to achieve a more controlled response, and to increase energy dissipation, as rocking systems typically have very low inherent damping.
- The use of energy dissipation devices produces a flag-shaped hysteresis curve for the response of the controlled rocking system and the shape of this response is influenced by various parameters including the contribution of the energy dissipation devices to the base rocking moment.
- The stiffness of the system during various stages of the response has been described by previous work on controlled rocking frame systems and adapted to account for the unique ratcheting behaviour of the GNG device.
- The equations describing this response are implemented in the numerical model developed in Chapter 7.

7. Rocking Model Development

7.1. Summary

This chapter presents the development of a finite element flexible rocking model, incorporating effects of gravity forces, post-tensioning and energy dissipation devices. OpenSEES software was used to produce the model and a custom material model recreating the behaviour of the GNG device was developed and incorporated into the software. A design hazard spectrum was produced for a ULS seismic event in the Wellington region, and a series of response metrics are presented for a sample structure analysis. This sample analysis is used to introduce model parameters, explain response metrics and describe the model.

This chapter further addresses research question 4: Can a model be developed to describe the GNG hysteretic performance, together with that of a rocking wall?

7.2. Model introduction

A two-dimensional flexible rocking frame model was created using OpenSEES software [OpenSEES 2007] and an overview is presented in **Figure 7.1**. The purpose of the model is to provide a computationally inexpensive, yet suitable approximation of the response of a flexible rocking frame when exposed to a range of ground motion recordings. This model allows for the examination of the effects of the Grip 'n' Grab device on structure response and the capacity requirements for the device to operate correctly for the duration of an earthquake event.

The flexible rocking model developed is based on the assumption of point to point rocking about the two outer edges of the frame. Effectively the rocking interface is assumed to have some flexibility, but the locations of the rocking pivots are fixed. This is expected to be a suitable simplification in the case of steel frames, where the frames are constructed to avoid significant deformation of the shape of the structure near the rocking edges, and where suitable horizontal supports are provided. The central element at the base of the frame model represents the post tensioning.

The model incorporates elements to simulate the behaviour of the rocking frame, GNG-dissipater systems and post-tensioning elements, with appropriate vertical and horizontal masses. A leaning column is included to model the seismic mass of the main structure connected to the rocking frame. The mass of the leaning column is modelled at the same height as the frame mass, as implemented in similar rocking studies [Hall et al. 2010, Wiebe 2013]. The rocking mechanism and the behaviour at the base of the frame was the focus of the model. Therefore, the form of the rocking frame itself was kept simple. While higher mode effects could be considered, the influence of higher modes is expected

to have limited influence on the base rotation and the required capacity of the GNG dissipative element.

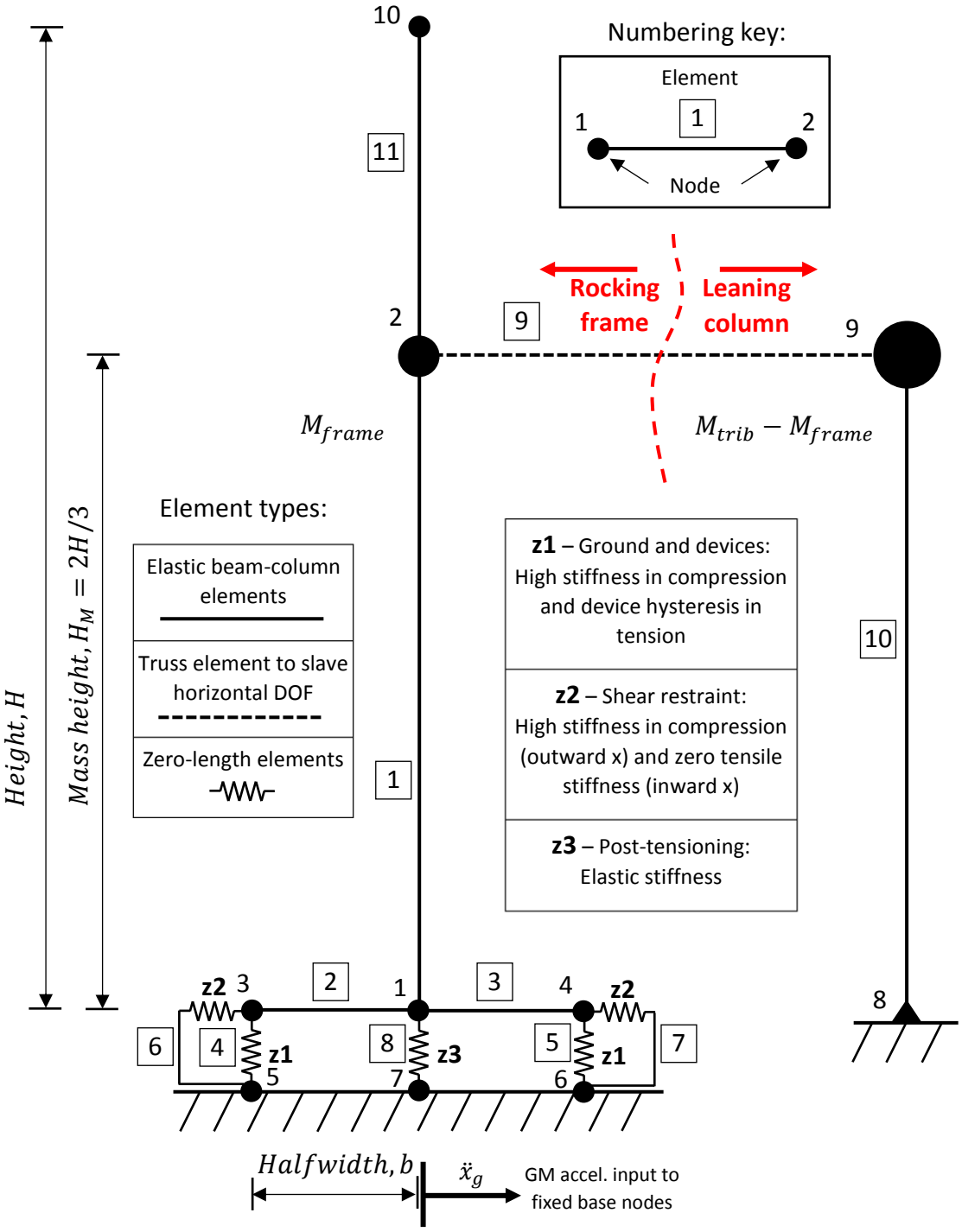

Figure 7.1 *Flexible rocking model implemented in OpenSEES.*

Elastic beam-column elements with a P-delta geometric transformation were used for the frame and leaning column elements. A truss element was used to connect the leaning column and frame masses. This method was selected to slave the horizontal DOF of the two nodes rather than implementing the

'equalDOF' command in OpenSEES because it removed some small force spikes from the results, that were not considered physically realistic.

Rocking occurs about nodes 5 and 6, shown in **Figure 7.1**, for counter-clockwise and clockwise base rotation respectively. The behaviour at the base of the rocking frame was defined using zero-length elements, connecting the three base nodes to three fixed nodes on the ground. The material models implemented at each of the zero-length elements are described later in subsection 7.4.

7.3. Model parameters

A total seismic tributary mass of $M_{trib} = 21 \times M_{frame}$ was used, and the frame mass, $M_{frame} = 100\ tonnes$, was assigned to a node at two thirds of the total height of the frame. This effective height was selected to provide a simple modelling approach focussed on first mode effects. The remaining part of the tributary mass, $M_{LC} = 20 \times M_{frame}$, was assigned to node 9 at the same height on the leaning column. These values were selected to give a broadly accurate estimate of the relative contributions of the rocking frame and tributary masses found in a real construction. Multiple rocking frames could be used in a given design application to reduce the loading experienced by any one rocking frame.

After assigning the frame and leaning column masses, a nominal mass of 1000 kg was assigned to the remaining nodes in unfixed x and y DOFs to provide numerical stability. These masses were selected to reduce force spikes in the results (which did not necessarily have physical significance), and avoid poorly scaled matrices in the computation. Rotation masses were zero. The elastic modulus of the frame elements was set to $E = 200\ GPa$, a common physical value for many variants of AISI steel. The area of the frame elements was $A = 0.1\ m^2$ and the half-width is $b = 2.5m$, to give a total frame width of 5 metres.

There is no clear general consensus on an exact value for inherent damping to most accurately model rocking behaviour. Some general structural design standards, such as NZS1170.5, reference 5% of critical damping. However, experimental work has shown that lower equivalent viscous damping values, perhaps in the range of 1-3% [Marriott et al. 2008], provide a good estimate of inherent damping in some rocking systems. Unique details of a particular controlled rocking system design will also affect this value. Rayleigh damping of 3% critical was applied for periods of 10% and 100% of the first mode period, to the model developed in this thesis.

Viscous damping was applied to the model to represent multiple damping mechanisms that occur in the physical system, such as any inelastic strain in the frame, inherent viscous damping, and damping due to rocking impacts. Impact damping can be modelled separately via a coefficient of restitution,

which is the ratio of the angular velocities immediately before and immediately after impact. Experimental values from testing by Kalliontzis et al. [2016] ranged from 0.86 to 0.95.

Considering impact damping separately to inherent damping, where inherent damping is modelled via equivalent viscous damping, may be useful to understand the individual effects of impact damping. However, the impact on the overall behaviour that would be seen by modelling impact damping separately, and reducing the applied viscous damping proportionately, is not expected to be significant. Further, the presence of added supplemental damping, through the use of the GNG dissipater system, reduces the sensitivity of the results to specific damping assumptions. With greater values of overall damping in the system, the effect of small changes to the applied inherent viscous damping is reduced.

7.4. Material models

Several zero-length elements were used to define the behaviour at the base of the frame. The following features were defined: horizontal supports, post-tensioning, ground interaction, and the energy dissipation devices. **Figure 7.2** to **Figure 7.5** show indicative results from a study described later in this Chapter, and each feature is described in more detail below.

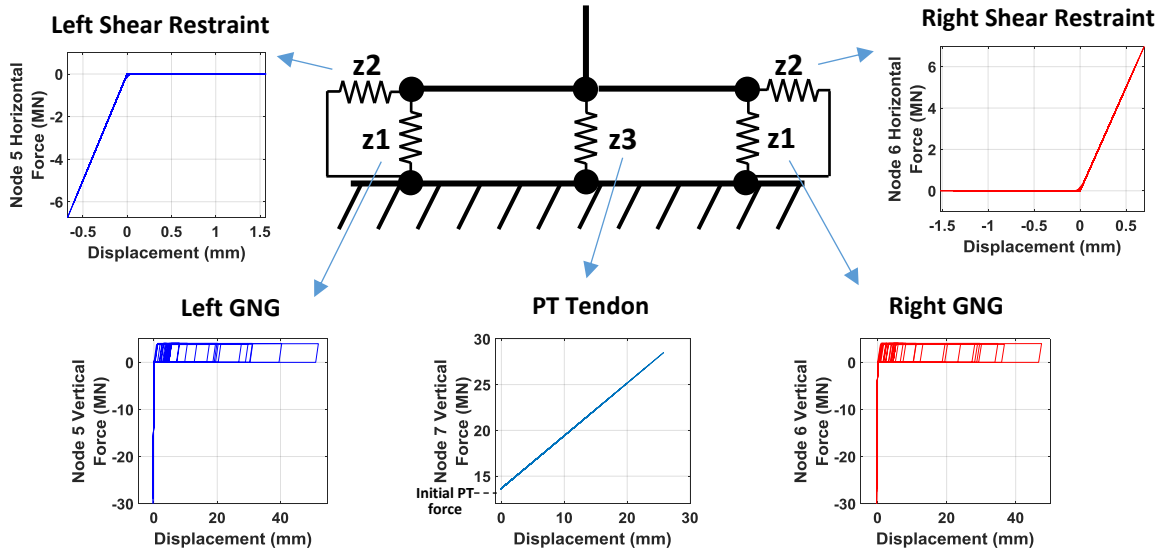

Figure 7.2 *Constitutive material models defining frame-ground interaction from a sample study. Clockwise from right: RHS shear restraint, RHS ground contact and GNG device, post-tensioning, LHS ground contact and GNG device, LHS shear restraint.*

7.4.1. Horizontal supports

Elastic-No-Tension (ENT) elements were used to represent supports to transfer horizontal shear forces at the rocking edges (elements 6 and 7), and appear as **z2** in **Figure 7.1** and **Figure 7.2**. A high elastic

stiffness of $K_{horz} = 1e10\ \frac{N}{m}$ was defined for displacements away from the centre of the frame (that is, negative displacements for the LHS rocking edge, and positive displacements for the RHS rocking edge), to simulate contact with the support. This value provided reasonable maximum horizontal deflections away from the frame centre at the rocking edges of up to ~3 mm.

No stiffness was applied for displacements towards the centre of the frame (that is, positive displacements for the LHS rocking edge, and negative displacements for RHS rocking edge), to allow for base rotation following uplift. These conditions on the horizontal motion of the rocking edges represent the presence of a support to transfer horizontal shear and prevent slippage, such as a trough or block. Complex sliding behaviour at the base of the rocking frame is not captured. **Figure 7.3** shows the horizontal force-displacement relationships for the two rocking edges.

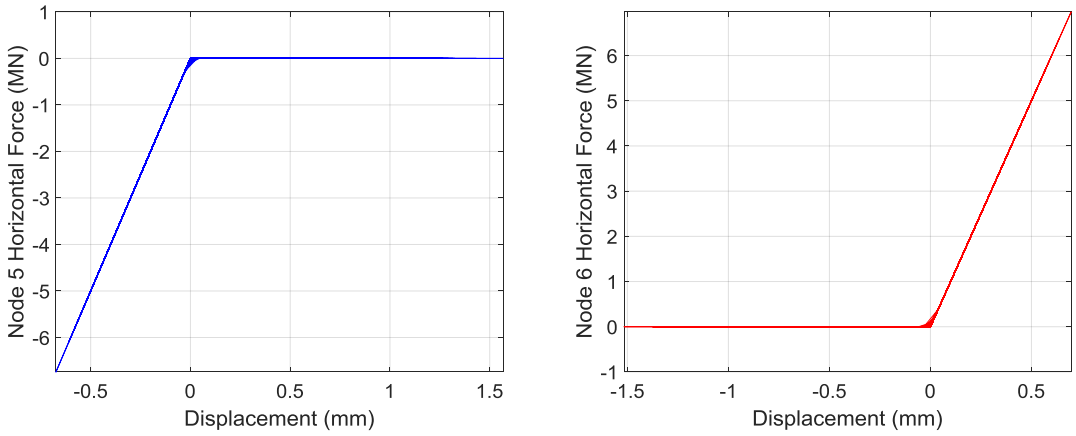

Figure 7.3 *Force-displacement relationships for the horizontal supports at the rocking edges, from a sample study: a) LHS (node 5) and b) RHS (node 6).*

7.4.2. GNG and rocking edge

The GNG material model described in Chapter 3 was recreated as a custom material in OpenSEES, with a few changes. The Menegotto-Pinto model was replaced with a simplified algorithm which does not incorporate curvature in the hysteretic loop around the yield point. Removing this feature allowed for a simpler algorithm and does not affect the ability to capture the main aspects of the GNG-dissipater system behaviour. For the simulations outlined below, a custom build of OpenSEES was compiled to incorporate the GNG material model. This material model will be available in the next release of the OpenSEES software downloadable executable file (date TBD), along with all the existing built-in OpenSEES material models. The two files added to the OpenSEES source code are provided in Appendix C.

A combination of two material constitutive models were used in parallel to model the vertical behaviour at the rocking edges (elements 4 and 5), and appear as **z1** in Figure 7.1 and Figure 7.2. An ENT model was used to simulate contact with the ground, and the GNG material model, which incorporates changes to the displacement datum when ratcheting occurs, was used to model the response during uplift. The vertical stiffness representing the ground was set to $K_{ground} = 1e11\ \frac{N}{m}$. This value provided reasonable maximum negative vertical deflections (into the ground) at the rocking edges of up to ~2 mm.

A post-yield stiffness to initial stiffness ratio of $\beta_{GnG} = 0.02\%$ was selected for the GNG devices. This value was selected to represent a yielding steel dissipative element and model the small amount of strain hardening observed in common steels. Figure 7.4 shows the vertical force-displacement relationship at the LHS rocking edge.

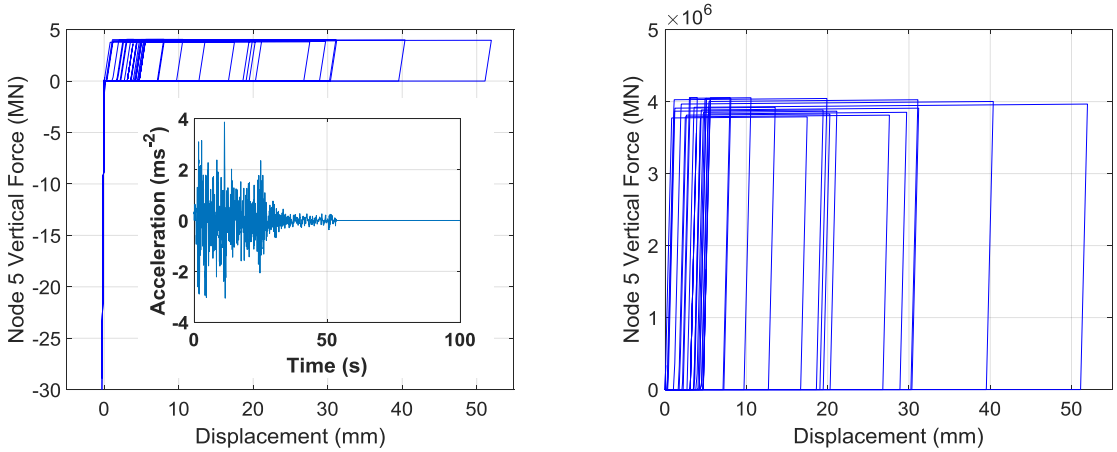

Figure 7.4 *The parallel ENT and GNG material models used to represent the vertical response at the rocking edges, from a sample study:*

a) The full hysteresis, and b) a close up of the positive displacement behaviour, controlled by the GNG. The ground motion input used to produce these results, record la01: Imperial Valley, is shown inset.

7.4.3. Post-tensioning

A linear post-tensioning relationship was modelled at the base of the rocking frame (element 8), with an elastic stiffness (E_{PT}) for positive displacements to simulate post-tensioning force during uplift, and appears as **z3** in **Figure 7.1** and **Figure 7.2**. The initial post-tensioning force was applied as an initial strain in the material constitutive model. Although linear behaviour is modelled, an Elastic-Perfectly-Plastic (EPP) element was used to allow for the application of the initial strain.

Large yield strains were set to avoid plastic behaviour with this element type. Therefore, non-linear behaviour of post-tensioning tendons is not captured. It is assumed that post-tensioning elements will

operate within the linear range of strain. **Figure 7.5** shows the post-tensioning model, where the force at zero displacement represents the initial post-tensioning force.

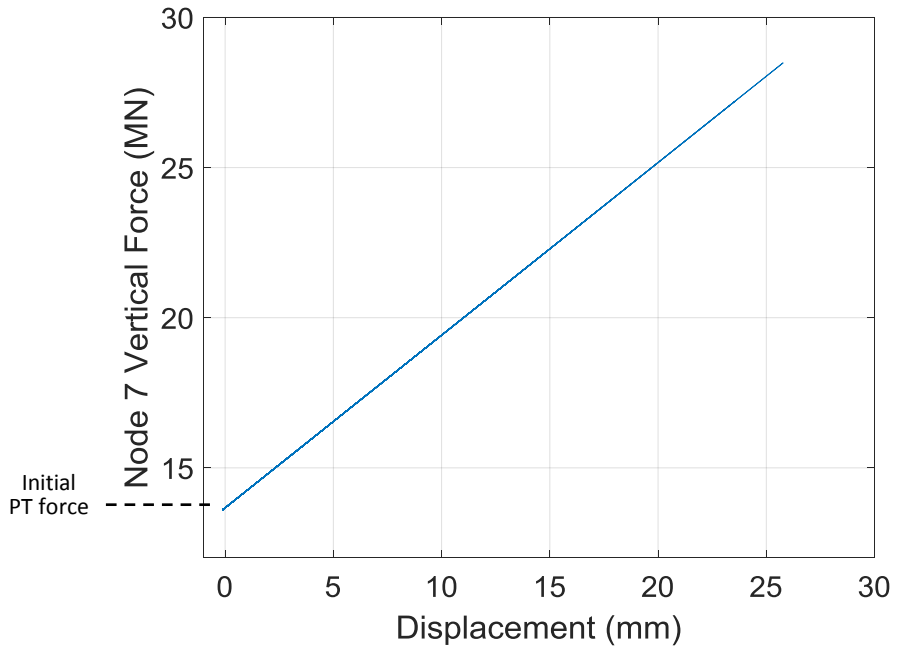

Figure 7.5 *The elastic post-tensioning model with initial strain, from a sample study.*

7.5. Analysis settings

The time step used in the analysis is $dt = 0.001$ seconds. This value was selected as it avoided numerical instability and provided a suitable sampling rate for input ground motion data. Smaller timesteps did not significantly change the results, based on a convergence study. Further, the smallest initial fixed base period of any structure modelled was 0.2 s. Therefore, the selected timestep is 0.5% of the smallest period simulated and adequately captures the response behaviour. The OpenSEES Newmark integrator object is used with constant values $\gamma = 0.5$ and $\beta = 0.25$ to implement the average acceleration method, and an energy increment convergence test was enabled with a tolerance of 1e-12 and maximum number of iterations before failure of 100. These details are shown in **Table 7.1** with the other OpenSEES analysis settings.

Table 7.1 OpenSEES analysis command settings

Analysis setting	Command
constraints	Plain
numberer	RCM
system	BandGeneral
test	EnergyIncr 1e-12 100 0
algorithm	Newton
integrator	Newmark 0.5 0.25
analysis	Transient

7.6. Design spectra

An elastic site hazard spectrum for horizontal loading, $C(T)$, was created using the guidance of the New Zealand earthquake design actions standard NZS1170.5 [SNZ 2004]. As presented in the standard:

$$\mathrm{C(T)} = \mathrm{C_h(T)} \times \mathrm{Z} \times \mathrm{R} \times \mathrm{N(T, D)} \qquad (7.1)$$

where $\mathrm{C_h(T)}$ is the spectral shape factor, Z is the hazard factor, R is the return period factor, and $\mathrm{N(T, D)}$ is the near-fault factor.

Values were chosen to represent a structure located on shallow soil (site subsoil class C) in the CBD of the Wellington, New Zealand region within 2km of the nearest major fault. The structure has a design working life of 50+ years, an importance level of 3 (this is a moderately important structure that may contain people in crowds or contents of high value to the community), and is assumed to be undergoing an ULS earthquake event. This combination of factors gives an annual probability of exceedance of 1/1000, and the corresponding return period factor is 1.3. These conditions are summarised in **Table 7.2**, and the resulting spectra is shown in **Figure 7.6**.

Table 7.2 Site conditions used to create the elastic site hazard spectrum.

Site variable	Value
Soil type	*C (shallow soil)*
Hazard factor, Z	*0.40*
Return period factor, R_u	*1.3*
Distance from nearest major fault, D	$\leq 2\ km$

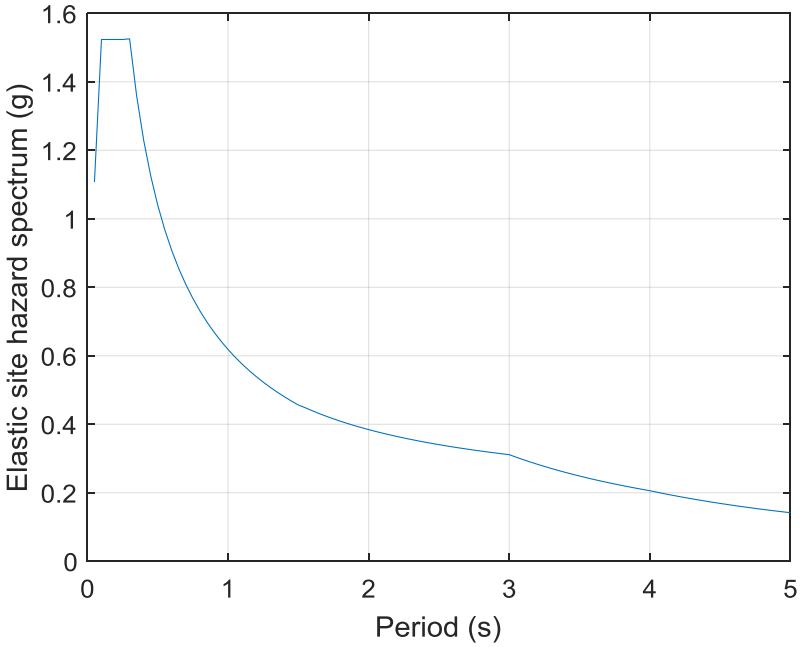

Figure 7.6 *The elastic site hazard spectrum for a Wellington based structure, produced from NZS1170.5.*

A conventional SDOF linear elastic spectra approach was used. The full suite of 60 earthquake recordings from the SAC project [Sommerville et al. 1997], padded to a uniform record length of 100 seconds, was used to create response spectra. An SDOF 'lollipop' model with the same mass ($M = M_{trib} = 2100$ tonnes) as the flexible rocking model and a damping ratio of $\zeta = 0.05$ was used to find the peak accelerations for models with a range of periods. While the flexible rocking model uses an inherent damping of 3% critical, the records were scaled based upon 5% critical damping to provide the same ground motions as any other conventional structure in the same location. These peak accelerations were scaled to match the elastic site hazard spectrum in **Figure 7.6**. A unique scale factor was determined for each ground motion recording at each structural fundamental period considered. A sample of the scaled records, for a structure with a fundamental period of 0.7 seconds, is presented in **Figure 7.7**.

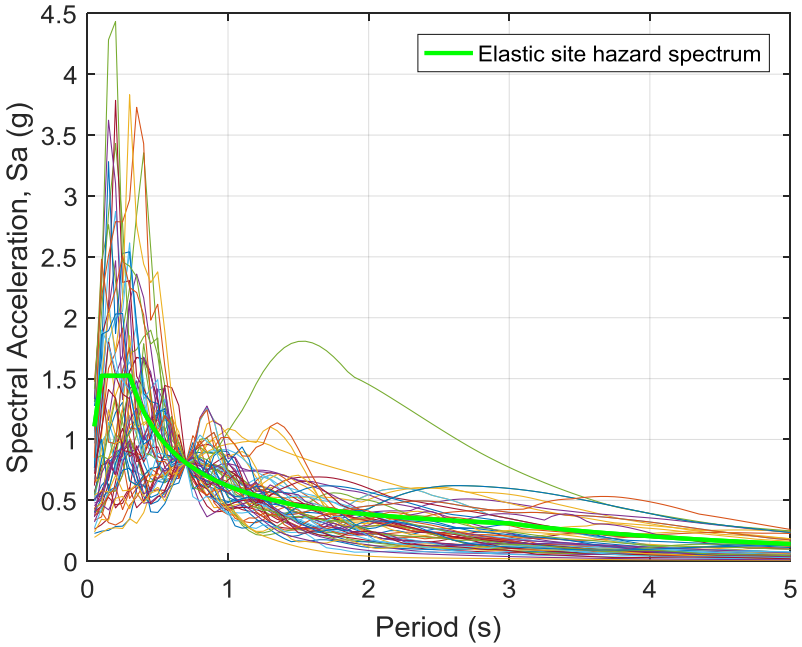

Figure 7.7 *A sample of the ground motion records scaled for a structure period of 0.7 seconds.*

7.7. Sample structure

In this subsection, results are presented for a sample structure using the flexible rocking model. The values selected to define this sample structure are presented in **Table 7.3** and represent some common physical values. Stiffness ratios between the post-uplift, pre-yield stiffness and the initial stiffness ($\propto$), and between the post-uplift, post-yield stiffness and the initial stiffness (γ), of 0.8 and 0.1 respectively, are applied to create an appropriately proportioned hysteretic response for the overall system. The initial stiffness of the structure is defined using the structure period and tributary mass:

$$K_{initial} = \left(\frac{2\pi}{T_n}\right)^2 M_{trib} \qquad (7.2)$$

As per the suggestions of the SCNZ rocking frame design guide discussed in Section 6.5.2.2, the contribution of energy dissipation devices to the moment at uplift $\left(\frac{M_{ED}}{M_{uplift}}\right)$ is modelled as 34% in the simulations completed. This value is based largely on the presence of residual compressive forces in the energy dissipation devices, which do not exist when using the GNG device, so the choice could be more open in this case. However, this value of 34% is used initially to provide a useful baseline, and the effect of changing this parameter is investigated during the parameter studies presented in Chapter 8.

A preference is also shown in the SCNZ rocking frame design guide for a frame aspect ratio (AR) of 4. A GNG rack pitch size (P) of 5 mm is selected. This pitch size is between the two pitch sizes tested with the advanced prototype GNG device of 10 mm and 3 mm, and represents a realistic construction size without requiring significant manufacturing complexity. Additionally, to meet the design objective of avoiding uplift during an SLS event ($R_s = 0.25$), a force reduction factor, R, of 4.0 is applied.

Table 7.3 *Values of the parameterised variables selected for the sample model*

Variable	Sample value
T_n	0.7 s
AR	4.0
P	5 mm
$\frac{M_{ED}}{M_{uplift}}$	34 %
R	4.0
$\propto$	0.8
γ	0.1

Chosen from the suite of scaled records, the ground motion acceleration input profile from Imperial Valley (la01) was used to demonstrate the response of the sample structure. The scaled ground motion record has a peak absolute acceleration of $3.87\ m/s^2$ occurring at 11.44 seconds into the record, and is shown in **Figure 7.8**. The '*UniformExcitation*' command in OpenSEES was used to apply the acceleration profile to all nodes fixed in the lateral degree of freedom.

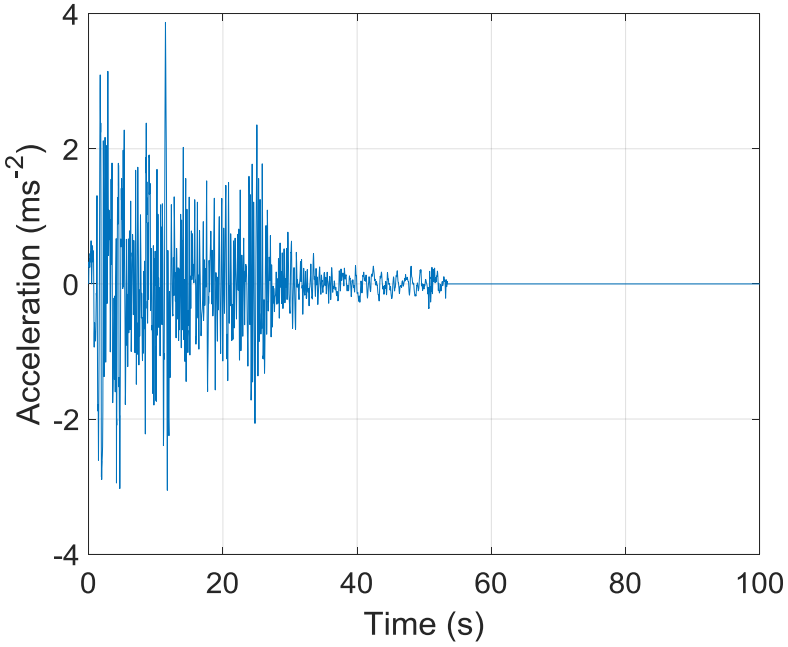

Figure 7.8 *The scaled ground motion acceleration record input to the fixed base nodes (period = 0.7 s, record la01: Imperial Valley).*

The total roof drift, or drift at the top of the rocking frame (node 10) due to both flexure and base rotation, and the uplift at the two rocking edges (nodes 3 and 4) are presented in **Figure 7.9** and **Figure 7.10** respectively. As expected from the ground motion input, most of the transient behaviour occurs during the first 30 seconds of this padded 100 second record. The frame drift reached a peak absolute value of 1.41% at 12.33 seconds. This represents a peak displacement at the top of the 20 m high frame of 0.28 m. The peak uplift at the corresponding rocking edge occurs at the same time and is 52 mm, at the left rocking edge. The peak uplift at the right rocking edge is 47.5 mm, and occurs at 13.05 seconds. The devices are located at the outer corners of the rocking frame, so the eccentricity of the devices from the rocking edge is equal to the frame width of 5 m.

There is no residual roof drift or base uplift at the end of the time-history analysis. The post tensioning provides a restoring force in the rocking system, which is not resisted by the dissipaters due to the lack of compressive forces in the GNG devices. Re centring can also be achieved in traditional tension compression systems when designed appropriately with enough restoring force to overcome the compression forces in the dissipater. The absence of residual drifts was observed for all of the time-history analyses presented in this thesis, including the parameter study results presented in Chapter 8. A comparison between some key quantities over time is provided in **Figure 7.11**, where the ground motion acceleration, roof drift and uplift are presented in parallel with a common x axis. Only results for the first 50 seconds of the response are shown in **Figure 7.11** to emphasise the most active period of the response.

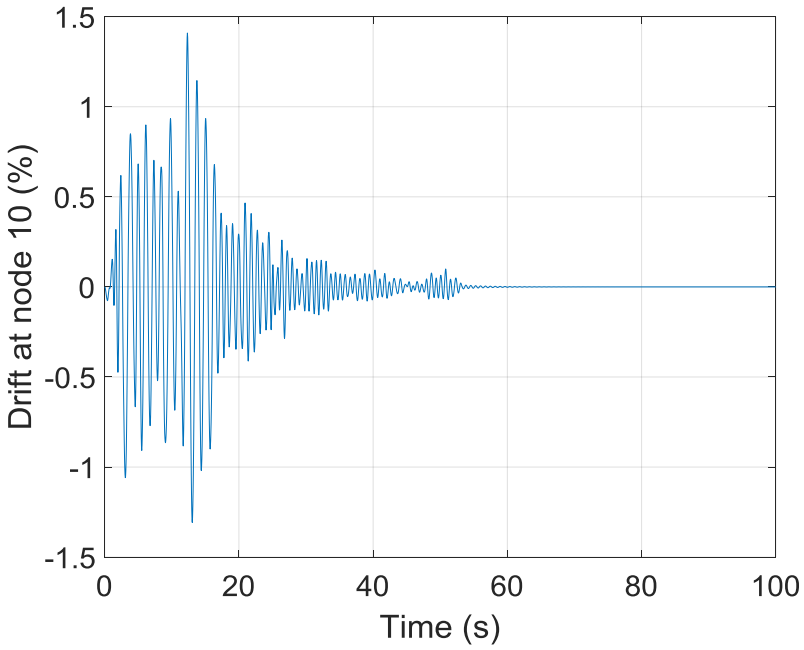

Figure 7.9 *Frame top (Node 10) drift*

(pitch = 5 mm, period = 0.7 s, aspect ratio = 4, R = 4, ζ = 3%, record la01: Imperial Valley).

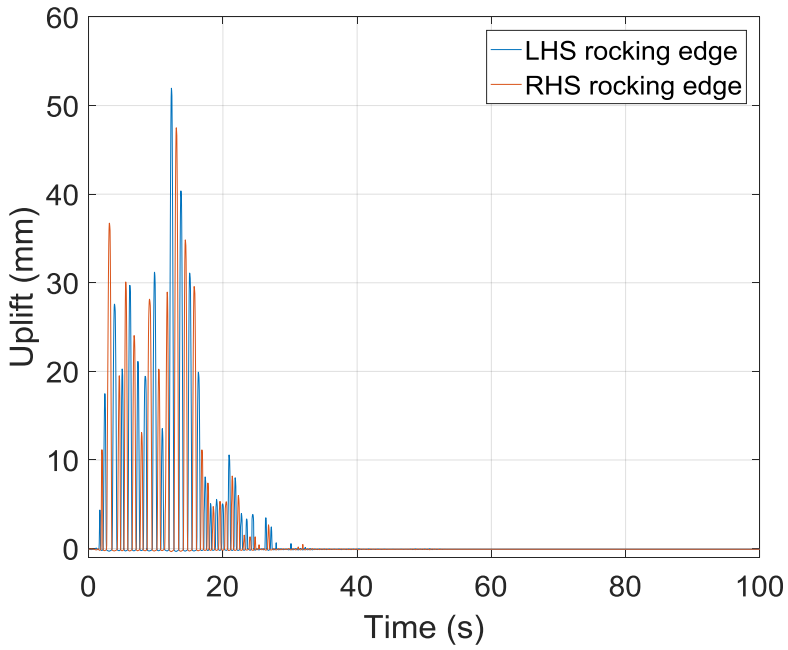

Figure 7.10 *Base rocking uplift on left (Node 3) and right (Node 4) sides of the frame*

(pitch = 5 mm, period = 0.7 s, aspect ratio = 4, R = 4, ζ = 3%, record la01: Imperial Valley).

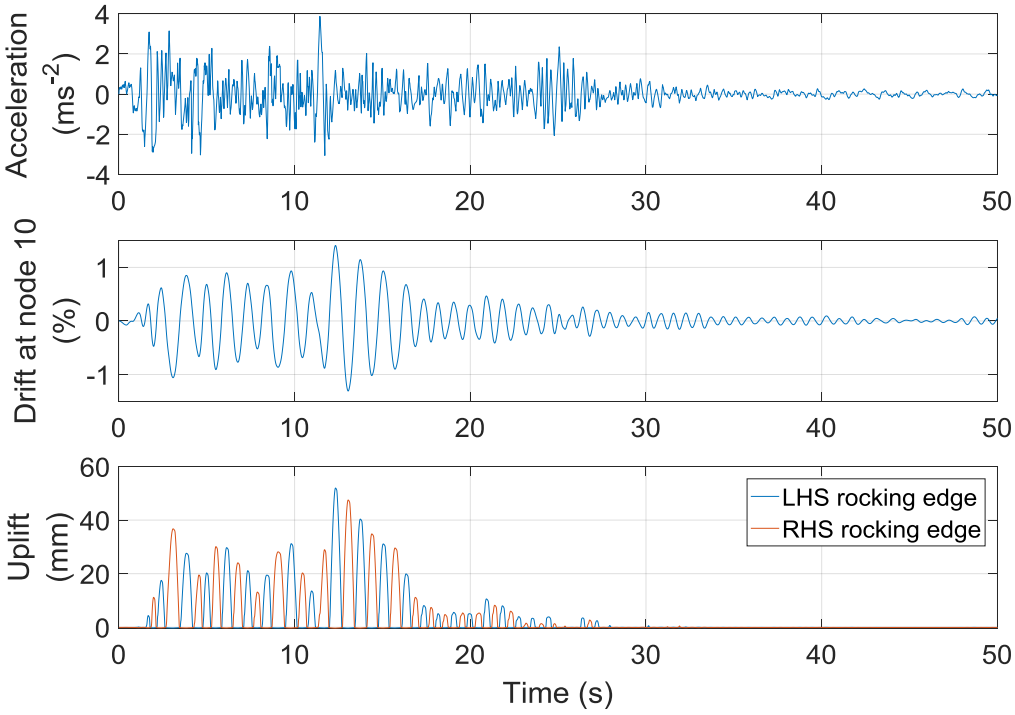

Figure 7.11 *Comparison of the ground motion record, roof drift and uplift for the first 50 seconds of the response (pitch = 5 mm, period = 0.7 s, aspect ratio = 4, R = 4, ζ = 3%, record la01: Imperial Valley).*

The force displacement hysteresis plot for the rocking system is shown in **Figure 7.12**. The positive force information is all from the horizontal compression only spring on the right hand side of the frame (element 7), while that in the negative direction is from the horizontal compression only spring on the left hand side of the frame (element 6). This is consistent with positive displacement being aligned toward the right side. The forces provided are the base shear force of the frame, and there is no force at the uplifted edge. Drift values are taken from the top of the frame (Node 10). The following features of the hysteresis curve are noted:

1) The roof drift is approximately linear with the rocking base node horizontal force before uplift occurs at the first kink at point A on **Figure 7.12**. There is some variation from a linear response due to dynamic effects and effects of non-fundamental modes due to the many degrees of freedom in the model.
2) After uplift, the slope changes as the system stiffness is now controlled by the stiffness of the GNG-dissipater system and the post-tensioning. The first kink is less pronounced due to the high ratio between the post-uplift, pre-yield stiffness and the initial stiffness ($\propto$).
3) At the second kink, labelled as point B on **Figure 7.12**, the GNG-dissipater system starts sliding, or yielding if using steel dissipaters, so only the post-tensioning provides stiffness. This effect occurs at a base node horizontal force approximately 50% greater than the uplift force since the GNG device was providing one third of the uplift resisting moment.

4) On return, after point C on **Figure 7.12**, energy is dissipated by the GNG-dissipater system, shown by the enclosed flag shape in the hysteresis loop. The GNG device carries tension force only.

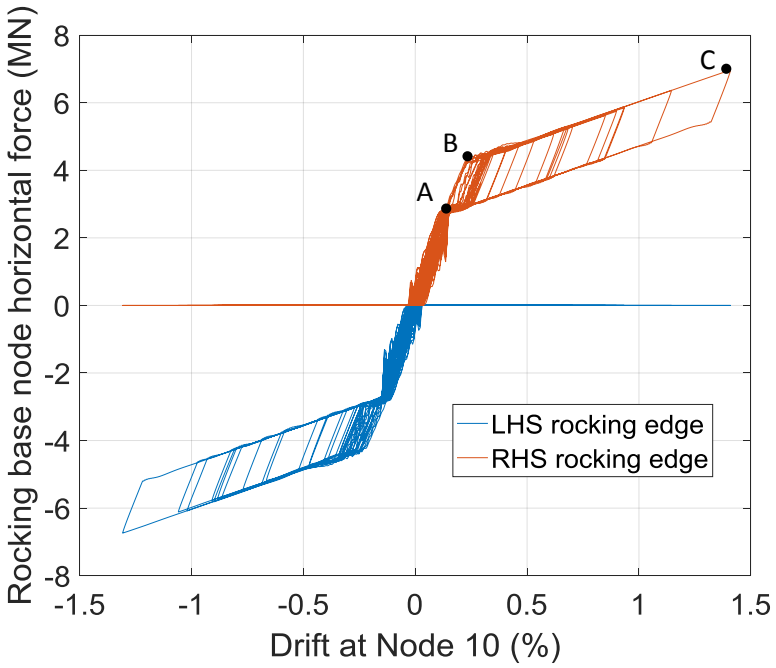

Figure 7.12 *A force-displacement plot of the flexible rocking frame (pitch = 5 mm, period = 0.7 s, aspect ratio = 4, R = 4, ζ = 3%, record la01: Imperial Valley).*

The cumulative inelastic displacement demand in the dissipaters is shown in **Figure 7.13**. The total inelastic demand was 303.2 mm and 306.9 mm in the dissipaters at the left and right hand rocking edges respectively. For an elongation to fracture of 20% in the dissipaters, these plastic demand values represent required dissipater lengths of 1516 mm and 1535 mm to avoid fracture and facilitate correct material response for the duration of the event, in the devices at the respective edges. Alternatively, a friction connection of other method of energy dissipation could be used.

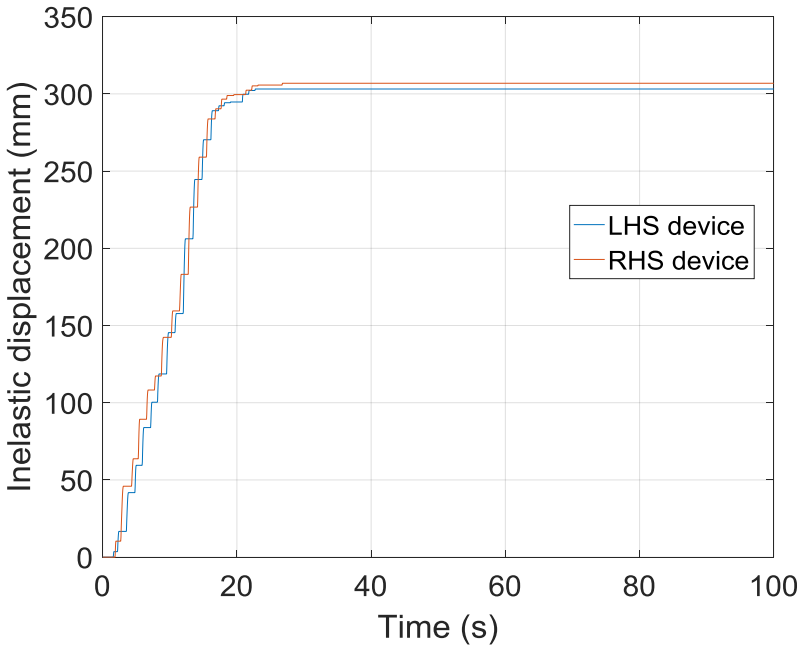

Figure 7.13 *Cumulative plastic strain in the dissipater elements*

(pitch = 5 mm, period = 0.7 s, aspect ratio = 4, R = 4, ζ = 3%, record la01: Imperial Valley).

The cumulative inelastic displacement demand in the critical device of 306.9 mm was 6.08 times that if the roof moved monotonically to the same peak drift of 1.4%. The static pushover response for a displacement profile of 0, +1.4%, -1.4%, 0 drift is shown in **Figure 7.14**. This hysteretic response in **Figure 7.14** appears idealised in comparison to **Figure 7.12** due to the absence of dynamic and higher mode effects. The inelastic displacement in the dissipaters during this static analysis was 50.5 mm.

There were a total of 60 and 61 ratcheting actions in the left and right devices, respectively. With a tooth pitch of 5 mm, these ratcheting values represent a total of 300 mm and 305 mm of toothed rack required, in the respective devices, to facilitate a correct ratcheting response for the full duration of the ground motion event. The total number of ratcheting actions in the GNG devices during the event is shown in **Figure 7.15**.

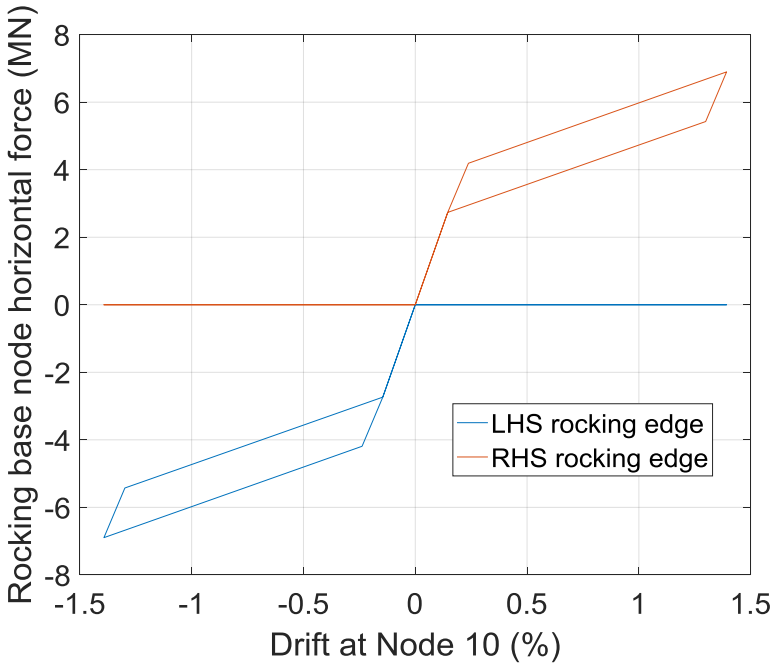

Figure 7.14 *Static cyclic hysteresis response*

(pitch = 5 mm, period = 0.7 s, aspect ratio = 4, R = 4).

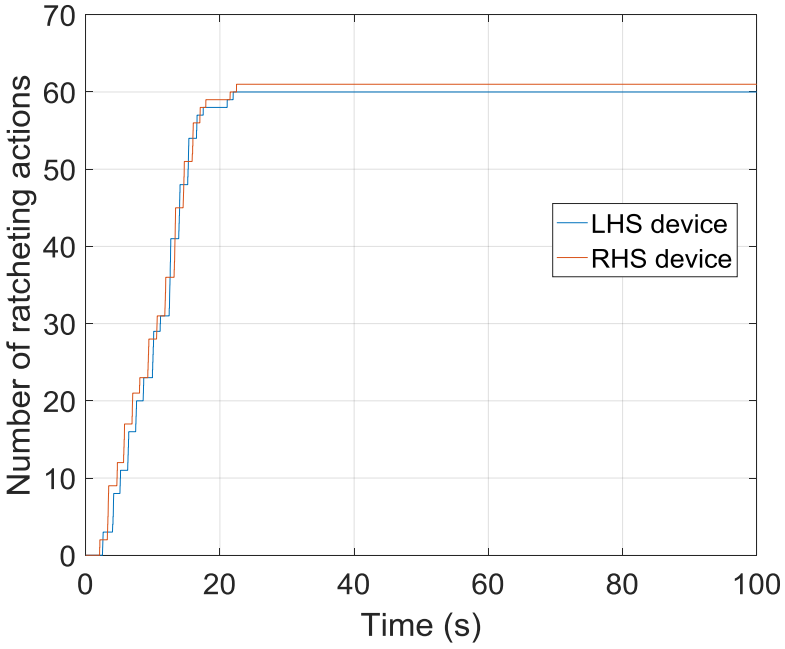

Figure 7.15 *Cumulative ratchet count in the GNG devices*

(pitch = 5 mm, period = 0.7 s, aspect ratio = 4, R = 4, ζ = 3%, record la01: Imperial Valley).

The simulation was repeated for a structure without supplementary energy dissipation devices. This model was achieved by replacing the material response of the two vertical rocking edge zero length elements z1 with an elastic no tension model using the vertical stiffness of the ground, $K_{ground} =$

$1e11\frac{N}{m}$, as specified in Section 7.4.2. The contribution of the post tensioning and the weight force to the moment at uplift was increased to 100%. The force displacement hysteresis plot for the rocking system without supplementary energy dissipation devices is shown in **Figure 7.16**, alongside the force displacement hysteresis plot for the rocking system with GNG supplementary energy dissipation devices, as originally presented in **Figure 7.12**.

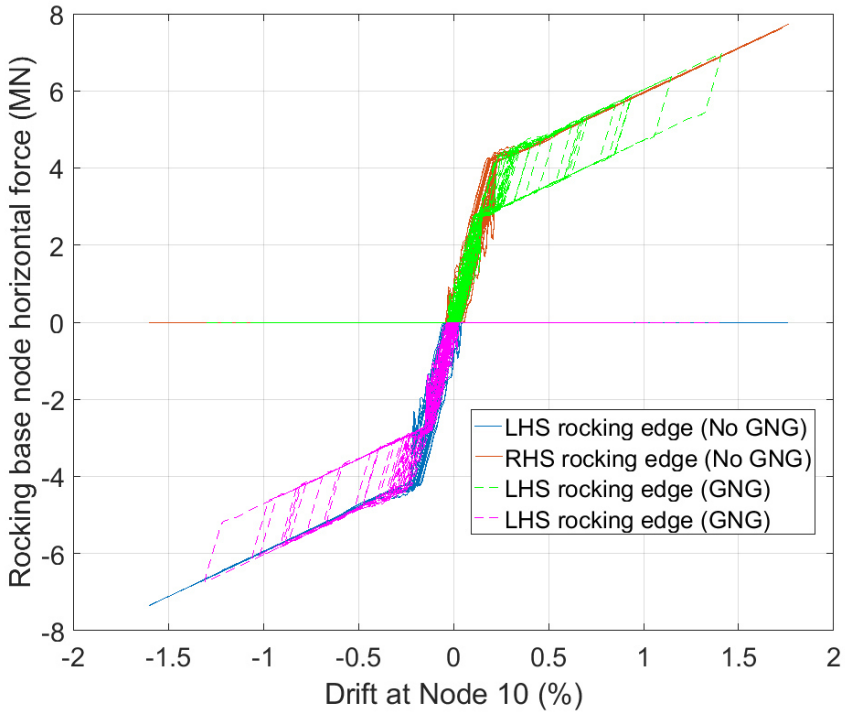

Figure 7.16 *A force-displacement plot of the flexible rocking frame without supplementary energy dissipation devices: (pitch = 5 mm, period = 0.7 s, aspect ratio = 4, R = 4, ζ = 3%, record la01: Imperial Valley).*

The maximum rocking base horizontal force and maximum roof drift, in the rocking system without supplementary energy dissipation devices, were 7.727 MN and 1.761 % respectively. In the rocking system with GNG supplementary energy dissipation devices, the maximum rocking base horizontal force and maximum roof drift were 6.967 MN and 1.409 % respectively. These results represent an increase of approximately 11% in the base horizontal force and an increase of about 25% in the peak drift response during this specific ground motion, due to the absence of the GnG. This comparative response is not intended to be a conclusive comparison, but instead provide a basic initial comparison to broadly indicate the potential contribution of the GnG to overall structural response.

7.8. Conclusions

This chapter has presented the development of a finite element computational model used to capture rocking wall and Grip ‘n’ Grab behaviour. OpenSEES software was used to produce the model, including a custom GNG material model developed during this research. A design hazard spectrum

was produced for a ULS seismic event in the Wellington region, and a sample structure analysis was used to introduce model parameters, explain response metrics and describe the model. These actions further address research question 4:

Can a model be developed to describe the GNG hysteretic performance, together with that of a rocking wall?

- The full hysteretic behaviour of the GNG device, including tooth pitch effects, is successfully captured by the constitutive material model algorithm added to the local OpenSEES build and incorporated into future OpenSEES releases.
- The unique GNG material model, together with standard OpenSEES elements, allowed the rocking frame GNG system to be successfully modelled.
- Key uplift and system behaviour was able to be captured in the resulting, computationally inexpensive, model.
- A design hazard spectrum was produced for a ULS seismic event in the Wellington region and a suite of 60 ground motion records were scaled accordingly to provide a broad range of possible input ground motions for future analyses outlined in Chapter 8.
- The detailed understanding and verification of the model forms a basis for parameter studies with multiple earthquake records, to better quantify the performance and parameter selection options for design.

8. System Response and Analysis

8.1. Summary

In this chapter the finite element flexible rocking model developed in Chapter 7 is implemented to complete a series of parameter studies consisting of 18600 individual time-history analyses in total to assess the behaviour of the GNG devices when combined with the rocking frame system. The study details are described and results for key quantities such as roof deflection, roof drift, uplift due to rocking, ratcheting and dissipater demand are presented and discussed. A brief statistical analysis is completed on the dissipater demand data to provide a basis for dissipater design capacity recommendations.

Approximate peak uplift values for a monotonic pushover analysis, for the rocking model described in Chapter 7, are found using the methods of SCNZ 110:2015 and NZS 1170.5, and compared to the results of the simulations. This comparison allows the time-history analysis results to be applied to current methods, and the cumulative inelastic capacity required in the dissipater and the rack can then be estimated.

Separate studies of the effects of the contribution of the dissipater to the resisting moment at uplift, and the effects of the force reduction factor, on the dissipater and rocking system responses are completed. This chapter also outlines some practical considerations for implementing the GNG device with a controlled rocking frame system, including the configuration of the GNG-dissipater system in the rocking frame system, and its connection to the frame.

This chapter addresses research questions 5 and 6: What is the system response, including the cumulative plastic demand generated in the dissipative element, and how does this vary with key design parameters such as the ratchet pitch size? How should GNG rocking wall systems be designed?

8.2. Main parameter study

8.2.1. Study details

During development of the parameter study, broad combinations of model input parameters were considered. While a large range of input parameters was desired to provide as much information as possible, poor choices of parameters in combination can lead to model instability, skew the results, and impact the general conclusions of the analysis. It is important to consider parameters in combination to ensure physically reasonable inputs to the model, and therefore, useful results.

One important combination of parameters is the aspect ratio and period of a structure. Some unrealistic combinations of these two parameters can lead to failed analyses or very large peak roof

drift values. For example, a rocking frame with an aspect ratio of 1 and a period of 2.0 seconds does not make much physical sense. The period suggests a frame height of around 20 storeys or ~60 m, and a rocking frame with the same width is not a realistic design to consider. Further, the use of a fixed frame width in the analyses needs to be considered when setting other parameters to ensure a sensible model that could represent a real structure.

For the final analyses, a range of four aspect ratios were selected, from 2 up to a maximum aspect ratio of 8. For the fixed frame width simulated, this range produced structures of four different heights. Eurocode 8 [BSI 2004] suggests the fundamental period of vibration T_1 of buildings with heights of up to 40 m can be approximated by the following expression:

$$T_1 = C_t H^{0.75} \tag{8.1}$$

where H is the height in metres, and $C_t = 0.05$ for rocking frames, as they are not encompassed by the other specified categories of moment-resisting concrete frames, moment-resisting steel frames or eccentrically braced steel frames. Another estimate of initial fundamental period is provided in the commentary to NZS1170.5 [SNZ 2004]:

$$T_1 = 1.25 k_t {h_n}^{0.75} \tag{8.2}$$

where $k_t = 0.05$ for rocking frames, as they are not encompassed by the other specified categories of moment-resisting concrete frames, moment-resisting steel frames or eccentrically braced steel frames, and h_n is the height in metres from the structure base to the uppermost seismic weight or mass. This equation is specified for the ultimate limit state, which matches the conditions chosen for the design spectra produced in Chapter 7, and used to scale the input ground motion records. The code equations defined by Equation (8.1) and Equation (8.2) are usually designed to provide a lower bound on the actual period of a structure, in order to provide a conservative design approach where the highest likely design force is found when using equivalent static analysis.

The four aspect ratios selected for the parameter study have corresponding heights of 10, 20, 30, and 40 metres. The selected structure heights represent buildings ranging from approximately 3 to approximately 13 stories, assuming an average storey height of 3 m. Using a range of plus or minus 25% from both Equation (8.1) and Equation (8.2), several structure periods were selected for simulation with each aspect ratio, to provide a suitable range of realistic parameters. Period steps of 0.1 seconds were used for simplicity. The simulated aspect ratio and period combinations are presented in **Figure 8.1**, and **Table 8.1** shows the full combinations of variables used in the parameter study. Note that the 'BSI + 25%' and 'NZS' lines in **Figure 8.1** are equal. A schematic of the selected structures, following the modelling approach described in detail in Chapter 7 (sections 7.1 to 7.5), with

the seismic mass applied at two-thirds of the frame height, is shown in **Figure 8.2**. The leaning column details, which induced P-Delta effects and was discussed in Chapter 7, are applied to each structure, but are omitted from **Figure 8.2** for clarity.

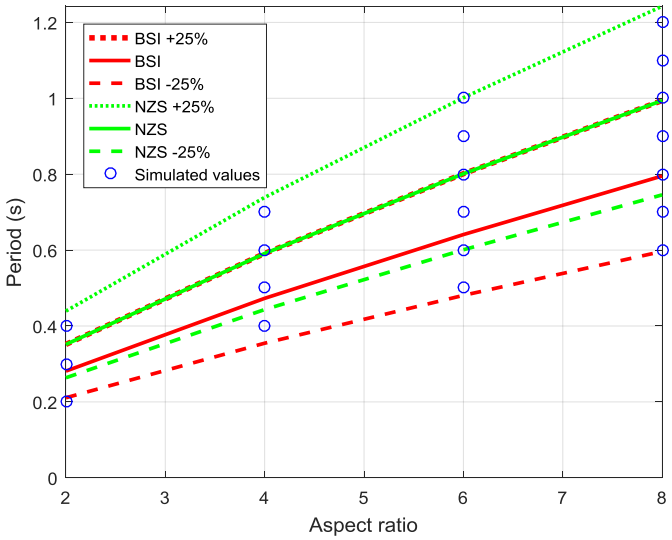

Figure 8.1 *Combinations of aspect ratio and period selected for simulation.*

Table 8.1 *Properties of the simulated structures.*

Aspect ratio	Height (m)	Period (s)	GNG Pitch (mm)
2	10	0.2, 0.3, 0.4	1, 2, 5, 10, 20
4	20	0.4, 0.5, 0.6, 0.7	1, 2, 5, 10, 20
6	30	0.5, 0.6, 0.7, 0.8, 0.9, 1.0	1, 2, 5, 10, 20
8	40	0.6, 0.7, 0.8, 0.9, 1.0, 1.1, 1.2	1, 2, 5, 10, 20

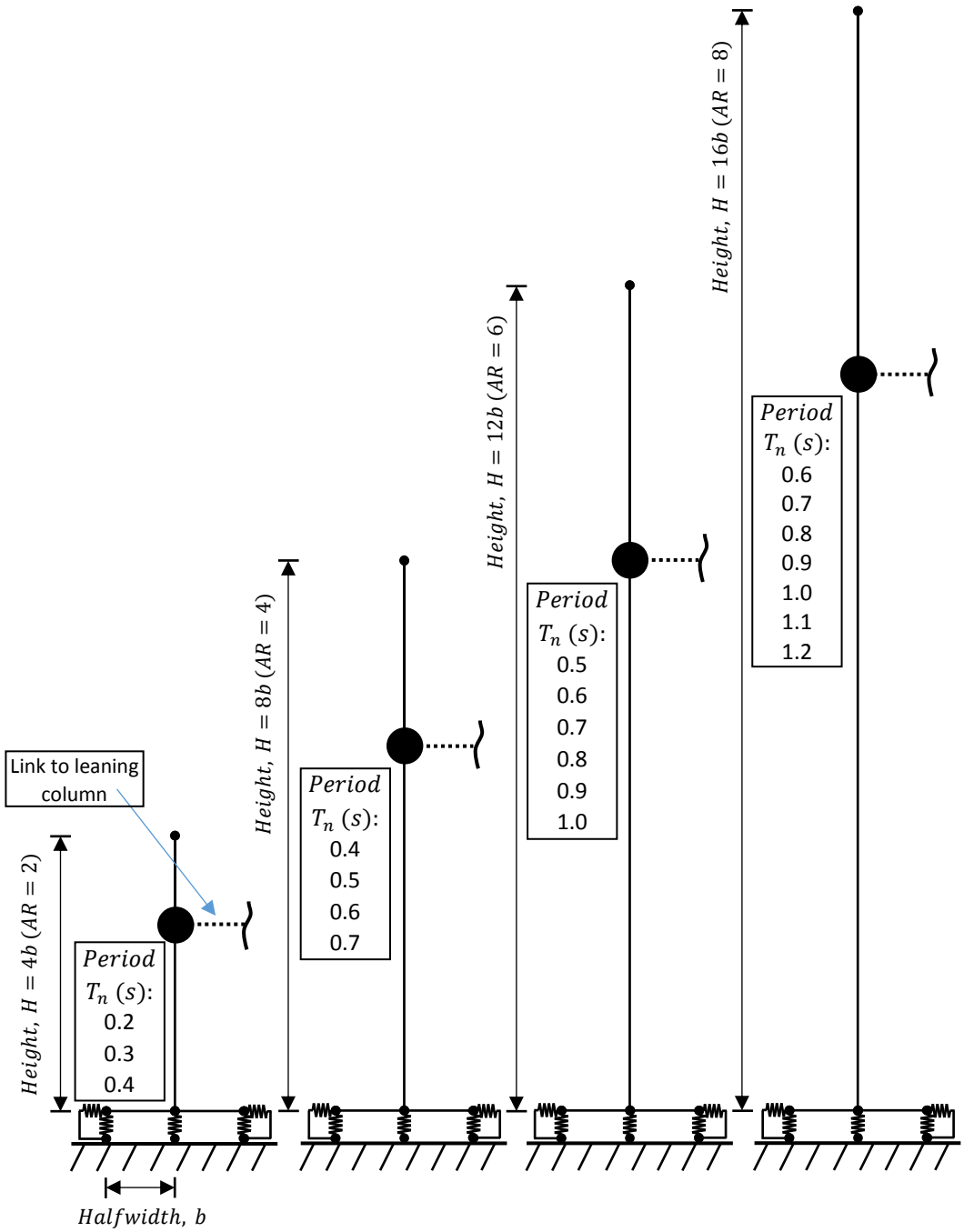

Figure 8.2 *Schematics for the four aspect ratios used in the parameter study, with leaning columns omitted for clarity.*

The smallest pitch size used with the two GNG prototypes was 3 mm. Smaller pitch sizes could be constructed, and the numerical analysis provides an opportunity to investigate the effects and possible benefits of smaller pitch sizes. Each structure was simulated with 5 different GNG rack pitch sizes, as shown in **Table 8.1**, and for the full suite of 60 SAC ground motion recordings, scaled to the elastic site hazard spectrum for a Wellington based ULS event, as described in Chapter 7. The force reduction factor applied is 4, as per the sample study presented in Chapter 7. A total of 6000 full time-history analyses were completed in this main parameter study. The quantities of roof deflection,

roof drift (with reference to the frame height) due to flexure and base rotation, frame base rotation, base uplift from rocking, ratchet behaviour and dissipater behaviour, described in Chapter 7 for a sample study, are all presented and discussed below. Geometric mean values over the 60 ground motions are presented for all results unless otherwise stated. This study focusses on a single rocking frame, and multiple rocking frames could be used in a given design application to reduce the loading experienced by any one rocking frame.

Given the large amount of data produced by the parameter study analyses completed, benchmark structure properties were selected in order to focus the presentation and discussion of the results. The benchmark structure GNG tooth pitch size is 5 mm. This pitch size is between the two pitch sizes tested with the advanced prototype GNG2 device, which were 10 mm and 3 mm, and represents a realistic construction size without significant manufacturing complexity. This selection reduces the number of figures with similar information presented in the main body of the text, while allowing for the demonstration of any trends associated with changes in structure period or aspect ratio.

Results for an aspect ratio of 4, which is selected as the benchmark aspect ratio for these analyses, are presented when observing trends associated with changes in pitch size. This aspect ratio is selected due to the preference expressed in the SCNZ rocking frame design guide [Wiebe et al. 2015]. When results are presented for a single pitch size or aspect ratio the value of this parameter is displayed on the plot and/or in the caption. A sample of the .tcl files used for the OpenSEES analysis are provided in Appendix D, and a wider selection of results for multiple aspect ratios and pitch sizes is presented in Appendix E.

8.2.2. Roof deflection, roof drift, base rotation, and uplift

Figure 8.3 shows the geometric mean peak roof deflection results over the suite of 60 ground motion records for the range of aspect ratios and periods simulated. These results are obtained from the simulation outputs for Node 10 at the top of the frame model, as defined in Chapter 7. For a pitch size of 5 mm, the geometric mean of the peak roof deflection ranged from 0.14 m (aspect ratio = 2, period = 0.2 s) to 0.57 m (aspect ratio = 8, period = 1.2 s). Results where the period range assessed overlaps for structures with different aspect ratios appear effectively overlaid in **Figure 8.3**. This trend shows that structures with the same period and different aspect ratios experienced similar peak roof deflections. The flexural stiffness of the structure was determined using the fundamental period in this study, so these overlaid results match expectations.

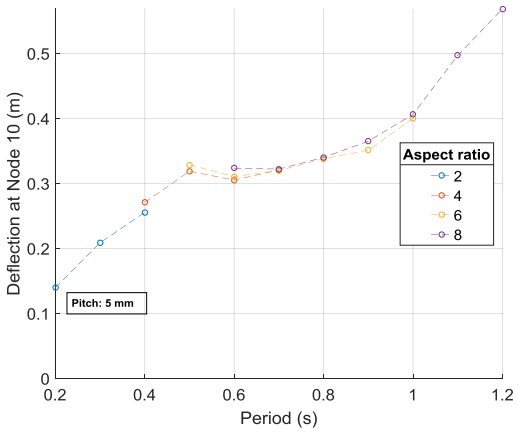

Figure 8.3 *Geometric mean of peak roof deflections (pitch = 5 mm, R = 4, ζ = 3%).*

With the results for each aspect ratio, there is a general trend of larger peak deflections for longer period structures. This result suggests that the decrease in stiffness with increasing period, which when considered independently, acts to increase deflections, is more significant than the decrease in the horizontal design action coefficient that occurs with increasing period, beyond the initial plateau on the elastic site hazard spectrum produced in Chapter 7, which when considered independently, acts to reduce deflections.

The decreases in stiffness and horizontal design action coefficient are compared in Figure 8.4 and Figure 8.5. Figure 8.4 shows the values of the two quantities for the range of periods considered in the analyses, while Figure 8.5 shows the percentage decrease in each value when compared to the value for the previous period. There is no change in the elastic site hazard spectrum value between the first two periods of 0.2 s and 0.3 s, as seen in the initial plateau in **Figure 8.4**. The exponential changes presented in **Figure 8.4** make it difficult to compare the relative changes in each quantity. However, **Figure 8.5** clearly shows that the relative decrease in stiffness outpaces the relative decrease in the horizontal design action coefficient across the full range of period values considered in the analyses. The more significant relative change in the stiffness, when compared to the relative change in the horizontal design action coefficient, confirms that a trend of increasing deflection with increasing period is to be expected, and matches the observed results.

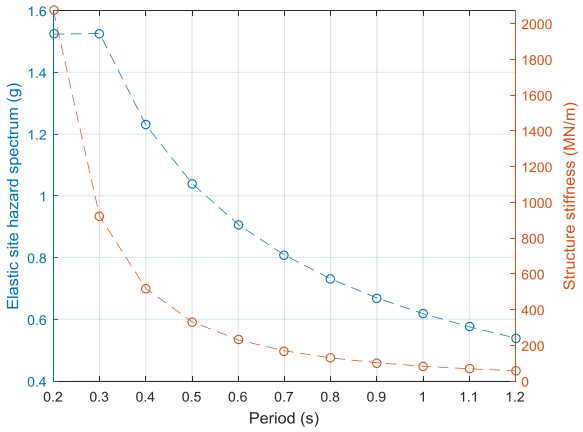

Figure 8.4 *Structure stiffness and elastic site hazard spectrum for the period range considered.*

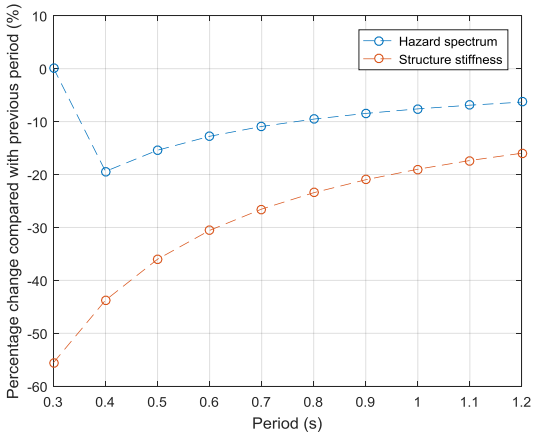

Figure 8.5 *Relative changes in structure stiffness and elastic site hazard spectrum with period.*

Figure 8.6 shows the effect of the tooth pitch size on the peak roof deflections. Increasing pitch size is shown to increase the peak roof deflection, with the greatest increase for the structures with an aspect ratio of 4 seen at a period of 0.4 seconds, where a pitch size of 20 mm caused a 16% greater geometric mean peak roof deflection, compared to a pitch size of 1 mm. This result is consistent with expectations, as the larger pitch size leads to greater free-travel and delayed engagement of the GNG device mechanism during repeated loading cycles.

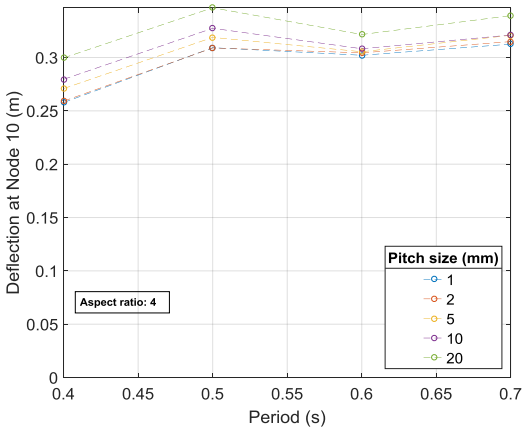

Figure 8.6 *Geometric mean peak roof deflections, showing the effect of pitch size (aspect ratio = 4, R = 4, ζ = 3%).*

Figure 8.7 presents the peak roof drift results, obtained using the deflection of the top of the frame (Node 10) as defined in Chapter 7, showing the contribution from rigid body rotation at the base as well as the total peak roof drift as a result of both rigid body rotation and elastic deflection. Across the range of aspect ratios and periods simulated, with a GNG rack pitch of 5 mm, the geometric mean of the total peak roof drift ranged from 0.81%, for the structure with an aspect ratio of 8 and a period of 0.7 s, to 2.56%, for the structure with an aspect ratio of 2 and a period of 0.4 seconds.

Across all results, rigid body rocking contributes around 75% of the total roof drift. The portion of the total roof drift contributed by base rotation of the rocking frame generally decreases slightly with increasing period. The portion of the total peak roof drift contributed by base rotation of the rocking frame is defined by:

$$\frac{\Delta_{rotation}}{\Delta_{total}} \times 100\% \qquad (8.3)$$

where Δ_{total} is the total peak roof drift due to flexure and base rotation, and $\Delta_{rotation}$ is the peak roof drift due to base rotation alone, or rigid body motion. A comparison of the contribution to total roof drift arising from base rotation, for the lowest and highest periods simulated for each aspect ratio, is presented in **Table 8.2**.

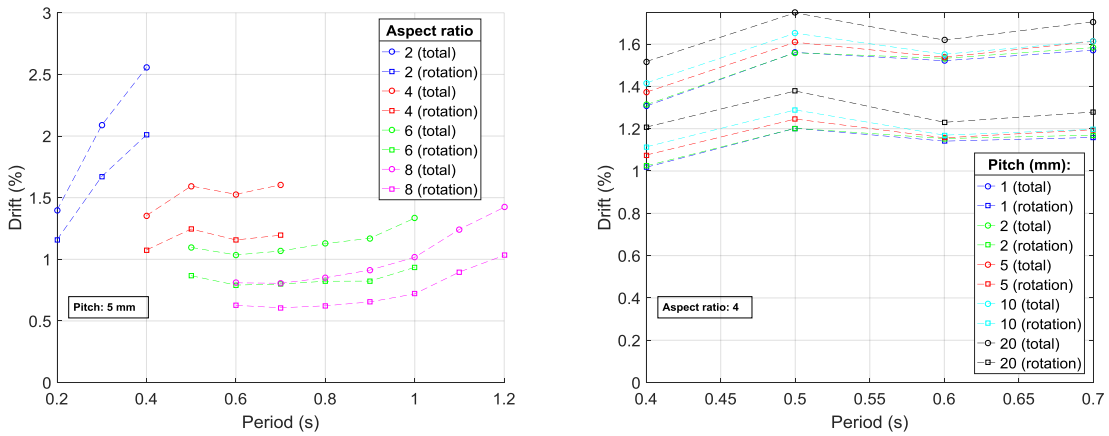

Figure 8.7 *Geometric mean peak roof drifts, showing the contribution to roof drift from base rotation (R = 4, ζ = 3%): a) effect of aspect ratio (pitch = 5 mm), and b) effect of pitch size (aspect ratio = 4).*

Table 8.2 *Percentage contributions of base rotation to total roof drift.*

Aspect ratio	Lowest period	Highest period
2	82.9% (0.2 s)	78.6% (0.4 s)
4	79.4% (0.4 s)	74.5% (0.7 s)
6	79.1% (0.5 s)	70.1% (1.0 s)
8	77.5% (0.6 s)	72.6% (1.2 s)

The effect of GNG rack pitch size on both the total and base rotation component of roof drift is illustrated in **Figure 8.7**b. Increasing pitch size is shown to increase the peak roof drift. The general trends of **Figure 8.7** are visible in the plots for multiple other properties subsequently presented and discussed. This repeated trend is due to the direct relationship between the peak roof drift and other parameters such as the base rotation, base uplift, ratchet demand and dissipater demand.

Figure 8.8a presents the geometric mean peak base rotation angles over the suite of 60 ground motion records for the range of aspect ratios and periods simulated. The peak rotation values follow similar trends with respect to changing period, aspect ratio, and pitch size as the roof drift data presented above. For a pitch size of 5 mm, the geometric mean of the peak base rotation angle ranged from 0.0061 radians, for the structure with an aspect ratio of 8 and a period of 0.7 s, to 0.02 radians, for the structure with an aspect ratio of 2 and a period of 0.4 seconds.

Increasing the aspect ratio has an associated increase in height given the selected modelling approach of using a fixed width for the rocking frame. The larger aspect ratio for a given structural period is seen to reduce the peak base rotation angle in the cases where the same period is simulated for different

aspect ratios. This can be explained by the greater flexural displacement available prior to uplift in taller structures.

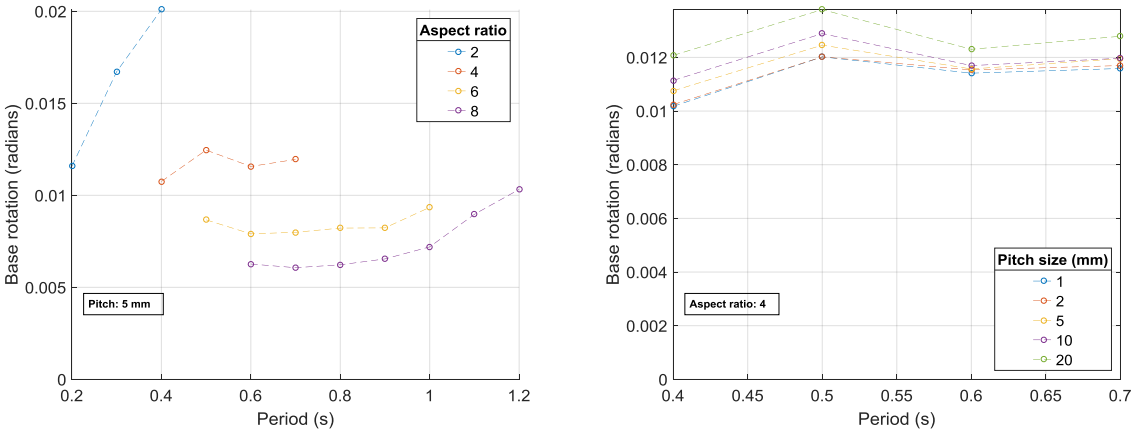

Figure 8.8 *Geometric mean base rotation angles (R = 4, ζ = 3%):*

a) effect of aspect ratio (pitch = 5 mm), and b) effect of pitch size (aspect ratio = 4).

The effect of pitch size on the peak base rotation angle is illustrated in **Figure 8.8**b. There is a clear trend of increasing base rotation with increasing pitch size, with the greatest increase for the structures with an aspect ratio of 4 seen at a period of 0.4 seconds, where a pitch size of 20 mm caused a 19% greater geometric mean peak base rotation, compared to a pitch size of 1 mm. This behaviour matches expectations, as the larger pitch sizes lead to larger average free-travel and a slightly delayed engagement in the device, reducing the initial resistance to base rotation on loading cycles after ratcheting has occurred on a previous response cycle.

Peak uplift values for the left (LHS) and right hand side (RHS) rocking edges are presented in Figure 8.9. The results for the left and right hand side devices are similar, but not quite the same. This level of random variation meets expectations. The peak uplift values follow similar trends to the peak roof drift values. Generally, greater peak uplifts occurred for structures with longer periods. Across the range of aspect ratios and periods simulated, with a pitch of 5 mm, the geometric mean of the peak uplift, for the device mounted on either side of the frame, ranged from 26.1 mm, for the structure with an aspect ratio of 8 and a period of 0.8 s, to 93.5 mm, for the structure with an aspect ratio of 2 and a period of 0.4 seconds.

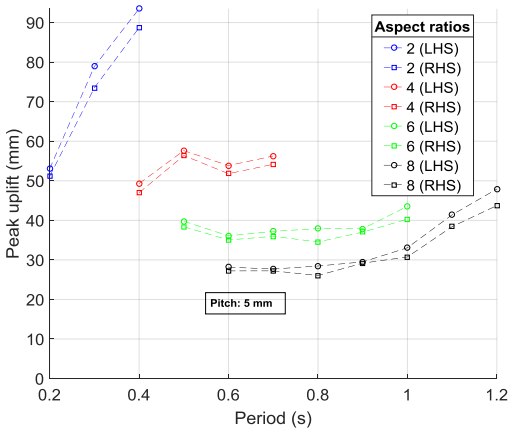

Figure 8.9 *Geometric mean peak uplift, for left and right sides (pitch = 5 mm, R = 4, ζ = 3%).*

The effect of pitch size on peak uplift due to base rotation is shown in **Figure 8.10**. The peak uplift is taken as the largest uplift to occur on either side of the frame during the analysis. Generally, greater peak uplift occurs for larger GNG rack pitch sizes as expected, due to the increase in average free-travel on any given cycle. The increase in geometric mean peak base uplift due to a larger pitch size, for the structures with an aspect ratio of 4, was up to 21.5%, when comparing the demand with a GNG rack size of 20 mm to the demand for a GNG rack size of 1 mm. This result occurred for the structure with a period of 0.4 s. A summary of the increase in peak uplift due to GNG rack size, for this structure, which saw the largest effect out of the structures with an aspect ratio of 4, is presented in **Table 8.3**. The impact on the ratcheting behaviour of the GNG is discussed in the next section.

Table 8.3 *Effect of pitch size on peak uplift.*

Parameter	**Values**				
Pitch (mm)	1	2	5	10	20
Peak uplift (mm)	45.0	45.5	48.1	50.4	54.6
$\frac{peak\ uplift}{peak\ uplift_{pitch=1mm}} \times 100$ (%)	100	101.2	107.0	112.0	121.5

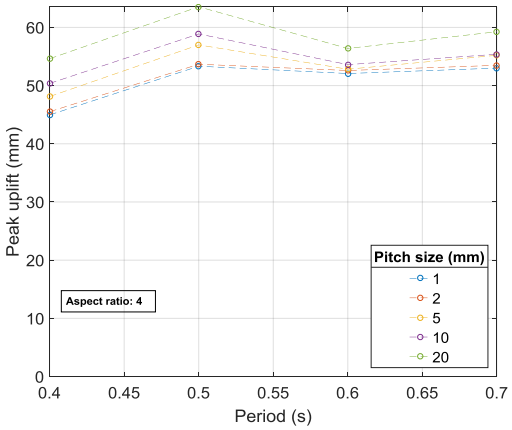

Figure 8.10 *Geometric mean peak uplift*

(aspect ratio = 4, R = 4, ζ = 3%).

8.2.3. Ratcheting

The number of occurrences of ratcheting or 'ratchet count', in the GNG devices at the left and right hand side rocking edges is presented in Figure 8.11. This value is an output from the custom material model algorithm developed for the GNG device behaviour and compiled into the OpenSEES software. Larger base rotation, and subsequently larger peak uplift, leads to a higher number of ratcheting actions as the device undergoes a greater range of motion during re-seating of the rocking wall. Across the range of aspect ratios and periods simulated, with a pitch of 5 mm, the geometric mean of the ratchet count, for the device mounted on either side of the frame, ranged from 14.6, for the structure with an aspect ratio of 8 and a period of 0.8 s, to 67.8, for the structure with an aspect ratio of 2 and a period of 0.4 seconds. Non-integer values occur because these are geometric mean values, but each individual time-history response has an integer value for this metric.

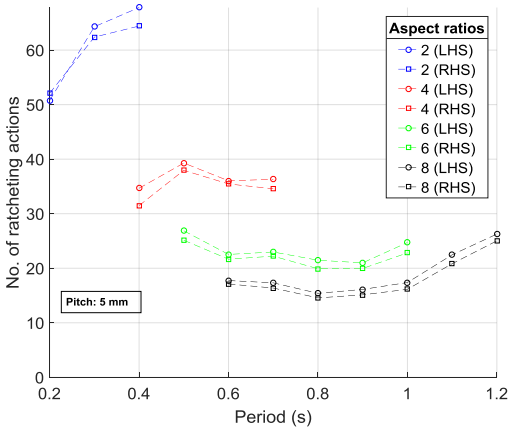

Figure 8.11 *Geometric mean ratchet count, for left and right side devices*

(pitch = 5 mm, R = 4, ζ = 3%).

The effect of pitch size on the ratchet count is shown in **Figure 8.12**. The geometric mean value from all GNG devices, both left and right sides, is presented. The ratchet count is approximately inversely proportional to the pitch size. The GNG rack demand x_{rack} is the length of toothed rack required for consistent operation of the GNG device for the duration of the ground motion. This value is found by multiplying the ratchet count $N_{ratchet}$ by the pitch size p:

$$x_{rack} = N_{ratchet} \times p \tag{8.4}$$

Some small additional length of the rack, less than the tooth pitch, may be required to avoid interference of components during any small amount of additional compressive motion after the last ratchet action has occurred. However, this section would not need to contain the tooth profile for correct operation.

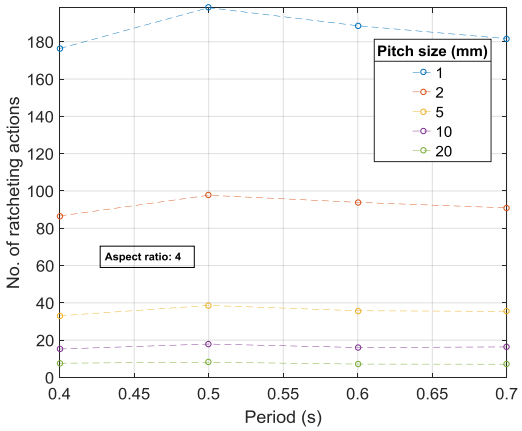

Figure 8.12 *Geometric mean ratchet count, for all devices (both sides) (aspect ratio = 4, R = 4, ζ = 3%).*

Using the relationship in Equation (8.4), Figure 8.13 shows the GNG rack demand for a pitch size of 5 mm. Similar trends for increasing GNG rack demand are observed as for other related quantities. For the structures with a pitch size of 5 mm, in analyses where ratcheting occurred, geometric means of GNG rack demand ranged from 72.8 mm (aspect ratio = 8, period = 0.8 s) to 339 mm (aspect ratio = 2, period = 0.4 s). The devices are located at the outer corners of the rocking frame, so the eccentricity of the devices from the rocking edge is equal to the frame width of 5 m, as described in Chapter 7.

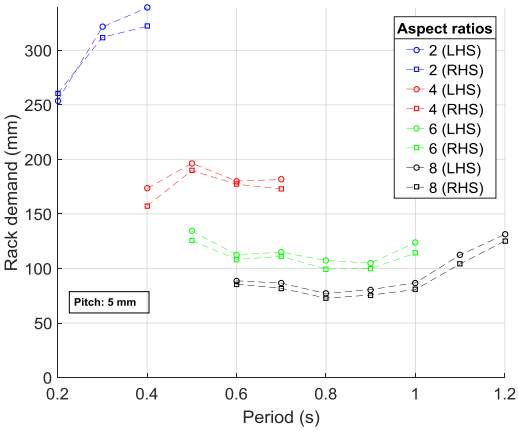

Figure 8.13 *Geometric mean GNG rack demand, for left and right side devices (pitch = 5 mm, R = 4, ζ = 3%).*

In most cases, a smaller pitch size leads to greater GNG rack demand. This result is expected as x_{rack} is likely to be a larger proportion of the total compressive travel as the pitch size reduces and more ratchet actions occur. However, it is possible for a GNG device with a larger pitch size to experience greater rack demand and less free-travel after undergoing the same loading and unloading displacement. For example, if the magnitude of compressive motion occurring during unloading after elastic recovery is 5.5 mm, this would result in a single ratcheting action for a GNG device with a rack pitch size of 5 mm, increasing the rack demand by 5 mm, and giving an expected free-travel on the next loading cycle of 0.5 mm. Alternatively, if a GNG device with a rack pitch size of 2 mm were to undergo the same loading and unloading cycle, the compressive displacement of 5.5 mm would result in two ratcheting actions, increasing the rack demand by only 4 mm, and the free-travel on the next loading cycle would be 1.5 mm. Thus, for some loading cycles, a device with a larger pitch size can experience a greater increase in GNG rack demand and a reduced free-travel on the following loading cycle. **Figure 8.14** demonstrates this effect.

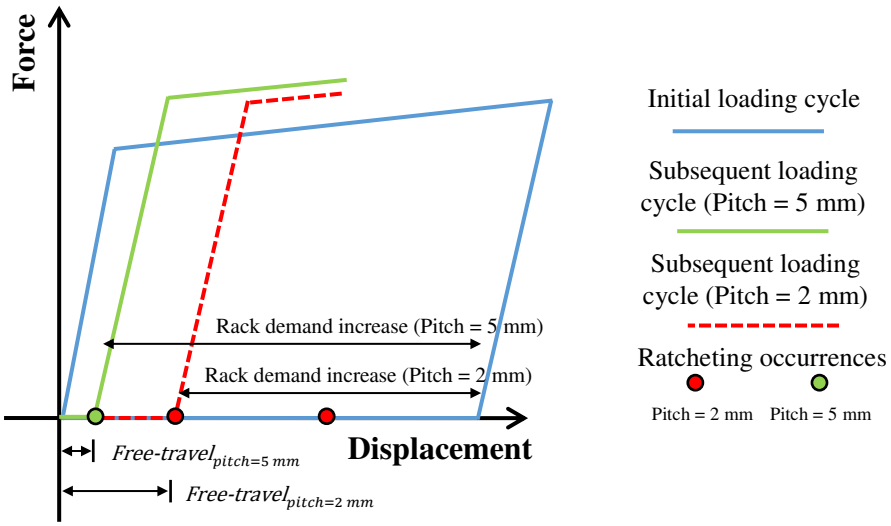

Figure 8.14 *Pitch size effect on GNG rack demand and free-travel.*

Also, when a device does experience additional free-travel on subsequent cycles, the reduced initial resistance to motion may allow for greater peak response of the system during that cycle, and potentially greater rack demand, and inelastic demand in the dissipater, as a result. The early engagement of the device may have the advantage of preventing momentum building up in the base rotation motion. Further, any difference in behaviour of the device during the early stages of the seismic response could lead to randomly compounding unfavourable occurrences, such as repeated near-misses of ratcheting not quite occurring. A comparison of the force displacement hysteresis for the rocking system, with two different pitch sizes is provided in Figure 8.15. This example is taken from the results of the structure with an aspect ratio of 4 and a period of 0.6 s, exposed to record la02 (Imperial Valley), for pitch sizes of 1 mm and 5 mm respectively, and represents an example of a larger rack demand and inelastic dissipater demand occurring in a system with a larger GNG rack pitch size.

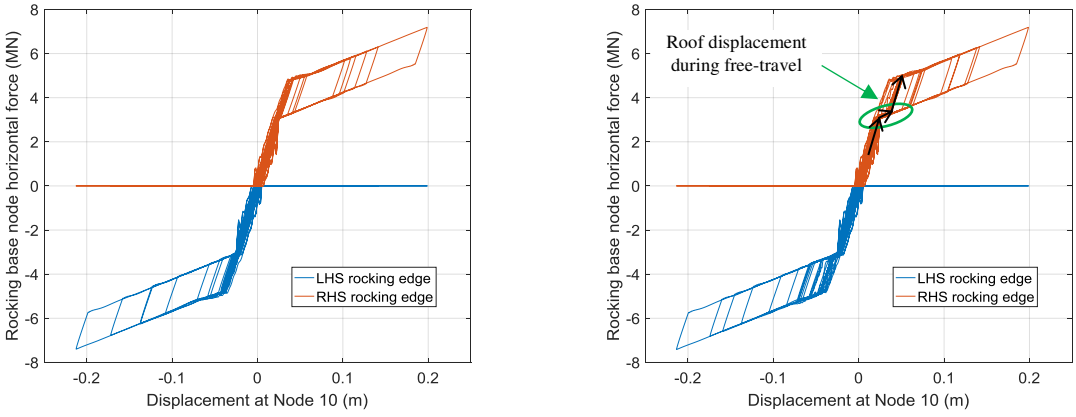

Figure 8.15 *System hysteresis comparison (aspect ratio = 4, period = 0.6 s, R = 4, ζ = 3%, record la02): a) pitch size = 1 mm, and b) pitch size = 5 mm.*

The displacement of the frame roof during the occurrence of free-travel in the GNG-dissipater system is highlighted in **Figure 8.15**b and described in **Figure 8.16**. This displacement can be much larger than the free-travel in the GNG-dissipater system, depending on the aspect ratio of the rocking frame. It is observed that significant displacement of the frame roof can occur during free-travel, altering the system response significantly and potentially leading to greater demand in the dissipater. The system with the larger GNG rack pitch size experienced additional smaller uplift and loading cycles that are not present in the results for the system with the smaller pitch size.

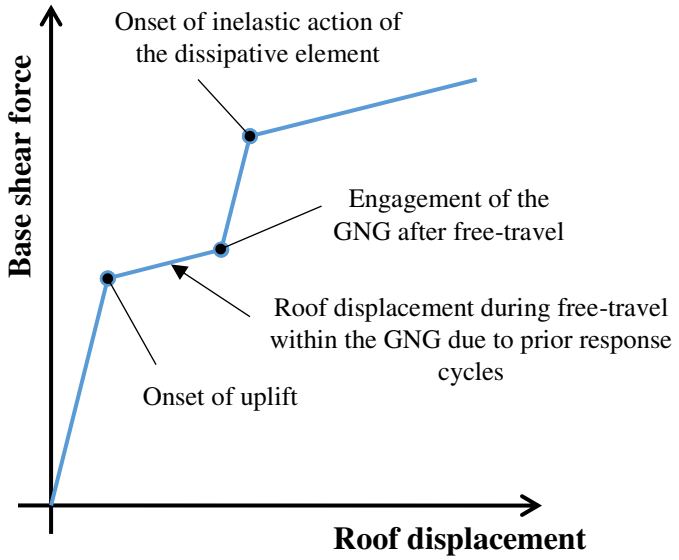

Figure 8.16 *Schematic showing roof displacement occurring during free-travel of the GNG.*

The effect of pitch size on the GNG rack demand is shown in **Figure 8.17**. The geometric mean value from all GNG devices, both left and right sides, is presented. Rack demand is generally reduced with increasing GNG pitch size, though not universally as discussed above. The rack demand is an important factor to consider when designing the GNG-dissipater system for any application. A GNG-dissipater system designed with insufficient capacity to meet the required demand in the rack could stop providing the desired ratcheting response, leading to disengagement of this system, preventing any energy dissipation from occurring.

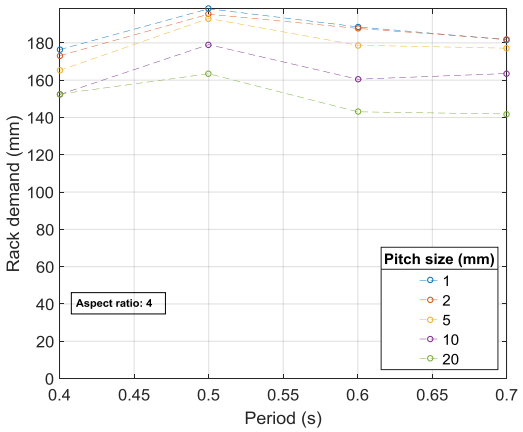

Figure 8.17 *Geometric mean GNG rack demand, for all devices (both sides) (aspect ratio = 4, R = 4, ζ = 3%).*

8.2.4. Inelastic dissipater demand

Figure 8.18 shows the geometric mean inelastic dissipater demand in the GNG devices. This value represents the total plastic deformation capacity required in the energy dissipation mechanism to ensure consistent operation of the GNG device for the duration of the ground motion, without fracture of the dissipater. This value is an output from the custom material model algorithm developed for the GNG device behaviour and compiled into the OpenSEES software. Across the range of aspect ratios and periods simulated, with a pitch of 5 mm, the geometric mean of the inelastic dissipater demand, for the device mounted on either side of the frame, ranged from 77.2 mm, for the structure with an aspect ratio of 8 and a period of 0.8 s, to 344.5 mm, for the structure with an aspect ratio of 2 and a period of 0.4 seconds.

The inelastic dissipater demands are generally similar to the GNG rack demands. While demand in the rack is induced during compressive motion after elastic recovery, demand in the dissipater is induced during tensile motion following yield. The magnitude of these respective motions can be very similar in systems with little strain hardening in the dissipater, such as the 0.02% value used in these analyses. The results for an aspect ratio of 4 in **Figure 8.18** broadly match the results presented earlier in **Figure 8.17**.

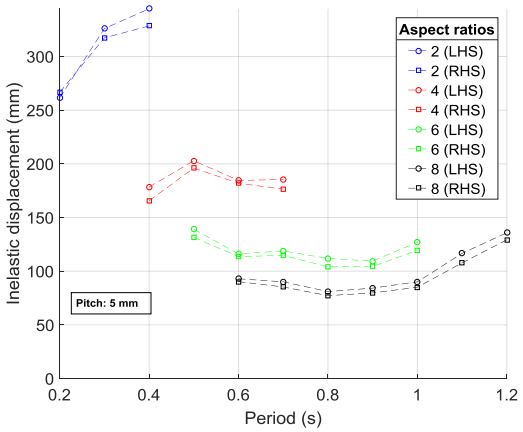

Figure 8.18 *Geometric mean inelastic dissipater demand, for left and right side devices (pitch = 5 mm, R = 4, ζ = 3%).*

The effect of pitch size on the inelastic dissipater demand is shown in **Figure 8.19**. The geometric mean value from all GNG devices, both left and right sides, is presented. In most cases, a smaller pitch leads to greater inelastic demand in the dissipater, due to a reduction in free-travel from the reduced pitch size. However, as mentioned previously in the discussion about GNG rack demand, it is possible for a device with a larger pitch size to experience a greater cumulative inelastic dissipater demand over the duration of a seismic event. In Figure 8.19, such an outcome is seen in the results for a period of 0.5 s, with the pitch size of 5 mm leading to a slightly greater geometric mean inelastic dissipater demand than the 1 mm and 2 mm pitch devices in the same analysis. However, most results show the expected trend of lower inelastic displacement resulting from the larger pitch size.

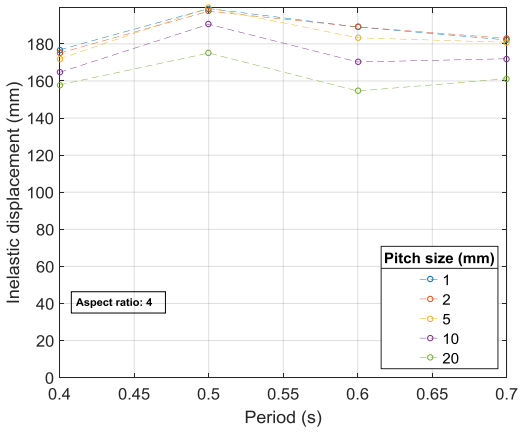

Figure 8.19 *Geometric mean inelastic dissipater demand, for all devices (both sides) (aspect ratio = 4, R = 4, ζ = 3%).*

In **Figure 8.20** the geometric mean of the relative inelastic demand in the dissipater is shown for the range of pitch sizes simulated. The geometric mean value from all GNG devices, both left and right sides, is presented. The data presented has been normalised to the demand for a pitch size of 1 mm

in the GNG device. The geometric mean demand in the GNG devices with a pitch size of 20 mm was typically around 85% of the demand in the same structure with a GNG rack pitch size of 1 mm. The influence of pitch size on inelastic dissipater demand could be amplified in cases with smaller uplift displacements, due to the increased size of the pitch relative to uplift.

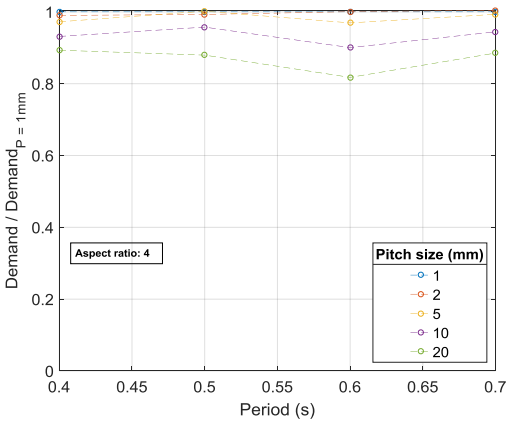

Figure 8.20 *Geometric mean relative dissipater demand, for all devices (both sides) (aspect ratio = 4, R = 4, ζ = 3%).*

8.2.5. Demand ratio

The ratio between the total cumulative inelastic demand in the dissipater and the peak uplift due to rocking recorded during the corresponding simulation is referred to as the 'demand ratio'. This ratio is of particular interest in the design of a rocking system implementing the GNG device, as it provides a convenient guide for the required capacity. The results below will form the basis for design recommendations outlined later in this chapter.

Figure 8.21 shows a comparison of the inelastic dissipater demand and peak uplift values in both the LHS and RHS devices for the 6000 analyses completed. Dashed lines are plotted indicating demand ratios of 1 and 10. Almost all of the simulated data fits within this range. Only 56 of 6000 simulations, that is 0.93%, exceed a demand ratio of 10. This result suggests that a design demand ratio of 10 would be suitable in most cases, without considering the dependency on GNG rack pitch size or other factors, which may allow for less conservative values in particular cases.

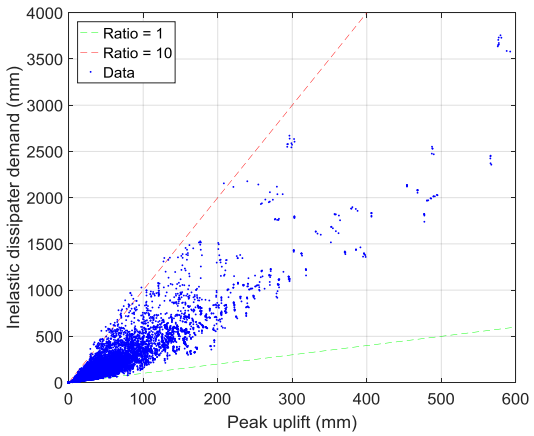

Figure 8.21 *Inelastic dissipater demand and peak uplift, for all devices (both sides) (R = 4, ζ = 3%)*

Figure 8.22 presents the geometric mean values of the demand ratio for the completed analyses, grouped by aspect ratio. The geometric mean value from all GNG devices, both left and right sides, is presented. The pitch has a significant effect on the demand ratio, where a larger pitch reduces the demand ratio. This influence could be amplified in cases with smaller uplift displacements, due to the increased size of the pitch relative to uplift.

The demand ratio for the structure with an aspect ratio of 2 and a period 0.2 s ranges from 5.3 for a pitch size of 1 mm, to 4.1 for a pitch size of 20 mm. This represents a reduction of 23% in the demand ratio due to the increased pitch size. In contrast, the demand ratio for the structure with an aspect ratio of 8 and a period 1.2 s ranges from 3.1 for a pitch size of 1 mm, to 2.2 for a pitch size of 20 mm. This represents a reduction of 29% in the demand ratio due to the increased pitch size.

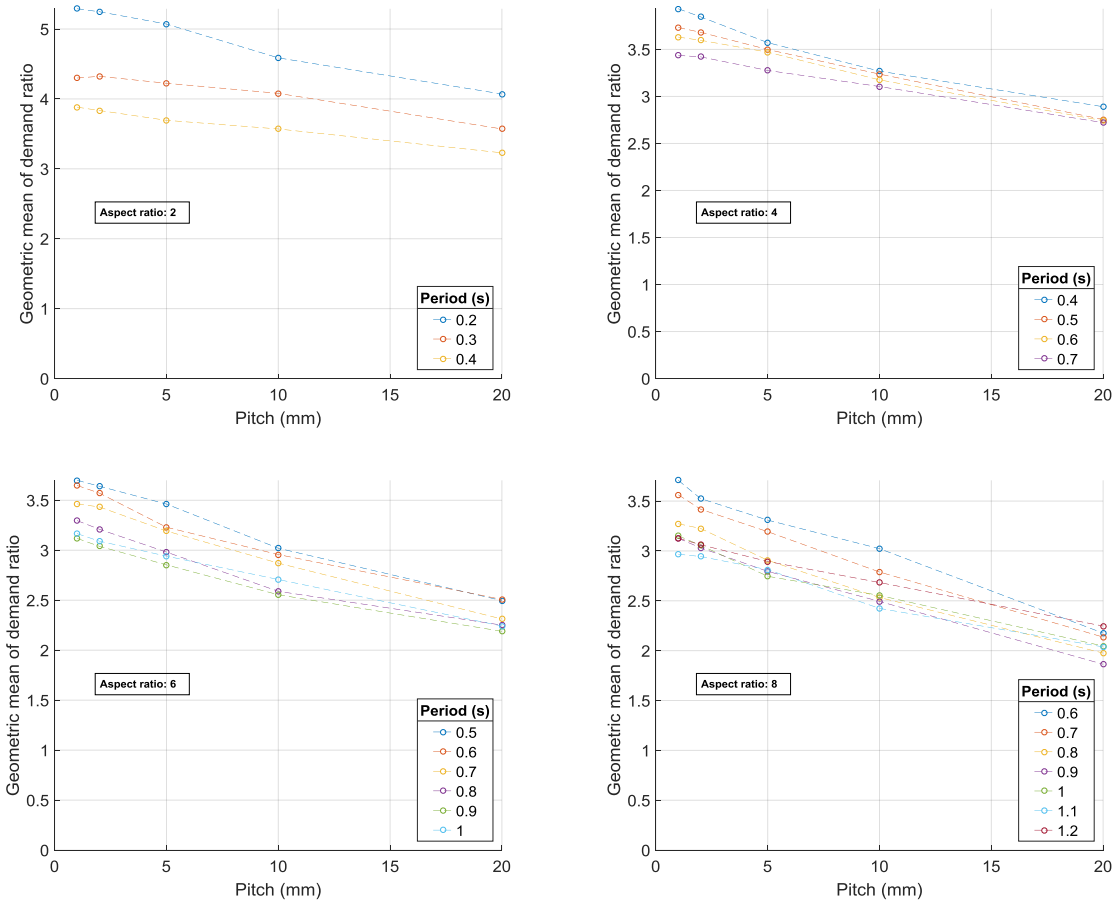

Figure 8.22 *Geometric mean of demand ratio, for all devices (both sides) (R = 4, ζ = 3%): a) aspect ratio = 2, b) aspect ratio = 4, c) aspect ratio = 6, and d) aspect ratio = 8.*

The spread of the demand ratio values is illustrated in **Figure 8.23**. **Figure 8.23** shows the demand ratio for each device from each of the 60 ground motion records simulated, giving a total of 120 series lines. These individual analyses results are shown alongside the geometric mean results. Results for the structure with an aspect ratio of 2 and a period of 0.2 s were selected to present here as they contain the largest spread of aspect ratio values. Some of the results exceed a demand ratio of 10, and in some analyses the demand ratio is greater than twice the geometric mean result. Further statistical analysis is presented below.

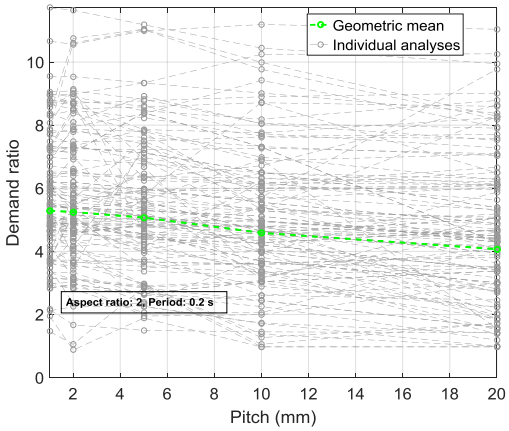

Figure 8.23 *Demand ratio spread*

(aspect ratio = 4, period = 0.2 s, R = 4, ζ = 3%).

A log-normal distribution analysis was used to assess the demand ratio data and provide summary statistics, forming a basis for tentative dissipater design capacity guidelines, provided later in this chapter. A log-normal distribution was chosen over a normal distribution due to the absence of a physical basis for negative values, making an additive standard deviation unsuitable. As a result, geometric mean and multiplicative standard deviation values are implemented in the analysis. For a sample of n individual values of data x, the geometric mean [Limpert et al. 2001] is defined as:

$$\bar{x}^* = exp\left(\frac{1}{n}\sum_{i=1}^{n} log(x_i)\right) = \left(\prod_{i=1}^{n} x_i\right)^{\frac{1}{n}} \qquad (8.5)$$

where i is the sample number. The resulting multiplicative standard deviation [Limpert et al. 2001] is then:

$$s^* = exp\left(\left[\frac{1}{n-1}\sum_{i=1}^{n}\left[log\left(\frac{x_i}{\bar{x}^*}\right)\right]^2\right]^{\frac{1}{2}}\right) \qquad (8.6)$$

Summary statistics for the entire data set are shown in **Table 8.4**. A log-normal distribution also produced a better match with expected confidence intervals, compared to a normal distribution. The resulting true confidence intervals, that is the actual percentage of results which fall within the respective distribution, are presented in **Table 8.5**. The symbol $*/$ represents multiply/divide. The lower limit of one log-normal standard deviation distribution is $\bar{x}^*/s^*$ and the upper limit is $\bar{x}^* * s^*$.

Table 8.4 Summary statistics of the demand ratio analysis.

Parameter	Value
Minimum	0.86
Maximum	12.74
Geometric mean, $\bar{x}^*$	3.12
Multiplicative standard deviation, s^*	1.64

Table 8.5 Log-normal distributions and confidence intervals.

Log-normal distribution	Theoretical confidence interval	True confidence interval
$\bar{x}^* */s^*$	68.3%	69.6%
$\bar{x} */(s^*)^2$	95.5%	94.3%
$\bar{x} */(s^*)^3$	99.7%	100%

Figure 8.24 shows the cumulative distribution function of the demand ratio data, and a distribution fit based on the summary statistics presented in **Table 8.4**. Using the 'logncdf' function to produce the distribution fit in MATLAB requires using the natural log of the geometric mean and multiplicative standard deviation values shown in **Table 8.4**. The distribution fit shown captures the spread of the data well. The simulation data is presented as markers only, with no line between points. However, the simulation data appears similar to a plotted line due to the close grouping of the 6000 data points that make up the dataset. **Figure 8.25** shows a histogram of the demand ratio data with a superimposed probability density function. Again, it can be seen that the log-normal distribution fitted to the results is a good representation of the underlying demand ratio information.

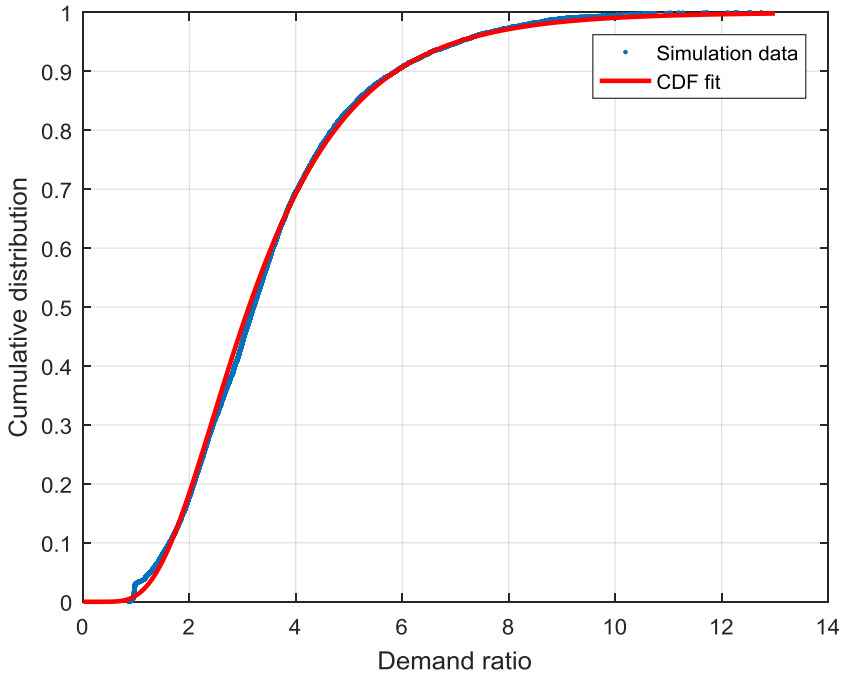

Figure 8.24 *Cumulative distribution function of the demand ratio data, showing the CDF fit.*

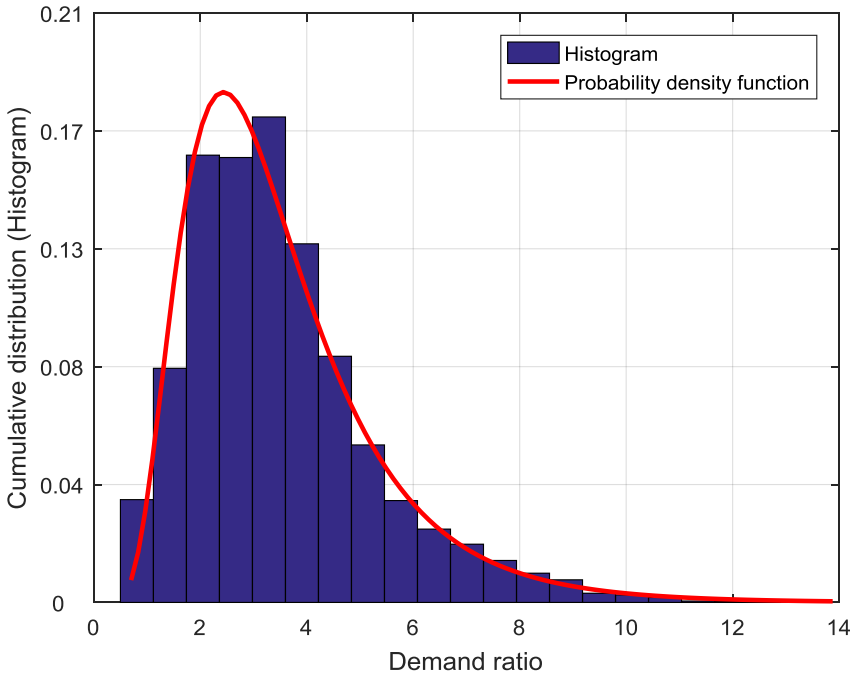

Figure 8.25 *Histogram and probability distribution of the demand ratio data. The y-axis shown applies to the histogram.*

The limits of the distributions for the three confidence intervals examined are shown in **Table 8.6**. While the distributions cover a certain amount of the data, defined by the confidence interval, a dissipater designed with a certain demand ratio capacity will be suitable for any required demand up to the design value. The percentage of simulations with a demand ratio less than the upper limit of

each distribution range is shown in **Table 8.6** as the 'cases captured'. This value is significantly larger than the corresponding confidence interval for the first 2 distributions.

Table 8.6 *Cases captured by 3 standard deviation distributions of the demand ratio data.*

	Limits of the distribution		Cases captured (%)
Distribution	**Lower**	**Upper**	**(demand < upper limit)**
$\bar{x}^* * / s^*$	1.90	5.13	84.7
$\bar{x} * / (s^*)^2$	1.15	8.44	98.2
$\bar{x} * / (s^*)^3$	0.70	13.88	100

From **Table 8.6** it can be seen that over 98% of the demand ratios recorded are below the upper limit of the $\bar{x} * / 2s^*$ distribution of 8.44. This data indicates that a dissipater designed with a plastic capacity of greater than 8.44 times the peak uplift experienced during a ULS seismic event would have sufficient inelastic capacity for the event in over 98% of cases. In addition, from the maximum value shown in Table 8.4, it is seen that a dissipater designed with a plastic capacity of over 12.74 times the peak uplift would survive the event intact in all of the simulated cases. This analysis provides a strong basis for tentative dissipater design capacity guidelines, which are provided later in this chapter.

Table 8.7 shows the influence of the pitch size on the geometric mean and multiplicative standard deviation of the inelastic demand ratio. There is a slight increase in the standard deviation with increasing pitch. In contrast, the geometric mean of the demand ratio varies significantly with the pitch size. For a pitch size of 20 mm, the geometric mean demand ratio is only 70% of the geometric mean demand ratio for a pitch size of 1 mm. A pitch size of 2 mm gives a demand ratio 98% of the demand ratio for a pitch size of 1 mm.

Table 8.7 *Pitch size influence on demand ratio.*

Parameter	**Values**				
Pitch (mm)	1	2	5	10	20
$\bar{x}^*$	3.54	3.48	3.27	2.97	2.47
s^*	1.55	1.56	1.58	1.64	1.74
$\frac{\bar{x}^*}{\bar{x}^*_{pitch=1mm}} \times 100$ (%)	100	98.09	92.22	83.79	69.71

Using a larger pitch size reduces the inelastic capacity required in the dissipater. However, less energy would be absorbed by the dissipater, possibly leading to greater peak displacements and potentially

increasing damage. Given the improved energy dissipation and reasonable ease of manufacture for small pitch sizes, it is recommended to use the smallest possible pitch size that has robust characteristics where the teeth and device can carry the required force.

8.3. Code-based method results and capacity recommendation

8.3.1. Peak uplift approximation from code methods

The ULS peak lateral deflections of the structure, and the peak base uplift, can be estimated using guidance from the SCNZ 110:2015 rocking frame design guide [Wiebe et al. 2015] and NZS 1170.5 [SNZ 2004]. Some simplification of the process has been made to apply it to the model structure described in Chapter 7. Relevant sections of the two code documents are stated where appropriate. A guide to the parameters used in the approximation of the code method to determine the peak base uplift is provided in **Table 8.8**, and a schematic of the ULS peak lateral deflection estimated from the codes is provided in **Figure 8.26**.

Table 8.8 *Parameters in the approximation of the code method to find peak base uplift.*

Symbol	Description
T_1	Initial fixed-base structure period of first mode
R	Force reduction factor (response modification factor)
μ	Structural ductility factor
S_p	Structural performance factor
k_μ	Inelastic spectrum scaling factor
$C_d(T_1)$	Horizontal design action coefficient
$C(T_1)$	Ordinate of elastic site hazard spectrum
V	Horizontal seismic base shear
W_t	Seismic weight of structure
K_1	Initial fixed-base structure stiffness
M_t	Seismic mass of structure
Δ_y	Elastic lateral roof deflection
Δ	Peak lateral roof deflection
$\Delta_{rotation}$	Lateral roof deflection due to base rotation at peak lateral roof deflection
θ_{base}	Peak base joint rotation
H	Structure height
x_{uplift}	Peak uplift due to base rotation
B	Half-width of the rocking frame
x_{ED}	Inelastic capacity required in the dissipater
ν_{demand}	Inelastic capacity factor

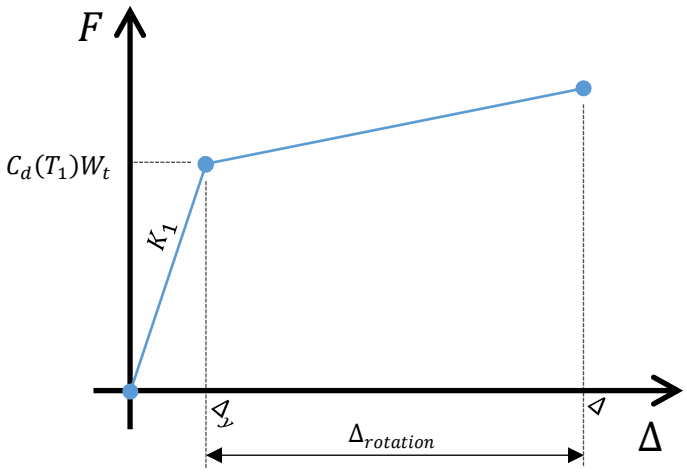

Figure 8.26 *Schematic of ULS peak lateral deflection estimated from code method.*

First, several rearrangements are made to find an appropriate combination of the structural ductility factor μ and structural performance factor S_p (SCNZ 110:2015 Section 5, NZS1170.5 Section 4), along with the inelastic spectrum scaling factor k_μ (NZS1170.5 Section 5), which represent the assumed force reduction factor R:

$$S_p = \begin{cases} 1.3 - 0.3\mu & for\ 1.0 < \mu < 2.0 \\ 0.7 & for\ \mu > 2.0 \end{cases} \tag{8.7}$$

$$k_\mu = \begin{cases} \mu & for\ T_1 \geq 0.7\ s \\ \dfrac{(\mu - 1)T_1}{0.7} + 1 & for\ T_1 < 0.7\ s \end{cases} \tag{8.8}$$

Where the relationship between the inelastic spectrum scaling factor, the structural performance factor and the force reduction factor is approximated from the application of the various factors to scale the ordinate of the elastic site hazard spectrum to find the horizontal design action coefficient (NZS1170.5 Section 5):

$$C_d(T_1) = \frac{C(T_1)S_p}{k_\mu} \tag{8.9}$$

$$R \approx \frac{k_\mu}{S_p} \tag{8.10}$$

This representation of the force reduction factor is consistent with the scaling of the ordinate of the elastic site hazard spectrum used in the time-history analyses presented in this thesis. The horizontal seismic shear acting at the base of the structure is then determined using the equivalent static method (NZS1170.5 Section 6):

$$V = C_d(T_1)W_t \tag{8.11}$$

With the lumped mass approximation used in the model, the elastic deflection at the mass (located at two-thirds of the height) can be calculated using the initial fixed base stiffness, and multiplied by 1.5 to find the elastic deflection at the top of the frame. This value is scaled by the deflection multiplier of 1.3 for self-centring systems to account for the effect of torsion:

$$K_1 = \left(\frac{2\pi}{T_1}\right)^2 M_t \tag{8.12}$$

$$\Delta_y = 1.3\left(\frac{V}{K_1} \times \frac{3}{2}\right) \tag{8.13}$$

The ULS deflection is calculated as the elastic deflection including torsion scaled by the structural ductility factor and by an additional displacement multiplier of 1.3 (SCNZ 110:2015 Section 5):

$$\Delta = 1.3\mu\Delta_y \tag{8.14}$$

The ULS deflection due to base rotation is now found by deducting the elastic roof displacement from the estimated peak roof displacement (SCNZ 110:2015 Section 5):

$$\Delta_{rotation} = \Delta - \Delta_y \tag{8.15}$$

The peak base joint rotation angle is estimated by dividing the deflection due to base rotation by the building height (SCNZ 110:2015 Section 5):

$$\theta_{base} = \frac{\Delta_{rotation}}{H} \tag{8.16}$$

Finally, this rotation angle is associated with a gap opening, or peak base uplift, equal to the base joint rotation angle multiplied by the frame width, for a dissipater located at the outer edge of the frame:

$$x_{uplift} = 2B\theta \tag{8.17}$$

8.3.2. Comparison of peak uplift values from simulations and code methods

Figure 8.27 shows a comparison of the peak uplift values obtained from the approximate code method described above and the geometric mean values from the OpenSEES simulations outlined previously, with a GNG rack pitch size of 1 mm. The results using the smallest GNG pitch size simulated provide the most appropriate comparison to the approximate code values, as there is no consideration of pitch size and free-travel in the general code methods since these are unique features of the GNG device. **Figure 8.28** presents the ratio of the geometric mean peak uplift values from the simulations to the code peak uplift values. The ratios displayed in **Figure 8.28** are obtained using the data in **Figure 8.27**.

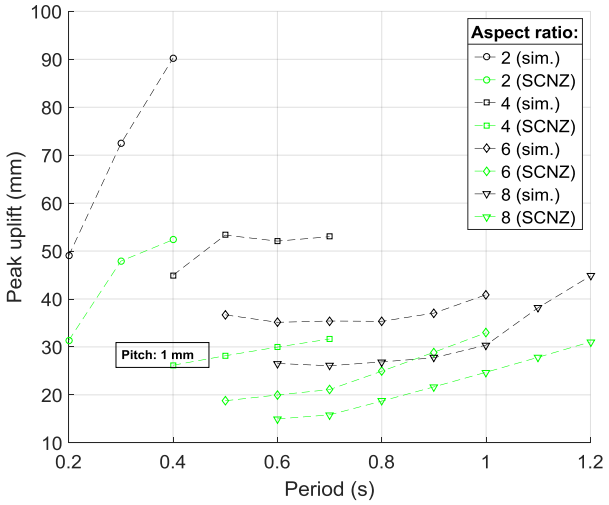

Figure 8.27 *SCNZ 110:2015 peak uplift values and OpenSEES simulation geometric mean peak uplift values (pitch = 1 mm, R = 4, ζ = 3%).*

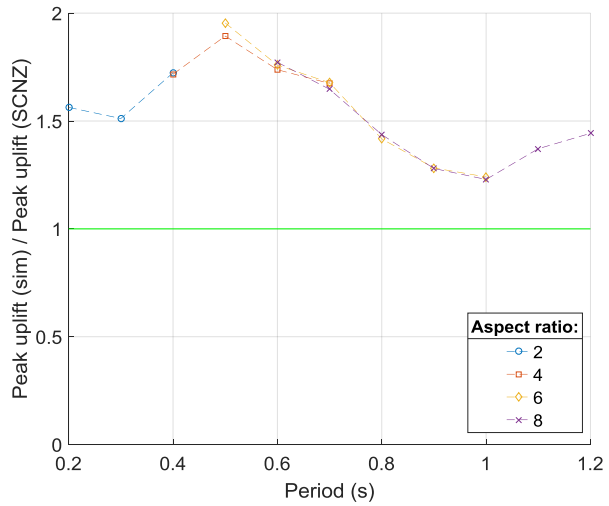

Figure 8.28 *Ratio of OpenSEES simulation geometric mean peak uplift values to SCNZ peak uplift values (pitch = 1 mm, R = 4, ζ = 3%).*

In general, larger peak uplift values were found in the simulations than using the SCNZ method. The closest match between simulation and code values was found for a period of 1.0 s. This is seen clearly in **Figure 8.28** where the ratio between the simulation and code results drops towards unity. The geometric mean simulated peak uplift results were between 123% and 196% of the values obtained using the approximate code method.

The GNG pitch size affects the ratio between the simulation and SCNZ values, in line with the trend of increasing uplift with increasing pitch size as previously discussed and shown in Table 8.3 and Figure 8.10. As a result, increasing the pitch size increased the ratio between the simulated results and the SCNZ results. The shape of the plot line was generally the same, with some separation of the series

lines for different aspect ratios, which did not overlap so well for the larger pitch sizes. For comparison the results for the largest pitch size simulated, 20 mm, are shown in **Figure 8.29**. For a pitch size of 5 mm, the minimum and maximum values are respectively 127% and 208%. For the 20 mm pitch, the geometric mean of the simulated results ranged from 139% to 227% of the SCNZ values. The variation in the ratio between the uplift values obtained from the OpenSEES simulations and the SCNZ method for the range of pitch sizes considered is presented in **Table 8.9**.

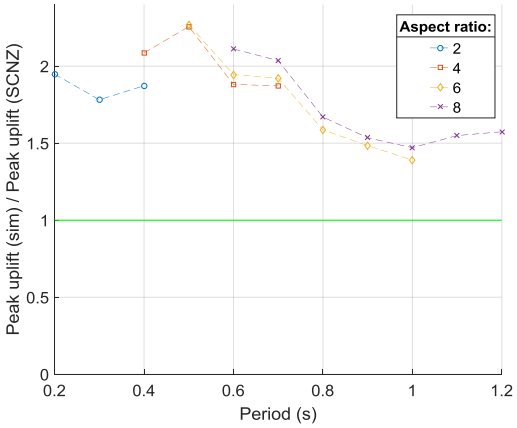

Figure 8.29 *Ratio of OpenSEES simulation geometric mean peak uplift values to SCNZ peak uplift values (pitch = 20 mm, R = 4, ζ = 3%).*

Table 8.9 *Variation of ratio of geometric mean simulated peak uplift values to SCNZ peak uplift values.*

Pitch size	Min.	Max.
1 mm	123%	196%
2 mm	123%	199%
5 mm	127%	208%
10 mm	130%	219%
20 mm	139%	227%

There is generally quite high variation between the simulation and the code-based results. However, there are several factors that contribute to this variation, and it may be reasonable given the approximate nature of the calculation and the influence of selected variables on the results. The OpenSEES model captures dynamic effects that are not recreated by the equivalent static method detailed in the code documents. The choice of ground motion recording files input to the simulated structures will affect the exact values. Additionally, the simplified application of the code method to the lumped mass model used in the simulations will introduce additional uncertainty. Further, the application of the inelastic spectrum scaling factor (k_μ) formula to periods near the boundary of the

two formulas provided in NZS1170.5, at 0.7 s, could increase the error in the approximation. Applying the SCNZ approximations to structures with very short periods, such as the lowest structure period modelled of 0.2 s, may yield less reliable results also. While the flexible rocking model uses an inherent damping of 3% critical, the records were scaled based upon 5% critical damping to provide the same ground motions as any other conventional structure in the same location. The fact that the baseline rocking structure has less inherent damping than is assumed in the design codes contributes to the differences in uplift results observed.

In summary, there were a number of assumptions and simplifications applied to the model which may affect how closely the results match the values found using the code-based methods. The existing code based approach for rocking walls does not make any consideration for the effect of the GNG mechanism, as it was not designed with the GNG in mind. Given the differences between the type of system considered in the code based method and the GNG system modelled in the numerical analysis completed in this thesis, the results were not expected to match. The aim was to see how values from the existing method compared to the values from the numerical analysis, in order to assess the value of using the existing methods, with the addition of a couple of additional factors, to provide a preliminary assessment of the cumulative demand, rather than making a detailed critique of the existing code methods. A more detailed model would be appropriate for improving the SCNZ method.

The spread of the peak uplift ratios is shown in Figure 8.30, with the individual results from each ground motion recording shown for each aspect ratio and period combination simulated, for a GNG rack pitch size of 1 mm, giving a total of 1200 individual time-history analysis results. There is a significant spread of values observed across the data presented, with some extreme outlier results showing peak uplift ratios of over 10 in rare cases. The spread of peak uplift ratios is also displayed in **Table 8.10**, which shows the percentage of ratios of peak uplift from individual time-history analyses, compared to code-based results, that were greater than a range of integer values.

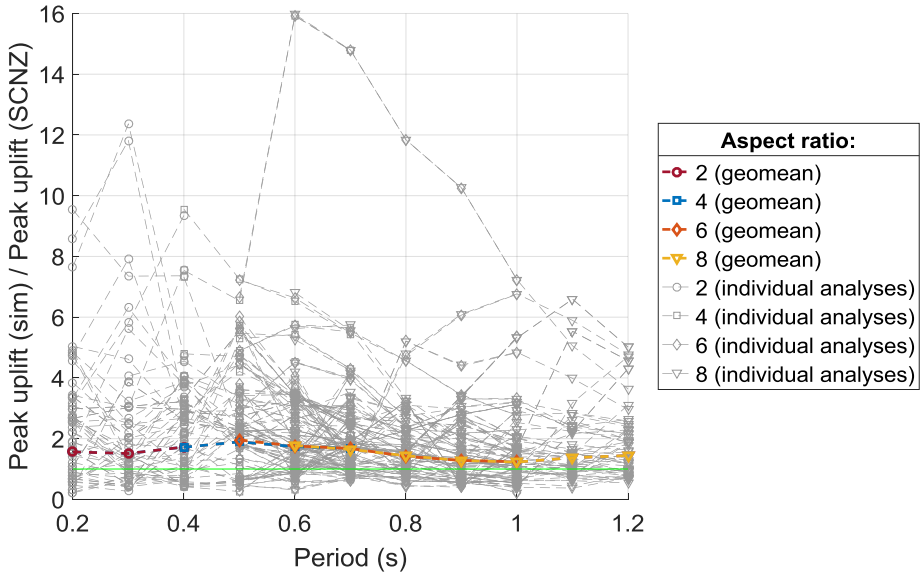

Figure 8.30 *Spread of ratio of OpenSEES simulation geometric mean peak uplift values to SCNZ peak uplift values (pitch = 1 mm, R = 4, ζ = 3%).*

Table 8.10 *Spread of peak uplift ratios.*

Reference	% of peak uplift ratios > reference
1	75.83
2	42.17
3	21.83
4	10.75
5	6.33
6	3.33

8.3.3. Recommended capacity in the dissipater and rack

Using the findings of the statistical analysis of the demand ratio presented earlier in this chapter and the comparison between simulated and code-based peak uplift values in the previous section, the inelastic capacity required in the dissipater can be estimated. After applying the equivalent static methods detailed in the design codes, a multiplier of 2 is suggested to be applied to the peak uplift values. This factor is suggested to account for the difference between the approximate code-based peak uplift values and the geometric mean of the simulated values of peak uplift outlined above. In most considered cases, larger peak uplifts were calculated from the time-history analyses than from the code-based approach. A factor of 2 applied to the code-based values provides a conservative design approach by ensuring that the code-based values are not below the values obtained via full

time-history analysis. Almost all of the ratios between geometric means of simulated peak uplift values and code-based peak uplift values were less than 2 for pitch sizes of 5 mm or less, as presented in Table 8.9. As discussed in the previous section, there are a number of assumptions and simplifications unique to the flexible rocking model used in these time-history analyses which can affect the variation between the simulated results and the code-based values.

The updated peak uplift value should then be multiplied by an inelastic capacity factor (ν_{demand}) to find the required inelastic demand in the dissipater (x_{ED}). A value of $\nu_{demand} = 10$ is recommended. The geometric mean of the demand ratio in the completed analyses ranged between 1.9 and 5.3, depending on the structure aspect ratio, period, and GNG rack pitch size. However, the ratio provided from the geometric mean only covers around half the response cases and a demand ratio in the dissipater of 10 was shown to be suitable for safe operation of the GNG system in over 99% of the analyses completed during the main parameter study.

Thus, the following equation is offered as a tentative recommendation:

$$x_{ED} = x_{rack} = 2x_{uplift}\nu_{demand} \tag{8.18}$$

This value should also be used for the required demand in the GNG rack (x_{rack}). This recommendation is made based upon the simulation of ULS events, and aftershocks and MCE motions will also need to be considered in design. Larger uplifts are expected during MCE events, but a similar demand ratio may be appropriate. A force reduction factor of 4 was used in the analyses to produce this equation, and a study of the effect of the force reduction factor follows.

8.4. Effect of response reduction factor

8.4.1. Roof deflection, roof drift, base rotation, and uplift

The main parameter study, which used a force reduction factor of 4, was repeated with force reduction factors of 2 and 6 to compare the results and assess the effect of the force reduction factor on the system response, involving an additional 12000 individual time-history analyses. The geometric mean peak roof deflection results from the three force reduction factor studies are presented in **Figure 8.31**. These results are obtained from the simulation outputs for Node 10 at the top of the frame model, as defined in Chapter 7. As seen previously in **Figure 8.3**, structures with the same period and different aspect ratios experienced similar peak roof deflections. The geometric mean peak deflections for the lowest and highest periods considered in the simulations, which were 0.2 s and 1.2 s respectively, are presented in **Table 8.11**. Higher deflections are recorded for larger force reduction factors, as expected due to the reduced threshold for uplift.

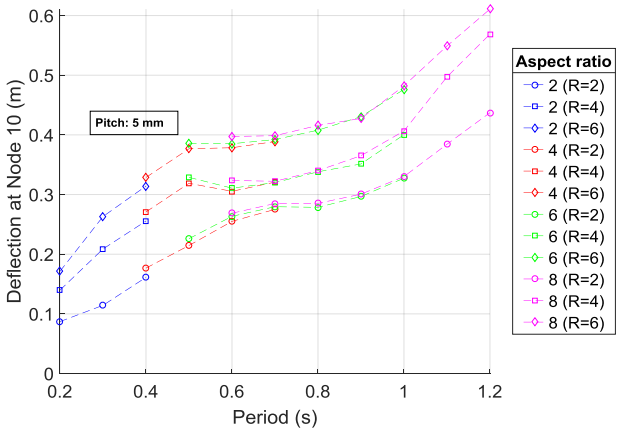

Figure 8.31 *Geometric mean peak roof deflections (pitch = 5 mm, ζ = 3%).*

Table 8.11 *Geometric mean peak roof deflections at min. and max. periods (pitch = 5 mm, ζ = 3%).*

R value	Roof deflection (T = 0.2 s) [m]	Roof deflection (T = 1.2 s) [m]
2	0.087	0.437
4	0.140	0.569
6	0.171	0.611

Figure 8.32 presents the total peak roof drift results, as a result of both rigid body rotation and elastic deflection, obtained using the deflection of the top of the frame (Node 10) as defined in Chapter 7. For any given aspect ratio, a larger structure period generally led to increased peak roof drift, and increasing the force reduction factor also increased the peak roof drift. For all of the force reduction factors modelled, the lowest total peak roof drift occurred with the structure with the lowest period of the structures with the highest aspect ratio, while the highest total peak roof drift occurred with the structure with the highest period of the structures with the lowest aspect ratio. This result is consistent with the mechanics previously outlined. The reduction in stiffness with increasing period was shown in **Figure 8.5** to be more significant than the reduction in elastic site hazard spectrum, and the peak roof deflection was shown to be largely independent of the aspect ratio, as seen in **Figure 8.3** and **Figure 8.31**, meaning a reduction in drift with increasing aspect ratio. The lowest and highest drifts for each reduction factor are presented in **Table 8.12**.

The maximum acceptable drift of 2.5% at ULS specified in NZS1170.5 was not always achieved. A broad study was undertaken to assess a wide range of structures, and not all results were expected to meet this standard. For the highest force reduction factor of 6, the geometric mean peak base rotation of a structure with an aspect ratio of 2 and a period of 0.4 seconds was 3.1%.

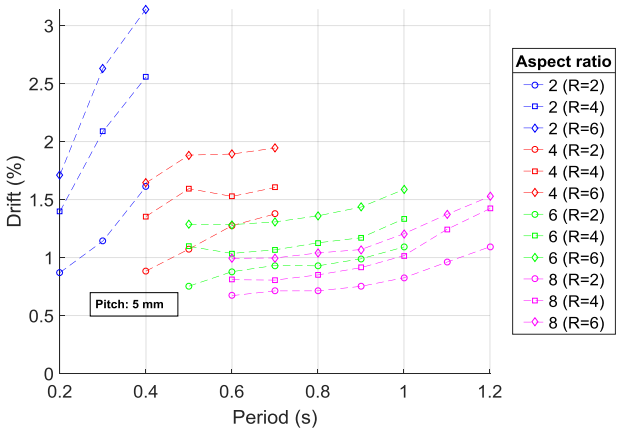

Figure 8.32 *Geometric mean peak roof drifts (pitch = 5 mm, ζ = 3%).*

Table 8.12 *Max. and min. geometric mean peak roof drifts (pitch = 5 mm, ζ = 3%).*

R value	Max. (AR = 2, T = 0.4 s) [%]	Min. (AR = 8, T = 0.6 s) [%]
2	1.61	0.67
4	2.56	0.81
6	3.14	0.99

The percentage of the total roof drift caused by base rotation is presented in **Figure 8.33**. The same trend of a slight reduction in the percentage of total roof drift caused by base rotation with increasing period, as presented previously in **Table 8.2** for the results of the main parameter study, is observed for all of the force reduction factors simulated. As expected, an increase in force reduction factor from 2 to 4 produced a significant increase in the contribution of base rotation to the total peak roof drift. Most of the peak roof drift due to flexure occurs prior to uplift, and is similar for each of the reduction factors simulated. However, increasing the force reduction factor lowers the force threshold for uplift, resulting in a significant increase in the roof drift due to base rotation. As a result, the relative size of the roof drift due to base rotation compared to the total roof drift increases significantly. A further increase in the force reduction factor, from 4 to 6, has a much less significant impact on the percentage of total roof drift caused by base rotation. The highest percentage of total roof drift caused by base rotation occurs for the lowest period structure simulated and increases from 70% for a force reduction factor of 2, to 83% and 86% for force reduction factors of 4 and 6 respectively.

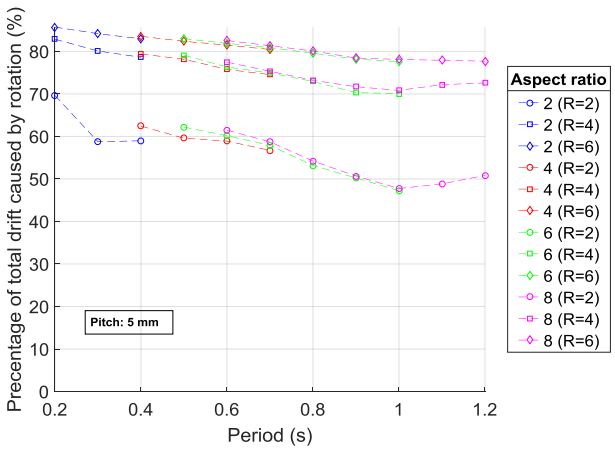

Figure 8.33 *Geometric mean contribution to peak roof drift from base rotation (pitch = 5 mm, ζ = 3%).*

The geometric mean peak base rotations and uplifts are presented in **Figure 8.34** and **Figure 8.35** respectively. These quantities are closely related to the peak roof deflection and peak roof drift results previously presented and the same trends are visible. The ranges of peak base rotation and peak uplift are displayed in **Table 8.13**. The period with the smallest geometric mean peak base rotation and uplift varied across the force reduction factors simulated.

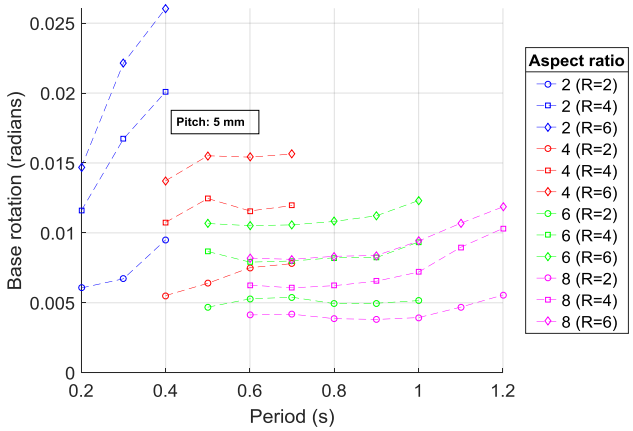

Figure 8.34 *Geometric mean peak base rotation angles (pitch = 5 mm, ζ = 3%).*

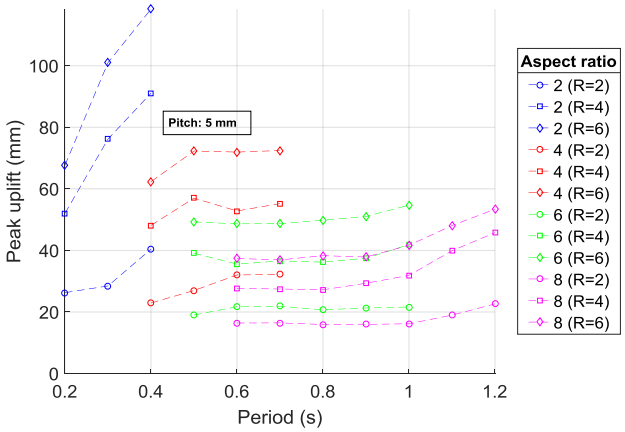

Figure 8.35 *Geometric mean peak uplift, using both left and right sides (pitch = 5 mm, ζ = 3%).*

Table 8.13 *Range of geometric mean peak base rotations and peak uplifts (pitch = 5 mm, ζ = 3%).*

R value	Rotation (radians)	Uplift (mm)
2	0.0038 – 0.0095	15.9 – 40.4
4	0.0061 – 0.0201	27.2 – 91.1
6	0.0081 – 0.0261	36.9 – 118.4

Figure 8.36 presents the ratio of the geometric mean peak uplift values from the simulations, with a GNG rack pitch size of 1 mm, to the peak uplift values obtained from the approximate SCNZ method described in Section 8.3.1. The results using the smallest GNG pitch size simulated provide the most appropriate comparison to the approximate code values, as there is no consideration of pitch size and free-travel in the general code methods since these are unique features of the GNG device. An increase in the force reduction factor resulted in an increase in the ratio between simulation and SCNZ results. There is greater disparity between the SCNZ and simulated results for higher force reduction factors. However, there was one outlier result for a period of 0.2 seconds where this ratio between simulation and SCNZ uplifts was slightly larger for a force reduction factor of 2 than for a force reduction factor of 4. The simulated results for a force reduction factor of 2 ranged from 76% to 161% of the SCNZ values, where the upper limit was due to the outlier result mentioned above. The next highest result was only 131% of the SCNZ value. This range was 123% to 196% for a force reduction factor of 4, and 144% to 226% for a force reduction factor of 6. The period with the smallest and largest ratio between simulated and SCNZ results varied across the force reduction factors simulated. The results for a reduction factor of 4 match the previously presented results in **Figure 8.28**.

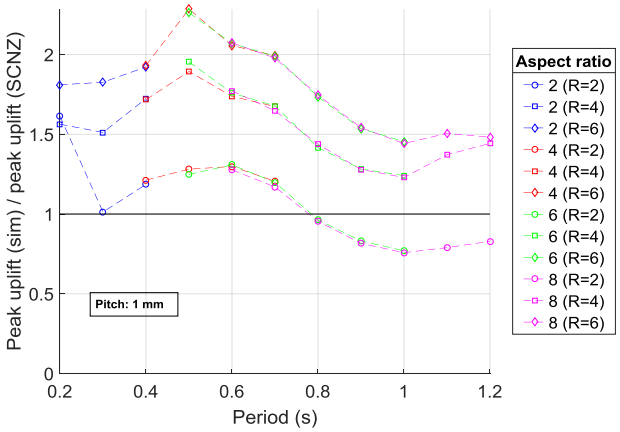

Figure 8.36 *Ratio of OpenSEES simulation geometric mean peak uplift values to SCNZ peak uplift values (pitch = 1 mm, ζ = 3%).*

8.4.2. Inelastic dissipater demand and demand ratio

The geometric mean of the absolute value of the inelastic demand in the dissipater is shown in **Figure 8.37** for the three force reduction factors simulated. For some structures, particularly for structures with the lower period values within the range used for each aspect ratio, there was a similar increase in the geometric mean of inelastic demand in the dissipater when increasing the force reduction factor from 2 to 4 as there was when increasing the force reduction factor from 4 to 6. As discussed previously, and seen in **Figure 8.33**, the percentage of the total roof drift contributed by base rotation was similar for the force reduction factors of 4 and 6, after a large increase when increasing the force reduction factor from 2 to 4. These results suggest that beyond a certain force reduction factor value, there may be some weak linear correlation between the increase in force reduction factor and the increase in inelastic demand in the dissipater.

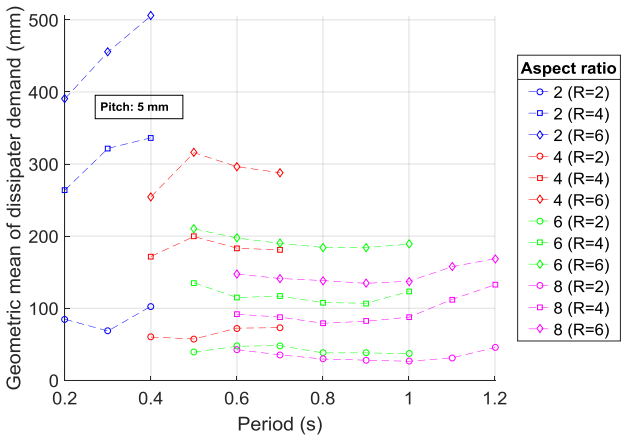

Figure 8.37 *Geometric mean inelastic dissipater demand, for all devices (both sides) (pitch = 5 mm, ζ = 3%).*

Figure 8.38 presents the geometric mean values of the demand ratio for the completed analyses. The geometric mean value from all GNG devices, both left and right sides, is presented. These results are obtained using the demand and uplift data previously presented in Figure 8.35 and Figure 8.37. As with some previously presented quantities, increasing the force reduction factor led to increased demand ratios. The series lines for a force reduction factor of 2 were not as smooth as those for the other two force reduction factors considered. Greater demand ratios are generally seen for shorter structure periods, as with the results from the initial R = 4 parameter study presented in Figure 8.22. The ranges of demand ratio are displayed in Table 8.14, and there was some variation in the aspect ratio and period which produced the lowest geometric mean demand ratio for each force reduction factor.

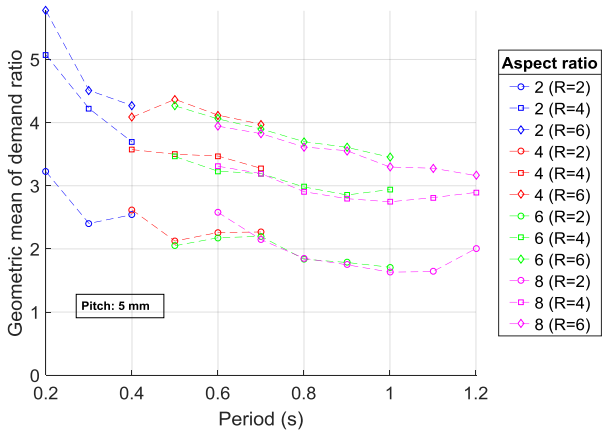

Figure 8.38 *Geometric mean of demand ratio, for all devices (both sides) (pitch = 5 mm, ζ = 3%).*

Table 8.14 *Range of geometric mean demand ratios (pitch = 5 mm, ζ = 3%).*

R value	Max.	Min.
2	3.22 (AR = 2, T = 0.2 s)	1.63 (AR = 8, T = 1.0 s)
4	5.07 (AR = 2, T = 0.2 s)	2.75 (AR = 8, T = 1.0 s)
6	5.77 (AR = 2, T = 0.2 s)	3.16 (AR = 8, T = 1.2 s)

Results of the geometric mean of the demand ratio from the simulations normalised to the SCNZ uplift values are presented in **Figure 8.39**. These values are calculated by dividing the geometric mean demand values obtained from the analyses, and presented in **Figure 8.37**, by the peak uplift values calculated using the approximate SCNZ method described in Section 8.3.1. This process is equivalent to multiplying the geometric mean demand ratios shown in **Figure 8.38** by the ratios between the simulation and SCNZ uplift values presented in **Figure 8.36**. As with the geometric mean demand ratios

normalised to the peak uplifts of the respective analyses presented in **Figure 8.38**, there is generally a greater demand ratio observed for shorter periods and higher force reduction factors. The ranges of demand ratio are displayed in **Table 8.15**, and there was some variation in the aspect ratio and period which produced the lowest geometric mean demand ratio for each force reduction factor.

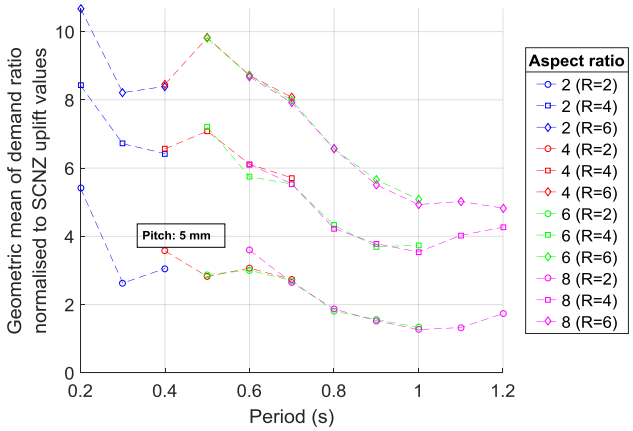

Figure 8.39 *Geometric mean of demand ratio, normalised to SCNZ uplift values (pitch = 5 mm, ζ = 3%).*

Table 8.15 *Range of geometric mean demand ratios, normalised to SCNZ uplift values (pitch = 5 mm, ζ = 3%).*

R value	Max.	Min.
2	5.41 (AR = 2, T = 0.2 s)	1.27 (AR = 8, T = 1.0 s)
4	8.42 (AR = 2, T = 0.2 s)	3.54 (AR = 8, T = 1.0 s)
6	10.68 (AR = 2, T = 0.2 s)	4.83 (AR = 8, T = 1.2 s)

A comparison of the inelastic dissipater demand and peak uplift values in both the LHS and RHS devices is presented in **Figure 8.40**, with lines included to show demand ratios of 1 and 10. The results are shown for each of the force reduction factor studies separately, and then all of the results together. **Figure 8.40**b shows the same data as **Figure 8.21** presented earlier in the main parameter study with a force reduction factor of 4. **Figure 8.40**d shows that the demand ratio generally increases as the force reduction factor increases, as reported earlier, with more demand ratios from individual time-history analyses greater than 10 (to the left of the upper dashed line) observed for a force reduction of 6, compared to a force reduction factor of 4. While only 0.93% of individual simulation results had demand ratios of greater than 10, when using a force reduction factor of 4, as reported earlier, this value increased to 1.70% when using a force reduction factor of 6. For a force reduction factor of 2, only 7 out of 6000 analyses, or 0.12%, showed a demand ratio of greater than 10. These

results show that a factor of $v_{demand} = 10$ in Equation (8.18) is suitable for force reduction factors up to at least 6.

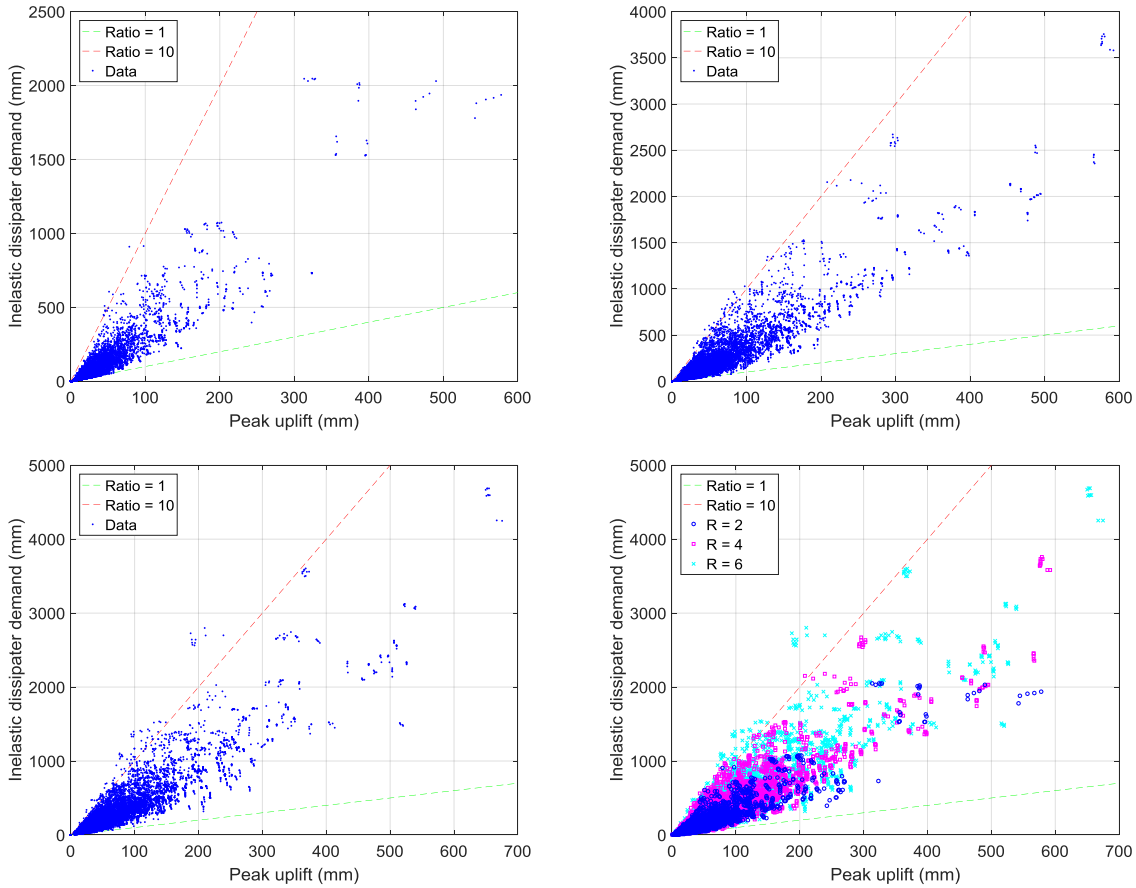

Figure 8.40 *Inelastic dissipater demand vs peak uplift for all time-history analyses (ζ = 3%): a) R = 2, b) R = 4, c) R = 6, and d) all results.*

8.5. Effect of dissipater strength

8.5.1. Study details

A separate study was completed to assess the impact of the dissipater strength, specifically, the contribution of the dissipater to the moment at uplift (abbreviated to 'dissipater contribution' in some of the following discussion), on the system response. For this study a sample structure was selected from the range of structures simulated in the main parameter study. The selected structure has an aspect ratio of 4 and a period 0.7 s, as well as the other properties outlined in **Table 8.16**. A range of dissipater contributions to moment at uplift of 0 to 90% were simulated. A value of 0% indicates a yield force in the dissipater of 0 N, whereas 90% indicates that 90% of the base moment at uplift comes from the dissipater. Post-tensioning force and stiffness values were calculated for each analysis to ensure the same base rocking moment was maintained. While large moment contributions from traditional tension-compression energy devices could cause substantial permanent or residual

displacements, the use of GNG devices removes the residual compressive forces allowing for effective re-centring even when the energy devices contribute a large percentage of the resistance to uplift.

The full suite of 60 SAC ground motion recordings, scaled based on NZS1170.5, was again used. This produced a total of 600 full time history analyses in the study. The quantities of roof deflection, roof drift (due to flexure and base rotation), base rotation, base uplift from rocking, ratchet behaviour and dissipater behaviour, are all presented and discussed below. Geometric mean values over the 60 ground motions are presented for all results unless otherwise stated.

Table 8.16 *Properties of the simulated structure for the dissipater strength study.*

Parameter	Value
Aspect ratio	4
Height (m)	20
Period (s)	0.7
Pitch (mm)	5
Dissipater contribution to uplift moment (%)	0, 10, 20, 30, 40, 50, 60, 70, 80, 90

8.5.2. Roof deflection, roof drift, base rotation, and uplift

Figure 8.41 shows the geometric mean peak roof deflections over the suite of 60 ground motion records for the range of dissipater contributions to uplift moment simulated. These results are obtained from the simulation outputs for Node 10 at the top of the frame model, as defined in Chapter 7. The geometric mean of the peak roof deflection ranged from 0.41 m, for no contribution from the dissipater, to 0.27 m, for the dissipater contributing 90% of the resisting moment at uplift, which is a reduction of 34%. Increasing the device contribution to the resisting moment at uplift reduced the peak roof deflection of the frame, with this effect becoming less significant as the device contribution to moment at uplift approaches 100%. A similar trend is observed for other related quantities such as the roof drift, base rotation, base uplift, ratchet count and demand, inelastic dissipater demand, and demand ratio. These results are presented briefly below.

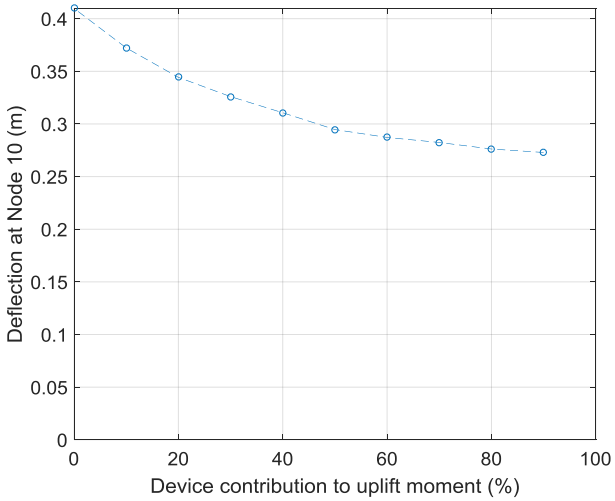

Figure 8.41 *Geometric mean peak roof deflections (aspect ratio = 4, period = 0.7 s, pitch = 5 mm, R = 4, ζ = 3%).*

The geometric mean of the peak roof drift, obtained using the deflection of the top of the frame (Node 10) as defined in Chapter 7, is shown in **Figure 8.42** and ranged from 2.05%, for no dissipater contribution, to 1.37%, for a dissipater contribution of 90%, which is a reduction of 33%. At the lowest dissipater contribution, base rotation accounted for 77% of the total roof drift, while at the highest dissipater contribution, this value reduced slightly to 72%.

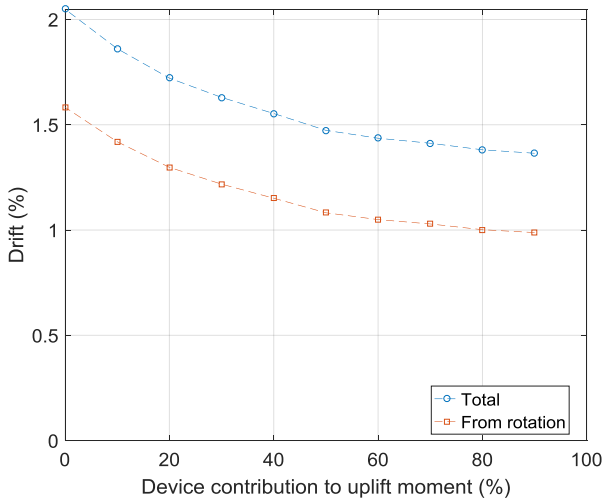

Figure 8.42 *Geometric mean peak roof drifts, showing the contribution to roof drift from base rotation and the total roof drift (aspect ratio = 4, period = 0.7 s, pitch = 5 mm, R = 4, ζ = 3%).*

Figure 8.43 presents the geometric mean peak base rotation angles over the suite of 60 ground motion records for the range of dissipater contributions to uplift moment simulated. The geometric mean of the peak base rotation angle ranged from 0.0158 radians, for no contribution from the dissipater, to 0.0099 radians, for the dissipater contributing 90% of the resisting moment at uplift,

which is a reduction of 37%. Increasing the device contribution to the resisting moment at uplift reduced the peak base rotation of the frame, with this effect becoming less significant as the device contribution to moment at uplift approaches 100%.

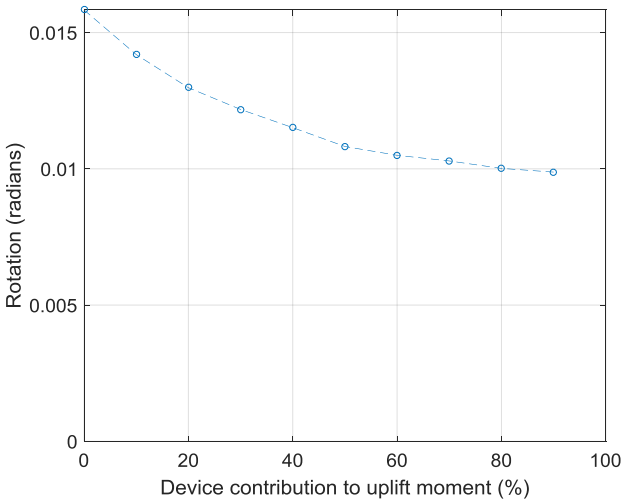

Figure 8.43 *Geometric mean peak base rotation angles (aspect ratio = 4, period = 0.7 s, pitch = 5 mm, R = 4, ζ = 3%).*

The spread of the base rotation is illustrated in **Figure 8.44**. **Figure 8.44** shows the base rotation from each of the 60 ground motion records simulated. These individual analyses results are shown alongside the geometric mean results. In several individual analyses the base rotation is greater than twice the geometric mean result, with one result being around 6 to 9 times the geometric mean, depending on the device contribution to moment at uplift.

The highest base rotations shown in **Figure 8.44** were recorded from simulations using the la40 record. After the scaling process outlined in Chapter 7, this particular record has a significantly higher PGA than some other scaled records. The inability of the SDOF model used for the scaling of the records to capture the complex behaviour of rocking and dynamic effects in the system can lead to significant variation in the peak magnitudes of the scaled ground motion records. The inclusion of extreme cases in the simulation results is a conservative approach, as it can lead to overestimation of system response and required capacity.

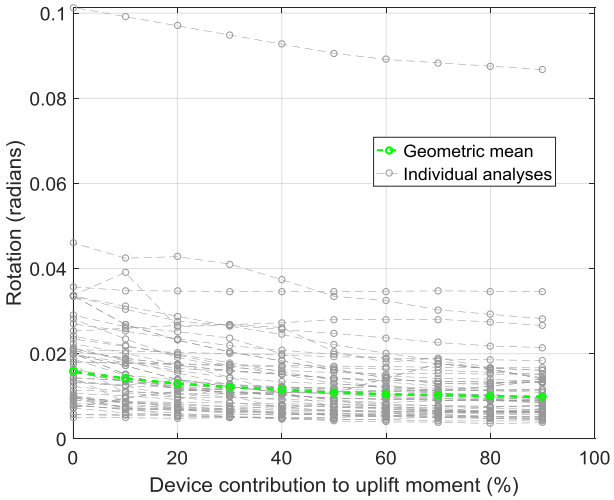

Figure 8.44 *Peak base rotation angle spread*

(aspect ratio = 4, period = 0.7 s, pitch = 5 mm, R = 4, ζ = 3%).

The geometric mean of the peak uplift is presented in **Figure 8.45**. These peak uplift values ranged from 76.1 mm, for no dissipater contribution, to 43.2 mm, for a dissipater contribution of 90%, for the left hand side device, which is a reduction of 43%. Similar values were recorded for both the left and right side devices, with a reduction of 40% seen in the right hand side device. Overall, the peak uplift is reduced by ~40%, for the system considered.

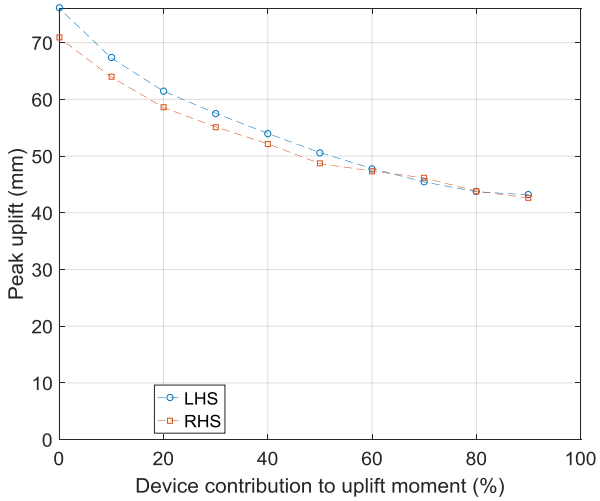

Figure 8.45 *Geometric mean peak uplifts, for left and right sides*

(aspect ratio = 4, period = 0.7 s, pitch = 5 mm, R = 4, ζ = 3%).

8.5.3. Ratcheting

The geometric mean number of ratcheting actions ranged from 83.6, for no dissipater contribution, to 18.8, for a dissipater contribution of 90%. A pitch size of 5 mm was used in these simulations, and these values are presented in **Figure 8.46**. The geometric mean value from all GNG devices, both left

and right sides, is presented. There is a large reduction in ratcheting actions with initial increases in the device contribution to uplift moment, with this effect reducing with further increases in device contribution.

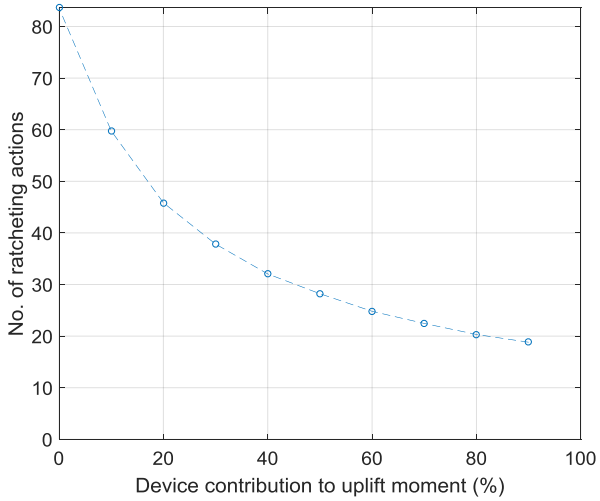

Figure 8.46 *Geometric mean ratchet count, for all devices (both sides) (aspect ratio = 4, period = 0.7 s, pitch = 5 mm, R = 4, ζ = 3%).*

The geometric mean GNG rack demand ranged from 418 mm, for no dissipater contribution, to 94 mm, for a dissipater contribution of 90%. These values are presented in **Figure 8.47**, and are obtained from the ratchet count data shown in Figure 8.46 using Equation (8.4). The reductions in ratchet count expressed in **Figure 8.46** led to corresponding reductions in GNG rack demand in **Figure 8.47**. The geometric mean value from all GNG devices, both left and right sides, is presented. The proportional reduction in GNG rack demand with increasing device contribution is quantified in **Table 8.17**.

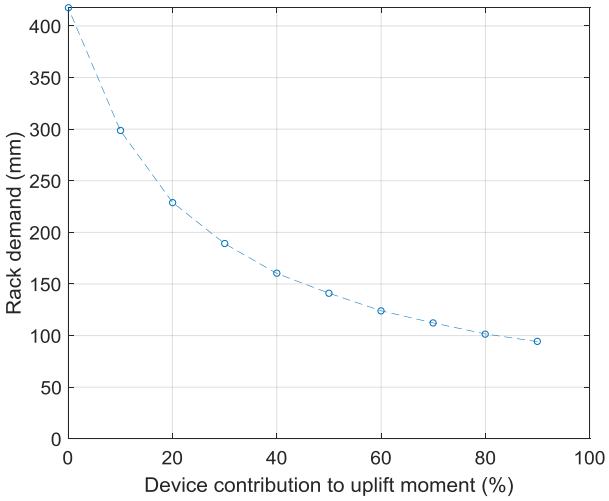

Figure 8.47 *Geometric mean GNG rack demand, for all devices (both sides) (aspect ratio = 4, period = 0.7 s, pitch = 5 mm, R = 4, ζ = 3%).*

Table 8.17 *Changes in GNG rack demand with increasing device contribution to uplift moment.*

Parameter	**Values**									
$\frac{M_{ED}}{M_{uplift}} \times 100\%$	0	10	20	30	40	50	60	70	80	90
x_{rack} (mm)	418.0	298.9	229.2	189.2	160.3	141.1	124.0	112.3	101.6	94.1
$\frac{x_{rack}}{x_{rack,M_{ED}=0}} \times 100\%$	100	71.5	54.8	45.3	38.3	33.8	29.7	26.9	24.3	22.5

8.5.4. Inelastic dissipater demand and demand ratio

The inelastic dissipater demand is shown in **Figure 8.48** and ranged from 423 mm, for no dissipater contribution, to 96.9 mm, for a dissipater contribution of 90%. The geometric mean value from all GNG devices, both left and right sides, is presented. The inelastic displacement values in the dissipater are very similar to the GNG rack demand values in **Figure 8.47**, and show the same trend of reduction with increasing device contribution to uplift moment described previously.

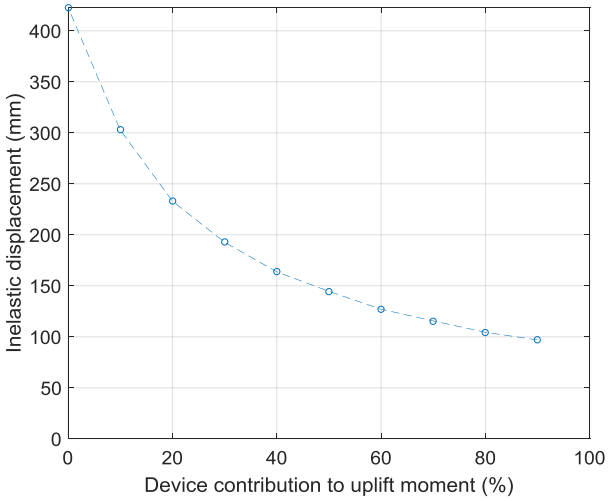

Figure 8.48 *Geometric mean inelastic dissipater demand, for all devices (both sides) (aspect ratio = 4, period = 0.7 s, pitch = 5 mm, R = 4, ζ = 3%).*

The demand ratio, shown in **Figure 8.49**, ranged from 5.8, for no dissipater contribution, to 2.3, for a dissipater contribution of 90%. The geometric mean value from all GNG devices, both left and right sides, is presented. Similar to previously presented quantities, the demand ratio shows a parabolic trend with the value levelling out as the device contribution to uplift moment approaches 100%. The spread of the demand ratio is displayed in **Figure 8.50**. **Figure 8.50** shows the demand ratio for each device from each of the 60 ground motion records simulated, for a total of 120 series lines. These individual analyses results are shown alongside the geometric mean results. In several individual analyses the demand ratio is greater than twice the geometric mean result.

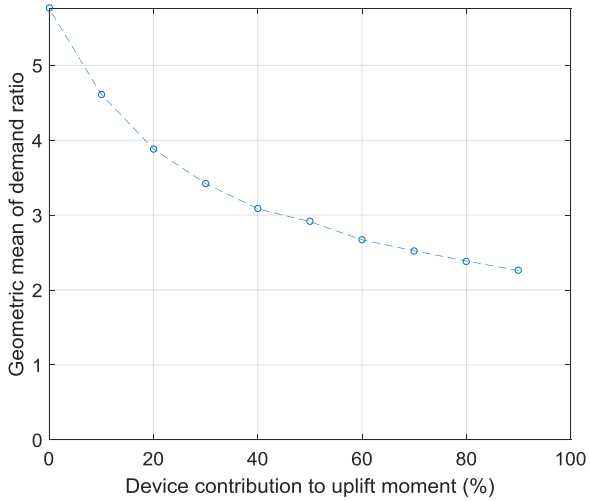

Figure 8.49 *Geometric mean demand ratio, for all devices (both sides) (aspect ratio = 4, period = 0.7 s, pitch = 5 mm, R = 4, ζ = 3%).*

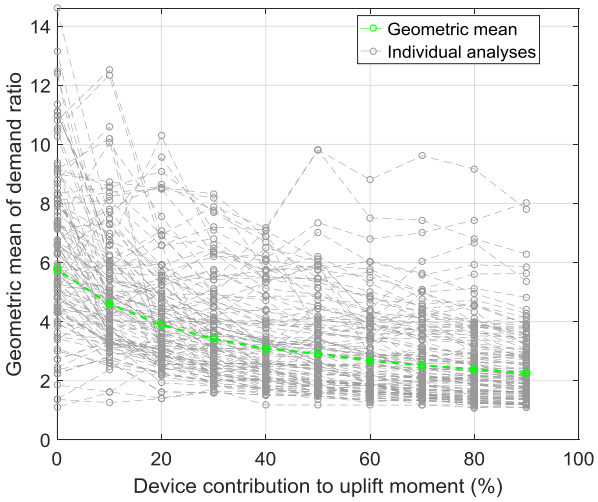

Figure 8.50 *Demand ratio spread*

(aspect ratio = 4, period = 0.7 s, pitch = 5 mm, R = 4, ζ = 3%).

8.5.5. Energy dissipation

The approximate amount of energy dissipated by the GNG devices was calculated using the product of the inelastic displacement in the dissipater and the yield force of the dissipater. Strain hardening effects were also considered in the calculation. The small increases in yield force experienced by the dissipater following yielding lead to increased energy dissipation on subsequent cycles of the response, once yielding has previously occurred. The approximation used is:

$$E = x_{ED,inelastic}\left(F_{yield,initial} + 0.5\beta x_{ED,inelastic}K_{ED}\right) \qquad (8.19)$$

where $x_{ED,inelastic}$ is the inelastic dissipater displacement, $F_{yield,initial}$is the initial yield force in the dissipater, β is the post-yield to pre-yield stiffness ratio of the dissipater, and K_{ED} is the pre-yield stiffness of the dissipater. This approach was chosen as it can be readily calculated using a few key outputs from the parameter study analyses. The full time-history information for each individual analysis was not saved, in order to reduce file run times and aid post-processing.

The geometric mean energy dissipation ranged from 84 kJ, for no dissipater contribution, to 974 kJ, for a dissipater contribution of 90%. There is still some energy dissipation recorded when the dissipater is not contributing to the resisting moment at uplift in the system. This is due to the small amount of strain hardening that is modelled in the dissipater, outlined in Chapter 7, even when the initial yield force is set to zero. The strain hardening leads to a small enclosed area in the GNG hysteresis loop, and a small amount of energy dissipation. The energy dissipation for a 0% device contribution to uplift moment was 9% of the value for a 90% device contribution to uplift moment. The energy dissipation data is presented in **Figure 8.51**, and shows a rapid increase in energy dissipation occurs up to a device contribution to moment at uplift of ~50%, with slowly reducing gains

beyond this value. The geometric mean value from all GNG devices, both left and right sides, is presented.

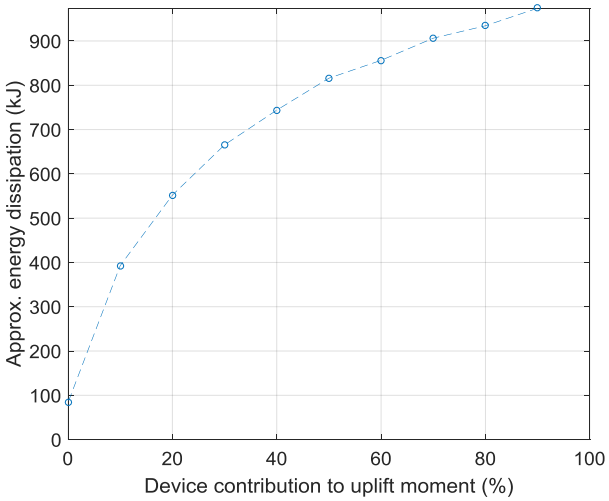

Figure 8.51 *Geometric mean energy dissipation, for all devices (both sides) (aspect ratio = 4, period = 0.7 s, pitch = 5 mm, R = 4, ζ = 3%).*

This result indicates that a significant increase in the amount of energy absorbed by the dissipater could be achieved by increasing the contribution of the dissipater to the resisting moment at uplift above the approximate currently applied value of 33%, introduced in Chapter 7. This recommended value of 33% is based largely on the presence of residual compressive forces in the energy dissipation devices, which do not exist when using the GNG device, so the choice could be more open in this case. An increase in dissipater contribution from 30% to 60% would achieve an increase in energy dissipation from 666 kJ to 856 kJ. This represents an additional 29% energy dissipation. Further, an increase in the contribution to the resisting moment at uplift from the dissipater leads to an increased yield force and greater elastic deformation capacity, when assuming consistent material properties. This increased elastic deformation capacity, and its contribution to mitigating energy transferred to the structure, is not captured here.

Figure 8.52 shows the geometric mean, across the suite of 60 scaled ground motion records, of the equivalent viscous damping for each value of the device contribution to uplift moment. The equivalent viscous damping was calculated using Equation (8.20) [Pekcan et al. 1999]:

$$\xi_{hyst} = \frac{1}{4\pi}\frac{E_D}{E_S} \qquad (8.20)$$

where E_D is the curve area enclosed by the flag-shaped hysteresis response, and E_S is the area under the equivalent linear elastic hysteresis response, using the maximum force and displacement. The value of E_D was calculated by reconstructing the maximum hysteresis response from each individual

time-history analysis using the saved maximum force and displacement values from the hysteresis response and the properties of the system.

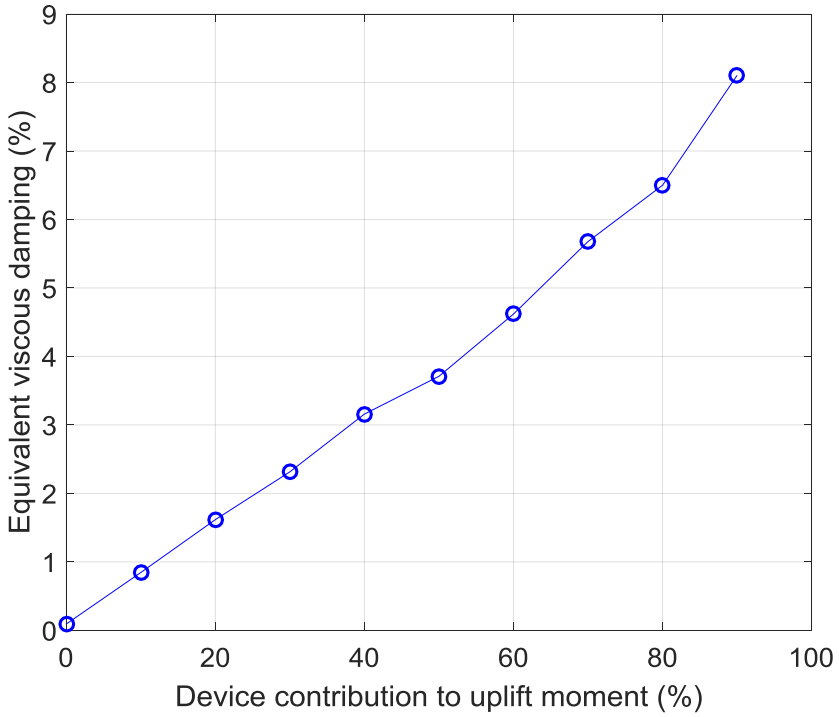

Figure 8.52 *Geometric mean equivalent viscous damping: (aspect ratio = 4, period = 0.7 s, pitch = 5 mm, R = 4, ζ = 3%).*

The geometric mean of the equivalent viscous damping ranged from 0.09% for a device contribution to uplift moment of 0%, up to 8.11% for a device contribution to uplift moment of 90%. Strain hardening modelled in the dissipater leads to a small amount of energy dissipation, and some small equivalent viscous damping, even when the dissipater is not contributing to the resisting moment at uplift in the system.

8.6. System configuration

8.6.1. Device placement

Figure 8.53 shows four approximate system configurations of a controlled rocking system with post-tensioning and energy dissipation devices. The energy dissipation devices or post-tensioning could each be attached at either the outer corners of the frame or at the centreline. In the example controlled rocking system described in Chapter 6, and modelled in the numerical analyses outlined in Chapter 7 and in this chapter, the GNG-dissipater systems are located at the outer edges of the rocking frame. The configuration shown in Figure 8.53a was modelled in the analyses described in this chapter, and is the focus of the discussion below. This is just one option for the configuration of the system, and other options may be more suitable in specific cases.

The placement of the energy dissipation devices at the outer edges of the frame, as in Figure 8.53a and Figure 8.53b, is seen in practice and provides the advantage of spreading the inelastic demand in the dissipater(s) over two devices rather than a single device, which may be used when locating the device at the centreline of the rocking frame, and may provide easier access depending on the exact design. The placement of the energy dissipation devices at the outer edges of the frame means that the device(s) at each side are only engaged during rocking motion about one of the rocking edges. The demand guidelines provided earlier in this chapter are only applicable for the positioning of the devices at the outer edges of the rocking frame, as they are based upon analysis of this configuration.

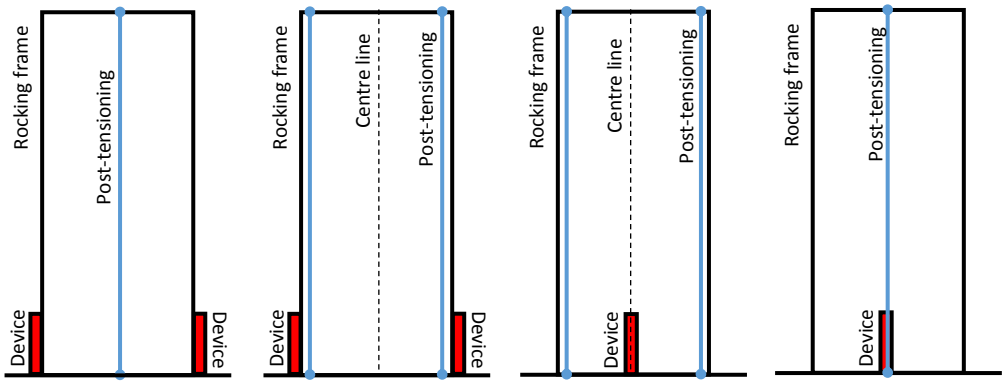

Figure 8.53 *Example controlled rocking system configurations:*
a) devices at outer edges and PT at centre, b) devices and PT at outer edges, c) device at centre and PT at outer edges, and d) device and PT at centre.

It can be convenient for access to apply the post-tensioning along a different line of action to the devices. The exact location of the post-tensioning does not have a significant impact on the system behaviour, and two different post-tensioning positions can be designed to provide equivalent stiffness and restoring forces in the controlled rocking system. Locating the post-tensioning further from the rocking edge(s) increases the elongation in the post-tensioning and so a greater elastic capacity may be required. Increasing the eccentricity of the post-tensioning from the rocking edge(s) also reduces the pre-stress forces required to provide a certain contribution to the base moment at uplift of the system.

Positioning of the energy dissipation device(s) at the centre of the rocking frame, as in Figure 8.53c and Figure 8.53d, is expected to approximately halve the peak uplift and inelastic dissipater demand during any given loading cycle. However, the device(s) would be engaged during rocking about either rocking edge, as opposed to engagement for rocking about only one of the rocking edges, as is the case with the devices located at the outer edges of the rocking frame. Therefore, a dissipater located at the centre of the frame would be active for twice as many cycles as a dissipater located at the edge

of the frame, and experience around half the uplift per cycle, resulting in similar cumulative inelastic demands.

If the devices are located at the centre of the frame, the eccentricity of the device from the rocking edge is halved. Halving the eccentricity means that twice the yield force in the dissipater would be required to provide the same contribution to the base rocking moment at uplift, compared to placement of the devices at the outer edges of the rocking frame. Further, the reduction in peak uplift experienced by the devices increases the influence of the pitch size on the inelastic demand in the dissipater, due to the increased size of the pitch relative to the uplift.

8.6.2. Connection options

In **Figure 8.54** a connection detail is shown with the pawl or collet subassembly, containing the ratcheting mechanism and described in detail in Chapter 2.3.2 and Chapter 4.2.2 for the two GNG prototypes respectively, attached to the rocking frame. In this case the dissipater subassembly, containing the rack and dissipater and described in detail in Chapter 2.3.1 and Chapter 4.2.1, is connected to the ground near the outer edge at the base of the rocking frame. The GNG-dissipater system at the right side is shown in **Figure 8.54** and the connection detail at the left side is symmetric about the centreline of the frame.

The initial position of the GNG-dissipater system is shown in **Figure 8.54**a and the effect of increased length in the dissipater subassembly due to inelastic demand in the dissipater is shown in **Figure 8.54**b. Additional space in the housing of the pawl or collet subassembly is required to allow for the increase in the subassembly length. Alternatively, an open top to the ratchet subassembly may be suitable to reduce the required size of the housing if any sealing or environmental concerns are addressed. This alteration would be better suited to the first prototype, given the reliance on the cover plate to position the spring in the GNG2 prototype. Failure to provide sufficient space for dissipater elongation could result in the top of the ratchet subassembly pressing on the dissipater subassembly during joint closure and preventing re-centring. Depending on the amount of uplift expected, pinned joints connecting the dissipater subassembly to the ground and connecting the ratchet subassembly to the frame may be required to prevent misalignment of the GNG-dissipater system during base rotation.

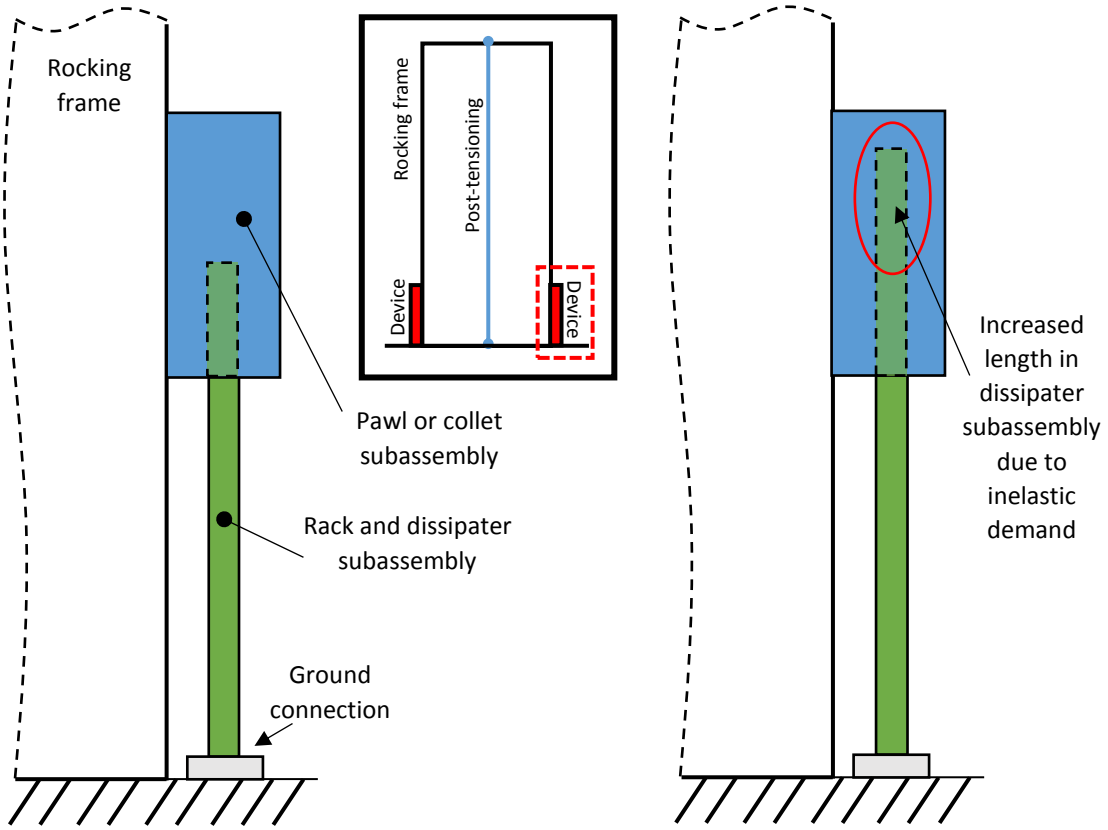

Figure 8.54 *GNG-dissipater connection detail with pawl or collet subassembly connected to the frame: a) initial position, and b) following inelastic demand in the dissipater. Device location shown in insert.*

When assembling this connection, the collet subassembly can be attached to the frame first before inserting the rack into the correct position in contact with the collets. The dissipater can then be threaded or otherwise connected into the rack. Finally the lower end of the dissipater can be attached to the ground.

Figure 8.55 shows an alternative connection detail with the pawl or collet subassembly attached to the ground. In this case the dissipater subassembly is connected to the rocking frame. The GNG-dissipater system at the right side is shown in Figure 8.55 and the connection detail at the left side is symmetric about the centreline of the frame.

The initial position of the GNG-dissipater system is shown in Figure 8.55a and the effect of increased length in the dissipater subassembly due to inelastic demand in the dissipater is shown in Figure 8.55b. Again, additional space in the housing of the ratchet subassembly is required to allow for the increase in the subassembly length due to cumulative inelastic displacement of the dissipative element. Alternatively, an open space in the ground below the ratchet subassembly may be suitable to reduce the required size of the housing if any sealing or environmental concerns are addressed. As with the

previous connection option, failure to provide sufficient space for elongation of the dissipater could result in the bottom of the ratchet subassembly pressing on the dissipater subassembly during joint closure and preventing re-centring. Depending on the amount of uplift expected, pinned joints connecting the dissipater subassembly to the rocking frame and connecting the ratchet subassembly to the ground may be required to prevent misalignment of the GNG-dissipater system during base rotation.

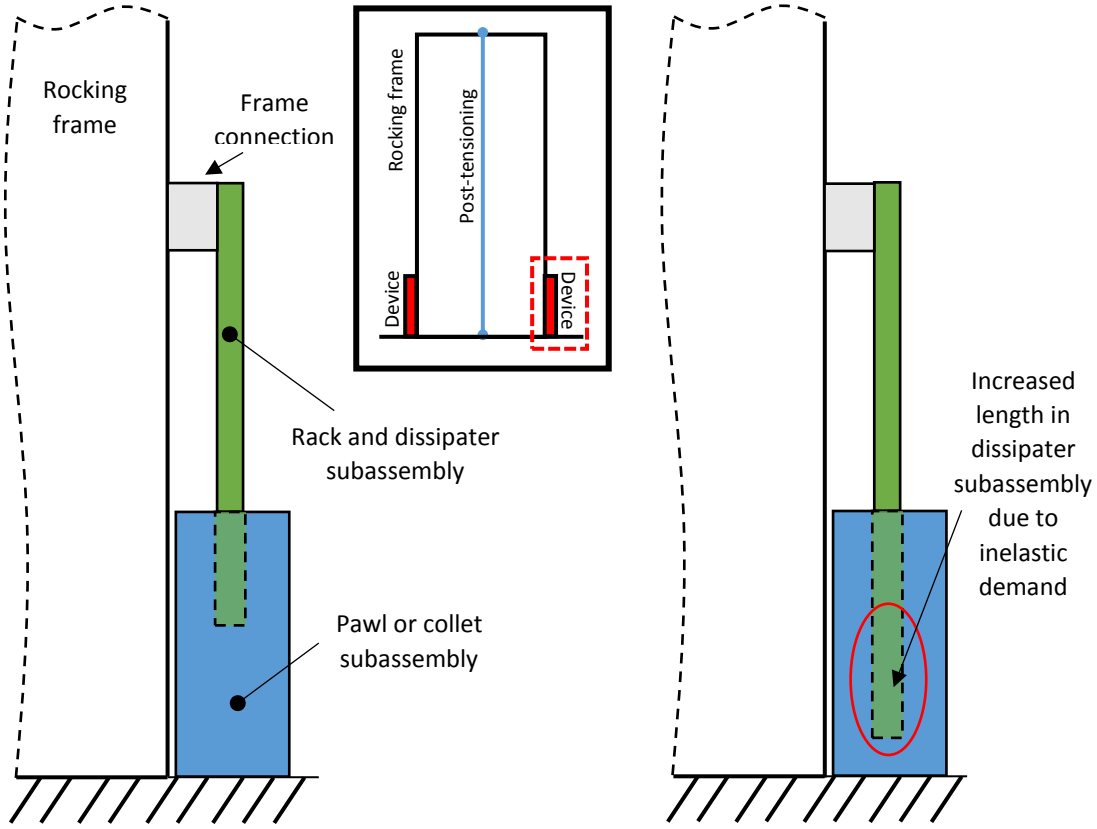

Figure 8.55 *GNG-dissipater connection detail with pawl or collet subassembly connected to the ground: a) initial position, and b) following inelastic demand in the dissipater. Device location shown in insert.*

When assembling this connection, the collet subassembly can be attached to the ground first before inserting the rack into the correct position in contact with the collets. The dissipater can then be threaded or otherwise connected into the rack. Finally the upper end of the dissipater can be attached to the frame. This orientation, with the rack being pushed downward into the collet subassembly to achieve the desired initial position, may provide an easier assembly process than the previous connection shown in **Figure 8.54**. When resetting the rack position after rocking has occurred during a seismic event, and possibly resetting or replacing the dissipater depending on the dissipater

selected, accessing the collet subassembly from above provides more convenient access than accessing it from below as required in the previous connection option.

8.7. Conclusions

This chapter has presented the findings of parameter studies conducted using the finite element model developed in Chapter 7. The influence of a range of device and structure parameters on the system response, and important relationships were investigated, and a brief statistical analysis was completed on the dissipater demand data. The effect of the contribution of the dissipater to the resisting moment at uplift, and the effect of the force reduction factor were also investigated. Some practical considerations for implementing the GNG device, including the configuration of the GNG-dissipater system in the rocking frame system, and its connection to the frame were discussed. These actions address research questions 5 and 6, and specific outcomes to note are listed for each research question below:

What is the system response, including the cumulative plastic demand generated in the dissipative element, and how does this vary with key design parameters such as the pitch size?

- A series of simulated structures with varying aspect ratios, periods and GNG rack pitch sizes were exposed to a suite of 60 scaled ground motion records in several parameter studies, with a total of 18600 individual time-history analyses.
- Peak roof deflection and related quantities were generally seen to increase with increasing pitch size, and with increasing period.
- Using a force reduction factor of 4, geometric mean base rotations ranged from 0.0061 to 0.02 radians, for structures with a GNG rack pitch size of 5 mm.
- Using a force reduction factor of 4, geometric mean peak total roof drifts (due to flexure and base rotation) ranged from 0.81% to 2.56%, for structures with a GNG rack pitch size of 5 mm. Base rotation typically contributed 70 to 80% of the total peak roof drift.
- Using a force reduction factor of 4, geometric mean base uplift due to rocking ranged from 26.1 mm to 93.5 mm, for structures with a GNG rack pitch size of 5 mm.
- Using a force reduction factor of 4, the demand in the GNG rack and the inelastic demand in the dissipater were less than 10 times the peak base uplift in over 99% of the analyses.
- Increasing the force reduction factor was shown to increase all of the reported system response quantities, including roof drift, uplift, inelastic dissipater demand and demand ratio.
- A significant increase in response was observed for an increase in force reduction factor from 2 to 4, with less significant increases in most response quantities occurring with a further increase in force reduction factor to 6.

- Increasing the contribution of the GNG devices to the base moment at uplift was shown to reduce peak roof drift, base rotation and uplift. GNG rack demand and inelastic dissipater demand were also reduced.
- There was a significant increase in the amount of energy absorbed by the dissipater with increasing contribution to base rocking moment up to a contribution of around 50%. After this point there was increased energy dissipation, but at a reduced rate.
- An increase in dissipater contribution from 30% to 60% achieved an increase in energy dissipation of ~29%.

How should GNG rocking wall systems be designed?

- Using a force reduction factor of 4, ULS peak lateral deflections were found to generally be around 123 to 196% of the values found by applying approximate code methods to the numerical model developed in Chapter 7.
- It is tentatively suggested that peak uplift values found from code methods are multiplied by an inelastic capacity factor of $\nu_{demand} = 10$, and by an additional factor of 2 due to variation between code-based and time-history analysis results, to find a suitable GNG rack capacity and inelastic dissipater capacity for field deployment of the GNG system with a rocking frame when subjected to ULS conditions. Additional considerations should be given to an MCE event and the associated inelastic demand.
- Various configurations of the controlled rocking frame systems incorporating the GNG could be used, and the most likely implementation of the GNG device will involve placing the GNG-dissipater system at the outside edges of the rocking frame.
- Two potential connection methods are suggested with the GNG mechanism attached to the edges of the rocking frame and the dissipater connected to the ground, or vice versa. Connecting the GNG mechanism to the ground may allow for easier setup and provide more convenient access for maintenance following an earthquake.

9. Conclusions

9.1. Summary

This thesis details the development of a ratcheting, tension-only mechanism for use with seismic energy dissipation systems. The development is taken from initial design concepts through to construction and testing of two prototype devices. A material model algorithm was developed to simulate the hysteretic response of the devices and a finite element flexible rocking system model was also developed to model the behaviour of a controlled rocking system instrumented with the GNG device. The results of the testing of the two prototype devices, and the numerical analyses, show the potential of the GnG concept to be a favourable option in supplementary damping and bracing systems. The research questions outlined in Chapter 1 have been addressed and the findings of this research are summarised below.

9.2. Tension-only device design

The following developments address research question 1, which was defined in Chapter 1 as:

1) Can devices be designed and built to dissipate energy under tensile earthquake loading without carrying compressive loads, and with reduced take-up on subsequent loading cycles to maximise energy dissipation?

Two different GnG prototype designs were implemented to provide a ratcheting, tension-only mechanism for use with seismic energy dissipation systems to address the concerns outlined in Chapter 1, which included the potential for buckling and the presence of residual compressive forces. Designed to offer resistance to loading in tension, while offering negligible resistance to compressive motion, the resulting low residual compression forces upon joint closure contribute to reducing residual structural displacements. Upon reloading, dissipater engagement will be more rapid than a simple steel dissipater due to the ratcheting mechanism, as the absence of residual compressive loads reduces the elastic take-up before yielding occurs and provides consistent, repeatable rocking behaviour. This effect leads to greater energy dissipation.

The design and manufacture of the GnG prototypes represents the transition of the GnG concept from a novel hysteresis loop in a computational study, into a pair of fully functioning devices capable of producing a desired hysteretic response. The initial prototype focussed on creating a functional device and involved a conservative design approach using a simple and reliable rack and pawl engagement interface. Pitch sizes of 40 mm and 20 mm were implemented with the first prototype design, and the same pawls were used with the two different racks with varying pitch sizes.

The second, more advanced GNG2 prototype device uses axial symmetry and a different engagement mechanism to provide several advantages over the initial prototype, simplifying the assembly process and providing improved performance. The device employs a simple and reliable rack and collet engagement interface, providing a larger contact interface and improving robustness in operation. The later design offers more effective operation, is less sensitive to potential alignment issues, and will be easier to reset the position of the rack as required after field engagement that has led to inelastic action within the dissipative element.

Additional threaded connections were used in the second prototype to reduce the use of fasteners and provide better ease of assembly. Smaller rack and collet interfaces, with pitch sizes of 10 mm and 3 mm, were used with the second prototype, and a different set of rack-specific collets is used with each rack. Careful detailed design was used in both prototypes to ensure a low-cost and easy to machine device, to increase likelihood of uptake.

9.3. Device engagement and behaviour

The following developments address research question 2, which was defined in Chapter 1 as:

2) Can the devices respond with appropriate speed of engagement for use during seismic loading of structures?

High speed camera footage and accelerometer recordings of the ratcheting mechanism were used to assess engagement timing in the first prototype with two different pitch sizes of 20 mm and 40 mm. The pawls showed rapid engagement, while experiencing a short period of misalignment of less than 33 ms. This brief misalignment is not likely to significantly impact performance during a typical earthquake, and could be addressed in future design developments. Overall, the pairs of pawls acted closely in unison producing solid engagement. Accelerometer recordings were also taken during testing with the second prototype, and approximately synchronised behaviour of the collets was observed. Due to the axial symmetry of the ratcheting mechanism in the second prototype, it is believed that the collets on this prototype act in greater unison than the pawls on the first prototype.

The following developments address research question 3, which was defined in Chapter 1 as:

3) Can the experimental devices exhibit desirable hysteresis behaviour, similar to theoretical predictions?

The ratcheting mechanism was shown to work as designed, providing rapid engagement during multi-cycle loading, reducing the free-travel prior to engagement on subsequent loading cycles, and increasing the energy dissipation capacity of the system. The observed hysteretic behaviour closely matched the idealised behaviour model presented in Chapter 2, with more complex material yielding

behaviour observed in the physical system. Robust, repeatable operation of both mechanisms, with redundancy in engagement, was observed.

A yielding steel dissipater element was designed to be used with the ratcheting devices during experimental testing outlined in Chapters 3 and 5, and the same dissipater design was used with both prototypes to ensure direct comparison of performance between devices. A total of 14 yielding steel dissipater elements were tested in a monotonic compression and cyclic testing schedule to demonstrate the function of the ratcheting mechanisms and assess the hysteretic behaviour of the dissipater elements and the overall GNG-dissipater system, with nine yielding dissipaters tested to fracture. The dissipaters were heat treated with a full annealing cycle to give maximum ductility in the relatively short length that was used due to testing machine limitations. This process resulted in yield forces of ~45 kN and ultimate tensile forces of ~65 kN in the dissipater elements.

As intended by design, the steel dissipater yielded only in tension. Furthermore, while the test was cyclic, the dissipater behaviour approximates a piecewise version of a standard monotonic tensile test due to the GNG device removing significant compressive loading in the dissipater. In particular, the maximum compressive forces are limited to less than 2% of the ultimate tensile forces. No damage to the assembly beyond the dissipater was observed. The system can be designed for use with various other energy dissipation mechanisms and at higher force levels as required.

Pawl and collet mechanisms have been tested with pitch sizes ranging from 3 to 40 mm, with smaller pitch sizes showing an increase in energy dissipation and inelastic displacement demand in the dissipater. 40 mm and 20 mm pitch racks were tested with the first prototype, while smaller pitch sizes of 10 mm and 3 mm were tested with the second prototype. The 3 mm pitch size was selected to broadly represent a practical lower bound in pitch size using traditional manufacturing options.

The enclosed hysteretic energy dissipation for the 10 mm and 3 mm rack pitch sizes was compared, with each system undergoing the same sine-wave displacement input profile until dissipater fracture. Use of the reduced pitch setup was shown to reduce free-travel and increase engagement of the energy dissipation system, resulting in increased energy dissipation. During the four cycles completed with the 3mm pitch rack, the energy dissipation per cycle was between 143% and 164% of the energy dissipated using the 10mm pitch rack during the same loading cycle, due to the GNG-dissipater system with the smaller pitch experiencing less free-travel. A comparison to a theoretical maximum, representing a device with no free-travel, suggests that an additional 15-26% of energy dissipation could be achieved per cycle during the first three cycles, prior to dissipative element fracture on the fourth cycle, when benchmarked against the theoretical device with an infinitely small pitch and no free-travel.

9.4. GNG and rocking wall modelling

The following developments address research question 4, which was defined in Chapter 1 as:

4) Can a model be developed to describe the GNG hysteretic performance, together with that of a rocking wall?

A bi-linear material model algorithm was created and adapted to incorporate the ratcheting behaviour of the GNG device. The resulting hysteretic response showed a good match with experimental results, while not capturing the full extent of non-linear yielding behaviour due to effects such as strain hardening within the dissipative element. This hysteretic model provides a means of modelling the GNG-dissipater system response, which can be used to undertake dynamic structural simulations to assess performance and displacement demands within the dissipater.

Supplementary damping mechanisms are frequently implemented along with rocking systems to achieve a more controlled response, and to increase energy dissipation, as rocking systems typically have very low inherent damping. The use of energy dissipation devices produces a flag-shaped hysteresis curve for the response of the controlled rocking system and the shape of this response is influenced by various parameters including the contribution of the energy dissipation devices to the base rocking moment. Idealised controlled rocking system mechanics and hysteresis behaviour, including the stiffness of the system during various stages of the response, has been described by previous work on controlled rocking frame systems and was adapted to account for the unique tension-only, ratcheting behaviour of the GNG devices developed in this thesis.

OpenSEES software was used to develop a finite element flexible rocking model, incorporating effects of gravity forces, post-tensioning and energy dissipation devices. The full hysteretic behaviour of the GNG device, including tooth pitch effects, was successfully captured by the GNG constitutive material model algorithm developed during this research. This custom material model was added to the local build of OpenSEES and will be available in the next public release of the software (release date TBD). The unique GNG material model, together with standard OpenSEES elements, allowed the rocking frame GNG system to be successfully modelled. Key uplift and system behaviour was able to be captured in the resulting, computationally inexpensive, model. The detailed understanding and verification of the model forms a basis for parameter studies with multiple earthquake records, to better quantify the performance and parameter selection options for design.

9.5. Dissipater demand

The following developments address research question 5, which was defined in Chapter 1 as:

5) What is the system response, including the cumulative plastic demand generated in the dissipative element, and how does this vary with key design parameters such as the ratchet pitch size?

A design hazard spectrum was produced for a ULS seismic event in the Wellington region and a suite of 60 ground motion records were scaled accordingly to provide a broad range of possible input ground motions for numerical analyses. The finite element flexible rocking model developed in Chapter 7 was implemented to complete a parameter study consisting of 6000 individual time-history analyses on a series of simulated structures with varying aspect ratios, periods and GNG rack pitch sizes. The study details were described and results for key quantities such as roof drift, uplift due to rocking, ratcheting and dissipater demand were presented and discussed. A brief statistical analysis was completed on the dissipater demand data to provide a basis for design recommendations.

Peak roof deflection and related quantities were generally seen to increase with increasing pitch size, and with increasing structural period. For structures with a GNG rack pitch size of 5 mm, which was used as a representative result, geometric means of some key system parameters, using a force reduction factor of 4, were as follows:

- peak base rotations ranged from 0.0061 to 0.02 radians, resulting in peak uplift at the line of action of the dissipaters, which were located at the outer edges of the frame, ranging from 26.1 mm to 93.5 mm
- peak total roof drifts (due to flexure and base rotation) ranged from 0.81% to 2.56%

Base rotation typically contributed 70 to 80% of the total peak roof drift, with the remainder coming from elastic flexure of the rocking frame. Using a force reduction factor of 4, the demand in the rack and the inelastic demand in the dissipater were less than 10 times the peak base uplift in over 99% of the analyses.

The main parameter study was repeated for multiple force reduction factors, involving an additional 12000 time-history analyses. An increase in the force reduction factor from 2 to 4 was shown to produce significant increases in roof deflection, roof drift, base rotation and uplift, as well as the percentage of total roof drift caused by base rotation. Smaller increases in these quantities were observed for a further increase in force reduction factor from 4 to 6. The demand ratio increased with increasing force reduction factor.

A separate study of the effect of the contribution of the dissipater to the resisting moment at uplift was also presented. Increasing the contribution of the GNG devices to the base moment at uplift was shown to reduce peak rotation, roof drift and uplift, with reductions of at least 33% observed when

comparing a dissipater contribution of 90% of the moment at uplift to a 0% contribution. Rack demand and inelastic dissipater demand were also reduced. There was a significant increase in the amount of energy absorbed by the dissipater with increasing contribution to base rocking moment up to a contribution of around 50%. After this point there was increased energy dissipation, but at a reduced rate. An increase in dissipater contribution from 30% to 60% achieved an increase in energy dissipation of ~29%. Increasing the dissipater contribution beyond the presently suggested value of ~33% would achieve greater energy dissipation, with any previous concerns about residual compressive forces in the energy dissipation devices ameliorated by using the GNG device.

9.6. Implementation

The following developments address research question 6, which was defined in Chapter 1 as:

6) How should GNG rocking wall systems be designed?

A series of basic stress calculations for the two prototype designs, focussing on the unique design interfaces of the ratcheting mechanism and high stress areas, and related to pitch size and the number of teeth engaged, are provided. These are specific to the particular device designs used in this thesis.

Some practical considerations for implementing the GNG device with a controlled rocking frame system have been outlined. Various configurations of controlled rocking frame systems incorporating the GNG could be used, and the most likely implementation of the GNG device will involve placing the GNG-dissipater system at the outside edges of the rocking frame. Two potential connection methods are suggested with the GNG mechanism attached to the edges of the rocking frame and the dissipater connected to the ground, or vice versa. Connecting the GNG mechanism to the ground may allow for easier setup and provide more convenient access for maintenance following an earthquake.

Approximate peak uplift values for the rocking model described in Chapter 7 were found using the methods of SCNZ 110:2015 and NZS 1170.5, and compared to the numerical results. ULS peak lateral deflections calculated from the time-history analyses were found to generally be around 123% to 196% of the values found by applying approximate code methods to the numerical model developed in Chapter 7, for a force reduction factor of 4. It is tentatively suggested that peak uplift values found from code methods are multiplied by an inelastic capacity factor of $\nu_{demand} = 10$, and by an additional factor of 2 due to variation between code-based and time-history analysis results, to find a suitable rack capacity and inelastic dissipater capacity for field deployment of the GNG system with a rocking frame. If the rack travel and inelastic dissipater capacity are designed using this criteria, the time-history results indicate that this will be sufficient in 99% of ULS events.

9.7. Conclusions

In summary, the unique contributions from this research and thesis to the earthquake engineering field include:

- The GNG devices developed use single direction engagement to provide resistance to system displacements while allowing for re-centring and closure of rocking joints. Concerns around buckling and residual compressive forces in the dissipater are ameliorated. The ratcheting mechanism reduces the take-up prior to engagement on cycles after previous engagement of the dissipater element has occurred, increasing resistance to displacement and improving energy dissipation capability. Other tension-only systems have been considered in the literature, but the need for a simple, low-cost solution remains and the robust design and development of the GNG devices addresses this need.
- The GNG ratcheting, tension-only devices developed provide a unique solution which can be implemented with a range of energy dissipation mechanisms as desired. The ratcheting mechanism itself is generalisable and could be attached to the dissipater element through a range of interfaces, depending on what is required for a given application.
- The completed schedule of monotonic compressive and cyclic experiments, with 14 yielding steel dissipaters, has provided insight into operational issues and design considerations. Careful detailed design was used in both prototypes to ensure a low-cost and easy to machine device, to increase likelihood of uptake.
- The GNG material model algorithm developed allows for the device behaviour to be simulated in numerical analysis, providing a basis for the inclusion of a GNG device within a structural design.
- The finite element controlled rocking system model developed can be used to simulate the behaviour of a rocking frame and provide insight into GNG behaviour in a rocking structure and the impact on the overall behaviour of the controlled rocking system. The study of rocking system response and demand in the GNG devices completed in this thesis provides a tentative guide for implementation and required capacity in deployment.

10. Directions of Future Research

10.1. Summary

The research presented in this thesis has provided significant development and insight into the design and implementation of GNG ratcheting, tension-only devices for use with seismic energy dissipation systems. Further opportunities to expand the knowledge of the earthquake engineering field in this area exist and have been identified during the completion of this research. Some specific issues to be considered in future research developments are outlined below.

10.2. Design revision

The exact details of the physical design of the GNG device are unique to this research and have been shown to provide the desired system hysteretic behaviour in a robust fashion. However, mechanical design can be as much of an art as a science, and the particular designs presented in this thesis will not be the most effective, and cost-effective, ways to achieve the desired system performance. Further work on refining the design of the ratcheting mechanisms presented in this thesis could improve the performance and manufacturability of the devices and reduce the cost of construction. Any improvements in this area will be beneficial in maximising uptake by the earthquake engineering profession. However, there is not a single design solution that is optimal for all applications. The design may need to be developed together with the structural application and the associated connection details to obtain the best solution for a specific structure.

Avoiding corrosion and preserving the integrity of the mechanism during deployment in structural systems is a key issue to consider. Paint or protective coatings could be applied to metal parts and future design of the main housing component of the ratchet mechanism could include appropriate sealing and improve the coverage of the other components to address this issue. Future design work can include a more detailed investigation of durability and corrosion issues.

10.3. Use of other dissipaters

The GNG devices designed and constructed in this research were tested using a series of yielding steel dissipaters as the energy dissipation mechanism in the GNG-dissipater system. The GNG ratcheting mechanism is not specific to yielding steel elements and is intended to be implemented with a range of energy dissipation mechanisms as appropriate in different applications. Testing of GNG-dissipater systems incorporating a range of different energy dissipation mechanisms, such as sliding friction connections or lead extrusion dampers, will provide further insight into the suitability of these dissipaters for use with the GNG device and any unique dissipater design considerations required for optimal operation.

10.4. Large-scale system testing

The monotonic compression and cyclic testing schedule completed with the GNG-dissipater systems constructed during the research showed the ratcheting, tension-only mechanisms to function as intended by design, with hysteretic behaviour closely matching the idealised behaviour model presented in Chapter 2. These tests were restricted to the GNG-dissipater system. An additional series of tests using a full or partial scale model structure to examine the behaviour of the GNG-dissipater system when connected in-situ in a structural application would provide further insight into any additional implementation issues or design considerations not previously identified.

10.5. System sensitivities

The parameter studies completed during this research, consisting of 1000s of individual time-history analyses, and presented in Chapter 8, provide a solid basis for recommendations on the implementation of the GNG in controlled rocking system applications. However, the complex nature of these simulations results in a wide range of variables that can impact the response recorded in the analysis and many assumptions and limitations must be applied to the model to fully define the system and complete the required computations. Further investigation of the sensitivity of the system response to a range of additional variables would provide a more rigorous basis for applying the device in a wide range of applications and systems. Some inputs of particular interest that could be investigated in further analyses include:

- Distribution of the seismic mass throughout the model structure height
- Inherent damping of the rocking system
- Selection of ground motion records used in the analyses, including consideration of directionality and duration among other factors
- Investigation of different ratios between the system stiffness during different stages of rocking, such as between the initial pre-uplift stiffness and the post-uplift stiffness and post-uplift, post-device-yield stiffness
- Impact damping during re-contact of the rocking edges with the ground

10.6. Higher mode effects and frame design

The work in this thesis has focussed on base rocking and the behaviour of energy dissipaters connected to the base of the rocking frame, using a lumped mass model. A rocking base controls the first mode response of the structure, but higher modes can increase structural shear forces and bending moments, even when the base moment is limited. These higher mode effects become more important for taller structures, with their associated longer periods and higher spectral displacements. Further modelling with multiple lumped masses or a more continuous mass distribution over the height of the

structure would provide insight into the effect of the response of higher modes on the overall system behaviour, including storey shears and bending moments.

It is not anticipated that such analyses will lead to significant differences in base rotation or inelastic dissipater demand. However, such analyses will have a greater influence on the design of the rocking walls or frames, including determining appropriate demands and design capacity. A more realistic model of the details of the rocking frame design beyond the behaviour at the base could be developed, and a case study of this detailed rocking frame model could be completed to examine effects of the GNG device behaviour on the full system. Also, a detailed design example, covering the design of the rocking frame and the GNG dissipater system for a given main structure, could be developed.

10.7. Code method approximations

A tentative guideline of required inelastic dissipater capacity has been made, including a factor to account for variation between peak uplift values obtained via time-history analyses and via code method approximations. A deeper investigation of the influence of various system parameters, such as structural ductility and force reduction factors, on the accuracy of code-based approximations could allow for an assessment of the suitability of current code-based methods. In particular, the design methodology for the estimation of peak displacements outlined in SCNZ 110:2015, which is an integral part of the current design process, could be applied to a large range of simulated structures to provide this data.

10.8. Field deployment

The true value of this research will be realised when it is implemented in professional practice. Practitioner interest has been shown during the design stages of this research, and this research has provided an introduction to the inclusion of GNG devices in a controlled rocking frame structure. Completing the process of detailed design and construction for a seismic resistance system incorporating GNG devices, in either a new building design or the retrofit of an existing structure, will complete the journey from inspiration to implementation for this research and provide value to the earthquake engineering community and beyond.

References

Beck, J. L. and Skinner, R. I. (1974). "Seismic response of a reinforced concrete bridge pier designed to step." Earthquake Engineering and Structural Dynamics **2**(4): 343-358.

Black, C. J., Makris, N. and Aiken, I. D. (2004). "Component testing, seismic evaluation and characterization of buckling-restrained braces." Journal of Structural Engineering **130**(6): 880-894.

BSI, B. S. I. (2004). Eurocode 8: Design of structures for earthquake resistance. Part 1: General rules, seismic actions and rules for buildings.

Buchanan, A. H., Bull, D., Dhakal, R., MacRae, G. A., Palermo, A. and Pampanin, S. (2011). Base Isolation and Damage-Resistant Technologies for Improved Seismic Performance of Buildings. Christchurch, New Zealand, University of Canterbury.

Calvi, G. M. (2010). L'Aquila earthquake 2009: reconstruction between temporary and definitive. NZSEE 2010 Annual Conference. Wellington, New Zealand.

CERC (2012). Volume 3: Low-damage building technologies. Christchurch, New Zealand, Canterbury Earthquakes Royal Commission.

Chang, K. C., Soong, T. T., Lai, M. L. and Nielsen, E. J. (1993). "Viscoelastic dampers as energy dissipation devices for seismic applications." Earthquake Spectra **9**(3): 371-371.

Clifton, G. C. (2005). Semi-rigid joints for moment-resisting steel framed seismic-resisting systems. PhD Thesis, University of Auckland.

Clough, R. W. and Huckelbridge, A. A. (1977). Preliminary Experimental Study of Seismic Uplift of a Steel Frame. Washington, D.C., USA, National Science Foundation, American Iron and Steel Inst.

Constantinou, M. C., Soong, T. T. and Dargush, G. F. (1998). Passive Energy Dissipation Systems for Structural Design and Retrofit. Monograph Series, No. 1, Multidisciplinary Center for Earthquake Engineering Research, Buffalo, N.Y.

Constantinou, M. C. and Symans, M. D. (1992). Experimental and Analytical Investigation of Seismic Response of Structures with Supplemental Fluid Viscous Dampers, State University of New York at Buffalo.

Constantinou, M. C. and Symans, M. D. (1993). "Experimental study of seismic response of buildings with supplemental fluid dampers." Structural Design of Tall Buildings **2**(2): 93-93.

Cousins, W. J. and Porritt, T. E. (1993). "Improvements to lead-extrusion damper technology." Bulletin of the New Zealand National Society for Earthquake Engineering **26**(3): 342-348.

duPont, W. and Noy, I. (2015). "What Happened to Kobe? A Reassessment of the Impact of the 1995 Earthquake in Japan." Economic Development and Cultural Change **63**(4): 777-812.

Eatherton, M. R., Fahnestock, L. A. and Miller, D. J. (2014). Self-centering buckling restrained brace development and application for seismic response mitigation. 10th U.S. National Conference on Earthquake Engineering: Frontiers of Earthquake Engineering, NCEE 2014, July 21, 2014 - July 25, 2014, Anchorage, AK, United states, Earthquake Engineering Research Institute.

Eatherton, M. R. and Hajjar, J. F. (2014). "Hybrid simulation testing of a self-centering rocking steel braced frame system." Earthquake Engineering and Structural Dynamics **43**(11): 1725-1742.

Eatherton, M. R., Ma, X., Krawinkler, H., Deierlein, G. G. and Hajjar, J. F. (2014). "Quasi-static cyclic behavior of controlled rocking steel frames." Journal of Structural Engineering (United States) **140**(11).

English, B. (2013). 2014 Budget: Budget Policy Statement. N. Z. Treasury, New Zealand Government.

Fastenal (2005). Technical Reference Guide. Winona, Minnesota, U.S.

Gledhill, S. M., Sidwell, G. K. and Bell, D. K. (2008). The damage avoidance design of tall steel frame buildings - Fairlie terrace student accommodation project, Victoria University of Wellington. The 2008 New Zealand Society for Earthquake Engineering Conference. Wellington, New Zealand.

Grigorian, C. E., Yang, T. S. and Popov, E. P. (1993). "Slotted bolted connection energy dissipators." Earthquake Spectra **9**(3): 491-491.

Gultom, R. and Ma, Q. T. (2015). Biaxial pseudodynamic tests of a post-tensioned rocking column with externally mounted energy dissipators. 2015 NZSEE Annual Technical Conference: New Dimensions in Earthquake Resilience. Rotorua, New Zealand.

Gunning, M. and Weston, D. (2013). Assessment of Design Methodologies for Rocking Systems, ENCI493 Report. Christchurch, New Zealand, University of Canterbury.

Hao, H. (2015). "Development of a New Nonbuckling Segmented Brace." International Journal of Structural Stability and Dynamics **15**(8).

Horwich, G. (2000). "Economic lessons of the Kobe earthquake." Economic Development and Cultural Change **48**(3): 521-542.

Housner, G. W. (1963). "Behavior of inverted pendulum structures during earthquakes." Seismological Society of America -- Bulletin **53**(2): 403-417.

Huckelbridge, A. A. (1977). Earthquake Simulation Tests of a Nine Story Steel Frame with Columns Allowed to Uplift. Washington, D.C., USA, National Science Foundation.

Jarrah, M., Khezrzadeh, H., Mofid, M. and Jafari, K. (2019). "Experimental and numerical evaluation of piston metallic damper (PMD)." Journal of Constructional Steel Research **154**: 99-109.

Kalliontzis, D., Sritharan, S. and Schultz, A. (2016). "Improved Coefficient of Restitution Estimation for Free Rocking Members." Journal of Structural Engineering (United States) **142**(12).

Kang, J.-D. and Tagawa, H. (2013). "Seismic response of steel structures with seesaw systems using viscoelastic dampers." Earthquake Engineering and Structural Dynamics **42**(5): 779-794.

Kelly, J. M., Skinner, R. I. and Heine, A. J. (1972). "Mechanisms of energy absorption in special devices for use in earthquake resistant structures." Bulletin of the New Zealand Society for Earthquake Engineering **5**(3): 63-73.

Kelly, J. M. and Tsztoo, D. F. (1977). Earthquake Simulation Testing of a Stepping Frame with Energy-Absorbing Devices. Washington, D.C., USA, National Science Foundation.

Latham, D. A., Reay, A. M. and Pampanin, S. (2013). Kilmore Street Medical Centre: application of a posttensioned steel rocking system. Steel Innovations Conference 2013. Christchurch, New Zealand.

Latour, M., Rizzano, G., Santiago, A. and Simoes da Silva, L. (2019). "Experimental response of a low-yielding, self-centering, rocking column base joint with friction dampers." Soil Dynamics and Earthquake Engineering **116**: 580-592.

Lee, D. and Taylor, D. P. (2001). "Viscous damper development and future trends." Structural Design of Tall Buildings **10**(5): 311-320.

Lei, J. S., Luo, W. X., Jiang, J. L. and Zhang, W. (2014). Seismic performance analysis of steel frame with wedge devices based on the energy dissipation. 4th International Conference on Civil Engineering, Architecture and Building Materials, CEABM 2014, May 24, 2014 - May 25, 2014, Haikou, China, Trans Tech Publications Ltd.

Limpert, E., Stahel, W. A. and Abbt, M. (2001). "Log-normal Distributions across the Sciences: Keys and CluesOn the charms of statistics, and how mechanical models resembling gambling machines offer a link to a handy way to characterize log-normal distributions, which can provide deeper insight into variability and probability—normal or log-normal: That is the question." BioScience **51**(5): 341-352.

Ma, J., Karaman, I. and Noebe, R. D. (2010). "High temperature shape memory alloys." International Materials Reviews **55**(5): 257-315.

MacRae, G. A. and Clifton, G. C. (2015). Research on seismic performance of steel structures. Steel Innovation Conference. Auckland, New Zealand.

MacRae, G. A., Clifton, G. C., Mackinven, H., Mago, N., Butterworth, J. and Pampanin, S. (2010). "The sliding hinge joint moment connection." Bulletin of the New Zealand Society for Earthquake Engineering **43**(3): 202-212.

Mar, D. (2010). Design examples using mode shaping spines for frame and wall buildings. 9th US National and 10th Canadian Conference on Earthquake Engineering 2010, Including Papers from the 4th International Tsunami Symposium, July 25, 2010 - July 29, 2010, Toronto, ON, Canada, Earthquake Engineering Research Institute.

Marriott, D., Pampanin, S., Bull, D. and Palermo, A. (2008). "Dynamic testing of precast, post-tensioned rocking wall systems with alternative dissipating solutions." Bulletin of the New Zealand Society for Earthquake Engineering **41**(2): 90-103.

Menegotto, M. and Pinto, P. (1973). Method of analysis for cyclically loaded reinforced concrete plane frames including changes in geometry and non-elastic behavior of elements under combined normal force and bending. IABSE Symposium on the Resistance and Ultimate Deformability of Structures Acted on by Well-defined Repeated Loads. Lisbon, Portugal.

Midorikawa, M., Azuhata, T., Ishihara, T. and Wada, A. (2006). "Shaking table tests on seismic response of steel braced frames with column uplift." Earthquake Engineering and Structural Dynamics **35**(14): 1767-1785.

Midorikawa, M., Ishihara, T., Azuhata, T., Takai, S., Kanagawa, M., Hori, H., Kusakari, T. and Asari, T. (2010). Three-dimensional shaking table tests on three-story reduced-scale steel rocking frames. 9th US National and 10th Canadian Conference on Earthquake Engineering 2010, Including Papers from the 4th International Tsunami Symposium, July 25, 2010 - July 29, 2010, Toronto, ON, Canada, Earthquake Engineering Research Institute.

Muto, K., Umemura, H. and Sonobe, Y. (1960). Study of the overturning vibration of slender structures. The 2nd World Conference on Earthquake Engineering, Tokyo and Kyoto, Japan.

Oberg, E., Jones, F. D., Horton, H. L. and Ryffell, H. H. (2000). Machinery Handbook. New York, NY, Industrial Press Inc.

OpenSEES (2007). Open System for Earthquake Engineering Simulation. http://opensees.berkeley.edu, University of California, Berkeley: Pacific Earthquake Engineering Research Center (PEER).

Pampanin, S. (2012). "Reality-check and renewed challenges in earthquake engineering: Implementing low-damage systems - From theory to practice." Bulletin of the New Zealand Society for Earthquake Engineering **45**(4): 137-160.

Pekcan, G., Mander, J. B. and Chen, S. S. (1999). "Fundamental considerations for the design of non-linear viscous dampers." Earthquake Engineering and Structural Dynamics **28**(11): 1405-1425.

Phocas, M. C. and Pocanschi, A. (2003). "Steel frames with bracing mechanism and hysteretic dampers." Earthquake Engineering and Structural Dynamics **32**(5): 811-825.

Phocas, M. C. and Sophocleous, T. L. (2013). Cable bracing design in adaptable dual control systems. 9th World Conference on Earthquake Resistant Engineering Structures, ERES 2013, July 8, 2013 - July 10, 2013, A Coruna, Spain, WITPress.

Poon, D. C. K., Shieh, S., Joseph, L. M. and C., C. (2004). Structural design of Taipei 101, The world's tallest building. Tall Buildings in Historical Cities - Culture & Technology for Sustainable Cities, Seoul, South Korea.

Priestley, M. J. N. (1991). "Overview of PRESSS research program." PCI Journal **36**(4): 50-57.

Priestley, M. J. N., Sritharan, S. S., Conley, J. R. and Pampanin, S. (1999). "Preliminary results and conclusions from the PRESSS five-story precast concrete test building." PCI Journal **44**(6): 42-67.

Rad, A. A., Macrae, G. A., Yeow, T. Z. and Bull, D. K. (2015). "Seismic behavior of steel buildings with out-of-plumb." Earthquake Engineering and Structural Dynamics **44**(14).

Robinson, W. H. and Greenbank, L. R. (1975). "Properties of an extrusion energy absorber." Bulletin of the New Zealand Society for Earthquake Engineering **8**(3): 187-191.

Robinson, W. H. and Greenbank, L. R. (1976). "Extrusion energy absorber suitable for the protection of structures during an earthquake." Earthquake Engineering and Structural Dynamics **4**(3): 251-259.

Rodgers, G. W., Solberg, K. M., Chase, J. G., Mander, J. B., Bradley, B. A., Dhakal, R. P. and Li, L. (2008). "Performance of a damage-protected beam-column subassembly utilizing external HF2V energy dissipation devices." Earthquake Engineering and Structural Dynamics **37**(13): 1549-1564.

Ryan, K. L. and Dao, N. D. (2016). "Influence of Vertical Ground Shaking on Horizontal Response of Seismically Isolated Buildings with Friction Bearings." Journal of Structural Engineering (United States) **142**(1).

SEAOC (1995). Vision 2000: Performance-Based Seismic Engineering of Buildings. Sacramento, California, Structural Engineers Association of California.

Shen, K. L., Soong, T. T., Chang, K. C. and Lai, M. L. (1995). "Seismic behaviour of reinforced concrete frame with added viscoelastic dampers." Engineering Structures **17**(5): 372-380.

Sitler, B., MacRae, G. A., Takeuchi, T., Matsuri, R., Westeneng, B. and Jones, A. (2017). Buckling restrained brace connection and stability performance issues. 16th World Conference on Earthquake Engineering, 16WCEE. Santiago, Chile.

SNZ (2004). NZS 1170.5:2004 Structural Design Actions Part 5: Earthquake actions - New Zealand. Wellington, New Zealand, Standards New Zealand.

SNZ (2004). NZS 1170.5 Supp 1:2004 Structural Design Actions Part 5: Earthquake actions - New Zealand - Commentary. Wellington, New Zealand, Standards New Zealand.

Sommerville, P., Smith, N., Punyamurthula, S. and Sun, J. (1997). Development of ground motion time histories for phase II of the FEMA/SAC steel project. Sacramento, Calif. : SAC Joint Venture, 1997.

Symans, M. D., Charney, F. A., Whittaker, A. S., Constantinou, M. C., Kircher, C. A., Johnson, M. W. and McNamara, R. J. (2008). "Energy dissipation systems for seismic applications: Current practice and recent developments." Journal of Structural Engineering **134**(1): 3-21.

Tagawa, H., Yamanishi, T., Takaki, A. and Chan, R. W. K. (2016). "Cyclic behavior of seesaw energy dissipation system with steel slit dampers." Journal of Constructional Steel Research **117**: 24-34.

Tait, J. D., Sidwell, G. K. and Finnegan, J. F. (2013). Case study - Elevate apartments - A rocking 15 storey apartment building. Steel Innovations Conference 2013. Christchurch, New Zealand.

Tamura, Y., Fujii, K., Ohtsuki, T., Wakahara, T. and Kohsaka, R. (1995). "Effectiveness of tuned liquid dampers under wind excitation." Engineering Structures **17**(9): 609-621.

Thammarak, P., Mai, T. T., Htun, L. H. and Khine, M. T. (2017). Development, and testing of cam-grip type, compression-free energy dissipative brace. 16th World Conference on Earthquake Engineering, 16WCEE. Santiago, Chile.

TheMathworksInc. (2016). MATLAB R2016a. Natick, MA, USA.

Tian, L., Gao, G., Qiu, C. and Rong, K. (2018). "Effect of hysteresis properties of shape memory alloy-tuned mass damper on seismic control of power transmission tower." Advances in Structural Engineering.

Tremblay, R., Poirier, L.-P., Bouaanani, N., Leclerc, M., Rene, V., Fronteddu, L. and Rivest, S. (2008). Innovative viscously damped rocking braced steel frames. The 14th World Conference on Earthquake Engineering. Beijing, China.

USGS (2008). The ShakeOut Scenario: U.S. Geological Survey Open-File Report 2008-1150 and California Geological Survey Preliminary Report 25. http://pubs.usgs.gov/of/2008/1150/, United States Geological Survey.

USGS (2015). UCERF3: A New Earthquake Forecast for California's Complex Fault System - USGS Fact Sheet-2015-3009. https://dx.doi.org/10.3133/fs20153009, United States Geological Survey.

Wada, A., Yamada, S., Fukuta, O. and Tanigawa, M. (2001). Passive controlled slender structures having special devises at column connections. The 7th International Seminar on Seismic Isolation, Passive Energy Dissipation and Active Control of Vibrations of Structures. Assisi, Italy.

Wiebe, L. (2008). Mitigation of higher mode effects in self-centring walls by using multiple rocking sections. Master of Earthquake Engineering Thesis, University Institute for Advanced Studies, University of Pavia.

Wiebe, L. (2013). Design of controlled rocking steel frames to limit higher mode effects. PhD Thesis, University of Toronto.

Wiebe, L. (2015). Controlled rocking steel braced frames: connecting research and practice. Steel Innovations Conference 2015. Auckland, New Zealand.

Wiebe, L. and Christopoulos, C. (2014). Controlled rocking systems for enhanced seismic resilience: State of the art. 2014 International Conference on Sustainable Development of Critical Infrastructure, IC-SDCI 2014, May 16, 2014 - May 18, 2014, Shanghai, China, American Society of Civil Engineers (ASCE).

Wiebe, L., Sidwell, G. and Gledhill, S. (2015). SCNZ 110:2015 Design guide for controlled rocking steel braced frames, Steel Construction New Zealand.

Xiao, Y., MacRae, G. A., Hamada, N., Priestley, M. J. N. and Seible, F. (1992). Rocking and Capacity Test of Model Bridge Pier, University of California, San Diego.

Xu, Z. D., Liao, Y. X., Ge, T. and Xu, C. (2016). "Experimental and theoretical study of viscoelastic dampers with different matrix rubbers." Journal of Engineering Mechanics **142**(8): 1-12.

Zhao, J. X., Cousins, J. W. and Robinson, W. H. (2000). Using a lead-based damper to increase near-source ground motion resisting capacity of existing base-isolated structures. The 12th World Conference on Earthquake Engineering. Auckland, New Zealand.

Appendix A Prototype device engineering drawings

A1 GNG1 prototype engineering drawings

The following appendix contains the engineering drawings used to produce the first GNG prototype device. Note that the yielding steel dissipater component was labelled in the original design as the 'fuse'. The part and assembly drawings attached include:

1. Main support body
2. Pawl pin
3. Pawl
4. Rack (40 mm pitch size)
5. Cover plate
6. Upper tongue
7. Upper rack support
8. Lower rack support
9. Dissipater (labelled as fuse)
10. Lower tongue
11. Rack (20 mm pitch size)
12. GNG1 assembly

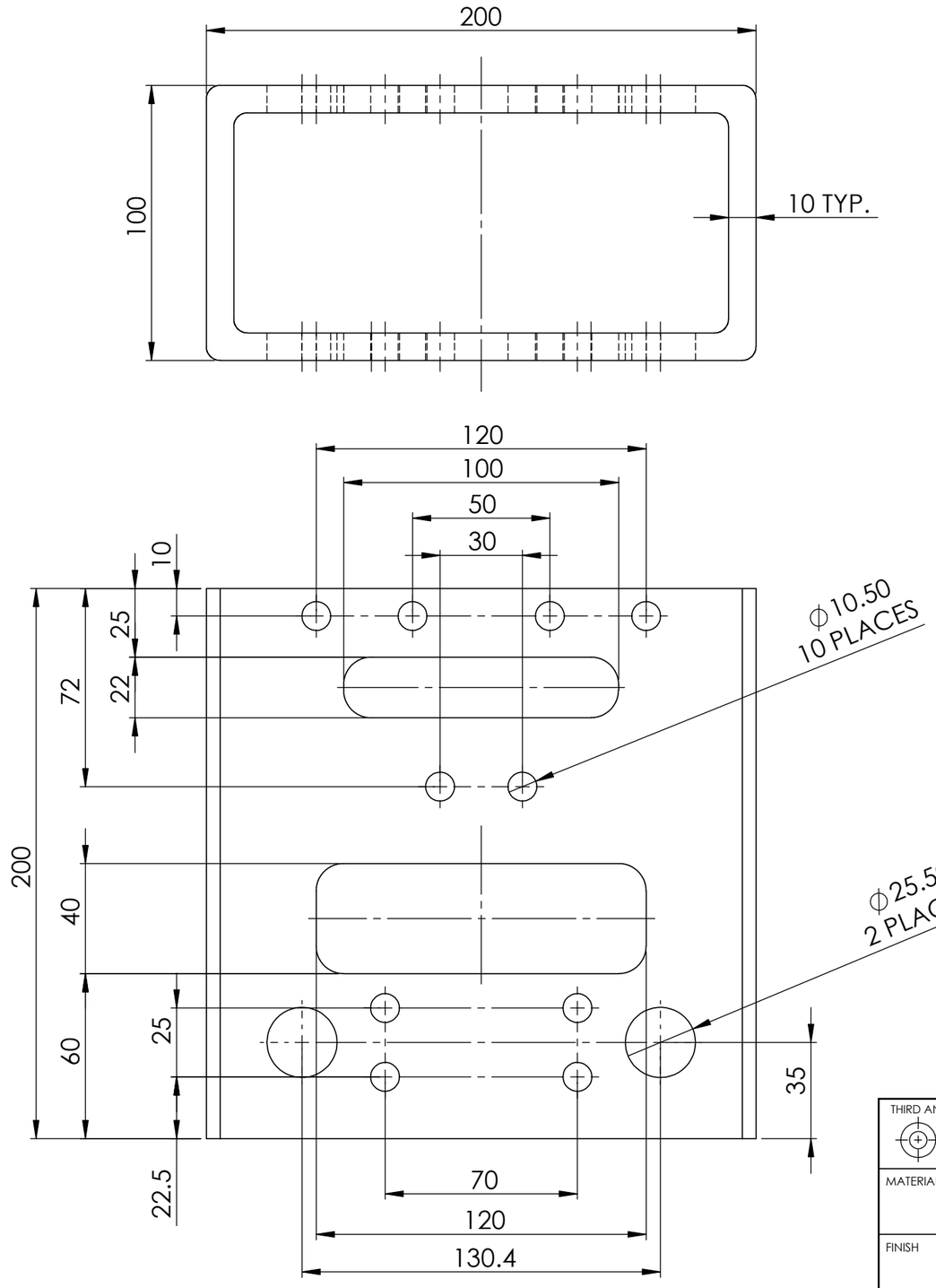

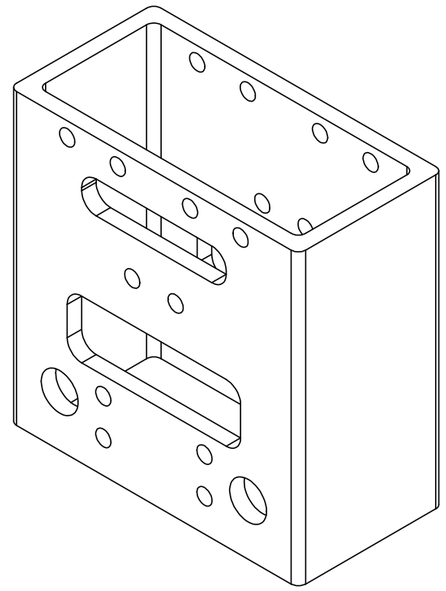

ALL FEATURES THROUGH
BOTH SIDES OF RHS
--EXCEPT TOP SLOT--

THIRD ANGLE PROJECTION

MATERIAL: 200 x 100 x 10.0 RHS

FINISH: AS MACHINED

TOLERANCE (UNLESS OTHERWISE SPECIFIED)
DECIMAL mm
.X ± .1 **.XX** ± .05 **.XXX** ± .010 **ANG.** ± 1°

UNIVERSITY OF CANTERBURY ©
DEPARTMENT OF MECHANICAL ENGINEERING

MAIN SUPPORT

DESIGN	DWG NO.	REV
JARROD COOK	RF-02-01	--
DRAWN: JARROD COOK	PROJECT: RATCHET FUSE	
SUPERVISOR: GEOFF RODGERS	ISSUE DATE: 20 JUNE 2014	DRAWING NOT TO SCALE
		SHEET: 1 OF 12

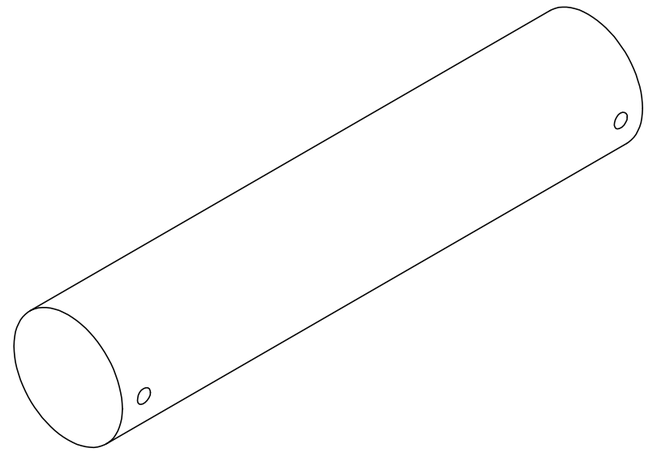

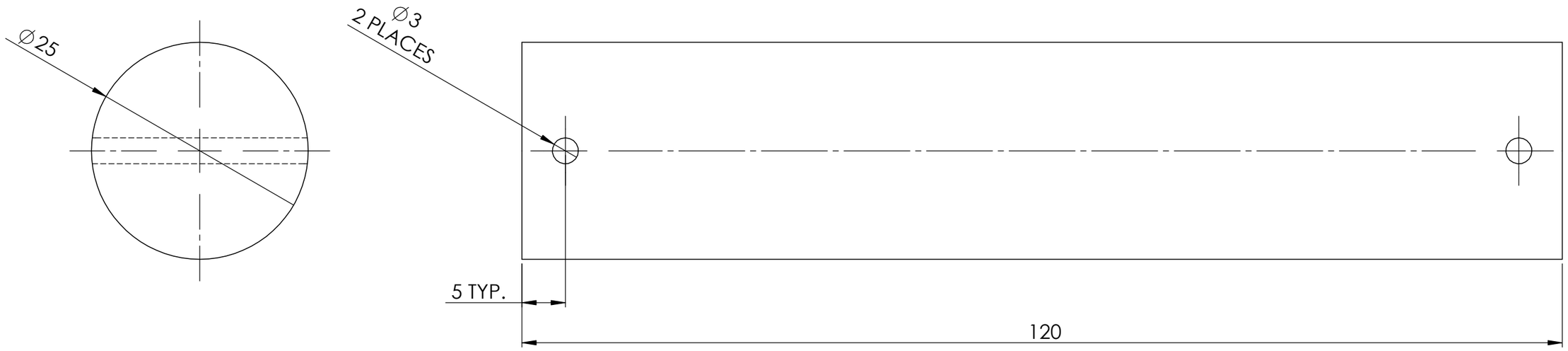

THIRD ANGLE PROJECTION	THIS DOCUMENT IS ISSUED IN STRICT CONFIDENCE ON CONDITION THAT IT IS NOT COPIED, REPRINTED, OR DISCLOSED TO A THIRD PARTY EITHER WHOLLY OR IN PART WITHOUT THE WRITTEN CONSENT OF UNIVERSITY OF CANTERBURY	UNIVERSITY OF CANTERBURY © DEPARTMENT OF MECHANICAL ENGINEERING	UNIVERSITY OF CANTERBURY Te Whare Wānanga o Waitaha CHRISTCHURCH NEW ZEALAND
MATERIAL: AISI 4140 OR EQUIVALENT - 2 REQUIRED		PAWL PIN	
FINISH: AS MACHINED		DESIGN: JARROD COOK	DWG NO.: RF-02-02
			REV: --
TOLERANCE (UNLESS OTHERWISE SPECIFIED) DECIMAL mm		DRAWN: JARROD COOK	PROJECT: RATCHET FUSE
.X ± .1 .XX ± .05 .XXX ± .010 ANG. ± 1°		SUPERVISOR: GEOFF RODGERS	ISSUE DATE: 17 JUNE 2014
		DRAWING NOT TO SCALE	SHEET: 2 OF 12

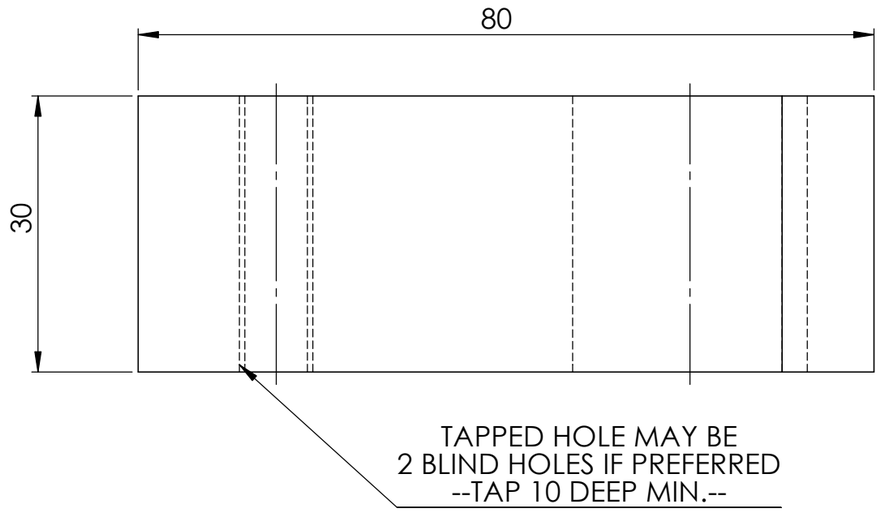

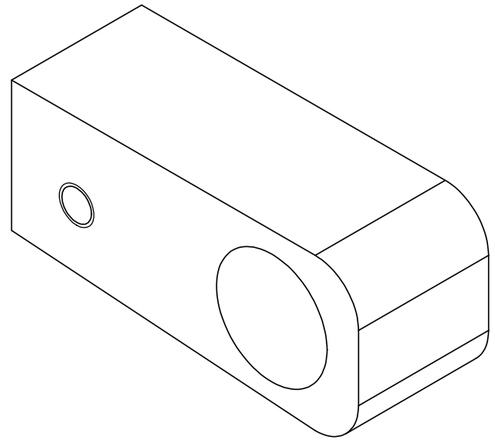

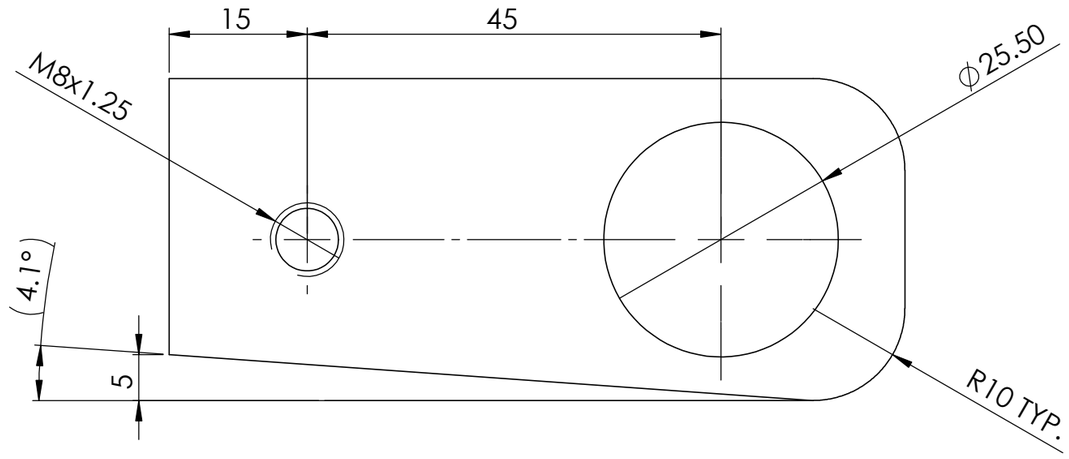

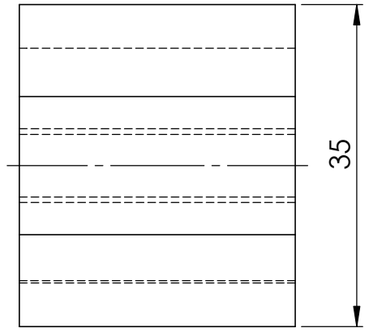

THIRD ANGLE PROJECTION	THIS DOCUMENT IS ISSUED IN STRICT CONFIDENCE ON CONDITION THAT IT IS NOT COPIED, REPRINTED, OR DISCLOSED TO A THIRD PARTY EITHER WHOLLY OR IN PART WITHOUT THE WRITTEN CONSENT OF UNIVERSITY OF CANTERBURY	UNIVERSITY OF CANTERBURY © DEPARTMENT OF MECHANICAL ENGINEERING		UNIVERSITY OF CANTERBURY Te Whare Wānanga o Waitaha CHRISTCHURCH NEW ZEALAND
MATERIAL: AISI 4140 OR EQUIVALENT - 4 REQUIRED		PAWL		
FINISH: AS MACHINED		DESIGN: JARROD COOK	DWG NO.: RF-02-03	REV: --
TOLERANCE (UNLESS OTHERWISE SPECIFIED) DECIMAL mm		DRAWN: JARROD COOK	PROJECT: RATCHET FUSE	
.X ± .1 .XX ± .05 .XXX ± .010 ANG. ± 1°		SUPERVISOR: GEOFF RODGERS	ISSUE DATE: 17 JUNE 2014	DRAWING NOT TO SCALE / SHEET: 3 OF 12

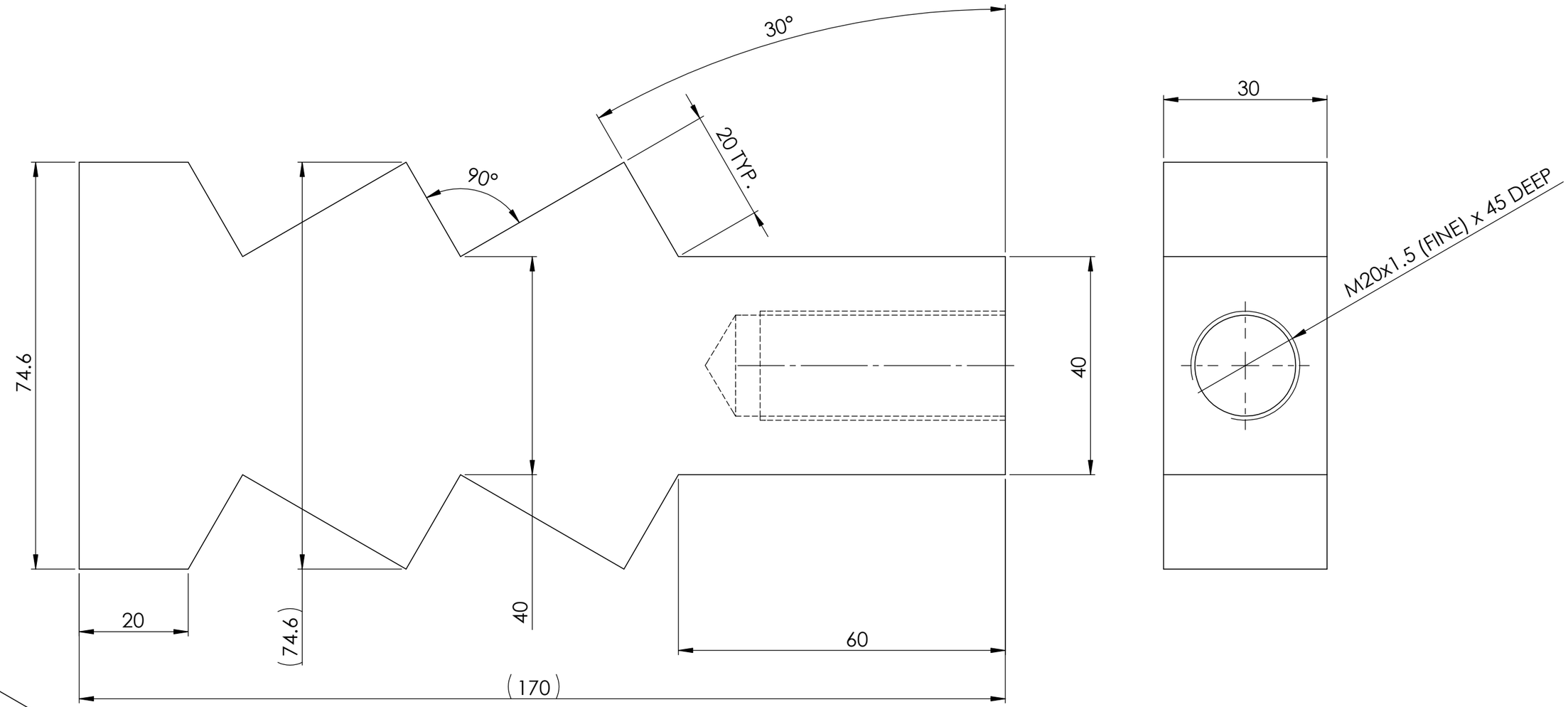

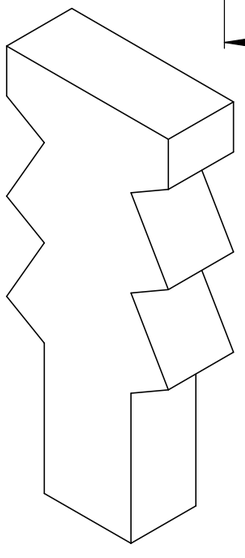

THIRD ANGLE PROJECTION

MATERIAL: AISI 4140 OR EQUIVALENT PREFERRED
AISI 1040 OR EQUIVALENT MINIMUM - 2 REQUIRED

FINISH: AS MACHINED

TOLERANCE (UNLESS OTHERWISE SPECIFIED)
DECIMAL mm
.X ± .1 **.XX** ± .05 **.XXX** ± .010 **ANG.** ± 1°

UNIVERSITY OF CANTERBURY ©
DEPARTMENT OF MECHANICAL ENGINEERING

RACK - P40

DESIGN	DWG NO.	REV
JARROD COOK	RF-02-04	--
DRAWN: JARROD COOK	PROJECT: RATCHET FUSE	
SUPERVISOR: GEOFF RODGERS	ISSUE DATE: 17 JUNE 2014	DRAWING NOT TO SCALE
		SHEET: 4 OF 12

UNIVERSITY OF CANTERBURY
Te Whare Wānanga o Waitaha
CHRISTCHURCH NEW ZEALAND

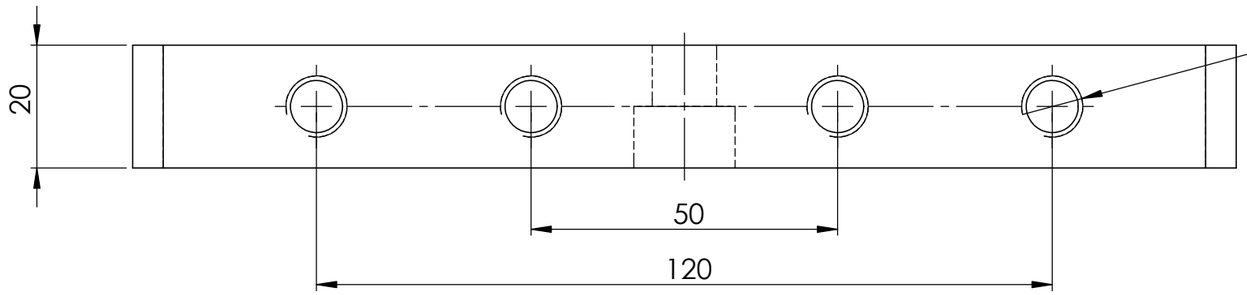

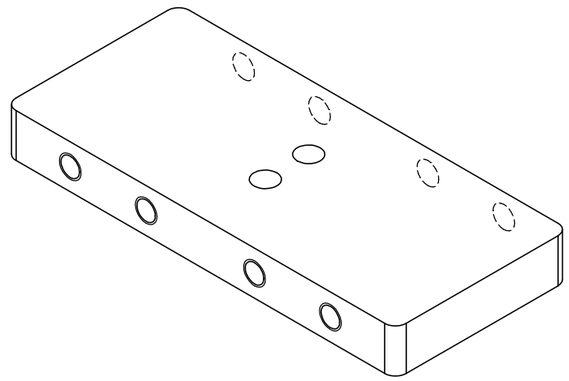

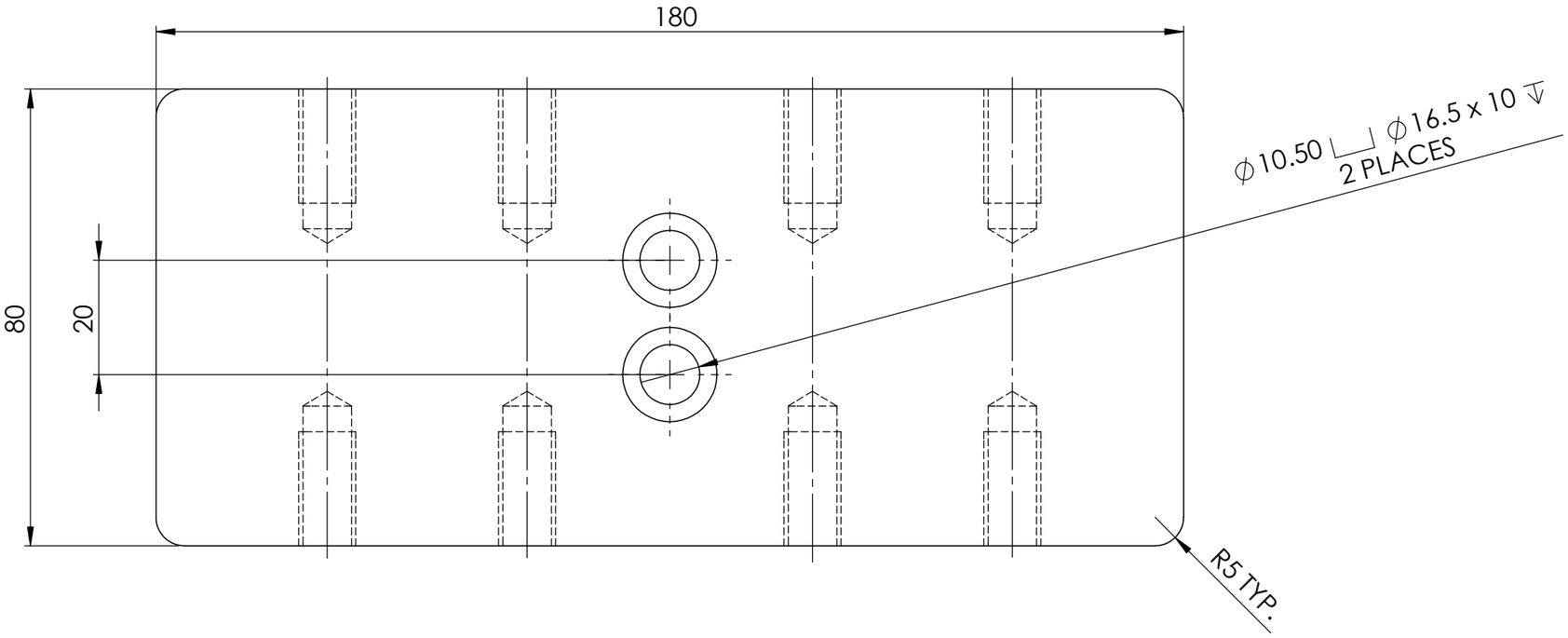

MATERIAL: AISI 1040 OR EQUIVALENT

FINISH: AS MACHINED

TOLERANCE (UNLESS OTHERWISE SPECIFIED)

DECIMAL mm

.X ± .1 **.XX** ± .05 **.XXX** ± .010 **ANG.** ± 1°

UNIVERSITY OF CANTERBURY ©
DEPARTMENT OF MECHANICAL ENGINEERING

UNIVERSITY OF CANTERBURY
Te Whare Wānanga o Waitaha
CHRISTCHURCH NEW ZEALAND

COVER PLATE

DESIGN	DWG NO.	REV
JARROD COOK	RF-02-05	--
DRAWN: JARROD COOK	PROJECT: RATCHET FUSE	
SUPERVISOR: GEOFF RODGERS	ISSUE DATE: 20 JUNE 2014	DRAWING NOT TO SCALE
		SHEET: 5 OF 12

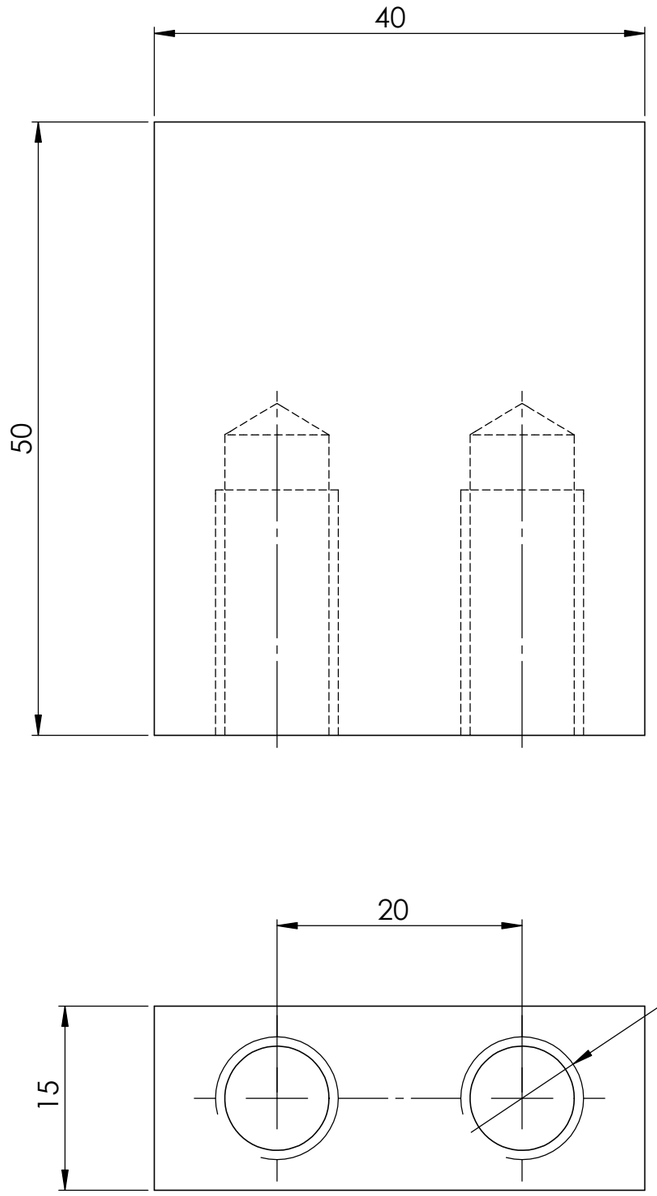

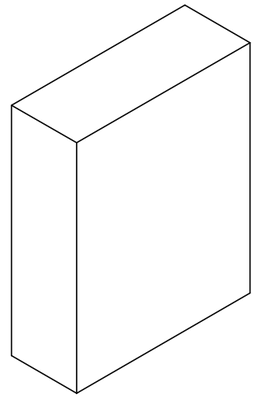

MATERIAL: AISI 1040 OR EQUIVALENT - 2 REQUIRED

FINISH: AS MACHINED

TOLERANCE (UNLESS OTHERWISE SPECIFIED)

DECIMAL mm

.X ± .1 **.XX** ± .05 **.XXX** ± .010 **ANG.** ± 1°

UNIVERSITY OF CANTERBURY ©
DEPARTMENT OF MECHANICAL ENGINEERING

UPPER TONGUE

DESIGN: JARROD COOK	DWG NO.: RF-02-06	REV: --	
DRAWN: JARROD COOK	PROJECT: RATCHET FUSE		
SUPERVISOR: GEOFF RODGERS	ISSUE DATE: 17 JUNE 2014	DRAWING NOT TO SCALE	SHEET: 6 OF 12

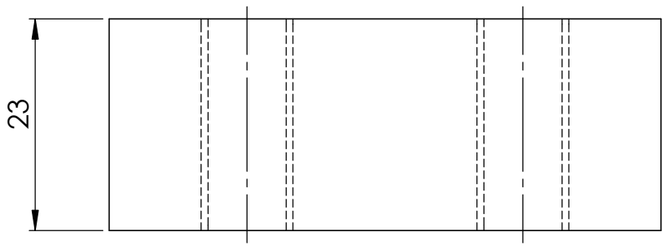

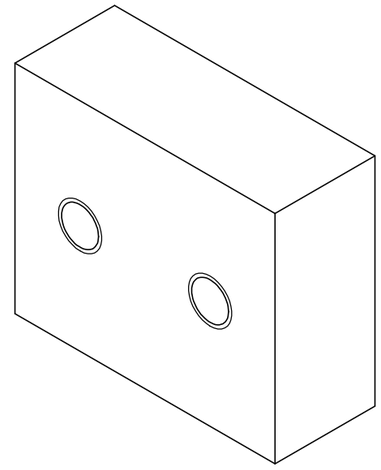

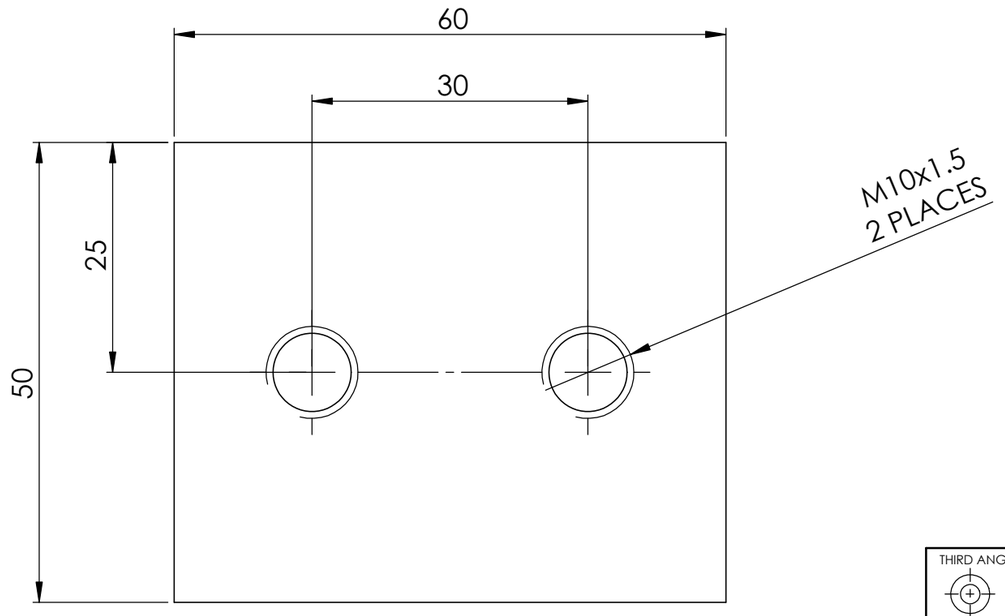

THIRD ANGLE PROJECTION

UNIVERSITY OF CANTERBURY ©
DEPARTMENT OF MECHANICAL ENGINEERING

UNIVERSITY OF CANTERBURY
Te Whare Wānanga o Waitaha
CHRISTCHURCH NEW ZEALAND

MATERIAL: AISI 1040 OR EQUIVALENT - 2 REQUIRED

FINISH: AS MACHINED

TOLERANCE (UNLESS OTHERWISE SPECIFIED)
DECIMAL mm
.X ± .1 **.XX** ± .05 **.XXX** ± .010 **ANG.** ± 1°

UPPER RACK SUPPORT

DESIGN	DWG NO.	REV
JARROD COOK	RF-02-07	--
DRAWN: JARROD COOK	PROJECT: RATCHET FUSE	
SUPERVISOR: GEOFF RODGERS	ISSUE DATE: 17 JUNE 2014	DRAWING NOT TO SCALE
		SHEET: 7 OF 12

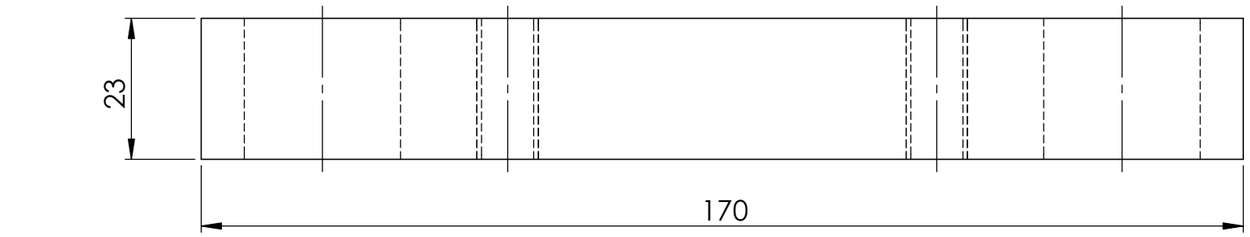

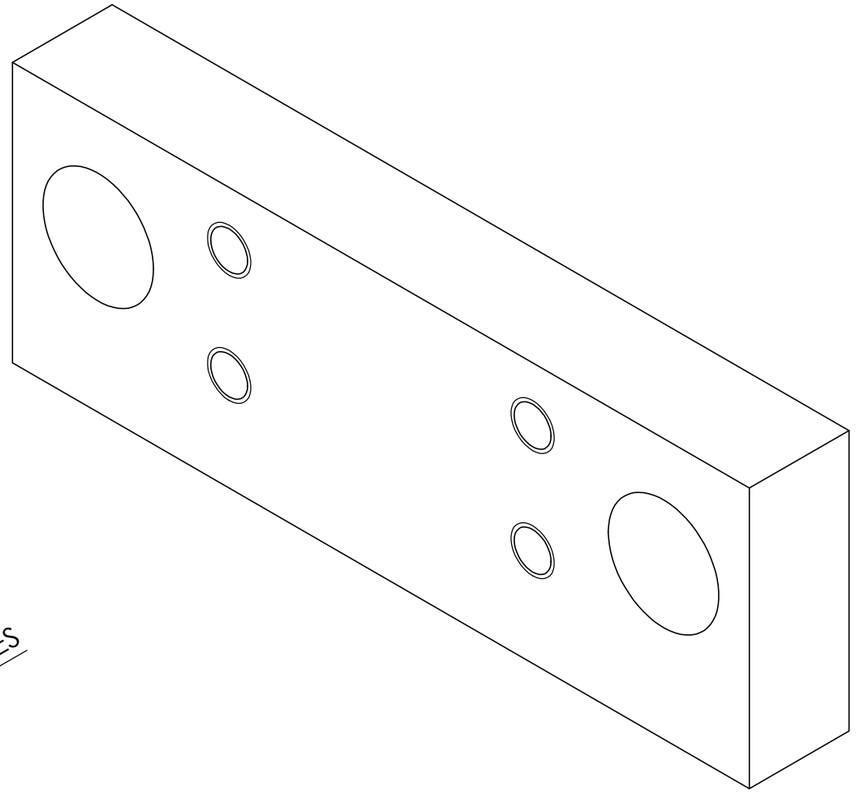

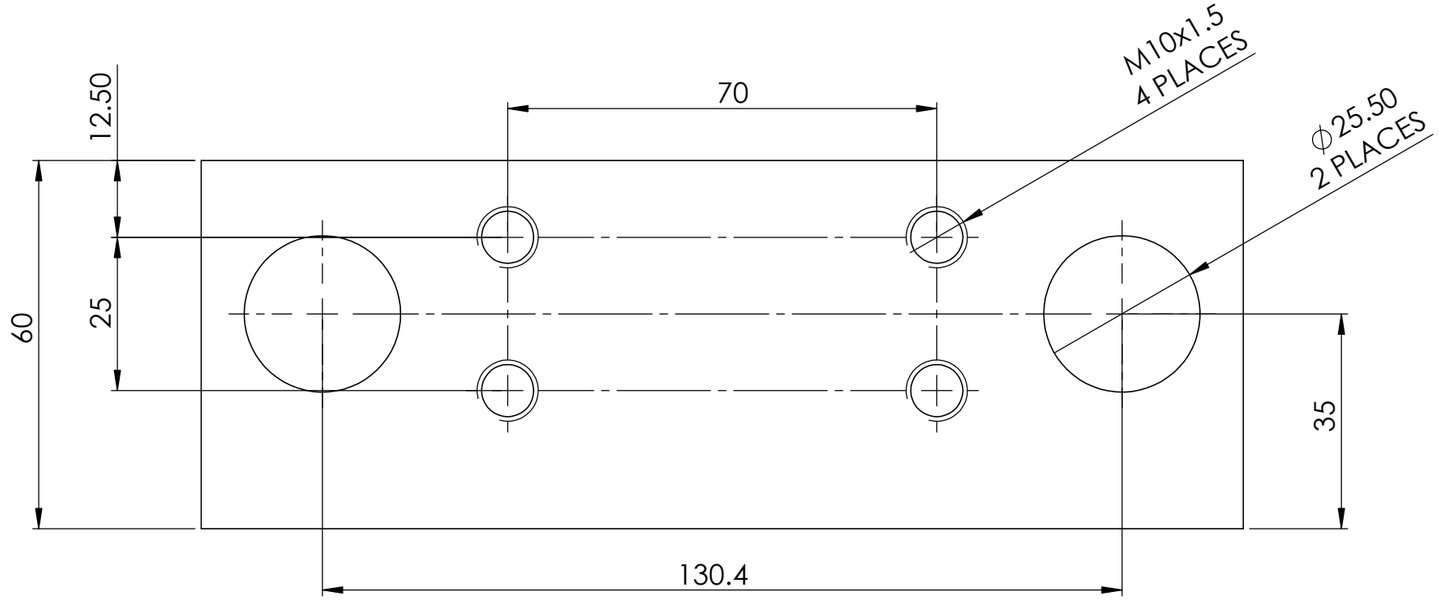

THIRD ANGLE PROJECTION

UNIVERSITY OF CANTERBURY ©
DEPARTMENT OF MECHANICAL ENGINEERING

UNIVERSITY OF CANTERBURY
Te Whare Wānanga o Waitaha
CHRISTCHURCH NEW ZEALAND

MATERIAL: AISI 1040 OR EQUIVALENT - 2 REQUIRED

LOWER RACK SUPPORT

FINISH: AS MACHINED

TOLERANCE (UNLESS OTHERWISE SPECIFIED)
DECIMAL mm
.X ± .1 .XX ± .05 .XXX ± .010 ANG. ± 1°

DESIGN	DWG NO.	REV
JARROD COOK	RF-02-08	--
DRAWN: JARROD COOK	PROJECT: RATCHET FUSE	
SUPERVISOR: GEOFF RODGERS	ISSUE DATE: 17 JUNE 2014	DRAWING NOT TO SCALE
		SHEET: 8 OF 12

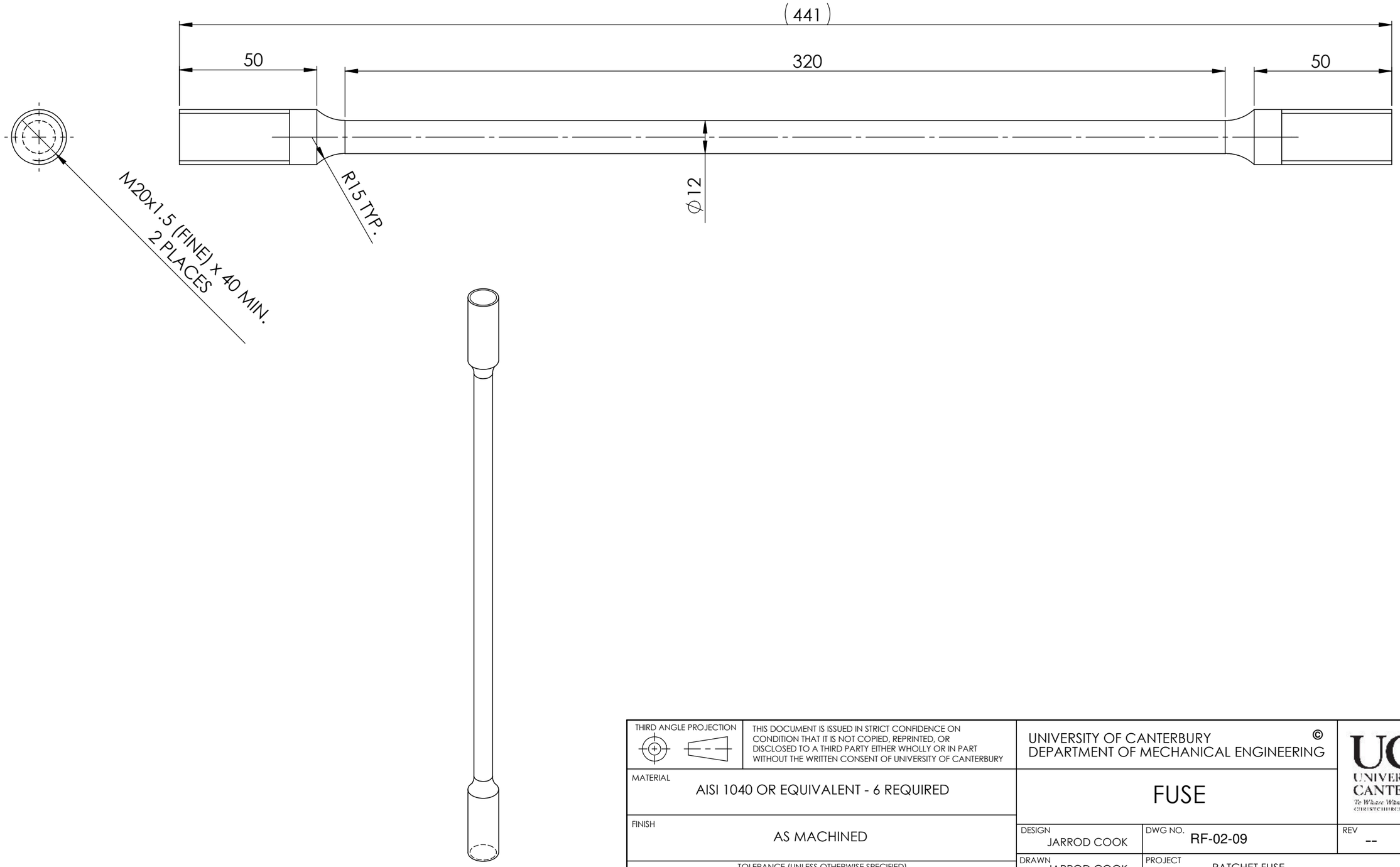

THIRD ANGLE PROJECTION

UNIVERSITY OF CANTERBURY ©
DEPARTMENT OF MECHANICAL ENGINEERING

UNIVERSITY OF CANTERBURY
Te Whare Wānanga o Waitaha
CHRISTCHURCH NEW ZEALAND

MATERIAL: AISI 1040 OR EQUIVALENT - 6 REQUIRED

FUSE

FINISH: AS MACHINED

TOLERANCE (UNLESS OTHERWISE SPECIFIED)
DECIMAL mm
.X ± .1 .XX ± .05 .XXX ± .010 ANG. ± 1°

DESIGN	DWG NO.	REV
JARROD COOK	RF-02-09	--
DRAWN: JARROD COOK	PROJECT: RATCHET FUSE	
SUPERVISOR: GEOFF RODGERS	ISSUE DATE: 17 JUNE 2014	DRAWING NOT TO SCALE
		SHEET: 9 OF 12

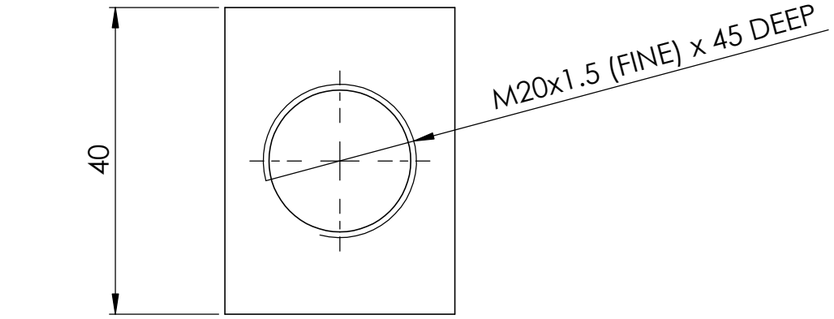

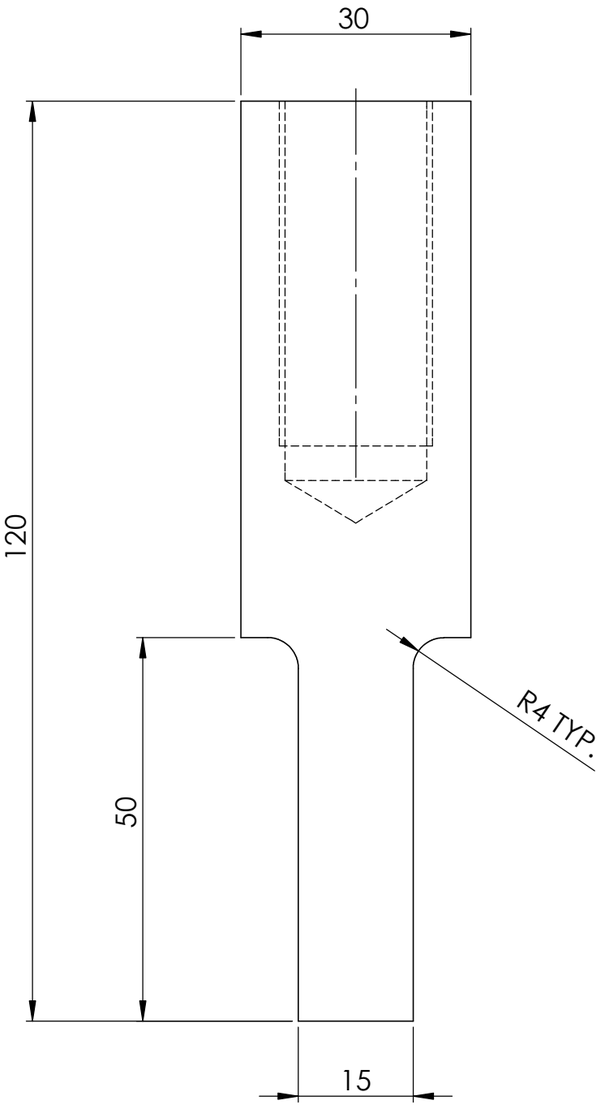

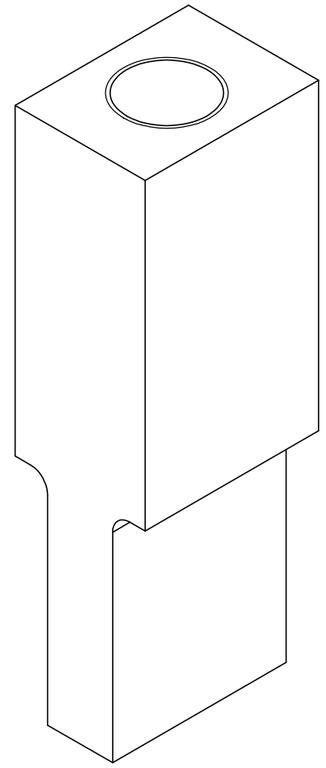

THIRD ANGLE PROJECTION

MATERIAL: AISI 1040 OR EQUIVALENT

FINISH: AS MACHINED

TOLERANCE (UNLESS OTHERWISE SPECIFIED)

DECIMAL mm

.X ± .1 **.XX** ± .05 **.XXX** ± .010 **ANG.** ± 1°

UNIVERSITY OF CANTERBURY ©
DEPARTMENT OF MECHANICAL ENGINEERING

LOWER TONGUE

DESIGN	DWG NO.	REV
JARROD COOK	RF-02-10	--
DRAWN: JARROD COOK	PROJECT: RATCHET FUSE	
SUPERVISOR: GEOFF RODGERS	ISSUE DATE: 17 JUNE 2014	DRAWING NOT TO SCALE
		SHEET: 10 OF 12

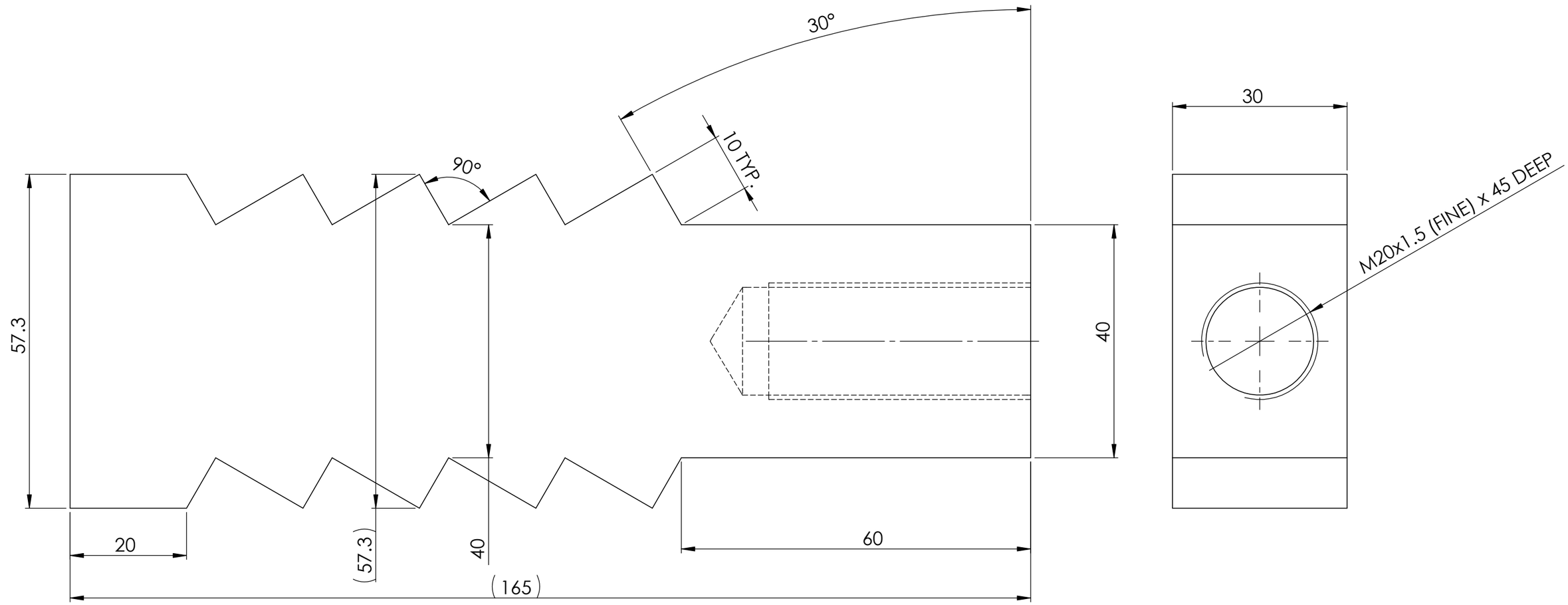

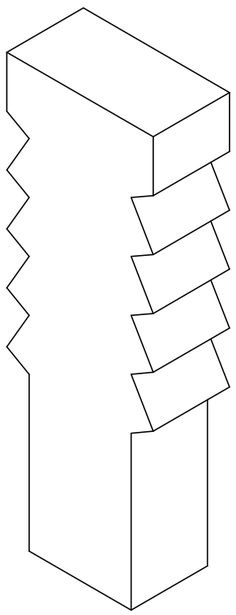

THIRD ANGLE PROJECTION

MATERIAL: AISI 4140 OR EQUIVALENT PREFERRED
AISI 1040 OR EQUIVALENT MINIMUM - 2 REQUIRED

FINISH: AS MACHINED

TOLERANCE (UNLESS OTHERWISE SPECIFIED)
DECIMAL mm
.X ± .1 .XX ± .05 .XXX ± .010 ANG. ± 1°

UNIVERSITY OF CANTERBURY ©
DEPARTMENT OF MECHANICAL ENGINEERING

RACK - P20

DESIGN	DWG NO.	REV
JARROD COOK	RF-02-11	--
DRAWN: JARROD COOK	PROJECT: RATCHET FUSE	
SUPERVISOR: GEOFF RODGERS	ISSUE DATE: 17 JUNE 2014	DRAWING NOT TO SCALE
		SHEET: 11 OF 12

UC UNIVERSITY OF CANTERBURY
Te Whare Wānanga o Waitaha
CHRISTCHURCH NEW ZEALAND

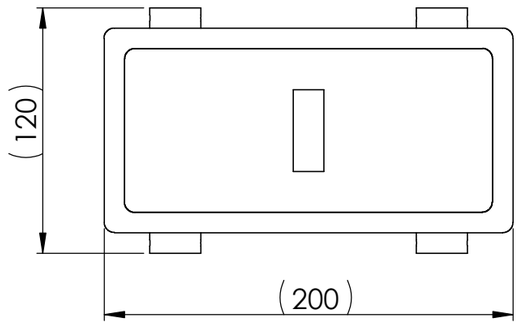

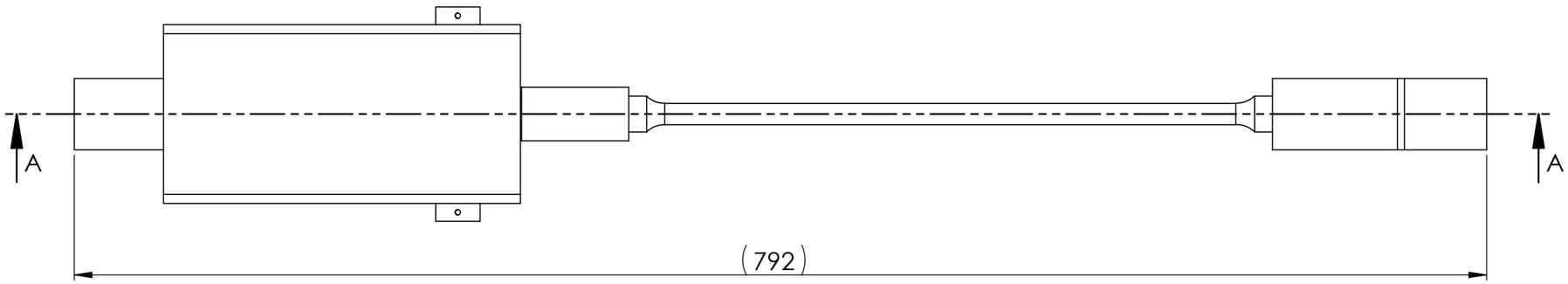

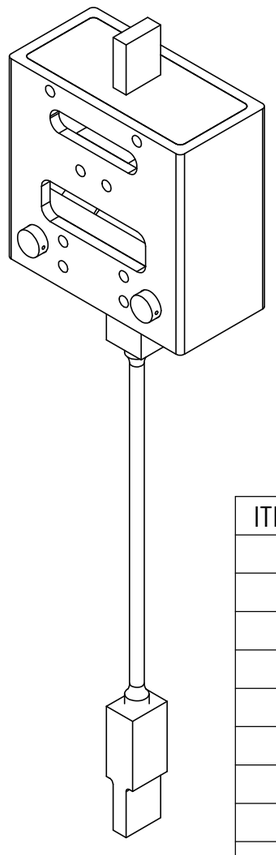

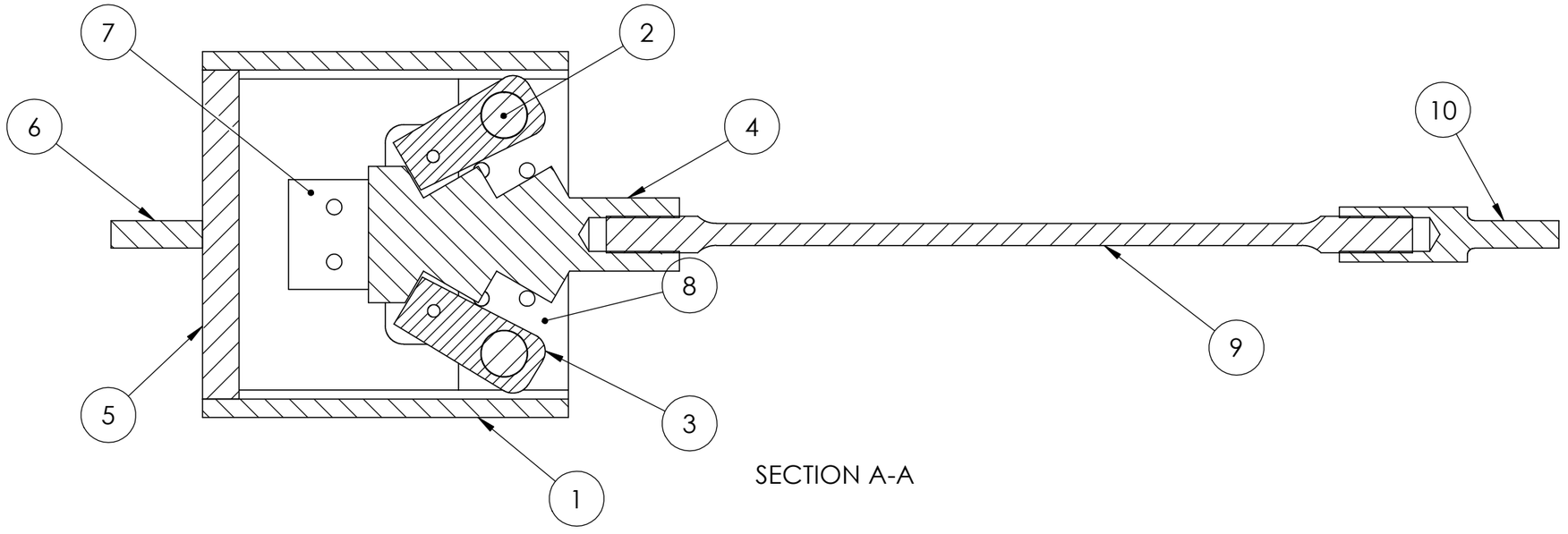

SECTION A-A

ITEM NO.	PART NAME	QTY.
1	MAIN SUPPORT	1
2	PAWL PIN	2
3	PAWL	4
4	RACK	4
5	COVER PLATE	1
6	UPPER TONGUE	2
7	UPPER RACK SUPPORT	2
8	LOWER RACK SUPPORT	2
9	FUSE	6
10	LOWER TONGUE	1

4 RACKS REQUIRED
--2 OF EACH DESIGN--

SPRINGS AND FASTENERS NOT SHOWN

THIRD ANGLE PROJECTION

UNIVERSITY OF CANTERBURY ©
DEPARTMENT OF MECHANICAL ENGINEERING

UNIVERSITY OF CANTERBURY
Te Whare Wānanga o Waitaha
CHRISTCHURCH NEW ZEALAND

RATCHET ASSEMBLY

MATERIAL: --

FINISH: --

TOLERANCE (UNLESS OTHERWISE SPECIFIED)
DECIMAL mm
.X ± -- .XX ± -- .XXX ± -- ANG. ± --

DESIGN	DWG NO.	REV
JARROD COOK	RF-02-12	--

DRAWN	PROJECT		
JARROD COOK	RATCHET FUSE		
SUPERVISOR: GEOFF RODGERS	ISSUE DATE: 17 JUNE 2014	DRAWING NOT TO SCALE	SHEET: 12 OF 12

A2 GNG2 prototype engineering drawings

The following appendix contains the engineering drawings used to produce the second GNG prototype device. Note that the yielding steel dissipater component was labelled in the original design as the 'fuse'. The part and assembly drawings attached include:

1. GNG2 assembly
2. Main support body
3. Collet guide
4. Collet (10 mm pitch size)
5. Rack (10 mm pitch size)
6. Cover plate
7. Reset collar
8. Spring-bearing washer (labelled as spring washer)
9. Collet (3 mm pitch size)
10. Rack (3 mm pitch size)

NOTES - (UNLESS OTHERWISE SPECIFIED)

1. ALL DIMENSIONS IN MILLIMETERS.
2. GD&T AS PER ISO1101-2004.
3. BREAK ALL SHARP EDGES.

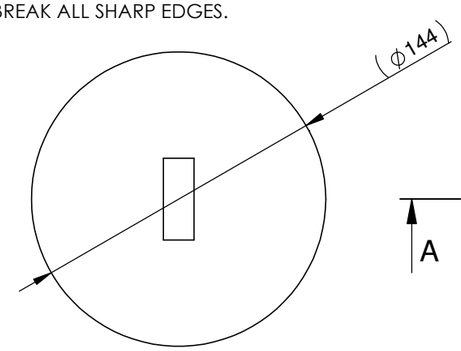

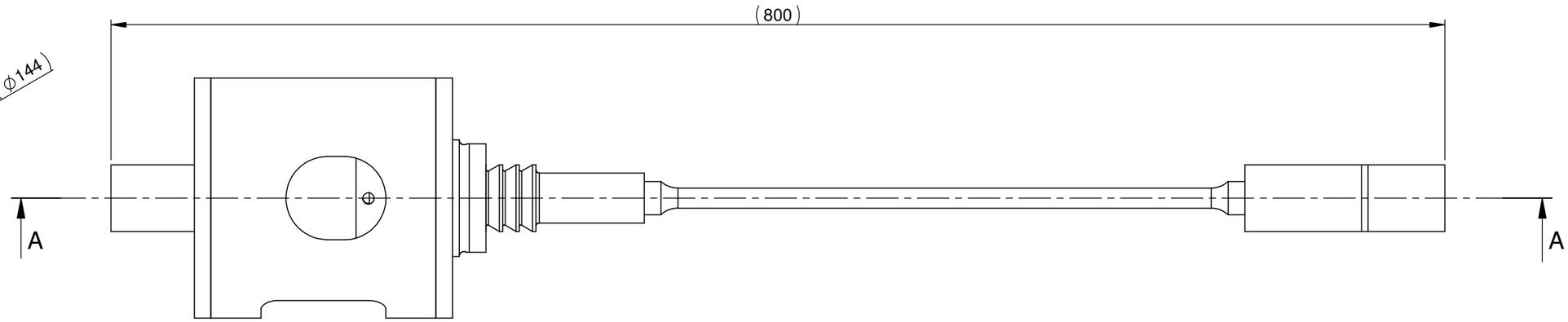

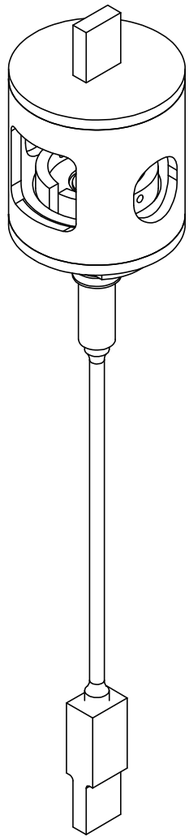

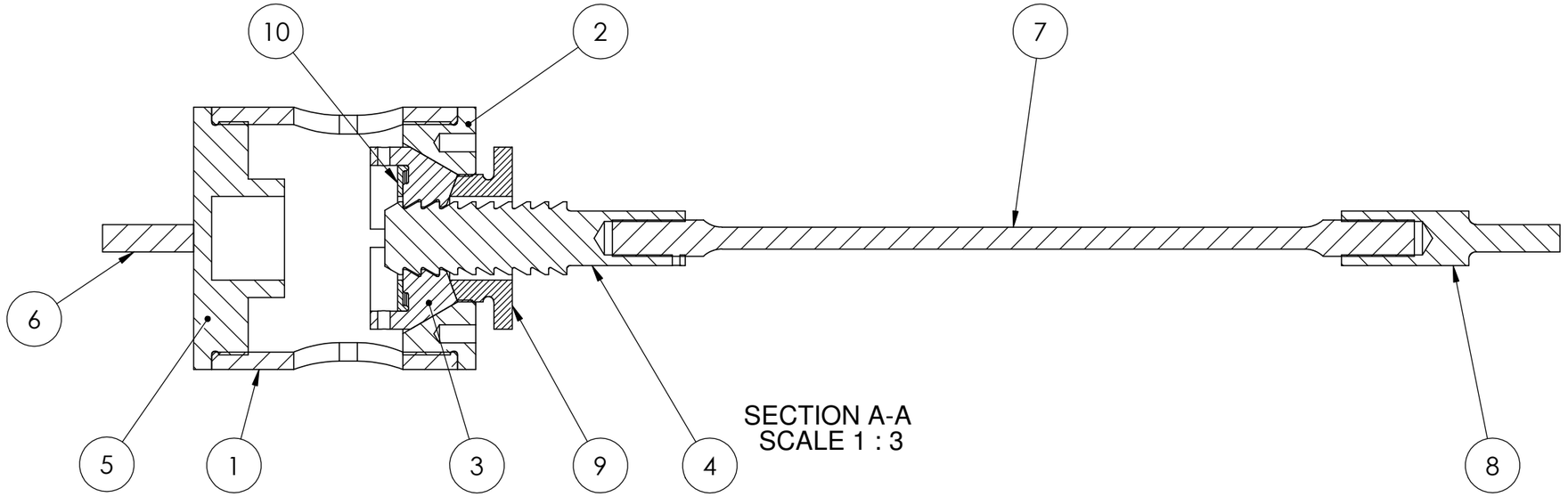

SECTION A-A
SCALE 1 : 3

ITEM NO.	PART	QTY.
1	MAIN SUPPORT	1
2	COLLET GUIDE	1
3	COLLET	2
4	RACK	1
5	COVER PLATE	1
6	UPPER TONGUE	1
7	FUSE	1
8	LOWER TONGUE	1
9	RESET COLLAR	1
10	SPRING WASHER	1

NB. EXISTING TONGUES AND FUSES TO BE USED

NB. FROM SINGLE TURNED PART

FASTENERS AND COMPRESSION SPRING OMITTED

THIRD ANGLE PROJECTION

MATERIAL: REFER TO PART DRAWINGS

FINISH: REFER TO PART DRAWINGS

TOLERANCE (UNLESS OTHERWISE SPECIFIED)

DECIMAL mm

.X ± .1 **.XX** ± .03 **.XXX** ± .010 **ANG.** ± 1°

UNIVERSITY OF CANTERBURY ©
DEPARTMENT OF MECHANICAL ENGINEERING

RATCHET FUSE ASSEMBLY

DESIGN: JARROD COOK	DWG NO.: RFA-11	REV: REV1	
DRAWN: JARROD COOK	PROJECT: RATCHET FUSE - AXISYMMETRIC		
SUPERVISOR: GEOFF RODGERS	ISSUE DATE: 19DEC14	DRAWING NOT TO SCALE	SHEET: 1 OF 8

NOTES - (UNLESS OTHERWISE SPECIFIED)

1. ALL DIMENSIONS IN MILLIMETERS.
2. GD&T AS PER ISO1101-2004.
3. BREAK ALL SHARP EDGES.

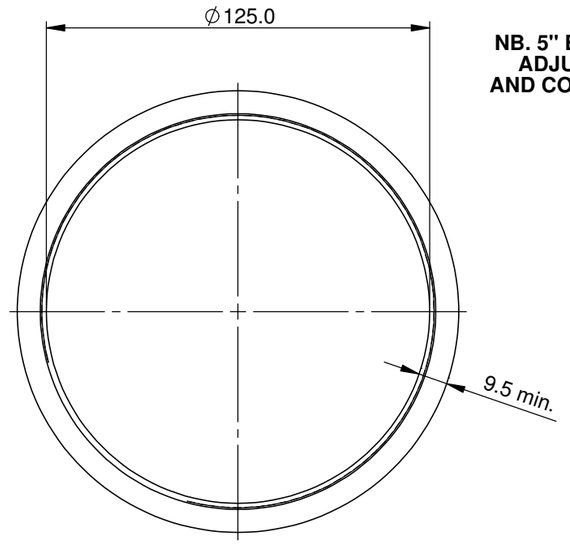

**NB. 5" BORE ACCEPTABLE:
ADJUST COVER PLATE
AND COLLET GUIDE TO SUIT**

NB. 0.375" OR 0.500" OK

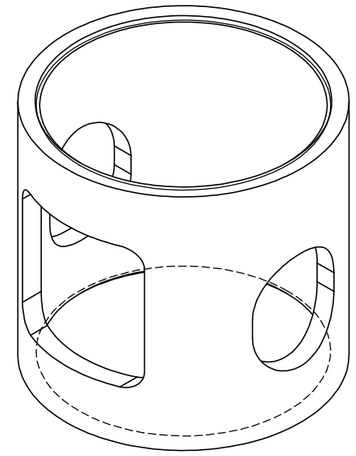

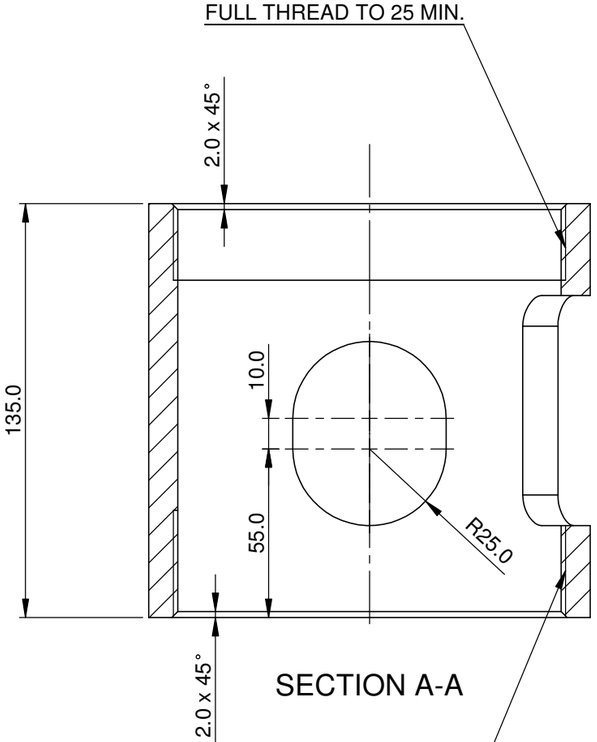

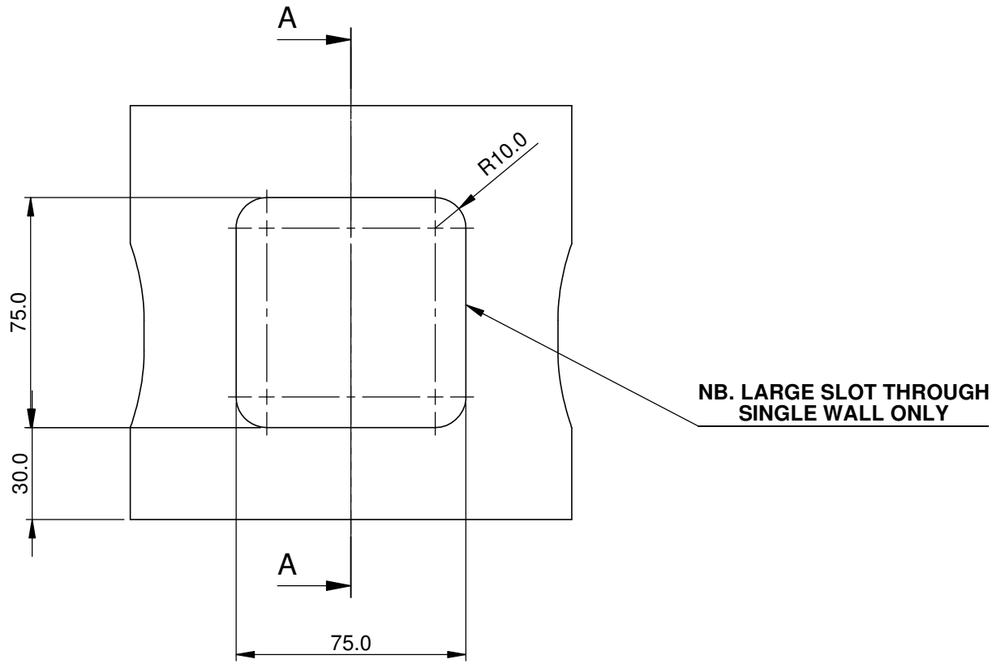

**NB. LARGE SLOT THROUGH
SINGLE WALL ONLY**

THIRD ANGLE PROJECTION

UNIVERSITY OF CANTERBURY ©
DEPARTMENT OF MECHANICAL ENGINEERING

UNIVERSITY OF CANTERBURY
Te Whare Wānanga o Waitaha
CHRISTCHURCH NEW ZEALAND

MATERIAL: AISI 1040 OR EQUIVALENT MINIMUM

FINISH: AS MACHINED

TOLERANCE (UNLESS OTHERWISE SPECIFIED)
DECIMAL mm
.X ± .1 **.XX** ± .05 **.XXX** ± .010 **ANG.** ± 1°

MAIN SUPPORT

DESIGN	DWG NO.	REV
JARROD COOK	RFA-02	REV1
DRAWN: JARROD COOK	PROJECT: RATCHET FUSE - AXISYMMETRIC	
SUPERVISOR: GEOFF RODGERS	ISSUE DATE: 19DEC14	DRAWING NOT TO SCALE
		SHEET: 2 OF 8

NOTES - (UNLESS OTHERWISE SPECIFIED)

1. ALL DIMENSIONS IN MILLIMETERS.
2. GD&T AS PER ISO1101-2004.
3. BREAK ALL SHARP EDGES.

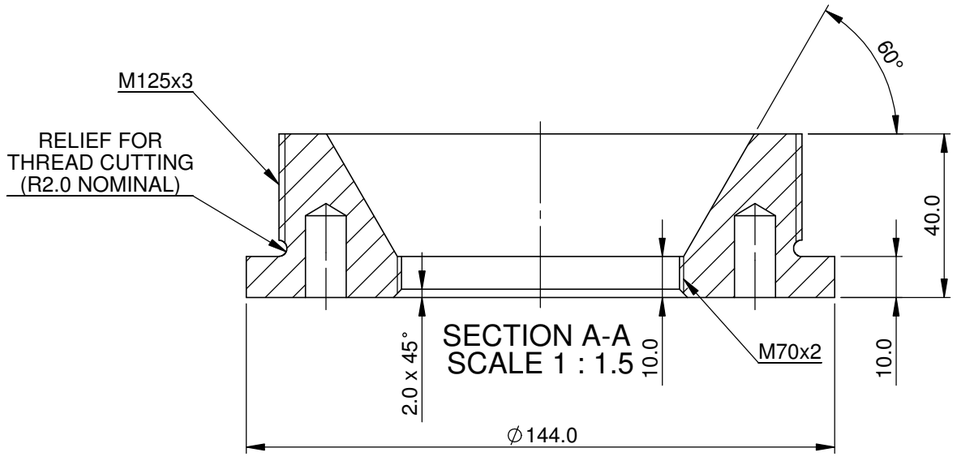

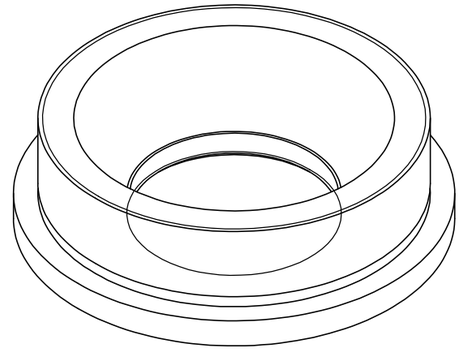

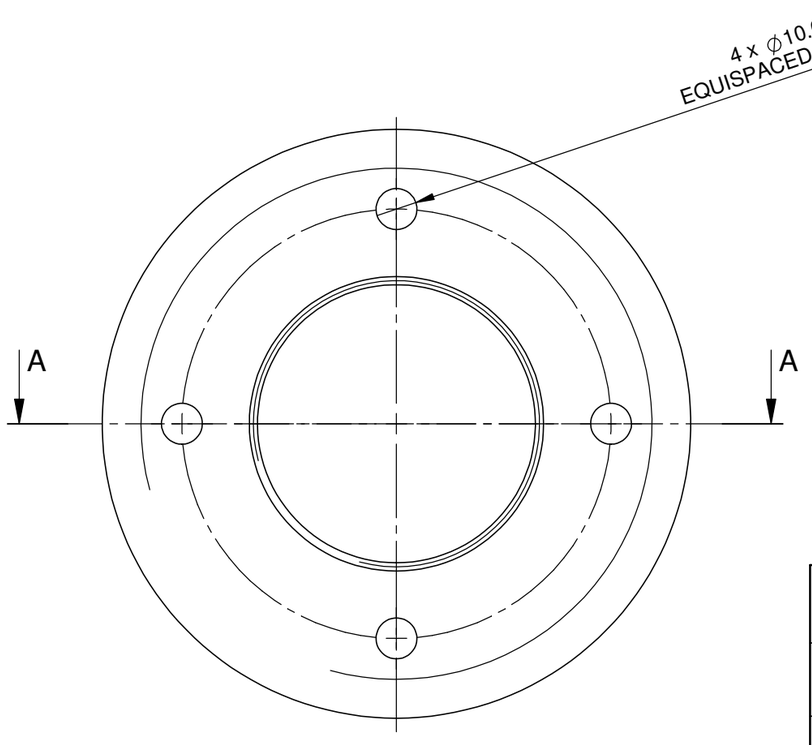

UNIVERSITY OF CANTERBURY ©
DEPARTMENT OF MECHANICAL ENGINEERING

UNIVERSITY OF CANTERBURY
Te Whare Wānanga o Waitaha
CHRISTCHURCH NEW ZEALAND

MATERIAL: AISI 4140 OR EQUIVALENT PREFERRED
AISI 1040 OR EQUIVALENT MINIMUM

FINISH: AS MACHINED

TOLERANCE (UNLESS OTHERWISE SPECIFIED)
DECIMAL mm
.X ± .1 .XX ± .05 .XXX ± .010 ANG. ± 1°

COLLET GUIDE

DESIGN: JARROD COOK	DWG NO.: RFA-03	REV: REV1	
DRAWN: JARROD COOK	PROJECT: RATCHET FUSE - AXISYMMETRIC		
SUPERVISOR: GEOFF RODGERS	ISSUE DATE: 19DEC14	DRAWING NOT TO SCALE	SHEET: 3 OF 8

NOTES - (UNLESS OTHERWISE SPECIFIED)

1. ALL DIMENSIONS IN MILLIMETERS.
2. GD&T AS PER ISO1101-2004.
3. BREAK ALL SHARP EDGES.

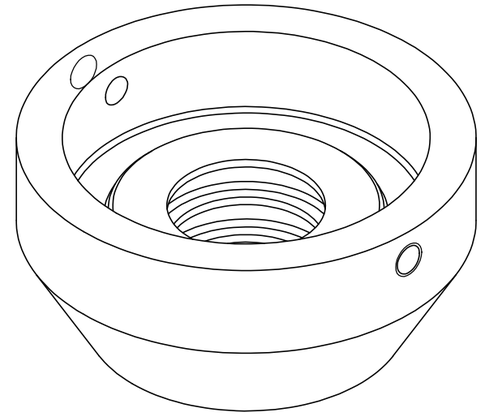

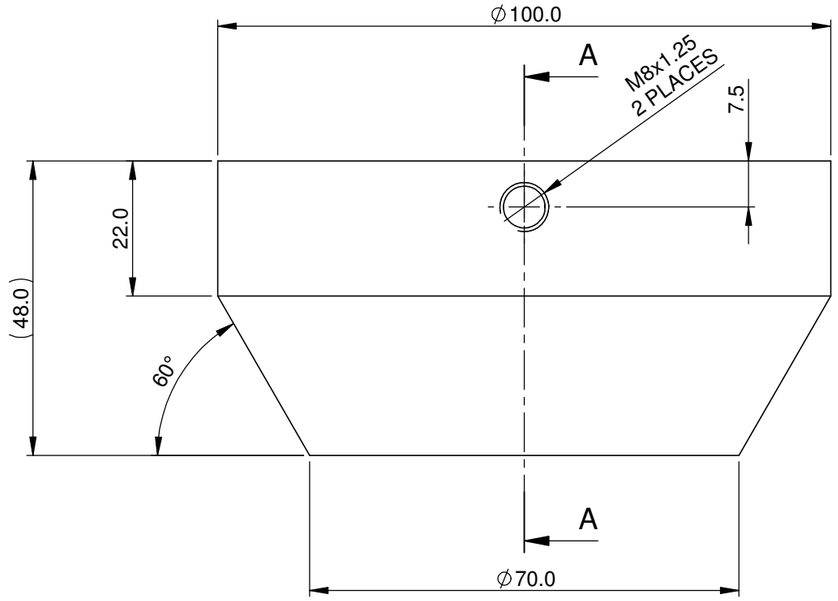

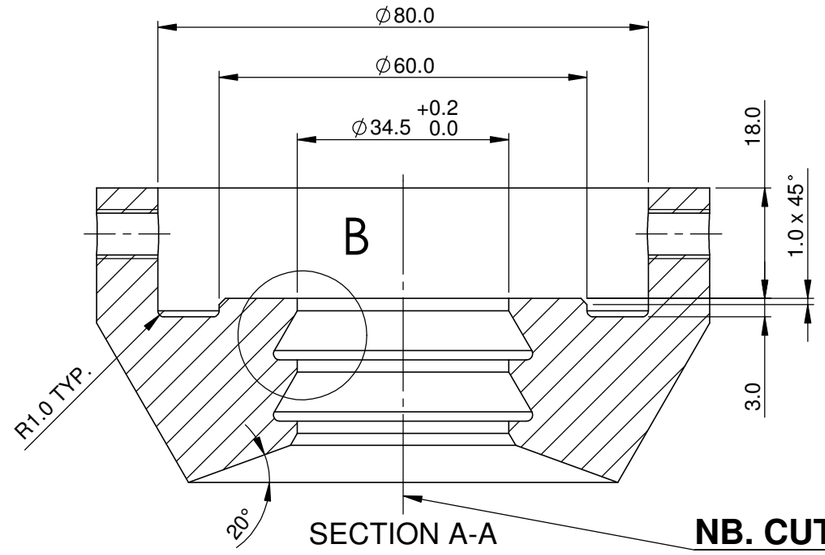

SECTION A-A **NB. CUT**

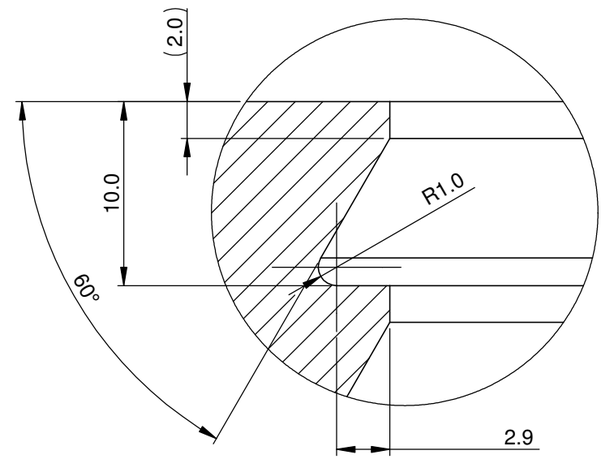

DETAIL B
SCALE 3 : 1

THIRD ANGLE PROJECTION	THIS DOCUMENT IS ISSUED IN STRICT CONFIDENCE ON CONDITION THAT IT IS NOT COPIED, REPRINTED, OR DISCLOSED TO A THIRD PARTY EITHER WHOLLY OR IN PART WITHOUT THE WRITTEN CONSENT OF UNIVERSITY OF CANTERBURY	UNIVERSITY OF CANTERBURY © DEPARTMENT OF MECHANICAL ENGINEERING	UNIVERSITY OF CANTERBURY Te Whare Wānanga o Waitaha CHRISTCHURCH NEW ZEALAND
MATERIAL: AISI 4140 OR EQUIVALENT		COLLET	
FINISH: AS MACHINED		DESIGN: JARROD COOK / DWG NO.: RFA-04	REV: REV1
TOLERANCE (UNLESS OTHERWISE SPECIFIED) DECIMAL mm: .X ± .1 .XX ± .05 .XXX ± .010 ANG. ± 1°		DRAWN: JARROD COOK / PROJECT: RATCHET FUSE - AXISYMMETRIC	
		SUPERVISOR: GEOFF RODGERS / ISSUE DATE: 19DEC14 / DRAWING NOT TO SCALE	SHEET: 4 OF 8

NOTES - (UNLESS OTHERWISE SPECIFIED)

1. ALL DIMENSIONS IN MILLIMETERS.
2. GD&T AS PER ISO1101-2004.
3. BREAK ALL SHARP EDGES.

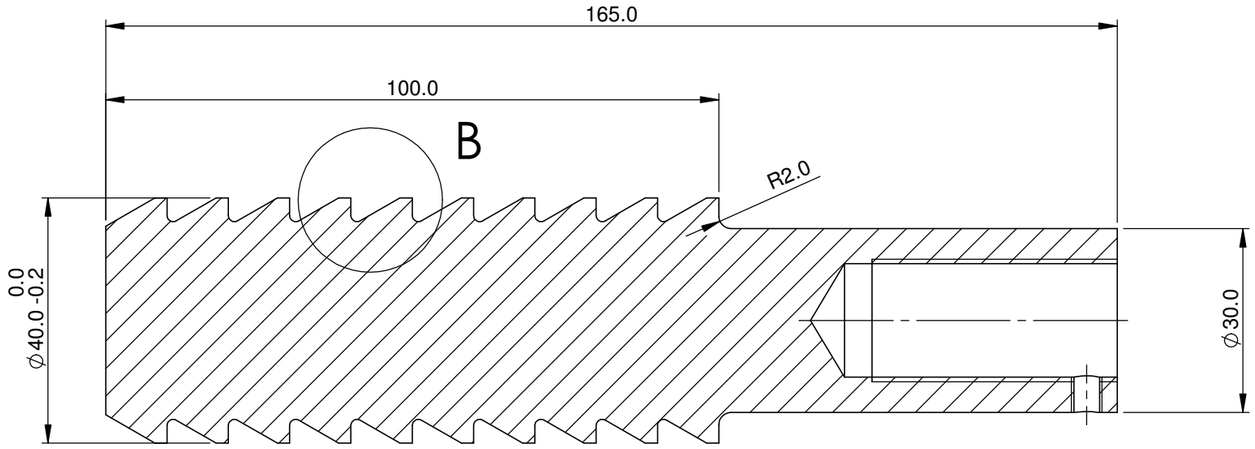

SECTION A-A
SCALE 1 : 1

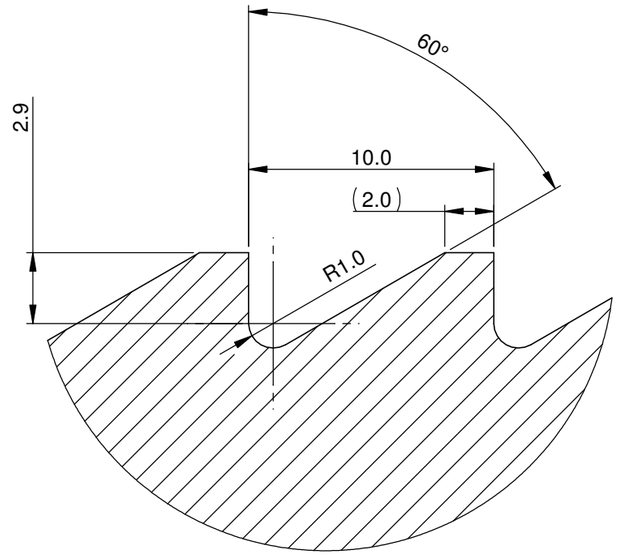

DETAIL B
SCALE 4 : 1

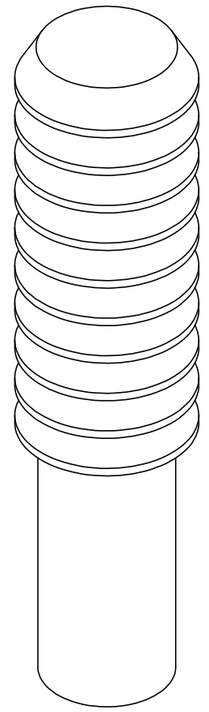

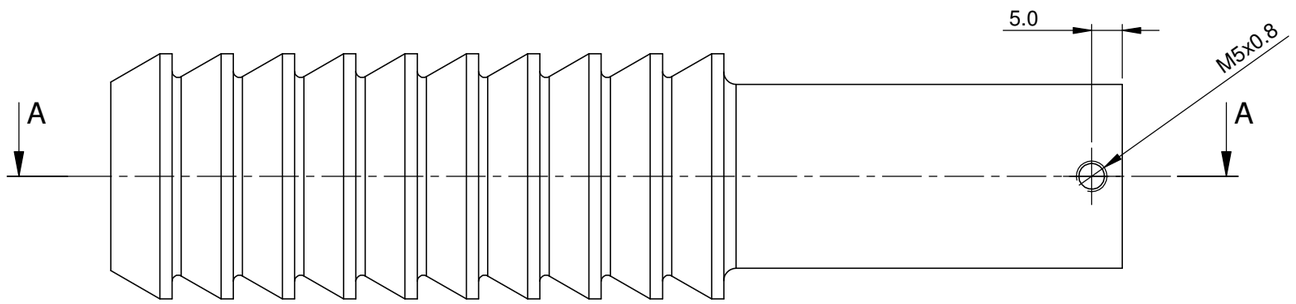

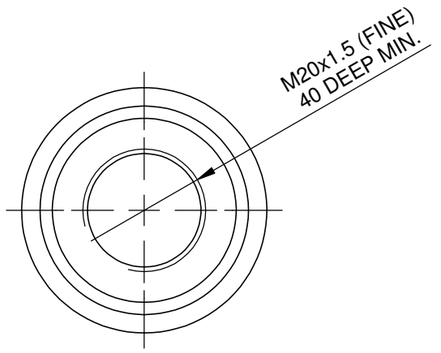

THIRD ANGLE PROJECTION		UNIVERSITY OF CANTERBURY © DEPARTMENT OF MECHANICAL ENGINEERING	UNIVERSITY OF CANTERBURY Te Whare Wānanga o Waitaha CHRISTCHURCH NEW ZEALAND
MATERIAL: AISI 4140 OR EQUIVALENT		RACK	
FINISH: AS MACHINED		DESIGN: JARROD COOK	DWG NO.: RFA-08 / REV: REV1
TOLERANCE (UNLESS OTHERWISE SPECIFIED) DECIMAL mm: .X ± .1 .XX ± .05 .XXX ± .010 ANG. ± 1°		DRAWN: JARROD COOK	PROJECT: RATCHET FUSE - AXISYMMETRIC
		SUPERVISOR: GEOFF RODGERS	ISSUE DATE: 19DEC14 / DRAWING NOT TO SCALE / SHEET: 5 OF 8

NOTES - (UNLESS OTHERWISE SPECIFIED)

1. ALL DIMENSIONS IN MILLIMETERS.
2. GD&T AS PER ISO1101-2004.
3. BREAK ALL SHARP EDGES.

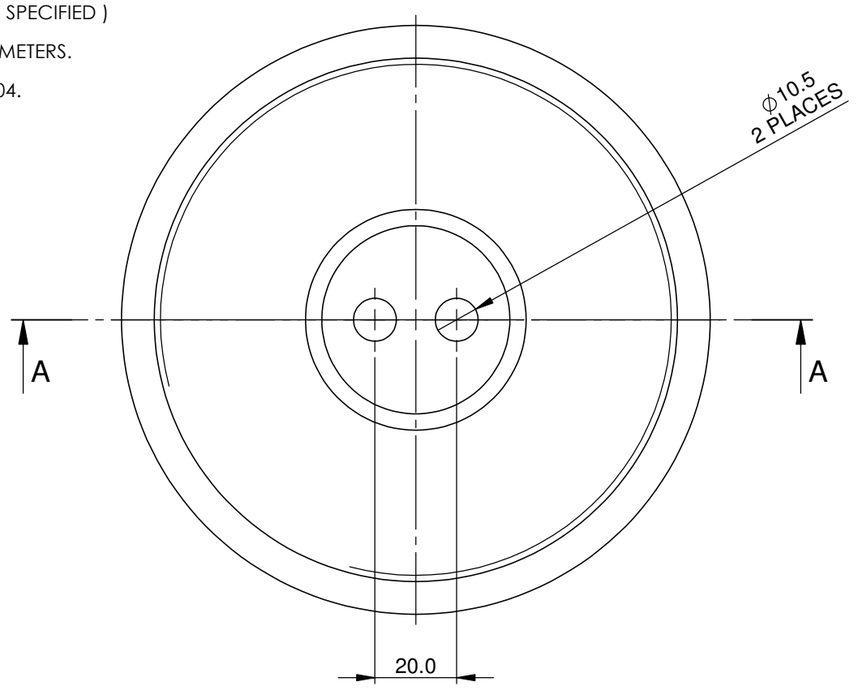

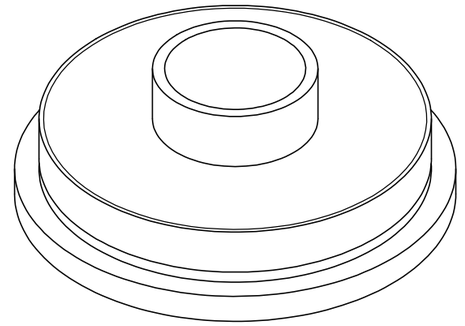

NB. REDUCED DIAMETER

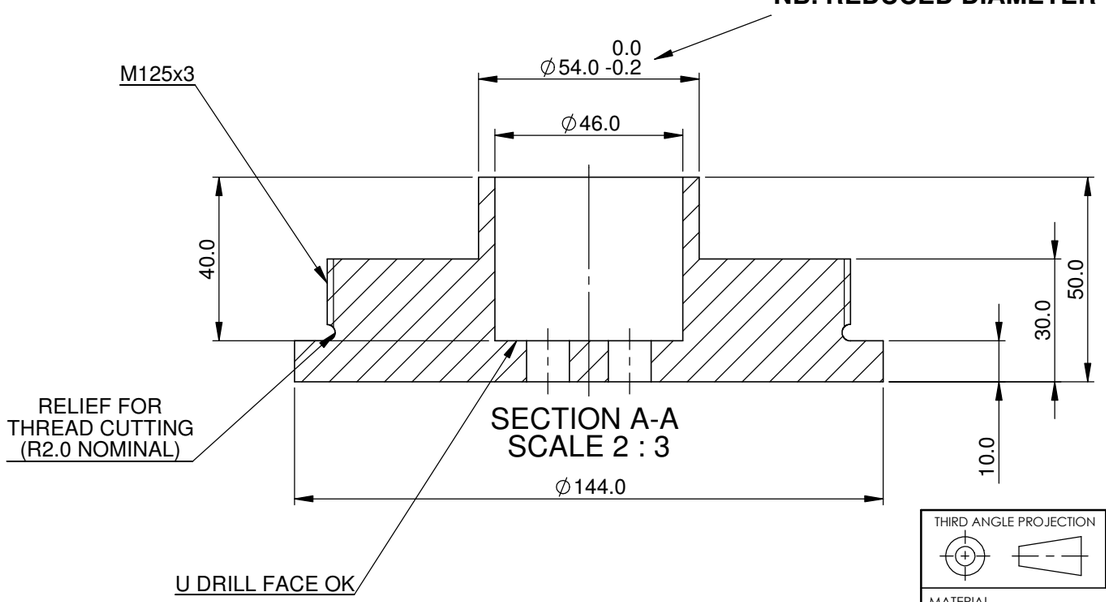

THIRD ANGLE PROJECTION

MATERIAL: AISI 1040 OR EQUIVALENT

FINISH: AS MACHINED

TOLERANCE (UNLESS OTHERWISE SPECIFIED)

DECIMAL mm

.X ± .1 **.XX** ± .05 **.XXX** ± .010 **ANG.** ± 1°

UNIVERSITY OF CANTERBURY ©
DEPARTMENT OF MECHANICAL ENGINEERING

COVER PLATE

DESIGN	DWG NO.	REV
JARROD COOK	RFA-06	REV1

DRAWN	PROJECT
JARROD COOK	RATCHET FUSE - AXISYMMETRIC

SUPERVISOR	ISSUE DATE		SHEET
GEOFF RODGERS	02FEB15	DRAWING NOT TO SCALE	6 OF 8

NOTES - (UNLESS OTHERWISE SPECIFIED)

1. ALL DIMENSIONS IN MILLIMETERS.
2. GD&T AS PER ISO1101-2004.
3. BREAK ALL SHARP EDGES.

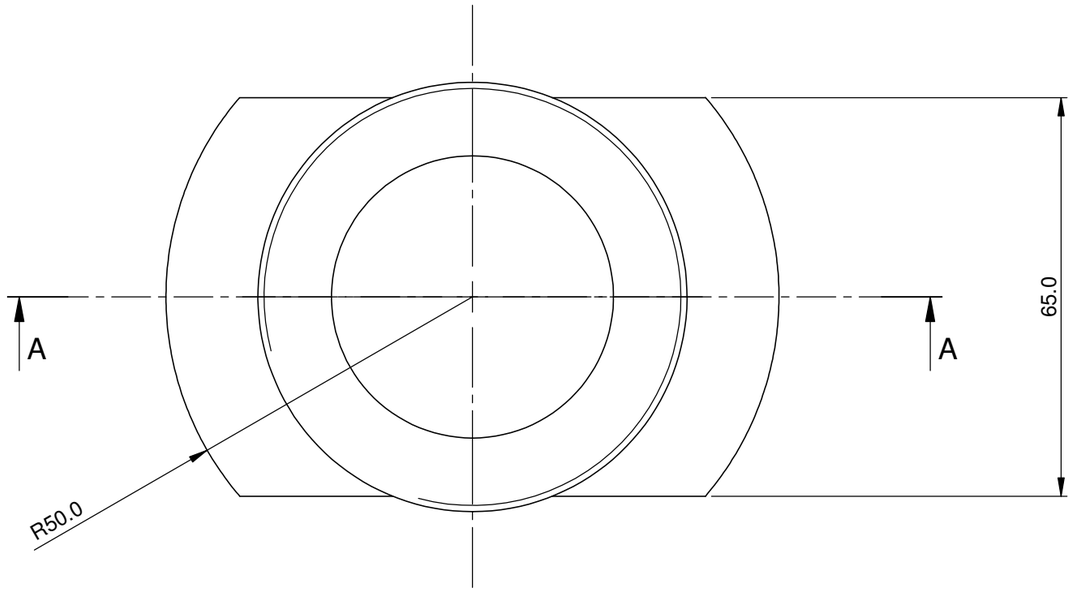

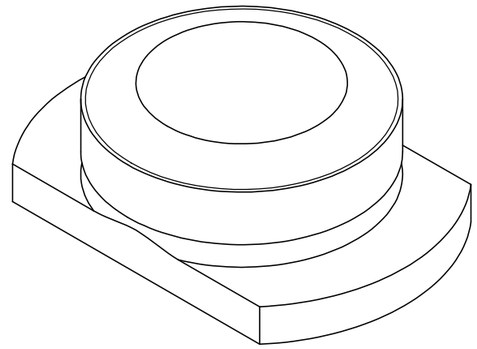

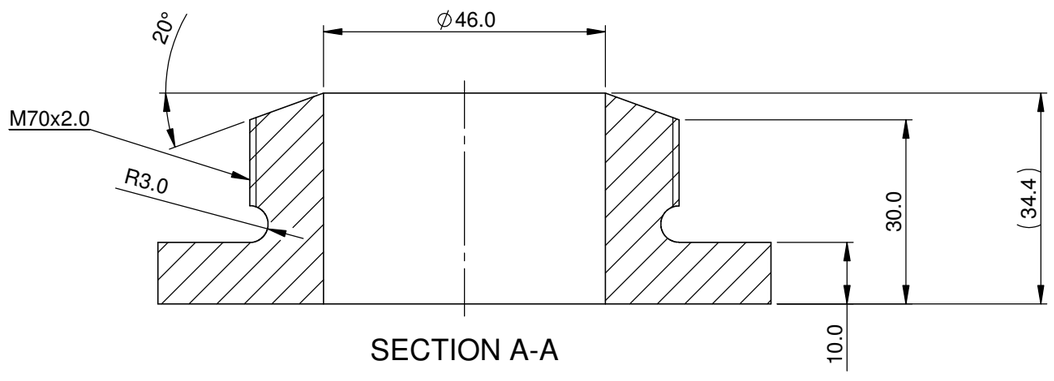

SECTION A-A

THIRD ANGLE PROJECTION

MATERIAL: AISI 1040 OR EQUIVALENT

FINISH: AS MACHINED

TOLERANCE (UNLESS OTHERWISE SPECIFIED)

DECIMAL mm

.X ± .1 **.XX** ± .05 **.XXX** ± .010 **ANG.** ± 1°

UNIVERSITY OF CANTERBURY ©
DEPARTMENT OF MECHANICAL ENGINEERING

RESET COLLAR

DESIGN: JARROD COOK	DWG NO.: RFA-07		REV: REV1
DRAWN: JARROD COOK	PROJECT: RATCHET FUSE - AXISYMMETRIC		
SUPERVISOR: GEOFF RODGERS	ISSUE DATE: 19DEC14	DRAWING NOT TO SCALE	SHEET: 7 OF 8

NOTES - (UNLESS OTHERWISE SPECIFIED)

1. ALL DIMENSIONS IN MILLIMETERS.
2. GD&T AS PER ISO1101-2004.
3. BREAK ALL SHARP EDGES.

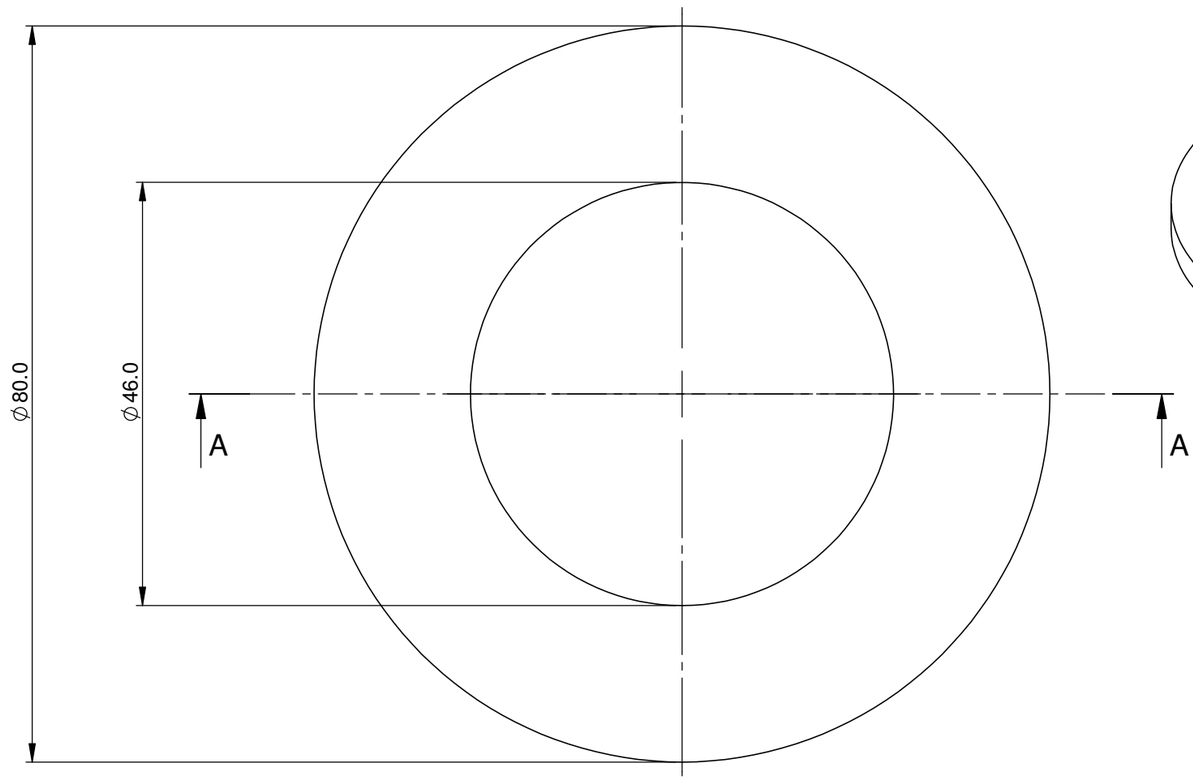

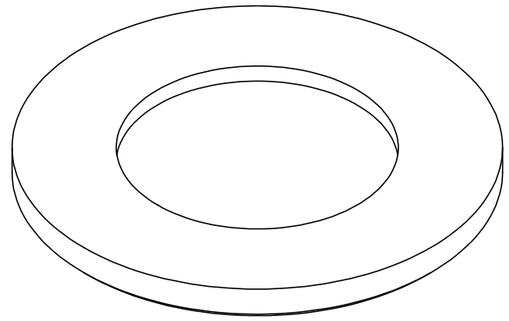

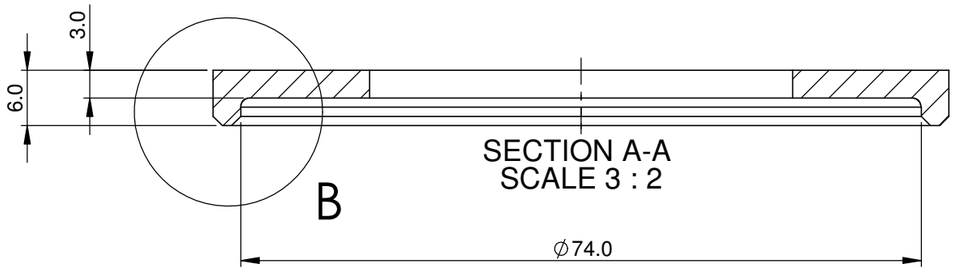

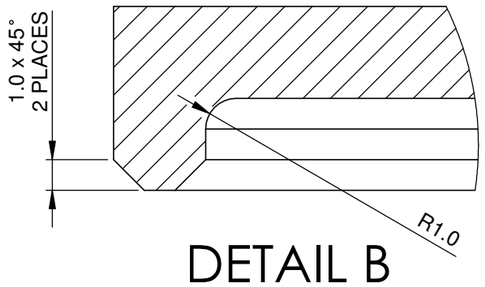

DETAIL B
SCALE 5 : 1

THIRD ANGLE PROJECTION

UNIVERSITY OF CANTERBURY ©
DEPARTMENT OF MECHANICAL ENGINEERING

UNIVERSITY OF CANTERBURY
Te Whare Wānanga o Waitaha
CHRISTCHURCH NEW ZEALAND

MATERIAL: AISI 1040 OR EQUIVALENT

FINISH: AS MACHINED

TOLERANCE (UNLESS OTHERWISE SPECIFIED)
DECIMAL mm
.X ± .1 .XX ± .05 .XXX ± .010 ANG. ± 1°

SPRING WASHER

DESIGN	DWG NO.	REV
JARROD COOK	RFA-05	REV1
DRAWN: JARROD COOK	PROJECT: RATCHET FUSE - AXISYMMETRIC	
SUPERVISOR: GEOFF RODGERS	ISSUE DATE: 19DEC14	DRAWING NOT TO SCALE / SHEET: 8 OF 8

NOTES - (UNLESS OTHERWISE SPECIFIED)

1. ALL DIMENSIONS IN MILLIMETERS.
2. GD&T AS PER ISO1101-2004.

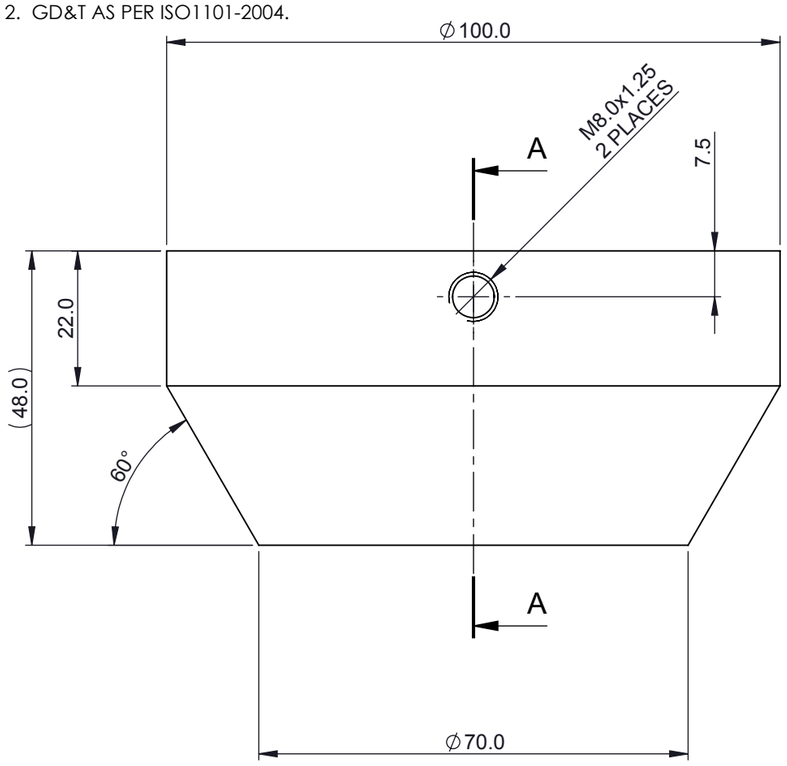

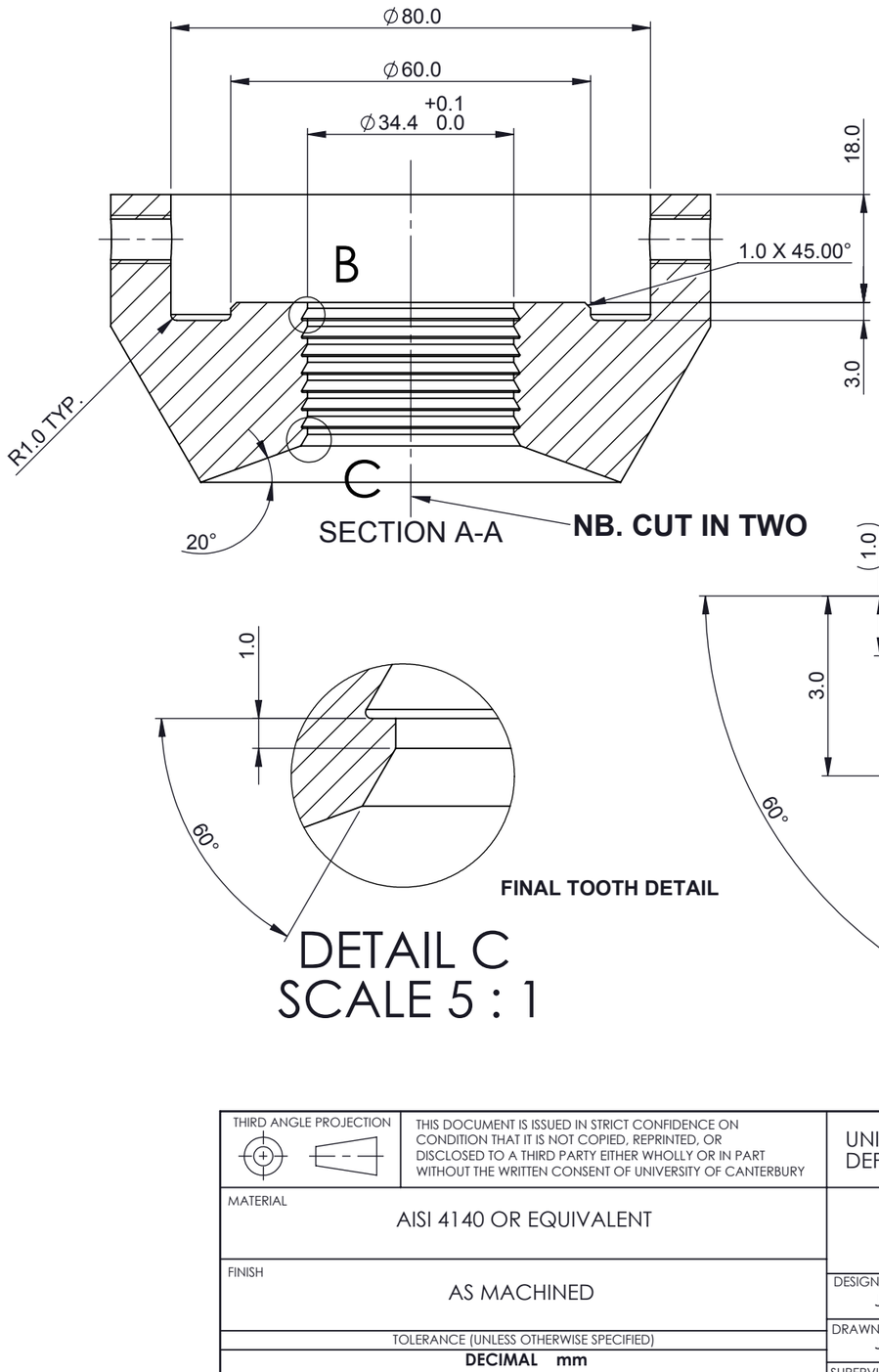

NB. CUT IN TWO

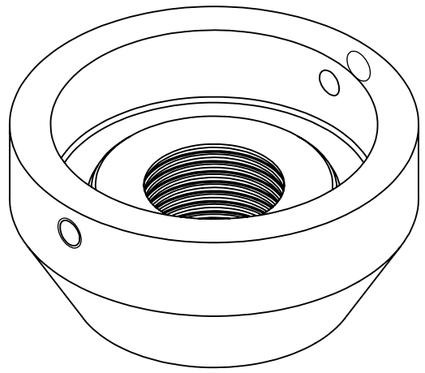

FINAL TOOTH DETAIL

DETAIL C
SCALE 5 : 1

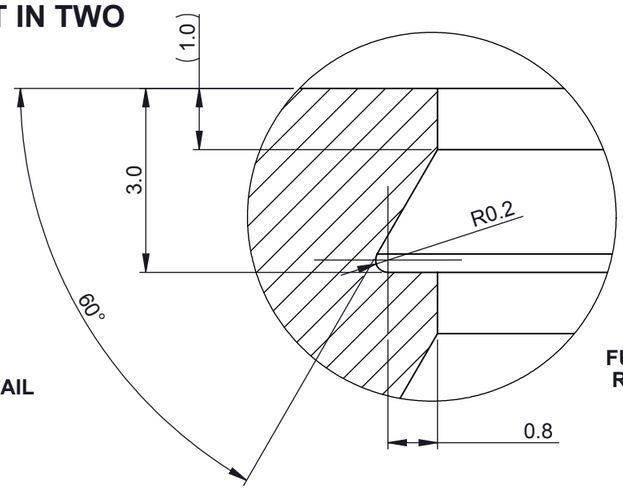

FULL TOOTH DETAIL REPEATED 7 TIMES

DETAIL B
SCALE 10 : 1

NB. TWO CUT PIECES TO BE MILLED TO SUIT 45 MM DIMENSION SHOWN

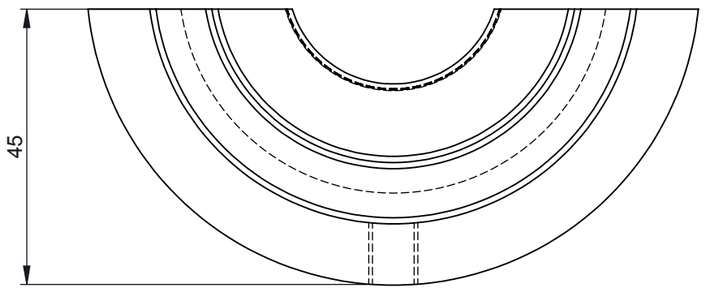

THIRD ANGLE PROJECTION		UNIVERSITY OF CANTERBURY © DEPARTMENT OF MECHANICAL ENGINEERING	UNIVERSITY OF CANTERBURY
MATERIAL: AISI 4140 OR EQUIVALENT		COLLET P3	
FINISH: AS MACHINED		DESIGN: JARROD COOK	DWG NO.: RFA-12 / REV: REV1
TOLERANCE (UNLESS OTHERWISE SPECIFIED) DECIMAL mm: .X ± .1 .XX ± .05 .XXX ± .010 ANG. ± 1°		DRAWN: JARROD COOK	PROJECT: RATCHET FUSE - AXISYMMETRIC
		SUPERVISOR: GEOFF RODGERS	ISSUE DATE: 19 MAY 2015 / DRAWING NOT TO SCALE / SHEET: 1 OF 1

NOTES - (UNLESS OTHERWISE SPECIFIED)

1. ALL DIMENSIONS IN MILLIMETERS.
2. GD&T AS PER ISO1101-2004.

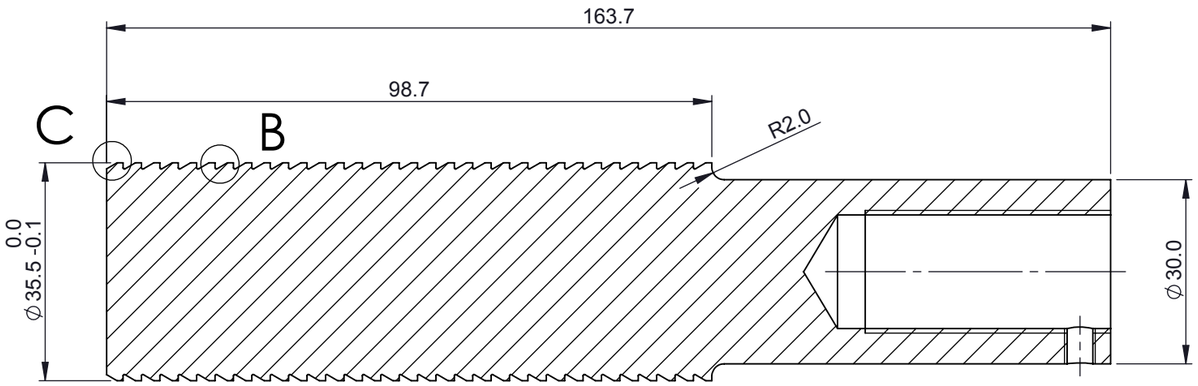

SECTION A-A
SCALE 1 : 1

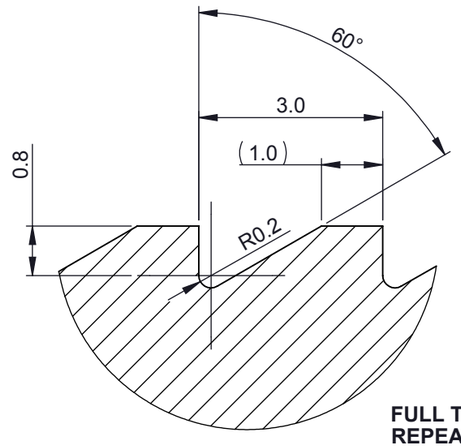

FULL TOOTH DETAIL
REPEATED 32 TIMES

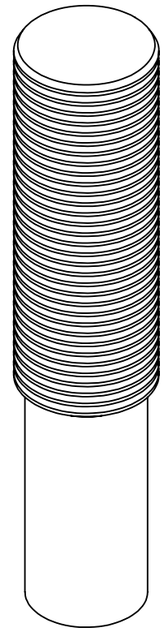

DETAIL B
SCALE 10 : 1

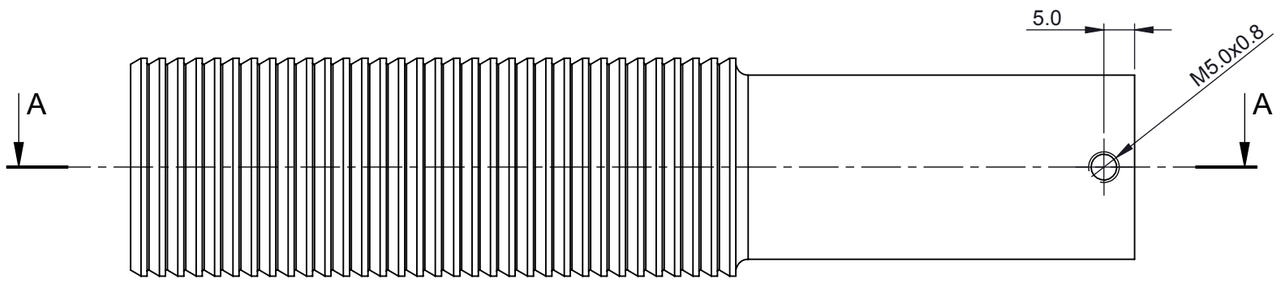

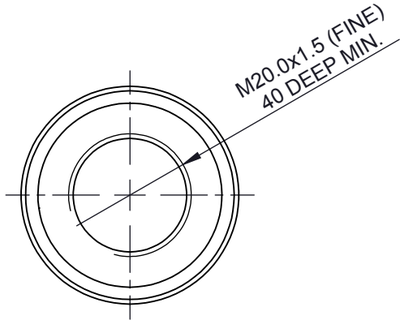

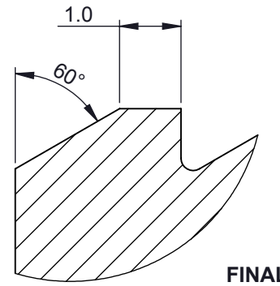

FINAL TOOTH DETAIL

DETAIL C
SCALE 10 : 1

THIRD ANGLE PROJECTION	THIS DOCUMENT IS ISSUED IN STRICT CONFIDENCE ON CONDITION THAT IT IS NOT COPIED, REPRINTED, OR DISCLOSED TO A THIRD PARTY EITHER WHOLLY OR IN PART WITHOUT THE WRITTEN CONSENT OF UNIVERSITY OF CANTERBURY	UNIVERSITY OF CANTERBURY © DEPARTMENT OF MECHANICAL ENGINEERING	UC UNIVERSITY OF CANTERBURY
MATERIAL: AISI 4140 OR EQUIVALENT		RACK P3	
FINISH: AS MACHINED		DESIGN: JARROD COOK / DWG NO.: RFA-13 / REV: REV1	
TOLERANCE (UNLESS OTHERWISE SPECIFIED) DECIMAL mm: .X ± .1 .XX ± .05 .XXX ± .010 ANG. ± 1°		DRAWN: JARROD COOK / PROJECT: RATCHET FUSE - AXISYMMETRIC	
		SUPERVISOR: GEOFF RODGERS / ISSUE DATE: 19 MAY 2015 / DRAWING NOT TO SCALE / SHEET: 1 OF 1	

Appendix B System stiffness rearrangement

The following appendix contains the rearrangement omitted from Chapter 6 in the main text in the interest of clarity. Both stiffness ratios α and γ can be defined, and the required values of K_{PT} and K_{ED} calculated, using both versions of Equation (6.14). The resulting equations are presented below and were used in the numerical model presented in Chapter 7.

$$K_{PT}{d_{PT}}^2 + K_{ED}{d_{ED}}^2 = \frac{\alpha K_0 h^2}{1-\alpha} + W_{trib}H_W \tag{B.1}$$

$$K_{PT}{d_{PT}}^2 + \beta K_{ED}{d_{ED}}^2 = \frac{\gamma K_0 h^2}{1-\gamma} + W_{trib}H_W \tag{B.2}$$

(B.1) - (B.2):

$$(1-\beta)K_{ED}{d_{ED}}^2 = \frac{\alpha K_0 h^2}{1-\alpha} - \frac{\gamma K_0 h^2}{1-\gamma}$$

$$K_{ED} = \frac{\frac{\alpha K_0 h^2}{1-\alpha} - \frac{\gamma K_0 h^2}{1-\gamma}}{(1-\beta){d_{ED}}^2}$$

Substitute K_{ED} into (B.1):

$$K_{PT}{d_{PT}}^2 + \left(\frac{\frac{\alpha K_0 h^2}{1-\alpha} - \frac{\gamma K_0 h^2}{1-\gamma}}{(1-\beta){d_{ED}}^2}\right){d_{ED}}^2 = \frac{\alpha K_0 h^2}{1-\alpha} + W_{trib}H_W$$

$$K_{PT} = \frac{\frac{\alpha K_0 h^2}{1-\alpha} + W_{trib}H_W - \left(\frac{\frac{\alpha K_0 h^2}{1-\alpha} - \frac{\gamma K_0 h^2}{1-\gamma}}{(1-\beta){d_{ED}}^2}\right){d_{ED}}^2}{{d_{PT}}^2}$$

K_{ED} and K_{PT} are now defined in terms of the system geometry and the desired stiffness ratios.

Appendix C OpenSEES material model files

C1 Header file: GNGMaterial.h

The following appendix contains the header file for the GNG material model algorithm added to the OpenSEES software.

// 'Grip n Grab' ratcheting, tension-only device material model
// - file edited from EPPGapMaterial file
// Jarrod Cook, University of Canterbury, Christchurch, New Zealand

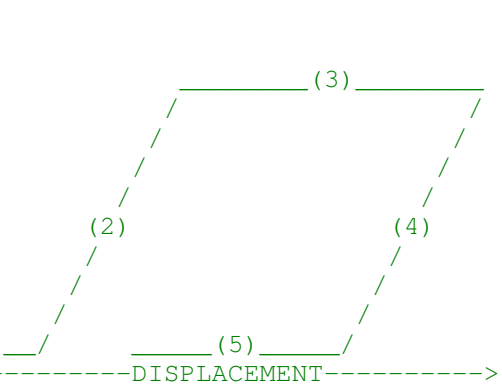

// LOADING
//   BELOW ENGAGEMENT THRESHOLD (1)
//   ELASTIC REGION (2)
//   BEYOND YIELD (3)
// UNLOADING
//   ELASTIC RECOVERY (4)
//   BELOW ENGAGEMENT THRESHOLD (5)

```
#ifndef GNGMaterial_h
#define GNGMaterial_h

#include <UniaxialMaterial.h>
#include <Information.h>

class GNGMaterial : public UniaxialMaterial
{
  public:

    //full constructor
    GNGMaterial(int tag, double E, double sigY, double P, double eta);

    //null constructor
    GNGMaterial();

    //destructor
    ~GNGMaterial();

    const char *getClassType(void) const {return "GNGMaterial";};

    int setTrialStrain(double strain, double strainRate = 0.0);
    double getStrain(void);
    double getStress(void);
    double getTangent(void);
```

```
    double getInitialTangent(void);

    int commitState(void);
    int revertToLastCommit(void);
    int revertToStart(void);

    UniaxialMaterial *getCopy(void);

    int sendSelf(int commitTag, Channel &theChannel);
    int recvSelf(int commitTag, Channel &theChannel,
         FEM_ObjectBroker &theBroker);

    void Print(OPS_Stream &s, int flag =0);

    Response* setResponse (const char **argv, int argc, OPS_Stream &theOutput);
    int getResponse (int responseID, Information &matInfo);

  protected:

  private:

    double commitStrain;
    double trialStrain;
    double E;
    double sigY;
    double P;
    double eta;
    double epsY;
    double epsE;
    double epsP;
    double sigP;
    double pdemand; //cumulative plastic demand
    int nratchet; //ratchet count

    double trialStress;      // current trial stress
    double trialTangent;     // current trial tangent

};


#endif
```

C2 Main file: GNGMaterial.cpp

The following appendix contains the main file for the GNG material model algorithm added to the OpenSEES software.

// 'Grip n Grab' ratcheting, tension-only device material model
// - file edited from EPPGapMaterial file
// Jarrod Cook, University of Canterbury, Christchurch, New Zealand

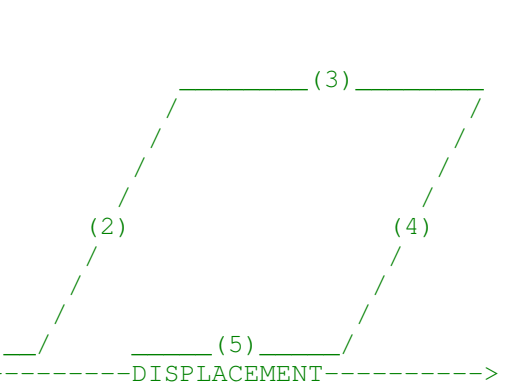

// LOADING
//   BELOW ENGAGEMENT THRESHOLD (1)
//   ELASTIC REGION (2)
//   BEYOND YIELD (3)
// UNLOADING
//   ELASTIC RECOVERY (4)
//   BELOW ENGAGEMENT THRESHOLD (5)

/* ** */

//Include Directives
//The first part of the file contains the list of includes. It is necessary to have an
//#include directive for each class and api file that is used within the .cpp file and
//is not included in the header.

#include <stdlib.h>

#include <GNGMaterial.h>
#include <Vector.h>
#include <Channel.h>
#include <math.h>
#include <float.h>
#include <elementAPI.h>
#include <OPS_Globals.h>

//Added when trying to add args to eleResponse
#include <MaterialResponse.h>
#include <Information.h>
#include <string.h>
#include <ID.h>
#include <FEM_ObjectBroker.h>
#include <OPS_Stream.h>

```
//External Procedure
//This is the all importat extenal procedure that the interpreter will parse when it
//comes accross your element on the command line. You need to parse the command line,
//create a material using the command line arguments you parsed and then return this
//material. The name of the procedure must be OPS_YourClassName (no exceptions). If this
//procedure is missing or the name is incorrect, your material will fail to load.

//NOTE: parsing the command line is easy with some other procedures that are defined in
//the elementAPI.h file. In the example we show how to get integer and double values from
//the command line. Other options such as character strings and obtaining the number of
//input arguments are also available.

static int numGNGMaterials = 0;

void* OPS_GNGMaterial()
{

    if (numGNGMaterials == 0) {
        numGNGMaterials++;
        opserr << "Grip 'n' Grab device installed in this structure!\n";
    }

    // Pointer to a uniaxial material that will be returned
    UniaxialMaterial *theMaterial = 0;

    int numArgs = OPS_GetNumRemainingInputArgs();
    if (numArgs < 4) {
    opserr << "Invalid #args,  want: uniaxialMaterial GNG tag E sigY P <eta>\n";
    return 0;
    }

    int tag;
    double dData[4];
    dData[3] = 0.0; // setting default eta to 0.

    int numData = 1;
    if (OPS_GetIntInput(&numData, &tag) != 0) {
    opserr << "WARNING invalid tag for uniaxialMaterial GNG" << endln;
    return 0;
    }

    numData = OPS_GetNumRemainingInputArgs();
    if(numData > 4) numData = 4;
    if (OPS_GetDoubleInput(&numData, dData) != 0) {
    opserr << "Invalid data for uniaxial GNG \n";
    return 0;
    }

    // Parsing was successful, allocate the material
    theMaterial = new GNGMaterial(tag, dData[0], dData[1], dData[2], dData[3]);
    if (theMaterial == 0) {
    opserr << "WARNING could not create uniaxialMaterial of type GNG\n";
    return 0;
    }

    return theMaterial;
}

//full constructor
GNGMaterial::GNGMaterial(int tag, double e, double sigY0, double p, double eta0)//, int accum)
:UniaxialMaterial(tag,MAT_TAG_GNG),
 commitStrain(0.0), trialStrain(0.0), E(e), sigY(sigY0), P(p), eta(eta0), epsE(0.0)
{
    epsP = 0.0;
    sigP = 0.0;
    pdemand = 0.0; //cumulative plastic demand
    nratchet = 0; //ratchet count

    if (E == 0.0) {
      opserr << "GNGMaterial::GNGMaterial -- E is zero, continuing with E = sigY/0.002\n";
      if (sigY != 0.0)
```

```
        E = fabs(sigY)/0.002;
      else {
        opserr << "GNGMaterial::GNGMaterial -- E and sigY are zero\n";
        exit(-1);
      }
    }
    else

      epsY = epsE + sigY/E;

    if (sigY*P<0) { // To Remove...
      opserr << "GNGMaterial::GNGMaterial -- Alternate signs on sigY and E encountered,
      continuing anyway\n";
    }

        if ( (eta >= 1) || (eta <= -1) ) {
          opserr << "GNGMaterial::GNGMaterial -- value of eta must be -1 <= eta <= 1,
          setting eta to 0\n";
          eta = 0;
        }

}

//null constructor
GNGMaterial::GNGMaterial()
:UniaxialMaterial(0,MAT_TAG_GNG),
 E(0.0), sigY(0.0), P(0.0), eta(0.0), epsE(0.0)
{

pdemand = 0.0;
nratchet = 0;

}

//Destructor
//Then we provide the destructor. In the destructor all memory that the the object created
//or was passed to it in the constructor must be destroyed. For this example we have no
//such memory. We could have left the destructor out entirely. Hoowever, it is good
//practice to leave it in your source code.

//destructor
GNGMaterial::~GNGMaterial()
{
  // does nothing
}

//setTrialStrain() Method
//This, as mentioned, is the method called when the element has computed a new strain
//for the element. The element will make subsequent calls to getStress() and getTangent()
//to obtain new values of these for the new strain. This is typically the most complicated
//method to write and to determine the theory for before you even write the code. All
//subsequent methods are trivial.

int
GNGMaterial::setTrialStrain(double strain, double strainRate)
{

  // set the trial strain
  trialStrain = strain;

  // determine trial stress and tangent

  // LOADING
  if (trialStrain > epsP) {

    // BEYOND YIELD (3)
    if (trialStrain >= epsY) {
        trialStress = sigY + eta*E*(trialStrain-epsY); // PLASTIC
        trialTangent = eta*E;

    // BELOW ENGAGEMENT THRESHOLD (1)
```

```
    } else if (trialStrain <= epsE) {
        trialStress = 0; // NO STRESS
        trialTangent = 0;

    }
    // ELASTIC REGION (2)
    else {
        trialStress = E*(trialStrain-epsE); // ELASTIC
        trialTangent = E;
    }

  }
  // UNLOADING
  else {

    // BELOW ENGAGEMENT THRESHOLD (5)
    if (trialStrain <= epsE) {
        trialStress = 0; // NO STRESS
        trialTangent = 0;

    // ELASTIC RECOVERY (4)
    } else {
        trialStress = E*(trialStrain-epsE); // ELASTIC
        trialTangent = E;
    }
  }

  if (trialStrain < 0) {

      trialTangent = 0;

  }

  return 0;

}

//Trivial Methods
//Next comes 3 rather simple methods that return basic information computed in the
//setTrialStrain(). You do of course have the option to ignore the setTrialStrain()
//method and compute the stress and tangent quantities again in the interests of
//saving memory.

//send back the strain
double
GNGMaterial::getStrain(void)
{
    return trialStrain;
}

//send back the stress
double
GNGMaterial::getStress(void)
{
  return trialStress;

}

//send back the tangent
double
GNGMaterial::getTangent(void)
{
  return trialTangent;
}

//send back the tangent
double
GNGMaterial::getInitialTangent(void)
{
  if (epsE > 0.0)
    return 0.0;
```

```
  else
    return E;
}

//Methods Dealing With Current State
//As mentioned, when the algorithm finds a solution state as it goes from one
//converged solution to the next. As it attempts to find these solutions it goes
//through a number of trial steps (each setTrialStrain() is invoked in each of these
//steps). Once it finds a trial step that is on the solution path it will stop and
//invoke commitState() on the material. Any state variables that the material uses
//needs to be updated at this time. Should the algorithm fail to find a solution it
//may return to the last converged step or indeed the start. You the developer must
//provide code so that your mateial can indeed go back to these states and report
//correct getTangent() and getStress() values for subsequent analysis atte,pts.

int
GNGMaterial::commitState(void)
{
    //update state variables for next step

// LOADING
if (trialStrain > epsP) {

    // BEYOND YIELD (3)
    if (trialStrain >= epsY) {
        epsE = trialStrain - trialStress/E; // UPDATE X AXIS CROSSING

        if (epsP > epsY) { //UPDATE CUMULATIVE PLASTIC DEMAND
            pdemand = pdemand + trialStrain - epsP;
        }
        else {
            pdemand = pdemand + trialStrain - epsY;
        }

    }

// UNLOADING

} else {

    // BELOW ENGAGEMENT THRESHOLD (5)
    if (trialStrain <= epsE) {
        if (trialStrain < (epsE - P)) { // CHECK FOR RATCHETING

            epsE = epsE - P; //*****LIMITED TO SINGLE RATCHET*****// max dy/dt appears to be
            < 5e-4

            epsY = epsE + sigY/E; // NEW YIELD STRAIN

            nratchet = nratchet + 1;
        }

    // ELASTIC RECOVERY (4)
    } else {
        if (sigP > sigY) {
            sigY = sigP; // NEW YIELD STRESS
            epsY = epsE + sigY/E; // NEW YIELD STRAIN
        }
    }
}

    epsP = trialStrain;
    sigP = trialStress;

    commitStrain = trialStrain;

    return 0;

}
```

```
int
GNGMaterial::revertToLastCommit(void)
{

    trialStrain = commitStrain;

    return 0;
}


int
GNGMaterial::revertToStart(void)
{
    commitStrain = 0.0;
    trialStrain = 0.0;

    pdemand = 0.0;
    nratchet = 0;

    epsP = 0.0;
    sigP = 0.0;
    epsE = 0.0;

    epsY = epsE + sigY/E;

    return 0;
}

//getCopy() Method
//This is the method called by each element or section to get unique copies of a material.

UniaxialMaterial *
GNGMaterial::getCopy(void)
{
    GNGMaterial *theCopy = new GNGMaterial(this->getTag(),E,sigY,P,eta);
    theCopy->trialStrain = trialStrain;

    theCopy-> epsP = epsP;
    theCopy-> sigP = sigP;
    theCopy-> epsE = epsE;
    theCopy-> sigY = sigY;
    theCopy-> epsY = epsY;
    theCopy-> pdemand = pdemand;
    theCopy-> nratchet = nratchet;

    return theCopy;
}

//Methods Dealing With Databases/Parallel Processing
//There are two methods provided which are required if the user wishes to use the
//database or parallel procesing features of the OpenSees applications. If neither
//are to be used, the developer need simply return a negative value in both methods.
//The idea is that the material must pack up it's information using Vector and ID
//objects and send it off to a Channel object. On the flip side, the receiving blank
//element must receive the same Vector and ID data, unpack it and set the variables.

int
GNGMaterial::sendSelf(int cTag, Channel &theChannel)
{
    //we place all the data needed to define the material and its state
    //into a vector object
  int res = 0;
  static Vector data(12);
  data(0) = this->getTag();
  data(1) = commitStrain;
  data(2) = E;
  data(3) = sigY;
  data(4) = P;
  data(5) = eta;
  data(6) = epsY;
  data(7) = epsE;
```

```
  data(8) = epsP;
  data(9) = sigP;
  data(10) = pdemand;
  data(11) = nratchet;

  //send the vector object to the channel
  res = theChannel.sendVector(this->getDbTag(), cTag, data);
  if (res < 0)
    opserr << "GNGMaterial::sendSelf() - failed to send data\n";

  return res;
}

int
GNGMaterial::recvSelf(int cTag, Channel &theChannel,
                      FEM_ObjectBroker &theBroker)
{
    //receive the vector object from the channel which defines material
    //parameters and state
  int res = 0;
  static Vector data(12);
  res = theChannel.recvVector(this->getDbTag(), cTag, data);
  if (res < 0)
    opserr << "GNGMaterial::recvSelf() - failed to recv data\n";
  else {
    this->setTag((int)data(0));
    commitStrain = data(1);
    trialStrain = commitStrain;
    E = data(2);
    sigY = data(3);
    P = data(4);
    eta = data(5);
    epsY = data(6);
    epsE = data(7);
    epsP = data(8);
    sigP = data(9);
    pdemand = data(10);
    nratchet = (int)data(11);

  }

  return res;
}

//Methods Dealing With Output
//Information is obtained by the user when the print command is invoked by the user
//and also when the user issues the recorder command. When the print command is invoked
//the Print method is invoked. This method simply prints information about the element,
//and then asks the material to do likewise.

void
GNGMaterial::Print(OPS_Stream &s, int flag)
{
    if (flag == OPS_PRINT_PRINTMODEL_MATERIAL) {
        s << "GNG tag: " << this->getTag() << endln;
        s << "  E: " << E << ", kinematic hardening ratio: " << eta << endln;
        s << "  sigY: " << sigY << endln;
        s << "  P: " << P << endln;
        s << " plastic demand: " << pdemand << endln;
        s << " ratchet count: " << nratchet << endln;
    }

    if (flag == OPS_PRINT_PRINTMODEL_JSON) {
        s << "\t\t\t{";
        s << "\"name\": \"" << this->getTag() << "\", ";
        s << "\"type\": \"GNG\", ";
        s << "\"E\": " << E << ", ";
        s << "\"eta\": " << eta << ", ";
        s << "\"sigY\": " << sigY << ", ";
        s << "\"P\": " << P << ", ";
        s << "\"plastic demand\": " << pdemand << ", ";
```

```
        s << "\"ratchet count\": " << nratchet << ", ";
    }
}

//Responses available to recorders

Response*
GNGMaterial::setResponse(const char **argv, int argc, OPS_Stream &theOutput)
{

    if (strcmp(argv[0],"demand") == 0) {

        return new MaterialResponse(this, 11, this->getStrain());

      }
    else if (strcmp(argv[0],"ratchetCount") == 0) {

        return new MaterialResponse(this, 12, this->getStrain());

      }

          //by default, See if the response is one of the defaults
      Response *res =  UniaxialMaterial::setResponse(argv, argc, theOutput);

      if (res != 0)      return res;
      else {
          opserr<<"error in GNGMaterial::setResponse"<<endln;
          return 0;
      }

}

int
GNGMaterial::getResponse(int responseID, Information &matInfo)
{

    if (responseID==11) {

        return matInfo.setDouble(pdemand);

    }
    else if (responseID==12) {

        return matInfo.setDouble(nratchet);

    }

    else {

      // Just call the base class method ... don't need to define
      // this function, but keeping it here just for clarity
      return UniaxialMaterial::getResponse(responseID, matInfo);

    }

}
```

Appendix D Sample OpenSEES analysis files

D1 Model file: finalData.tcl

The following appendix contains a sample model file used to complete the time-history analyses in OpenSEES software.

```
# THE FINAL ANALYSIS
#
# clear previous variables and commands
wipe

# establish model domain with 2 dimensions
model BasicBuilder -ndm 2

#**********Input parameters****************************************

set LCfactor 20;

#*****Fixed or derived:*****

set pi [expr 2.0*asin(1.0)];     # Definition of pi
set g 9.81;                      # gravity acc.

# Frame parameters
set Kground 1e11;                # ground stiffness
set Khorz 1e10;                  # horizontal support stiffness
set A 0.1;                       # area of frame elements
set E 200e9;
set M 1e5;                       # frame mass
set W [expr $M*$g];              # weight force of frame
set damping 0.03;                # critical damping ratio
set B 2.5;                       # half width
set nodeMassx 1e3;               # nominal node mass - x dof
set nodeMassy 1e3;               # nominal node mass - y dof
set nodeMassz 0;                 # nominal node mass - z dof

set MAll [expr ($LCfactor + 1) * $M];
set H [expr $aspectRat*2*$B];    # height
set HM [expr $H*2/3];            # mass height
set wn [expr 2*$pi/$Tn];         # natural frequency (fixed base)

set Kinitial [expr $wn*$wn*$MAll];  # initial system stiffness
set Icol [expr $Kinitial*$HM*$HM*$HM/(3*$E)];
set H2 [expr $H - $HM];
set Icol2 [expr $Kinitial*$H2*$H2*$H2/(3*$E)];

set IbeamNom [expr $Kinitial*$B*$B*$B/(3*$E)];      # inertia of beam elements
set Ibeam [expr 128*$IbeamNom]; # the beams have greater flexural stiffness than the
columns, creates reasonable response
set Ibeam 10.0;

# Moment at uplift
set Mover [expr $Gup*$g*$MAll*$HM/$R];
set MW [expr $W*$B];
set MED [expr $Mover*(100 - $PTper)/100];
set MPT [expr $Mover - $MW - $MED];
set Fyielddev [expr $MED/(2*$B)];
set initialFPT [expr $MPT/$B];

# Leaning column parameters
set L [expr 3*$B];               # distance to leaning column
set massLC [expr $LCfactor*$M]; # mass of leaning column
set WLC [expr $massLC*$g];       # weight force of leaning column
set WAll [expr $MAll*$g];        # weight force of full system

# Rigid link to LC
set Arigid 1000.0;               # define area of truss section (make much larger than A of
frame elements)
set Irigid 100000.0;             # moment of inertia for p-delta columns  (make much larger
than I of frame elements)
set Erigid 200e9;                # steel Young's modulus

# post-yield stiffness ratio
set bGNG 2e-4;

# Device and PT stiffnesses for uplift stiffness ratios alpha and gamma
set alpha 0.8;
```

```
set gamma 0.1;
set const1 [expr $HM*$HM/$B/$B/4/(1-$bGNG)];
set const2 [expr ($alpha*$Kinitial)/(1-$alpha) - ($gamma*$Kinitial)/(1-$gamma)];
set Edev [expr $const1*$const2];
set const3 [expr $HM/$B/$B];
set const4 [expr ($gamma*$Kinitial*$HM)/(1-$gamma) + $WAll];
set EPT [expr $const3*$const4 - 4*$bGNG*$Edev];

# no implied relation between Fy and W! (just that devices are at edges and PT is at centre)
set initialStrainPT [expr -$initialFPT / $EPT]; # initial strain

#**********Node placement*************************************

# Rocking frame
#       no. x    y
node    1   0    0;       # base centre (frame)
node    2   0    $HM;     # mass (frame)
node    3   -$B  0;       # left foot (frame)
node    4   $B   0;       # right foot (frame)
node    5   -$B  0;       # left foot (ground)
node    6   $B   0;       # right foot (ground)
node    7   0    0;       # base centre (ground)
node    10  0    $H;      # roof (frame)

# Leaning column
#       no. x    y
node    8   $L   0;       # base of leaning column
node    9   $L   $HM;     # top of leaning column (mass)

#**********Nodal masses*************************************

# Rocking frame
#       node    x           y           z
mass    1       $nodeMassx  $nodeMassy  $nodeMassz;     # bottom centre (frame)
mass    2       $M          $M          $nodeMassz;     # mass height
mass    3       $nodeMassx  $nodeMassy  $nodeMassz;     # left foot
mass    4       $nodeMassx  $nodeMassy  $nodeMassz;     # right foot
mass    10      $nodeMassx  $nodeMassy  $nodeMassz;     # roof

# Leaning column
#       node    x           y           z
mass    8       0           0           $nodeMassz;     # base of leaning column (pinned)
mass    9       $massLC     $massLC     $nodeMassz;     # top of leaning column (mass)

#**********Fixity conditions*************************************

# Rocking frame
#   node    x   y   z
fix 5       1   1   1;  # ground below left foot - fully fixed
fix 6       1   1   1;  # ground below right foot - fully fixed
fix 7       1   1   1;  # ground below base centre - fully fixed

# Leaning column
#   node    x   y   z
fix 8       1   1   0;  # base of leaning column - pinned

#**********Geometric tranfromations*************************************

# Tags
set transfTag_C 1; # column tag
set transfTag_B 2; # beam tag

# PDelta
geomTransf PDelta $transfTag_C; #0 0 -1
geomTransf PDelta $transfTag_B; #0 1 0

# Linear
# geomTransf Linear $transfTag_C;
# geomTransf Linear $transfTag_B;

#**********Material models*************************************
```

```
# high compressive stiffness rocking edge
set rockMatTag 1
uniaxialMaterial ENT $rockMatTag $Kground

# elastic post-tensioning
set PTMatTag 2
uniaxialMaterial Elastic $PTMatTag $EPT

# high compressive stiffness horizontal support at rocking edges
set supportMatTag 3
uniaxialMaterial ENT $supportMatTag $Khorz

# nominal small stiffness elastic material to provide stability in zero stiffness plastic
cases
set nominalKMatTag 25
uniaxialMaterial Elastic $nominalKMatTag 1

# device hysteresis GNG - LHS
set GNGLHSMatTag 4
uniaxialMaterial GNG $GNGLHSMatTag $Edev $Fyielddev $Pitch $bGNG
set GNGLHSrockMatTag 5
uniaxialMaterial Parallel $GNGLHSrockMatTag $rockMatTag $GNGLHSMatTag $nominalKMatTag

# device hysteresis GNG - RHS
set GNGRHSMatTag 6
uniaxialMaterial GNG $GNGRHSMatTag $Edev $Fyielddev $Pitch $bGNG
set GNGRHSrockMatTag 7
uniaxialMaterial Parallel $GNGRHSrockMatTag $rockMatTag $GNGRHSMatTag $nominalKMatTag

# elastic post-tensioning with inital strain (large yield strains to avoid plastic behaviour)
set PTisMatTag 8
uniaxialMaterial ElasticPP $PTisMatTag $EPT 1000 -1000 $initialStrainPT

# define truss material for link to leaning column
set TrussMatTag 9
uniaxialMaterial Elastic $TrussMatTag $Erigid;

#**********Elements****************************************

# Frame elements
element elasticBeamColumn 1     1 2     $A $E $Icol     $transfTag_C;   # vertical frame
element
element elasticBeamColumn 11    2 10    $A $E $Icol2    $transfTag_C;   # vertical frame
element - above mass
element elasticBeamColumn 2     1 3     $A $E $Ibeam    $transfTag_B;   # left horizontal
frame element
element elasticBeamColumn 3     1 4     $A $E $Ibeam    $transfTag_B;   # right horizontal
frame element

# Rocking edge elements
element zeroLength 4 5 3 -mat $GNGLHSrockMatTag -dir 2; # left rocking edge (vertical)
element zeroLength 5 6 4 -mat $GNGRHSrockMatTag -dir 2; # right rocking edge (vertical)
element zeroLength 6 5 3 -mat $supportMatTag    -dir 1; # left rocking edge (horizontal)
element zeroLength 7 6 4 -mat $supportMatTag    -dir 1 -orient -1 0 0 0 -1 0;   # right
rocking edge (horizontal)

# Base centre element
element zeroLength 8 7 1 -mat $PTisMatTag       -dir 2;     # PT element

# Rigid link to leaning column
element truss  9 2 9 $Arigid $TrussMatTag;  # rigid pinned element between the 2 masses
(produces cleaner curve than equalDOF command)
# equalDOF 2 9 1; # node slaved in x-direction to roof node of frame

# Leaning column
element elasticBeamColumn  10  8  9 $Arigid $Erigid $Irigid $transfTag_C;   # rigid pinned
column

#**********Gravity loading*********************************
```

```
# Gravity loading
pattern Plain 1 Linear {
    load 2 0 -$W 0;      # weight force applied to top point of frame (-y)
    load 9 0 -$WLC 0;    # weight force applied to leaning column
}

#**********Analysis commands*****************************************

constraints Plain;              # constraint equation setting
numberer Plain;                 # numbering scheme used to assemble the system of equations
system BandGeneral;             # system of equations
algorithm Linear;               # solution algorithm
integrator LoadControl 0.1;     # incremental solution via load control (steps of 0.1 * load
pattern)
analysis Static;                # type of analysis
set ok [analyze 10];            # analyze 10 steps (of 0.1 * load pattern)
loadConst -time 0;              # sets loads constant and resets times to 0.0 (gravity load
always applied)
puts "Gravity load applied"

#**********Eigenvalues*****************************************

set Eigenvalue [eigen -fullGenLapack 1]
puts "Eigenvalue: [format {%0.4E} $Eigenvalue]"

#**********Damping properties*****************************************

set omega1 [expr {sqrt(abs($Eigenvalue))}]; # high frequency bound (root of first eigenvalue
- fundamental period)
set omega2 [expr {$omega1/10}]; # low frequency bound (10 * fundamental period)
set alphaM [expr {2*$damping*$omega1*$omega2/($omega1 + $omega2)}]; # mass proportional
damping term
set betaK 0;            # stiffness proportional damping term
set betaKinit 0;        # initial stiffness proportional damping term
set betaKcomm [expr {2*$damping/($omega1 + $omega2)}];  # committed stiffness proportional
damping term
rayleigh $alphaM $betaK $betaKinit $betaKcomm ;# Rayleigh damping command

#*********************************Outputs*****************************************

# puts "Kinitial: $Kinitial"

set Krigidrock [expr $EPT*$B*$B + $Edev*(2*$B)*(2*$B) - $WAll*$HM]
# puts "Krigidrock: $Krigidrock"
set Krock [expr 1 / (($HM*$HM/$Krigidrock) + (1/$Kinitial))]

set KrigidrockYield [expr $EPT*$B*$B + $bGNG*$Edev*(2*$B)*(2*$B) - $WAll*$HM]
# puts "KrigidrockYield: $KrigidrockYield"
set KrockYield [expr 1 / (($HM*$HM/$KrigidrockYield) + (1/$Kinitial))]

# set Kuplift [expr $EPT*$B*$B/$H/$H]
# puts "Kuplift: $Kuplift"
# set KW [expr -($W+$WLC)/$H]
# puts "KW: $KW"
# set Kequiv [expr $Kuplift + $KW]
# puts "Kequiv: $Kequiv"
```

D2 Parameter study file: run_finalData.tcl

The following appendix contains a sample analysis file used to run part of the parameter study in OpenSEES software.

```
# THE FINAL ANALYSIS

#**********File settings*****************************************

# Save file settings
set recorderdir "finalResults";# recorder directory name
file mkdir $recorderdir ;# create results directory
set GMdir "GM/AllEQs/"

set f [open scaleFactors1.txt r];
set scaleFactors1 [split [string trim [read $f]]];
close $f;

# Force at uplift in g (multiplied by Wtrib by H (and divided by R) to get moment at uplift)
set f [open Gups.txt r];
set Gups [split [string trim [read $f]]];
close $f;

set maxPeriods 100;
set periodStep 0.05;

# Create result files
set testResults [open $recorderdir/testResults.txt w]
# Node displacements
set nodeD [open $recorderdir/nodeD.txt w]
# Node reactions
set nodeR [open $recorderdir/nodeR.txt w]
# Node accelerations
set nodeA [open $recorderdir/nodeA.txt w]

#**********Time settings*****************************************

set dt_analysis 1e-3;   # time step for transient analysis
set max_time 100.0;     # maximum time

#**********Loading pattern*****************************************

# Reduction factor
set R 4;

# Set uplift PT contribution (percentage)
set PTper 66;

# Select ground motion records
set GMFiles [glob -nocomplain -directory $GMdir -type f *.txt];

# Define aspect ratios
set aspectRats [list 2 4 6 8];
set NARs [llength $aspectRats];

# Define natural periods (seconds)
set Tns {{0.2 0.3 0.4} {0.4 0.5 0.6 0.7} {0.5 0.6 0.7 0.8 0.9 1.0} {0.6 0.7 0.8 0.9 1.0 1.1
1.2}};
set NTns [llength $Tns];

# Define Pitches (metres)
set Pitchs [list 1e-3 2e-3 5e-3 10e-3 20e-3];

# Preallocate analyses counter
set theCtr 0;

# Start the clock
set startTAll [clock seconds]

# Loop ground motion records
foreach gMotion $GMFiles {

    # Set current ground motion record
    set gMotionName [string range $gMotion 0 end-4 ]
    set gMotionNumber [string range $gMotion 12 end-4 ]
```

```
# Loop structure aspect ratios
for {set i 0} {$i < $NARs} {incr i 1} {

    # Set current aspect ratio
    set aspectRat [lindex $aspectRats $i]

    foreach Tn [lindex $Tns $i] {

        # Set uplift force
        set indexRef [expr round($Tn/$periodStep) -1]; # index for scale factor and
        uplift force lists
        set Gup [lindex $Gups $indexRef]; # Uplift force in g

        # Set scale factor
        set ScaleFactorRef [expr (($gMotionNumber-1)*$maxPeriods) + $indexRef -1];
        set scaleFactor [lindex $scaleFactors1 $ScaleFactorRef];

        # Loop device pitches
        foreach Pitch $Pitchs {

            # Load the model and run gravity analysis
            source finalData.tcl

            # ---earthquake ground motion---
            timeSeries Path 2 -dt $dt_analysis -filePath $gMotion -factor $scaleFactor
            -prependZero
            pattern UniformExcitation 2 1 -accel 2

            #**********Recorders**********

            # Node displacements
            recorder EnvelopeNode -file $recorderdir/nodeDisps.txt  -node 1 2 3 4 9 10
            -dof 1 2 3 disp
            # Node reaction forces
            recorder EnvelopeNode -file $recorderdir/nodeReactions.txt  -node 1 2 3 4 5
            6 7 8 9 10 -dof 1 2 reaction
            # Node accelerations
            recorder EnvelopeNode -file $recorderdir/nodeAccels.txt -node 1 2 3 4 9 10
            -dof 1 2 accel

            #**********Analysis commands**************************************

            constraints Plain;                  # constraint equation setting
            numberer RCM;                       # numbering scheme used to assemble the
            system of equations
            system BandGeneral;                 # system of equations
            test EnergyIncr 1e-12 100 0;        # convergence test
            algorithm Newton;                   # solution algorithm
            integrator Newmark 0.5 0.25;        # Newmark Beta integration scheme with
            constant average acceleration
            analysis Transient;                 # type of analysis

            # run the analysis
            set startT [clock seconds]
            set ok [analyze [expr {int($max_time/$dt_analysis/2)}] $dt_analysis]
            puts "50% complete"
            set ok [analyze [expr {int($max_time/$dt_analysis/2)}] $dt_analysis]
            puts "Done!"

            set endT [clock seconds]
            puts "Execution time: [expr $endT-$startT] seconds."

            #**********Display commands**************************************

            # Write results to file
            set demandLeft [eleResponse 4 material 1 material 2 demand]
            set demandRight [eleResponse 5 material 1 material 2 demand]
            set ratLeft [eleResponse 4 material 1 material 2 ratchetCount]
            set ratRight [eleResponse 5 material 1 material 2 ratchetCount]
            puts $testResults "$gMotionNumber $Tn $scaleFactor $aspectRat $Pitch $PTper
            [format {%0.4E} $Fyielddev] $ok [format {%0.2f} $Eigenvalue] $demandLeft
```

```
                $demandRight $ratLeft $ratRight"

                wipe;

                #**********Write analysis recorder results to analyses results files

                # Node displacements
                set f [open $recorderdir/nodeDisps.txt];
                set nodeDNow [split [string trim [read $f]] "\n"];
                close $f;
                puts $nodeD "[lindex $nodeDNow end]"

                # Node reaction forces
                set f [open $recorderdir/nodeReactions.txt];
                set nodeRNow [split [string trim [read $f]] "\n"];
                close $f;
                puts $nodeR "[lindex $nodeRNow end]"

                # Node accelerations
                set f [open $recorderdir/nodeAccels.txt];
                set nodeANow [split [string trim [read $f]] "\n"];
                close $f;
                puts $nodeA "[lindex $nodeANow end]"

                # Update counter
                set theCtr [expr $theCtr+1];
            }
        }
    }
}

set endTAll [clock seconds]
puts "Total execution time for $theCtr analyses: [expr $endTAll-$startTAll] seconds."

close $testResults
close $nodeD
close $nodeR
close $nodeA

wipe ;# this will kill the recorders which will cause them to close the files
```

Appendix E Additional parameter study results

The following appendix shows additional result plots from the time-history analyses completed in the main parameter study in OpenSEES software, with a force reduction factor of 4.

E1 Roof deflection

E1.1 Results by pitch

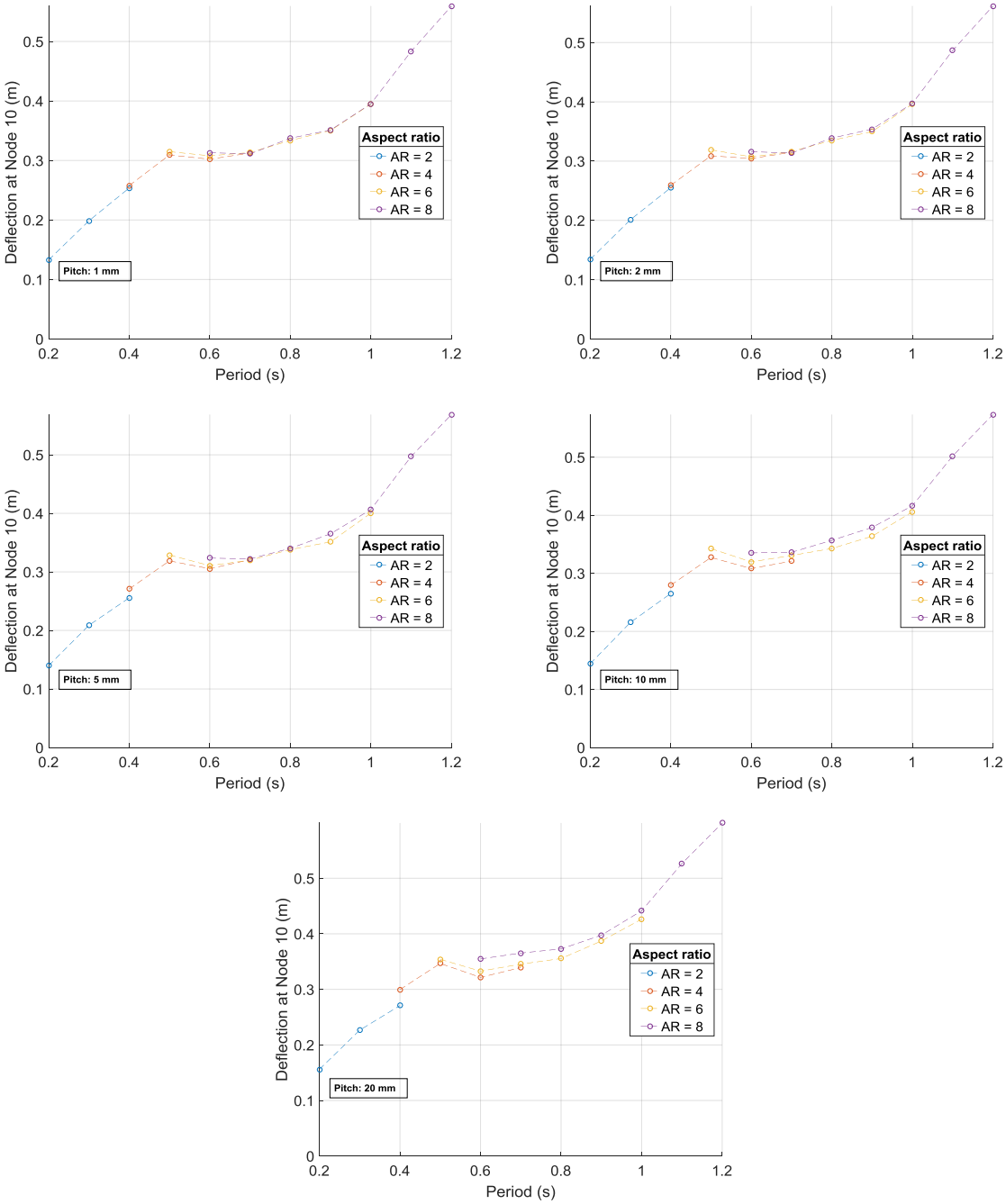

Figure E.1 *Geometric mean peak roof deflections (R = 4, ζ = 3%):*
a) pitch = 1 mm, b) pitch = 2 mm, c) pitch = 5 mm, d) pitch = 10 mm, and e) pitch = 20 mm.

E1.2 Results by aspect ratio

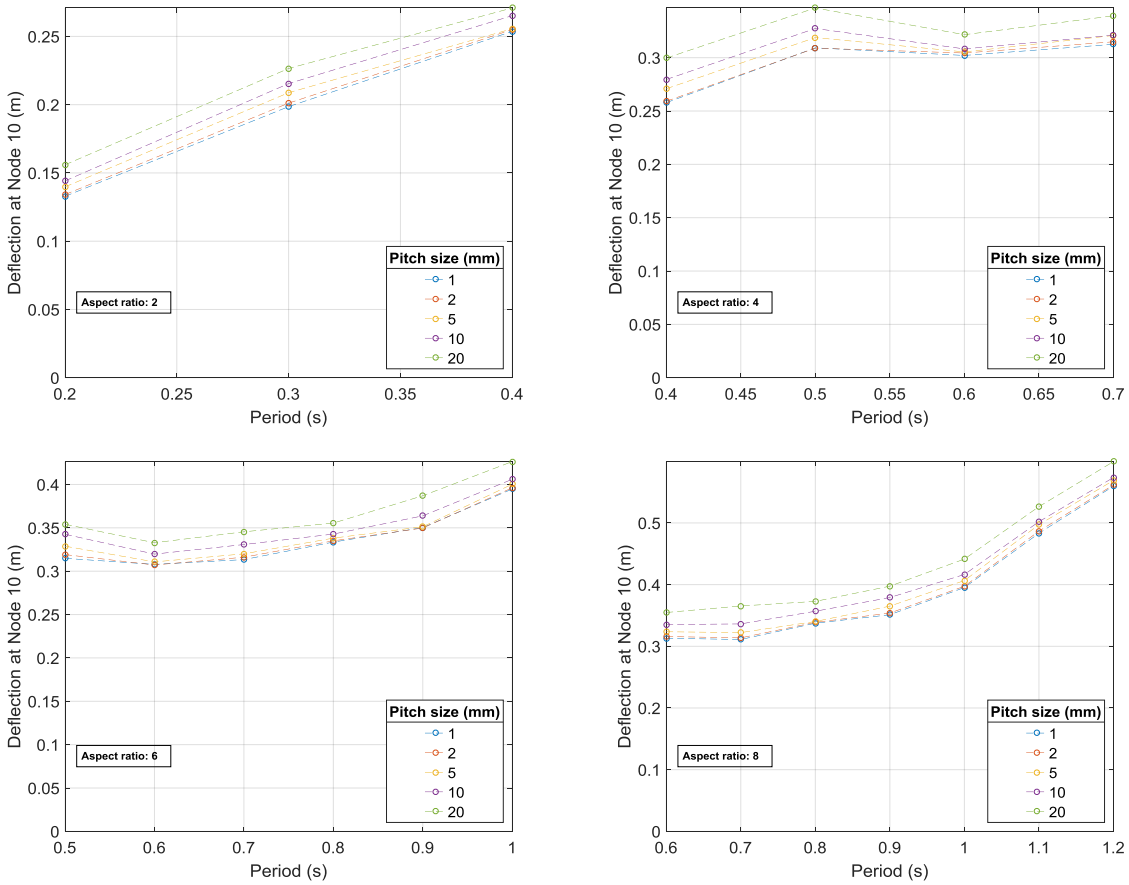

Figure E.2 *Geometric mean peak roof deflections (R = 4, ζ = 3%):*
a) aspect ratio = 2, b) aspect ratio = 4, c) aspect ratio = 6, and d) aspect ratio = 8.

E2 Roof drift

E2.1 Results by pitch

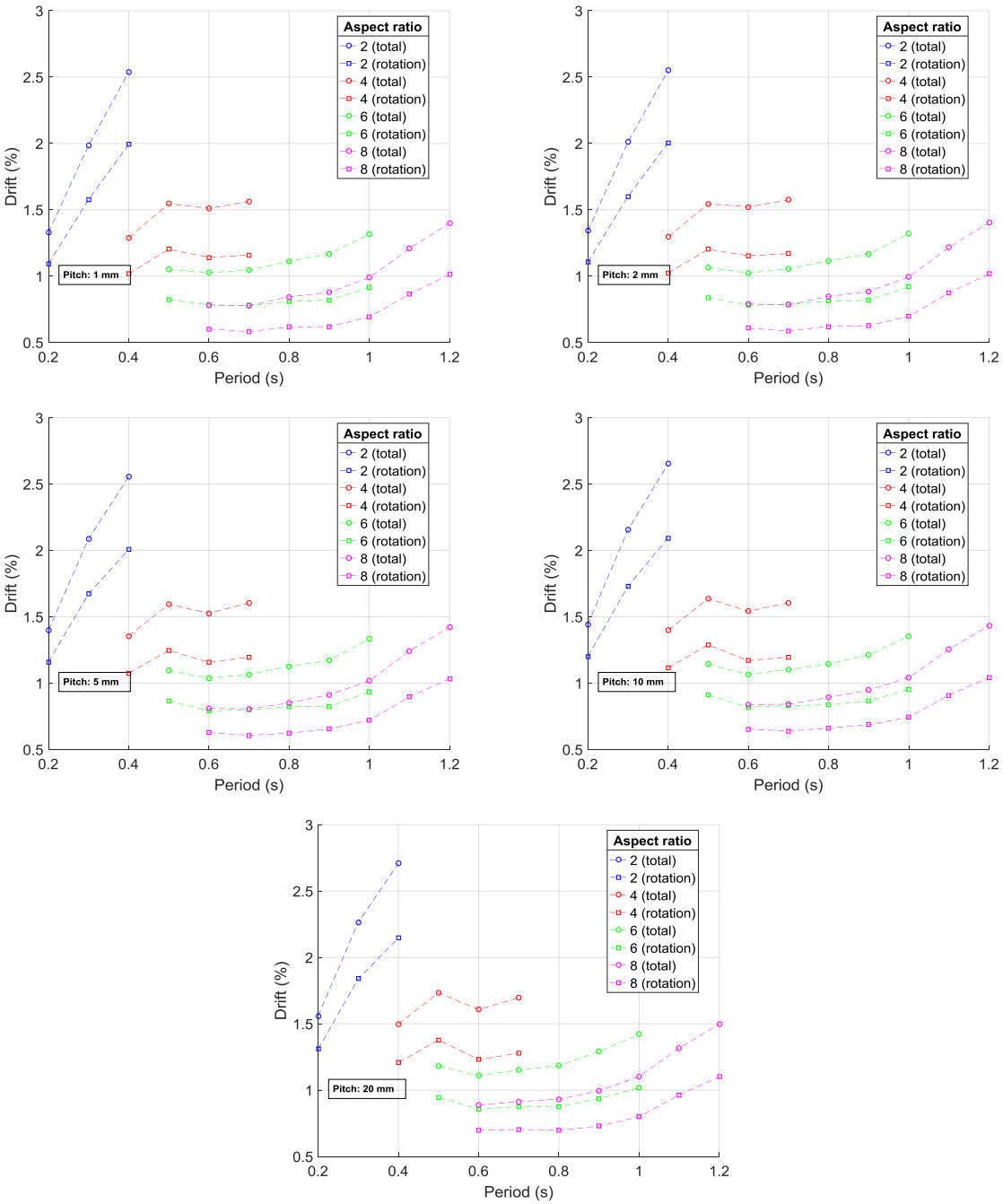

Figure E.3 *Geometric mean peak roof drifts, showing the contribution to roof drift from base rotation (R = 4, ζ = 3%): a) pitch = 1 mm, b) pitch = 2 mm, c) pitch = 5 mm, d) pitch = 10 mm, and e) pitch = 20 mm.*

E2.2 Results by aspect ratio

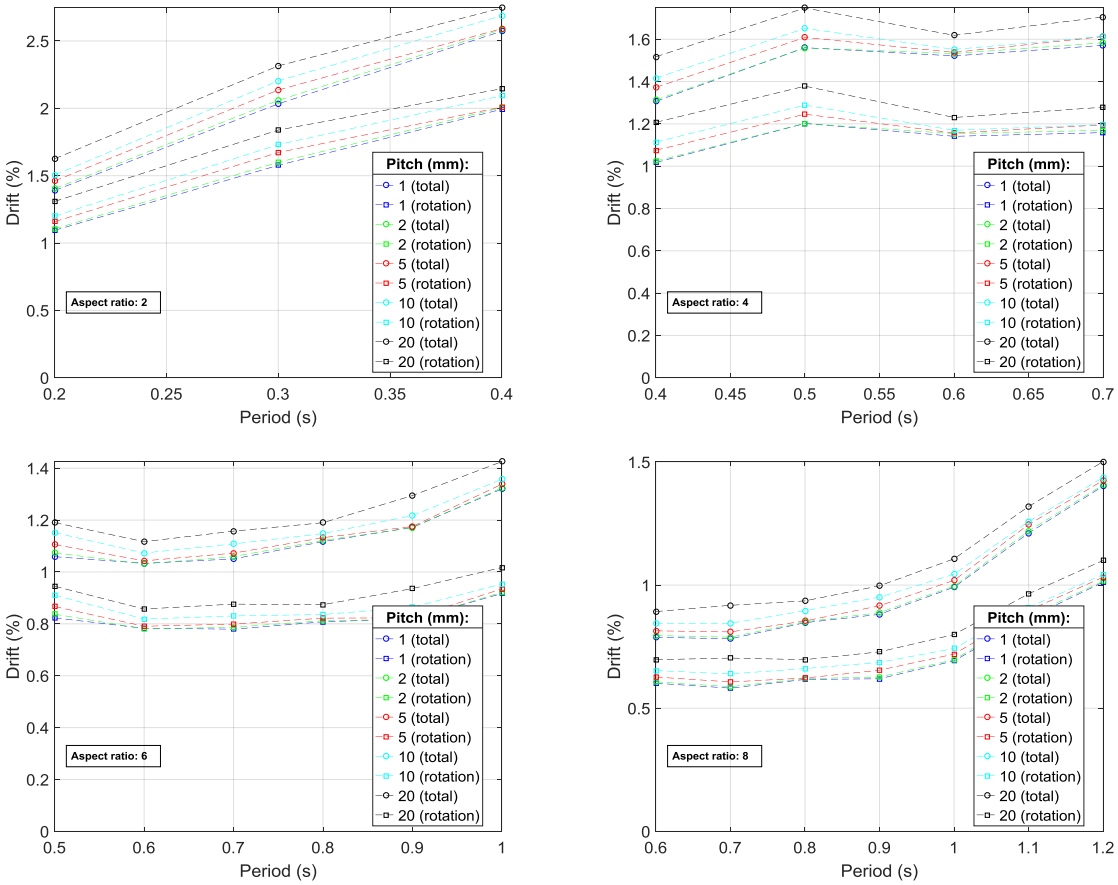

Figure E.4 *Geometric mean peak roof drifts, showing the contribution to roof drift from base rotation (R = 4, ζ = 3%): a) aspect ratio = 2, b) aspect ratio = 4, c) aspect ratio = 6, and d) aspect ratio = 8.*

E3 Base rotation

E3.1 Results by pitch

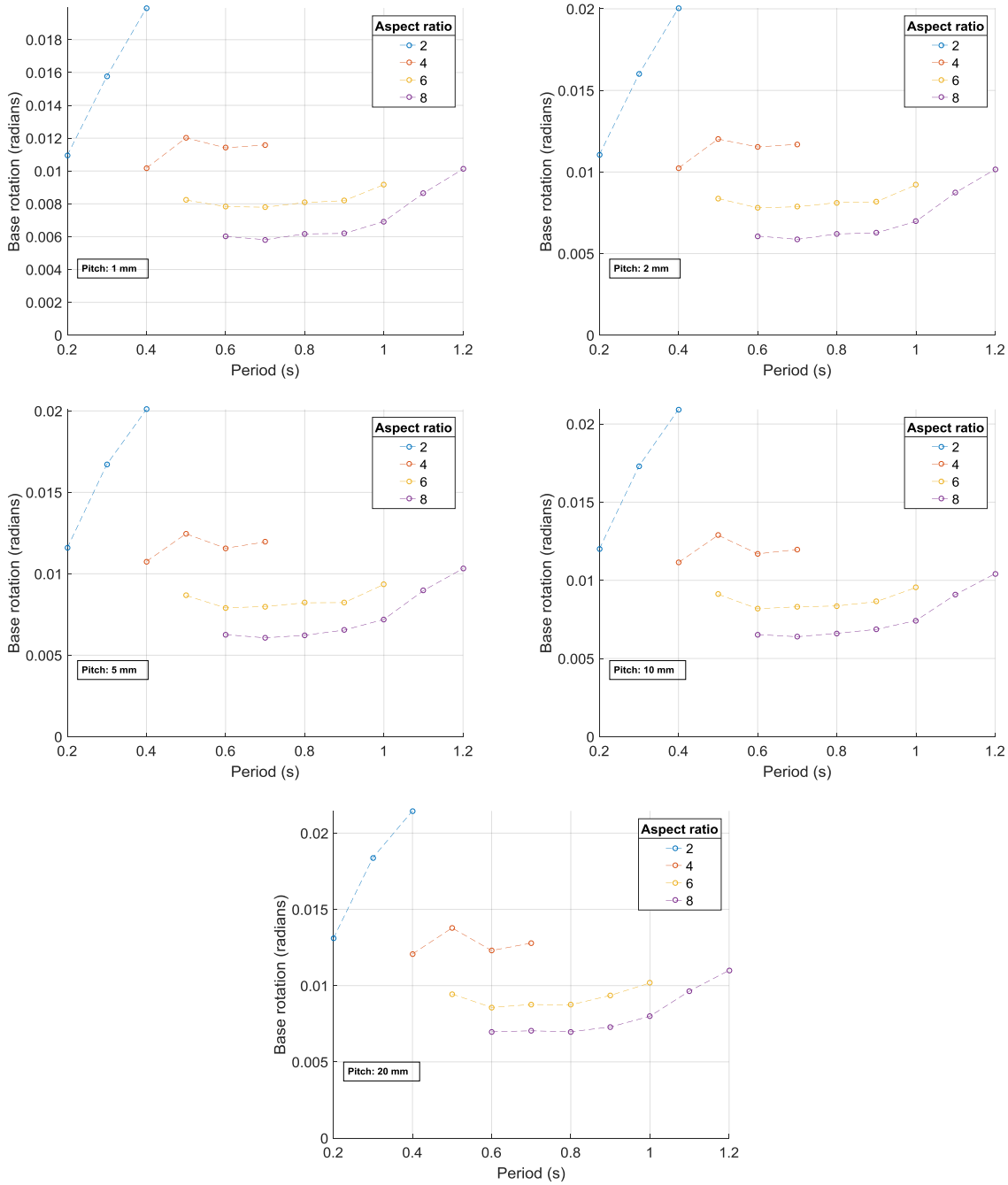

Figure E.5 *Geometric mean base rotation angles (R = 4, ζ = 3%):*
a) pitch = 1 mm, b) pitch = 2 mm, c) pitch = 5 mm, d) pitch = 10 mm, and e) pitch = 20 mm.

E3.2 Results by aspect ratio

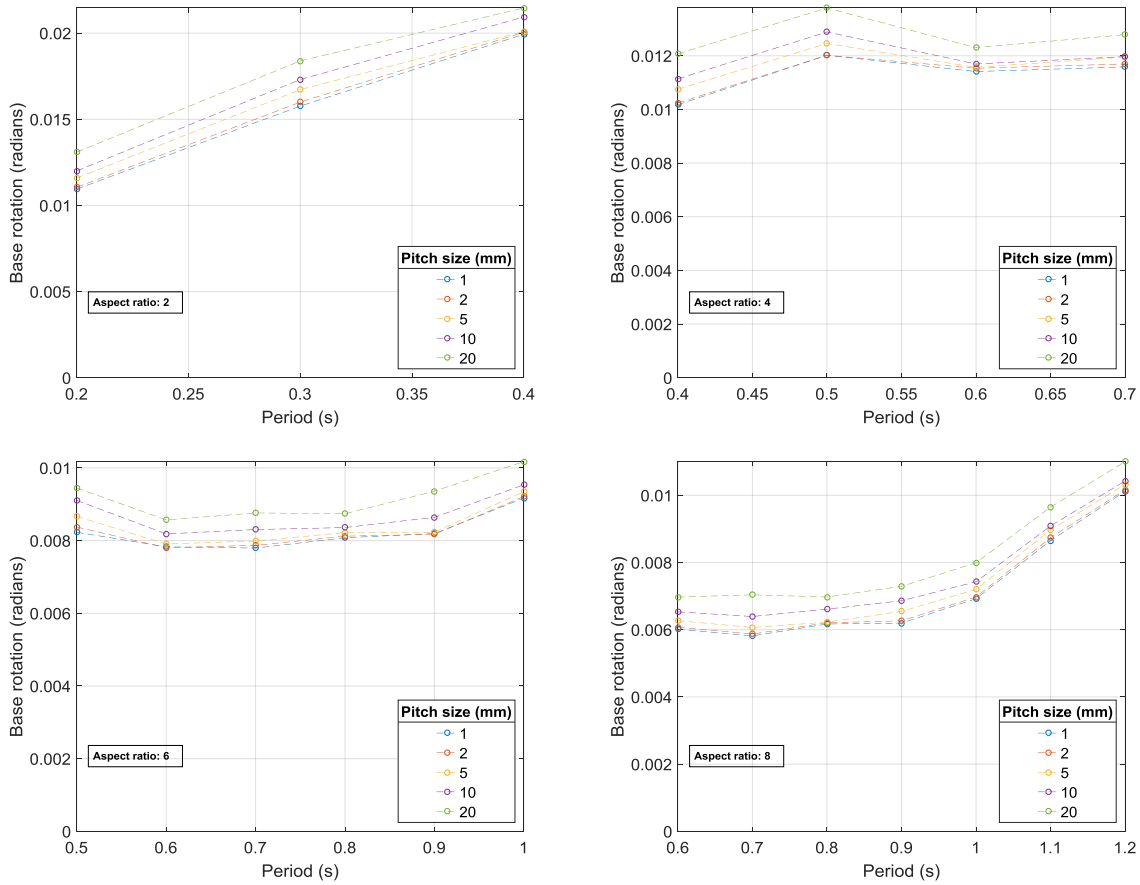

Figure E.6 *Geometric mean base rotation angles (R = 4, ζ = 3%):*
a) aspect ratio = 2, b) aspect ratio = 4, c) aspect ratio = 6, and d) aspect ratio = 8.

E4 Uplift

E4.1 Results by pitch

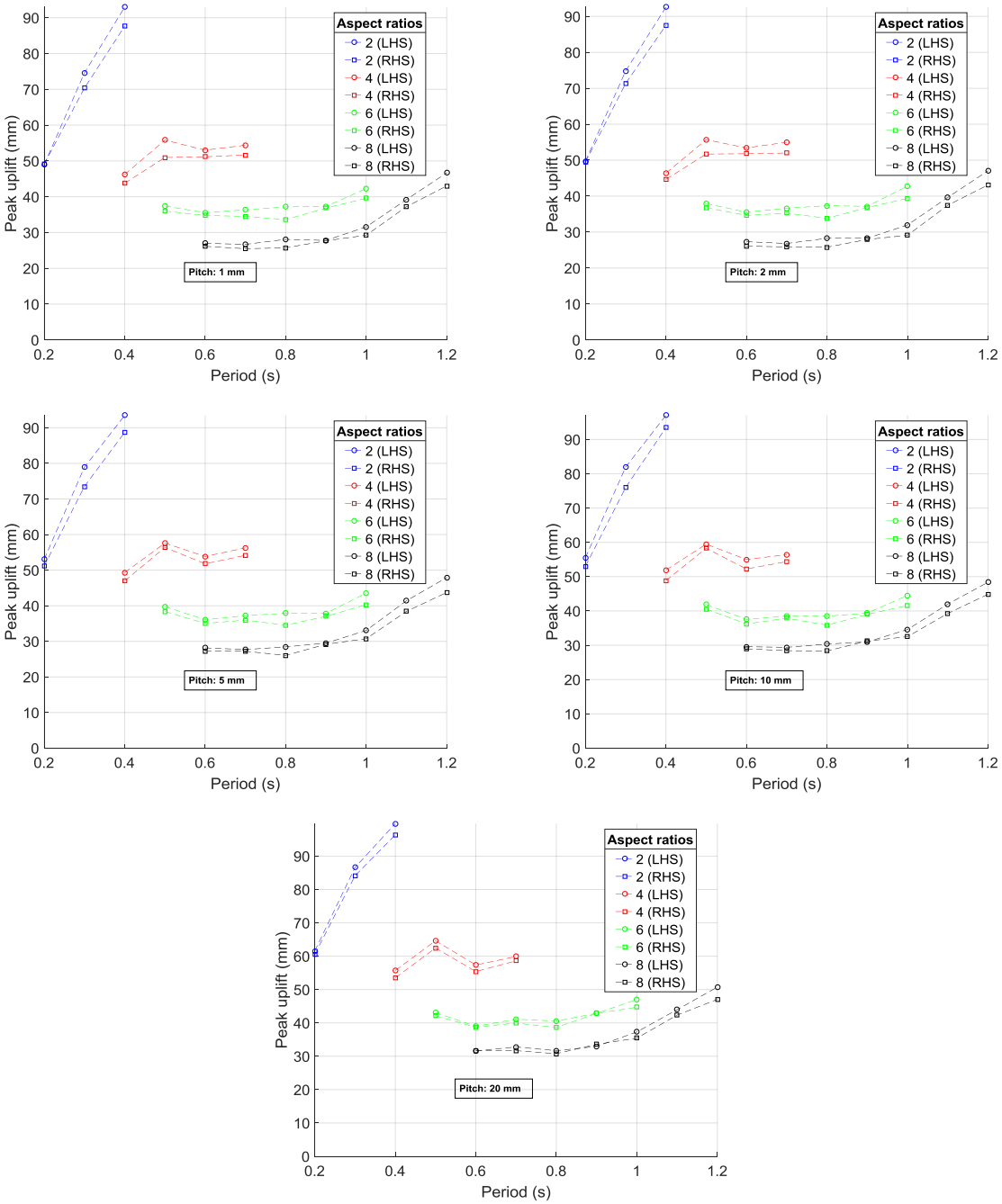

Figure E.7 *Geometric mean peak uplift (R = 4, ζ = 3%):*
a) pitch = 1 mm, b) pitch = 2 mm, c) pitch = 5 mm, d) pitch = 10 mm, and e) pitch = 20 mm.

E4.2 Results by aspect ratio

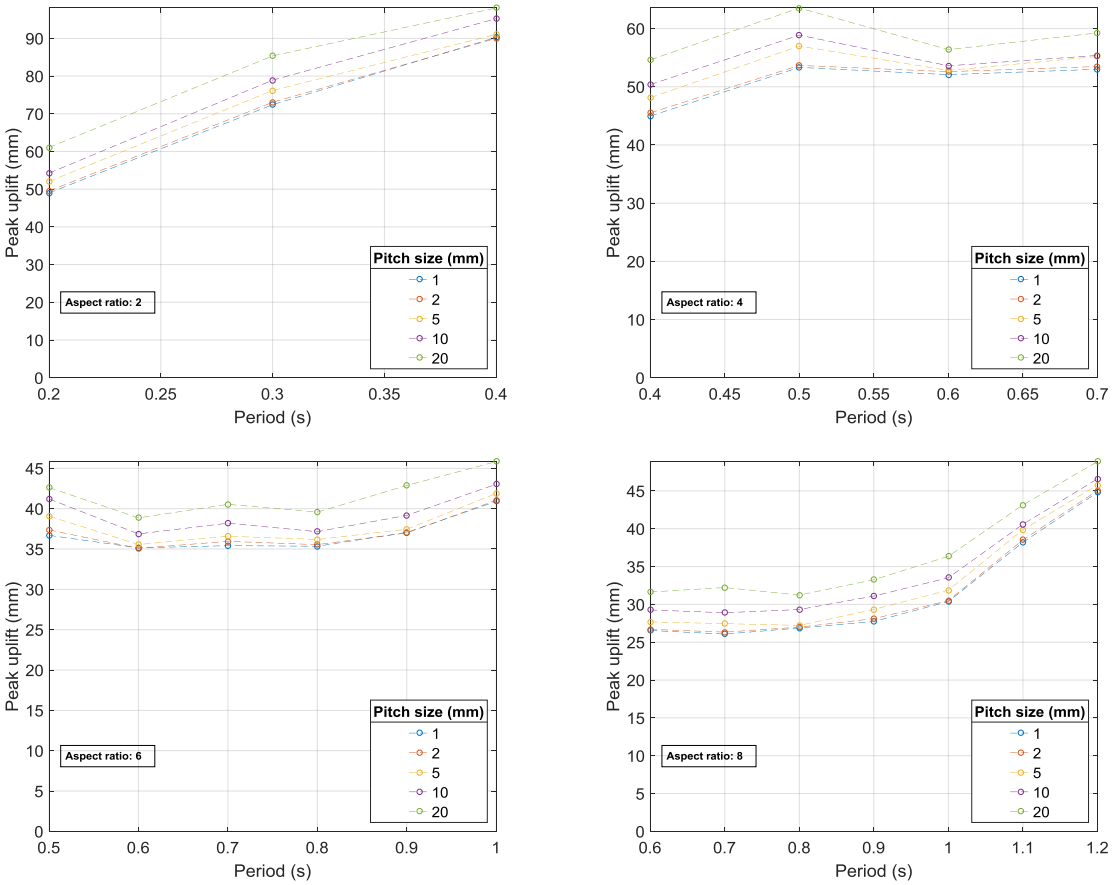

Figure E.8 *Geometric mean peak uplift (R = 4, ζ = 3%):*
a) aspect ratio = 2, b) aspect ratio = 4, c) aspect ratio = 6, and d) aspect ratio = 8.

E5 Ratchet count

E5.1 Results by pitch

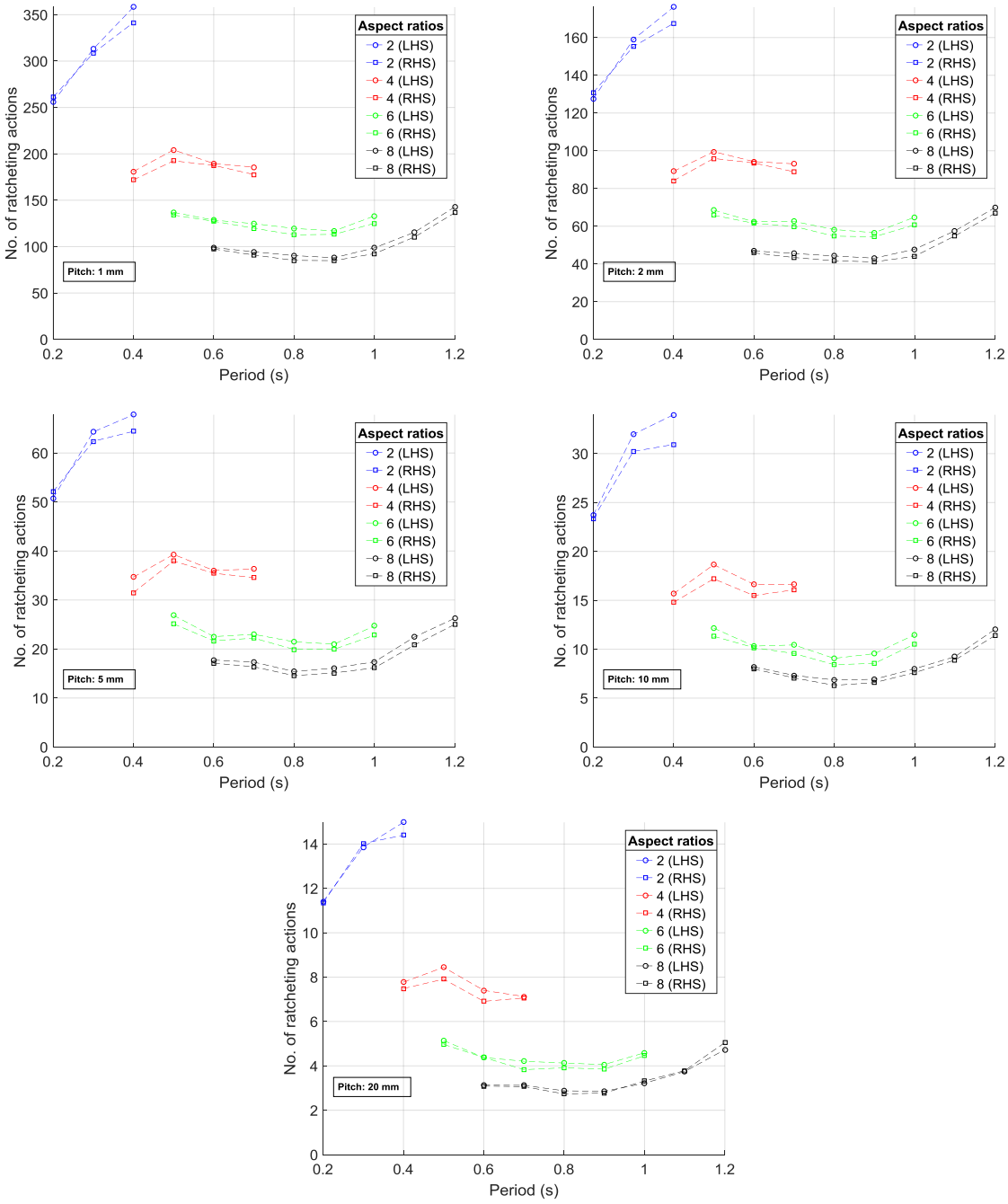

Figure E.9 *Geometric mean ratchet count(R = 4, ζ = 3%):*
a) pitch = 1 mm, b) pitch = 2 mm, c) pitch = 5 mm, d) pitch = 10 mm, and e) pitch = 20 mm.

E5.2 Results by aspect ratio

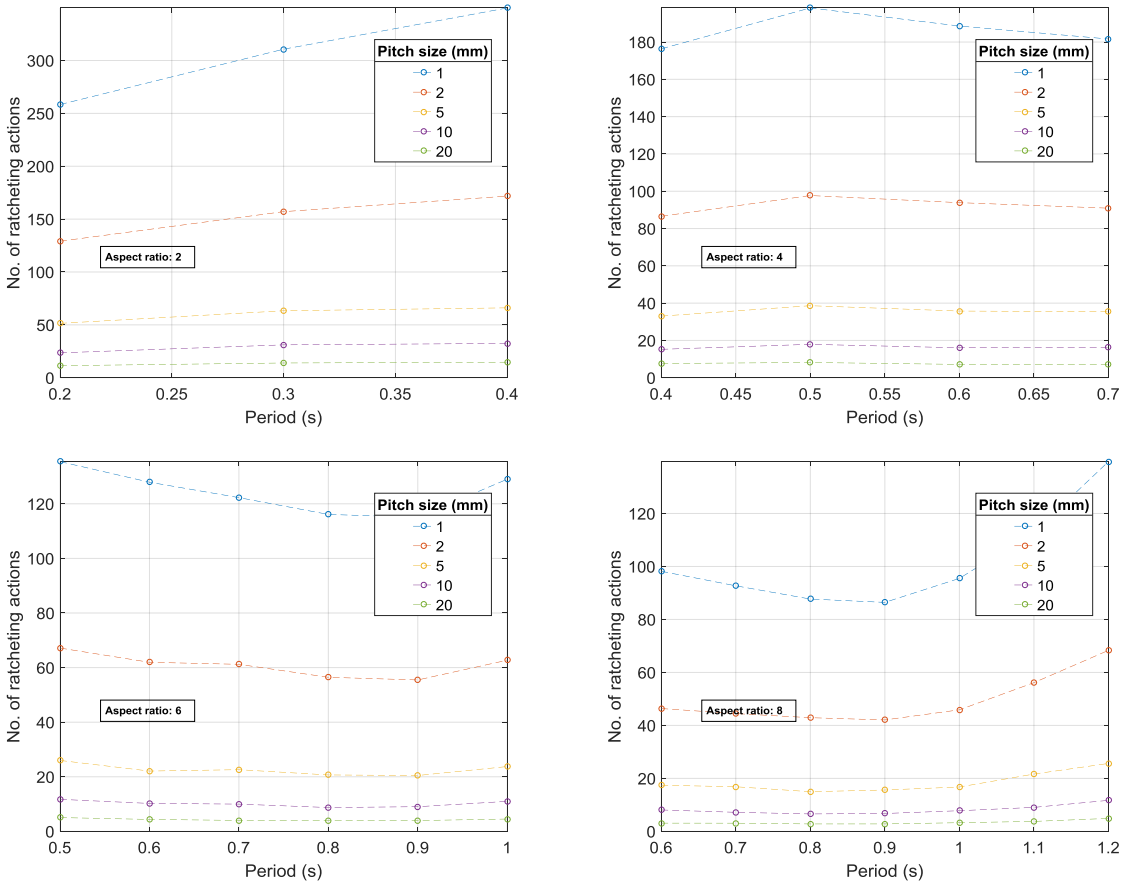

Figure E.10 *Geometric mean ratchet count (R = 4, ζ = 3%):*
a) aspect ratio = 2, b) aspect ratio = 4, c) aspect ratio = 6, and d) aspect ratio = 8.

E6 Rack demand

E6.1 Results by pitch

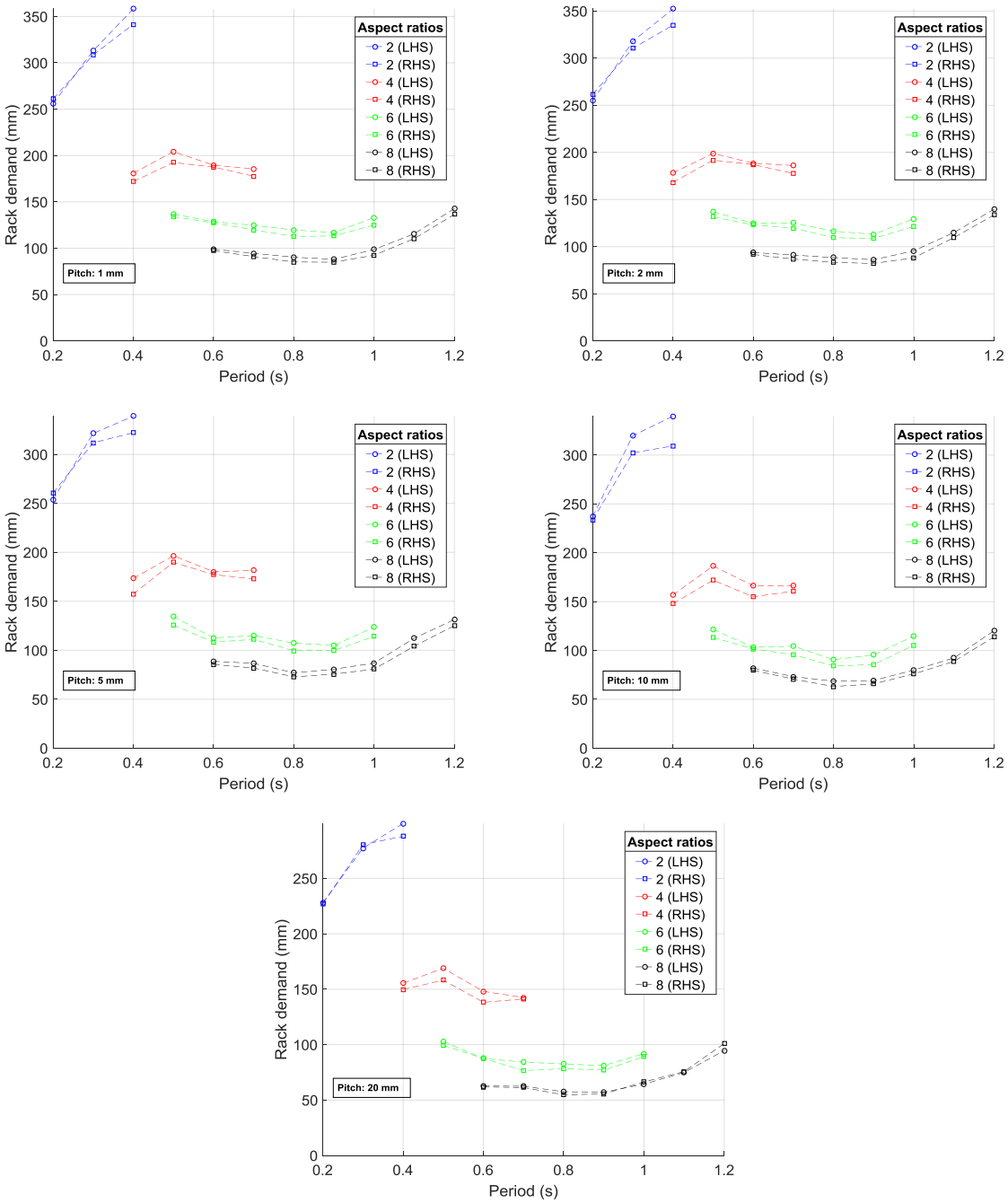

Figure E.11 *Geometric mean GNG rack demand (R = 4, ζ = 3%):*
a) pitch = 1 mm, b) pitch = 2 mm, c) pitch = 5 mm, d) pitch = 10 mm, and e) pitch = 20 mm.

E6.2 Results by aspect ratio

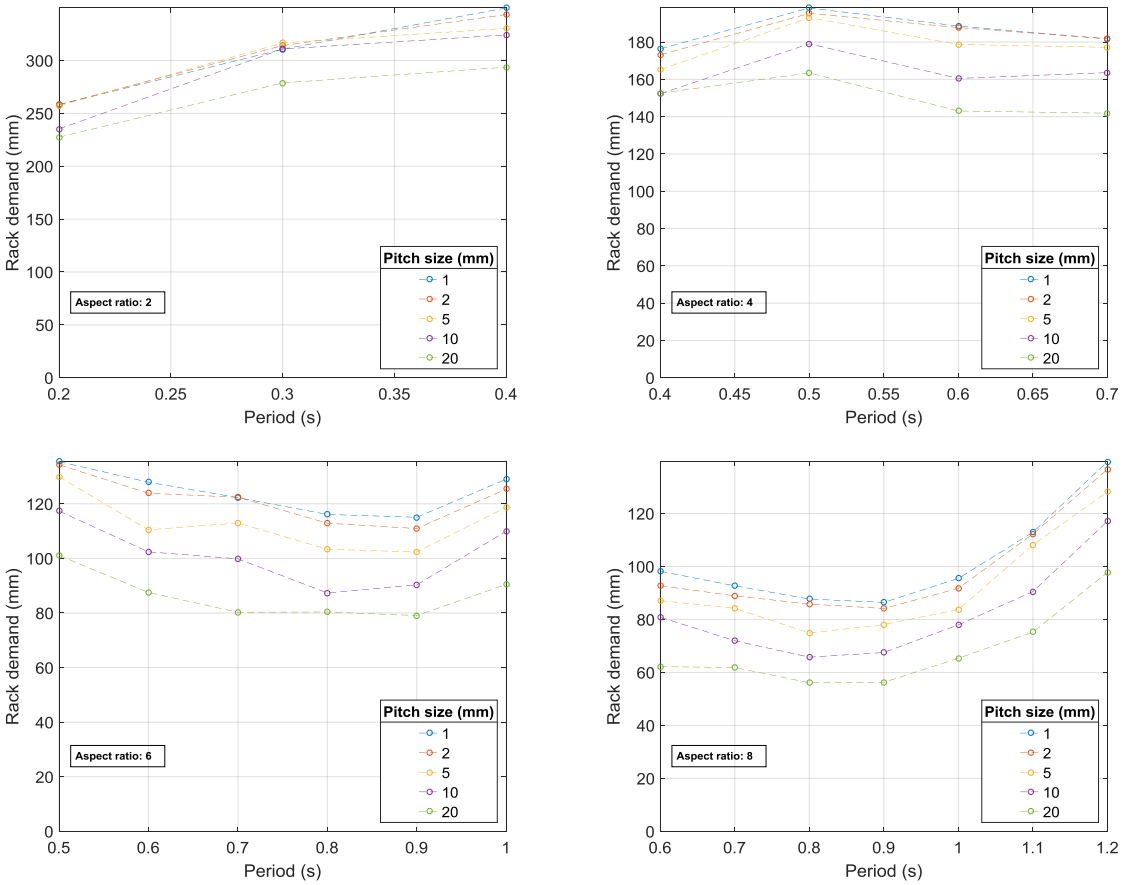

Figure E.12 *Geometric mean GNG rack demand (R = 4, ζ = 3%):*
a) aspect ratio = 2, b) aspect ratio = 4, c) aspect ratio = 6, and d) aspect ratio = 8.

E7 Dissipater demand

E7.1 Results by pitch

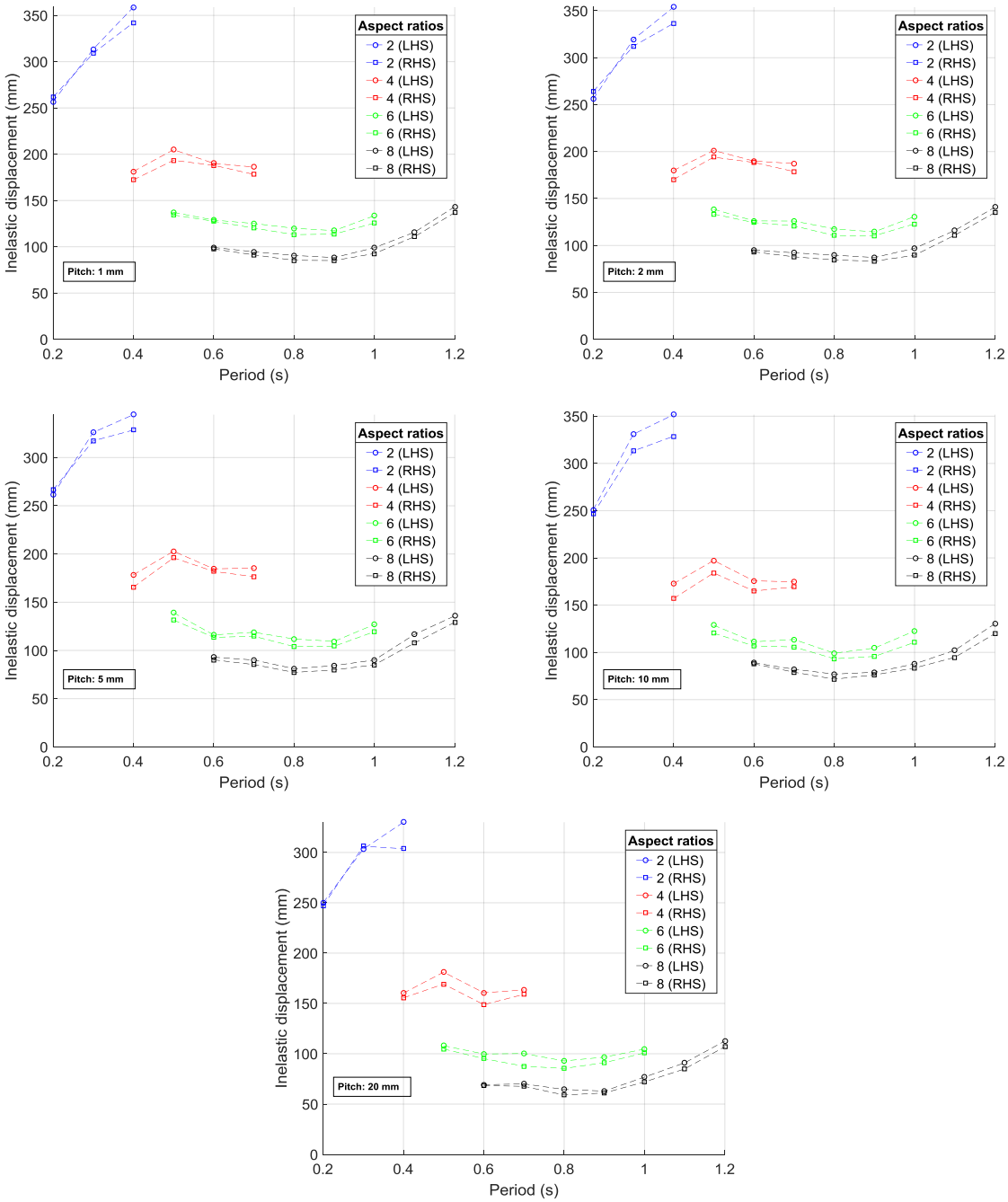

Figure E.13 *Geometric mean inelastic dissipater demand (R = 4, ζ = 3%):*
a) pitch = 1 mm, b) pitch = 2 mm, c) pitch = 5 mm, d) pitch = 10 mm, and e) pitch = 20 mm.

E7.2 Results by aspect ratio

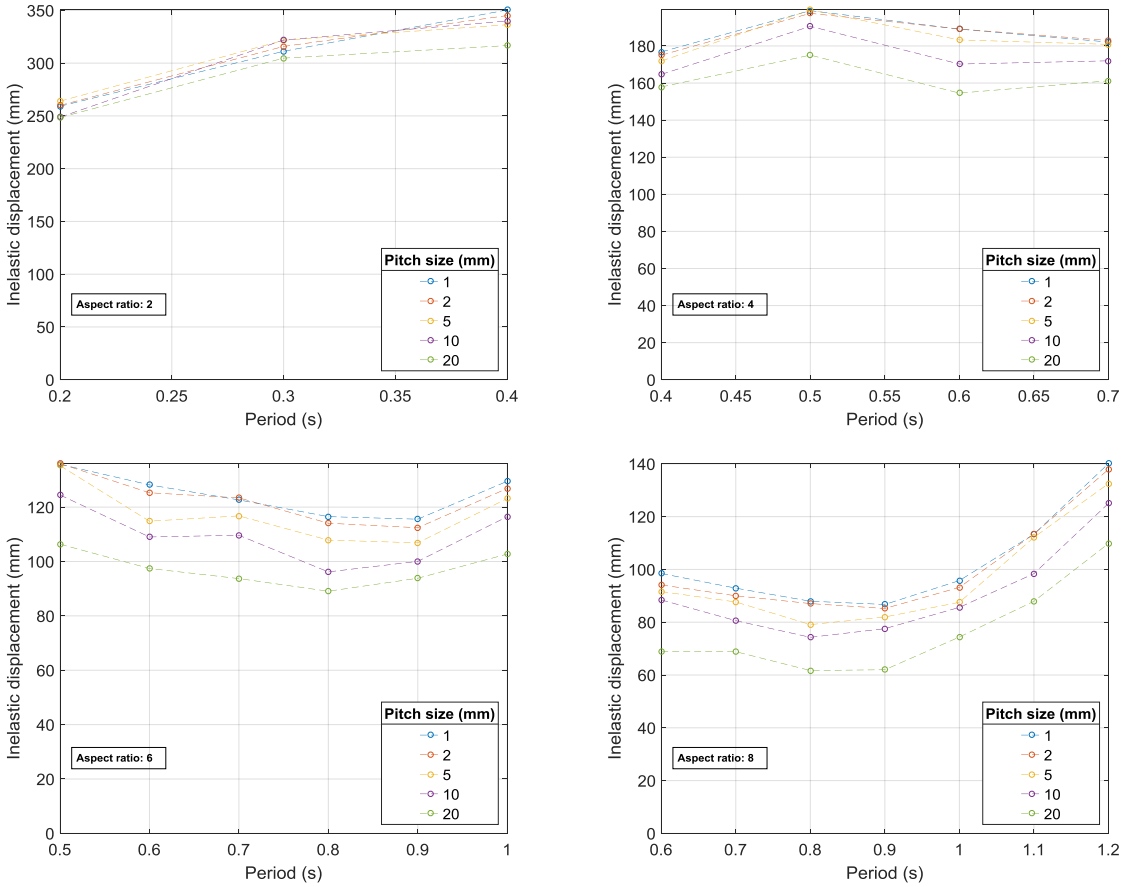

Figure E.14 *Geometric mean inelastic dissipater demand (R = 4, ζ = 3%): a) aspect ratio = 2, b) aspect ratio = 4, c) aspect ratio = 6, and d) aspect ratio = 8.*

E8 Relative dissipater demand

E8.1 Results by aspect ratio

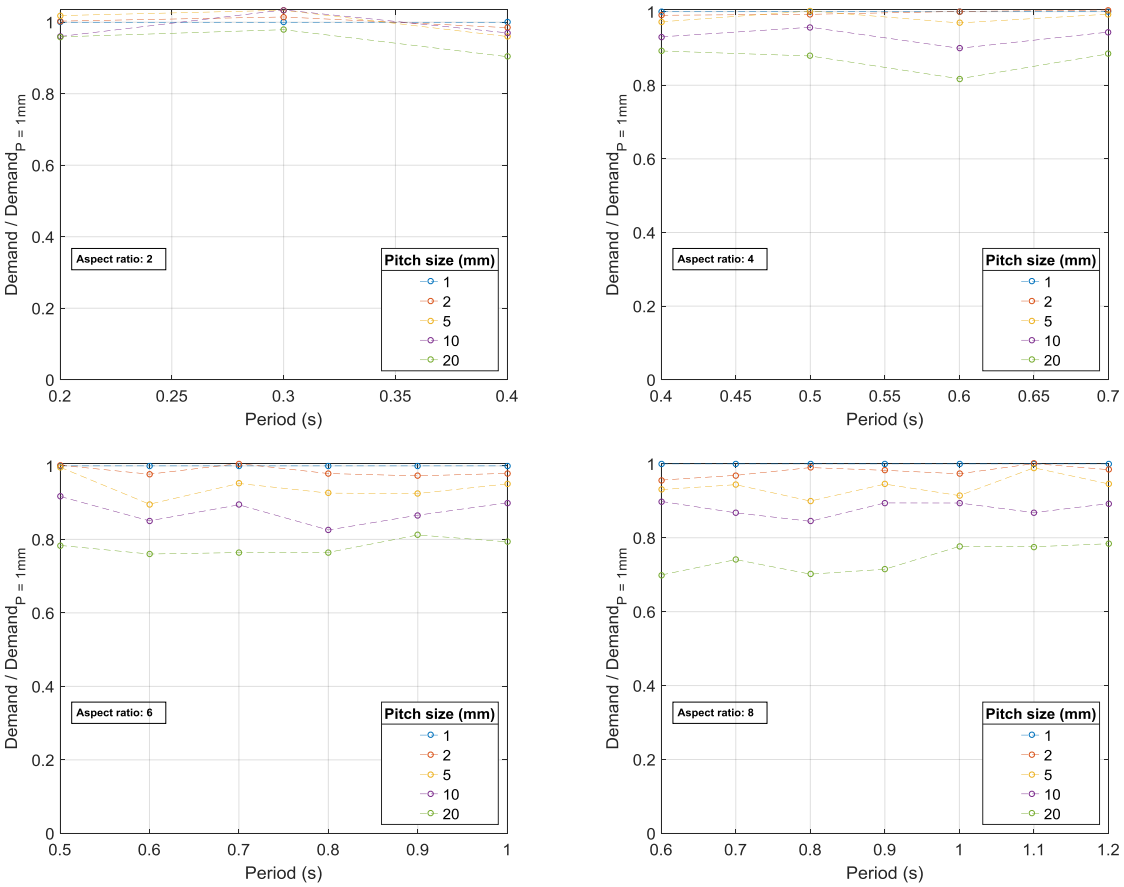

Figure E.15 *Geometric mean relative dissipater demand (R = 4, ζ = 3%): a) aspect ratio = 2, b) aspect ratio = 4, c) aspect ratio = 6, and d) aspect ratio = 8.*

E9 Demand ratio

E9.1 Results by pitch

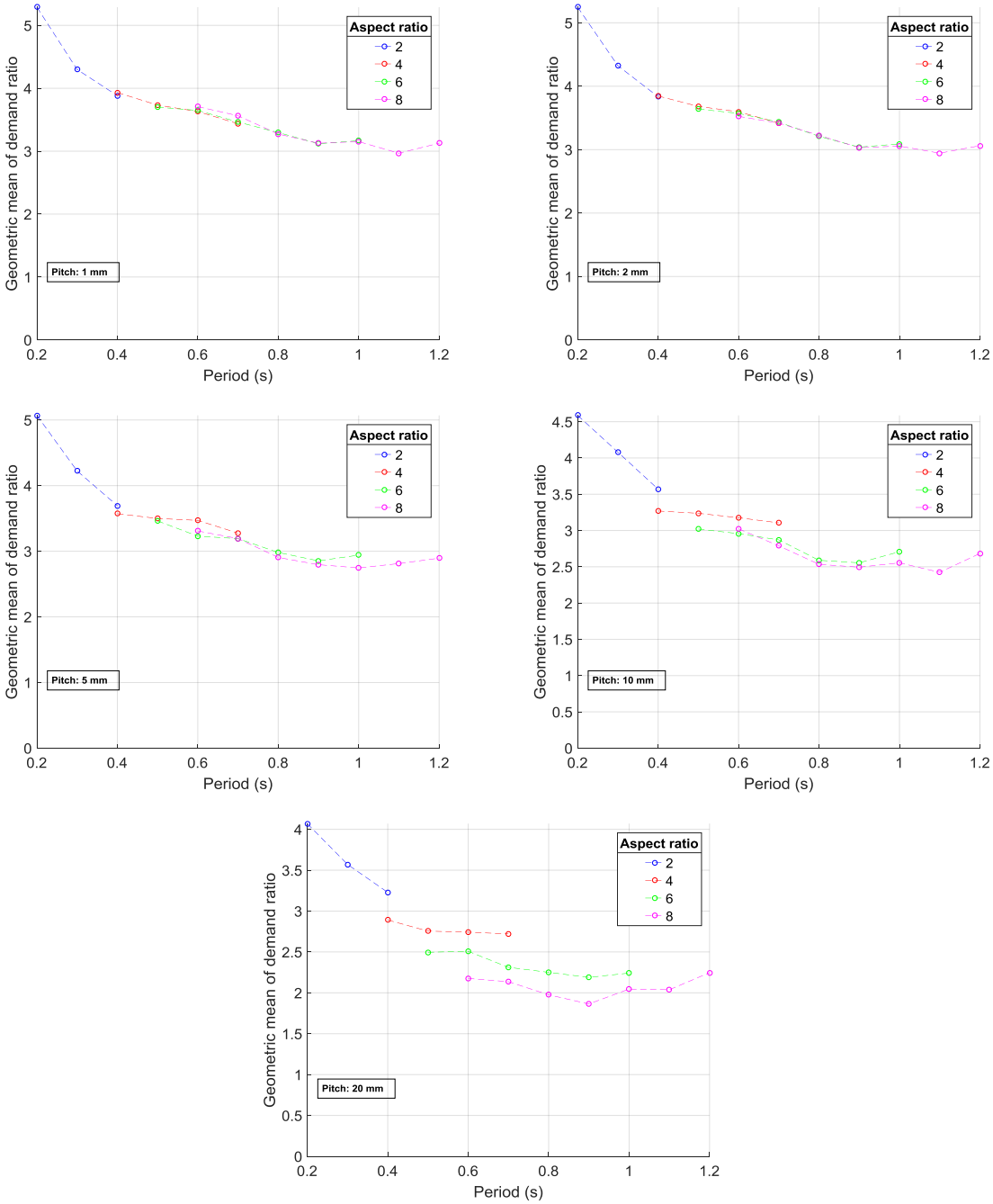

Figure E.16 *Geometric mean of demand ratio (R = 4, ζ = 3%):*
a) aspect ratio = 2, b) aspect ratio = 4, c) aspect ratio = 6, and d) aspect ratio = 8.